JOURNAL OF APPLIED PHYSICS

Vol. 31, No. 1 January, 1960

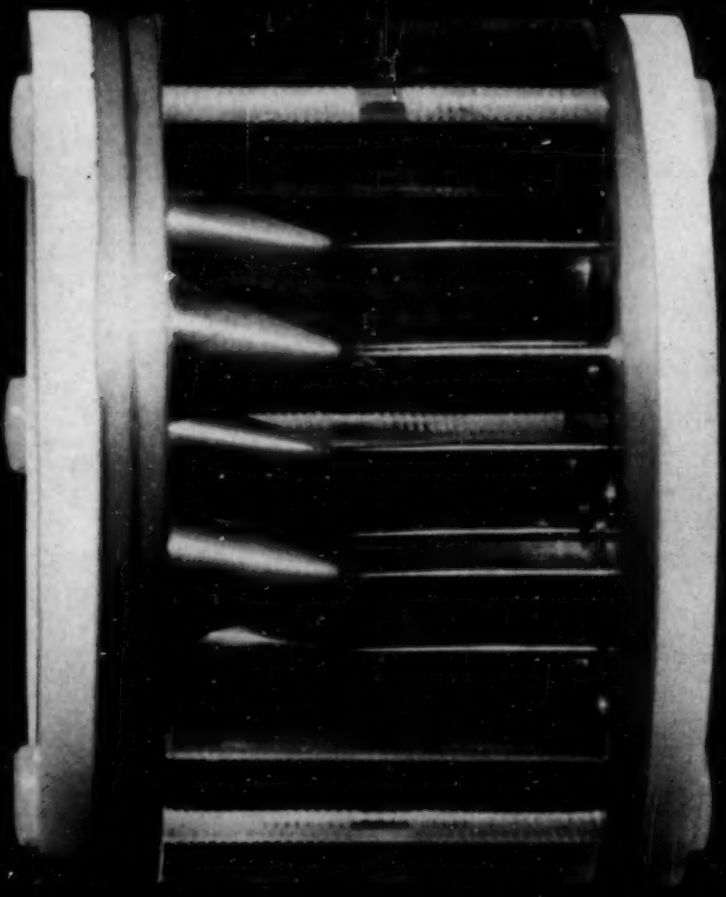

Ion Drag Pump. See Page 136.

NORELCO

and ELECTRON PROBE MICROANALYSIS

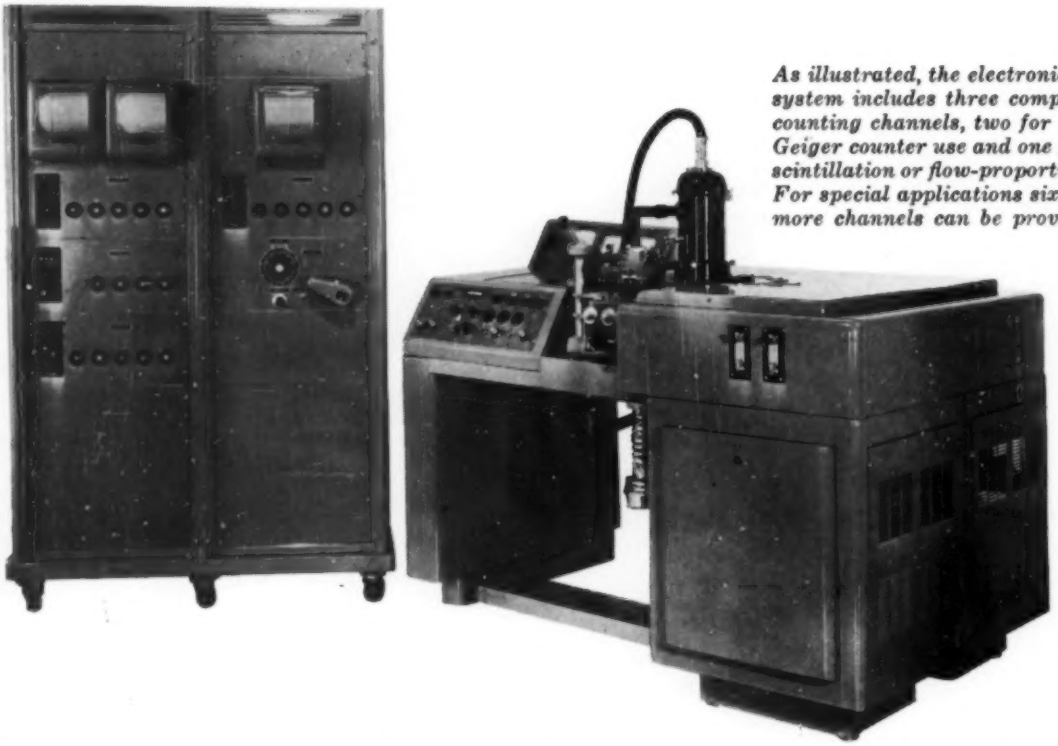

As illustrated, the electronics system includes three complete counting channels, two for Geiger counter use and one for scintillation or flow-proportional. For special applications six or more channels can be provided.

Elemental domains — the intrusion or incursion of one metal into another; the existence or degree of intergranular corrosion of stainless steels, grain boundaries, unique micro-inclusions and other conditions of metals, all pose vital questions—now answerable with the high resolution Norelco Electron Probe Microanalyzer. In a space-age era, the development of new metals and alloys of special characteristics is absolutely essential to the continued progress of our space program and is in fact necessary to meet the daily cries for better, stronger, lighter metals required for competitive advantage.

The Norelco Electron Probe Microanalyzer is a multichannel micro-beam X-ray analytical instrument utilizing an electron optical system which provides an energy source of finite, controllable minute size for the excitation of characteristic X-radiations of an area of sample one micron or less in diameter. It is designed to analyze for elements from magnesium (Atomic #12) upward in the periodic table.

While the Micro Probe Analyzer is of unique design and performs a highly specialized role, most of its constituent parts are drawn from a variety of proven, reliable Norelco X-ray spectrographic and electron-optical instruments. These, individually, have been tried and tested in literally thousands of executions. Electronic components, controls, lens system, electron gun filament, meters, etc. are essentially basic items, easily replaced and quickly furnished. On the basis of the outstanding past performance of Norelco instruments, and secure in the technical "Know-how" and experience of our engineering staff, this instrument is offered on the basis that you convince yourself of the applicability of this latest Norelco instrument to your particular problems. *Write today for complete information, specifications and price.*

Norelco®
Serving Science and Industry

PHILIPS ELECTRONIC INSTRUMENTS

A Division of Philips Electronics and Pharmaceutical Industries Corp.

750 SOUTH FULTON AVENUE, MOUNT VERNON, N. Y.

In Canada: Research & Control Instruments • Philips Electronics Industries Ltd. • 116 Vanderhoof Ave. • Leaside, Toronto 17, Ont.

JOURNAL OF APPLIED PHYSICS

Vol. 31, No. 1 JANUARY, 1960

In This Issue

Calculation of Efficiency of Thermoelectric Devices . . . . B. Sherman, R. R. Heikes, and R. W. Ure, Jr. 1
Waves on a Filamentary Electron Beam in a Transverse-Field Slow-Wave Circuit . . . . A. E. Siegman 17
Ion-Bombardment Etching of Silicon and Germanium . . . . . J. A. Dillon, Jr., and R. M. Oman 26
Dipole Mode of Minority Carrier Diffusion with Reference to Point Contact Rectification . . B. R. Gossick 29
Some Properties of Zinc Sulfide Crystals Grown from the Melt . . . Arrigo Addamiano and Manuel Aven 36
Flat Panel Vacuum Thermal Insulation . . . . . H. M. Strong, F. P. Bundy, and H. P. Bovenkerk 39
Outgassing Caused by Electron Bombardment of Glass . . . . . B. Johnson Todd, Jack L. Lineweaver, and John T. Kerr 51
Particle Interaction in Magnetic Recording Tapes . . . . . J. G. Woodward and E. DellaTorre 56
Determination of Molecular Field Coefficients in Ferrimagnets . . . . . G. T. Rado and V. J. Folen 62
Explanation for the Low-Temperature Behavior of the Anisotropy of Iron . . . . . W. J. Carr, Jr. 69
Time-Dependent Electron Flow . . . . . M. C. Pease 70
Formation of Cesium Antimonide. I. Electrical Resistivity of the Film of Cesium-Antimony System . . . . Kiyoshi Miyake 76
Scattering by Nonspherical Particles . . . . . J. Mayo Greenberg 82
Rectangular Hysteresis Loop Ferrites with Large Barkhausen Steps . Aaron P. Greifer and William J. Croft 85
Interaction between Arsenic and Aluminum in Germanium . . . . . J. O. McCaldin 89
Dislocations in Two Types of CdS Crystals . . . . . D. C. Reynolds and S. J. Czyzak 94
Elastic Constants of Single Crystal Beryllium . . . . . J. F. Smith and C. L. Arbogast 99
Field Dependence of Photoelectric Emission from Tantalum . . . . . J. L. Gumnick and D. W. Juenker 102
Shapes of Etch Hillocks and Pits and Their Correlation with Measured Etch Rates . . . . . B. A. Irving 109
Interferometric Determination of Twist and Polytype in Silicon Carbide Whiskers . . . . D. R. Hamilton 112
Defects in Dislocations Produced by Focusing Collisions in f.c.c. Lattices . . . . . G. Leibfried 117
Impurity Effects upon Mobility in Silicon . . . . . R. A. Logan and A. J. Peters 122
Flow Rates Using Nuclear or Electron Paramagnetic Resonance Techniques with Applications to Biological and Chemical Processes . . . . . J. R. Singer 125
Interaction of Atomic Hydrogen with Glass . . . . . T. W. Hickmott 128
Ion Drag Pumps . . . . . Otmar M. Stuetzer 136
X-Ray Study of Ferromagnetic Domains in Cobalt Zinc Ferrite . . . . . Kenneth M. Merz 147
Magnetization of the Compound TiFe . . . . . M. V. Nevitt 155
Asymmetrical Triple Probe Method for Determining Energy Distribution of Electron in Plasma . . . . . Takayoshi Okuda and Kenzo Yamamoto 158
Figure of Merit for Thermionic Energy Conversion . . . . . N. S. Rasor 163
Specific Heat of High Purity Iron by a Pulse Heating Method . . . . . D. C. Wallace, P. H. Sidles, and G. C. Danielson 168
Angular Distribution of Sputtered Material . . . . . G. K. Wehner and D. Rosenberg 177
Model for Switching and Polarization Reversal in Colemanite . . . . . H. H. Wieder 180
Variation in Ferroelectric Characteristics of Lead Zirconate Titanate Ceramics Due to Minor Chemical Modifications . . . . . Robert Gerson 188
Dislocation Structure and the Formation and Strength of Sodium Chloride Whiskers . . . . W. W. Webb 194
Novel Mechanism for Mass Transport during Whisker Growth—Cesium Chloride from Aqueous Films . . . . . W. W. Webb and N. P. Bertolone 207

Letters to the Editor:

Hall Mobility of Holes in AgBr . . . . . Roland C. Hanson and Frederick C. Brown 210
Thermal Expansion of Silicon . . . . . Leon Maissel 211
Influence of X-Rays on the Electrification of NaCl Crystals . . . . . Anna Szaynok 211
Growth of InSb Crystals in the (111) Polar Direction . . . . . H. C. Gatos, P. L. Moody, and M. C. Lavine 212
Spontaneous Magnetizations of Some Gadolinium Alloys . . . . . Sigurds Arajs and D. S. Miller 213
Alternative Forms of Some Exponential and Power Functions for Graphical Representation . . . . . C. C. Harris 215
Dislocation Arrays in Depth and Recrystallization Produced by Surface Deformation of Single Crystals of Copper at High Temperature . . . . . John M. Bailey and Allan T. Gwathmey 215
Behavior of InSb Surfaces during Heat Treatment . . . . . D. Haneman 217
Minority Carrier Current in a Linearly Graded Drift Field . . . . . David P. Kennedy 218
Low Melting Sulfide-Halogen Inorganic Glasses . . S. S. Flaschen, A. David Pearson, and William R. Northover 219
Evanescent Modes in a Partially Filled Gyromagnetic Rectangular Wave Guide . . . . . Chen To Tai 220
Reviving the Classical Theory of Friction by a Modern Dislocation Theory of Deformation Revision . . . . . John H. Dismant 221
Maser Behavior: Temperature and Concentration Effects . . . . . T. H. Maiman 222

Books Reviewed 223
Announcements 224
Index to Advertisers xxx

JOURNAL OF APPLIED PHYSICS

A journal of general physics and its applications to other sciences and to industry

Published by the

American Institute of Physics

GOVERNING BOARD

Chairman

Ralph A. Sawyer

Members

Walter S. Baird
J. G. Baker
Jesse W. Beams
R. H. Bolt
Harvey Brooks
J. W. Buchta
J. H. Dillon
Vernet E. Eaton
Herbert A. Erf
S. A. Goudsmit
W. W. Havens, Jr.
Winston E. Kock
R. Bruce Lindsay
Walter C. Michels
C. J. Overbeck
G. E. Pake
Joseph B. Platt
Ralph A. Sawyer
John Strong
George E. Uhlenbeck
V. F. Weisskopf

ADMINISTRATION

Elmer Hutchisson
Director

Henry A. Barton
Associate Director

Wallace Waterfall
Secretary and Treasurer

Ruth. F. Bryans
Publication Manager

W. C. Kelly
Director of Education Projects

Eugene H. Kone
Director of Public Relations

Alice Mastropietro
Circulation Manager

Kathryn Setze
Assistant Treasurer

Edward Tober
Manager, Production and Distribution

Theodore Vorburger
Advertising Manager

Emily Wolf
Office Manager

Editor

James A. Krumhansl

Editorial Board

J. H. Crawford
Arthur Kantrowitz
A. F. Kip
J. E. Goldman
J. L. Tuck
C. A. Wert
Herman A. Haus
C. Lester Hogan
R. S. Rivlin

THE JOURNAL OF APPLIED PHYSICS is devoted to general physics and its applications to other sciences, to engineering, and to industry. Previous to 1937, this journal was called PHYSICS.

The JOURNAL OF APPLIED PHYSICS welcomes articles of two distinct kinds: (1) Descriptions of new results in experimental or theoretical physics which are of general interest to physicists. The author should explain his contribution in such a way that a physicist or engineer in another field of specialization can appreciate its objectives and essential features. (2) Critical reviews of particular areas of physics or surveys of extensive investigations at a single laboratory. Authors contemplating writing such should correspond with the Editor before they begin writing.

The JOURNAL OF APPLIED PHYSICS welcomes letters to the editor which describe in a few words the content of laboratory reports and theses and which tell readers how they may obtain copies of such reports.

Manuscripts should be submitted to the Editor, James A. Krumhansl, Rockefeller Hall, Cornell University, Ithaca, New York. Authors should read the "Information for Contributors," facing page 1 of the January issue, before writing articles or letters. The *Style Manual* of the American Institute of Physics is also helpful to writers preparing manuscripts for journals published by the American Institute of Physics. It can be obtained for $1.00 from the American Institute of Physics, 335 East 45 Street, New York 17, New York.

Corrected proofs and all correspondence concerning papers in the process of publication should be addressed to the Publication Manager, American Institute of Physics, 335 East 45 Street, New York 17, New York.

Subscriptions, renewals, and orders for back numbers should be addressed to the American Institute of Physics, 335 East 45 Street, New York 17, New York.

Subscription Price	**U.S. and Canada**	**Elsewhere**
To members of member organizations of the American Institute of Physics and Affiliated Societies ..	$12.00	$13.00
To all others	14.00	16.00

Back Number Prices

Yearly back number rate when complete year is available: $17.00.
Single copies: $1.75 each (exception: March, 1958—$3.00 each).

Changes of address should be sent to the American Institute of Physics.

Advertising rates supplied on request. Orders, advertising copy, and cuts should be sent to the American Institute of Physics.

Second-class postage paid at Lancaster, Pa.

Component Specification: ARNOLD

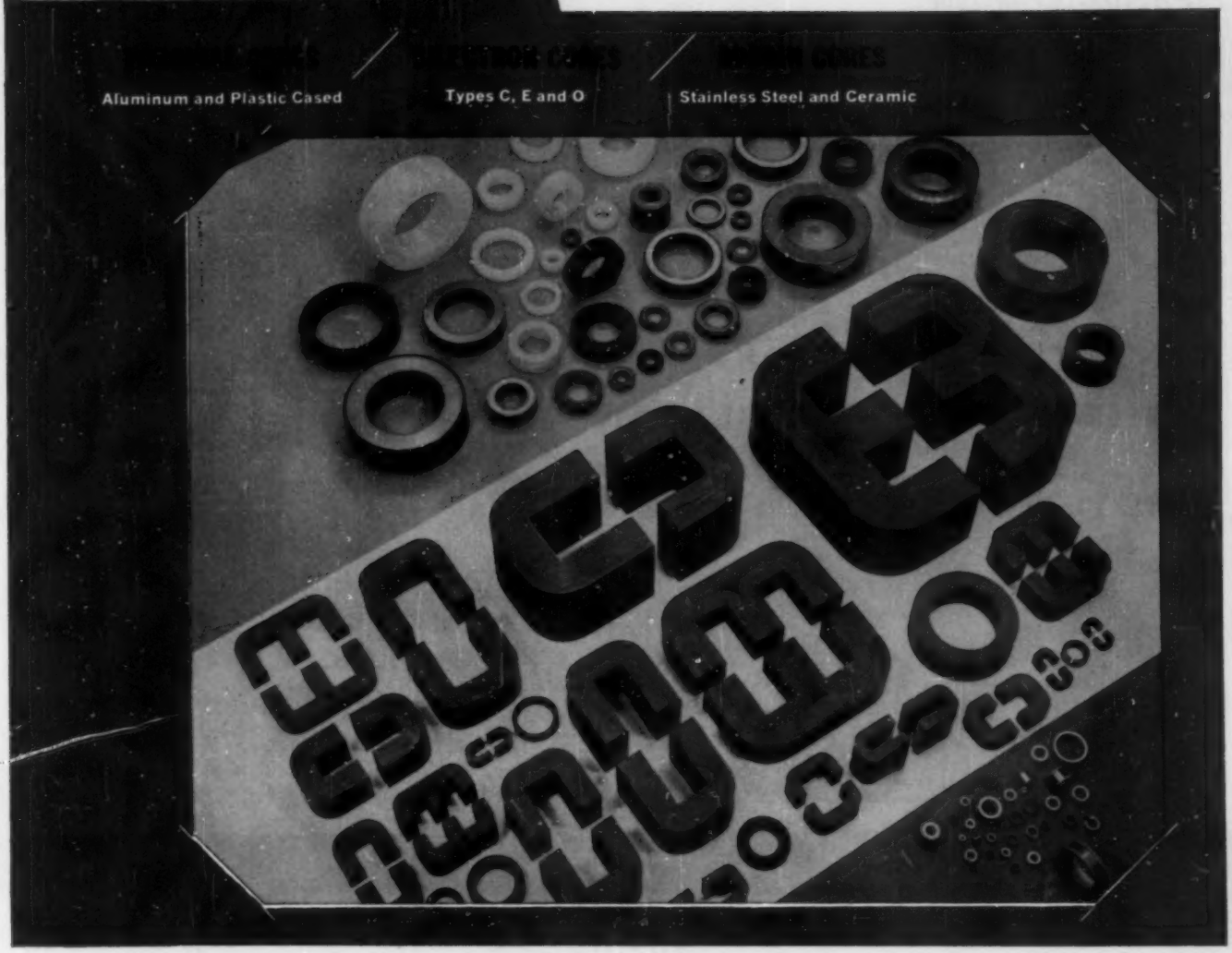

The ARNOLD LINE-UP includes ANY TAPE CORES you need

APPLICATIONS

We'll welcome your inquiries on your Tape Wound Core requirements for Pulse and Power Transformers, 3-Phase Transformers, Magnetic Amplifiers, Current Transformers, Wide-Band Transformers, Non-Linear Retard Coils, Reactors, Coincident Current Matrix Systems, Static Magnetic Memory Elements, Harmonic Generators, etc.

ENGINEERING DATA

For data on the various types of Arnold Tape Cores, write for these Bulletins:

SC-107A—*Silectron Cores, Types C, E and O*

TC-101A—*Toroidal Cores, of Supermalloy, Deltamax and 4-79 Mo-Permalloy*

TC-108A—*Bobbin Cores*

TC-113A—*Supermendur Tape Cores*

ADDRESS DEPT. J-01

Arnold produces Silectron C, E and O cores, aluminum and plastic cased toroidal cores of high-permeability materials, and bobbin-wound cores to meet whatever your designs may require in tape thickness, material, core size or weight.

As a fully integrated producer, Arnold controls every manufacturing step from the raw material to the finished core . . . and modern testing equipment permits 100% inspection of cores before shipment.

Wide selections of cores are carried in stock as standard items for quick delivery; both for engineering prototypes to reduce the need for special designs, and for production-quantity shipments to meet your immediate requirements.

• *Let us help you solve your tape core problems.* Check Arnold, too, for your needs in Mo-Permalloy or iron powder cores, and for cast or sintered permanent magnets made from Alnico or other materials. Just write or call *The Arnold Engineering Company, Main Offices, Marengo, Illinois.*

7521 C

ARNOLD

SPECIALISTS in MAGNETIC MATERIALS

BRANCH OFFICES and REPRESENTATIVES in PRINCIPAL CITIES

Find them FAST in the YELLOW PAGES

Physicists consider

THE THERMAL UTILIZATION OF A HETEROGENEOUS REACTOR

To understand thermal utilization in a heterogeneous reactor, where the neutron absorption rate is a function of energy and the thermal neutron energy spectrum varies as it passes from a moderating region to an absorbing region, the physicists at the Bettis Atomic Power Laboratory are pursuing extensive theoretical and experimental studies.

If you are a theoretical or experimental physicist and are interested in pursuing a career in reactor physics and you are a U. S. Citizen, write to: Mr. M. J. Downey, Bettis Atomic Power Laboratory, Box 1526, Dept. B-26, Pittsburgh 30, Pennsylvania.

$$f = \frac{\int\int \Sigma_a^{Fuel}(\vec{x}, E)\ \Phi\ (\vec{x}, E)\ dE d\vec{x}}{\int\int \Sigma_a^{Total}(\vec{x}, E)\ \Phi\ (\vec{x}, E)\ dE d\vec{x}}$$

BETTIS ATOMIC POWER LABORATORY

Westinghouse

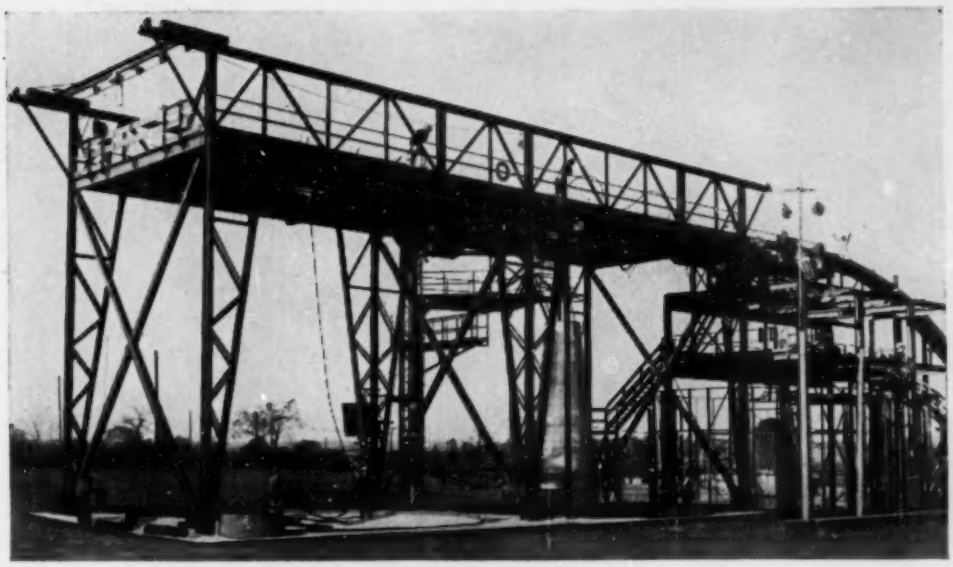

SHIP WITHOUT AN OCEAN

How do you lay a cable on the ocean floor—a cable that is connected to scores of large, heavy amplifiers? How do you "overboard" such a system in a continuous operation, without once halting the cable ship?

Bell Telephone Laboratories engineers must answer these questions in order to lay a new deep-sea telephone system designed to carry many more simultaneous conversations. They're experimenting on dry land because it is easier and more economical than on a ship. Ideas that couldn't even be attempted at sea are safely tested and evaluated.

In one experiment, they use a mock-up of the storage tank area of a cable ship (above). Here, they learn how amplifiers (see photo right), too rigid and heavy to be stored with the cable coils *below* decks, must be positioned *on* deck for trouble-free handling and overboarding.

Elsewhere in the Laboratories, engineers learn how best to grip the cable and control its speed, what happens as the cable with its amplifiers falls through the sea, and how fast it must be payed out to snugly fit the ocean floor. Oceanographic studies reveal the contours of the ocean bottom. Studies with naval architects show how the findings can be best put to work in actual cable ships.

This work is typical of the research and development effort that goes on at Bell Labs to bring you more and better communications services.

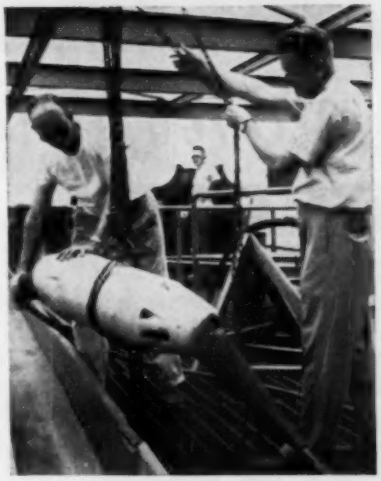

Experimental amplifier about to be "launched" from "cable ship." Like a giant string of beads, amplifiers and connecting cable must be overboarded without stopping the ship.

BELL TELEPHONE LABORATORIES

WORLD CENTER OF COMMUNICATIONS RESEARCH AND DEVELOPMENT

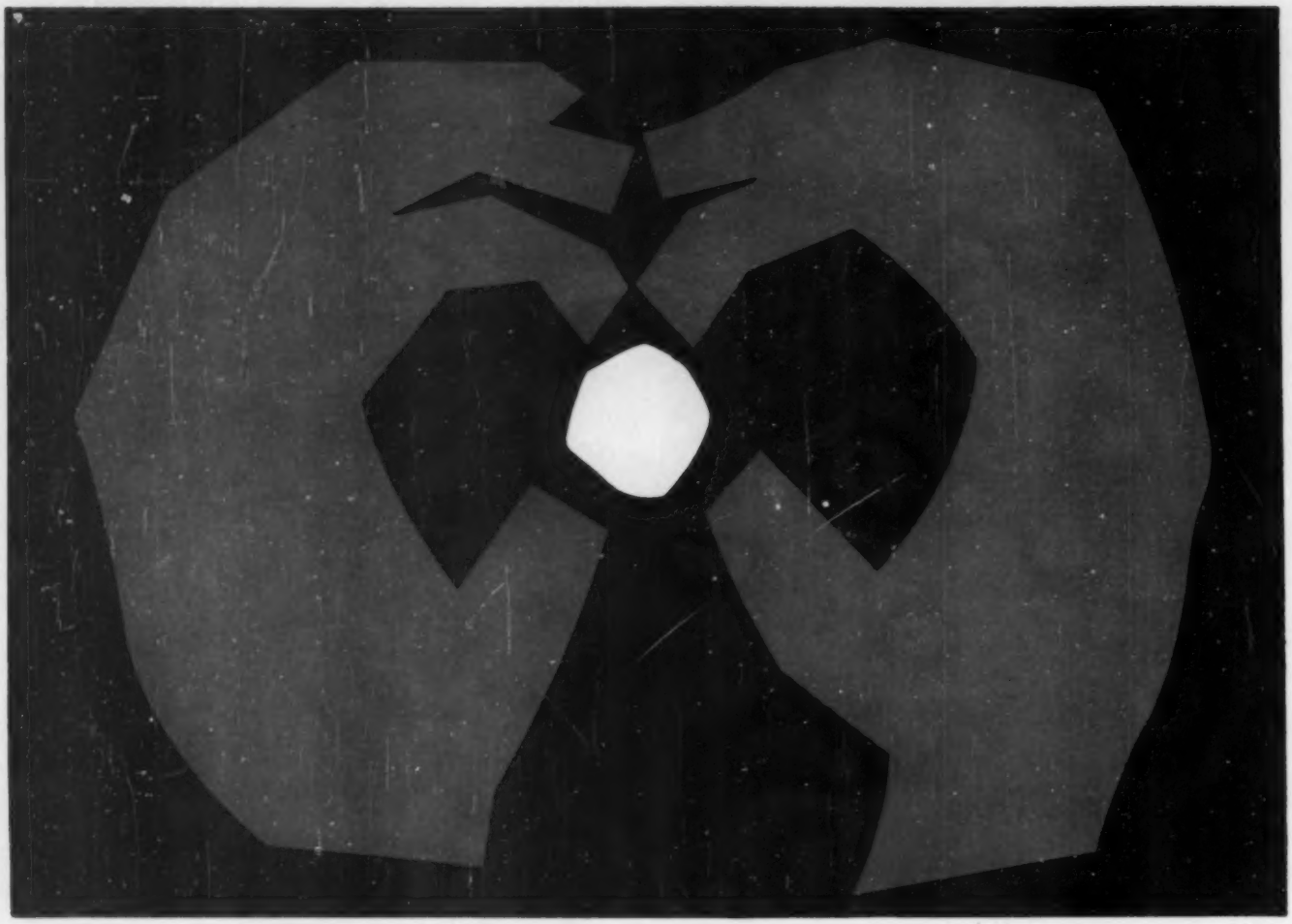

CRL manipulators...

AS OBEDIENT AS YOUR HAND!

Slave ends of CRL Manipulators obey perfectly—duplicate the natural motions of the operators' hands—make operation of the system amazingly simple. An operator becomes perfectly adept with practically no training.

Simplicity of operation is only one of several reasons research and production organizations all over the world specify CRL Manipulators. The system is versatile. Accessories such as special-purpose tongs, load hooks, motion locks, and protective booting allow adaption to a great variety of purposes. A continuous program of improvement . . . uncompromising workmanship . . . and standardized, interchangeable parts provide more reasons why you should consider CRL Manipulators for handling hazardous materials.

Central Research Laboratories will be glad to advise you on the handling of radioactive materials, explosives, hazardous chemicals, biological materials—in the layout of hot cells—in other research areas, too. For complete information, write CRL today.

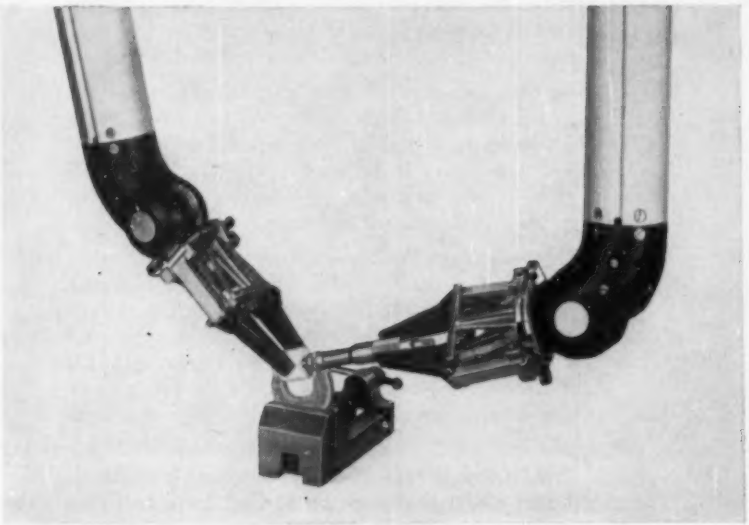

Central Research Manipulators from basic Argonne National Laboratory design

Central Research
laboratories, inc.
Red Wing, Minnesota, Dept. 301

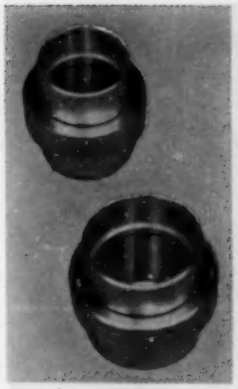

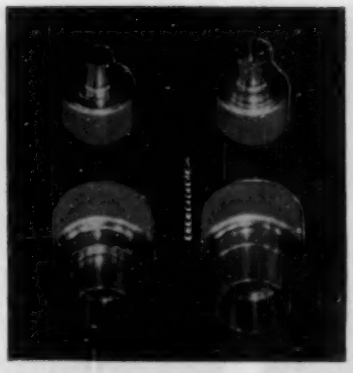

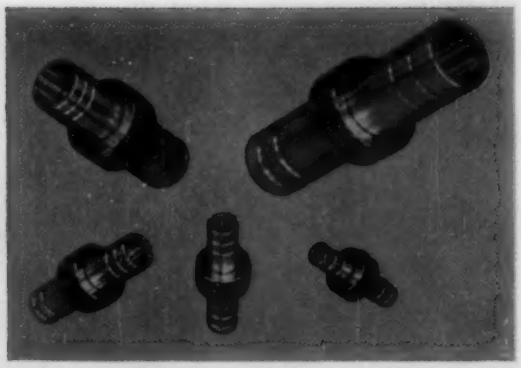

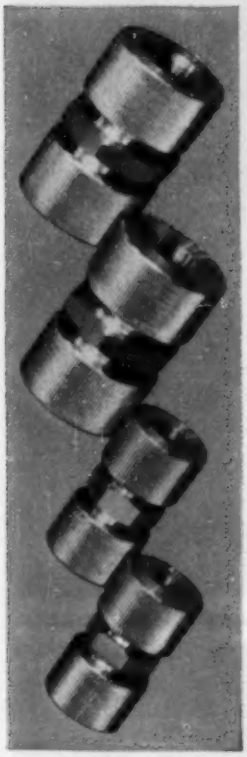

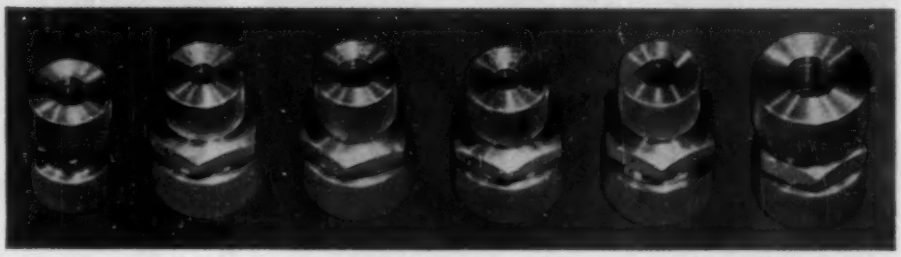

DEPENDABLE... VACUUM-TIGHT
for metal to glass, glass to glass,
metal to metal...
and all to rubber tubing.

CENCO VACUUM CONNECTORS

These precision made connectors will meet practically every need for a vacuum-tight seal between components of a vacuum system. Especially useful in making seal with a glass stem of a thermocouple, Pirani, ionization or other type of vacuum gage. These connectors may be easily tightened by hand without need for any special wrench.

Available in a variety of types and sizes for connecting metal to glass, glass to glass, or metal to metal, and all to rubber tubing.

Write for details and prices.

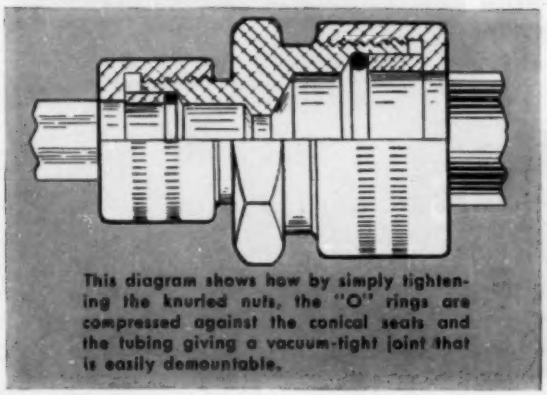

This diagram shows how by simply tightening the knurled nuts, the "O" rings are compressed against the conical seats and the tubing giving a vacuum-tight joint that is easily demountable.

cenco

CENTRAL SCIENTIFIC CO.
A Subsidiary of Cenco Instruments Corporation
1718-A Irving Park Road • Chicago 13, Illinois
Branches and Warehouses—Mountainside, N. J. Boston • Birmingham • Santa Clara • Los Angeles • Tulsa Houston • Toronto • Montreal • Vancouver • Ottawa

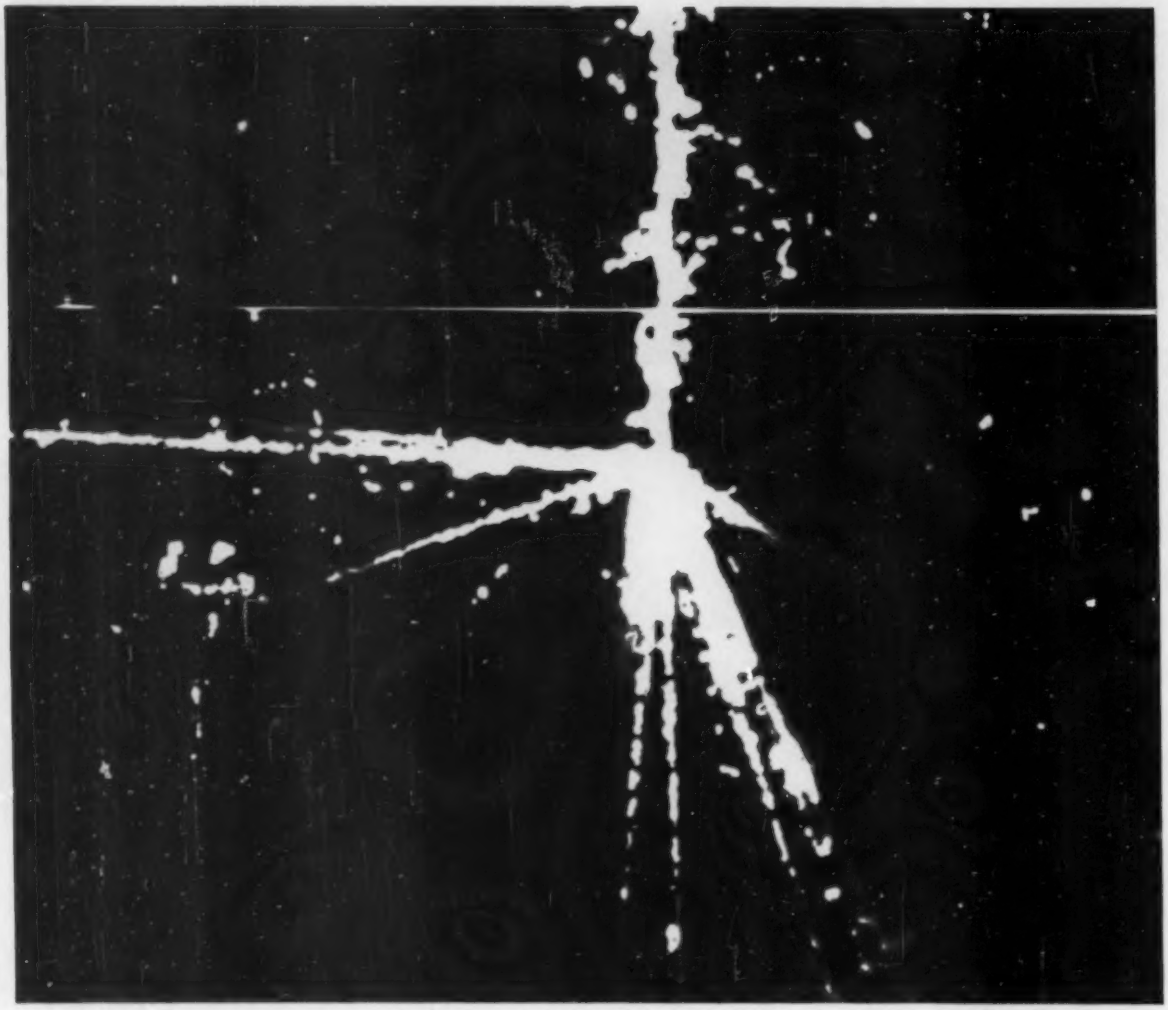

BASIC RESEARCH AT LOS ALAMOS INCLUDES NUCLEAR PLATE STUDIES OF HIGH ALTITUDE RADIATION PHENOMENA.

FOR EMPLOYMENT
INFORMATION WRITE:
PERSONNEL DIRECTOR,
DEPARTMENT 60-8

los alamos
scientific laboratory
OF THE UNIVERSITY OF CALIFORNIA
LOS ALAMOS, NEW MEXICO

The

Avco-Everett Research Laboratory

announces

it is expanding its activities
to explore and bring to engineering fruition,
new concepts in Satellite and
Space Vehicle Design,
Electric Propulsion for Space Vehicles,
and Generation of Electricity
for both Ground Station and Space Application
through MHD.

IF THIS OPPORTUNITY
INTERESTS YOU, WRITE:

DR. ARTHUR KANTROWITZ, DIRECTOR
AVCO-EVERETT RESEARCH LABORATORY
2385 REVERE BEACH PARKWAY
EVERETT 49, MASSACHUSETTS

MECHANICAL RADIATION

By R. B. LINDSAY, Brown University. *McGraw-Hill International Series in Pure and Applied Physics.* Ready in February.

The book provides an introduction to wave motion at the senior-graduate level, using mechanical radiation as the principal vehicle, but laying stress on these aspects common to all kinds of wave propagation. Mechanical relation is presented in the broad sense in integrated form by bringing together a unified treatment of the most significant radiation aspects of acoustics. Though the principal emphasis throughout is theoretical, the author has not allowed the mathematical analysis to dominate the physical meaning of the results.

RADIOISOTOPE TECHNIQUES

By RALPH T. OVERMAN, Oak Ridge Institute of Nuclear Studies; and HERBERT M. CLARK, Rennselaer Polytechnic Institute. Ready in January.

A laboratory textbook designed to give the principles and typical procedures of working with radioactive materials. Discussions and techniques are included relative to the detection of radiation, errors in radioactivity measurements, the preparation of radioactive sources, the laboratory characterizations of radiation, the standardization of radioactive sources and the calibration of radiation detectors, the rates of radioactive processes, radiochemical separation methods, and applications of radioisotopes. Approximately 1,000 references to literature dealing with these techniques are included.

MISSILE AERODYNAMICS

By JACK N. NIELSEN, VIDYA, Inc. *McGraw-Hill Series in Missile and Space Technology.* Ready in March.

This volume presents a rational and connected account of principles of missile aerodynamics. It treats the subjects of bodies, wings, and tails and the interactions between them which are particularly important for missiles. Various methods are presented for determining the airflow about missiles, including the vortices which are frequently very prominent in the flow. The book is directed at the supersonic speed range, although most of the results are also applicable to subsonic speeds.

BOUNDARY LAYER THEORY, *Second Edition*

By HERMANN SCHLICHTING, University of Braunschweig, Germany. Translated by Dr. J. KESTIN, Brown University. *McGraw-Hill Mechanical Engineering Series.* Ready in April.

A general up-dating of a reference book written principally for practicing and research engineers doing advanced work in Fluid Mechanics, and for students of aerodynamics and such allied subjects as require a thorough knowledge of the dynamics of viscous flow. The book gives a connected and logical exposition of that branch of Fluid Mechanics which deals with flows in boundary layers.

Send for copies on approval

McGraw-Hill
BOOK COMPANY, INC.
330 West 42nd Street New York 36, N.Y.

dial any output from 0-1000V within 1%

KEITHLEY Model 240 High-voltage Supply combines convenience, accuracy, wide range

This convenient supply brings new speed, ease and accuracy to laboratory tests. Typical applications include calibration of meters and dc amplifiers, supplying potentials for photomultiplier tubes and ionization chambers. Other uses include furnishing potentials for high resistance measurements, and for diode and capacitor leakage resistance tests.

The Model 240 output delivers 0 to 1000 volts at up to 10 milliamperes. Three calibrated dials on the front panel select the desired output voltage in one volt steps, with accuracy of 1% or 100 millivolts. Greater accuracy may be obtained with a potentiometer provided for setting the output with an accurate voltmeter.

Polarity is selectable. The switch includes an "OFF" position, facilitating timed measurements. An overload relay cuts off the output at 12 milliamperes within 50 milliseconds. Connectors are provided on front and rear panels.

SPECIFICATIONS

DC OUTPUT VOLTAGE: Positive or negative, 0 to 1000 volts, in one volt steps.

OUTPUT CURRENT: 0 to 10 milliamperes.

ACCURACY: Within 1% above 10 volts, within 100 millivolts below 10 volts.

LOAD REGULATION: 0.02% for 0 to 10 ma.

RIPPLE: Less than 3 mv RMS above 5 cps.

OUTPUT IMPEDANCE: 0.15 ohms at 10 volts, rising linearly to 15 ohms at 1000 volts.

STABILITY: Within 0.02 volts ± 0.02% the first hour, or in subsequent 24-hour periods.

LINE REGULATION: Output change, less than 0.02 volts for a line change of 105 to 125 V.

RACK mounting, shown above with accessory end frames, bench mounting.

PRICE $325.00

SEND TODAY FOR COMPLETE DETAILS

KEITHLEY INSTRUMENTS, INC.
12415 EUCLID AVENUE • CLEVELAND 6, OHIO

The nation's largest industrial computational facility

. . . important part of a unique research environment that can multiply your scientific accomplishments

Wherever you are carrying on scientific investigations, we doubt if you can call on advanced facilities and complementary scientific skills equal to those available at the Research Laboratories.

Here, leaders in a variety of scientific disciplines provide assistance in many areas that relate to your primary field of research. In addition, the nation's largest industrial computational facility can take over the routine of solving difficult calculations — routine that might otherwise burden you for months.

The Research Laboratories are organized to respect the time and abilities of men working in advanced scientific areas. If you appreciate an environment where a scientist can focus full mental power on scientific accomplishment, we would like to hear from you.

ATTRACTIVE OPENINGS
in many areas . . .

Solid State Physics
Plasma Physics
Gaseous Electronics
Chemical Kinetics
Particle Physics
Nuclear Engineering
Surface Chemistry
Cryogenics
Energy Conversion

Please write to Mr. W. M. Walsh, or phone Hartford, Conn., JAckson 8-4811, Ext. 7145

RESEARCH LABORATORIES
UNITED AIRCRAFT CORPORATION
400 Main Street, East Hartford 8, Conn.

UAC RESEARCH
. . . symbol of creative research

Kodak reports on:

finding an organic compound when you aren't sure what you want . . . the stable base of photography . . . four views of a 1920 Bavarian postage stamp

A devil of a job

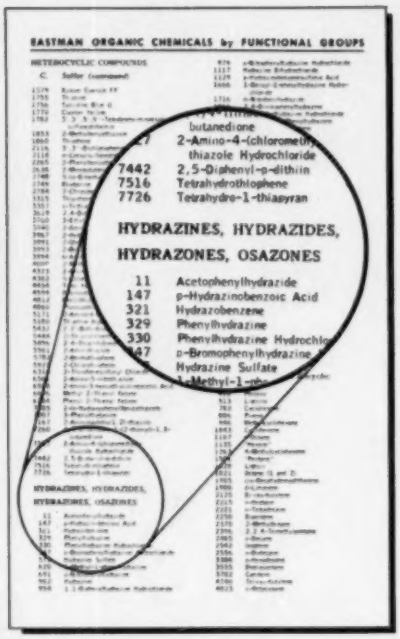

See a typical page from the new "Eastman Organic Chemicals Classified by Functional Groups."

Putting this book together was one devil of a job. It should have been done 25 years ago, but we'd kept putting it off and putting it off.

The job was not done by a committee. One man decided how it ought to be done and issued appropriate orders to his helpers. We hope he has done a good job. Some other chemist would have done it some other way. The other way would have seemed far more sensible to the other chemist. That's the trouble with committees (although they *do* have their uses). If a committee had had to agree on the scheme, you would not now be able to obtain a copy of *Eastman Organic Chemicals Classified by Functional Groups* by merely asking Distillation Products Industries, Eastman Organic Chemicals Department, Rochester 3, N. Y. (Division of Eastman Kodak Company).

There are some 3700 Eastman Organic Chemicals for laboratory use. To look one up in our regular alphabetical "Eastman Organic Chemicals List No. 41" for availability, package size, price, structural formula, and MP or BP, you must know what specific compound you want and how we interpret *Chemical Abstracts* nomenclatural rules in naming it. This isn't always easy.

Now, if you first consult ". . . by Functional Groups," you see gathered together in one handily comprehensible list all the compounds we offer that contain a given functional group. Each compound appears under each of the functional groups it contains.

We think we have done a good thing for chemistry and for business.

Wall Street cheery

Factory Photos

Firms Spur Camera Use To Solve Test, Sales, Production Problems

headlined the first column of *The Wall Street Journal* on the penultimate morning of last summer.

"Industry sources expect retail sales of equipment and supplies for industrial photographic use will reach some $250 million this year, up from about $100 million five years ago," the story said. (That's a very short time ago. These very discourses have been appearing for six years in this periodical.)

Feeling well disposed toward *The Wall Street Journal*, we laid it aside and took action to maintain the trend. Of "supplies" that *The Wall Street Journal* mentioned, none is older than photographic plates—our original product. For the love of challenge, we decided to get ready for the printer a chart that would put the photographic plate right into the spearhead of photography's onslaught on current technology.

The chart is now ready. You may have a copy with our compliments for your photo department wall. Indicate interest to Eastman Kodak Company, Special Sensitized Products Division, Rochester 4, N. Y. It takes 29" x 16½" to set out enough information about our 75 species of plates to permit industry and technology some intelligent basis for choice. You will receive the chart accompanied by a little pamphlet on dimensional stability entitled "Physical Characteristics of Kodak Glass Plates." Gist of the pamphlet's message: if there were no such thing as the glass photographic plate, it would be necessary to invent it.

About the new x-ray films

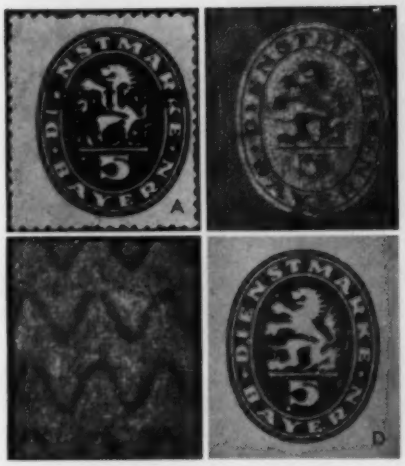

Bavarian stamp of 1920 (Scott No. 052). A. Visible light photograph. The design is green and the "Deutsches Reich" overprint is black. B. Soft x-ray radiograph. Details of both design and paper visible. Design is "negative," indicating absorption of x-rays by the ink. C. Electron radiograph. Only the details of the paper are shown. D. Electron-emission radiograph. The design is "positive," indicating a relatively high electron emission from some heavy element in the ink. The overprint cannot be seen.

This is a clever scheme to snare the attention of those who use philately for a hobby and radiation for a livelihood. Having gained your attention, we must reward you for it. The reward takes the form of a handsome 24-page book which contains not only a discussion of the above illustrations but (much more important) of general techniques for radiography by emitted electrons, transmitted electrons, soft x-rays, hard x-rays, and gamma rays; and (most important) operating data about the several new and newly improved Kodak films for all manner of radiography and x-ray diffraction.

Request a copy of the Second Supplement *to "Radiography in Modern Industry" from Eastman Kodak Company, X-ray Division, Rochester 4, N. Y. To have it make full sense, it helps to have a copy of the book that the supplement supplements. This hard-cover, thoroughly indexed, 136-page affair is sold by x-ray dealers for $5. If you already own it and have sent in the postcard that came with it, you doubtless have already received and read the supplement and have been wasting your time for the past 90 seconds.*

Price quoted is subject to change without notice.

Kodak
TRADE MARK

This is another advertisement where Eastman Kodak Company probes at random for mutual interests and occasionally a little revenue from those whose work has something to do with science

PHYSICISTS

THE MITRE CORPORATION

Invites you to investigate the varied opportunities available in the pioneering areas of large-scale system design and development

Organized under the sponsorship of the Massachusetts Institute of Technology, with a staff nucleus of the men who designed and developed the SAGE System, MITRE is engaged in continuing system programs of unprecedented scope and complexity. The principal responsibility of this non-profit organization is to provide the necessary scientific and managerial guidance for command action required to insure a technically compatible, integrated air defense mission system.

To fulfill this vital function MITRE employs a multi-discipline approach in the design, development and evaluation of the sub-systems, equipments and components from which these large-scale, real-time air defense systems are evolved. These detection systems, computers, data links, communications and advanced weapons must be integrated into the system matrix in a manner that assures their functional compatibility—individually and collectively. It must be further ascertained that every part of the system contributes its maximum operational efficiency to the air defense mission for which it was designed.

As an integral part of these activities, physicists find a professional environment in which to advance the state of the art while pursuing independent research in:

- **PHYSICAL ELECTRONICS**
- **SOLID STATE PHENOMENA**
- **ATMOSPHERIC PHYSICS**
- **ELECTRONIC CIRCUITRY**
- **PHOTO CONDUCTIVITY**
- **OPTICS**

The system oriented scientist will also find significant opportunities available with MITRE's expanding scientific community.

Openings are available at the MITRE facilities
in suburban Boston, Massachusetts – Fort Walton Beach, Florida – and Montgomery, Alabama

To arrange an immediate confidential interview, please send resume to Dana N. Burdette, Personnel Director, Dept. 1-C

THE MITRE CORPORATION
244 Wood Street – Lexington 73, Massachusetts

HARSHAW MANUFACTURES A COMPLETE LINE OF SCINTILLATION AND OPTICAL CRYSTALS

SCINTILLATION *Mounted* NaI(T1) *Crystals*

Crystal detectors designed for the most sophisticated counting problems. Our physics and engineering group are available to assist you in your special detector problems.

More detailed information is contained in our 32-page book, "Harshaw Scintillation Phosphors." We invite you to write for your free copy!

STANDARD LINE
(Hermetically Sealed Crystal Assemblies)
- The accepted standard of the industry
- Proven through years of service in research, medical and industrial applications
- unparalleled performance
- dependability
- consistent good quality.

INTEGRAL LINE
(Crystal photo multiplier tube combination assembly)
- Improved resolution
- Ready to use plug-in unit
- Permanently light sealed
- Capsule design facilitates decontamination
- Close dimensional tolerances
- Harshaw guaranteed

***Large Crystal* MATCHED WINDOW LINE**
(Designed primarily for crystals 4" dia. and larger)
- "Small crystal" performance achieved through improved optical design
- Low mass containers
- Available in standard aluminum or complete low background assemblies
- Convenient mounting flange
- Ready to use

Every Harshaw crystal is a product of our experience in crystal growing technology since 1936

Other Phosphors Available from The Harshaw Chemical Company

ROUGH CUT THALLIUM ACITVATED SODIUM IODIDE CRYSTA' BLANKS • EUROPIUM ACTIVATED-LITHIUM IODIDE (NORMAL) • EUROPIUM ACTIVATED LITHIUM IODIDE (96% Li^6 ENRICHED) • THALLIUM ACTIVATED CESIUM IODIDE • THALLIUM ACTIVATED POTASSIUM IODIDE • ANTHRACENE • PLASTIC PHOSPHORS

OPTICAL *Crystals*

For Infrared and Ultra Violet Transmitting Optics

"HARSHAW QUALITY" INHERENT IN EACH HARSHAW-GROWN CRYSTAL GUARANTEES THE MOST EFFICIENT OPTICAL TRANSMISSION POSSIBLE THROUGH:

1) Negligible light scattering in crystals, permitting higher sensitivity and improved resolution
2) Freedom from absorptions caused by trace impurities in crystal optics
3) Minimum strain

"HARSHAW QUALITY" meets the demand for uniformity of optical properties such as dispersion and refractive index.

Prices, specifications, or other information will be sent in answer to your inquiry.

The following infrared and ultra violet transmitting crystals are available; others are n the process of development:

SODIUM CHLORIDE • SODIUM CHLORIDE MONOCHROMATOR PLATES POTASSIUM BROMIDE • POTASSIUM BROMIDE PELLET POWDER • (through 200 on 325 mesh) • POTASSIUM CHLORIDE • OPTICAL SILVER CHLORIDE • THALLIUM BROMIDE IODIDE • LITHIUM FLUORIDE • LITHIUM FLUORIDE MONOCHROMATOR PLATES • CALCIUM FLUORIDE • BARIUM FLUORIDE • CESIUM BROMIDE • CESIUM IODIDE

Additional information on the physical and optical properties of the above crystals is available in our 36-page booklet "Synthetic Optical Crystals". Send for your free copy.

HARSHAW

THE HARSHAW CHEMICAL CO.
Crystal Division • Cleveland 6, Ohio

RESEARCH AT COLLINS

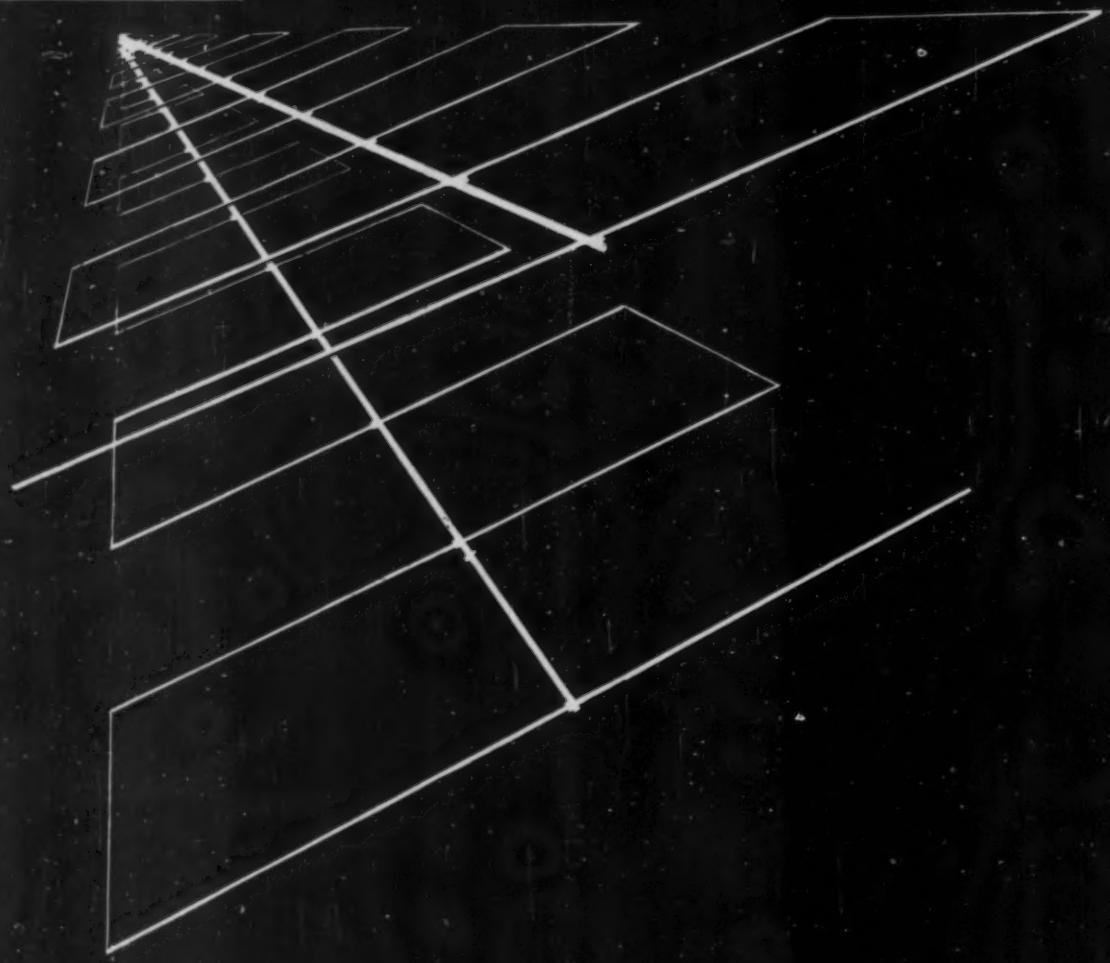

THE UNUSUAL SHAPE OF PROGRESS

Yesterday's basic and applied research in antennas has become today's technology in broadband antenna design at Collins Radio Company. Pictured here is a Collins Logarithmic Periodic Antenna. It performs functions previously requiring a large number of antennas. The Logarithmic Periodic concept is based on a structural geometry in which the electrical characteristics repeat periodically as the log of the frequency. Since only minor changes occur over each period, the characteristics are essentially constant over the entire frequency range.

Collins Radio Company Research Laboratories in Cedar Rapids, Iowa, direct far ranging programs in circuits, advanced systems, antennas and propagation, mechanical sciences, and mathematics toward advancing scientific knowledge and developing new technologies. Collins provides freedom of activity in basic research for the physicist and engineer capable of looking beyond the apparent limits of today's science. In applying the new concepts thus created, Collins has attained an enviable position of leadership in electronics. Unique professional opportunities are now being offered. Your inquiry is invited. Write today for more information.

COLLINS

COLLINS RADIO COMPANY • CEDAR RAPIDS, IOWA • DALLAS, TEXAS • BURBANK, CALIFORNIA

SCIENTIFIC INSTRUMENTS FOR RESEARCH AND DEVELOPMENT

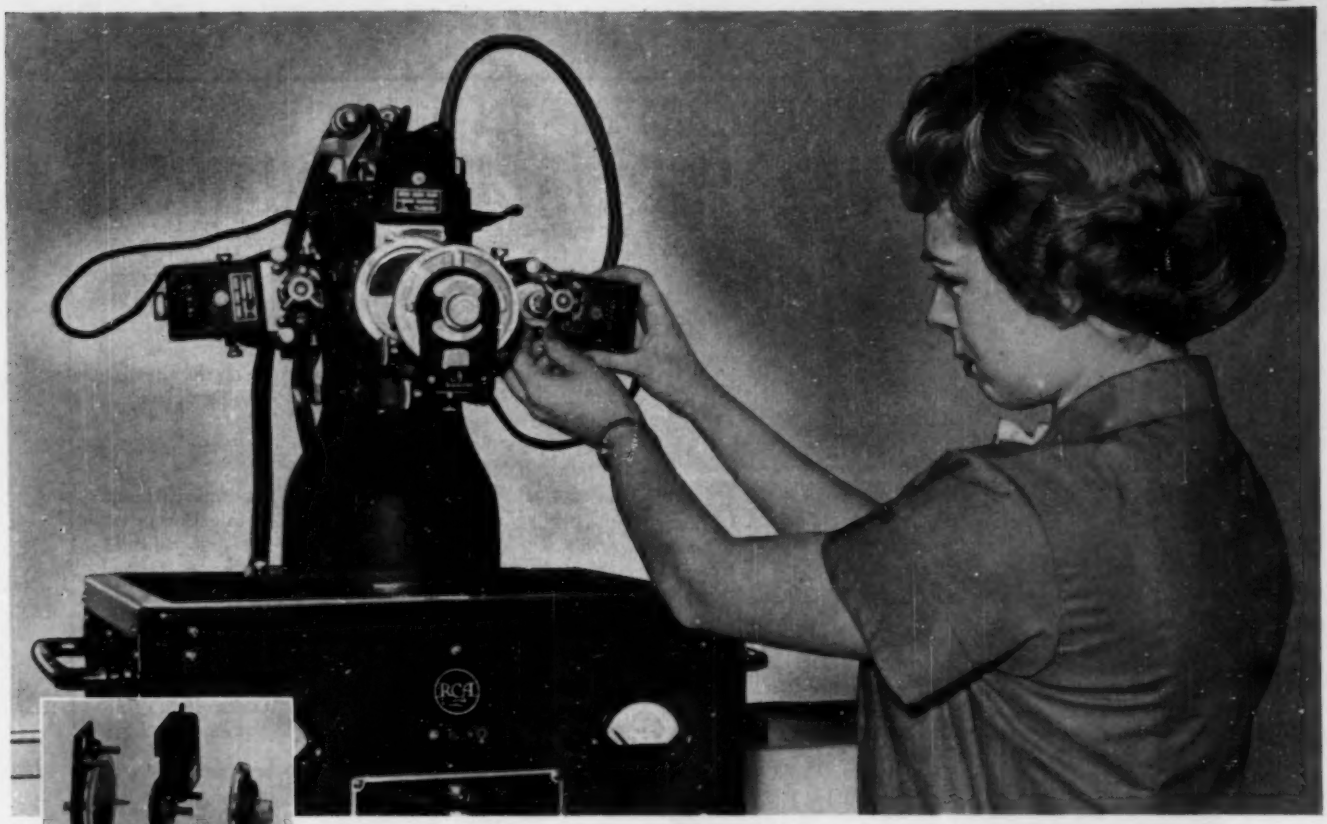

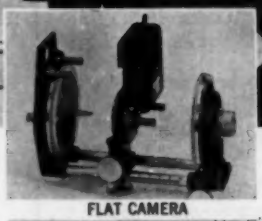

FLAT CAMERA

CYLINDRICAL CAMERA

GUINIER CAMERA

STRESS CAMERA

STEREO-MICROCAMERA

NOW FOR AS LITTLE AS $4,000!

Complete RCA X-Ray Diffraction Equipment for all Types of Film Studies

Think of it—a complete x-ray diffraction facility for film studies can be yours now for less than $4,000.00. A typical installation could include: a Crystalloflex II X-Ray Diffraction Generator complete with two powder cameras, a flat camera, and a stereo-microcamera, a copper target x-ray tube and camera carriers. Other combinations, with prices varying according to the selection, could include both one and two radian cylindrical cameras, flat cameras and the very versatile 70mm. film with one radian cylindrical camera which can be used for powder diffraction, symmetrical back reflection work and rotating crystal layer line diagrams. A wide variety of additional cameras, x-ray tubes with other targets, and attachments for special specimen handling are also available.

Cameras used with the Crystalloflex II can be operated simultaneously at four x-ray ports, each of which is equipped with an individually timed shutter. Rating of this compact table model is 25 to 60 KV in 5 KV steps. Tube current control is continuous from 0 to 40ma. Overall size of the unit is 24″ wide x 32″ high x 22″ deep. The Crystalloflex II can also be tilted so that the tube may be operated horizontally. All these features make this generator an excellent tool for chemists, metallurgists, physicists and biologists whose research projects usually entail a high volume and wide variety of film work.

RCA also offers the Crystalloflex IV console model generator, and the world's most complete line of attachments and accessories for x-ray diffraction and spectroscopy including an exceptionally versatile group of cameras, pole figure goniometer, single crystal layer line and microfluorescence attachments.

Contract services on RCA X-Ray diffraction equipment and electron microscopes are available through eleven regional offices of the RCA Service Company.

For more information about this advanced equipment or a quotation on your requirements, write: Radio Corporation of America, Dept. C-65, Building 15-1, Camden, N.J.

RCA Tmk(s) ®

RADIO CORPORATION of AMERICA

CAMDEN 2, N. J.

QUIET - VIBRATIONLESS - ALL-PURPOSE
WELCH DUO-SEAL® VACUUM PUMPS

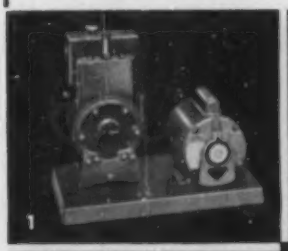

The complete line of Duo-Seal Vacuum Pumps is shown here. Descriptions and prices below.

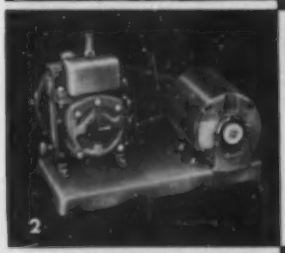

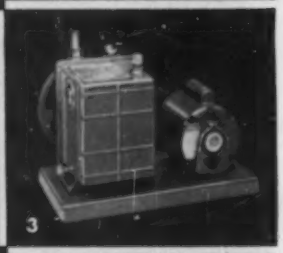

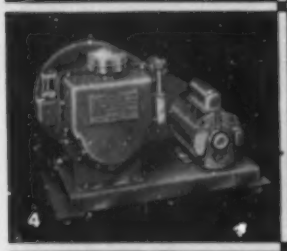

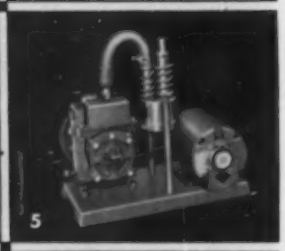

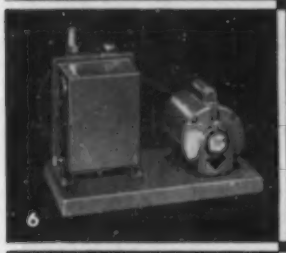

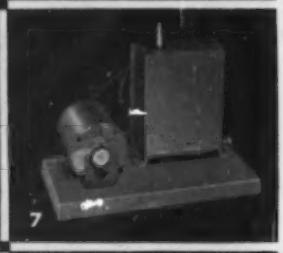

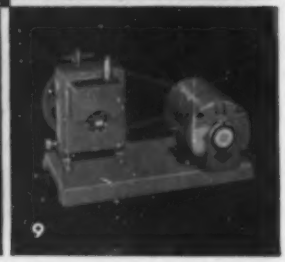

Whether it's in the laboratory, on a busy production line, in a classroom, reduced noise level means greater efficiency, higher quality work. Duo-Seal Vacuum Pumps are *quiet*. Welch engineers took noise and vibration out of the vacuum pump right on the drawing board. The result is a pump that runs as quietly as an electric motor.

Quiet operation means greater efficiency

Quiet, vibrationless operation means pumps that run smoothly year after year with virtually no maintenance beyond a periodic oil change. Duo-Seal pumps, built to close tolerances, actually improve with use, the seal and vanes become more highly polished and the fit more perfect.

There is a Duo-Seal pump available for almost every purpose, for every budget, from noncritical classroom problems to most exacting high-vacuum industrial-production and laboratory vacuum requirements.

Welch Pumps are best because:
Every pump is triple tested.
Specified performance guaranteed.
Lowest cost per year of use.
Highest vacuum of any mechanical pump.
Quietest mechanical pump made.

1. 1405 (2 speeds available) two-stage, No. 1405H. 0.05 micron, 33.4 liters per minute. $230.00. No. 1405B. 0.1 micron, 58 liters per minute. $255.00

2. 1400B—two-stage, 0.1 micron, 21 liters per minute. $133.00

3. 1402B—two-stage, vented exhaust, 0.1 micron, 140 liters per minute. $310.00

4. 1397B—two-stage, vented exhaust, 0.1 micron, 375 liters per minute. $645.00

5. 1392—mechanical and diffusion pump assembly, two-stage (each element) 0.001 micron, 600 liters per minute. (at 0.1 micron) $275.00

6. 1403B—single-stage, 5 microns, 100 liters per minute. $245.00

7. 1404H—Wegner Pump single-stage, 20 microns, 33.4 liters per minute. $150.00

8. 1406H—single-stage, 5 microns, 33.4 liters per minute. $150.00

9. 1410B—Wegner Pump single-stage, 20 microns, 21 liters per minute. $100.00

For complete specifications, request our pump catalog.

W. M. WELCH SCIENTIFIC COMPANY
DIVISION OF W. M. WELCH MANUFACTURING COMPANY
ESTABLISHED 1880
1515 Sedgwick Street, Dept. C-1 Chicago 10, Illinois U. S. A.
Manufacturers of Scientific Instruments and Laboratory Apparatus

Journal of Applied Physics

JAMES A. KRUMHANSL, *Editor*

Board of Editors

J. L. CRAWFORD
ARTHUR KANTROWICZ
A. F. KIP
J. E. GOLDMAN
J. L. TUCK
C. A. WERT
HERMAN A. HAUS
C. LESTER HOGAN
R. S. RIVLIN

VOLUME 31

JANUARY–DECEMBER, 1960

Published by the
AMERICAN INSTITUTE OF PHYSICS
Incorporated

INFORMATION FOR CONTRIBUTORS

1. **Other sources of information.** The *Style Manual* of the American Institute of Physics is available from the A. I. P. at $1.00 per copy. Authors should obtain a copy of it. The *Style Manual* contains many helpful suggestions for preparing manuscripts, a list of abbreviations in use by the A.I.P. journals, and a list of special symbols for which type is available. Authors should also study the form and style of printed articles in the *Journal*.

2. **Manuscripts.** Manuscripts must be in English, typewritten, double-spaced, on one side of the page, on 8 1/2- × 11-inch durable, opaque, white paper. The typed original, not a carbon or ditto-process copy, should be submitted. Wide margins should be provided to permit editorial instructions to the printer. Editorial work will be speeded if a duplicate is submitted in addition to the original, but please do not submit more than one duplicate. An author should adopt a particular way of writing his name in the "by-line" and use this same name for all his publications. This practice makes indexes more useful and less confusing.

3. **Figures.** Line drawings should be planned for reduction to the 3-inch column width. They preferably should be 6 inches or 9 inches wide and must not be larger than 8 1/2 × 11 inches. Lettering and symbols should be large enough so that they will be at least 1/16 inch high after reduction. Lines should be broad and black, since a narrow line will appear as a broken, gray line after reduction.

The original line drawings must be submitted. They must be in india ink on white or pale blue tracing paper or tracing cloth. Coordinate paper should not be used.

Photographs of apparatus should be used sparingly, since a good line drawing tells more than most photographs. Oscillograph photographs should be avoided in most cases by making a line drawing from the photograph. Pictures should be glossy prints with a maximum black and white contrast and should be rectangular in shape. Do not write heavily on the backs of pictures or clip or staple them so as to mar the picture. The Editor will be glad to consider suggestions for cover photographs.

Plan figures to use space efficiently. Avoid wasting space, particularly at the top or bottom.

Write on the back or margin of each illustration the figure number and the author's name. Figures should be numbered consecutively. Figure captions should be typed, double-spaced, and included as the last page of the manuscript. Captions are sent to the printer, but figures are sent to the photoengraver. Lettering or lines cannot be added to nor deleted from the drawing or photograph submitted.

The editorial review of a paper will be expedited if copies of figures can be provided. These copies are not necessary, but permit retaining originals of the figures in the Editor's office during review of the paper. (Such copies are *not a substitute* for the original drawings and glossy prints.)

Please refer to figures in the text by the abbreviation "Fig. 1" etc., except at the beginning of a sentence where "Figure" is not abbreviated.

4. **Mathematics.** All but the simplest mathematical expressions should be carefully printed in by hand. Be sure to distinguish between capital and small letters. Indicate clearly superscripts by a penciled ∨ sign under the superscripts and subscripts by a penciled ∧ sign over the subscript. Avoid complicated subscripts and superscripts, subscripts to subscripts, and superscripts to superscripts. Avoid repetition of a complicated expression by use of an appropriate symbol for the expression. Identify Greek letters in the margin, and identify unusual symbols by number (see the list of available symbols in the *Style Manual*). Use fractional exponents instead of root signs. Use the solidus (/) for simple fractions to save vertical space. Remember that the typesetter is neither a physicist nor a mathematician.

5. **References.** References should appear as footnotes, numbered consecutively and arranged thus:

[1] A. B. Smith, Phys. Rev. 41, 852 (1932).
[2] H. Lamb, *Hydrodynamics* (Cambridge University Press, Cambridge, England, 1940), sixth edition, pp. 573, 645.

A list of the abbreviations for the names of journals appears in the *Style Manual*.

6. **Tables.** All but the simplest tabular material should be organized into separate tables. Tables should be numbered with Roman numerals and typed on sheets at the end of the running text. Each table must have a caption, typed at the top of the table, which makes the data in the table intelligible without reference to the text. Avoid complicated column headings. If necessary, use symbols which are explained in the caption.

7. **Abstract.** An abstract must accompany each article. It should be adequate as an index and as a summary. It should give all subjects, major and minor, concerning which new information is presented. It should give the conclusions of the article and all numerical results of general interest. An abstract is usually reprinted verbatim in abstract journals. Therefore, great care should be used in writing it.

8. **Letters to the Editor.** Letters have the same requirements as manuscripts with two exceptions: (1) The original and one copy of the manuscript and figures are required (rather than just suggested, as in the case of regular articles). (2) No abstract is used.

9. **Publication charge.** Authors' institutions or companies are asked to pay a publication charge of $30 per printed page for articles and $30 per page per Letter (with a minimum of $30 per Letter), for which they will receive 100 reprints without covers.

10. **Correspondence and alterations.** Send manuscripts to the Editor, James A. Krumhansl, National Carbon Research Laboratories, P. O. Box 6116, Cleveland 1, Ohio. The Editor welcomes the responsibility some laboratories take for the excellence of manuscripts sent out, but he prefers to correspond directly with the author rather than through executives or through the reports division of the author's laboratory. Please do not send to the Editor any correspondence about proof, reprints, or publication charge.

If your paper is accepted for publication, you will be notified by the Editor. Any alterations can be made at this time. You will also be notified when your paper is sent to the American Institute of Physics. *All* subsequent correspondence about your paper should be addressed to Miss Ruth F. Bryans, Publication Manager, American Institute of Physics, 335 East 45th Street, New York 17, New York.

11. **Proof of articles** (but not of Letters to the Editor) will be sent to you and should be returned promptly to the Publication Manager, A.I.P. A few alterations in proof are unavoidable, but the cost of making extensive alterations or of correcting mistakes caused by careless preparation of the manuscript will be charged to the author.

12. **Check list.**

(a) Typed, original manuscript.
(b) Original line drawings of figures, not larger than 8 1/2 × 11 inches.
(c) Abstract.
(d) Typed list of figure captions.
(e) Mathematical expressions explained for the printer.
(f) Greek letters and unusual symbols identified in the margin.
(g) Additional copy of manuscript and figures *desired* for papers and *required* for Letters.

Journal
of
Applied Physics

Volume 31, Number 1 January, 1960

Calculation of Efficiency of Thermoelectric Devices

B. Sherman, R. R. Heikes, and R. W. Ure, Jr.
Westinghouse Research Laboratories, Pittsburgh 35, Pennsylvania
(Received May 11, 1959)

A procedure has been developed for the exact calculation of the efficiency of thermoelectric generators and cooling devices in which the parameters of the materials have arbitrary temperature dependence. High speed computer techniques are found necessary. Approximate methods are reviewed and their discussion extended. A number of examples are worked out by both the exact and approximate methods. Comparison of these results show that the approximate methods agree with the exact method to about 5% in the case of power generation and to about 15% in the case of the refrigeration coefficient of performance. However, in the case of the maximum heat pumping rate deviations as large as a factor of 2 are found.

I. INTRODUCTION

IN this paper methods will be presented for calculating the performance of a Seebeck-effect thermoelectric generator and of a Peltier-effect thermoelectric cooling device. Examples of these devices are shown schematically in Fig. 1. They operate between two temperatures T_h and T_c where $T_h > T_c$. The problem of the heat transfer between the heating or cooling medium and the junctions will not be considered. The temperatures T_h and T_c are the actual temperatures at the junctions between the active arms p and n and the metal straps to which they are soldered (labeled T_h and T_c in Fig. 1). It will be assumed that the junction resistance is negligible compared to the bulk resistance of the arms. It will also be assumed that each arm has perfect thermal insulation around it so that there is no heat transfer across the cylindrical surface of the arms. The arms are assumed to have uniform cross-sectional area along their length. This latter restriction has been made in the light of the work of Gelhoff, Justi, and Kohler[1] showing that the performance of a thermoelectric device is not improved by making the elements in a noncylindrical shape.

Formulas for the performance of these devices have been given before[2-5] but it has always been assumed that the Seebeck coefficient[6] α, the electrical resistivity ρ, and the thermal conductivity k of the p and n arms are independent of temperature. In this paper the general case where all three parameters are arbitrary functions of temperature will be considered.

In Sec. II, the problem will be stated explicitly in a form which is most suitable for the rest of the paper. The formulas for the case of parameters independent of temperature will be given. Although these have been given before, they are included here for the sake of completeness. In Sec. III, it will be shown that the same formulas can be derived by minimization of the entropy production.

Three approaches to the general problem of arbitrary temperature variation of the parameters will be considered. The first two of these have been given before. One approach has been to insert average values of the appropriate parameters into the formulas derived for the case of parameters independent of temperature. This will be outlined in Sec. IV and will

[1] Gelhoff, Justi, and Kohler, Abhandl. braunschweig. wiss. Ges. **2**, 156 (1950). *Note added in proof.*—A. H. Boerdijk has recently given a more complete proof of this topic [J. Appl. Phys. **30**, 1080 (1959)].

[2] E. Altenkirch, Physik. Z. **12**, 920 (1911).

[3] D. K. Coles, Westinghouse Research Rept. R-94468-5-A. (unpublished).

[4] A. F. Ioffe, *Semiconductor Thermoelements and Thermoelectric Cooling* (Infosearch, Ltd., London, England, 1957).

[5] F. E. Jaumot, Jr., Proc. Inst. Radio Engrs. **46**, 538 (1958).

[6] This coefficient is commonly called the thermoelectric power. However, it is not a "power" but a material coefficient. We prefer to call it the Seebeck coefficient by analogy with the closely related Thomson and Peltier coefficients. The term Seebeck coefficient has been recommended by the joint IRE-AIEE Task Group on Thermoelectric Devices.

Copyright © 1960 by the American Institute of Physics.

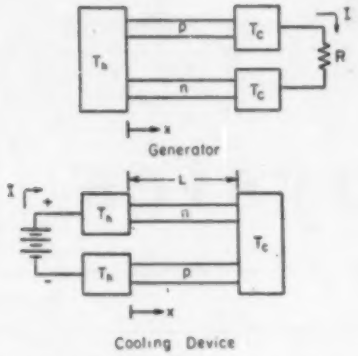

FIG. 1. Schematic drawing of a Seebeck-effect thermoelectric generator and a Peltier-effect thermoelectric cooling device. The elements marked T_h and T_c are heat reservoirs and have zero electrical resistance. The elements marked p and n are the p-type and n-type thermoelectric materials.

be called Approach 1—Average Parameters. If the device is broken up into an infinite number of stages exact formulas for the performance can be derived; this approach will be considered in Sec. V and will be called Approach 2—Infinite Staging. A new procedure has been developed by us. It is designated Approach 3—Exact, and will be discussed in Sec. VI. The results of the three methods will be compared in Sec. VII.

II. STATEMENT OF PROBLEM

The efficiency of a thermoelectric generator is defined as

$$\eta = P_0/q_h, \tag{1}$$

where P_0 is the electrical power output and q_h is the rate of heat removal from the high temperature heat reservoir (T_h in Fig. 1). In the constant parameter case this heat removal rate can be expressed as the sum of the Peltier heat absorbed at the hot junction plus the thermal conduction heat minus the fraction of the Joule heat which returns to the hot junction. In the general case there are two complications. (1) The Thomson heat, which is proportional to the temperature derivative of the Seebeck coefficient, is no longer zero.[7] (2) The Joule heat, Thomson heat, and thermal conduction heat cannot be considered separately, since the differential equation governing the temperature distribution in the arms is no longer linear. Since the Thomson heat and Joule heat actually pass to the junctions by the thermal conduction process, the rate of heat removal is given by

$$q_h = \pi_h I - k_p(T_h)T_p'(0) - Ak_n(T_h)T_n'(0), \tag{2}$$

where $\pi_h = \pi_{np}(T_h)$ is the Peltier coefficient of the couple at temperature T_h, I is the total current, $k_p(T)$ is the thermal conductivity of the arm p at temperature T, and $T_p'(0) = dT_p/dx$ at $x=0$.

In both the power generation and cooling cases the length of each arm is L and the x coordinate varies from 0 at the hot junction T_h to L at the cold junction T_c. Arm p has unit cross-sectional area and arm n has area A.

By the first Kelvin relation,

$$\pi_{np}(T) = -\pi_{pn}(T) = T\alpha_{pn}(T), \tag{3}$$

where $\alpha_{pn}(T)$ is the Seebeck coefficient of the couple at temperature T. The temperature distribution in the arms is given by the solution of the equation[8]

$$(d/dx)[k(T)T'(x)] - \tau(T)JT'(x) + \rho(T)J^2 = 0, \tag{4}$$

where $\tau(T)$ is the Thomson coefficient at temperature T and J is the electrical current density. The relation between the Thomson coefficient and the Seebeck coefficient is given by the second Kelvin relation

$$\tau(T) = Td\alpha/dT, \tag{5}$$

where α is the absolute Seebeck coefficient of the material. The Seebeck coefficient of the couple is given by $\alpha_{pn} = \alpha_p - \alpha_n$. The current densities in the two arms are

$$J_p = I \quad \text{and} \quad J_n = -I/A. \tag{6}$$

The power output is given by

$$P_0 = I^2R, \tag{7}$$

where R is the load resistance. The total current is

$$I = \frac{\int_{T_c}^{T_h} \alpha_{pn}(T)dT}{R + \int_0^L [\rho_p(T) + A^{-1}\rho_n(T)]dx}. \tag{8}$$

In the following sections the maximum value of η for given L, T_c, and T_h will be found as A and R are varied.

For the case of k and τ independent of temperature and for $\rho(T) = \rho_0 + \rho_1 T$, Burshtein has shown that the temperature gradient at $x=0$ is[9]

$$T'(0) = \left(T_h + \frac{\rho_0}{\rho_1}\right)\left(\frac{\tau J}{2k} + CJ \operatorname{ctnh} CJL\right) + \left(T_c + \frac{\rho_0}{\rho_1}\right)CJ\left(\exp\left[-\frac{\tau JL}{2k}\right]\right)\operatorname{csch} CJL, \tag{9}$$

where $C = (2k)^{-1}(\tau^2 - 4\rho_1 k)^{\frac{1}{2}}$. For $J \ll 2k/\tau$ and $J \ll 1/CL$,

[7] For a general review of the Thomson effect, Seebeck effect, and Peltier effect and their interrelations see, for example, Zemansky, *Heat and Thermodynamics* (McGraw-Hill Book Company, Inc., New York, 1943); C. A. Domenicali, Rev. Modern Phys. **26**, 237 (1954); or reference 4.

[8] C. A. Domenicali, J. Appl. Phys. **25**, 1310 (1954).

[9] A. I. Burshtein, Soviet Phys.-Tech. Phys. **2**, 1397 (1957); Zhur. tekh. Fiz. **27**, 1510 (1957).

(9) can be written

$$T'(0)=\frac{-\Delta T}{L}+\frac{J^2L}{2k}\left[\rho_0+\rho_1\frac{2T_h+T_c}{3}\right]$$
$$+\frac{\tau J}{2k}\left[\Delta T-\frac{J^2L^2(\rho_0+\rho_1T_c)}{6k}-\frac{\tau JL\Delta T}{6k}\right]+\cdots. \quad (10)$$

The first term is due to the conducted heat in the absence of a current, the second the Joule heat, and remainder the Thomson heat. The temperature distribution in this case is a superposition of the normal linear curve in the absence of a current, a distribution which has a maximum near the center of the bar produced by the Joule heat, and a contribution from the Thomson heat. The first Thomson heat term in (10) is the result of the normal linear distribution, the second is caused by the gradient produced by the Joule heat, and the third by the gradient produced by the Thomson heat itself. In some cases of practical interest the second term is of the same order of magnitude as the first and cannot be neglected.

Only in the case $\tau=0$ and $\rho_1=0$ is a simple answer obtained for the efficiency η. From (1), (2), (3), (6), (7), and (10), the efficiency in the case α, ρ, and k independent of temperature ($\tau=0$) can be written

$$\eta=\frac{I^2R}{\alpha_{pn}T_hI+\Delta TL^{-1}(k_p+Ak_n)-I^2L(\rho_p+\rho_nA^{-1})/2}. \quad (11)$$

By the use of (8) which relates I and R, this expression can be maximized with respect to the load resistance R and the area A. The optimum efficiency is

$$\eta=\frac{T_h-T_c}{T_h}\frac{(1+\bar{T}z)^{\frac{1}{2}}-1}{(1+\bar{T}z)^{\frac{1}{2}}+(T_c/T_h)}, \quad (12)$$

where $\bar{T}=(T_h+T_c)/2$ and

$$z=\left[\frac{\alpha_{pn}}{(\rho_pk_p)^{\frac{1}{2}}+(\rho_nk_n)^{\frac{1}{2}}}\right]^2. \quad (13)$$

The values of A and R which optimize the efficiency are

$$A=(\rho_nk_p/\rho_pk_n)^{\frac{1}{2}}, \quad R=(1+\bar{T}z)^{\frac{1}{2}}(\rho_p+\rho_nA^{-1})L. \quad (14)$$

The first factor in (12) is the Carnot cycle efficiency while the second is called the thermocouple efficiency. Examination of (12) reveals that the material parameters enter into the efficiency only in the combination denoted by z. This quantity is called the figure of merit of a couple.

For the cooling device, (4), (9), and (10) still hold. However, the current densities are given by

$$J_p=-I \quad \text{and} \quad J_n=I/A. \quad (15)$$

Instead of the efficiency the quantity of interest is the coefficient of performance φ defined as

$$\varphi=q_c/P_i, \quad (16)$$

where q_c is the rate of heat removal from the cold junction by the device and P_i is the electrical power input. The heat pumped is given by

$$q_c=\pi_cI+k_p(T_c)T_p'(L)+Ak_n(T_c)T_n'(L), \quad (17)$$

where $\pi_c=\pi_{np}(T_c)$. The applied voltage is

$$E=\int_{T_c}^{T_h}\alpha_{pn}(T)dT+I\int_0^L[\rho_p(T)+A^{-1}\rho_n(T)]dx, \quad (18)$$

and the power input is $P_i=EI$.

There are three different problems which are of interest for cooling devices. (I) What is the maximum coefficient of performance when operating between two given temperatures? (II) What is the maximum temperature difference which the device can attain? For the case of α, ρ, and k independent of temperature, this maximum temperature difference can be calculated directly. In the numerical calculation of the general case, the temperature of one end must be held constant. In this paper, the hot junction temperature will be maintained and the minimum T_c which gives $q_c=0$ will be calculated. (III) When operating between two given temperatures what is the maximum heat per unit cross-sectional area which the device will pump, i.e., what is the maximum of $q_c/(1+A)$? In all three problems the maximum is obtained by varying A and either I or E.

For the case of α, ρ, and k independent of temperature, the solution of these three problems can easily be derived from (3) and (10) and (15)–(18). The results are summarized in Table I.

III. CONSIDERATIONS OF ENTROPY PRODUCTION

The above derivation presented in terms of maximization of the over-all efficiency tends to conceal the importance of the irreversible phenomena (Joule heating and thermal conduction). Therefore, it is worthwhile to briefly discuss an alternative approach.

For a reversible process the entropy production is of course zero. For an irreversible process the rate of entropy production may be used as a measure of the irreversibility. It will now be shown that the conditions for maximum generator efficiency derived in the preceding section can also be obtained by minimizing the entropy production per unit work output. Or, in other words, the conditions derived above are precisely the conditions which minimize the irreversible processes.

If q_h and q_c are the heat flows from the hot and cold reservoir, respectively, the rate of entropy production $\dot{S}$ per unit power output of a thermoelectric generator can be written for $L=1$

$$\frac{\dot{S}}{P_0}=\left[-\frac{q_h}{T_h}+\frac{q_c}{T_c}\right]\Big/I^2R, \quad (19)$$

TABLE I.

			E	A
I	$\varphi_{\max}=\dfrac{T_c}{T_h-T_c}\dfrac{(1+\bar{T}z)^{\frac{1}{2}}-(T_h/T_c)}{(1+\bar{T}z)^{\frac{1}{2}}+1}$	(1)	$\dfrac{\alpha\Delta T(1+\bar{T}z)^{\frac{1}{2}}}{(1+\bar{T}z)^{\frac{1}{2}}-1}$	$\left(\dfrac{\rho_n k_p}{\rho_p k_n}\right)^{\frac{1}{2}}$
II	$\Delta T_{\max}=zT_c^2/2$	(2)	αT_h	$\left(\dfrac{\rho_n k_p}{\rho_p k_n}\right)^{\frac{1}{2}}$
III	$\left(\dfrac{q_c}{1+A}\right)_{\max}=\dfrac{1}{L(1+A)}\left[\dfrac{\alpha^2T_c^2}{2(\rho_p+A^{-1}\rho_n)}-\Delta T(k_p+Ak_n)\right]$	(3)	αT_h	$\dfrac{\rho_n B+\{(\rho_n/\rho_p)[1+B(\rho_n-\rho_p)]\}^{\frac{1}{2}}}{1-B\rho_p}$ where: $B=2(k_p-k_n)\Delta T/\alpha^2T_c^2$

where

$$q_h=(k_p+Ak_n)\Delta T-1/2(\rho_p+\rho_nA^{-1})I^2+\alpha T_hI \quad (20)$$

and

$$q_c=-(k_p+Ak_n)\Delta T-1/2(\rho_p+\rho_nA^{-1})I^2-\alpha T_cI. \quad (21)$$

It is seen that the last term (the Peltier heat), being reversible, does not contribute to $\dot{S}$. Upon minimization of $\dot{S}/P_0$ by varying R and A, the criteria given by (14) are again obtained. Thus, this choice of parameters minimizes the irreversible processes and therefore gives the maximum efficiency by allowing a closer approach to the Carnot cycle.

IV. APPROACH 1—AVERAGE PARAMETERS

An obvious possibility is simply to substitute average values for all the parameters occurring in the equations derived for the constant parameter case. For z one can substitute

$$z_h=\left[\frac{\langle\alpha_{pn}\rangle}{\langle\rho_pk_p\rangle^{\frac{1}{2}}+\langle\rho_nk_n\rangle^{\frac{1}{2}}}\right]^2, \quad (22)$$

where $\langle x\rangle$ is the temperature average value of $x(T)$. Joffe[10] purports to prove that for small τ the Thomson heat is correctly taken into account if $\langle\alpha\rangle$ is used in the calculation of z. However, his proof is not valid since he neglects the second part of the Thomson heat term in (10). He also states that to a first approximation the temperature dependence of ρ and k can be taken into account by replacing ρk by $\langle\rho k\rangle$. However, no proof is given. Nonetheless, z_h will be used rather than $\langle z\rangle$, the average value of $z(T)$. In Sec. VII it will be shown that these approaches give surprisingly accurate results in some cases, and serious disagreement in other cases.

V. APPROACH 2—INFINITE STAGING*

A rather different approach to the problem has been taken by Coles[3] and Zener.[11] In their work the efficiency is calculated by breaking up the working temperature interval into an infinite number of stages. If the calculation is done in this manner they claim that (1) the result is exact even for arbitrary temperature variation of α, ρ, and k, and that (2) the result is an upper limit on the efficiency obtainable with a single set of materials over the given temperature range. These two points, however, are not proved in the work referred to. In this section their approach will be outlined and, in addition, proofs will be indicated for the two claims.

To solve this problem it is first necessary to know the efficiency of a single stage in which the physical parameters have arbitrary temperature variation and in which ΔT and L both approach zero while $\Delta T/L$ remains finite. In this case the parameters may be expanded into a power series in t where $t=(T-T_c)$. Terms of the other t^2 will be dropped. For example the Thermal conductivity can be written $k=k_0+k_1t$, where $k_0=k(T_c)$ and $k_1=(dk/dT)_{T=T_c}$. With these substitutions (4) reduces to

$$k_0\frac{d^2t}{dx^2}-\tau_0J\frac{dt}{dx}+\rho_0J^2+k_1\left(\frac{dt}{dx}\right)^2+\left\{k_1\frac{d^2t}{dx^2}-\tau_1J\frac{dt}{dx}+\rho_1J^2\right\}t=0. \quad (23)$$

Since (a) ΔT approaches zero and $0\leq t\leq\Delta T$ and (b) the bracket remains finite, the last term can be made arbitrarily small. Hence it can be omitted. By the use of the standard substitution $p=dt/dx$, it can easily be shown that the first integral of the remaining differential equation is of the form $f(p)=x$. Since $0\leq x\leq L$ and L approaches zero, the change in p over the stage can be made as small as desired by choosing L small. Thus as L approaches zero, dt/dx approaches $\Delta T/L$.

[10] Reference 4, p. 114.

* *Note added in proof.*—After this paper was submitted for publication, a paper by A. H. Boerdijk was published in which the results of this section are given. However, the approach to the problem is somewhat different in the two treatments, Boerdijk's work being more abstract than ours [J. Appl. Phys. **30**, 1080 (1959)].

[11] C. Zener, *Proceedings of the Washington Conference on Thermoelectricity* (John Wiley & Sons, Inc., New York) (to be published).

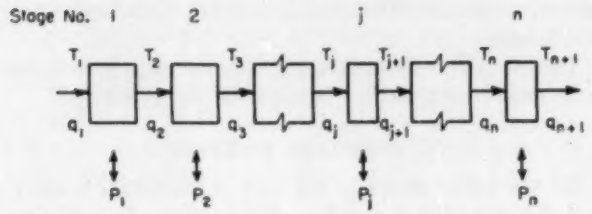

FIG. 2. An n-stage thermoelectric device showing the notation for the interstage heat fluxes q and temperatures T. For a generator T_1 is the hot temperature T_h and T_{n+1} is the cold temperature T_c. For a cooling device, the cold temperature T_c is T_1 and the hot temperature T_h is T_{n+1}.

Hence from (1) and (2), the efficiency is

$$\eta=\frac{I^2R}{\pi_h I+(k_{0p}+Ak_{0n})\Delta TL^{-1}}. \tag{24}$$

If (24) is now optimized with respect to R and A one finds

$$\eta=\frac{\Delta T}{T}\cdot\frac{(1+Tz)^{\frac{1}{2}}-1}{(1+Tz)^{\frac{1}{2}}+1}. \tag{25}$$

Expression (25) is exact. Therefore, one may now calculate the efficiency of an infinite stage generator as shown schematically in Fig. 2.

From (1) and (25), the power output of the jth stage is

$$P_j=\frac{\delta T_j}{T_j}\cdot\frac{(1+T_jz)^{\frac{1}{2}}-1}{(1+T_jz)^{\frac{1}{2}}+1}q_j\equiv\epsilon(T_j)\frac{\delta T_j}{T_j}q_j, \tag{26}$$

where $\delta T_j=T_j-T_{j+1}$. The heat flowing into the $(j+1)$th stage is then

$$q_{j+1}=q_j-P_j=q_j\left[1-\epsilon(T_j)\frac{\delta T_j}{T_j}\right]. \tag{27}$$

Therefore the heat leaving the cold junction of the device is

$$q_0=q_{n+1}=q_1\prod_{j=1}^{n}\left[1-\epsilon(T_j)\frac{\delta T_j}{T_j}\right]. \tag{28}$$

In the limit $n\to\infty$ $(\delta T\to 0)$, (28) reduces to

$$q_0=q_1\exp\left[-\int_{T_c}^{T_h}\epsilon(T)dT/T\right]. \tag{29}$$

Hence the efficiency is

$$\eta_\infty=\frac{q_1-q_0}{q_1}=1-\exp\left[-\int_{T_c}^{T_h}\epsilon(T)dT/T\right]. \tag{30}$$

As the calculation of the coefficient of performance of an infinite stage cooling device is quite similar, only the result will be given here; it is

$$\varphi=\left\{\exp\left[\int_{T_c}^{T_h}\frac{dT}{T\epsilon(T)}\right]-1\right\}^{-1}. \tag{31}$$

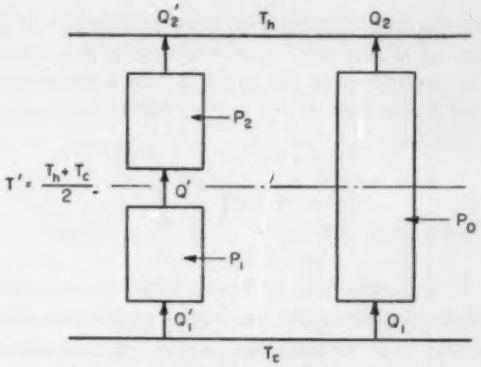

FIG. 3. Schematic diagram showing comparison of two stage and single stage devices.

If, now ϵ is independent of temperature, (30) and (31) take on particularly simple forms. One finds for the efficiency of a generator

$$\eta=\frac{T_h^{\epsilon}-T_c^{\epsilon}}{T_h^{\epsilon}}, \tag{32}$$

and for the coefficient of performance of a refrigerator

$$\varphi=\frac{T_c^{1/\epsilon}}{T_h^{1/\epsilon}-T_c^{1/\epsilon}}. \tag{33}$$

Thus, in the generator case, for example, the efficiency is simply the Carnot efficiency using "effective temperature" T_h^{ϵ} and T_c^{ϵ} in place of T_h and T_c.

It remains to demonstrate that the infinite stage device does give the maximum efficiency (or coefficient of performance) for given thermocouple materials. As the proof of this point is rather cumbersome, although straightforward, it will only be outlined here. In order to be able to carry the argument through analytically, the case of temperature independent parameters will be considered. The method used is simply to show that it is always beneficial to break up a given temperature interval into two stages. Establishment of this result would, of course, prove that infinite staging gives the maximum performance. If reference is made to Fig. 3, the ratio of the coefficients of performance for the single stage and two stage device may be written

$$\frac{\varphi_{SS}}{\varphi_{TS}}=\frac{Q_1}{P_0}\left\{\frac{P_1}{Q_1'}+\frac{P_2}{Q'}+\frac{P_1P_2}{Q_1'Q'}\right\}, \tag{34}$$

where, for example,

$$\frac{Q_1'}{P_1}=\frac{T_c}{T'-T_c}\cdot\frac{\{1+[T'-(\Delta T/2)]z\}^{\frac{1}{2}}-(T'/T_c)}{\{1+[T'-(\Delta T/2)]z\}^{\frac{1}{2}}+1}. \tag{35}$$

The terms in (35) can now be expanded in a power series in $\Delta T/T$. In order to evaluate (34) it is necessary to go to second order in $\Delta T/T$ as the first-order term turns out to be zero. If one carries out these expansions, it is found that

$$\frac{\varphi_{SS}}{\varphi_{TS}}=1-A\left(\frac{\Delta T}{T}\right)^2, \tag{36}$$

where A is a positive number. Thus, it is seen that infinite staging gives the maximum performance.

The fact that infinite staging gives the maximum efficiency can also be understood on the basis of minimum entropy production. In Sec. III it was seen that the choice of load resistance and area ratio of the arms which gave maximum efficiency also minimized the irreversible effects or, in other words, minimized the entropy production. In the present problem the two adjustable parameters of the single stage device have been replaced by an essentially infinite number of parameters. It is this fact which allows for minimization of the irreversible effects and a consequent maximization of efficiency.

In Sec. VII, the results for infinite staging will be compared with those for single stage operation.

VI. APPROACH 3—EXACT

In the power problem we wish to maximize η as A and R are varied through positive values. In addition to the maximizing values of A and R and the maximum value of η we want the quantities $-k_p(T_h)T_p'(0)$ and $-Ak_n(T_h)T_n'(0)$ and the temperature distributions $T_p(x)$ and $T_n(x)$ corresponding to these maximizing values.

The functions $\alpha_{pn}(T)$, $k_i(T)$, and $\rho_i(T)$ $(i=p,\ n)$ are positive in the interval I extending from $T=T_c$ to $T=T_h$, and the products $\gamma_i=\rho_i k_i$ are of order of magnitude 10^{-4}. The functions $\tau_i(T)$ need not be of one sign in I; the order of magnitude of τ_i is also 10^{-4}. We restrict the functions and parameters in the Eq. (4) in such a way that the solution $T(x)$ is a decreasing function of x.

Introducing (2), (3), (6), and (8) into (1) we get

$$\eta=\frac{\int_{T_c}^{T_h}\alpha_{pn}(T)dT-J_p\int_0^L\rho_p(T)dx+J_n\int_0^L\rho_n(T)dx}{-(1/J_p)k_p(T_h)T_p'(0)+(1/J_n)k_n(T_h)T_n'(0)+\alpha_{pn}(T_h)T_h}. \tag{37}$$

Using (4) we have

$$J_i\int_0^L\rho_i(T)dx=-\int_{T_c}^{T_h}\tau_i(T)dT$$

$$-\frac{1}{J_i}[k_i(T_c)T_i'(L)-k_i(T_h)T_i'(0)], \tag{38}$$

and introducing (38) into (37)

$$\eta=1-\frac{\pi_c-(1/J_p)k_p(T_c)T_p'(L)+(1/J_n)k_n(T_c)T_n'(L)}{\pi_h-(1/J_p)k_p(T_h)T_p'(0)+(1/J_n)k_n(T_h)T_n'(0)}. \tag{39}$$

The function

$$y_i(T)=-k_i(T)/J_i x_i'(T) \tag{40}$$

is positive if $i=p$ and negative if $i=n$ and satisfies the equation

$$y_i'(T)=-\tau_i(T)-\frac{\gamma_i(T)}{y_i(T)} \tag{41}$$

and the condition

$$\int_{T_c}^{T_h}\frac{k_i(T)}{y_i(T)}dT=-\int_{T_c}^{T_h}J_i x_i'(T)dT=J_i L. \tag{42}$$

In terms of y_p and y_n the efficiency is

$$\eta=1-\frac{y_p(T_c)-y_n(T_c)+\pi_c}{y_p(T_h)-y_n(T_h)+\pi_h}. \tag{43}$$

Taking $y_p(T_h)$ and $y_n(T_h)$ as independent variables we may formulate the maximum problem as follows: find the maximum of η as defined by (43), where $y_p(T_h)=\xi_p$ and $y_n(T_h)=\xi_n$ are independent variables subject to the restrictions $\xi_p\geqq 0$, $\xi_n\leqq 0$ and $y_i(T_c)$ is determined in terms of ξ_i by solving (41) subject to the condition $y_i(T_h)=\xi_i$. Thus, writing $y_i(T_c)=y_i(T_c,\xi_i)$ to make the dependence on ξ_i clear,

$$\eta=1-\frac{y_p(T_c,\xi_p)-y_n(T_c,\xi_n)+\pi_c}{\xi_p-\xi_n+\pi_h}. \tag{44}$$

The maximizing ξ_p and ξ_n immediately determine the maximum η, and they determine J_p and J_n through (42). From this we get, after some simple calculations using (6), (8), and (38),

$$\begin{aligned} A&=-J_p/J_n,\\ R&=\frac{\eta}{J_p}(\xi_p-\xi_n+\pi_h),\\ -k_p(T_h)T_p'(0)&=J_p\xi_p,\\ -Ak_n(T_h)T_n'(0)&=-J_p\xi_n. \end{aligned} \tag{45}$$

Through each point (T_h,ξ_i), with $\xi_i\neq 0$, there passes an integral curve of (41) which does not intersect the T axis in I and passes through the point $[T_c,y_i(T_c,\xi_i)]$. For suppose T_0 is the first zero to the left of T_h of the integral curve $y_i(T)$ for which $y_i(T_h)=\xi_i>0$ (a similar argument will hold for $\xi_i<0$). Then $y_i'(T)$ and $y_i(T)$ are positive in the right vicinity of T_0 and the equation

$$y_i(T)y_i'(T)+y_i(T)\tau_i(T)+\gamma_i(T)=0$$

implies a contradiction as $T\to T_0$, since $\gamma_i(T)>0$. If $\xi_i=0$ then the integral curve of (41) has a vertical tangent and one branch lies entirely above and the other entirely below the T axis in $T_c\leqq T<T_h$. Increasing ξ_i raises the integral curve throughout I; otherwise two integral curves would intersect, thus producing two solutions of (41) through the point of intersection. The integral curves diverge to the right, or alternatively converge to the left, over I. It is for this reason that we have chosen the ordinates at T_h as the independent variables in restating the maximum problem rather than the ordinates at T_c. For if we use numerical procedures to solve (41), and we shall do so, it reduces the error to work from right to left rather than from left to right. To prove this property let (T_1,y_1) and (T_2,y_2) be any two points on an integral curve $y_i(T)$, which $T_c\leqq T_1<T_2\leqq T_h$. Then

$$y_2=y_1+\int_{T_1}^{T_2}y_i'(T)dT=y_1-\int_{T_1}^{T_2}\left(\tau_i+\frac{\gamma_i}{y_i}\right)dT,$$

from which we get

$$\frac{dy_2}{dy_1}=1+\int_{T_1}^{T_2}\frac{\gamma_i}{y_i^2}\frac{dy_i}{dy_1}dT.$$

Since γ_i/y_i^2 and dy_i/dy_1 are both positive we have $dy_2/dy_1>1$, and this proves the divergence property.

We derive an approximate solution of (41) as follows. We write (41) as an integral equation

$$y_i(T)=\xi_i+\int_T^{T_h}\tau_i(T)dT+\int_T^{T_h}\frac{\gamma_i(T)}{y_i(T)}dT, \quad (46)$$

whose solution can be obtained by forming the sequence

$$y_i^{(n)}(T)=\xi_i+\int_T^{T_h}\tau_i(T)dT+\int_T^{T_h}\frac{\gamma_i(T)}{y_i^{(n-1)}(T)}dT. \quad (47)$$

We get a good first approximation by taking $\tau_i=0$ in (41) and solving exactly the resulting equation. This is plausible since τ_i is of order of magnitude 10^{-4}. This exact solution is

$$y_i^{(1)}(T)=\pm\left[\xi_i^2+2\int_T^{T_h}\gamma_i(T)dT\right]^{\frac{1}{2}}, \quad (48)$$

where the sign is chosen to coincide with that of ξ_i. Since $dy_i^{(1)}/dT=-\gamma_i/y_i^{(1)}$ we get the second approximation explicitly

$$y_i^{(2)}(T)=\int_T^{T_h}\tau_i(T)dT+y_i^{(1)}(T). \quad (49)$$

We can suppose $y_i^{(2)}(T)$ is a good approximation to $y_i(T)$ if the first term on the right of (49) is small compared to $y_i^{(1)}(T)$. If $\tau_i(T)$ is of one sign in I we can make a stronger statement. Suppose $\tau_i(T)\geqq 0$; then an inspection of (41) shows that $y_i(T)\geqq y_i^{(1)}(T)$ in the left vicinity of T_h. Furthermore this inequality persists throughout I. For if not we would have, at the first point of intersection to the left of T_h,

$$\frac{dy_i}{dT}-\frac{dy_i^{(1)}}{dT}=-\tau_i(T)\leqq 0,$$

and this contradicts the fact that the slope of $y_i(T)$ would exceed that of $y_i^{(1)}(T)$ at such a point. Subtracting (41) from

$$\frac{dy_i^{(2)}}{dT}=-\tau_i-\frac{\gamma_i}{y_i^{(1)}}$$

we get

$$\frac{d}{dT}[y_i^{(2)}-y_i]=\gamma_i\frac{y_i^{(1)}-y_i}{y_i^{(1)}y_i}\leqq 0.$$

Thus $y_i^{(2)}(T)-y_i(T)$ is a decreasing function of T in I, and since this difference is zero at T_h we have $y_i^{(2)}(T)\geqq y_i(T)$. Hence $\tau_i(T)\geqq 0$ in I implies $y_i^{(2)}(T)\geqq y_i(T)\geqq y_i^{(1)}(T)$; an analogous argument shows that $\tau_i(T)\leqq 0$ implies $y_i^{(2)}(T)\geqq y_i(T)\geqq y_i^{(1)}(T)$. It follows then that $y_i(T)$ differs from $y_i^{(1)}(T)$ or $y_i^{(2)}(T)$ by less than

$$\left|\int_T^{T_h}\tau_i(T)dT\right|.$$

We seek now to solve the maximum problem using the approximation $y_i^{(2)}(T)$. Setting $T=T_c$ in (49) we have

$$y_i^{(2)}(T_c,\xi_i)=\int_{T_c}^{T_h}\tau_i(T)dT \pm\left[\xi_i^2+2\int_{T_c}^{T_h}\gamma_i(T)dT\right]^{\frac{1}{2}}, \quad (50)$$

where the sign is chosen to coincide with that of ξ_i. Thus writing

$$\zeta=\pi_c+\int_{T_c}^{T_h}[\tau_p(T)-\tau_n(T)]dT,$$
$$c_i^2=2\int_{T_c}^{T_h}\gamma_i(T)dT, \quad (51)$$

we get for η the expression

$$\eta=1-\frac{(\xi_p^2+c_p^2)^{\frac{1}{2}}+(\xi_n^2+c_n^2)^{\frac{1}{2}}+\zeta}{\xi_p-\xi_n+\pi_h}=1-\frac{A}{B}. \quad (52)$$

We wish to maximize η for $\xi_p\geqq 0$ and $\xi_n\leqq 0$. We note first that $\pi_h>0$. If $\zeta>\pi_h$ then $\eta<0$ and this situation cannot occur in actuality. Also if $\zeta<0$ and $c_p+c_n<|\zeta|$ then $A=0$ has real solutions and thus η can be made equal to 1; thus situation also cannot occur in reality. In all other cases a maximum exists and can be found by setting the partial derivatives to 0

$$\frac{1}{B^2}\left[\frac{B\xi_p}{(\xi_p^2+c_p^2)^{\frac{1}{2}}}-A\right]=0, \quad \frac{1}{B^2}\left[\frac{B\xi_n}{(\xi_n^2+c_n^2)^{\frac{1}{2}}}+A\right]=0.$$

From these two equations we derive

$$\frac{\xi_p}{(\xi_p^2+c_p^2)^{\frac{1}{2}}}=\frac{-\xi_n}{(\xi_n^2+c_n^2)^{\frac{1}{2}}}=\frac{(\xi_p^2+c_p^2)^{\frac{1}{2}}+(\xi_n^2+c_n^2)^{\frac{1}{2}}+\zeta}{\xi_p-\xi_n+\pi_h}, \quad (53)$$

and these yield

$$\xi_h=-\frac{c_n}{c_p}\xi_p, \quad (54)$$

$$\pi_h\xi_p=c_p^2+c_pc_n+\zeta(\xi_p^2+c_p^2)^{\frac{1}{2}}. \quad (55)$$

Thus

$$\xi_p=\frac{c_p}{\pi_h^2-\zeta^2}\{\pi_h(c_p+c_n)\pm\zeta[(c_p+c_n)^2+\pi_h^2-\zeta^2]^{\frac{1}{2}}\}. \quad (56)$$

Inspection of (55) yields the following choice of sign in (56):

$$\pi_h>\zeta>0, \quad +,$$
$$\zeta<0, \quad \pi_h>|\zeta|, \quad -,$$
$$\zeta<0, \quad \pi_h<|\zeta|, \quad +.$$

Thus the maximum η is, using (53)

$$\eta_{\max}=1-\frac{\xi_p}{(\xi_p^2+c_p^2)^{\frac{1}{2}}}, \quad (57)$$

where ξ_p is given by (56). Inserting the maximizing ξ_p and ξ_n in (49) we get the corresponding $y_p(T)$ and $y_n(T)$; these can be used to give us the desired quantities (45), using (42) to calculate J_p and J_n. From (57) we can get some idea of the order of magnitude of the maximizing ξ_p and ξ_n. Solving for ξ_p we get

$$\xi_p=\frac{1-\eta}{[1-(1-\eta)^2]^{\frac{1}{2}}}\left[2\int_{T_c}^{T_h}\gamma_p(T)dT\right]^{\frac{1}{2}},$$

where $\eta=\eta_{\max}$. Taking η between 0.03 and 0.30, taking $\gamma_p(T)=10^{-4}$, and taking a representative difference $T_h-T_c=400$ we get values of ξ_p between 1.12 and 0.28; ξ_n is of the same order of magnitude. Equation (41) implies that the corresponding $y_i(T)$ will be close to horizontal straight lines.

We consider now the numerical solution over I of

$$y'(T)=-\tau(T)-\frac{\gamma(T)}{y(T)} \quad (58)$$

subject to the condition $y(T_h)=\xi$. Let the interval I be divided into n equal subintervals of length $h=(T_h-T_c)/n$, with T_k the left end point of the kth interval. From (58) we get

$$y(T_k)=y(T_{k+1})+\int_{T_k}^{T_{k+1}}\tau(T)dT+\int_{T_k}^{T_{k+1}}\frac{\gamma(T)}{y(T)}dT. \quad (59)$$

Applying the trapezoidal rule to the second integral on the right of (59) we get the following recursion relation which generates quantities z_k starting with $z_{n+1}=\xi$:

$$z_k=z_{k+1}+\int_{T_k}^{T_{k+1}}\tau(T)dT+\frac{h}{2}\left(\frac{\gamma_k}{z_k}+\frac{\gamma_{k+1}}{z_{k+1}}\right). \quad (60)$$

Here $\gamma_k=\gamma(T_k)$. This method of solving (58) is sometimes called the modified Euler method. The method is obviously inapplicable should $\xi=0$, and for very small values of ξ the accuracy will be insufficient. In this event we can proceed by calculating $y^{(2)}(T_h-1)$ and then solving (58) over the range $T_c\leqq T\leqq T_h-1$, using $y^{(2)}(T_h-1)$ as the initial value. In order to make a proper choice of h we need to make an error analysis of method (60). We defer this analysis to the end of the section.

We obtain a numerical solution to the problem of maximizing η as follows. For the initial ξ_p and ξ_n we use the values (56) and (54). Next we calculate $y_p(T_c,\xi_p)$ and $y_n(T_c,\xi_n)$ using method (60) and then calculate η by (44). Then on the assumption that these initial values of ξ_p and ξ_n bring us fairly near the maximum we probe for the maximum by trial and error. After the maximizing ξ_p and ξ_n and the maximum η are obtained we use the corresponding functions $y_p(T)$ and $y_n(T)$ to calculate J_p and J_n by (42), using numerical methods to evaluate the integrals. Then quantities (45) are calculated, and finally the temperature distributions $T_i(x)$ are obtained from

$$x_i(T)=\frac{1}{J_i}\int_T^{T_h}\frac{k_i(T)}{y_i(T)}dT. \quad (61)$$

Thus we have a complete numerical solution of the power problem.

We consider now the refrigeration problem. The assertions, in the power problem, regarding the signs and orders of magnitude of the functions ρ_i, k_i, τ_i, and α_{pn} apply to the refrigerator problem also. The range T_c to T_h will be about 60 to 80°. However we abandon the restriction that $T_i(x)$ be a decreasing

function in those parts of the problem dealing with the minimization of T_c and the maximization of $q_c/(1+A)$.

In terms of the variables ξ_p and ξ_n we may write

$$\varphi=\frac{\omega}{1-\omega}, \tag{62}$$

where

$$\omega=\frac{y_p(T_c,\xi_p)-y_n(T_c,\xi_n)+\pi_c}{\xi_p-\xi_n+\pi_h}. \tag{63}$$

Thus the problem of maximizing φ relative to variations in I and A is equivalent to maximizing ω subject to variations in $\xi_p\leqq 0$ and $\xi_n\geqq 0$. Introducing the functions $y_i^{(2)}(T_c,\xi_i)$ into (63) we get the approximate maximizing values ξ_p and ξ_n given by (56) and (54), with the minus sign chosen in (56). From this point we may proceed by using (60) and trial and error probing to maximize ω and φ. E is given by

$$E=\pi_h-\pi_c+\xi_p-y_p(T_c,\xi_p)-\xi_n+y_n(T_c,\xi_n), \tag{64}$$

and the temperature distribution by (61). J_p and J_n are determined by (42) and

$$I=-J_p, \quad A=-J_p/J_n. \tag{65}$$

In the second and third refrigeration problem we abandon the restriction that $T_i(x)$ be a decreasing function. Inspection of (4) shows that $T_i(x)$ can have no minimum; this follows by carrying out the differentiation of the first term, using the fact that $k_i>0$ and $\rho_i>0$, and observing that at a minimum $T_i'(x)=0$ and $T_i''(x)\geqq 0$. Hence $T_i(x)$ may increase to a maximum, starting from the point $(0,T_h)$, and then decrease to (L,T_c). The corresponding integral curve $y_i(T)$ behaves as follows: if $i=p$ then $\xi_p>0$ and $y_p(T)$ issues from the point (T_h,ξ_p), proceeds to the right and intersects the T axis at T_p^*, and then goes to the left intersecting $T=T_h$ at ξ_p^* and $T=T_c$ at $y(T_c,\xi_p)$. The integral curve $y_n(T)$ behaves similarly and we adopt a similar notation for it.

The second refrigeration problem may be phrased, in terms of ξ_p and ξ_n, as follows; find the minimum value of T, where T is implicitly defined by

$$\alpha_{pn}(T)T+y_p(T,\xi_p)-y_n(T,\xi_n)=0. \tag{66}$$

Here ξ_p and ξ_n may assume any values, and $y_p(T,\xi_p)$ and $y_n(T,\xi_n)$ are determined, when $\xi_p>0$ and $\xi_n<0$, by the convention described above. However to each $\xi_p>0$ and to each $\xi_n<0$ there corresponds a $\xi_p^*<0$ and $\xi_n^*>0$ such that $y_p(T,\xi_p)=y_p(T,\xi_p^*)$ and $y_n(T,\xi_n)=y_n(T,\xi_n^*)$. For this reason the range of values assumed by T, as defined by (66), is not changed if we impose the restriction $\xi_p\geqq 0$ and $\xi_n\geqq 0$. Hence we need only find the minimum value of T subject to this restriction. We will show that the minimizing values are $\xi_p=\xi_n=0$; thus T is the solution of

$$\alpha_{pn}(T)T+y_p(T,0)-y_n(T,0)=0. \tag{67}$$

We have

$$\frac{\partial}{\partial T}[\alpha_{pn}(T)T+y_p(T,\xi_p)-y_n(T,\xi_n)]\frac{\partial T}{\partial \xi_p}+\frac{\partial y_p(T,\xi_p)}{\partial \xi_p}=0. \tag{68}$$

Since

$$\frac{\partial}{\partial T}\alpha_{pn}(T)T=\alpha_{pn}(T)+\alpha_{pn}'(T)T=\alpha_{pn}(T)+\tau_p(T)-\tau_n(T),$$

$$\frac{\partial}{\partial T}y_i(T,\xi_i)=-\tau_i(T)-\frac{\gamma_i(T)}{y_i(T,\xi_i)},$$

we may write (68)

$$\left[\alpha_{pn}(T)+\frac{\gamma_n(T)}{y_n(T,\xi_n)}-\frac{\gamma_p(T)}{y_p(T,\xi_p)}\right]\frac{\partial T}{\partial \xi_p}+\frac{\partial y_p(T,\xi_p)}{\partial \xi_p}=0. \tag{69}$$

Since

$$\alpha_{pn}(T)\geqq 0, \quad y_n(T,\xi_n)>0, \quad y_p(T,\xi_p)<0, \quad \frac{\partial y_p(T,\xi_p)}{\partial \xi_p}\geqq 0,$$

we get $\partial T/\partial \xi_p\leqq 0$. Similarly we can show that $\partial T/\partial \xi_n\geqq 0$. Thus T is a decreasing function of ξ_p and an increasing function of ξ_n and therefore achieves its minimum value when $\xi_p=\xi_n=0$. The practical solution of (67) for the minimium T can be accomplished by evaluating the left side of (67) starting at T_c and working down, first in five degree steps and then in one degree steps. This might require 5 to 10 evaluations. Of course use of the method (60) to evaluate $y_p(T,0)$ and $y_n(T,0)$ requires that we start with $\xi_i=y_i^{(2)}(T_h-1)$. To calculate J_i we have

$$J_iL=\int_{T_{\min}}^{T_h-1}\frac{k_i(T)}{y_i(T,0)}dT+\int_{T_h-1}^{T_h}\frac{k_i(T)}{y_i(T,0)}dT. \tag{70}$$

The first integral on the right of (70) can be numerically evaluated; the second integral we approximate by

$$\int_{T_h-1}^{T_h}\frac{k_i(T)}{y_i^{(2)}(T,0)}dT=\int_{T_n-1}^{T_h}\frac{k_i(T)dT}{\int_T^{T_h}\tau_i(T)dT\pm\left(2\int_T^{T_h}k_i(T)dT\right)^{\frac{1}{2}}}, \tag{71}$$

where the choice of sign is $+$ if $i=n$ and $-$ if $i=p$. The

integral on the right of (71) we approximate by

$$\int_{T_k-1}^{T_k} \frac{k_i dT}{\tau_i(T_k-T)\pm[2\gamma_i(T_k-T)]^{\frac{1}{2}}} = \frac{2k_i}{\tau_i}\log\left[1\pm\frac{\tau_i}{(2\gamma_i)^{\frac{1}{2}}}\right], \quad (72)$$

where, on the right of (72), the choice of sign is + if $i=n$ and − if $i=p$, and τ_i, k_i, and γ_i are the average values of $\tau_i(T)$, $k_i(T)$, and $\gamma_i(T)$ over the interval $T_k-1\leqq T\leqq T_k$. The quantities I and A are given by (65). E is given by (64) with $\xi_p=\xi_n=0$ and T_c replaced by $T_{\min}$; thus, using (67), $E=\pi_k$.

In the third refrigeration problem we have

$$\frac{q_c}{1+A}=\frac{y_p(T_c,\xi_p)-y_n(T_c,\xi_n)+\pi_c}{J_n^{-1}-J_p^{-1}}. \quad (73)$$

If we impose the restriction $\xi_p\leqq 0$ and $\xi_n\geqq 0$ then (73) is maximized for $\xi_p=\xi_n=0$, since $y_p(T_c,\xi_p)$ is maximized and $-J_p^{-1}$ minimized when $\xi_p=0$ and $-y_n(T_c,\xi_n)$ is maximized and J_n^{-1} minimized when $\xi_n=0$. Hence the maximum of (73) is attained when $\xi_p\geqq 0$ and $\xi_n\leqq 0$. We find this maximum by probing, taking T_p^* and T_n^* as the independent variables.† Thus we choose a value $T_p^*\geqq T_k$ and calculate the upper branch $y_p^+(T)$ of the integral curve $y_p(T)$ from T_p^* to T_n and the lower branch $y_p^-(T)$ from T_p^* to T_c, using the procedures described for the second refrigeration problem. This gives us the quantity $y_p(T_c,\xi_p)$, and J_p is given by

$$J_pL=\int_{T_c}^{T_p^*}\frac{k_p(T)}{y_p^-(T)}dT-\int_{T_k}^{T_p^*}\frac{k_p(T)}{y_k^+(T)}dT. \quad (74)$$

In the same way a choice of T_n^* yields the quantities $y_n(T_c,\xi_n)$ and J_n, with J_n given by

$$J_nL=\int_{T_c}^{T_k^*}\frac{k_n(T)}{y_n^+(T)}dT-\int_{T_k}^{T_n^*}\frac{k_n(T)}{y_n^-(T)}dT. \quad (75)$$

Thus (73) can be calculated and its maximum determined by probing. E, I, and A are given by (64) and (65), q_c is obtained from (73) by multiplying by $1+A$.

We conclude with some remarks on the error in the numerical procedure (60) We may write (59)

$$y_k=y_{k+1}+\int_{T_k}^{T_{k+1}}\tau(T)dT+\frac{h}{2}\left(\frac{\gamma_k}{y_k}+\frac{\gamma_{k+1}}{y_{k+1}}\right)-\frac{1}{12}h^3y''(T_k^*) \quad (76)$$

where $y_k=y(T_k)$ and $T_k\leqq T_k^*\leqq T_{k+1}$. Writing $E_k=z_k-y_k$ and substracting (76) from (60) we get

$$E_k=E_{k+1}-\frac{1}{2}h\left(\frac{\gamma_{k+1}}{y_{k+1}z_{k+1}}E_{k+1}+\frac{\gamma_k}{y_kz_k}E_k\right)+\frac{1}{12}h^3y''(T_k^*) \quad (77)$$

If we write

$$a_k=\left(1-\frac{h\gamma_{k+1}}{2y_{k+1}z_{k+1}}\right)\Big/\left(1+\frac{h\gamma_k}{2y_kz_k}\right),$$

$$b_k=\frac{1}{12}h^3y''(T_k^*)\Big/\left(1+\frac{h\gamma_k}{2y_kz_k}\right),$$

then (77) becomes

$$E_k=a_kE_{k+1}+b_k,$$

and we derive from this

$$E_1=a_1a_2\cdots a_nE_{n+1}+a_1a_2\cdots a_{n1}b_n+a_1a_2\cdots a_{n-2}b_{n-1}+\cdots+a_1b_2+b_1. \quad (78)$$

We suppose now that h is so small that all quantities $h\gamma_k/2y_kz_k$ are less than 1 (they are all positive since z_k and y_k will agree in sign). Then writing

$$s_k=\min(h\gamma_{k+1}/2y_{k+1}z_{k+1},\quad h\gamma_k/2y_kz_k),$$

we have

$$0<a_k\leqq\frac{1-s_k}{1+s_k}\leqq e^{-2s_k}.$$

Taking absolute values in (78) we have

$$|E_1|\leqq|E_{n+1}|a_na_{n-1}\cdots a_1+\sum_{k=1}^{n}\frac{|b_k|}{a_k}(a_ka_{k-1}\cdots a_1)$$

$$\leqq|E_{n+1}|\exp(-2\sum_{k=1}^{n}s_k)+\sum_{k=1}^{n}\frac{h^3|y''(T_k^*)|}{12[1-(h\gamma_{k+1}/2y_{k+1}z_{k+1})]}\times\exp(-2\sum_{j=1}^{k}s_k). \quad (79)$$

The right side of (79) approximates

$$|E_{n+1}|\exp\left(-\int_{T_c}^{T_k}\frac{\gamma}{y^2}dT\right)+\frac{h^2}{12}\int_{T_c}^{T_k}\frac{|y''|\exp\left(-\int_{T_c}^{T}(\gamma/y^2)dT\right)}{1-(h\gamma/2y^2)}dT. \quad (80)$$

If we introduce some simplifying assumptions the upper bound (80) to $|E_1|$ can be modified into various convenient forms. Assume $y''(T)$ is of one sign in I and

† This maximum need not exist; see the discussion in Sec. VII.

TABLE II.

ϑ	$y^{(0)}(T_c)$	$y^{(1)}(T_c)$	$y(T_c)$	z_1	(81)	(83)	$\lvert y(T_c)-z_1\rvert$
			$T_h-T_c=400$, $h=4$				
1.00	0.9992	1.0392	1.	1.	1.0×10^{-7}	5.1×10^{-6}	0
0.10	0.2600	0.3000	0.2717490	0.2717538	8.4×10^{-4}	5.0×10^{-4}	4.8×10^{-6}
0.03	0.2444	0.2844	0.2581528	0.2582170	5.0×10^{-3}	1.4×10^{-3}	6.4×10^{-5}
			$T_h-T_c=900$, $h=9$				
1.00	0.9963	1.0863	1.	1.	2.5×10^{-6}	5.3×10^{-6}	0
0.10	0.3459	0.4359	0.375594	0.375610	5.0×10^{-3}	2.4×10^{-3}	1.6×10^{-5}
0.03	0.3353	0.4253	0.367301	0.367497	4.1×10^{-2}	8.4×10^{-3}	2.0×10^{-4}

write $M=\max\gamma(T)/2y^2(T)$, where for the purpose of estimating M we take $y(T)=y^{(2)}(T)$. Then (80) is not in excess of

$$|E_{n+1}|+\frac{h^2}{12(1-hM)}\left|\int_{T_c}^{T_h}y''(T)dT\right|$$
$$=|E_{n+1}|+\frac{h^2}{12(1-hM)}|y'(T_h)-y'(T_c)|$$
$$=|E_{n+1}|+\frac{h^2}{12(1-hM)}\left|\tau(T_h)+\frac{\gamma(T_h)}{y(T_h)}-\left[\tau(T_c)+\frac{\gamma(T_c)}{y(T_c)}\right]\right|. \quad (81)$$

Here $y(T_h)=\xi$ and $y(T_c)$ is estimated by $y^{(2)}(T_c)$. Thus (81) is an upper bound to the error in calculating $y(T_c)$ using (60); except when the initial ξ is estimated from $y^{(2)}(T)$, $E_{n+1}=0$. For small values of ξ, neglect of the exponential term in (80) may cause the upper bound (81) to be unnecessarily large. We take the exponential term into account by taking $y(T)=y^{(1)}(T)$ in (80); this is plausible since, when ξ is small, the error involved in applying (60) to solve (58) should be of the same order of magnitude in the two cases $\tau=10^{-4}$ and $\tau=0$. Since

$$\exp\left[-\int_{T_c}^{T}\frac{\gamma}{(y^{(1)})^2}dT\right]=\exp\left[+\int_{T_c}^{T}\frac{1}{y^{(1)}}\frac{dy^{(1)}}{dT}dT\right]=\frac{y^{(1)}(T)}{y^{(1)}(T_c)},$$

the quantity (80) is not in excess of

$$|E_{n+1}|\frac{y^{(1)}(T_h)}{y^{(1)}(T_c)}+\frac{h^2}{12(1-hM)}\left|\int_{T_c}^{T_h}\frac{y^{(1)}(T)}{y^{(1)}(T_c)}\frac{d^2y^{(1)}}{dT^2}dT\right|$$
$$=|E_{n+1}|\frac{y^{(1)}(T_h)}{y^{(1)}(T_c)}+\frac{h^2}{12(1-hM)}\left|\frac{y^{(1)}(T_h)}{y^{(1)}(T_c)}y^{(1)\prime}(T_h)-y^{(1)\prime}(T_c)-\frac{1}{y^{(1)}(T_c)}\int_{T_c}^{T_h}\left(\frac{dy^{(1)}}{dT}\right)^2dT\right|. \quad (82)$$

We have now

$$\int_{T_c}^{T_h}\left(\frac{dy^{(1)}}{dT}\right)^2dT=\int_{T_c}^{T_h}\frac{\gamma^2}{[y^{(1)}]^2}dT=\gamma^*\int_{T_c}^{T_h}\frac{\gamma}{[y^{(1)}]^2}dT$$
$$=\gamma^*\log\frac{y^{(1)}(T_c)}{y^{(1)}(T_h)},$$

where γ^* is some intermediate value between $\max\gamma(T)$ and $\min\gamma(T)$. Thus (80) is not in excess of

$$|E_{n+1}|\frac{y^{(1)}(T_h)}{y^{(1)}(T_c)}+\frac{h^2}{12(1-hM)}\left|\frac{\gamma(T_c)-\gamma(T_h)}{y^{(1)}(T_c)}-\frac{\gamma^*}{y^{(1)}(T_c)}\log\frac{y^{(1)}(T_c)}{y^{(1)}(T_h)}\right|. \quad (83)$$

To compare the two bounds (81) and (83) we construct Table II below. Here $\tau(T)=-10^{-4}$, $\gamma(T)=10^{-4}$, and we take two representative ranges $T_h-T_c=400$ and $T_h-T_c=900$ with subdivisions into 100 intervals in each case. Also $E_{n+1}=0$. We note from Table II that the upper bounds (81) and (83) are considerably in excess of the actual error $|y(T_c)-z_1|$.

The assumption that $y''(T)$ is of one sign is true if τ and γ are constant. The assumption is plausible when τ and γ do not vary much over I. When it is not reasonable to make the assumption it becomes necessary to experiment with the subinterval size h. In this connection we note from (80) that halving h reduces the error by a factor of approximately $\frac{1}{4}$. Thus if z_1 and z_1^* are the calculated values using subdivisions of size h and $h/2$ then $y(T_c)-z_1^*=[y(T_c)-z_1]/4$, from which we deduce that $y(T_c)-z_1=4(z_1^*-z_1)/3$ and $y(T_c)-z_1^*=(z_1^*-z_1)/3$. The right sides estimate the error when subdivisions of size h and $h/2$ are used.

VII. DISCUSSION

(a) Power Generation

Throughout this section L will be taken as 1 cm.

Calculations have been made for three different power generators. The properties of the thermoelectric

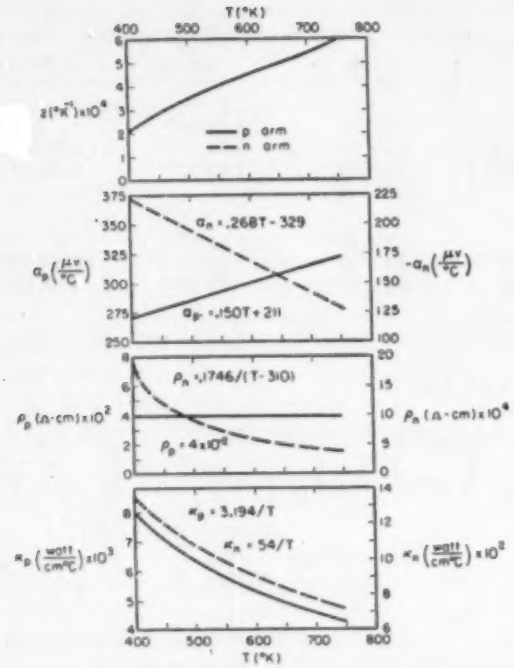

FIG. 4. Properties of the thermoelectric materials in the example I generator.

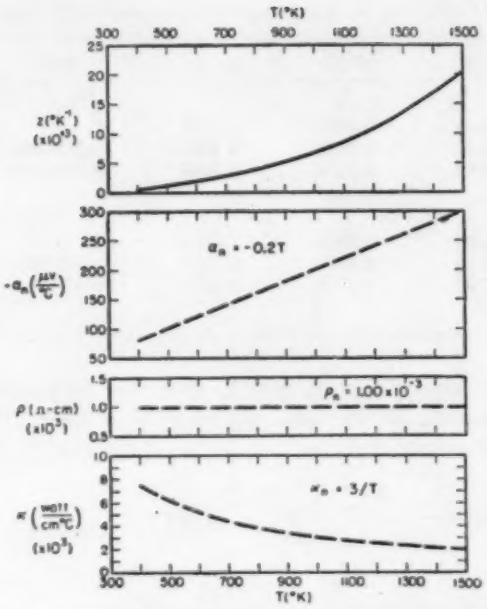

FIG. 6. Properties of the thermoelectric materials in the example III generator. The p arm is the same material at the p arm of example II.

materials are shown in Figs. 4, 5, and 6 with the results of the calculations displayed in Tables III and IV. The materials used in example I have properties similar to those for InSb and MnTe while the materials for examples II and III are hypothetical with properties appreciably better than any known at present.

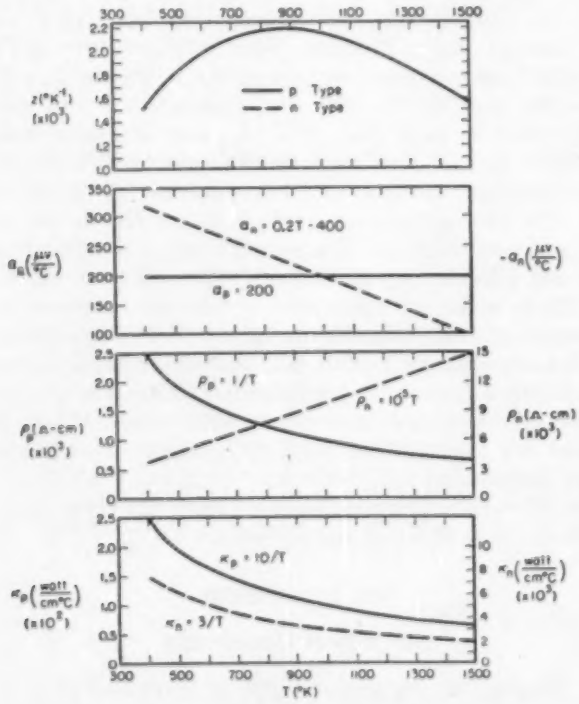

FIG. 5. Properties of the thermoelectric materials in the example II generator.

Examination of Table III shows that the efficiency calculated for the average parameters (Approach 1) is quite close to the exact value. It should be remarked that z_{Av} as given by (22) can be quite different from the average value of $z(T)$. For instance, in example III, z_{Av} is $4.25\times10^{-3}°C^{-1}$ while $\langle z(T)\rangle$, the average value of $z(T)$, is $7.62\times10^{-3}°C^{-1}$. The efficiency calculated by using $\langle z(T)\rangle$ in (12) is 0.44 which is 30% higher than the exact value.

In order to get some idea of the nonlinearity of the temperature distribution under operating conditions the temperature profiles for example II are shown in Fig. 7.

In the three examples calculated here the efficiency with infinite staging is only slightly larger than with

TABLE III. Maximum efficiency of three thermoelectric generators calculated by the three methods described in Secs. IV–VI. The parameters of the thermoelectric materials are shown in Figs. 4, 5, and 6. The generator of example I works between 400 and 750°K while examples II and III run between 400 and 1500°K. The percentage difference between the value and the exact value of Approach 3 is shown in parenthesis. In Tables III to IX, the values calculated by the exact method have been rounded off to the same number of significant figures as used in the approximate calculations.

	Approach 1 Average parameters	Approach 2 Infinite staging	Approach 3 Exact
Example I	0.031 (+7%)	0.033 (+14%)	0.029
Example II	0.25 (−4%)	0.26 (0)	0.26
Example III	0.36 (+6%)	0.36 (+6%)	0.34

a single stage. Thus for these cases little would be gained by going to multiple staging.

(b) Refrigeration

Calculations have been made for four different hypothetical sets of materials made into thermoelectric cooling devices. The properties of the materials are shown graphically in Fig. 8. In all four cases the device runs between 270 and 330°K. The materials of case *A* are similar to presently available materials. The other three cases were constructed by reversing the sign of the temperature dependence of α and ρ or both while approximately maintaining the same average value over the operating temperature range. Clearly, the

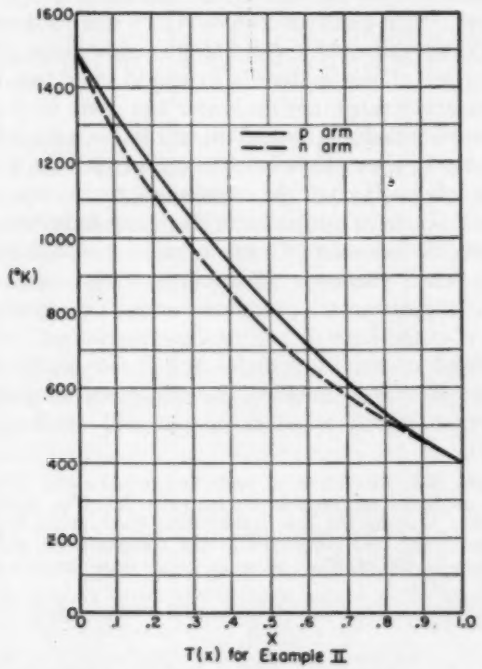

FIG. 7. Temperature distribution in the two arms of the example II generator when the current and area are adjusted to maximize the efficiency.

limited data for the four cases studied are not sufficient to draw firm conclusions; however, it is worthwhile to list the various factors involved in considering the results. Some tentative conclusions will then be made.

The first factor to consider is the sign of the Thomson coefficient. In cases *A* and *D* the Thomson effect is such as to draw heat from the cold reservoir while in cases *B* and *C* heat is given to the cold reservoir. As a result of this effect, *A* and *D* should have better performance.

Because of the procedure used in setting up these examples (the average value of α is approximately the same in all four cases) the Peltier coefficient at the cold end is low in case *A* and *D* and high in case *B* and *C*. This effect implies better performance for *B* and *C*.

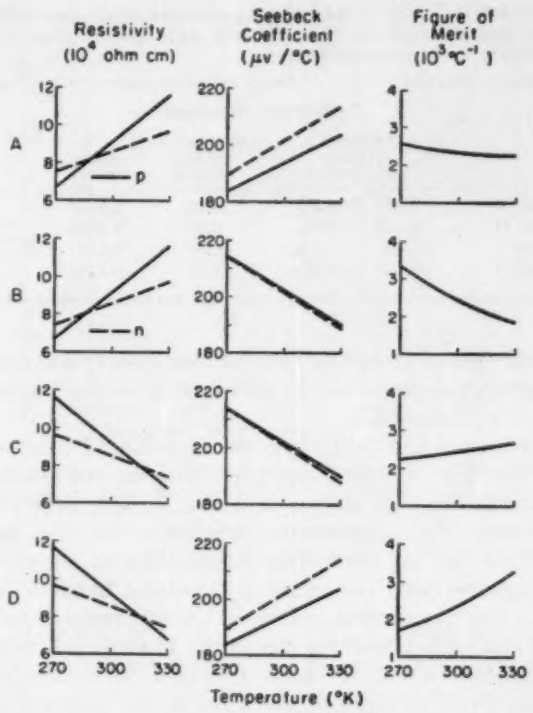

FIG. 8. Properties of the thermoelectric materials in the four cooling devices. The thermal conductivity of the p arm is 0.015 w/cm°C and of the n arm $(3.05–0.00247)10^{-2}$. The absolute value of the Seebeck coefficient of the n arm is plotted.

A third consideration is the temperature dependence of the resistivity. Examination of (10) shows that, for the case of k and τ independent of temperature and ρ linear with temperature, the temperature dependence of the resistivity affects the fraction of both the Joule and Thomson heats going to the cold junction. Case *A* and *B* should have better performance as far as the distribution of the Joule heat is concerned. If the Thomson effect produces heat in the arm, better performance will be obtained if a large fraction of the Thomson heat goes to the hot end, and vice versa.

TABLE IV. Values of the various parameters which maximize the efficiency of the three thermoelectric generators described in Table III.

	Approach 1 Average parameters	Approach 3 Exact
Example I		
Current I (amp)		1.22
Area of n arm, A (cm²)	0.034	0.036
Load resistance, R (ohms)	0.069	0.071
Example II		
Current I (amp)		55
Area of n arm, A (cm²)	5.0	4.5
Load resistance, R (ohms)	5.0×10^{-3}	5.1×10^{-3}
Example III		
Current, I (amp)		65
Area of n arm, A (cm²)	1.67	2.2
Load resistance, R (ohms)	4.0×10^{-3}	4.8×10^{-3}

TABLE V. Values of the relevant parameters of the thermoelectric cooling devices adjusted to maximize the coefficient of performance. The properties of the thermoelectric materials are given in Fig. 8. The percentage difference between the approximate and exact values is shown in parenthesis.

	Coefficient of performance, φ			Area of n arm A		Applied voltage E		Current I	
	Approach 1 average parameters	Approach 2 infinite staging	Approach 3 exact	Approach 1 average parameters	Approach 3 exact	Approach 1 average parameters	Approach 3 exact	Approach 1 average parameters	Approach 3 exact
Case A	0.161 (−14%)	0.28	0.183	0.78	0.75	0.102	0.103	38	37
Case B	0.178 (+20%)	0.30	0.148	0.75	0.75	0.101	0.100	38	35
Case C	0.180 (+14%)	0.29	0.158	0.77	0.80	0.101	0.099	38	40
Case D	0.163 (−8%)	0.26	0.176	0.77	0.80	0.101	0.103	38	42

Thus case A should be favored over case D and case C over case B as far as the distribution of the Thomson heat is concerned.

The results of the calculation of problem I (discussed in Sec. II) i.e., the maximization of the coefficient of performance, are shown in Table V. The differences between the approximate methods and the exact calculations are somewhat larger than in the power generation case. The reason is as follows. In the cooling case the net cooling, which is the difference between the Peltier heat and the sum of the Joule and thermally conducted heats, is small compared to either term. Thus small changes in any term or the addition of a small Thomson heat is significant. However in the power case, the Peltier heat and the thermally conducted heat have the same sign and their sum is large compared to the Thomson and Joule heats. Thus a small change in any term has less effect on the result than in the cooling case. Examination of Table V indicates that the sign of the Thomson coefficient is the most important factor of those cited in the foregoing; that is, one wants the Thomson effect to absorb heat from the cold reservoir.

In contrast to the power generation cases the values for infinite staging are appreciably larger than for the single stage. For the case of material parameters independent of temperature, it is easily shown that if the coefficient of performance of a single stage device is small, a multistage device will have an appreciably larger coefficient of performance. However for large φ the difference between φ for a single stage device and for a multistage device is small. In all four cases calculated here, φ is small and hence the result that φ_∞ is appreciably larger than φ_1 is expected.

The results for problem II, the maximum temperature difference are given in Table VI. In this problem the devices operate over a wider temperature range and the properties of the materials averaged over this larger temperature range are no longer the same in the four cases. Nonetheless comparison of the last two columns in Table VI shows little correlation between the average figure of merit and the maximum temperature difference. Again in this problem it appears to be beneficial to have a favorable Thomson effect coupled with a small Peltier coefficient rather than the inverse.

An experimental procedure which is sometimes used with the hope of getting close agreement between measured material properties and device coefficient of performance is to measure the maximum temperature difference which a given couple will produce. An

TABLE VI. Values of various parameters of several thermoelectric cooling devices adjusted to produce the maximum temperature difference. The hot junction is held at 330°K. The sixth column gives the apparent figure of merit calculated from $z_{app}=2\Delta T_{max}/T_h^2$. The last column gives the figure of merit averaged over the range from the calculated cold junction temperature to 330°K. All other calculations were made by Approach 3-Exact.

	ΔT_{max} (°C)	Area of n arm A (cm²)	Applied voltage E (v)	Current I (amp)	Apparent figure of merit z_{app} (°C)$^{-1}$	Average figure of merit z_{Av} (°C)$^{-1}$
Case A	80	0.75	0.138	51	2.6×10^{-3}	2.4×10^{-3}
Case B	77	0.74	0.125	44	2.4×10^{-3}	2.6×10^{-3}
Case C	73	0.80	0.125	50	2.2×10^{-3}	2.4×10^{-3}
Case D	75	0.81	0.138	58	2.3×10^{-3}	2.2×10^{-3}

TABLE VII. Coefficient of performance calculated from the apparent figure of merit given in Table VI. The percentage difference between the approximate and exact values is shown in parenthesis. The properties of the thermoelectric materials are given in Fig. 8. The operating temperature range is 270 to 330°K.

	Apparent figure of merit from maximum ΔT z_{app}(°C^{-1})	Coefficient of performance	
		From z_{app}	Exact
Case A	2.6×10^{-3}	0.21 (+15%)	0.183
Case B	2.4×10^{-3}	0.176 (+19%)	0.148
Case C	2.2×10^{-3}	0.132 (−20%)	0.158
Case D	2.3×10^{-3}	0.154 (−14%)	0.176

TABLE VIII. Heat pumping rates which correspond to zero slope in the temperature distribution at the hot junction. The properties of the thermoelectric materials are given in Fig. 8. The operating temperature range is from 270 to 330°K.

	Heat pumping rate per unit area $q_c/(1+A)$ (w/cm²)	Area of n arm A (cm²)	Applied voltage E (v)	Current I (amp)
Case A	0.49	0.76	0.118	43
Case B	0.34	0.75	0.110	39
Case C	0.41	0.81	0.109	46
Case D	0.55	0.82	0.119	52

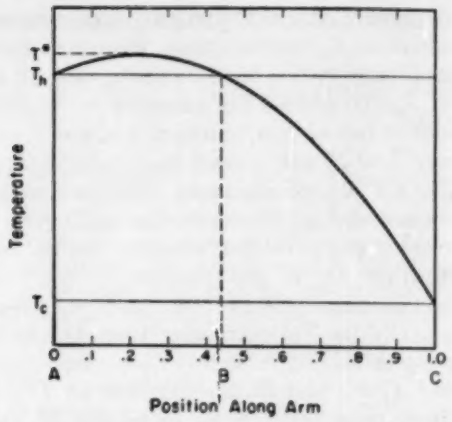

FIG. 9. Temperature distribution in a thermoelectric arm with the current adjusted to maximize the heat removed from the cold junction. The same heat can be removed from the cold junction by using only the portion of the arm from B to C and the same current. However, the power input is lower with the shorter arm.

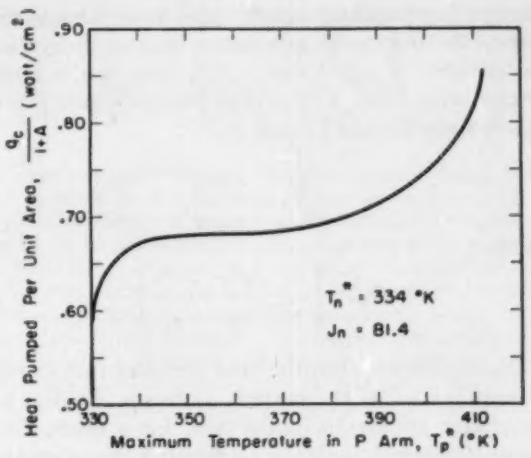

FIG. 10. The heat pumping rate per unit cross-sectional area for case D as a function of the maximum temperature in the p arm, T_p^*. Experimentally T_p^* is changed by changing the current in the p arm. The area of the n element is changed in order to maintain the current density in the n arm constant at 81.4 amp/cm².

apparent figure of merit is then obtained from (2) Table I and used to calculate the coefficient of performance from (1) Table I. In Table VII values are shown using this procedure. The values are somewhat worse than those obtained by averaging α and ρk. Better agreement might be found if the maximum temperature difference were measured with T_c fixed at 270°K rather than with T_h fixed at 330.

In the case of the maximum heat pumping rate the temperature distribution has a maximum value in the interior of the pellet as shown in Fig. 9. The same heat pumping rate can be achieved by using an element BC (Fig. 9), and using the same current as in the original pellet of length AC. However, the power input will be smaller. The largest heat pumping rate which can be achieved without benefiting from cutting the pellet shorter is that which gives a zero slope to the temperature distribution at the hot end. The values of the parameters which maximize $q_c/(1+A)$ with zero slope in the temperature distribution at T_h are shown in Table VIII.

The values of the parameters which maximize $q_c/(1+A)$ without this restrictive condition are shown in Table IX. For case D, a totally unexpected behavior was found. In Fig. 10, the heat pumping rate per unit area for case D is shown as a function of T_p^*, the maximum temperature in the p arm. Experimentally T_p^* is increased by increasing the current density, but T_p^* is a better independent variable for the machine calculation. For a given T_p^*, the maximum $q_c/(1+A)$ occurred with J_n close to 81.4 amp independent of the value of T_p^*. In the other three cases, $q_c/(1+A)$ had a maximum value as shown in Table IX and decreased regularly as T_p^* and T_n^* were increased beyond the values which give the maximum.

In order to show that this result is reasonable, the case of ρ, k, and τ independent of temperature will be considered. The solution of (4) for this case gives

$$\frac{k}{J}T'(1)=\frac{\tau\Delta T+\rho J}{\exp[-\tau J/k]-1}+\frac{\rho k}{\tau} \tag{84}$$

for $L=1$. If $\tau J<0$, then in the limit of large values of $|J|$, (84) becomes

$$\frac{k}{J}T'(1)=\frac{\rho k}{\tau}. \tag{85}$$

Thus at high current density, the heat delivered to

TABLE IX. Maximum heat pumping rates of several thermoelectric cooling devices as calculated by several methods. The calculation is made with $T_c=270$°K and $T_h=330$°K. The properties of the thermoelectric materials are given in Fig. 8. The values shown for case IV are the largest obtained under condition that $\rho_p>0$ at T_p^*.

	Heat pumping rate per unit area, $q_c/(1+A)$		Area n arm A		Applied voltage E		Current I		Maximum temp. in each element	
	Approach 1 average parameters	Approach 3 exact	Approach 1 average parameters	Approach 3 exact	Approach 1 average parameters	Approach 3 exact	Approach 1 average parameters	Approach 3 exact	T_p^*	T_h^*
Case A	0.46	0.55	0.83	0.74	0.131	0.139	55	51	332	332
Case B	0.51	0.36	0.83	0.74	0.133	0.123	56	44	331	331
Case C	0.51	0.47	0.83	0.89	0.133	0.129	56	62	334	332
Case D	0.46	0.86	0.83	5.2	0.131		55	42	412	334

the cold junction by the arm increases linearly with the current density in the arm rather than as the square of the current. If $\tau_p>0$ and $\tau_n<0$, then in the limit of large I with fixed A, the heat pumping rate per unit area is from (15), (17), and (85)

$$\frac{q_c}{1+A}=\frac{ID_{pn}}{1+A}, \tag{86}$$

where

$$D_{pn}=\left[\pi_c-\frac{\rho_p k_p}{\tau_p}+\frac{\rho_n k_n}{\tau_n}\right]. \tag{87}$$

If D_{pn} is positive, then the heat pumping rate increases without bound as the current increases. At first sight this might appear to imply that, for a given T_h, an arbitrarily large temperature difference can be attained, contrary to what has been proved in Sec. VI. However, with the above restrictions on the signs of the τ's, π_c becomes smaller for decreasing T_c and hence there will be a T_c below which D_{pn} is no longer positive.

The contract resistance, which has been neglected throughout this paper, will limit $q_c/(1+A)$ to finite values since the heat which is delivered to the cold junction by the contact resistance is proportional to J^2.

If D_{pn} is negative then the heat pumping rate is negative when $|J_p|$ and J_n are simultaneously large. However, for $|J_p|$ large and J_n finite, the heat pumping rate is given by

$$\frac{q_c}{1+A}=D_pJ_n+k_nT_n'(1), \tag{88}$$

where

$$D_p=\pi_c-\frac{\rho_p k_p}{\tau_p}. \tag{89}$$

If D_p is positive, the heat pumping rate remains finite and positive as J_p becomes large. However, there may be a maximum in the heat pumping rate at a finite value of J_p. To discuss the situation in the problems calculated in this section, values of ρ, k, and τ averaged between T_c and T^* will be used. In case D, D_p is positive for $T_p^*>374°K$ and increases with increasing T_p^*. Examination of Fig. 10 shows that $q_c/(1+A)$ begins to increase rapidly in the vicinity of this value of T_p^*. However D_n is also positive for $T_n^*>438°K$. The exact calculation shows that $q_c/(1+A)$ decreases monotonically for T_n^* increasing from 335 to 500°K, and $T_p^*=345°K$.

In case A, D_n, and D_p are negative for $T^*=330°K$ and become more negative for increasing T^*. In cases B and C, phenomena of this sort cannot occur since the Thomson coefficients have the wrong sign.

In all of these calculations on the cooling device better performance is obtained with a lower Peltier coefficient at the cold end coupled with a Thomson effect which absorbs heat. Thus it appears to be more efficient to have the Thomson effect absorb part of the Joule heat at the point where it is produced rather than conducting the Joule heat to the end of the bar and absorbing it by the Peltier effect.

VIII. ACKNOWLEDGMENT

We wish to thank Miss Lois Morgan of the laboratory computing staff for her very able programing of the problems discussed in this paper and for carrying out the calculations on the Datatron computer. We note particularly that the maximizing operations, which required some careful attention, were done by her.

JOURNAL OF APPLIED PHYSICS VOLUME 31, NUMBER 1 JANUARY, 1960

Waves on a Filamentary Electron Beam in a Transverse-Field Slow-Wave Circuit*

A. E. SIEGMAN
Stanford Electronics Laboratories, Stanford University, Stanford, California
(Received June 24, 1959)

The waves on a filamentary electron beam in a longitudinal dc magnetic field, and their interaction with a transverse-field slow-wave circuit, are studied in detail. All quantities are expressed in terms of circular polarization, with the circuit fields having arbitrary polarization. The beam is found to carry four waves: a positively polarized negative-energy slow cyclotron wave, a negatively polarized positive-energy fast cyclotron wave, and two synchronous ($\beta=\beta_e$) waves, one with positive polarization and positive energy, one with negative polarization and negative energy. The coupling of these waves to the circuit is described both in the manner of Pierce's longitudinal traveling wave tube (TWT) analysis and in a coupled-mode description. For the two special cases of positive or negative circularly polarized fields, only the appropriately polarized beam waves couple. A third special case of linear polarization is more complicated, but essentially only the two cyclotron waves couple. In each of the three cases one positive-energy and one negative-energy beam wave is involved. In each case the equations can be made identical with the longitudinal TWT equations. As one example, a positively polarized circuit can be used as a fast-wave coupler for an Adler-type parametric amplifier, and its design becomes formally identical with the longitudinal Kompfner dip problem. Published Kompfner dip data can be used. The beam-circuit interaction is found to be correctly described by considering only the apparent transverse motion of the beam's position, although the actual interaction mechanism involves both the true transverse interaction with the actual transverse electron velocities, and the longitudinal interaction of the dc beam velocity with the longitudinal ac fields off the dc beam axis. The latter leads to changes in longitudinal dc velocity of the electrons and thus accounts for the negative rf energies of two of the waves.

I. INTRODUCTION

THE phenomena that result when the space-charge waves on an electron beam interact with the longitudinal electric fields on a slow-traveling-wave circuit are well known from the work of Pierce[1] and others. The conventional longitudinal traveling-wave tube is the major example of this type of interaction.

The analogous problem for the case of transverse interaction between the transverse waves on a filamentary electron beam in an axial magnetic field and the transverse electric fields of a slow-wave circuit has not been studied in as much detail. This latter problem is of interest for its own sake, since the beam in this case carries four waves rather than the two waves of the space-charge case, and since the mechanism of interaction is somewhat more complicated. The problem may also be of practical interest. It is possible to build traveling-wave amplifiers, backward-wave oscillators, and other devices using transverse interaction, although such devices have not generally proven to be as important as longitudinal devices. In addition, a traveling-wave type of transverse coupler to the fast cyclotron wave may be useful in higher-frequency versions of a recently invented electron-beam parametric amplifier.[2]

The present paper develops a general analysis of the elementary problem of a filamentary electron beam in a purely transverse-field slow-wave circuit. The beam waves, the beam-circuit interaction, the interaction mechanism, and the relationship to the longitudinal case are studied in some detail. A number of interesting and novel conclusions are obtained, and these are summarized in the concluding section, Sec. IX.

II. ANALYTICAL MODEL, ASSUMPTIONS, AND DEFINITIONS

We consider an electron beam of zero spot size in the transverse direction traveling along the positive z axis with velocity u_0 under dc conditions. The beam is in an axial magnetic field B_0, which is arbitrarily chosen to point in the positive z direction. This choice results in the slow cyclotron beam wave being circularly polarized in the positive sense and the fast wave polarized in the negative sense.

The beam is assumed to be coupled to a slow-wave circuit which has purely transverse electric fields at the dc position of the beam. In the analysis, only transverse fields and transverse electron displacements and velocities are included formally. Longitudinal fields, longitudinal motions, and hence longitudinal space-charge effects, are ignored. However, the longitudinal ac electric fields off the axis are found to play a crucial role in the energy-exchange mechanism of the interaction, and this topic is discussed in some detail later on. The analysis is linearized and small signal, with $\exp(j\omega t)$ time dependence throughout, and the slow-wave circuit is assumed to propagate only a single mode at a velocity small compared to the velocity of light.

In the transverse plane we define a number of quantities describing the transverse motion of the beam and electrons as follows:

$\mathbf{r}_a=(x_a,y_a)$ = the transverse displacement of an individual electron,

$\mathbf{u}_a=d\mathbf{r}_a/dt$ = the transverse velocity of an individual electron,

$\mathbf{r}=(x,y)$ = the transverse displacement of the electron beam as a function of z,

* This research was supported by the U. S. Air Force through the Wright Air Development Center.

[1] J. R. Pierce, *Traveling-Wave Tubes* (D. Van Nostrand Company, Inc., Princeton, New Jersey, 1950).

[2] Adler, Hrbek, and Wade, Proc. Inst. Radio Engrs. 46, 1756 (1958).

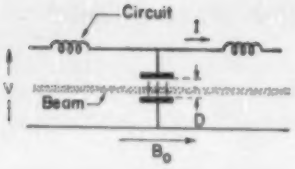

FIG. 1. Schematic drawing of the equivalent transmission line which replaces the slow-wave circuit in the analysis.

$\mathbf{u}=j\omega\mathbf{r}$ = the transverse velocity of the electron beam position as a function of z,

and

$\mathbf{v}=j\omega\mathbf{r}+u_0\partial\mathbf{r}/\partial z$ = the transverse velocity of the electrons in the beam at a distance z as a function of z.

Because the basic motions of an electron transverse to a magnetic field are rotational motions, it is most convenient to express the above quantities and any other transverse vectors in circularly rather than linearly polarized components. If any transverse vector $\mathbf{A}$ has linear components A_x, A_y, these will be related to the positive and negative circularly polarized components A_+ and A_- by the relations

$$A_x=A_++A_-, \qquad A_y=j(A_+-A_-)$$
$$A_+=\tfrac{1}{2}(A_x-jA_y), \quad A_-=\tfrac{1}{2}(A_x+jA_y). \tag{1}$$

The analysis follows the general approach of Pierce's analysis of the conventional traveling-wave tube,[1] i.e., find the fields induced on the slow-wave circuit by any modulation on the beam, find the modulation of the beam caused by any fields on the circuit, and then require that the two be self-consistent. The equations are then also expressed in the coupled-mode form which has been found convenient for traveling-wave tube and other problems.

III. BASIC ANALYSIS

(a) Circuit Equation

The slow-wave circuit is represented, as is usual, by an equivalent transmission line carrying voltage V and current I, such that $P=\frac{1}{2}\,\mathrm{Re}(VI^*)$ is the average power on the circuit. Figure 1 is a sketch of the physical system envisioned. The voltage V is related to the actual transverse electric fields at the beam position by a normalizing distance D and two dimensionless factors f_+ and f_- through the equations

$$E_x=-(f_++f_-)V/D$$
$$E_y=-j(f_+-f_-)V/D \tag{2}$$

or

$$E_+=-f_+V/D$$
$$E_-=-f_-V/D \tag{3}$$

with the requirement that

$$f_+f_+^*+f_-f_-^*=1. \tag{4}$$

The factors f_+ and f_- express the type of polarization which the circuit fields possess. The voltage V may be taken to be the electric potential at an arbitrarily chosen point on the slow-wave circuit structure. The two complex Eqs. (2) and (4) then determine the two complex factors f_+ and f_- and the factor D in terms of the real physical quantities E_x, E_y, and V.

It may be noted that arbitrary types of polarization are available on actual slow-wave circuits. Linearly polarized fields are readily obtained in planar types of circuits, while the ±1 space harmonics of the helix slow-wave circuit give circularly polarized purely transverse electric fields at the center of the helix. A helix with an elliptical cross section would very probably give elliptical polarization to the same harmonics. A structure such as a quadruply ridged wave guide, with slots or other modifications cut in the ridges to provide slow waves, propagates two degenerate modes corresponding to the two mirror symmetries of the structure about two longitudinal planes 90° apart. By varying the relative excitation of these two modes and by suitable strapping of the circuit, arbitrary polarization can be obtained.

The transmission line equations for the equivalent slow-wave circuit are

$$\partial V/\partial z=\mp j\beta_0Z_0I$$
$$\partial I/\partial z=\mp j(\beta_0/Z_0)V+J, \tag{5}$$

where β_0 and Z_0 are the propagation constant or wave number and characteristic impedance, respectively, of the circuit in the absence of the beam, and the top or bottom sign applies when the circuit is a forward- or backward-wave circuit, respectively. The induced current J per unit length in the slow-wave circuit due to modulation on the beam can be written as

$$J=-(2\rho_0/D)(f_+^*u_++f_-^*u_-)$$
$$=-(2\rho_0\omega/D)(f_+^*r_++f_-^*r_-). \tag{6}$$

Physically, this says that the induced current is caused by the total amount of electronic charge ρ_0 in a unit length of the beam moving towards the circuit with the velocity $\mathbf{u}$ which describes the motion of the beam's position. This is not the same as the actual transverse velocity of the electrons, and some questions may arise as to the correctness of the above expression. The expression will simply be stated here. Its validity is defended below in Sec. VI.

Combining Eqs. (5) and (6) and assuming that waves on the combined beam-circuit system propagate as $\exp(-j\beta z)$ leads to the *circuit equation*

$$\partial^2V/\partial z^2+\beta_0^2V=\mp(2\beta_0Z_0\rho_0\omega/D)(f_+^*r_++f_-^*r_-) \tag{7}$$

or

$$(\beta^2-\beta_0^2)V=(2\beta_0Z_0\rho_0\omega/D)(f_+^*r_++f_-^*r_-) \tag{8}$$

which give the circuit voltage V induced by the beam transverse displacement modulation $\mathbf{r}$.

(b) Electronic Equation

The force equation for an electron is

$$d^2\mathbf{r}_a/dt^2=-\eta[\mathbf{E}+(d\mathbf{r}_a/dt)\times\mathbf{B}], \tag{9}$$

where η is the charge-to-mass ratio for an electron. We define the cyclotron frequency ω_c, cyclotron wave number β_c, and synchronous wave number β_e as

$$\begin{aligned}\omega_c&=\eta B_0\\ \beta_c&=\omega_c/u_0\\ \beta_e&=\omega/u_0,\end{aligned} \tag{10}$$

where B_0 is the z-directed dc magnetic field. Noting that the operator d/dt applied to individual electron quantities becomes the operator

$$\begin{aligned}(d/dt)&=(\partial/\partial t)+(\partial/\partial z)(dz/dt)\\ &\approx j\omega+u_0(\partial/\partial z)\end{aligned} \tag{11}$$

when applied to quantities as functions of z, the transverse components of the force equation can be written in circular terms as

$$\begin{aligned}(\partial^2 r_+/\partial z^2)+j(2\beta_e+\beta_c)(\partial r_+/\partial z)-\beta_e(\beta_e+\beta_c)r_+&\\ =(\eta f_+V/u_0^2D)&\\ (\partial^2 r_-/\partial z^2)+j(2\beta_e-\beta_c)(\partial r_-/\partial z)-\beta_e(\beta_e-\beta_c)r_-&\\ =(\eta f_-V/u_0^2D).&\end{aligned} \tag{12}$$

Alternatively, the equations can be written in terms of the electron velocity $\mathbf{v}$ in the form

$$\begin{aligned}\partial v_+/\partial z+j(\beta_e+\beta_c)v_+&=(\eta f_+/u_0D)V\\ \partial v_-/\partial z+j(\beta_e-\beta_c)v_-&=(\eta f_-/u_0D)V.\end{aligned} \tag{13}$$

We will see later that the difference between Eqs. (12) and (13) arises from the fact that there are four waves on the beam which involve transverse displacement $\mathbf{r}$ of the electrons, but only two of these involve actual transverse velocity $\mathbf{v}$ of the electrons. Under the assumption of $\exp(-j\beta z)$ propagation, Eqs. (12) become

$$\begin{aligned}(\beta-\beta_e-\beta_c)(\beta-\beta_e)r_+&=-(\eta f_+/u_0^2D)V\\ (\beta-\beta_e+\beta_c)(\beta-\beta_e)r_-&=-(\eta f_-/u_0^2D)V.\end{aligned} \tag{14}$$

In the absence of a slow-wave circuit, the beam propagates two so-called synchronous[3] waves, both with $\beta=\beta_e$, and a slow and a fast cyclotron wave with respective wave numbers

$$\begin{aligned}\beta_{\text{slow}}&=\beta_e+\beta_c\\ \beta_{\text{fast}}&=\beta_e-\beta_c.\end{aligned} \tag{15}$$

Equations (14) show that the slow cyclotron wave couples only to the plus circularly polarized component of the circuit fields while the fast cyclotron wave couples only to the minus circularly polarized component. This is discussed in more detail below. Equations (14) together form the electronic equation for the beam.

(c) Secular Equation

Since the power flow on the slow-wave circuit is given by

$$P=VV^*/2Z_0=D^2(E_xE_x^*+E_yE_y^*)/4Z_0 \tag{16}$$

a transverse interaction impedance K_t can be defined as

$$K_t=Z_0(\beta_0D)^{-2}=(E_xE_x^*+E_yE_y^*)/(4\beta_0^2P). \tag{17}$$

Using this impedance, the circuit and electronic Eqs. (8) and (14) can be combined to give the secular equation

$$\beta^2-\beta_0^2=\mp\frac{K_tI_0}{V_0}\frac{\beta_0^3\beta_e}{(\beta-\beta_e)}\left[\frac{f_+f_+^*}{\beta-\beta_e-\beta_e}+\frac{f_-f_-^*}{\beta-\beta_e+\beta_e}\right], \tag{18}$$

where I_0 is the dc electronic beam current and V_0 is the dc beam voltage.

Some simplified cases of this equation are of interest. If the circuit fields are linearly polarized in the x direction, so that $f_+f_+^*=f_-f_-^*=\frac{1}{2}$, then the secular equation becomes

$$\beta^2-\beta_0^2=\mp\frac{K_tI_0}{V_0}\frac{\beta_0^3\beta_e}{(\beta-\beta_e-\beta_c)(\beta-\beta_e+\beta_c)}. \tag{19}$$

The synchronous wave term $(\beta-\beta_e)$ disappears, indicating that the synchronous waves are not excited by linearly polarized fields. On the other hand, if the fields have purely positive circular polarization, so that $f_+f_+^*=1$ and $f_-f_-^*=0$, then the secular equation becomes

$$\beta^2-\beta_0^2=\mp\frac{K_tI_0}{V_0}\frac{\beta_0^3\beta_e}{(\beta-\beta_e)\ (\beta-\beta_e-\beta_c)}. \tag{20}$$

The fast cyclotron wave is missing, since it does not couple to the plus polarized fields, and the synchronous wave reappears. If the fields are polarized in the opposite sense, it is the slow cyclotron wave which does not couple.

The secular equations for the special cases of linear or circular polarization are very similar to the secular equation of the longitudinal traveling-wave tube as given, for example, in Pierce's book.[1] If the quantity $\beta(4QC^2)^{\frac{1}{2}}$ in Pierce's notation is set equal to the reduced plasma wave number β_q, then Pierce's Eq. (7.10) for the longitudinal case can be written in the notation of the present paper as

$$\beta^2-\beta_0^2=\mp\frac{KI_0}{2V_0}\frac{\beta_0\beta_e\beta^2}{(\beta-\beta_e+\beta_q)(\beta-\beta_e-\beta_q)} \tag{21}$$

which is very similar to either (19) or (20) above.

[3] The word "synchronous" in this case refers to the fact that the synchronous beam waves have a phase velocity identical with the dc velocity u_0 of the electrons. No reference to any possible synchronism between a beam wave and a circuit wave is intended.

The linearly polarized case has been analyzed previously by Pierce in the same reference. The more general results of the present paper are in agreement with Pierce's analysis for the special case of linear polarization. Equation (19) is identical with Pierce's Eq. (13.23) under the assumption of purely transverse fields, i.e., in Pierce's notation $\alpha^2=\infty$, $\Phi^2=0$.

IV. COUPLED-MODE FORM OF THE ANALYSIS

In order to cast the above analysis in coupled-mode form,[4] we introduce the normalized mode variables

$$A_0=(2Z_0)^{-\frac{1}{2}}V=\text{circuit voltage amplitude},$$

$$A_1=jkv_+=-ku_0[\beta_e r_+-j(\partial r_+/\partial z)]$$
$$=\text{slow-cyclotron-wave amplitude},$$

$$A_2=jkv_-=-ku_0[\beta_e r_--j(\partial r_-/\partial z)]$$
$$=\text{fast-cyclotron-wave amplitude},$$

$$A_3=jk(v_++j\omega_c r_+)=-ku_0[(\beta_e+\beta_c)r_+-j\partial r_+/\partial z)] \quad (22)$$
$$=\text{first synchronous-wave amplitude},$$

and

$$A_4=jk(v_--j\omega_c r_-)=-ku_0[(\beta_e-\beta_c)r_--j\partial r_-/\partial z)]$$
$$=\text{second synchronous-wave amplitude},$$

where the "impedance" factor k for the beam modes is

$$k=(\omega I_0/2\eta\omega_c)^{\frac{1}{2}}. \quad (23)$$

Inverting these definitions gives

$$v_+=A_1/jk, \qquad v_-=A_2/jk$$
$$r_+=(A_1-A_3)/k\omega_c, \quad r_-=(A_4-A_2)/k\omega_c \quad (24)$$

i.e., $\mathbf{v}$ has components only from the two cyclotron waves while $\mathbf{r}$ has components from all four waves.

Introducing a coupling factor κ defined by

$$\kappa=(\omega I_0\beta_0^2K_i/2\omega_c u_0) \quad (25)$$

and making the assumption that the backward-traveling wave on the slow-wave circuit does not couple and can be neglected, the force equations (12) and (13) and the circuit Eq. (7) can be written in the coupled-mode form as

$$\partial A_1/\partial z+j(\beta_e+\beta_c)A_1=j\kappa f_+A_0$$
$$\partial A_2/\partial z+j(\beta_e-\beta_c)A_2=j\kappa f_-A_0$$
$$\partial A_3/\partial z+j\beta_eA_3=j\kappa f_+A_0$$
$$\partial A_4/\partial z+j\beta_eA_4=j\kappa f_-A_0 \quad (26)$$

and

$$\partial A_0/\partial z+j\beta_0A_0$$
$$=\pm j\kappa[f_+^*(A_3-A_1)+f_-^*(A_2-A_4)]. \quad (27)$$

We see that, as would be expected, the beam waves couple only to the appropriate component of the circuit voltage, and not to each other, while the circuit voltage couples to all of the beam waves. Furthermore, from Eq. (27) it is apparent that A_2 and A_3 are positive-energy waves, while A_1 and A_4 are negative-energy waves. The total average power flow along the beam circuit system is given by

$$P=\pm|A_0|^2-|A_1|^2+|A_2|^2+|A_3|^2-|A_4|^2. \quad (28)$$

That the z derivative of this quantity is zero can be easily verified using Eqs. (26) and (27). Of the two waves A_1 and A_3 which couple to the positively polarized component of the voltage, the slow cyclotron wave A_1 is the negative-energy wave, while the faster synchronous wave A_3 is the positive-energy wave. Of the negatively polarized waves A_2 and A_4, it is again the slowest wave A_4 which is the negative-energy wave, although this wave is the synchronous wave in this case.

Table I summarizes the important properties of the beam waves.

V. PHYSICAL DESCRIPTION OF THE BEAM WAVES

All four waves on the beam are necessary for a full description, since one may prescribe four independent initial conditions for the electrons. These four initial conditions may be the vector components of the initial displacement $\mathbf{r}\exp(j\omega t)$ and initial velocity $\mathbf{v}\exp(j\omega t)$ of the electrons at the plane $z=0$.

A physical description of the two cyclotron waves is as follows: In the two cyclotron waves A_1 and A_2, the individual electrons move axially at velocity u_0, while rotating about the z axis at frequency ω_c in orbits of radius r_c which is the same as the magnitude of the displacement vector $\mathbf{r}$. From Eqs. (24), if only A_1 or only A_2 is excited, we can write

$$r_+=A_1/k\omega_c \quad \text{or} \quad r_-=-A_2/k\omega_c$$
$$v_+=A_1/jk \quad \text{or} \quad v_-=A_2/jk \quad (29)$$

and from the laws of motion for an electron in a cyclotron orbit

$$|r_c|=|v|/\omega_c=A_1/k\omega_c \quad \text{or} \quad A_2/k\omega_c$$
$$=r_+ \quad \text{or} \quad r_-. \quad (30)$$

Figures 2(a) and 2(b) are snapshots of the beam with slow or fast waves, respectively. A center cylinder has been inserted to make the patterns clearer. The individual electrons move to the right with velocity u_0, and hence the pattern will have an axial component of velocity equal to u_0. However, the electrons also rotate clockwise at angular velocity ω_c, which gives an additional backward component of velocity to the slow-wave

TABLE I. The transverse waves on an electron beam. The four waves are arranged in order of decreasing phase velocity.

Wave	Symbol	Free β	Energy	Polarization
Fast cyclotron	A_2	$\beta_e-\beta_c$	+	−
Synchronous	A_4	β_e	−	−
Synchronous	A_3	β_e	+	+
Slow cyclotron	A_1	$\beta_e+\beta_c$	−	+

[4] J. R. Pierce, J. Appl. Phys. **25**, 179 (1954); Bell System Tech. J. **33**, 1343 (1954).

pattern and an additional forward component of velocity to the fast-wave pattern. The net result is that if one neglects individual electrons and merely watches the beam pattern, the pattern can be viewed as simply rotating at frequency ω, in a counterclockwise direction for the positively polarized slow wave and in a clockwise direction for the negatively polarized fast wave. Alternatively, the patterns can be viewed as moving forward with the phase velocities of the slow and fast waves, respectively. The pattern wavelengths and phase velocities which make all of these statements compatible are $\lambda_1/\lambda_e=v_1/u_0=(1+\omega_c/\omega)^{-1}$ for the slow wave and $\lambda_2/\lambda_e=v_2/u_0=(1-\omega_c/\omega)^{-1}$ for the fast wave, where λ_e is the distance traveled by an electron in one cycle of ω.

The two synchronous waves A_3 and A_4 are of an entirely different nature. The individual electrons have no transverse velocity at all, and no rotations at ω_c are involved. Snapshots of these waves would look very much like Figs. 2(a) and 2(b) so far as the shape of the pattern is concerned, but both patterns would have the same wavelength $\lambda_3=\lambda_4=\lambda_e$ and both would move at the same velocity $v_3=v_4=u_0$. One can imagine exciting similar waves in the stream of water from a garden hose by moving the nozzle in a clockwise or counterclockwise circle in the transverse plane at frequency ω, while the water molecules shoot straight out in an axial direction with no transverse component of velocity. This description makes it apparent why $\mathbf{v}$ has no components for these two waves.

VI. INTERACTION MECHANISM, AND THE VALIDITY OF THE INDUCED CURRENT EXPRESSION

This section is intended to prove the validity of the induced current expression used above in Sec. III(a), Eq. (6), and to explore the nature of the interaction and energy-exchange mechanism between beam and circuit. We will first demonstrate the source of the induced current expression

$$J=-(2\rho_0/D)(f_+^*u_++f_-^*u_-) \tag{31}$$

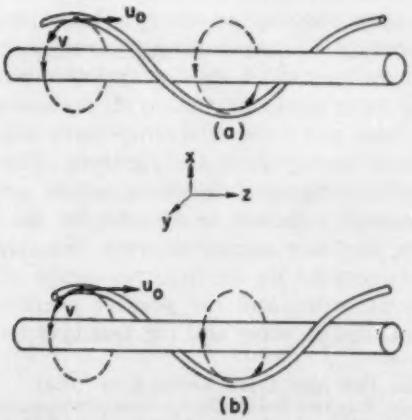

FIG. 2. Snapshots of the beam pattern for (a) slow and (b) fast cyclotron waves.

FIG. 3. The current induced in the capacitor is given by the enclosed charge and the transverse velocity of the beam position.

and then argue for its physical validity. In the process, the nature of the interaction mechanism will become much clearer. Consider first a pair of capacitor plates with a clump of charge between them, as shown in Fig. 3. Suppose that the electrons are contained in a cellophane bag, so to speak, so that they can be moved forcibly up and down. Then the induced current in the circuitry which might be connected to the plates, including the capacitance of the plates, would be given by Ramo's theorem,[5] and would be an expression something like the above expression. That the above expression is the correct one for the more general quadrupole case we have considered can be shown by the following argument. The rate of change with distance of the total power, real plus reactive, on the transmission-line equivalent circuit is given by

$$\frac{\partial}{\partial z}(P+jQ)\bigg|_{\text{circuit}}=\frac{1}{2}\frac{\partial}{\partial z}(VI^*)=\frac{1}{2}\left(V\frac{\partial I^*}{\partial z}+I^*\frac{\partial V}{\partial z}\right)$$

$$=\pm j\frac{1}{2}\left(\frac{\beta_0}{Z_0}VV^*-\beta_0Z_0II^*\right)$$

$$+j\omega\rho_0\frac{V}{D}(f_+r_+^*+f_-r_-^*), \tag{32}$$

where the first term clearly represents reactive energy storage in the passive elements of the transmission line and the second term represents real plus reactive power delivered to the line by the beam. On the other hand, the total power delivered to the circuit fields by the beam per unit length is asserted to be

$$\frac{\partial}{\partial z}(P+jQ)\bigg|_{\text{from beam}}=\frac{1}{2}\rho_0\mathbf{E}\cdot\mathbf{u}^*. \tag{33}$$

This says that the charge ρ_0 per unit length moves with the velocity $\mathbf{u}$, representing the motion of the beam position, in the transverse field $\mathbf{E}$. Expanding this expression yields

$$\frac{\partial}{\partial z}(P+jQ)\bigg|_{\text{from beam}}=j\omega\rho_0\frac{V}{D}(f_+r_+^*+f_-r_-^*). \tag{34}$$

The total power delivered by the beam equals the total power received by the circuit, including both real and reactive terms.

Objections have been made to the expression for power delivered by the beam, Eq. (33) above, on the

[5] S. Ramo, Proc. Inst. Radio Engrs. **27**, 584 (1939).

grounds that while the beam *position* moves in a transverse field $\mathbf{E}$ with velocity $\mathbf{u}$, the individual *electrons* do not move with transverse velocity $\mathbf{u}$. The actual or true transverse velocity of the electrons is $\mathbf{v}$. For some of the beam waves $\mathbf{v}=0$ even though $\mathbf{u}\neq 0$, as discussed in the previous section. One may well ask in this case how transverse fields can exchange energy with electrons which have no transverse velocity.

We will now show that the actual mechanism of energy exchange between the electrons and the circuit involves the interaction between the actual transverse velocity $\mathbf{v}$ of the electrons and the transverse fields, plus the interaction between the dc velocity u_0 and the z-directed ac electric fields which will be present off the dc beam position. However, when these exact expressions are totaled up for slow waves, they reduce to just the expression (33) used in the foregoing.

We consider first the true transverse interaction. The actual electron velocity $\mathbf{v}$ must be used in the expression

$$\begin{aligned}\frac{\partial}{\partial z}(P+jQ)\bigg|_{\text{true trans}} &= \frac{1}{2}\rho_0\mathbf{E}\cdot\mathbf{v}^* \\ &= \tfrac{1}{2}\rho_0\mathbf{E}\cdot(-j\omega\mathbf{r}^*+u_0\partial\mathbf{r}^*/\partial z) \\ &= \tfrac{1}{2}\rho_0\mathbf{E}\cdot(-j\omega+j\beta u_0)\mathbf{r}^* \\ &= j(\omega-\beta u_0)\rho_0(V/D) \\ &\quad\times(f_+r_+^*+f_-r_-^*). \quad (35)\end{aligned}$$

We must now also consider the interaction between the axial electron velocity u_0 and the z-directed ac electric fields which the beam will inevitably see if it moves off the dc beam position. If we assume slow waves, i.e., $\beta\ll k=\omega/c$, then the circuit fields can be assumed to be derived from a scalar potential and to have zero curl. We can, therefore, write $\partial E_z/\partial x=\partial E_x/\partial z=-j\beta E_x$ and $\partial E_z/\partial y=\partial E_y/\partial z=-j\beta E_y$. If the beam is displaced a small amount $(\Delta x,\Delta y)$ from its dc position, it interacts with the axial ac fields and gives up total power per unit length due to longitudinal interaction of

$$\frac{\partial}{\partial z}(P+jQ)\bigg|_{\text{long}} = \rho_0 u_0 E_z = \rho_0 u_0\left[\frac{\partial E_z}{\partial x}\Delta x+\frac{\partial E_z}{\partial y}\Delta y\right]. \quad (36)$$

Using the slow-wave assumptions just mentioned, and noting that the displacements are actually sinusoidal quantities

$$\Delta x=\mathrm{Re}[x\exp(j\omega t)]$$

and

$$\Delta y=\mathrm{Re}[y\exp(j\omega t)],$$

we can rewrite this equation as

$$\begin{aligned}\frac{\partial}{\partial z}(P+jQ)\bigg|_{\text{long}} &= \frac{1}{2}\rho_0 u_0(-j\beta E_x x^*-j\beta E_y y^*) \\ &= -j\beta u_0\rho_0(V/D)(f_+r_+^*+f_-r_-^*). \quad (37)\end{aligned}$$

Adding together the longitudinal and true transverse interactions yields the result

$$\frac{\partial}{\partial z}(P+jQ)\bigg|_{\text{long+true trans}} = j\omega\rho_0\frac{V}{D}(f_+r_+^*+f_-r_-^*) \quad (38)$$

which is just exactly the expression given in Eq. (33) above. The induced current from the beam can be correctly computed using only the transverse fields and the motion of the beam position. However, the actual mechanism involved is a combination of the true transverse velocities of the electrons plus interaction of the axial electron velocities with the axial ac electric fields which are always present off the dc beam position. This fact has been noted much earlier by Adler,[6] Wade,[7] and Fank.[8] Fank showed, for example, that in a transverse-field klystron, the induced current in the output gap can be gotten by considering either only the transverse fields in the gap or only the longitudinal fringing fields at the gap edges. Adler also points out the importance of the longitudinal fields.

This being the case, one might ask why the longitudinal ac motions of the electron can be neglected. The answer is that, in the transverse case, the interaction between longitudinal ac fields and longitudinal ac motions would involve the product of three ac quantities, since the ac field strength depends on the size of the ac transverse displacement. Therefore, this interaction can be neglected in a small-signal analysis.

One consequence of this interaction mechanism is that the ac power carried by, for example, the slow cyclotron wave is a negative quantity

$$P=-|A_1|^2=-(\omega I_0/2\eta\omega_c)|v_+|^2 \quad (39)$$

whereas the kinetic energy carried along by the transverse ac velocities of the electrons would be simply

$$P=(I_0/2\eta)|v_+|^2 \quad (40)$$

and would always be positive. One might ask how the slow cyclotron wave in the absence of a circuit can have positive kinetic energy associated with its ac velocities, and yet carry negative ac energy. The answer is that any slow-wave or transverse-gap structure which is used to initially establish the slow cyclotron wave on the beam will have axial components off the axis or in the fringing fields, and these axial components will abstract axial kinetic energy from the electrons. The average axial kinetic energy of the electrons will be less than u_0 by an amount sufficient to account for the negative energy of the slow cyclotron wave. Exactly similar arguments account for the negative energy of the one synchronous wave, and the positive energies of the other synchronous wave and the fast cyclotron wave.

[6] R. Adler, IRE Natl. Conv. Record **6**, 54 (1953).
[7] G. Wade, Stanford University (private communication).
[8] B. Fank, "Investigation of the transverse-field klystron," Tech. Rept. No. 305-1, Stanford Electronics Laboratories, Stanford University, Stanford, California (March 10, 1958).

Although one can postulate the existence of transverse waves involving no longitudinal effects, such waves cannot in fact be set up by practical structures without longitudinal interaction occurring.

We can obtain further insight into the interaction mechanism by considering a coupler which will excite only one or the other of the synchronous waves. An idealized form of such a coupler is shown in Fig. 4. The coupler consists of two circularly polarized quadrupole structures spaced ½ cyclotron wavelength apart and with the second quadrupole phased ½ cyclotron cycle behind the first. Assuming a length $2b$ for the quadrupole and an ideal step function shape for the transverse fields, the transverse fields in a quadrupole can be written as

$$E_x = -E_0[u(z+b)-u(z-b)]\cos\omega t$$
$$E_y = \pm E_0[u(z+b)-u(z-b)]\sin\omega t, \qquad (41)$$

where the top sign refers to positive, and the bottom to negative, circular polarization. If the transit time $\tau = 2b/u_0$ of an electron through the quadrupole is small, the transverse velocity given to an electron which passes through the center of the first quadrupole when E_x is a maximum is

$$v_x = \eta E_0 \tau. \qquad (42)$$

Since the fields are circularly polarized, all phases are alike and this particular choice of phase has no significance other than being a convenient one. This electron will then travel around a circular orbit in the transverse plane, as shown in the end view of Fig. 5. The electron will arrive at the second quadrupole ½ cyclotron cycle later, at a time when its fields have the same direction and phase as did the fields in the first quadrupole, and at a position y given by

$$y = 2v_x/\omega_c = 2\eta E_0 \tau/\omega_c. \qquad (43)$$

Since the transverse velocity of the electron has been reversed by the time it reaches the second quadrupole and since the second quadrupole has the same fields as the first, the transverse velocity will be just reduced to zero on passing through the second quadrupole, and the electron will emerge with transverse displacement but not transverse velocity. This is the condition for a synchronous wave.

However, in passing through the second quadrupole, the electron sees longitudinal fringing fields because it is off axis in the y direction. Assuming that the quadrupole fields are derivable from a potential and thus

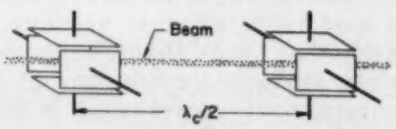

FIG. 4. A dual-quadrupole coupler which will excite either of the two synchronous waves.

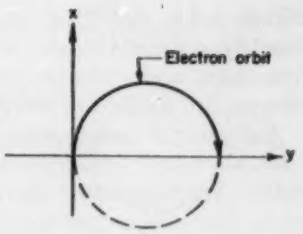

FIG. 5. The orbital transverse motion of an electron in the region between the two couplers.

have zero curl, one can write the z field of a quadrupole as a function of y as

$$E_z = (\partial E_z/\partial y)y = (\partial E_y/\partial z)y$$
$$= \pm E_0[\delta(z+b)-\delta(z-b)]y\sin\omega t. \qquad (44)$$

If the electron passes the center of the second quadrupole at relative time $t=0$, it will see the first delta function at time $(0-\tau/2)$ and the second at time $(0+\tau/2)$. Using the value of y computed above, the energy obtained by the electron from the longitudinal fields is

$$\Delta W = -\int eE_z(z)dz$$
$$= \pm eE_0(2\eta E_0\tau/\omega_c)\left[\sin(-\omega\tau/2)\int \delta(z+b)dx - \sin(\omega\tau/2)\int \delta(z-b)dz\right]$$
$$\approx \pm 2\eta e\omega\tau^2 E_0^2/\omega_c = \pm(e\omega\omega_c/2\eta)y^2. \qquad (45)$$

Noting that the radius r of the resulting synchronous wave is just $r=y$ and that the number of electrons passing per second is I_0/e, the power absorbed by the beam is

$$P = \pm(I_0/e)\Delta W$$
$$= \pm(\omega I_0/2\epsilon\omega_c)\omega_c^2 r^2 \qquad (46)$$
$$= \pm k^2\omega_c^2 r^2$$

which is identical with the beam power expression derived earlier. The beam power in the synchronous wave is positive or negative according as the wave is positively or negatively circularly polarized. Note also that in this case all electrons are slowed down by exactly the same amount. This furnishes further justification for ignoring ac quantities in the longitudinal direction.

VII. EQUIVALENCES WITH THE LONGITUDINAL TRAVELING-WAVE TUBE

Equivalences between longitudinal and transverse interaction have been noted earlier by Adler[6] and others, although Adler did not include any dc magnetic field. This section will show that the equations for transverse interaction in the present problem are formally identical with the longitudinal traveling-wave-tube equations for the case of circularly polarized circuit fields of

either sense and also, with some qualifications for linearly polarized fields. In each of the three cases, two beam modes, one positive-energy and one negative-energy, are coupled to the circuit.

For circular polarization, it is apparent from Eqs. (26), the coupled-mode equations, that two of the beam waves are completely uncoupled from the circuit in each case. The equations for the two cases, ignoring the uncoupled waves, are as follows:

(a) Positive circular polarization, $f_+=1$, $f_-=0$

$$\begin{aligned}\partial A_1/\partial z+j(\beta_e+\beta_c)A_1&=j\kappa A_0\\ \partial A_3/\partial z+j\beta_e A_3&=j\kappa A_0\\ \partial A_0/\partial z+j\beta_0 A_0&=\pm j\kappa(A_3-A_1).\end{aligned}\tag{47}$$

(b) Negative circular polarization, $f_+=0$, $f_-=1$

$$\begin{aligned}\partial A_2/\partial z+j(\beta_e-\beta_c)A_2&=j\kappa A_0\\ \partial A_4/\partial_z+j\beta_e A_4&=j\kappa A_0\\ \partial A_0/\partial z+j\beta_0 A_0&=\pm j\kappa(A_2-A_4).\end{aligned}\tag{48}$$

Each of these sets has essentially the same form as the coupled-mode equations for the conventional longitudinal-traveling-wave tube, as given by, for example, Gould.[9] By making proper identification between quantities such as transverse interaction impedance K_t, cyclotron frequency ω_c, and the like in the transverse case, and the equivalent quantities such as longitudinal interaction impedance K, plasma frequency ω_q, and the like in the longitudinal case, one can make the transverse and longitudinal problems formally identical. Note, however, that in the Pierce analysis all wave numbers are normalized with respect to the dc beam wave number β_e, which is halfway between the beam waves $\beta_e\pm\beta_q$. Thus, Pierce's quantities b, δ, and so on represent variations from β_e. In the transverse problem, to obtain exact equivalence, the normalization in the circularly polarized cases must be with respect to the wave number $(\beta_e\pm\frac{1}{2}\beta_c)$ which is halfway between the beam waves β_e and $\beta_e\pm\beta_c$. For the same reason, ω_c in the circular cases is analogous not to ω_q but to $2\omega_q$.

The case of linear polarization is slightly more complicated. The linear polarization condition is $f_+f_+^*=f_-f_-^*=\frac{1}{2}$. It is then convenient to write the coupled-mode equations in the form

$$\begin{aligned}\partial(f_+^*A_1)/\partial z+j(\beta_e+\beta_c)(f_+^*A_1)&=j\tfrac{1}{2}\kappa A_0\\ \partial(f_-^*A_2)/\partial z+j(\beta_e-\beta_c)(f_-^*A_2)&=j\tfrac{1}{2}\kappa A_0\\ \partial(f_+^*A_3)/\partial z+j\beta_e(f_+^*A_3)&=j\tfrac{1}{2}\kappa A_0\\ \partial(f_-^*A_4)/\partial z+j\beta_e(f_-^*A_4)&=j\tfrac{1}{2}\kappa A_0\\ \partial A_0/\partial z+j\beta_0 A_0=\pm j\kappa[&-(f_+^*A_1)+(f_-^*A_2)\\ &+(f_+^*A_3-f_-^*A_4)].\end{aligned}\tag{49}$$

[9] R. W. Gould, Proc. Inst. Radio Engrs. **47**, 419 (1959).

If the initial condition is that no synchronous waves are present, $A_3=A_4=0$, then from the above equations $f_+^*A_3$ and $f_-^*A_4$ will be excited equally by the circuit voltage A_0. Therefore, the last term of the final equation will be zero; i.e., the synchronous waves will not couple back into the circuit. They will, in fact, be carrying no net power, since if $f_+^*A_3=f_-^*A_4$, then the power in the synchronous waves will be

$$P_{3+4}=A_3A_3^*-A_4A_4^*=[(f_-f_-^*/f_+f_+^*)-1]A_4A_4^*=0.\tag{50}$$

However, in noise calculations, for example, the initial wave amplitudes may not be zero. Even if the synchronous waves are present at the input, they will not couple cumulatively to the circuit. From Eqs. (49) we can write

$$(f_+^*A_3-f_-^*A_4)=(f_+^*A_3-f_-^*A_4)_{z=0}\exp(-j\beta_e z)=C\exp(-j\beta_e z)\tag{51}$$

and solving this for A_3, we can then write the power on the two synchronous waves as

$$\begin{aligned}P&=A_3A_3^*-A_4A_4^*\\ &=2[CC^*+f_-CA_4^*\exp(-j\beta_e z)\\ &\qquad+f_-^*C^*A_4\exp(j\beta_e z)]\end{aligned}\tag{52}$$

which indicates that power is transferred away from and back to the waves in a quasi-periodic fashion with a wave number of $(\beta-\beta_e)$, where β is the wave number of A_4. The coupling is not quite the same as the usual coupling between a beam wave and a circuit wave. The power interchange is not cumulative.

The equivalences just discussed imply that, for linearly, positive circularly, or negative circularly polarized circuits, all of the usual traveling-wave-tube phenomena can be obtained, such as forward-wave amplification or backward-wave oscillation. This has long been recognized for the linear case, but does not seem to have been stated before for the circular cases; that these types of operation have not been unearthed and exploited to a greater extent is probably due to the fact that transverse interaction impedances and growth constants are usually smaller than for the longitudinal case.

VIII. CIRCULARLY POLARIZED FAST-WAVE COUPLER

In the type of transverse-interaction low-noise parametric amplifier developed by Adler *et al.*,[2] one requires a coupler which will transfer all the energy from an electrical circuit to the fast cyclotron wave. For broad band width, one might wish to accomplish this with a slow-wave circuit, and one is then considering a problem very similar to the Kompfner dip condition for the ordinary traveling-wave tube.[10] In fact, if one

[10] R. Kompfner, J. Brit. Inst. Radio Engrs. **10**, 283 (1950). Cf. also, H. R. Johnson, Proc. Inst. Radio Engrs. **43**, 684 (1957).

uses a negatively-polarized slow-wave circuit, the problem is to find a solution of the set of Eqs. (48) with initial conditions $A_0=1$, $A_2=A_4=0$, and the problem is formally *identical* with the Kompfner dip problem. For the ordinary traveling-wave tube, the Kompfner dip conditions require one to find values of CN and b such that

$$\sum_{i=1}^{3}\frac{\delta_i^2+4QC}{(\delta_i-\delta_j)(\delta_i-\delta_k)}\exp(2\pi\delta_i CN)=0, \tag{53}$$

where

$$\begin{aligned}\beta&=\beta_e(1+jC\delta),\\ \beta_0&=\beta_e(1+Cb-jCd)\\ C&=(KI_0/4V_0)^{\frac{1}{2}}\\ \omega_q/\omega C&=(4QC)^{\frac{1}{2}},\end{aligned} \tag{54}$$

and the δ_i's are the roots of

$$\delta^2=(-b+jd+j\delta)^{-1}-4QC. \tag{55}$$

For a negative-circularly polarized transverse coupler, the equivalent conditions are

$$\sum_{i=1}^{3}\frac{\bar{\delta}_i^2+p^2}{(\bar{\delta}_i-\bar{\delta}_j)(\bar{\delta}_i-\bar{\delta}_k)}\exp(2\pi\bar{\delta}_i\bar{C}N)=0, \tag{56}$$

where

$$\begin{aligned}\beta&=(\beta_e-\beta_e/2)(1+j\bar{C}\bar{\delta}),\\ \beta_0&=(\beta_e-\beta_e/2)(1+\bar{C}b-j\bar{C}d),\\ \bar{C}&=(K_tI_0/2V_0)^{\frac{1}{2}},\\ \omega_c/2\omega\bar{C}&=p,\end{aligned} \tag{57}$$

and the $\bar{\delta}_i$ are roots of

$$\bar{\delta}^2=(-f+j\bar{d}+j\bar{\delta})^{-1}-p^2. \tag{58}$$

The overhead bars have been used to distinguish the transverse case. The analogy between logitudinal and transverse cases is exact if one identifies p with $(4QC)^{\frac{1}{2}}$ and barred quantities with the corresponding unbarred quantities. Note the factor of two, however, in defining p, and the change in normalization of the wave numbers, as discussed in Sec. VII.

For large p, which corresponds to large space charge in the longitudinal case, the slower beam wave can be ignored and the transverse Kompfner dip condition becomes

$$\bar{C}N_{dip}=\tfrac{1}{4}(2p)^{\frac{1}{2}}=\tfrac{1}{4}(\omega_c/\omega\bar{C})^{\frac{1}{2}}. \tag{59}$$

Under similar conditions in the longitudinal case, the Kompfner dip condition has the equivalent form

$$CN_{dip}=\tfrac{1}{4}[2(4QC)^{\frac{1}{2}}]^{\frac{1}{2}}=\tfrac{1}{4}(2\omega_q/\omega C)^{\frac{1}{2}}. \tag{60}$$

For small values of p, the tables and graphs of CN_{dip} and b_{dip} as functions of $(4QC)^{\frac{1}{2}}$ and d which have been prepared for the longitudinal case can be used directly in the transverse case for design purposes. More generally, published data giving the δ_i's *vs* b, d, and QC are also directly usable.

IX. CONCLUSIONS

The results of the analysis may be summarized in the following statements:

1. A general analysis for the filamentary-beam transverse-interaction case has been developed, taking into account all possible polarizations of the slow-wave circuit fields. The analysis can be put into the form of Pierce's traveling-wave-tube analysis, or into coupled-mode form.

2. The beam is found to carry a fast and a slow cyclotron wave and two synchronous waves. The slow cyclotron wave and one synchronous wave are both positively polarized and carry negative and positive rf power, respectively. The fast cyclotron wave and the other synchronous wave are both negatively polarized and carry positive and negative rf power, respectively. The synchronous waves involve only transverse displacement, while the cyclotron waves involve transverse displacement and transverse velocity. The four waves couple to the circuit, but not to each other, while the circuit couples to all four waves. However, the coupling depends on the polarization of the circuit fields.

3. The current induced in the circuit by the beam in the transverse case is given correctly by considering the dc beam charge to be moving transversely at a velocity equal to the rate of change of the beam position. This is not the same as the true transverse velocity of the electrons. The actual interaction mechanism involves the true transverse interaction between the transverse fields and the true transverse electron velocities, plus the usually more important longitudinal interaction between the longitudinal dc electron velocity and the longitudinal rf electric fields which are inevitably present off the dc beam axis. Because of this mechanism of interaction, the rf energy carried by the beam waves is not simply the transverse kinetic energy of the electrons. In setting up any of the waves, the beam is inevitably speeded up or slowed down in the axial direction, and this accounts for the positive and negative rf energies of the various waves.

4. For three special polarizations of the circuit fields, only two of the four beam waves couple to the circuit, and the equations become essentially identical with the longitudinal traveling-wave-tube equations. For linear polarization, only the slow and fast cyclotron waves couple cumulatively. For positive circular polarization, only the slow cyclotron and the positively polarized synchronous waves couple. For negative circular polarization, only the negatively polarized synchronous and the fast cyclotron waves couple. In each case, one negative-energy wave and one positive-energy wave are involved.

5. Slow-wave-circuit coupling to the fast cyclotron

wave can be obtained by using a negatively polarized slow-wave circuit. By making the proper identifications, the problem becomes formally identical with the longitudinal Kompfner dip problem, and the published results for the Kompfner dip conditions can be used directly to design such a coupler. This type of coupling appears promising as a broad-band coupler for an Adler-type electron-beam parametric amplifier.

ACKNOWLEDGMENTS

The author is grateful to Dr. Glen Wade, who explained to him the nature of the interaction mechanism described in Sec. VI and the picture of the beam waves in Sec. V. Dr. Billy Kluver also furnished some stimulating arguments over the interaction mechanism. The work reported was supported by the U. S. Air Force through the Wright Air Development Center.

JOURNAL OF APPLIED PHYSICS VOLUME 31, NUMBER 1 JANUARY, 1960

Ion-Bombardment Etching of Silicon and Germanium*

J. A. Dillon, Jr., and R. M. Oman
Barus Research Laboratory, Department of Physics, Brown University, Providence 12, Rhode Island
(Received June 8, 1959)

Electron-microscope photographs of a germanium single crystal surface subjected to prolonged argon-ion bombardment under conditions used for surface cleaning disclosed etch patterns of a type completely different from those observed after chemical etching alone. The dimensions and distribution of the bombardment-induced pits were such that the patterns were not detectable either with an optical microscope or by low-energy electron diffraction. Approximately 93% of the surface remained undamaged. Bombardment of silicon and germanium at 500 ev for prolonged periods at higher current densities produced a different type of etching which may be associated with screw-type dislocations.

INTRODUCTION

In recent years special techniques, such as the ion-bombardment cleaning process,[1] have been developed to produce and maintain single-crystal surfaces which are substantially free of adsorbed impurities. In this process the surfaces were subjected to cycles of argon-ion bombardment (500 ev energy and 100 μa/cm^2 current density) and heat treatment in high vacuum. The cumulative ion bombardment given any of these surfaces was usually no longer than three hours. When the samples were examined following this treatment there was no evidence of any etching effects which could be attributed to the bombardment unless the surfaces were heavily oxidized.[2,3] The low-energy electron-diffraction studies did not indicate the appearance of planes developed by bombardment etching[4] although this technique is capable of observing the development of thermal etching.[5]

On the other hand, Wehner,[6] using higher current densities, longer bombardment times, and lower ion energies, reported the growth of characteristic etch pits on germanium surfaces bombarded by ions of mercury or argon. In an attempt to resolve this apparent disagreement between Wehner's results and those of the groups using ion bombardment as a surface-cleaning tool, we have undertaken a study of the effects of ion bombardment for longer periods or at higher current densities.

LOW-PRESSURE EXPERIMENTS

A (100), 42 ohm-cm (intrinsic) germanium crystal, which had been used in some of our earlier experiments and had been heated in high vacuum at 700°C for about 400 hr, was polished, chemically etched, and placed in the vacuum system.† The latter was the same apparatus used in our work-function measurements, and the vacuum conditions employed were as good as those used in the surface-cleaning experiments.[2] After baking the system and activating the three getter tubes, a pressure reading of 5×10^{-10} mm Hg was obtained. Argon gas from Pyrex flasks was adjusted to a pressure of 1×10^{-3} mm Hg by a metal vacuum valve. Ionization of the argon was facilitated by the use of two electron-gun arrangements. The system was continuously pumped during the bombardment which was first conducted at 500 ev and 100 μa/cm^2. Bombardment was

* This work is supported by the U. S. Air Force Cambridge Research Center, Air Research and Development Command, Bedford, Massachusetts.

[1] Farnsworth, Schlier, George, and Burger, J. Appl. Phys. **29**, 1150 (1958).

[2] J. A. Dillon, Jr., and H. E. Farnsworth, J. Appl. Phys. **28**, 174 (1957).

[3] S. P. Wolsky, Report on Seventeenth Annual Conference on Physical Electronics, Massachusetts Institute of Technology, 1957, p. 109.

[4] R. E. Schlier and H. E. Farnsworth, *Semiconductor Surface Physics* (University of Pennsylvania Press, Philadelphia, Pennsylvania, 1957), p. 3.

[5] H. E. Farnsworth, Phys. Rev. **44**, 417 (1933); **49**, 598 (1936).

[6] G. K. Wehner, J. Appl. Phys. **29**, 217 (1958).

† In the present experiments the samples were etched for about two minutes in a solution consisting of 100 parts fuming nitric acid, 16 parts 48% hydrofluoric acid, and 44 parts glacial acetic acid.

continued for one hour, and the tube was then evacuated and the getters reactivated to assure that the active gas partial pressure was kept to a minimum. This process was repeated until a total ion-bombardment time of seven hours was reached. The sample was removed from the vacuum system and examined at magnifications up to 600×. No evidence of bombardment etch pits was visible.

The sample was replaced in the vacuum system, and the process was repeated for an additional six hours at 100 ev and 100 $\mu a/cm^2$. Again observation of the surface with the optical microscope failed to reveal the presence of etch pits. The cumulative bombardment at this stage was about four times that used in the cleaning experiments. The sample was then sent to Fort Monmouth, New Jersey, where, through the courtesy of Dr. F. Leonhard, electron-microscope photographs were taken. The majority of the surface was perfectly smooth, but spread uniformly over about 40% of the surface were clusters of tiny pits which seem to be similar to those observed on a much larger scale by Wehner. A photograph of one of the pit clusters is shown in Fig. 1. The dimensions of the pits were of the order of tenths of a micron which would explain why they were not detected by the optical microscope. The over-all percentage of the surface occupied by pits was probably less than 5% which also explains why their development was not detected by electron diffraction. Beams contributed by such a small percentage of the surface might well be hidden in the background scattering, particularly if the pits were not well-developed.

It was not possible to obtain electron-microscope photographs of the surface just prior to the ion bombardment. Residual films from the replica technique introduce uncertainties which would make the results questionable unless the sample was again polished and etched. However, following the bombardment studies described, the sample was repolished and chemically

FIG. 1. Electron-microscope photograph of the surface of a (100) germanium crystal following argon-ion bombardment of 7 hr at 500 ev and 100 $\mu a/cm^2$ plus 6 hr at 100 ev and 100 $\mu a/cm^2$. Scale length 1 micron.

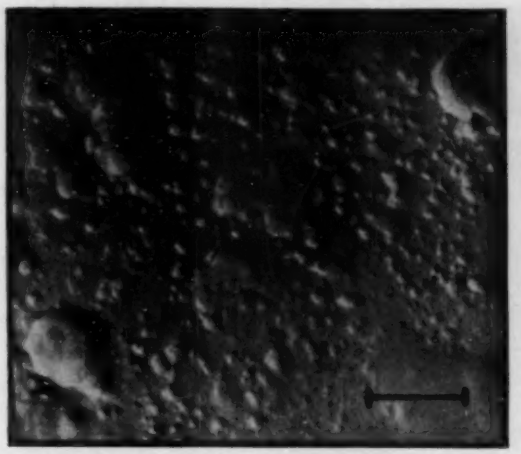

FIG. 2. Electron-microscope photograph of the surface of a (100) germanium crystal following chemical etching. Scale length 0.5 micron.

etched in exactly the same manner, and electron-microscope photographs were then obtained. The surface condition after chemical etching alone was completely different from that observed after the ion bombardment. About 99% of the surface was perfectly smooth, and the remainder contained a few patches of defects of the type shown in Fig. 2. Since both the nature and the distribution of the patterns were quite different on the two surfaces, it appears safe to assume that the ion bombardment caused the clusters of pits to develop. In any case it is evident that very little surface damage has been caused by ion bombardment under the conditions used in the surface-cleaning experiments.

When comparing the results of the bombardment-cleaning experiments with those of Wehner, one must note that there are marked differences not only in the current densities but also in the temperatures and ion energies employed.

In Wehner's experiments the best etch patterns were obtained when the samples were bombarded at energies between 60 and 100 ev. At higher energies, the pits produced by the low-energy bombardment became rounded and truncated. Wehner[7] has previously discussed the changes in the ejection patterns of sputtered material as a function of ion energy in the range of 100 ev to 400 ev for metal crystals. In order to explain the preferential ejection which leads to characteristic etch-pit development, one must assume that the surface damage created by the bombardment is annealed so rapidly that the ions in general are interacting with an undisturbed crystalline surface. The most favorable conditions for preferential ejection and characteristic etch-pit production are those in which the temperature of the sample is high and the ion energy low.‡ In his

[7] G. K. Wehner, Report on Seventeenth Annual Conference on Physical Electronics, Massachusetts Institute of Technology, 1957, p. 60.

‡ It is therefore possible that the 6-hr bombardment at 100 ev was most instrumental in developing the pits shown in Fig. 1.

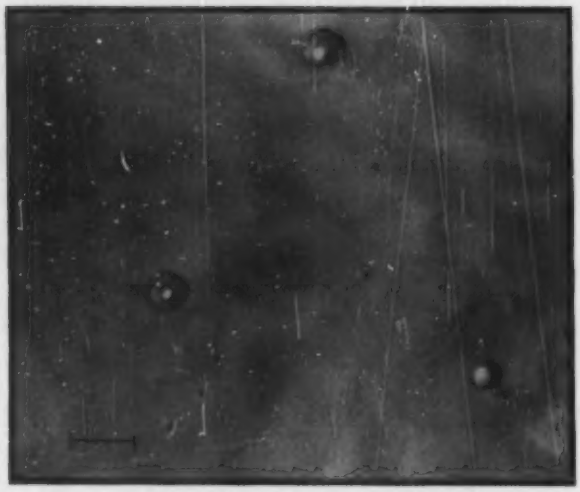

FIG. 3. Surface of (111) silicon crystal after 17 hr argon-ion bombardment at 500 ev and 1 ma/cm². Scale length 15 microns.

germanium studies[6] Wehner has satisfied both of these conditions since his samples were maintained at 300°C and the ion energy kept at a low value. For bombardment cleaning, higher energies and lower temperatures have usually been used. Thus it does not seem too surprising that in the latter experiments pitting usually has not been observed. Wolsky has used higher temperatures in his more recent bombardment cleaning,[8] but his current densities and bombardment times do not seem to have been sufficient to produce visible pits.

HIGH-PRESSURE EXPERIMENTS

Several crystals of both germanium and silicon have been subjected to ion bombardment at 500 ev and at current densities of the order of 1 ma/cm². To attain these densities the gas pressure was increased to about 10^{-1} mm Hg. This pressure region is not advisable for surface-cleaning experiments since the short mean free path introduces the possibility of backscattering some of the sputtered materials.

After bombardment times of about 20 hours, it was found that etch patterns developed which were circular on the (111) face, Fig. 3, oval on the (110) face, and of a distorted circular shape on the (100) face. The densities of these patterns were of the order of 10^2/cm² on the (111) and (110) faces and somewhat less on the (100) face. The patterns on the (111) and (100) faces had a structure which suggested that they might have been of the type observed by Meckel and Swalin,[9] and which may possibly be connected with screw-type dislocations. The density of the patterns on our surfaces was only one thousandth of that observed by Meckel and Swalin. The results were the same for both germanium and silicon, and seemed to be independent of the outgassing history of the samples. The results were not changed whether the gas employed was argon, oxygen, or a mixture of the two.

At these high-current densities and higher energies the mechanism of formation of the defect patterns must be quite different from that operating in the development of the characteristic pits. The surface damage is so extensive that one might envisage a mobile, amorphous surface layer, components of which could diffuse to active centers where accumulation would take place. In this way hillocks would be produced, and the work of Meckel and Swalin strongly suggests that screw-type dislocations play the roles of active centers.

SUMMARY

The appearance of etch patterns due to argon-ion bombardment of germanium and silicon have been observed under different conditions. A germanium sample bombarded at both 500 ev and 100 ev for prolonged periods under the conditions used in surface cleaning exhibited a number of tiny pits whose size and density were such that they were detected only by electron-microscope examination. This type of etching presumably represents the initial stages of the gross characteristic pitting reported by Wehner. Bombardment at 500 ev and higher current densities eventually produces larger pits of a different nature which may be associated with the accumulation of mobile surface atoms at locally active centers.

ACKNOWLEDGMENTS

We wish to thank Dr. F. Leonhard of Fort Monmouth, New Jersey for his kind assistance in electron microscopy and our colleague, Professor H. E. Farnsworth, for the use of certain apparatus which expedited these experiments. We also thank the staff members of the Air Force Cambridge Research Center for their continued support of this research.

[8] S. P. Wolsky, J. Appl. Phys. **29**, 1132 (1958).

[9] B. B. Meckel and R. A. Swalin, J. Appl. Phys. **30**, 89 (1959).

JOURNAL OF APPLIED PHYSICS VOLUME 31, NUMBER 1 JANUARY, 1960

Dipole Mode of Minority Carrier Diffusion with Reference to Point Contact Rectification

B. R. Gossick
Physics Department, Arizona State University, Tempe, Arizona
(August 5, 1959)

The dipole mode of minority carrier diffusion about a spherical emitter is presented. The current-voltage relationship, and frequency characteristics of this mode are determined. Compared with the unipole mode, which has been treated extensively, the dipole mode offers superior high-frequency performance, which is partially offset by an inferior dc characteristic curve. A representative numerical example gives 40 mμsec mean response time with the unipole mode and 0.5 mμsec with the dipole mode. It is proposed that the reproducibility of special diode characterictics might be improved by designing diodes to suppress either the unipole or dipole mode. Methods are suggested for the suppression of either mode.

I. INTRODUCTION

THE behavior of rectifying point contacts which inject minority carriers has been analyzed by solving the heat equation with only one space coordinate, *viz.*, the radial distance about the point.[1–6] The result is that in the work reported to date, all spherical harmonics in the general solution have been ignored save one. The intention here is to obtain an answer to the question: What is the relative importance of the dominant higher mode of excitation, as compared with the fundamental mode? The answer happens to have a significant bearing on diode performance, and therefore it is important.

Although we refer here to point contact rectifiers, the discussion applies not only to rectifiers with a metal point contact on *n*-type germanium, but to hemispherical alloy junctions, "gold-bonded" diodes, and in fact any semiconducting device with a rectifying barrier of the type indicated in Fig. 1. In the discussion hereafter, minority carriers will be represented by holes.

II. FEATURES OF UNIPOLE AND DIPOLE MODES OF HOLE INJECTION

Although the unipole mode has been used as a model for point contact rectification, it appears impossible to design a practical experiment to illustrate the case. We resort to a "dedanken experiment," in which an imaginary electrical connection couples a central sphere with one terminal of a generator, and a real electrical connection couples a surrounding concentric shell with the other terminal of the generator (Fig. 2). The central sphere is an injecting contact. The surrounding concentric shell is an ohmic contact, and the concentric layer in between is an *n*-type semiconductor. With such geometry, the flow of holes is radial from the spherical injecting contact, which typifies the unipole mode of minority carrier diffusion. The excess concentration of holes about the injecting sphere obeys, for the unipole mode, the relation

$$p(r)-p_e=p_e(e^{qV/kT}-1)r_0/r, \tag{1}$$

in which V represents applied voltage; k, T, and q denote respectively Boltzmann's constant, absolute temperature, and electronic charge; p_e denotes equilibrium hole concentration; r_0, the exterior boundary of the space charge region (Fig. 1); and r, the radial coordinate. The hole current through one hemisphere is given by the well-known Wagner[7] relation

$$I(V)=I_s(e^{qV/kT}-1). \tag{2}$$

The saturation current I_s stands for the expression $2\pi r_0\sigma_p kT/q$ in which σ_p gives the conductivity due to holes. The unipole mode of hole diffusion has been applied to rectifiers with geometric design typified by Fig. 3. The *n*-type semiconducting die is either a rectangular parallelopiped or right cylinder, with an ohmic contact across the bottom surface, and a rectifying point contact on the center of the opposite surface.

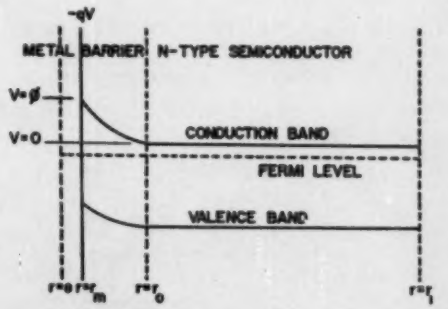

FIG. 1. Profile of potential energy of electrons shown with the diode in equilibrium. The radii r_m, r_0, and r_1 refer to the radius of the metal contact (r_m), the exterior radius of the space charge layer (r_0), and the distance between the center of the injecting contact and the boundary of the ohmic contact (r_1) as shown in Fig. 4.

* Work supported by U. S. Atomic Energy Commission Contract.

[1] P. C. Banbury, Proc. Phys. Soc. (London) **B66**, 833–840 (1953).
[2] Melvin Cutler, Phys. Rev. **96**, 255–259 (1954).
[3] H. L. Armstrong, J. Appl. Phys. **27**, 420 (1956).
[4] B. R. Gossick, J. Appl. Phys. **27**, 905–911 (1956).
[5] E. Hofmeister and E. Groschwitz, Z. angew. Phys. **10**, 109–114 (1958).
[6] Heinz Beneking, Z. angew. Phys. **10**, 216–225 (1958).
[7] C. Wagner, Physik. Z. **32**, 641 (1931).

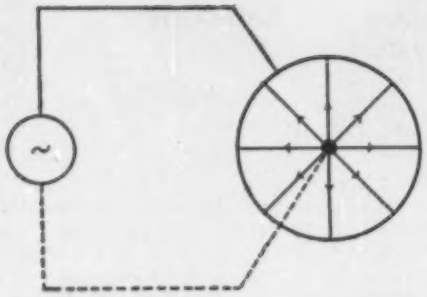

FIG. 2. Hypothetical arrangement to illustrate spherically symmetric diffusion of minority carriers, i.e., by the unipole mode.

The flow pattern of hole current injected from the point contact has been sketched to conform reasonably to the pattern required for the unipole mode shown in Fig. 2. However, such a pattern can be attained only with either a very large surface recombination velocity on the sides of the die, or by extending the ohmic contact to the sides. On the contrary, the free surfaces are normally etched to minimize leakage current about the point contact. Therefore, in practice, the current density is nonuniform across the surface of the emitting contact, less current being emitted from the sides and more being emitted from the center. It becomes evident in the next paragraph that such a departure from the unipolar flow pattern leads to the characteristic pattern of the dipole mode.

One can, at least in principle, design an experiment to illustrate the dipole mode of hole diffusion. Such an arrangement is shown in Fig. 4. The injecting contact floats electrically in the center of the semiconducting sample. While one hemisphere of this contact emits holes, the opposite hemisphere collects them. In order to discuss this case, it is necessary to introduce another coordinate, *viz.*, the angle θ between the applied field E and the radius vector r. The excess concentration of holes about the central sphere obeys, for the dipole mode, the relation

$$p(r,\theta)-p_e=p_e(e^{qV\cos\theta/kT}-1)r_0^2/r^2. \qquad (3)$$

As defined here, the term *applied voltage* V refers to one hemisphere in the case of the dipole mode (Fig. 4). The purpose for so defining applied voltage is to make it serve for the practical scheme illustrated in Fig. 6. The density of radial hole current at the edge of the space charge layer may be written

$$J(r_0,\theta)=2\sigma_p kT(e^{qV\cos\theta/kT}-1)(qr_0)^{-1}. \qquad (4)$$

We have also for the hole current through one hemisphere,

$$I(V)=2I_s[kT(e^{qV/kT}-1)(qV)^{-1}-1]. \qquad (5)$$

The current-voltage characteristic (5) is indeed different from the Wagner law (2), as may be seen in Fig. 5. The ultimate reverse current with the dipole mode is twice as great as that with the unipole mode, and the forward current with the dipole mode is somewhat lower as compared with the unipole mode. The dipole mode of hole diffusion is applicable to rectifiers with the geometric design sketched in Fig. 6. Once more, the n-type semiconducting die may be either a rectangular parallelopiped or right cylinder, with an ohmic contact across the bottom surface, and a rectifying contact on the center of the opposite surface. The flow pattern is just what might be expected with a well-etched die.

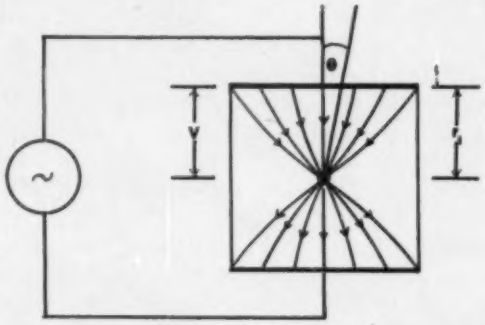

FIG. 4. Schematic arrangement to illustrate the diffusion of minority carriers by the dipole mode. A small spherical injecting contact floats electrically in the center of a semiconductor. The lower hemisphere of the central contact emits, while the upper hemisphere collects holes. The hole current which bypasses the spherical contact is not shown.

Therefore, from the viewpoint of the practitioner, the dipole mode of minority carrier diffusion merits as much study as the unipole mode.

The dipole mode exhibits a shorter injection recovery time than the unipole mode for the following reason. The excess holes obey the relation $1/r$ with the unipole mode, but are distributed as $1/r^2$ with the dipole mode. Hence the total injection is localized nearer the contact with the dipole mode, and can be collected faster when the diode is cut off. This advantage of the dipole mode is partially offset by a longer time constant for the space charge layer with forward bias, because the slope of (5) is less than the slope of (2) with $V>0$.

In order to illustrate briefly the main features of dipolar diffusion, some details have been brushed aside which will be considered in the following sections.

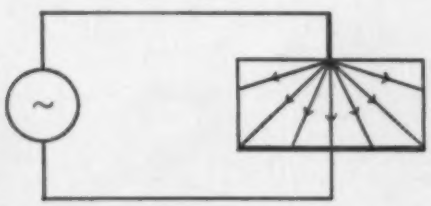

FIG. 3. Conventional point contact-semiconductor die arrangement with current flow pattern typical of the unipole mode.

III. DIPOLE SOLUTION OF THE HEAT EQUATION

The analysis which follows employs a set of initial postulates and corollaries stated in an earlier paper.[4] Only minority carriers will be discussed.

The equation of continuity for excess hole concentration $[p_1(r,\theta)=p(r,\theta)-p_e]$ provides the basis from which the hole current will be determined:

$$\partial p_1(r,\theta)/\partial t = D\nabla^2 p_1 - p_1/\tau. \tag{6}$$

Symbols D and τ denote, respectively, the diffusion coefficient and lifetime of holes. The initial statement (6) will be solved for the region outside an injecting sphere ($r_0<r$) as illustrated in Fig. 4. subject to the boundary conditions

$$p_1(r_1,\theta,t)\approx 0, \tag{7}$$

and

$$p_1(r_0,\theta,t)=p_e(e^{qV(t)\cos\theta/kT}-1). \tag{8}$$

The first boundary condition (7) specifies that the flow

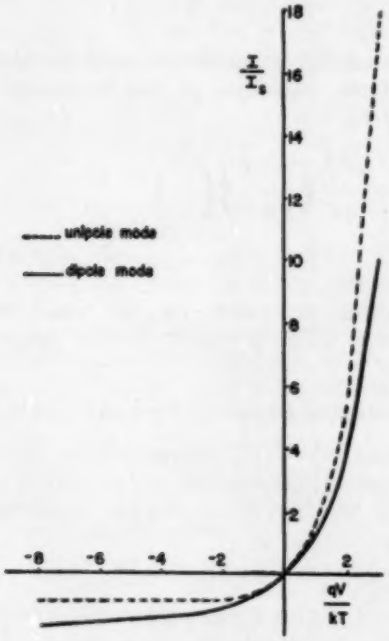

FIG. 5. Current-voltage characteristic curves for the unipole and dipole modes.

of holes from the injecting sphere must be stable. The second boundary condition (8) comes from the Boltzmann distribution.[4] For example, when the injecting sphere (Fig. 4) is polarized, it is surrounded by an electric dipole field. The dipole potential about the exterior surface of the space charge layer obeys the familiar relation $V(r_0,\theta)=V\cos\theta$, which has been used with the Boltzmann distribution to give (8).

Taking the Fourier transform of $p_1(r,\theta,t)$ as the product of two functions $R(r,j\omega)\ \Theta(\theta,j\omega)$, then it follows from (6) that these functions separately satisfy the differential equations

$$\frac{d^2Rr}{dr^2}-\left[\frac{1}{\Lambda^2}+\frac{l(l+1)}{r^2}\right]Rr=0, \tag{9}$$

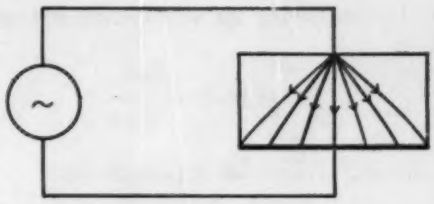

FIG. 6. Conventional point contact-semiconductor die arrangement with current flow pattern typical of the dipole mode.

and

$$\frac{1}{\sin\theta}\frac{d}{d\theta}\sin\theta\frac{d\Theta}{d\theta}+l(l+1)\Theta=0, \tag{10}$$

with

$$1/\Lambda^2=(1+j\omega\tau)/(D\tau), \tag{11}$$

and $l=0, 1, 2, 3, \cdots$. The solution of (10) consists of the well-known Legendre polynomials Θ_l of the first kind. An equation of the same form as (9) was solved by Poisson[5] in the course of investigating the asymmetric propagation of heat in a sphere. It was demonstrated later by Lommel[5] that, except for a factor $(\Lambda/jr)^{\frac{1}{2}}$, Poisson's solution consists of Bessel functions of order $(l+\frac{1}{2})$. For example, the function $R(r,j\omega)$ may be written

$$R_l(r,j\omega)=\{A_lH_{l+\frac{1}{2}}(jr/\Lambda)+B_lH_{l+\frac{1}{2}}(jr/\Lambda)^*\}(\Lambda/jr)^{\frac{1}{2}}, \tag{12}$$

in which $H_{l+\frac{1}{2}}(jr/\Lambda)$ is a Bessel function of the form for complex arguments introduced by Hankel, $H_{l+\frac{1}{2}}(jr/\Lambda)^*$ is the conjugate, A_l and B_l are constants to be evaluated from the boundary conditions.

The constants B_l vanish immediately from the boundary condition (7). Therefore, the Fourier transform of the excess hole concentration reduces to eigenfunctions of the form

$$p_1(r,\theta,j\omega)=A_lH_{l+\frac{1}{2}}(jr/\Lambda)\Theta_l(\Lambda/jr)^{\frac{1}{2}}. \tag{13}$$

Take now the dc case, which is formally obtained by making $V(t)$ a constant in the boundary condition (8) and forcing the angular frequency ω to vanish in the diffusion length Λ. The constants A_l are determined by expressing the boundary condition (8) by an expansion of (13), e.g.,

$$p_e(e^{qV\cos\theta/kT}-1)=(\Lambda/jr_0)^{\frac{1}{2}}\sum_{l=1}^{\infty}A_lH_{l+\frac{1}{2}}(jr_0/\Lambda)\Theta_l. \tag{14}$$

The unipole mode, with $l=0$, for which $\Theta_0=1$, has been discussed in an earlier paper.[4] It is excluded from the expansion (14) because it gives a spherically symmetric distribution of holes about the injecting sphere, and therefore cannot contribute to the solution for the dipole mode. The following procedure may be used to evaluate each constant A_l in (14). One multiplies both sides of (14) by $\Theta_{l'}$, and then integrates over the solid

[5] G. N. Watson, *Bessel Functions* (The Macmillan Company, Inc., New York, 1948), second edition.

angle 4π. By employing the well-known orthogonality relation

$$\int_0^{4\pi} \Theta_l \Theta_{l'} d\Omega = \frac{4\pi\delta_{ll'}}{2l+1} \tag{14a}$$

and the integral formula after Gegenbauer[8,9]

$$\int_0^{4\pi} e^{z\cos\theta} \Theta_l d\Omega = \frac{(2\pi)^{\frac{1}{2}}}{(-j)^l} \frac{J_{l+\frac{1}{2}}'(-jz)}{(-jz)^{\frac{1}{2}}} \tag{14b}$$

one obtains the constants. They are given by the relation

$$A_l = \left(\frac{2l+1}{2}\right)(j)^{l+1} \times p_e \left(\frac{2\pi r_0 kT}{\Lambda qV}\right)^{\frac{1}{2}} \frac{J_{l+\frac{1}{2}}'(-jqV/kT)}{H_{l+\frac{1}{2}}(jr_0/\Lambda)}. \tag{14c}$$

The diffusion current, as a function of applied voltage, is obtained by integrating the radial current density over one hemisphere of the space charge layer. The current, as presented here, is based only on the term for $l=1$, but, as the integral $\int_0^{2\pi} \Theta_2 d\Omega$ vanishes, we have neglected only the terms for which $l \geqslant 3$. The result may be written

$$I(V) = \tfrac{3}{4} I_s \left(1 + \frac{r_0}{\Lambda} + \frac{1}{1+(r_0/\Lambda)}\right) \times \left(\frac{qV}{kT}\cosh\frac{qV}{kT} - \sinh\frac{qV}{kT}\right)\left(\frac{kT}{qV}\right)^2, \tag{14d}$$

which takes the form

$$I(V) = \tfrac{3}{2} I_s \left(1 + \frac{r_0}{\Lambda} + \frac{1}{1+(r_0/\Lambda)}\right) \times \left[\frac{2}{3!}\frac{qV}{kT} + \frac{4}{5!}\left(\frac{qV}{kT}\right)^3 + \frac{6}{7!}\left(\frac{qV}{kT}\right)^5 + \cdots\right], \tag{14e}$$

with $qV/kT \ll 1$.

Note that the dipole mode, as based on Fig. 4, gives a current which is an odd function of applied voltage, in contrast to the unipole mode which displays an asymmetric dependence between current and voltage with the well known "forward" and "reverse" characteristics. However, the symmetry in the dipolar current-voltage function would no longer remain in a hemispherical system applicable to point contact rectifiers (see Fig. 6), but would give way to a "forward" and "reverse" characteristic typical of rectifiers. A mathematical model for analyzing such a hemispherical system is required, and the model proposed here proceeds from the boundary condition (8). As a starting point (8) gives the excess hole concentration at the exterior surface of the space charge layer. Since the dependence of excess holes on the coordinate θ is contained in the factor $(e^{qV\cos\theta/kT}-1)$, and the dependence on the radius can be approximated by the factor $1/r^2$, therefore the excess hole concentration may be written as (3) which leads to the dipolar rectifier formula (5).

Consider small voltage fluctuations of amplitude $V \ll kT/q$, about a fixed bias V_0. This case requires only a single term ($l=1$) of (13), e.g., the boundary condition (8) may be expressed as

$$p_e e^{qV_0\cos\theta/kT} qV\cos\theta/kT = -(2/\pi)^{\frac{1}{2}} A_1 e^{-r_0/\Lambda}\left(1+\frac{r_0}{\Lambda}\right)(\cos\theta)\Lambda^2/r_0^2, \tag{15}$$

which immediately gives the constant A_1, and permits expressing the transform of the fluctuation in hole concentration.

$$p_1(r,\theta,j\omega) = \frac{qVp_e}{kT}\left(\frac{\Lambda+r}{\Lambda+r_0}\right)\left(\frac{r_0}{r}\right)^2 \times \exp[(r_0-r)/\Lambda + qV_0\cos\theta/kT]. \tag{16}$$

The following expression for the small amplitude fluctuation of diffusion current density comes directly from (16):

$$I(t) = G(V_0)[1 + r_0/\Lambda + (1+r_0/\Lambda)^{-1}]Ve^{j\omega t}/2. \tag{17}$$

The conductance $G(V_0)$ represents the slope of the current-voltage characteristic (5) evaluated for a bias voltage V_0. The admittance for the dipole mode may be written

$$Y(j\omega) = j\omega C(V_0) + G(V_0)[1 + r_0/\Lambda + (1+r_0/\Lambda)^{-1}]/2, \tag{18}$$

in which $C(V_0)$ is the barrier capacitance with bias V_0. The transform $Y(j\omega)^{-1}$ may be regarded as a transfer function, and its inverse transform as a weighting function $f(t)$, after James and Weiss.[10] The physical significance of the weighting function $f(t)$, in this instance, is that it gives the voltage response to a unit impulse in current density. As before,[4] we use a method described by Elmore and Sands[11] to determine the mean response time, as weighted by the function $f(t)$, and obtain the relation

$$\langle t \rangle_{Av} = T_d + (r_0^2/2D), \quad \text{(dipole mode)} \tag{19}$$

in which T_d is the time constant of the space charge layer $C(V_0)/G(V_0)$. The term r_0^2/D will be called the

[9] The function $J_{l+\frac{1}{2}}'(-jz)$ in Gegenbauer's formula is a Bessel function of the first kind.

[10] H. M. James and P. R. Weiss, *Theory of Servomechanisms*, edited by James, Nichols, and Phillips (McGraw-Hill Book Company, Inc., New York, 1947), Chap. 2.

[11] W. Elmore and M. Sands, *Electronics* (McGraw-Hill Book Company, Inc., New York, 1949), p. 137.

diffusion time hereafter in this paper. The mean response time with the unipole mode, as reported earlier,[4] may be written

$$\langle t\rangle_u = T_u + (r_0/2)(\tau/D)^{\frac{1}{2}} \quad \text{(unipole mode)}. \quad (20)$$

The second term of (20) is one-half the geometric mean of the diffusion time and the bulk lifetime, which is $(D\tau)^{\frac{1}{2}}/r_0$ times as great (a large factor) as the corresponding term in (19). However, this advantage of the dipole over the unipole mode is somewhat offset by the ratio of the charging time constants T_d/T_u which increases with increasing forward bias.

At frequencies for which the relation $\omega r_0^2 \ll 2D$ holds, the admittance reduces to

$$Y(j\omega) = G(V_0)[1 + j\omega\langle t\rangle_u], \quad (21)$$

which has the frequency dependence of a simple relaxation process. At high frequencies ($\omega r_0^2 \gg 2D$) the admittance obeys the relation

$$Y(j\omega) = G(V_0)\left\{1 + \left(\frac{\omega r_0^2}{2D}\right)^{\frac{1}{2}} + j\left[\omega T_d + \left(\frac{\omega r_0^2}{2D}\right)^{\frac{1}{2}}\right]\right\}, \quad (22)$$

which has the same form as the corresponding admittance with the unipole mode.

IV. COMBINATION OF BOTH MODES

In practice it would be very difficult to confirm or disprove a formal solution for both modes operating simultaneously. The justification for sketching such a solution is that it reveals an important dependence of both frequency and amplitude response on variations in surface conditions. To treat both unipole and dipole modes simultaneously, it is necessary to rewrite the boundary condition (8) as follows

$$p_1(r_0,\theta,t) = p_e(\exp\{q[1-\beta+\beta\cos\theta]V(t)/kT\} - 1), \quad (23)$$

in which βV is the fraction of the applied voltage taken up by the dipole mode. By expressing (23) by the expansion of (13), *viz.*,

$$p_e(\exp\{q[1-\beta+\beta\cos\theta]V(t)/kT\} - 1)$$

$$= (\Lambda/jr_0)^{\frac{1}{2}} \sum_{l=0}^{\infty} A_l H_{l+\frac{1}{2}}(jr_0/\Lambda)\Theta_l, \quad (24)$$

the constants A_l can be evaluated, and, in principle, the hole concentration and, in turn, the hole current are determined. The essential difficulty which impedes the practical utilization of such a solution is the evaluation of β. The fraction β depends in a subtle way on the geometrical design of the point contact diode and the surface recombination velocity at all free surfaces of the semiconducting die. Most important of all, β is not truly constant, but varies with injection level. Therefore, the constants A_l which determine the relative magnitude of the modes contributing to the current can themselves vary during the operation. In this way, variations in frequency response might occur which would be unjustifiable by the theoretical expressions for dynamic behavior of the individual modes listed in the previous section and in an earlier paper.[4] Also, as surface condition is difficult to control, it might be expected that current-voltage characteristics representing various combinations of (2) and (5) might appear in diodes made under more or less similar conditions. It would appear that more reproducible characteristics might be obtained if diodes were designed deliberately to suppress either the unipole or dipole mode, as dictated by the application. Two simple geometric designs (Fig. 7) are shown, one to suppress the unipole mode, and the other to suppress the dipole mode.

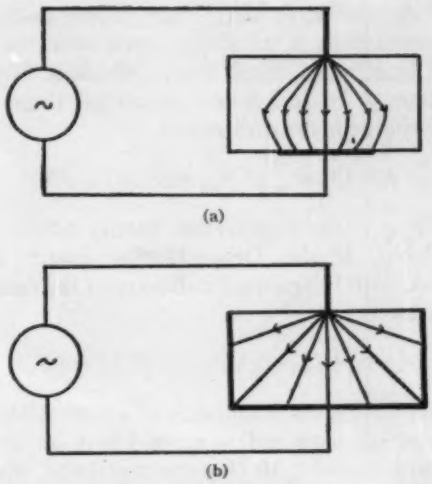

FIG. 7. (a) Point contact-semiconductor die arrangement designed to suppress the unipole mode. (b) Point contact-semiconductor die arrangement designed to suppress the dipole mode.

The solutions for the higher modes ($l > 1$) of minority carrier diffusion about a point contact should be unimportant as long as the radius of the space charge layer r_0 is small compared with the wavelength of the applied field. With the present size of injecting contacts and the frequency bands in use, the higher modes should be of minor concern.

V. DISCUSSION

The validity of approximations (3), (19), and (21) requires that the radius of the space charge layer r_0 be small compared with the diffusion length $(D\tau)^{\frac{1}{2}}$, i.e., the dc value of Λ. Furthermore, the radius of the space charge layer r_0 enters into the mean response time $\langle t\rangle_u$ with both unipole and dipole modes. Therefore, the magnitude of r_0 is of practical concern, and we are led to ask questions such as the following. Are there limits to the miniaturization of r_0? If so, what are the limits, and what do they indicate for attainable operating frequencies?

The limits on r_0 may be inferred from a study of the space charge surrounding disordered regions in germa-

nium.[12] According to that study, if the radius of the metal contact r_m is small compared with the Debye-Hückel length $(kT\epsilon)^{\frac{1}{2}}(q^2N)^{-\frac{1}{2}}$, in which N is the concentration of ionized donor impurities, then we have a space charge layer with radius

$$r_0=(3\varphi\epsilon r_m/qN)^{\frac{1}{2}}, \quad r_m\ll(kT\epsilon/q^2N)^{\frac{1}{2}} \tag{25}$$

in which φ is the equilibrium barrier height. On the other hand, if the Debye-Hückel length is small compared with the contact radius, or of the same order, then we have

$$r_0=r_m+(2\varphi\epsilon/qN)^{\frac{1}{2}}, \quad r_m\gtrsim(kT\epsilon/q^2N)^{\frac{1}{2}}. \tag{26}$$

Equation (25) gives a radius r_0 of extent 3500 A for a metal contact with radius r_m of 150 A on an n-type germanium die with 10 ohm-cm resistivity, while (26) gives a radius r_0 of 1400 A for the same contact on a 0.03 ohm-cm die. One might remark that r_0 is not a sensitive function of resistivity, because a reduction by more than two orders of magnitude in resistivity produced, in this instance, a reduction in r_0 of less than one order of magnitude. A reasonable conclusion is that r_0 cannot be reduced significantly below around 3000 A with n-type germanium suited for diodes.

The diffusion length $(D\tau)^{\frac{1}{2}}$ may be as much as 2500 times as great as the radius r_0 taking material with bulk lifetime 200 μsec, and diffusion coefficient 40 cm^2/sec. Therefore, the condition $(D\tau)^{\frac{1}{2}}\gg r_0$, required for the validity of (3), (19), and (21), can be met. Furthermore, the same figures for r_0 and D give a diffusion time $r_0^2/D\sim3\times10^{-11}$ sec, which indicates that diodes could be made to obey (21) up to a frequency of about 5 kMc/sec. At zero bias, the time constant of the space charge layer is about 5×10^{-10} sec with n-type germanium having resistivity of 10 ohm-cm regardless of the mode, which, with $r_0=3500$ A, gives attainable values of response time $\langle t\rangle_{Av}\sim5\times10^{-10}$ sec with the dipole mode as compared with $\langle t\rangle_{Av}\sim4\times10^{-8}$ sec with the unipole mode. The mean response time of the dipole mode is about two orders of magnitude smaller with this example, and by consideration of the general expressions for $\langle t\rangle_{Av}$, Eqs. (19) and (20) in Sec. III, it is evident that the dipole mode is inherently superior to the unipole mode for high frequency applications.

The motion of the boundary of the space charge layer with variations in applied voltage has been neglected thus far. As the boundary of the space charge layer is at the same time the bounding surface for current flow, the current for a given applied voltage is restricted by the area of this bounding surface. Therefore, motion of the space charge layer is of interest in connection with the current-voltage characteristics. While the size but not the shape of the space charge layer varies in the case of the unipole mode, both size and shape vary with applied voltage in the case of the dipole mode. As only the size of the space charge layer varies with the unipole mode, its dependence on applied voltage can be treated by expressing the exterior radius as the function $r_0(V)$. The departure from spherical form with the dipole mode is treated here by considering the space charge layer as a sphere with bounding radius equal to the average radial coordinate $\langle r_0(V)\rangle_{Av}$ of the exterior boundary. The average is taken over the range of the angular coordinate $0<\theta<\pi/2$. The expressions $r_0(V)$, for the unipole mode, and $\langle r_0(V)\rangle_{Av}$, for the dipole mode, may be approximated by the following modifications of (25) and (26):

$$\left.\begin{aligned} r_0(V)&=\left[\frac{3(\varphi-V)\epsilon r_m}{qN}\right]^{\frac{1}{2}}, \quad \text{(unipole)} && (27)\\ \langle r_0(V)\rangle_{Av}&=r_03\varphi\left[1-\left(\frac{\varphi-V}{\varphi}\right)^{\frac{1}{2}}\right](4V)^{-1}, \quad \text{(dipole)} && (28)\end{aligned}\right\} r_m\ll\left(\frac{kT\epsilon}{q^2N}\right)^{\frac{1}{2}}$$

$$\left.\begin{aligned} r_0(V)&=r_m+\left[\frac{2(\varphi-V)\epsilon}{qN}\right]^{\frac{1}{2}}, \quad \text{(unipole)} && (29)\\ \langle r_0(V)\rangle_{Av}&=r_m+\left(\frac{2\varphi\epsilon}{qN}\right)^{\frac{1}{2}}\frac{2\varphi}{3V}\left[1-\left(\frac{\varphi-V}{\varphi}\right)^{\frac{1}{2}}\right], \quad \text{(dipole)} && (30)\end{aligned}\right\} r_m\gg\left(\frac{kT\epsilon}{q^2N}\right)^{\frac{1}{2}}.$$

Equations (27)–(30) become inaccurate with increasing forward voltage because the hole concentration within the range $r_m<r<r_0$ has been neglected in the determination of these expressions. However, in the range of applied voltage over which motion of the space charge layer noticeably influences the hole current, Eqs. (27)–(30) are accurate.

As the space charge boundary is relatively insensitive to applied voltage, its effect on the expressions for dc current (2) with the unipole mode, and (5) with the dipole mode, can be accounted for by direct substitution of the appropriate radius, $r_0(V)$ or $\langle r_0(V)\rangle_{Av}$ from (27) through (30) for r_0 in the saturation current (I_s). This has been done with the current-voltage characteristic curves for reverse voltage, sketched in Figs. 8 and 9. These curves apply to diodes made of the same material, *viz.*, n-type germanium with 10 ohm-cm resistivity.

[12] B. R. Gossick, J. Appl. Phys. **30**, 1214 (1959).

A 0.3 v equilibrium barrier (φ) has been assumed in each example. Figure 8 refers to a low-frequency diode with 33.3-μ contact radius (r_m), which by (26) gives a 35-μ space charge bounding radius (r_0) with zero bias. Taking 200 μsec bulk lifetime (τ) and zero bias gives 4 μsec for the mean response time $\langle t \rangle_{av}$ with the unipole mode, and 0.15 μsec with the dipole mode (with reference only to Fig. 8).

The motion of the space charge layer with reverse bias $qV/kT = -2000$, which is -50 v at room temperature, makes the reverse current increase in magnitude from $-I_s$ to $-1.6I_s$ with the unipole mode, and from $-2I_s$ to $1.4(2I_s)$ with the dipole mode (Fig. 8). Figure 9 refers to a high-frequency diode with 150 A contact radius (r_m) which by (25) gives a 3500 A space charge

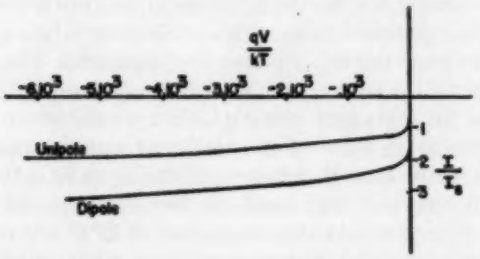

FIG. 8. Reverse current-voltage characteristics of both unipole and dipole modes for a large contact radius suitable for low frequency applications.

layer radius (r_0) with zero bias. Taking 200 μsec bulk lifetime (τ) and zero bias gives 40 mμsec for the mean response time $\langle t \rangle_{av}$ with the unipole mode and 0.5 mμsec with the dipole mode. In this case, the motion of the space charge layer with reverse bias $qV/kT = -2000$, makes the reverse current increase in magnitude from $-I_s$ to $-5.5I_s$ with the unipole mode, and from $-2I_s$ to $-4.1(2I_s)$ with the dipole mode (Fig. 9). The percentagewise variation in saturation current through its

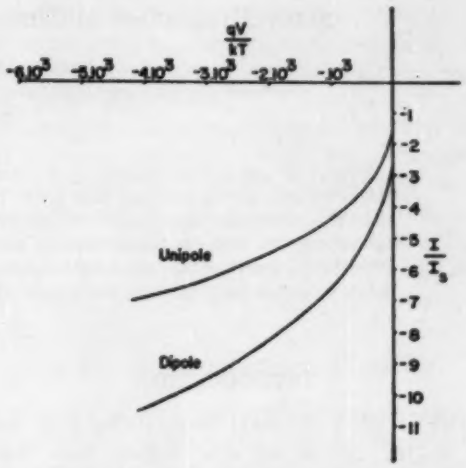

FIG. 9. Reverse current-voltage characteristics of both unipole and dipole modes for a small contact radius suitable for high frequency applications.

dependence on the space charge boundary is less with the dipole mode in both examples, the physical explanation being that the motion of the boundary with the dipole mode is restricted by a constraint at $\theta = \pi/2$ where it is held stationary. A final conclusion, which comes from a comparison of Figs. 8 and 9, is that a smaller (i.e., faster) contact inherently gives a larger magnitude of reverse current.

On the basis of this discussion it is clear that the dipole mode has characteristics which are distinctly different from and in certain respects superior to those of the unipole mode. Therefore, the experimental investigation of the dipole *versus* the unipole modes of minority carrier diffusion is obviously warranted.

ACKNOWLEDGMENTS

It is a pleasure to thank both H. C. Schweinler and A. T. Wager for helpful comments.

Some Properties of Zinc Sulfide Crystals Grown from the Melt

ARRIGO ADDAMIANO AND MANUEL AVEN
General Electric Company, Lamp Development Department, Nela Park, Cleveland, Ohio
(Received June 24, 1959)

Hexagonal zinc sulfide crystals were obtained by controlled cooling of melted zinc sulfide. Both pure and activated zinc sulfide powders were used. The density of pure melt grown crystals was found to be higher than that of natural zinc blende crystals or crystals grown by evaporation. The stability of the pure hexagonal crystals towards transformation to the cubic zinc-blende structure in the interval of temperature 700–1150°C was investigated. A full conversion to the cubic phase was never observed. The experimental evidence indicates the transition point to be above 1150°C.

INTRODUCTION

DIFFERENT methods of obtaining pure synthetic single crystals of zinc sulfide have been described[1–13] in the past few years. In a recent paper from this laboratory[14] it was indicated that zinc sulfide crystals can also be obtained by melting zinc sulfide powders at relatively low pressures. By this method zinc sulfide powders both pure and "doped" can be used as starting materials. We wish to report here some preliminary observations on different samples of pure and activated wurtzite crystals obtained from the melt.

EXPERIMENTAL

I. Pure ZnS Crystals

Pure hexagonal zinc sulfide crystals were obtained by controlled cooling of luminescent grade zinc sulfide powders (mp 1830±20°C) in an argon atmosphere at 150 psi using a somewhat modified version of the bomb where the melting point and triple point pressure of zinc sulfide were determined.[14] Some typical crystals are illustrated in Fig. 1.

For optical observations fused zinc sulfide rods were cut with a diamond saw and reduced to regular shapes, some 5×5×1.5 mm. The crystal surfaces were reduced to optical flats by grinding and polishing. Observations in polarized light between crossed nichols showed that the samples were homogeneous and apparently free from defects. Similar back-reflection Laue photographs were obtained with a narrow beam of x-rays impinging in different areas of the crystals repeatedly translated in a plane normal to the direction of the beam.

The density of the crystals was determined by the pycnometer and by the hydrostatic balance techniques. For comparison the densities of different single crystals grown from the vapor phase were measured. The values obtained for our crystals were in every case higher than those for the vapor phase grown crystals, which is not surprising in view of the fact that our crystals were apparently free of defects and, being polished, had a smaller surface area available for adsorption of gases. The pycnometric values measured at 22°C and referred to water at 22°C gave an average of 4.184±0.017 g/cc for our crystals and 4.037±0.037 g/cc for crystals supplied by Dr. W. W. Piper. The values obtained with the hydrostatic balance are between 4.13 and 4.14 g/cc for our samples and 4.089 g/cc for a large single crystal supplied by Dr. D. C. Reynolds.

These values may be compared with an x-ray density of 4.089 g/cc given by the ASTM File Index for pure wurtzite powders and 4.15_3 g/cc calculated from the cell dimensions of wurtzite as given by G. Aminoff.[15]

Analytical data on the luminescent powders used as starting materials and on the fused zinc sulfide rods were obtained by spectrographic analysis. Traces of B, Al, Cu, Cd, Fe, Mg, Pb, and Si, ranging from 1 to 15 ppm were detected in the zinc sulfide powders. For

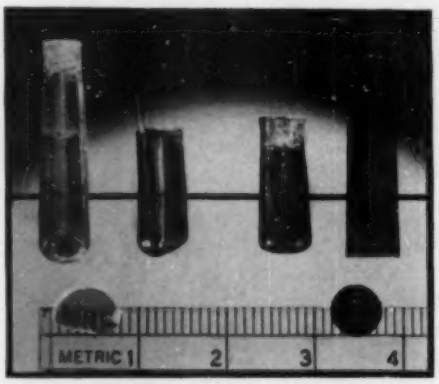

FIG. 1. Some samples of pure and activated zinc-sulfide obtained by controlled cooling of the melt.

[1] Greene, Reynolds, Czyzak, and Baker, J. Chem. Phys. **29**, 1375 (1958).
[2] D. C. Reynolds and S. J. Czyzak, Phys. Rev. **79**, 543 (1950).
[3] W. W. Piper, J. Chem. Phys. **20**, 1343 (1952).
[4] W. W. Piper and W. L. Roth, Phys. Rev. **92**, 503 (1953).
[5] A. Addamiano, Nature **179**, 493 (1957).
[6] Matsumura, Fujisaki, and Tanabe, Sci. Repts. Research Insts. Tohoku Univ. Ser. **A10**, 459 (1958).
[7] L. W. Strock and V. A. Brophy, Am. Mineral. **40**, 94 (1955).
[8] A. Kremheller, Sylvania Technologist **8**, 11 (1955).
[9] H. Müller, Neues Jahrb. Mineral. **84**, 43 (1952).
[10] J. Krumbiegel, Z. Naturforsch. **9a**, 903 (1954).
[11] R. Lorenz, Ber. deut. chem. Ges. **24**, 1507 (1891).
[12] A. Kremheller and A. Levine, Sylvania Technologist **10**, 67 (1957).
[13] Allen, Crenshaw, and Merwin, Am. J. Sci. **34**, 341 (1912).
[14] A. Addamiano and P. A. Dell, J. Phys. Chem. **61**, 1020 (1957).
[15] G. Aminoff, Z. Krist. **58**, 203 (1923).

the analysis of the melt product the zinc sulfide rods were cut in approximately equally thick parallel slices and the impurity content was examined for each slice separately.

The analysis showed that near spectroscopic purity was achieved in the preparation of the crystals. In fact only traces of B, Cu, Mg, and Si were detected in the fused zinc sulfide rods. Cooling the melted mass from its bottom upwards resulted in a segregation of copper impurities on the upper part of the crystals, while the reverse situation was true for silicon. The central portion of the rods contained no spectroscopically detectable impurities.

II. Zinc Sulfide Phosphors

The melting procedure is particularly suitable to the growth of crystal phosphors. We have obtained a variety of activated crystals either by melting powders of precipitated zinc sulfide wetted by a solution of the desired impurities and then taken to dryness, or by directly melting zinc sulfide phosphors of different composition. As an alternate route to the preparation of single crystal phosphors we have activated pure wurtzite crystals by diffusing impurities into them, either by long firing of the specimens embedded in suitably activated zinc sulfide powders, or by plating the crystals with the selected activators and allowing diffusion to take place at elevated temperatures.

When powders were used we obtained the same end product in all cases independently of whether crystal phosphors or precipitated zinc sulfide powders containing the correct amount of doping agents were used. Segregation of impurities during solidification of the melt was observed in many cases, even for low impurity concentration and for elements, like Mn, which can substitute for zinc by isomorphous replacement. Thus in the preparation of ZnS:Cu, Al phosphors, in which phosphor powders activated by 5×10^{-4} Cu and coactivated by 5×10^{-4} Al were used as starting materials, the rods of melted zinc sulfide were definitely inhomogeneous; most of the copper had concentrated in the upper (last frozen) parts of the crystals, which looked dark brown and were practically opaque, while the lower portions of the rods were transparent and had a green luminescence under 3650-A irradiation. This is in agreement with the analytical data on pure wurtzite crystals and shows that it should be possible to eliminate minute traces of copper present in ZnS powders by zone melting techniques or similar methods.

Zinc sulfide phosphors or unfired powders of equivalent composition with different concentrations of copper and bromine, copper and aluminum, manganese, copper and manganese, cobalt, samarium, gadolinium, lead, etc., have been used in other experiments. Copper activated, halogen-coactivated wurtzite crystals have shown green luminescence under 3650- or 2537-A excitation at room temperature. The color of the luminescence shifted to the blue at liquid nitrogen temperature or under x-ray excitation. In contrast, ZnS:Cu, Al phosphors were observed to emit in the green even at liquid nitrogen temperature.

Introducing activators by diffusion from the outside of pure wurtzite crystals, it was possible to prepare green-luminescing ZnS:Cu, Al crystals, blue emitting crystals activated by silver and coactivated by aluminum, "self-activated" blue crystals with aluminum or gallium, and copper-activated "self-coactivated" orange crystals (excitation by 3650-A radiation).

III. Phase Transformation Studies

The stability of wurtzite crystals was investigated on crystal specimens prepared as outlined in Sec. I. The crystals, originally transparent and colorless, were annealed at different temperatures from 700 to 1150°C in sealed containers. For experiments up to 900°C the crystals were sealed in fused silica tubes previously seasoned by firing in them pure zinc sulfide in H_2S atmosphere. The crystals were placed in the tubes and heated for five minutes at 500° in an H_2S stream to remove adsorbed air or water. After cooling to room temperature the tubes were sealed off with one atmosphere H_2S and inserted into the furnaces preheated to the desired temperatures.

Above 900° this method was found unsatisfactory because a progressive coloration of the crystals took place due to diffusion of impurities from the walls of the silica tubes on which they were resting. To prevent such contamination the wurtzite crystals were placed into crucibles of spectroscopically pure graphite provided with lids and then inserted into seasoned tubes of fused silica containing few grams of H_2S-fired pure zinc sulfide powder. After sealing off with one atmosphere H_2S, these tubes were introduced into the furnaces at the desired temperatures, with a temperature gradient along the tubes to keep the powder slightly cooler than the crucibles. By the use of this technique the crystals remained clear even after 400 hrs firing at 1150°C, while the zinc sulfide powders absorbed most of the volatile impurities and became luminescent.

At regular intervals the tubes were extracted from the furnaces and quickly cooled to room temperature. The crystals were examined under the polarizing microscope. If necessary the crystal surfaces were repolished. Back reflection Laue pictures were taken at the beginning of each experiment and compared with those obtained at later stages of the annealing process.

The results of this investigation are summarized in Table I.

These experiments point to a much greater stability of the hexagonal phase towards transformation to the cubic phase than reported by other investigators. Moreover, experiments 7 and 8 (cf. Table I) indicate that for pure wurtzite crystals obtained from the melt the transition point is higher than the often quoted

TABLE I. Summary of phase transformation studies for melt grown wurtzite crystals.

Experiment No.	Annealing temperature °C	Annealing time (hr)	Optical observations	X-ray pattern	Crystal container
1	700	740	Crystal stays clear and birefringent	No change	Silica tube
2	800	740	Crystal becomes olive green after 740 hr. Still birefringent	No change	Silica tube
3	900	213	Dark coloration and birefringence after 213 hr	No change	Silica tube
4	900	168	As above	No change	Silica tube
5	975	340	Crystal too dark for optical observations	No change	Silica tube
6	975	504	Crystal stays clear and birefringent	No change	Graphite crucible
7	1100	168	Crystal stays clear and birefringent	Signs of incipient transition visible (reflections with $h-k\neq 3n$ are diffuse)	Graphite crucible
8	1150	32	Crystal clear and birefringent	Reflections with $h-k\neq 3n$ are diffuse)	Graphite crucible
	1150	120	Crystal clear and birefringent	Intensity of diffuse reflections increased	
	1150	448	Crystal clear and birefringent	Diffuse reflections disappearing, sharp cubic reflections are now present.	

value of 1020±5°C obtained by Allen, Crenshaw, and Merwin.[13] It should be remembered that such value actually refers to a zinc-blende containing 0.15% iron impurity and that different impurities have a marked effect on the transition point. Our observations are in qualitative agreement with the work of Allen *et al.*[13] insofar as the transformation wurtzite→blende was observed to be sluggish by them also. Firing times of 40–66 hrs were reported to be necessary for the conversion to sphalerite of mineral samples fired between 800 and 950°C.

The exact determination of the transition temperature is complicated by recently discovered order-disorder phenomena accompanying the transformation.[16–20] Müller[9] gives 850°C for the temperature at which the transformation occurs at the highest rate, and 10–12 hr for a complete transformation to occur at that temperature. On the other hand Kremheller[8] observed that the transformation rate is a maximum at 900°C, with a firing time of 5 hr being required for a complete phase change. It is interesting to note that Kremheller observed conversion of the cubic to hexagonal ZnS at 975° in presence of chlorides, but no transformation even at 1175°, in the absence of chlorides. Moreover, in annealing hexagonal crystals he observed the appearance of a cubic phase even at 1130°C, i.e., 110° above the generally accepted transition point.

As the vapor pressure of zinc sulfide[21] is already of the order of three millimeters at 1150°, it is difficult to extend our observations to higher temperatures, particularly in view of the long firing times which seem to be required for the transformation wurtzite→blende.

SUMMARY AND CONCLUSIONS

Pure hexagonal zinc sulfide single crystals prepared by controlled cooling of melted zinc sulfide in an argon atmosphere at 150 psi have displayed good optical properties, high purity, high density, and high stability. Their conversion to the cubic phase could not be observed by prolonged firing at 700–1150°C, in contrast to the behavior of vapor grown crystals and natural minerals. An inversion point above 1150° is indicated by our observations. The reasons for the disagreement with the value reported in the literature are to be seen mainly in the higher purity of our crystals and their method of preparation.

Preliminary work on doped zinc sulfide has shown that segregation of impurities takes place during solidification. In particular copper is more soluble in liquid than in solid ZnS. The contrary seems to be true for silicon.

Crystal phosphors doped by various activators did not differ very much in their luminescent properties from conventional phosphor powders. Diffusion techniques gave good results in activating pure wurtzite crystals. There is some evidence to suggest that diffusion of impurities from the walls of the containers takes place when zinc sulfide crystals are fired in fused silica tubes without special precautions. Such impurities are probably present in crystals grown by the vapor phase and may be responsible for some differences observed in the stability of our crystals as compared to crystals grown by the vapor phase.

[16] C. Frondel and C. Palache, Am. Mineral. **35**, 29 (1950).
[17] R. S. Mitchell and A. S. Corey, Am. Mineral. **39**, 773 (1954).
[18] D. C. Buck and L. W. Strock, Am. Mineral. **40**, 192 (1955).
[19] H. Jagodzinski, Acta Cryst. **2**, 201 (1949); **2**, 208 (1949); **2**, 298 (1949).
[20] M. S. Paterson, J. Appl. Phys. **23**, 805 (1952).
[21] H. Spandau and F. Klanberg, Z. anorg. u. allgem. Chem. **295**, 309 (1958).

ACKNOWLEDGMENTS

We wish to thank Dr. I. Lee Smith, Dr. R. P. Taylor, and Miss J. R. Cooper of this laboratory for the spectrographic and pycnometric determinations, for the density determination by the immersion method, and for taking the Laue photographs of the wurtzite crystals. We are obliged to Dr. W. W. Piper (General Electric Research Laboratory, Schenectady, New York) and Dr. D. C. Reynolds (Aeronautical Research Laboratory WPAFB, Dayton, Ohio), who kindly supplied crystals grown by the vapor phase by two different techniques. The mechanical handling (cutting and polishing) of the fused zinc sulfide rods was done by Mr. G. W. Armstrong of this laboratory whom we thank.

JOURNAL OF APPLIED PHYSICS VOLUME 31, NUMBER 1 JANUARY, 1960

Flat Panel Vacuum Thermal Insulation

H. M. STRONG, F. P. BUNDY, AND H. P. BOVENKERK
General Electric Research Laboratory, Schenectady, New York

(Received June 8, 1959)

Evacuated mats of glass fiber made up of fibers of proper size and orientation are capable of supporting a compressive mechanical loading of at least one atmosphere and yet maintain a thermal conductivity of less than 10 microcalories/cm°C sec. The use of such a glass fiber mat as a filler makes possible an evacuated flat-panel thermal insulation which is comparable to a Dewar flask in insulation efficiency. The rate of heat transfer through a Dewar flask wall was reduced several-fold at liquid nitrogen temperatures and below by adding a 2-cm-thick layer of orientated and evacuated glass fiber mat to the outer surface.

This investigation showed that in evacuated glass fiber mats, supporting external atmospheric loading, the fiber to fiber contact area is less than 10^{-4} the mat area, making the contact pressure about 15 000 kg/cm². The effective length of the thermal conduction paths along the fibers is about four times the mat thickness. The mean pore size for gas molecule motion in the mat was found to be about 54×10^{-4} cm and 2×10^{-4} cm for mean fiber sizes of 14×10^{-4} cm and 0.2×10^{-4} cm, respectively. The radiation mean free paths for the same fiber sizes were found to be 150×10^{-4} cm and 52×10^{-4} cm, respectively. The thermal diffusivity is about 10^{-4} cm²/sec, which is much smaller than any other insulating material.

I. INTRODUCTION

ONE of the most effective types of thermal insulation known is a wall space evacuated to less than one micron pressure and having surfaces highly reflective to thermal radiation. In the form of the familiar Dewar flask, this type of insulation has been in use for over sixty years. However Dewar-type insulation is limited to cylindrical and spherical shaped vessels because of the necessity of supporting the atmospheric load by the inner and outer walls without any mechanical support in the evacuated space between. No insulation has appeared in flat panel form that approaches the vacuum type wall in insulation efficiency. Almost all of the other familiar insulations contain air, and regardless of their makeup have the conductivity of still air as their lower limit of conductivity. Few of them reach this lower limit and only the finest particle insulations such as the silica aero-gel of Kistler[1] have conductivities equivalent to, or slightly lower than that of still air. The lowest thermal conductivities can be reached only by removal of air.

A variation of the highly evacuated empty wall space is the moderately evacuated wall space containing lightly packed powders proposed by Smolukowski,[2] Langmuir,[3a] and Stanley[4] for cylindrical and spherical containers. While such a heat barrier is roughly equivalent to a Dewar-type wall, attempts to use powders to support flat evacuated walls[3,5,6] were not as successful because of the high thermal conductivity of the same powders when compacted by the atmospheric pressure load.

The possibility of discovering a supporting structure for flat evacuated walls that has great stress bearing capacity and exceedingly low thermal conductivity is very intriguing. The present report describes the authors' study of this and associated problems.

References of further interest in connection with this subject are text books on the kinetic theory of gases,[7,8] the early work of Smolukowski[9] and Knudsen[10] on the application of the kinetic theory of gases to explain

[1] S. S. Kistler, Nature **127**, 741 (1931); J. Phys. Chem. **39**, 79–85 (1935).

[2] M. Von Smolukowski, Krakauer Anz., 129(A) (1910); Max Jakob, *Heat Transfer* (John Wiley & Sons, Inc., New York, 1949), p. 90.

[3] Unpublished work of (a) I. Langmuir and (b) A. W. Hull, made available to authors.

[4] W. Stanley, powder filled vacuum wall flask, U. S. Patent 1,071,817 (1913).

[5] C. G. Munters, U. S. Patent 2,164,143 (1939).

[6] Blat, Bresler, and Ryabinin, J. Tech. Phys. (USSR) **15**, 916–23 (1945). Yu N. Ryabinin (thesis) from Kislorod (1944), No. 3, pp. 39–43.

[7] Saul Dushman, *Vacuum Technique* (John Wiley & Sons, Inc., New York, 1949).

[8] E. H. Kennard, *Kinetic Theory of Gases* (McGraw-Hill Book Company, Inc., New York, 1938).

[9] M. Von Smolukowski, Akad. Wiss. Wien **107**, 304 (1898); **108**, 5 (1899).

[10] M. Knudsen, Ann. Physik **34**, 593 (1911).

TABLE I. Comparison of approximate thermal conductivities in the temperature range 0° to 100°C.

Substance	Coefficient of thermal conduction, k in microcalories/cm°C sec
1. Structural materials	
Metals	100 000
Organic polymers	400
Ceramic and refractory materials	10 000
Glass	3 000
2. Insulations	
Air filled fibers, foams, etc., in common use	80
Still air 65°C	69
Finest powders 65°C (silica aero-gel)	60
Dewar flask (66°C inner T) (65°C outer T)	7 microcalories/cm² sec
Flat vacuum wall structure (max. value desired)	10

gaseous conduction, Smolukowski's[2] early experiments on gaseous conduction at reduced pressure in fine powders, papers by Kistler[1] on the properties of his silica aero-gel, tests on evacuated silica aero-gel for liquid air storage by Blat *et al.*,[6] and studies on mechanisms of conduction in air-filled, evacuated and heavy-gas-filled insulations by Verschoor and Greebler.[11]

II. PHYSICAL REQUIREMENTS

To be comparable with a Dewar flask in insulation quality, the mechanical supporting structure between the walls of a flat vacuum panel should have an effective thermal conductivity not exceeding 10 microcalories/cm°C sec.* Thus, the supporting structure must have very small contact areas and devious heat flow paths of high thermal resistance. Small contact areas imply high contact stresses attainable only with hard, strong materials which can maintain their properties under conditions of vacuum bake-out and long service life without creep. It is also desirable that the geometry of the supporting structure provide radiation baffling, and that it divide the space into cells small enough that gaseous thermal conduction would be negligible up to gas pressures of a few hundred microns.

In choosing a material to support flat walls against an atmospheric pressure load it is helpful to compare the approximate thermal conductivities of a variety of substances with the desired conductivity of the supporting structure. The values are noted in Table I.

Most glass, ceramic, and refractory materials are hard stable substances suitable for use in permanently evacuated containers and are the most favored choice for use in devising a vacuum wall support structure. It is clear from their thermal conductivity values that a suitably low thermal conductivity in these materials must be achieved through proper geometric distribution of the support material. It was found that a pad made of glass fibers oriented randomly in planes parallel to the pad (perpendicular to the temperature gradient) fulfilled all requirements.

The thermal conduction characteristic of a number of granular and fibrous substances taken from the authors' test results are shown in Table II. The tests were all made in a one to 10 micron vacuum with a tempearture range across the sample of about 20° to 110° or at an average temperature of 65°C. In some tests the sample supported the load of the atmospheric pressure; in others the atmospheric pressure load was not applied to the sample. From the numbers in the table it is readily seen that granular materials are sensitive to applied pressure while fibrous materials are not.

A glass column structure was proposed by Hull[3b] of this laboratory which has a solid thermal conductivity very close to 10. Each column consisted of two $\frac{3}{16}$-in.-diam glass beads in series, one on top of the other in the direction of heat flow. The columns were positioned three or four inches apart by a plate structure lying perpendicular to the direction of heat flow. In an open structure of this sort the wall surfaces are made reflecting and the air pressure kept below about 1 μ of mercury. To the authors' knowledge, this is the only structure for

TABLE II. Thermal conductivity of granular and fibrous materials in a 1 to 10 μ vacuum; average temperature approximately 65°C.

Material	Thermal conductivity, k, microcalories/cm°C sec	
	Loosely packed	1 atmos Compressive load
80 mesh foundry sand	8.7	86
Glass beads $\frac{3}{16}$-in. diam	27	98
Glass beads, 0.002-in. diam		50
Crushed Pyrex glass 20 mesh	7.1	23
Carborundum 150 mesh		220
Alumina 100–250 mesh		196
Diatomaceous earth and carbon black 3:1 mixture		51
Silica aero-gel		22
Duck feathers (eider down)		8.3
Asbestos lint		30
Cotton fibers		19
Stainless steel wool (fine)		26
Glass needles 125 μ diam		39
Glass fibers 14 μ diam (good orientation)	9.6[a]	6 to 8
Glass fibers 4 μ diam (good orientation)	4 to 5	3.9 to 5.2
Glass fibers 2 μ diam (good orientation)		5.4
Glass fibers 0.2 μ diam (good orientation)		4.6

[11] J. D. Verschoor and P. Greebler, Trans. Am. Soc. Mech. Engrs. 74, 961 (1952).

* The unit of thermal conductivity used throughout this report is the microcalorie/cm°C sec. This unit will not be repeated except where necessary for clarity. Thermal conductivity values given apply for an average temperature of the insulation within the range 0° to 100°C, usually about 70°C. Where there are exceptions or where the exact temperature is important to the discussion, the temperature will be given, otherwise not.

[a] Sample thickness under no load increased without much change in heat transfer, making the loosely packed k larger than the k under a compressive load. (See Sec. VI for description of test methods and definition of k.)

flat wall evacuated insulations other than a glass fiber mat approaching 10 in conductivity.

To account for the exceptionally low thermal conductivity of evacuated glass fiber structures, the mechanism of heat flow by gaseous, solid, and radiative conduction will be examined briefly in the sections that follow.

III. SOLID CONDUCTION IN GLASS FIBER SUPPORTS

An exact analysis of heat conduction along the solid paths in a random arrangement of fibers would be a very difficult task. It would be complicated by the existence of radiant heat transfer through the fibers, and at any point there may be an exchange between solid and radiative heat transfer. However, one can visualize an idealized structure consisting of a symmetrical array of uniform fibers like that shown in Fig. 1(a) in which the general heat flow is perpendicular to the fibers. An analysis of a structure of this sort helps to show how glass fiber mat can have so high a thermal resistance, and indicates approximate values of the areas of contact, contact pressures, and path lengths for heat flow.

At the points of intersection of the fibers there will be a tiny circular contact area whose radius b, is given by the Hertz formula[12]

$$b=1.13(SR/E)^{\frac{1}{3}},$$

in which S is the load per contact, R is radius of fiber, E is modulus of elasticity. The heat must pass through these tiny contact areas and along the fiber to the next contact as shown in Fig. 1(b). The heat flow is assumed to be evenly divided to the right and left.

Focusing attention on the flow to the right only, the symmetry of the flow lines is closely equivalent to the geometry for flow shown in Fig. 1(c) in which the ends of the fibers are pictured as being hemispherical and in contact end to end. The actual contact area between the two fibers is shared equally by the flow to the right and the flow to the left. Hence, the thermal resistance of one contact unit [Figs. 1(b) and 1(c)] is made up of the hemispherical end, with contact area one-half the actual contact area, and a length of fiber, l, equal to one-half the distance between successive fiber junctions. Since the heat leaving each contact point has the opportunity of flowing in two directions, the thermal resistance of each layer is that of two parallel paths, each path consisting of two contact units in series.

In Fig. 1(b), the area of contact due to the pressure flattening is given by the expression

$$\tfrac{1}{2}\pi b^2=(\pi/2)1.28(SR/E)^{\frac{1}{3}}. \tag{1}$$

This corresponds to a compression of the radius of the equivalent hemispherical end [see Fig. 1(c)] of an amount given by

$$\Delta R=(\text{area of contact}/2\pi R),$$
$$=(1.28/4)(S/E)^{\frac{1}{3}}R^{-1}. \tag{2}$$

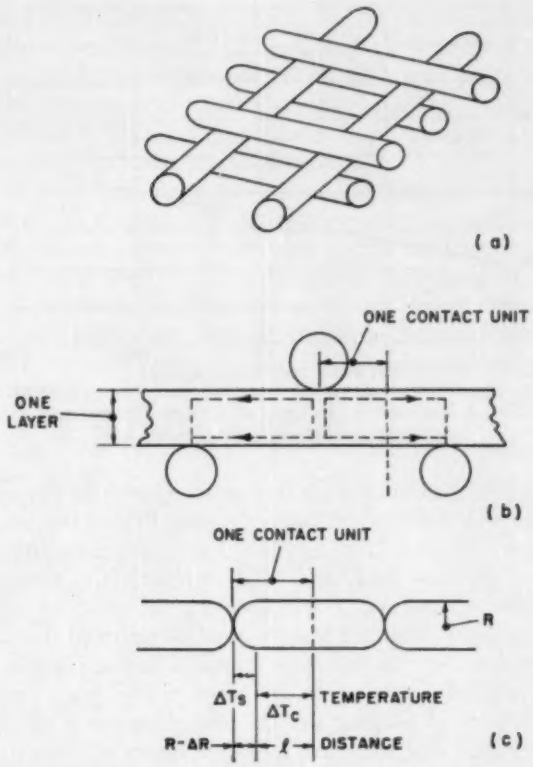

FIG. 1. Ideal glass fiber lattice. (a) A symmetrical lattice of glass fibers; (b) detail of a series of two fiber junctions showing the heat flow path; (c) an idealized fiber junction which is approximately equivalent thermally to the junction shown in (b).

The thermal resistance of one contact unit [Fig. 1(c)] was taken to be the sum of the thermal resistances of the hemispherical end ($\Delta T_s/q$) and the cylindrical portion ($\Delta T_c/q$), where q is the rate of heat flow through the fiber. This was found to be

$$\frac{\Delta T_s+\Delta T_c}{q}=\frac{\Delta T}{q}=\frac{1}{2\pi kR}\ln\frac{4R}{\Delta R}+\frac{l}{\pi kR^2}. \tag{3}$$

The first term on the right applies to the hemispherical end and the second term to the cylindrical portion. ΔT is the temperature drop across one contact unit.

The total rate of heat flow, Q, through a one square centimeter area of panel for a temperature difference ΔT across each contact unit will be $2nq$, where n is the number of fiber junctions in one square centimeter and the factor 2 accounts for the two parallel paths of heat flow entering and leaving each fiber junction. From Eq. (3), the value of Q is given by

$$Q=2nq=\frac{4\pi R^2k}{R\ln(4R/\Delta R)+2l}n\Delta T. \tag{4}$$

[12] See S. Timoshenko, *Strength of Materials* (D. Van Nostrand Company, Inc., New York, 1945), Part II, Chap. VII.

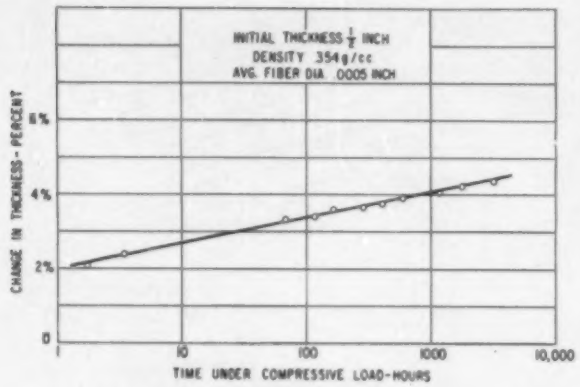

FIG. 2. Decrease in thickness of a glass fiber mat with time under an atmospheric pressure load.

Typical glass fiber mats having fibers with an average diameter of 0.00036 cm and occupying 10% of the space (density about 0.25 g/cm³) when supporting an atmospheric pressure load, had solid conductivities ranging between 4.5 and 5.2. For calculating the effective solid conductivity of such a mat, it must be assumed that all fibers have exactly the same diameter and are laid in a symmetrical lattice array as shown in Fig. 1(a). From the density of packing and the fiber diameter it can be determined that there are 2.78×10^3 layers of fibers in a mat one centimeter thick, and that the fibers in a single layer are spaced four fiber diameters apart so that $l=4R$. In each layer the fibers are laid parallel with 360 fibers to each centimeter. The number of fiber junctions between layers is therefore $(360)^2$ or 13×10^4. Each contact in supporting the atmospheric pressure must carry a burden of $10^3/13\times10^4$ g or 7.5 d.† The value of ΔR was obtained through the use of Eq. (2). The value of E used was 7×10^{11} d/cm².

Assuming a temperature difference of 1°C across the 1-cm-thick mat, the temperature difference across one contact unit, ΔT, will be 1.8×10^{-4}°C. Substitution of all the data in Eq. (4) gives for Q the value 10 microcalories/sec. Since the conditions chosen for calculating Q were a 1°C temperature difference across a 1-cm cube, this value of Q is also the value for the effective coefficient of solid conduction in microcalories/cm°C sec. The value 10 is to be compared with the values 4.5 to 5.2 obtained experimentally.

Tests on mats of fibers averaging 13×10^{-4} cm in diam gave "solid" conductivity values between 6 and 8 as compared to the theoretical value of 24. Fibers of 125×10^{-4} cm average diameter gave "solid" conductivity values around 18 contrasted to the theoretical value of about 300. The variation between the theoretical and experimental values is in the direction to be expected due to deviation from the perfect lattice assumed. Variation of diameters of the fibers and randomness of orientation in planes causes a smaller number of contacts than was assumed in the ideal lattice. The greater lateral stiffness of the larger fibers would be expected to enhance this effect still more.

The possibility of fiber breakage and eventual loss of insulating effect over a long period of use has been investigated for 3.6-μ- and 13-μ-diam fibers. Upon first loading the fibers a great many of them can be heard snapping if the ear is placed close to the fibers. The fiber snapping may continue for several hours but with steadily diminishing frequency until it eventually stops. The breakage continues longer for coarse fibers than for fine ones. After the initial adjustment period, the load distribution stabilizes. Evidently the fiber contacts are stressed nearly to their ultimate strengths even in the final stable state.

Measurements of the change in fiber mat thickness as a function of time have been taken and are shown in Fig. 2. Fiber breakage always ceases before any noticeable increase in solid conduction occurs. A number of vacuum insulation panels have been in use for nine years, and have been perfectly stable during this period. Many of them have been subjected to severe mechanical jarring without noticeable change in thickness or insulating value.

IV. GASEOUS CONDUCTION IN POROUS MEDIA

The mechanism of the thermal conductivities of gases was explained by the kinetic theory of gases largely through the efforts of Smolukowski[9] and Knudsen[10] at the turn of the century. (References 7 and 8 have detailed accounts of this work.) Two different types of gaseous conduction were distinguished, one a pressure independent region of conduction ranging from atmospheric pressure down to fairly low pressures, and the other a pressure dependent region at quite low pressures. The transition from the one type of conduction to the other occurs at pressures where the mean free path for collision between gas molecules is about equal to the mean free path for collisions between gas molecules and the walls of the container, or the particles of the porous structure inside the walled container.

The familiar expression giving the coefficient of thermal conductivity of a still gas, k, is

$$k_{\text{gas}}=A\rho C_v v_a L_g, \tag{5}$$

where ρ is the gas density, C_v the specific heat at constant volume, v_a the average molecular velocity, L_g the mean free path of gas molecules and A a numerical constant. Over a wide range of pressures, k is independent of pressure because L_g varies inversely with the pressure while ρ varies directly with the pressure. When the pressure is reduced below the point where $L_g\sim d$, the distance between the walls or particles against which molecules strike, k becomes proportional to the pressure. At these pressures the mean free path, L, of the molecules, taking into account both collisions between gas molecules and between gas molecules and solid barriers,

† The area of each contact was about 5×10^{-10} cm² and the pressure about 15 000 kg/cm².

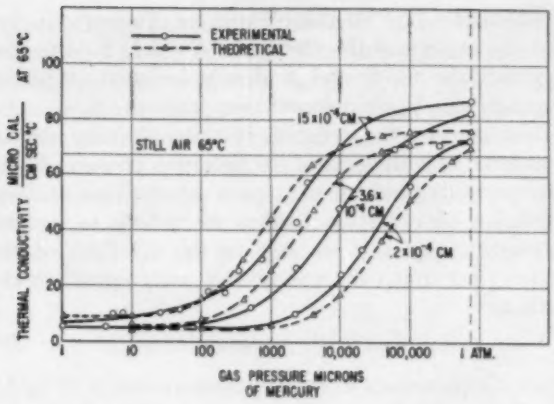

FIG. 3. Thermal conductivity as a function of residual air pressure in insulations of different fiber diameters. Theoretical curves obtained from Eq. (6).

becomes

$$L=L_g[d/(d+L_g)].$$

At pressures such that $L_g \ll d$, $L \approx L_g$. Thus, Eq. (5) taking into account the full range of pressure from atmospheric down may be written

$$k=A\rho C_v \bar{v}_a[L_g d/(d+L_g)]. \tag{6}$$

In writing Eq. (6), it is assumed that the accommodation coefficient between gas molecules and the particles is unity. If this coefficient is less than unity, the k calculated from Eq. (6) will be too large.

Equation (6) is useful for predicting the gaseous conduction in a porous medium as a function of pressure provided the pore dimension, d, is known. Conversely, it is useful for determining the size of pores in a finely-divided material if one knows how its thermal conductivity varies with the gas pressure. Kistler[1] made use of this relation to determine that the size of the pores in his silica aero-gel was about 5×10^{-6} cm.

For the glass fiber mats used in this work, it was possible to calculate the pore size d in the direction of heat flow and to predict the gas conduction within the mat for various pressures. With the optimum fiber arrangement as described in the previous section, the distance, d, a gas molecule can travel on the average in the direction of heat flow between collisions with glass fibers is given by

$$d=\pi R/2s,$$

in which R is the fiber diameter and s the fraction of space occupied by fibers. Fibers 14×10^{-4} cm in average diameter and packed to a space factor, s, of about 14% had a d value of 54×10^{-4} cm. Fibers that had an average diameter of 0.2×10^{-4} cm packed to a volume density of 9% had a d value of 2×10^{-4} cm. The predicted and experimental values of the thermal conductivity at different pressures are shown in Fig. 3.

At pressures of 1 to 10 μ of mercury in a glass fiber mat, the gas conduction is negligible and only the residual solid conduction and radiative heat transfer remain. Together these account for 5 to 9 units of heat transfer. This residual heat conduction must be included with the gas conduction computed for a particular pressure to obtain the estimated total conductivity of the glass fiber mat at that pressure.

It is evident from the calculated and experimental data that a space with glass fiber mats supporting an atmospheric pressure load need not be reduced in pressure below about 100 μ of mercury, depending on fiber size, to obtain negligibly low gas conductivity. This is a distinct advantage because pressures between 10 and 100 μ are rather easy to maintain in a vacuum insulation panel whereas to establish a permanent pressure of 1 μ or less would be more troublesome.

Equation (6) suggests the possibility of finding a material whose d value is so small that the gas conduction k at one atmosphere pressure might be reduced to $\frac{1}{10}$th its normal value. If this could be done, then there would hardly be need for making a vacuum type insulation in order to achieve greatly increased insulation efficiency. To make $d/d+L_g=\frac{1}{10}$, d must be equal to $L_g/9$. At atmospheric pressure, L_g is about 6×10^{-6} cm. If s is taken to be $\frac{1}{10}$, which experience shows is about as dense as small fibers can be packed, the fiber diameters turn out to be 10^{-7} cm. The smallest fibers made available to us averaged 200×10^{-7} cm in diam.

Probably the finest pore sizes yet produced in thermal insulation are in Kistler's silica areo-gel in which the pore size is estimated to be 50×10^{-7} cm. The thermal conductivity of this material is about 60.

V. HEAT TRANSFER BY RADIATION THROUGH FIBROUS MEDIA

It will be assumed that the insulation is made up of fibers of diameters smaller than the gaps of empty space between fibers. For simplicity it will be assumed that when radiation strikes a fiber a fraction ϵ (absorptivity or emissivity) is absorbed and later re-radiated as thermal radiation characteristic of the temperature of the fiber in which it was absorbed.

The projected sidewise area of the fibers in a volume element of thickness dr and unit area is $2sdr/\pi R$. Hence, the probability of radiation being absorbed while traveling across the element in the dr direction is $2s\epsilon dr/\pi R$, and the probability of its penetrating a distance r is

$$P(r)=\exp(-2s\epsilon r/\pi R). \tag{7}$$

Any preferred orientation of the fibers relative to the axis of the volume element will affect the probability of penetration at different angles θ to the axis. Thus, in general

$$P(r,\theta)=\exp[-2s\epsilon r f(\theta)/\pi R], \tag{8}$$

where $f(\theta)$ is a function characteristic of the fiber orientation.

Now consider a spherical element of an extensive

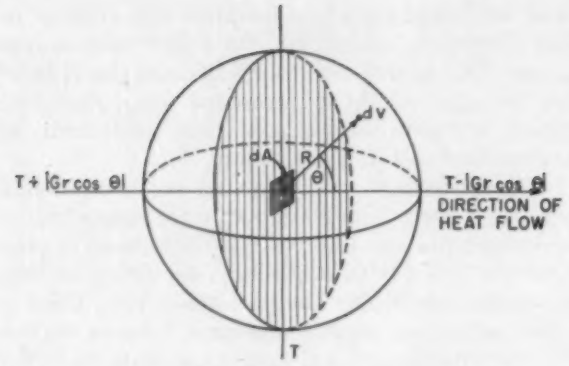

FIG. 4. Radiation through an element of area in an isothermal plane.

uniform volume of insulation which is conducting heat from left to right as shown in Fig. 4. Let the element of area dA at the center of the sphere lie in a plane of equal temperature T. It is assumed that there is a uniform temperature gradient G and that the radiation which passes through the element dA originates and is absorbed within the insulation itself.

The radiation which passes to the right through dA may be obtained by integrating the contributions of all the elements of volume in the half-space to the left. This comes out to be

$$\rightarrow dF_{\text{rad}}=dA\frac{4s\sigma\epsilon}{\pi R}\int_0^{\pi/2}\int_0^{\infty}\sin\theta\cos\theta f(\theta)\times\exp\left[-r\frac{2s\epsilon}{\pi R}f(\theta)\right][T+|Gr\cos\theta|]^4 dr d\theta. \quad (9)$$

The radiation which passes from right to left is given by a similar expression except that the temperature term is $[T-|Gr\cos\theta|]^4$. The net radiation transfer is the difference of the two integrals. Neglecting some of the small higher order terms this is found to be

$$dF_{\text{rad}}=dA\frac{8\pi R\sigma GT^3}{s\epsilon}\int_0^{\pi/2}\frac{\sin\theta\cos^2\theta}{f(\theta)}d\theta. \quad (10)$$

If the fibers are randomly oriented in all three dimensions $f(\theta)=1$, and

$$dF_{\text{rad}}=dA\,(8/3)(\pi R\sigma GT^3/s\epsilon). \quad (11)$$

If the fibers are oriented randomly in planes parallel to dA, then

$$f(\theta)=\cos^2\theta+(2/\pi)\sin^2\theta \quad (12)$$

and

$$dF_{\text{rad}}=dA\cdot 3.24\cdot(\pi R\sigma GT^3/s\epsilon). \quad (13)$$

If $dA=1$ and $G=1$ the expressions given in Eqs. (11) and (13) are just the thermal conductivities by radiation. Thus,

$$k_{\text{rad}}=H\cdot(\pi R\sigma T^3/s\epsilon), \quad (14)$$

in which $H=2.67$ for complete three dimensional random orientation of the fibers and $H=3.24$ for the case in which the fibers are randomly oriented in planes perpendicular to the temperature gradient.

Heat transfer by radiation in this case may also be considered as a diffusion of the radiation photons due to a temperature gradient in a space containing a uniform dispersion of radiation baffles. According to general diffusion theory the net flow in the direction of the gradient per unit time and unit of area normal to the gradient is

$$F_{\text{rad}}=(c\lambda/3)(d\rho_{\text{rad}}/dx), \quad (15)$$

where c is the velocity of the photons (velocity of light), λ is the mean free path between absorbing collisions of photons with fibers, and ρ_{rad} is the radiation density. From radiation theory, $\rho_{\text{rad}}=4\sigma T^4/c$. This, together with Eq. (15), gives the thermal conductivity by radiation in the form,

$$k_{\text{rad}}=(16/3)\lambda\sigma T^3, \quad (16)$$

which is to be compared with the equivalent expression in Eq. (14).

If we equate expressions (14) and (16), using $H=8/3$, which is the value for three dimensional random orientation of the fibers, a relationship between λ and the fiber pad parameters is obtained:

$$\lambda=\pi R/2\epsilon s. \quad (17)$$

Equation (16) offers the possibility of getting quantitative information about λ from experimental observations. When there is no heat conduction by gases the total heat flow per unit area and time is

$$F=(k_{\text{rad}}+k_{\text{solid}})G=[(16\lambda\sigma T^3/3)+k_{\text{solid}}]G. \quad (18)$$

Remembering that $G=dT/dx$, and integrating, the following relation between temperature and distance is obtained:

$$(4\lambda\sigma/3)T^4+k_{\text{solid}}T=Fx+\text{const.} \quad (19)$$

Typical graphs of this T *vs* x relationship are illustrated in Fig. 5. When the heat transfer by radiation is negligible and k_{solid} is independent of the temperature, T *vs* x is linear. If the heat transfer is by radiation only, the temperature gradient becomes smaller the higher the local temperature, and a nonlinear temperature distribution is established. As both modes of heat transfer occur in actual cases, the observed temperature distribution curves lie between the two extremes just described. If the temperatures are measured at three known positions in a sample conducting heat under steady state conditions of known heat flow rate, three simultaneous equations of the form of Eq. (19) can be written and solved for $4\lambda\sigma/3$, k_{solid}, and the constant of integration. Thus, from such experimental measurements λ and k_{solid} may be determined. Measurements of this type, reported later in this report, gave results which were in fair agreement with the theory.

A more refined theory of transfer of radiation through pads of fiber would have to take detailed account of the reflection of radiation from the fibers, the spectral distribution of the absorptivity of the fiber material, and the effect of the ratio of fiber diameter to wavelength of radiation on the absorption and scattering. Different fiber materials have a considerable range of infrared absorption bands, giving enough difference in total average absorption to show up experimentally (cf. Verschoor and Greebler).[11]

VI. APPARATUS AND METHODS

The thermal conductivity tests were made by the guarded hot plate method[13,14] adapted for making tests in vacuum.

A sketch of the apparatus is shown in Fig. 6. The guarded hot plate with a fixed bottom cold plate was enclosed in a steel vacuum chamber. The top cold plate was in the form of a piston which the external atmospheric pressure forced against the test sample to simulate exactly the compression the sample would receive in a vacuum flat panel. A flexible rubber ring diaphragm was used to make the vacuum seal for the piston and still permit free motion of the piston. Several thermocouple connections for measurement and control of temperature were taken through metal-glass seals in the side of the vacuum chamber. Copper tubing was brazed on to the top and bottom plates for circulating cooling water of regulated temperature.

Auxiliary equipment not shown in Fig. 6 included (1) a means for external support of the top plate so that the sample could be tested without any compressive load if desired; (2) stiff springs that could be used for exerting additional force on the piston in excess of the atmospheric pressure; (3) sensitive control equipment

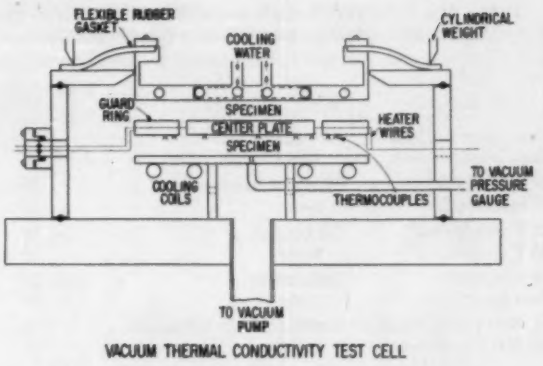

FIG. 6. Apparatus for testing thermal insulation in vacuum under atmospheric pressure load.

to keep the guard ring temperature within 1°C of the center plate temperature; (4) vacuum gauges for measuring pressure inside the sample and other parts of the apparatus; (5) a controlled air leak to enable tests to be made at air pressures ranging from one micron to one atmosphere; and (6) a thin stainless steel collar to rest on the bottom plate for containing granular materials.

The samples tested were usually 1 cm thick and 17.8 cm in diam. Each test was run for sufficient time to be sure that thermal equilibrium was reached. The coefficient of thermal conductivity, k, was calculated from the expression

$$k=(Q\times D)/(A\times\Delta T),$$

in which Q is the amount of power in calories per second to the center plate, D the thickness of sample on one side of the guarded hot plate, A the combined area of both sides of the hot plate, and ΔT the temperature difference between hot plate and cold plate.

VII. TEST RESULTS

A majority of the tests were made with one to ten microns air pressure within the sample, under atmospheric pressure loading and at an average temperature of about 65°C with the cooling water at 20°C and the hot plate at about 110°C. Unless otherwise noted, it will be understood that these were the conditions for the test. A few special tests on radiation effects were made in which either 95°C water or "dry-ice" cooled alcohol was circulated through the coolant tubes.

A number of the characteristics of vacuum types of insulation were studied and the results are given in a series of tables and graphs that follow. First in Table II are listed the thermal conductivities of a variety of substances in vacuum, a few of them in both the loosely packed condition and under atmospheric pressure loading to illustrate the difference in behavior between granular and fibrous types of panel-supporting materials. There are also given results on different glass fiber sizes. Compared to all the other substances tested, including many not given in Table II, properly oriented glass

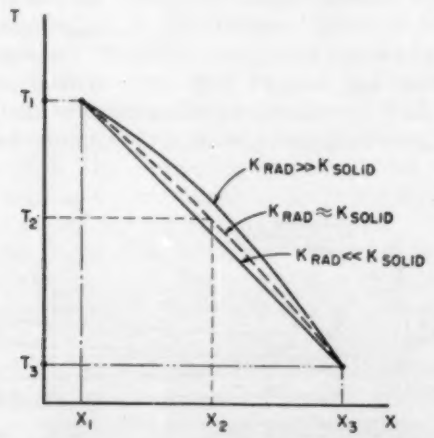

FIG. 5. Temperature *vs* distance in an evacuated glass fiber mat; x is measured along the thickness of the insulation.

[13] G. B. Wilkes, *Heat Insulation* (John Wiley & Sons, Inc., New York, 1950), p. 37.

[14] ASTMC-177-45 Standard Thermal Conductivity Test Apparatus; Guarded Hot Plate Method.

TABLE III. Influence of coatings on thermal conductivity of glass fiber while supporting atmospheric pressure.

Load material	Coating	k microcalories/ cm°C sec
Glass fabric woven	Lubricant	79
Glass fabric woven	none	20
PF insulation[a]	Phenolic binder	23
PF insulation[a]	none	10
TWF insulation[b]	Oil coated	18
TWF insulation[b]	none	10
Glass mat[c]	Lubricant	16
Glass mat[c]	none	12
No. 800 Pyrex wool	Small amount lubricant	8
No. 800 Pyrex wool	none	7

[a] Owens Corning preformed glass fiber batting.
[b] Owens Corning, "thermal wool fiber."
[c] Owens Corning glass fiber used for plastic reinforcement.

fiber of 14×10^{-4} cm diam or smaller had by far the lowest thermal conductivity when under a compressive load. In this size range the conductivity was not sensitive to fiber size or compressive load. The 125×10^{-4} cm fibers crumbled almost to a granular powder under the atmospheric pressure load and had a high thermal conductivity compared to the smaller diameter fibers.

The effect of residual air pressure on the thermal conductivities of glass fiber mats was studied by allowing air to leak into the test chamber while throttling the line connecting to the vacuum pump. In this way tests were made at a number of constant pressures ranging from one micron to one atmosphere within the sample. In Fig. 3 are shown the conductivities as a function of air pressure in the sample for glass fiber mats made up of well oriented fibers in three size ranges; 14×10^{-4}, 4×10^{-4}, and 0.2×10^{-4} cm diam. The samples were furnished by the Owens Corning Fiberglas Corporation, Newark, Ohio.

Virtually all glass fiber must have some kind of coating on it to prevent the fibers from "flying" and from cutting themselves to pieces. Such coatings cannot be tolerated in a permanently evacuated system since they evolve gases. They also increase the cross-sectional area for heat flow, particularly at the contact points, tending to increase the thermal conductivity of the mat. It is, therefore, essential to remove all coatings by heating before sealing them in a flat vacuum panel.

Tests illustrating the effect of coatings on thermal conductivity are given in Table III. Coatings on the fibers can increase the conductivity two to four times depending on the amount and on the fiber orientation.

Glass fiber may be prepared for use in vacuum panels by first removing the coating by heating, then compressing it to nearly its ultimate density and heating it to a temperature just above the strain point of the glass for a few minutes to permit all the fibers to adapt themselves to a densely packed condition. It is then a coherent and easily handled mat.

The influence of fiber orientation is illustrated in Table IV. The results of tests on fibers are given in which the desired orientation is compared to fibers lined up more or less parallel to each other and with orientations both parallel and perpendicular to the direction of heat flow. Fibers arranged randomly in planes perpendicular to the path of heat flow have the lowest thermal conductivity. Individual fibers should penetrate as few planes as possible in the mat since such penetration tends to short circuit those planes through which the fiber passes.

TABLE IV. Influence of fiber orientation on the thermal conductivity of glass fiber[a] while supporting atmospheric pressure load.

Material	k microcalories/ cm°C sec
Glass textile fibers, 6×10^{-4} cm diam laid parallel to each other but perpendicular to direction of heat flow	62
Glass textile fiber randomized in planes perpendicular to heat flow	8
Woven glass fabric 6×10^{-4} cm fibers	20
B fiber, 6×10^{-4} cm fiber arranged mostly parallel to heat flow	72
B fiber random orientation in planes perpendicular to heat flow	3.9 to 5.2
TWF 14×10^{-4} cm fiber diam randomized perpendicular to heat flow. Fibers penetrating several planes	10
HTI fiber improved orientation. Fibers randomized in planes perpendicualr to heat flow path. Fiber penetration of adjacent planes reduced	6 to 7

[a] All samples supplied by Owens-Corning Fiberglas Corporation.

VIII. EXPERIMENTAL STUDY OF RADIATION TRANSFER

The apparatus was arranged to make temperature measurements at three known positions along the heat flow path in the fiber pads under test. This was accomplished by making some modifications in the sandwich-type thermal conductivity test cell used for the standard thermal conductivity measurements. The modifications are illustrated in Fig. 7. The upper and lower fiber pad samples were each divided into two layers. Each layer was weighed to provide information on the layer thicknesses while under compressive load.

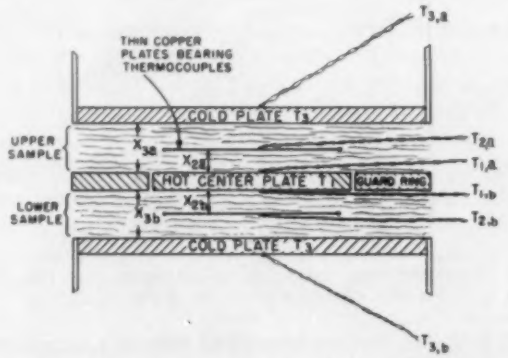

FIG. 7. Experimental setup for analyzing heat transfer by radiation and solid conduction.

TABLE V. Experimental data on heat transfer by radiation in evacuated glass fiber pads.

Fiber designation	Glass "needles"	Glass "thermal wool fiber"	"Glass B" fiber	Glass fiber "filter paper"
Average fiber diameter (cm)	125×10^{-4}	13×10^{-4}	3.6×10^{-4}	0.2×10^{-4}
Fiber orientation	Random	Roughly random in planes	Random in planes	Random in planes
Density (while supporting atmos load) (g cm^{-3})	1.15	0.50	0.25	0.26
s	0.44	0.19	0.096	0.10
λ(cm) [from experiment through Eq. (19)]	0.079	0.015	0.0069	0.0052
$\pi R/2s=\epsilon\lambda$	0.022	0.0054	0.0029	0.00016
ϵ (from $\epsilon\lambda$ vs λ)	0.28	0.36	0.42	0.031
k_{rad} at 10°C	15.0	3.4	1.15	0.85
k_{solid}	18	6.0	4.8	5.0
k_{rad}/k_{total} (evacuated insulation)	0.45	0.40	0.20	0.145
k_{rad}/k_{total} (air-filled insulation)	0.14	0.04	0.015	0.011

Thin disks of copper, bearing appropriate thermocouples, were placed between the layers to give the temperatures T_{2a} and T_{2b} at the distances x_{2a} and x_{2b} in the upper and lower pads, respectively. The temperatures of the hot center plate, T_1, and the cold plates, T_3, were measured with the usual thermocouples attached to them. Care was taken to get a uniform distribution of fiber over the area of the samples. The sample thicknesses were determined by direct measurement of the total thickness $(x_{3a}+x_{3b})$, under test conditions and taking the distances x_{2a}, x_{2b}, x_{3a}, and x_{3b} in proportion to the weights of the corresponding pads of fiber.

Table V lists the results obtained from the experimental tests on pads of different kinds of glass fibers. The average fiber diameters of the different samples ranged from 125×10^{-4} cm to 0.2×10^{-4} cm. The diameters of the fibers within a given sample had statistical distributions similar to that shown in Fig. 8 which is that for the "thermal wool fiber," listed in the second column of the table. The mean free paths λ of radiation were obtained by solution of simultaneous equations of the form of Eq. (19). The values of effective emissivity, ϵ, were obtained by insertion of the above value of λ in the relationship $\lambda=\pi R/2\epsilon s$ [Eq. (17)]. The last two rows of the table compare the fraction of heat transfer by radiation in the same glass fiber pads, evacuated and unevacuated. The greater importance of heat transfer by radiation in the evacuated insulations is striking.

The ϵ's obtained for the glass "needles," "thermal wool fiber," and the "B" fiber, 0.28, 0.36, and 0.42, respectively, are reasonable considering the competing effect of reflection at glancing angles of incidence. The low value of ϵ for the 0.2×10^{-4} cm diam fiber is to be expected because the diameter of this fiber is many times less than the wavelength of the most intense thermal radiation flux under the test conditions. Apparently after the average fiber diameter gets to be less than about half the wavelength of the most intense ambient thermal radiation, the mean free path of the radiation is set more by the amount of glass it has to go through rather than by the number of fibers.

This approximate lack of dependence of the mean free path of radiation on the average diameter of the fibers for diameters below about 4×10^{-4} cm may also be partially explained by the difference in distribution of numbers of fibers *vs* fiber mass per unit length as compared to the distribution of numbers of fibers *vs* fiber diameter. The greater portion of the mass of the glass is concentrated in the fibers of larger diameters, and, hence, the fiber population density is not so high as would be indicated by the gross density, space factor, and "mean fiber diameter." This explanation is strengthened by the observation that the mean free paths of gas molecules in pads of this same nominal 0.2×10^{-4} cm diam fiber, as indicated by experimental measurements, are higher than expected theoretically.

After the values of λ and k_{solid} are experimentally established for a given type of fiber pad, the thermal conductivity characteristics over a wide range of temperatures can be calculated. Figure 9 shows graphically the variation of the thermal conductivities of "TWF" fiber pads and "B" fiber pads with mean temperature using the values of λ and k_{solid} given in Table V. For comparison, experimental points are shown on the same graph. The agreement of the calculated and observed values indicates that the correct mechanism of heat transfer by radiation has been assumed. These data also show the greater radiation baffling effect of the finer

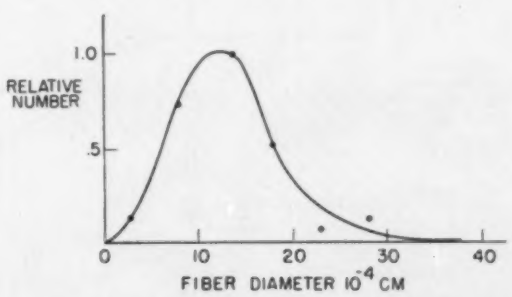

FIG. 8. Distribution of fiber sizes in a sample of thermal wool fiber.

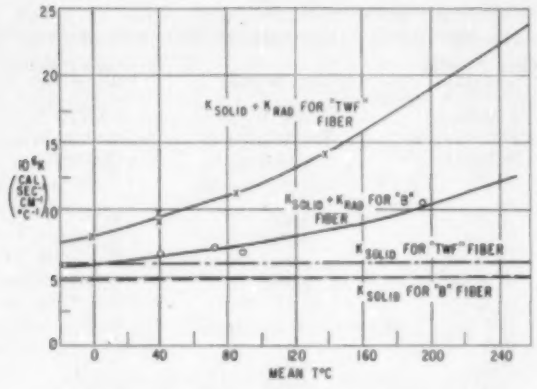

FIG. 9. Thermal conductivity of two types of fiber pads as a function of temperature.

"B" fiber although its gross density is less than that of the TWF fiber.

IX. THERMAL DIFFUSIVITY EFFECTS

The rate at which a wave of temperature change propagates through a medium is determined largely by the thermal diffusivity, $\alpha = k/c\rho$, of the medium, where c is the specific heat and ρ the density. The relatively high heat capacity and unusually low thermal conductivity of the evacuated fiber pad insulations described in this report cause them to have values of thermal diffusivity which are an order of magnitude or more smaller than those of conventional insulations, as shown in Table VI. Preliminary calculations indicated that time intervals of the order of minutes would be required for a temperature shock to penetrate one centimeter of the evacuated insulation. This appeared interesting enough to justify some quantitative tests of this phenomenon.

When a semi-infinite piece of homogeneous conducting medium, bounded by a plane face, and initially at a uniform temperature T_0 throughout (see Fig. 10), suddenly has its face temperature changed to T_1 and held at that value, a plane wave of temperature change propagates through the medium in a direction perpendicular to the face. Let this be taken as the x direction. In this simple case the solution of the heat flow equations[15] yields the following relationship:

$$\frac{T_1 - T}{T_1 - T_0} = \frac{2}{\sqrt{\pi}} \int_0^{\beta} \exp(-\beta^2) d\beta = f(\beta), \qquad (20)$$

in which $\beta = x/2(\alpha\tau)^{\frac{1}{2}}$, x is the distance from the face, α the thermal diffusivity, τ the time interval measured from the application of the temperature shock, and T the temperature at a given x and τ. A more convenient arrangement of the relationship is

$$\Delta T/\Delta T_0 = 1 - f(\beta), \qquad (21)$$

where ΔT_0 is the temperature change imposed at the face and ΔT is the change from the initial temperature at depth x and time τ.

A convenient way to solve Eq. (21) for a certain ΔT_0 is to take a given value of ΔT and find, by use of tables of the $f(\beta)$ function, the value of β which satisfies the equation. From this β and a given x the τ is obtained at which the ΔT occurs. In the experimental tests ΔT_0 was about 97°C, x was nearly 1 cm and α for the insulation was approximately 10^{-4} cm^2 sec^{-1}. The theoretical ΔT(°C) *vs* τ(sec) curve for this case is shown in Fig. 11. Note that there is practically no change in temperature during the first 360 sec, or 6 min.

TABLE VI. Values of thermal constants for various materials (20°C).

Material	k cal cm^{-1} sec^{-1} °C^{-1}	c cal g^{-1} °C^{-1}	ρ g cm^{-3}	α cm^2 sec^{-1}
Silver	0.974	0.0558	10.5	1.66
Aluminum	0.504	0.214	2.70	0.872
Steel	0.115	0.115	7.90	0.127
Marble	0.008	0.203	2.71	0.0145
Glass	0.0028	0.20	2.6	0.0054
Cork	0.00011	0.40	0.14	0.0020
Refrigerator glass fiber	0.000086	0.20	0.032	0.013
Evacuated glass fiber pad	0.0000060 to 0.0000080	0.20	0.25 to 0.40	0.00012 to 0.00010

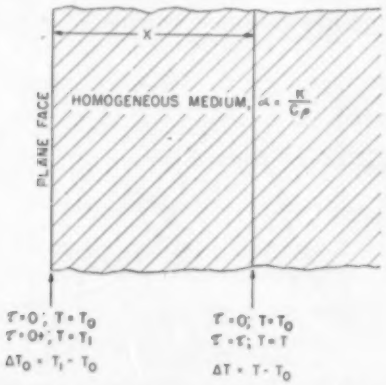

FIG. 10. Thermal diffusion in a homogeneous medium.

The experimental results are also shown in Fig. 11. The observed transit time of the thermal shock was closely that predicted by the theory, but the rate of temperature change from that time on was less than indicated by the theory because of the presence of the metal envelope of the insulation panel. The envelope had considerable heat capacity and much greater thermal conductivity than the filler and so decreased the rate of temperature change. This latter effect was verified by running some tests on an electric analog of the thermal system. The results of the analog computer are also shown in Fig. 11.

[15] Ingersoll, Zobel, and Ingersoll, *Heat Conduction*, McGraw-Hill Book Company, Inc., New York, 1948), Chap. 7.

X. MECHANICAL PROPERTIES OF EVACUATED PANELS

The pressure of the atmosphere holding the envelope of an evacuated panel firmly against the filler pad prevents the envelope from buckling easily and thus develops the "skin-strength" of the structure. For this reason evacuated panels having thin metal envelopes have unusual bending and torsional stiffness.

Although the envelope supplies most of the strength, the fibrous filler pad also contributes because of the fibers being locked together into a board-like structure by the compression. This is readily demonstrated by placing a pad of fibrous filler material in a flexible rubber envelope, sealing it off, and excuating. Before evacuation the assembly is quite limp and flexible while after evacuation it has about the stiffness and strength of loosely bonded fiber board.

Evacuated panels of glass fiber do not have the acoustic absorbing power of similar pads of air-filled insulation. There are two reasons for this: first, there can be no friction damping of the air motion of sound waves relative to the fibers because the fibers are in a vacuum; and second, the points of contact of the fibers are loaded so heavily by the pressure of the atmosphere that they react elastically rather than dissipatively to vibrations imposed upon the walls of the panel. The acoustic effect is pronounced enough that it is easy to distinguish between identical evacuated and unevacuated panels merely by thumping them.

TABLE VII Heat conduction in Dewar flask walls (5-liter Dewars)

	Standard Dewar No. 1	Standard Dewar No. 2	"Super-Dewar" (2 cm thick glass fiber layer)
Liquid nitrogen evaporation rate			
liter/day	0.691	0.672	0.341
cal/sec	0.306	0.297	0.1515
cal/cm² sec	1.91×10^{-4}	1.86×10^{-4}	0.810×10^{-4}
Liquid hydrogen evaporation rate			
liter/day		3.00	0.725
cal/sec		0.263	0.0633
cal/cm² sec		1.64×10^{-4}	0.339×10^{-4}
Liquid He evaporation rate			
liters/day		22.5	1.75
cal/sec		0.196	0.0153
cal/cm² sec		1.23×10^{-4}	0.082×10^{-4}

XI. IMPROVED DEWAR TYPE VACUUM WALL FLASK

Remarkably low heat transfer values can be obtained using a combination of a Dewar flask type radiation gap and an evacuated glass fiber layer. This structure for a five liter flask is illustrated in Fig. 12 and is called a "super-Dewar" flask.[16] The structure shown was designed for the storage of liquefied gases.

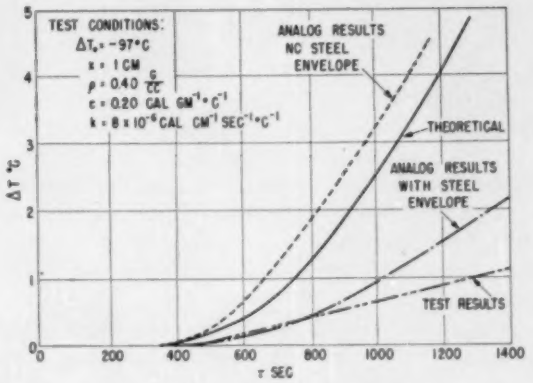

FIG. 11. Temperature *vs* time on one side of a vacuum panel after applying a thermal shock to the other side.

The gain in insulation efficiency over a standard Dewar increased with reduction of the internal temperature. For example, in comparing a five liter "super-Dewar" flask with a standard Dewar of like capacity by measuring the times required to evaporate five liters of a liquefied gas, it was found that liquefied nitrogen lingered two or three times longer in the "super-Dewar" than in the standard Dewar, hydrogen, four times longer, and helium over ten times longer.

It is important for the glass fiber layer to be on the high temperature side of the insulation because its function is to keep the temperature of the warmer side of the radiation gap as low as possible. Then the transfer of heat across the radiation gap is substantially reduced since total radiation across the gap is governed by the difference in the fourth powers of the two temperatures.

The comparative data for liquefied gas storage on the two types of flasks is given in Table VII. The two flasks used were identical standard Dewars initially. Both of them were tested on liquid nitrogen storage first then standard Dewar number one was modified by surrounding it with a two cm thick layer of evacuated "B" fiber glass to convert it to a super-Dewar. The glass fiber mat had properly oriented fibers as previously described and

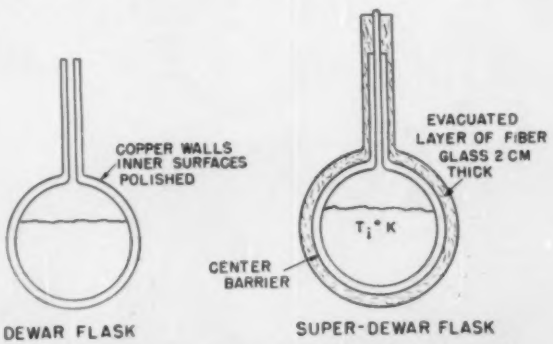

FIG. 12. Standard and super-Dewar structures.

[16] H. M. Strong and F. P. Bundy, US Patent 2,776,776.

its density was about 7 lb per cu ft. The reflecting surfaces of the three Dewars were polished copper. The data in Table VII clearly show the marked improvement in insulating effect due to the glass fiber layer.

In the absence of a temperature measurement on the middle wall, it is not possible to explain this remarkably low heat transfer rate in detail. But it is probable that the conductivity of the glass fiber layer near the inside surface was much reduced, possibly by as much as a factor of ten, at the liquefied gas temperatures over that measured at ~70°C.

Various modifications of this structure would be likely to show similar effects. For example, multiple radiation gaps or a powder filled outer space might be used. But the glass fiber mat offers structural simplicity because small compact pads of it may be used in direct contact with the inner vessel to support it mechanically without loss of insulation.

XII. CONCLUSIONS

In evacuated, flat, thermal insulating panels, the conduction of the internal structure required to support the walls against the crushing load of atmospheric pressure proved to be the most critical factor. Grits, powders, grills and various kinds of cellular structures all develop unacceptably high conductivities when under compressive loading of the atmosphere. Pads made of fine glass (or glass-like) fibers oriented randomly in planes perpendicular to the temperature gradient and pressure axis proved to have remarkably low thermal conductivity which was quite insensitive to loading. Glass fiber pads of this type, enclosed in flat metal envelopes gave thermal conductivities in the range of 4 to 10 microcalories/cm°C sec.

Several other properties of a glass fiber supporting structure are of considerable significance. The radiation baffling of a 1-cm-thick layer is equivalent to that of several highly reflecting surfaces. The pore space between fibers is small enough that internal gas pressures up to about 100 μ may be tolerated without significant impairment of insulating qualities. The thermal diffusivity of this type insulation is at least an order of magnitude lower than for common insulations due to the remarkably low thermal conductivity but relatively high capacity of the glass fiber mat.

Remarkably low heat transfer rates were obtained in Dewar flasks while storing liquefied gases by surrounding the flasks with an evacuated glass fiber blanket.

The stability, permanence of vacuum and high insulating efficiency of the glass fiber structure sealed in evacuated metal envelopes[17] has been well established over a period of nine years of use.

ACKNOWLEDGMENTS

The authors are grateful to A. W. Hull, the late I. Langmuir, M. Hebb, and A. J. Nerad for valuable discussions, and to the Owens-Corning Fiberglas Corporation for supplying samples of especially prepared glass fiber mats.

[17] H. M. Strong and F. P. Bundy, British Patent 715,174 and Canadian Patent 537,151.

JOURNAL OF APPLIED PHYSICS VOLUME 31, NUMBER 1 JANUARY, 1960

Outgassing Caused by Electron Bombardment of Glass

B. JOHNSON TODD, JACK L. LINEWEAVER, AND JOHN T. KERR
Corning Glass Works, Corning, New York

(Received June 17, 1959)

A flow system used for continuous measurement of the gases evolved from aluminized glass during bombardment with 20 kev electrons is described. The system is also suitable for gettering measurements. A cathode-ray tube containing the samples is sealed directly to the source of a mass spectrometer. Calibration of the first flow system built revealed the gettering of oxygen by the graphite-silicate conductive coating and the hot metal parts of the electron gun of the cathode-ray tube. This gettering was minimized in a second flow system. It was found that oxygen constitutes at least 95% of the gas evolved from each of five types of glasses investigated. Also, a graphite-silicate coating can play a dual role in a cathode-ray tube; when not bombarded by electrons it is an active getter for oxygen, but when bombarded it is a source of oxygen, carbon monoxide, and carbon dioxide.

INTRODUCTION

THE widespread use of glass in electron tubes containing oxide-coated cathodes and the increasing interest in prolonging the life of these cathodes have posed a number of questions with regard to the effect of the glass envelope on cathode life. In particular, with especial reference to cathode-ray tubes, the question has arisen as to what gases, if any, are evolved when glass which has been well baked out is subjected to electron bombardment. This paper describes the apparatus we are using to study the outgassing of glass caused by electron bombardment and presents outgassing data on five types of glasses.

In brief, a flow system in which a cathode-ray tube is sealed directly to the source of a mass spectrometer is used to obtain continuous measurement of the outgassing rate while the sample is bombarded with 20 kev electrons. The ion currents corresponding to ions of different m/e are monitored as a function of time while a television type raster scans the sample. Calibration of the first flow system built revealed the gettering of oxygen by the graphite-silicate coating and by the electron gun of the cathode-ray tube. This gettering, undesirable from the point of view of these measurements, was minimized in a second flow system. Oxygen constitutes at least 95% of the evolved gas; whereas the greater part of the gas evolved upon heating at bake-out temperatures has been found to be water.[1]

FLOW APPARATUS AND METHOD

First Apparatus

A schematic diagram of the apparatus is shown in Fig. 1. V_b is the expansion volume of the mass spectrometer[2] sample system which can be filled with a gas to some known pressure in the micron (Hg) range. V represents the volume of the mass spectrometer source in which ionization of the gas mixture to be analyzed takes place. The amplified current of ions with m/e characteristic of the gas of interest is proportional to the partial pressure of this gas in V. This amplified ion current, observed as divisions on a strip chart recorder, is the only time-dependent quantity directly observed in the experiments which follow. The quantities of interest, such as flow rate, have to be related to the observed ion current. V_c represents the volume of the cathode-ray tube containing the sample. A_1 and A_2 are stopcocks; A_3 and A_4 are Alpert valves.[3] Valve A_4 and the pumps which follow it are used to process the tube independently of the mass spectrometer pumping system. S_1, S_2, and S_3 represent the conductances of the various sections of connecting tubing. The analysis of the experiments which follows is correct provided the following inequalities are maintained,

$$S_1 \ll S_2 < S_3 \quad \text{and} \quad V < V_b. \tag{1}$$

A typical outgassing experiment consists of recording the ion current characteristic of the gas of interest as an electron beam scans a sample in V_c. Valves A_2 and A_4 are closed while valve A_3 is open so that the evolved gases are pumped continuously through the mass spectrometer source. Under these conditions, provided no gas is adsorbed in the system, the rate at which gas is evolved $\dot{Q}_{EV}$ in V_c is given by the equation

$$\dot{Q}_{EV} = \dot{Q}_L + (V+V_c)\dot{P} + (V_c/S_3)(\ddot{Q}_L + V\ddot{P}), \tag{2}$$

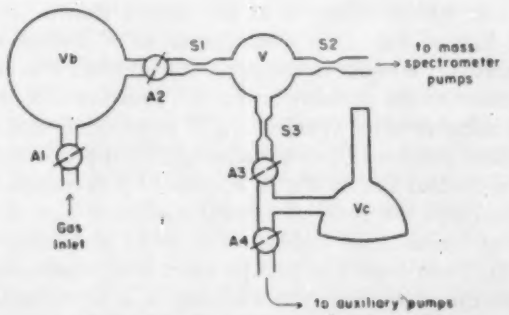

FIG. 1. Schematic drawing of first apparatus.

[1] B. J. Todd, J. Appl. Phys. **26**, 1238 (1955).

[2] The mass spectrometer is a Model 21-620 with glass sample system and automatic peak selector manufactured by Consolidated Electrodynamics Corporation, Pasadena, California. The gold leak used in batch analysis with this instrument was removed.

[3] D. Alpert, J. Appl. Phys. **24**, 860 (1953).

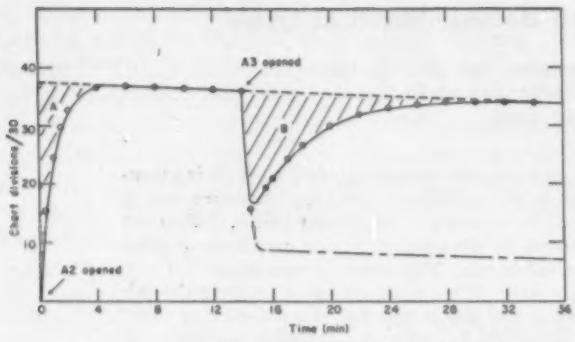

FIG. 2. Data obtained for argon at m/e of 40 with ionizing current of 20 μa when P_b^0 was 8 μ (Hg). System parameters are: V, 0.8 l; V_b, 3.0 l; V_c, 2.3 l; S_1, 1.5×10^{-4} l/sec; S_2, 1.5×10^{-2} l/sec; S_3, 6.0×10^{-2} l/sec. The data give values of F_S equal to 0.94 divisions/$\mu\mu$ (Hg)- l/sec and P_S equal to 13.7 divisions/mμ (Hg). The observed chart divisions are shown by the solid line. The circled points are values calculated from the foregoing parameters and the differential equations applying to the two and three conductance experiments. The good agreement between calculated and observed values indicates the validity of the assumptions used in determining the parameters.

where $\dot{Q}_L$ is the rate at which gas is leaving V, and $\dot{P}$ is the rate of change of the partial pressure in V. When $\dot{Q}_{EV}$ is known as a function of time, the amount of gas Q_{EV} evolved in any time interval is obtained by integration.

In order to evaluate the right side of Eq. (2) one needs, in addition to the volumes and S_3, two types of sensitivity factors: an ion current-flow rate sensitivity F_S and an ion current-source pressure sensitivity P_S. F_S is defined as the number of chart divisions per unit flow rate leaving V through S_2; P_S is the number of chart divisions per unit pressure in V. The function of V_b and S_1, which is a length of capillary tubing, is to provide a means for obtaining these sensitivity factors. V_b, V_c, and S_3 are calculated from the geometry of the system.

F_S is determined in the following way. With a known gas pressure P_b^0 in V_b and A_3 shut, A_2 is opened. The rate $\dot{Q}_E$ at which gas enters V when S_1 is much smaller than S_2 is given by

$$\dot{Q}_E=S_1P_b^0\exp(-S_1t/V_b)=\dot{Q}_L+V\dot{P}. \tag{3}$$

The ion current observed at any time t, shown by the solid line of Fig. 2, is proportional to P and also to $\dot{Q}_L$, since $\dot{Q}_L$ is equal to the product S_2P when P is large compared to the pressure on the low pressure side of S_2. Five minutes after opening A_2, $\dot{P}$ is so small that for practical purposes $\dot{Q}_E$ is equal to $\dot{Q}_L$. $\dot{Q}_E$ is proportional to the dashed line in Fig. 2 obtained by extrapolation of $\dot{Q}_L$. From the slope of a semilogarithmic plot of ion current against time and the value of V_b one can calculate S_1. Then from Eq. (3) the value of $\dot{Q}_L$ corresponding to the observed chart divisions can be calculated leading to F_S. S_1 is most quickly obtained by using hydrogen as the test gas, and then calculating S_1 for other gases using Graham's law.

If at some time after opening A_2 as described above, A_3 is opened to the previously evacuated V_c then the $\dot{Q}_L$ curve takes the shape shown by the solid line in Fig. 2. From this experiment, now involving all three conductances, one can calculate P_S provided the test gas is not adsorbed in V_c. After the sudden initial drop of P upon opening A_3, the pressure P_c in V_c is very nearly equal to P because of the relatively large conductance S_3. Also, because of the relatively small value of S_1, the solid line of Fig. 2 eventually becomes practically identical with the dashed line. Then to a close approximation the value of P when these two curves merge is equal to the shaded area B, expressed in pressure-volume units by means of F_S, divided by V_c. Knowing P for a given number of chart divisions one can calculate P_S.

S_2 is given by the equation

$$S_2=P_S/F_S. \tag{4}$$

If S_2 is known for one gas, values for other gases can be obtained from Graham's law. If S_2 and F_S are known for a particular gas, Eq. (4) permits calculation of P_S without admitting gas to V_c. This allows determination of P_S even for a gas which is adsorbed in V_c.

V_b and V_c can be determined rather easily from the geometry of the system. The geometry of V is less well known, but V can be determined from the shaded area A of Fig. 2. If N represents the chart divisions observed when Q_L first becomes practically equal to Q_E, then V is given by the equation

$$V=AP_S/NF_S. \tag{5}$$

This completes the evaluation of the parameters necessary for calculation of $\dot{Q}_{EV}$ from Eq. (2).

Second Apparatus

In an attempted measurement of P_S for oxygen by the three conductance experiment described above the ion current followed the unequally dashed curve of Fig. 2. In this instance a completed cathode-ray tube comprised V_c, and the persistently low ion currents observed after opening A_3 are the result of gettering in the tube. Obviously no getter had been added intentionally to the tube. This type of experiment was used to determine the source of the getter activity. We found that a blank glass envelope exhibited negligible gettering, but that both the graphite-silicate conductive coating used in the completed tube and the hot metal parts of the electron gun were extremely active getters. A tin oxide type conductive coating showed little getter activity, so this coating is used in place of the graphite-silicate. The activity of the gun parts is minimized by inserting an aperture between the gun and the rest of the tube. This aperture is large enough not to seriously interfere with the electron beam at beam currents less than 500 μa, but it has a relatively low gas conductance of 0.2 l/sec. At the same time the speed of evacuation

of V_c is greatly increased by replacing the A_3 Alpert valve with a valve of much higher conductance and by inserting a mercury diffusion pump between this valve and the mass spectrometer source. High conductance traps at −78°C are placed on either side of the mercury pump. Measurement of the diffusion pump speed at V_c gave a value of 1.5 l/sec. Comparison of this pumping speed with the conductance of the aperture shows that we should obtain 85% of any oxygen evolved in V_c.

A sketch of the glass valve used for A_3 in this second apparatus is shown in Fig. 3. The magnetically operated dome seats in a pool of molten silver chloride. When the silver chloride is frozen at 350°C the valve will stand an atmosphere pressure differential with no leak. We could not obtain this condition with any of several low melting alloys because they failed to wet the glass. With the dome up and the valve at room temperature, as it is used in outgassing measurements, there are no outgassing problems. However, with the valve hot so

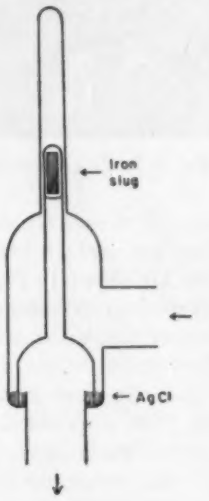

FIG. 3. Schematic drawing of high conductance valve.

that the dome can be moved in and out of the silver chloride, the outgassing is great enough to prevent gettering measurements. With a suitable valve one could carry out gettering measurements on this second system by leaving the mercury pump at room temperature.

If the gettering rate in V_c is assumed to be zero, which introduces a maximum error of 15%, then $\dot{Q}_{EV}$ is now given by

$$\dot{Q}_{EV}=\dot{Q}_L+V\dot{P}+(V_c/S_{H_2})(\ddot{Q}_L+V\ddot{P}), \qquad (6)$$

where S_{H_2} is the effective speed of the diffusion pump measured at V_c. The second apparatus is the one that has been used for all of the outgassing work. In most of the experiments $\dot{P}$ is small enough to make the last two terms of Eq. (6) negligible; in which case we have the much simpler calculation from the equation

$$\dot{Q}_{EV}=\dot{Q}_L. \qquad (7)$$

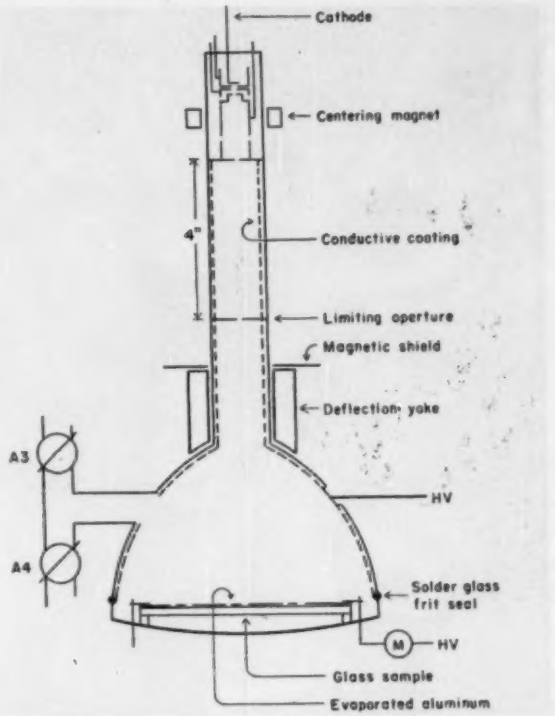

FIG. 4. Schematic drawing of cathode-ray sample tube.

CATHODE-RAY SAMPLE TUBE

A schematic diagram of the cathode-ray sample tube is shown in Fig. 4. The sample tube is made from a lead glass face plate and funnel. The glass samples are held in place against the face plate by a stainless steel rack which is anchored to two stainless steel pins sealed through the face plate. The rack can hold a single 4×5 in. sample or five 1×4 in. samples. The pins and rack provide the high voltage (HV) connection to the sample. A solder glass frit seal is used to seal the face plate to the funnel after sample installation. A solder glass frit seal is also used to seal in the limiting aperture. The electron gun is one-third of a color television gun assembly using an indirectly heated oxide-coated cathode. The high voltage is applied to the tin oxide type conductive coating on the inside funnel wall and then to the aperture and to the fourth grid of the gun by a conventional metal button assembly.

The control circuitry produces a standard television raster using electrostatic focusing and magnetic scanning of the electron beam. The electron beam is centered through the aperture with the external centering magnet. The magnetic shield prevents deflection of the beam by the yoke field until the beam has passed through the aperture. The raster area is variable from a 4×5 in. rectangle to any smaller size, and the raster can be placed on any area of the sample. A calibrated monitor tube is used to show the location of the raster on the sample area. The sample current, which is read on the meter M, is variable up to 500 μa, and is regu-

FIG. 5. Electron micrograph of directly aluminized Code No. 8603 glass surface after bake out and prior to electron bombardment. The length of the white bar is 1 μ.

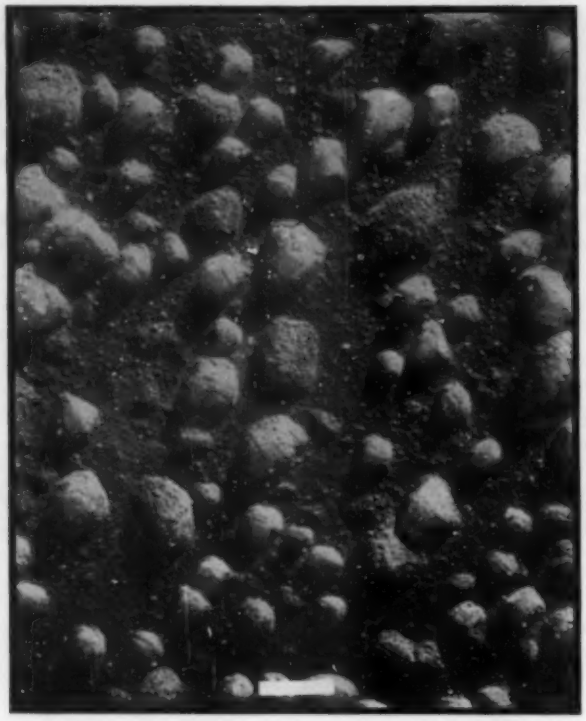

FIG. 6. Surface shown in Fig. 5 after electron bombardment.

lated to 1 μa by electronically controlling the cathode current. This sample current is equal to the current striking the sample minus any current due to secondary emission. The upper limit of 500 μa is set by the aperture diameter. The range of electron energy available is limited by the gun design and extends from 10 to 30 kev.

The tube is processed (baked out, gun outgassed by induction heating, and cathode activated) while pumping through A_4 with A_3 closed. After processing has been completed A_4 is shut and A_3 is opened. The system is then ready for outgassing measurements.

OUTGASSING MEASUREMENTS

Outgassing produced by bombardment with 20-kev electrons is of particular interest since this is within the range of energies used in television tubes. However, glass bombarded by 20-kev electrons acquires a negative charge which destroys the raster and diminishes the sample current. In order to avoid this the glass samples are coated with an aluminum film 1000 A thick. It was found that an evaporated aluminum film has very little oxygen gettering activity. Calculations based on the work of Spear[4] show that the 1000-A film transmits 96% of the incident 20 kev electrons, and that the average electron energy after transmission is 19.7 kev. In our first experiments the aluminum was evaporated directly on the glass. Electron micrographs of such a surface before and after electron bombardment are shown in Fig. 5 and Fig. 6. Comparison of the two micrographs indicates that the evolved gas is first trapped under the aluminum and has to raise blisters before it can escape. In order to minimize this trapping of gas the glass is first coated with a nitrocellulose film, then aluminized, and the nitrocellulose film later removed by heating. This leaves behind an aluminum film with much less adherence to the glass, and which does not blister upon electron bombardment. With all other parameters the same, the gas evolved using the second coating procedure is about three times that obtained with the directly evaporated film.

Figure 7 shows the outgassing data obtained on five types of glass. Each sample was 1 mm thick and had a 1000-A aluminum film applied using the nitrocellulose film technique. The samples were bombarded with 20 kev electrons while using a $3\times\frac{1}{4}$ in. raster and a sample current of 200 μa. Under these conditions at least 95% of the gas evolved is oxygen. The remainder of the gas is carbon monoxide and hydrogen, and part of this remainder represents background gas from the hot parts of the gun. We have qualitative data which show that the oxygen evolution increases rapidly with increasing temperature. All the samples of Fig. 7 had the same dimensions so that the temperature attained during bombardment should have been nearly the same, approximately 250°C, for each. The curves of Fig. 7 are the averages of two separate runs on each

[4] W. E. Spear, Proc. Phys. Soc. (London) **B68**, 991 (1955).

glass where the difference between the two runs was not greater than 15%.

Figure 8 shows the oxygen outgassing data obtained on glass samples coated with a graphite-silicate conductive coating approximately 40 μ thick rather than the aluminum film. The bombardment conditions were the same as those used for the aluminized samples of Fig. 7. These values would be higher than shown if the nonbombarded graphite-silicate area were not acting as a getter. Carbon monoxide and carbon dioxide are also evolved during bombardment of the graphite-silicate coating. However, the results for these two gases show poor reproducibility. The combined carbon monoxide-carbon dioxide evolution has varied from 2 to 200% of the oxygen evolved.

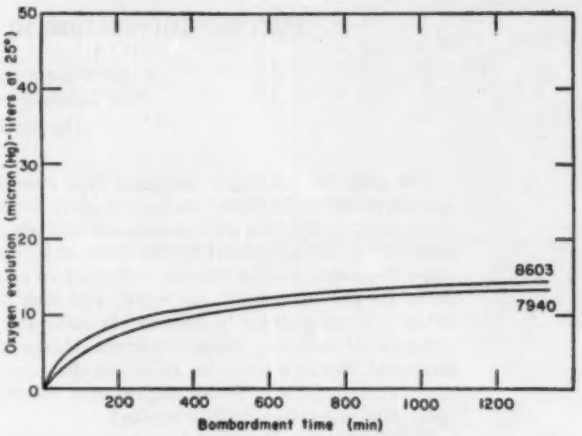

FIG. 8. Plot of oxygen evolved in μ (Hg)-l at 25°C *vs* time of bombardment in minutes for two glasses coated with a 40-μ thick graphite-silicate coating.

DISCUSSION

While our primary interest has been the outgassing measurements, the first apparatus described appears ideal for gettering measurements. The amount of gas gettered by samples in V_c can be determined by the three conductance type of experiment used in evaluating P_S. Information on the speed of gettering can be obtained as long as this speed is not limited by the conductance S_3.

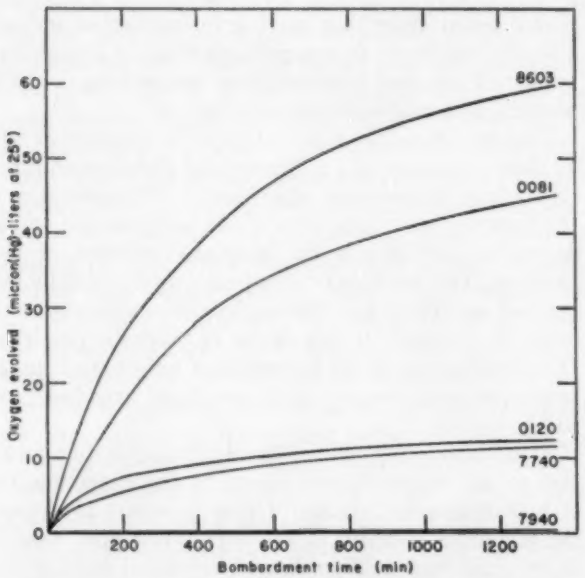

FIG. 7. Plot of oxygen evolved in μ (Hg)-l at 25°C *vs* time of bombardment in minutes for five glasses coated with 1000-A aluminum. The numbers are Corning Glass Works code numbers and refer to the following glass types: 7940, fused silica; 7740, Pyrex brand borosilicate; 0120, potash-soda-lead; 0081, soda-lime; 8603, lithia-alumina-silicate.

Code No. 7940 glass, fused silica, has the lowest outgassing rate of any of the glasses we have measured. The addition of other oxides necessary to produce glasses with lower softening points than silica results in increased oxygen evolution. No exact correlation has been obtained yet between glass composition and outgassing rate.

Calculations based on the work of Spear[4] and of Young[5] provide an estimate of 2 μ for the range of the 20 kev electrons in the glass samples. If all the oxygen contained in a 2-μ thick layer of Code No. 8603 glass, having an area equal to the raster size, were removed, one would obtain 670 μ (Hg)-l of oxygen. As shown in Fig. 7, about 10% of the oxygen contained in this 2-μ layer is evolved in 20 hr of bombardment.

The 40-μ thick graphite-silicate coating used on the samples shown in Fig. 8 should be sufficiently thick to completely shield the glass substrate from the 20-kev electrons. This shielding effect is shown by comparison of the two sets of data for Code No. 8603 glass. The data for fused silica show that the graphite-silicate coating is itself a source of oxygen when bombarded by electrons. Thus the graphite-silicate coating plays a dual role in cathode-ray tube operation. When bombarded by electrons it is a source of oxygen; when not bombarded it is an extremely active getter. The oxygen that can diffuse to the cathode surface is determined by the difference between these two competing processes.

The investigations are proceeding towards a study of binary and ternary glasses and measurement of the effect of variations in both temperature and electron energy on the outgassing rate.

ACKNOWLEDGMENTS

The electron micrographs were taken by Mr. G. B. Carrier. We also wish to thank Dr. J. L. Sheldon of Corning Glass Works and Dr. J. H. Turnbull of the Radio Corporation of America for helpful advice and discussion.

[5] J. R. Young, Phys. Rev. **103**, 292 (1956).

JOURNAL OF APPLIED PHYSICS VOLUME 31, NUMBER 1 JANUARY, 1960

Particle Interaction in Magnetic Recording Tapes

J. G. WOODWARD AND E. DELLATORRE
RCA Laboratories, Princeton, New Jersey
(Received July 13, 1939)

The magnetic coating of recording tape is assumed to be composed of an assemblage of small, single-domain particles. Each particle is assumed to have a symmetrical, square hysteresis loop when the reversible component of magnetization is neglected and when the particle is not influenced by the fields of neighboring particles. When influenced by the fields of its neighbors, the particle may exhibit an asymmetrical loop when the loop is plotted relative to an external applied field. In this case the positive and negative switching fields for the particle are not equal, and their difference gives an indication of the particle interaction. While it is not possible to measure the switching fields of a single particle on the recording tape, the distribution of switching fields in the assemblage of particles and the associated magnetic moment can be measured. The two switching fields and the magnetic moment define a 3-dimensional distribution function which describes the magnetic properties of the tape, and in terms of which both dc and anhysteretic magnetization processes may be described.

The distribution functions have been measured for two recording tapes. While the functions for the two tapes are markedly different in detail, both show that particle interaction is very appreciable in recording tapes and that it is a significant factor in determining the bulk magnetic properties and the recording performance of tapes.

I. INTRODUCTION

IN attempting to deduce the bulk magnetic behavior of recording-tape coatings and similar aggregates of magnetic particles from the properties of the individual particles, workers have usually found it convenient to neglect the interaction between particles. The validity of this procedure has been questioned from time to time but few indications as to the effects of particle interactions have been shown. Johnson and Brown[1] suggest particle interaction as a possible, but not sufficient, explanation of a lack of agreement between their measurements and predictions based on the Stoner-Wohlfarth model of noninteracting particles for their sample of packed γ-iron-oxide particles. However, they provide no estimate as to the magnitude of the interaction.

In computations based on an idealized distribution of particle sizes and orientations, Néel[2] has shown that particle interactions influence very appreciably the magnetic properties of pressed-powder permanent magnets. The parameters and materials selected for consideration by Néel are sufficiently similar to those of interest in magnetic-tape coatings to strengthen the belief that particle interaction in recording tapes is an important factor. Wohlfarth[3] has considered certain possible interaction mechanisms for near-spherical particles in weak interaction. Néel[4] has approached the problem by considering effects resulting from the interaction between dipoles in an ensemble of dipoles. At present, however, it is not possible to evaluate the effects of interaction in the oxide coatings of recording tapes on a purely theoretical basis. The measurements and analysis reported below show that particle interaction is, indeed, a highly significant factor, perhaps equal in importance to particle size and orientation, in determining the bulk properties of magnetic recording tapes.

The existence and effect of particle interaction will be shown in terms of a 3-dimensional distribution function whose independent variables are the positive and the negative switching fields of the particles and whose dependent variable is the magnetic moment of the particles. The distribution function is interpreted by the method suggested by Preisach[5] with modifications to make it applicable to aggregates of magnetic particles. Distributions measured by means of anhysteretic magnetization processes applied to samples of recording tape will be shown.

After considering the nature of the distribution function we will discuss briefly its use in the interpretation of bulk magnetization and demagnetization processes, the statistical stability of the distribution and, finally, the experiments yielding three-dimensional plots of the distributions for two different recording tapes.

II. DISTRIBUTION FUNCTION

It is convenient, though not necessary, to assume that the magnetic tape coating is composed of single-domain particles each of which has a single, strongly-preferred direction of magnetization. These particles will have some unspecified distribution in both their size and their orientation relative to the length of the tape, with the tape samples being in the commonly-used form of long, $\frac{1}{4}$-in.-wide strips. Each particle may be characterized by a magnetic moment and a rectangular hysteresis loop if we neglect the reversible component of magnetization since, to a first approximation, the reversible component does not contribute to the remanent induction on the

[1] C. E. Johnson, Jr., and W. F. Brown, J. Appl. Phys. **29**, 1699–1701 (1958).
[2] Louis Néel, Appl. Sci. Research **B4**, 13–24 (1954–55).
[3] E. P. Wohlfarth, Proc. Roy. Soc. (London) **A232**, 208–227 (1955).
[4] Louis Néel, Compt. rend. **246**, 2313–2325 (1958).
[5] F. Preisach, Z. Physik. **94**, 277–302 (1935).

tape. We will measure the components of magnetic moment as well as the fields along a direction parallel to the length of the tape.

When an external field, H, is applied parallel to the length of the tape, a particle will have a component of magnetic moment, $+m$, if $H \geq H_+$ and a component, $-m$, if $H \leq H_-$, where H_+ and H_- are the switching fields of the single-domain particle. In the absence of particle interaction $|H_+| = |H_-|$, and the rectangular loop for the particle is symmetrical. When interaction exists, the fields due to neighboring particles are added to the external field and will, in general, cause the loop for the particle under consideration to be displaced along the field axis as shown in Fig. 1.

We now take the positive and negative switching fields of the particles as two coordinate axes. At any instant each particle may be represented by a point having coordinates, H_+ and H_-, in the plane of these axes. In the absence of interaction all of the points fall on a line of unity slope. The distribution of points along this line is dependent on the size, shape and orientation distributions of the particles. When particle interaction is significant the points are spread over an appreciable area in the $H_+ - H_-$ plane. The greater the interaction fields experienced by the particles, the greater will be the spread of the points away from the line of unity slope. The types of loop asymmetry required to locate points in various regions of the $H_+ - H_-$ plane are shown in Fig. 2. Since all of the experimental measurements as well as most of the discussion which follows are concerned with particles whose point representations are contained in only one quadrant of the $H_+ - H_-$ plane, the coordinate axes have been chosen in Fig. 2 so as to place this region in the first quadrant. We note that particles whose point representations lie to the left of the 45° line labeled H_+' have their loops reversed; that is, for a positive external field these particles become negatively polarized. It seems unlikely that any particles composing the usual recording tapes would have the characteristics required to locate their point representations to the left of the H_+' line. For the present, however, we will not exclude the possibility of at least a few such particles existing in aggregates of other types of magnetic particles.

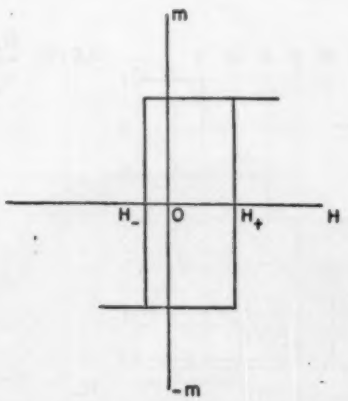

FIG. 1. Asymmetrical hysteresis loop for a particle interacting with its neighbors. H is the externally-applied field.

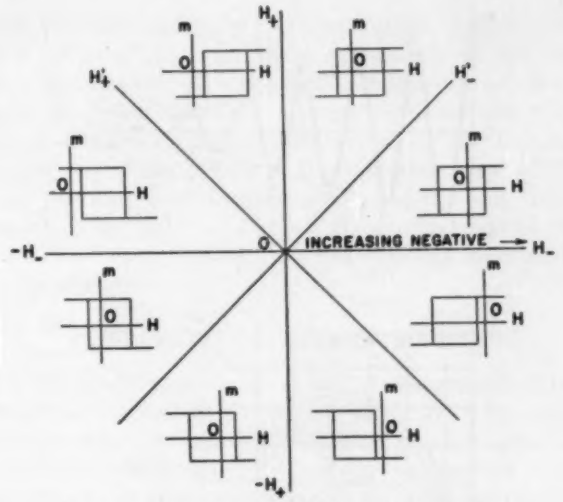

FIG. 2. Types of loop asymmetry associated with various regions of the $H_+ - H_-$ plane.

The magnitude of the magnetic moment of a particle may be associated with its point representation in the $H_+ - H_-$ plane in terms of a height above the plane at the point in question. When a very large number of particles are involved, the distribution in the $H_+ - H_-$ plane may be treated as a continuum, and the magnitudes of the moments of the particles whose points lie in an elementary area of the $H_+ - H_-$ plane may be summed to give the magnetic moment per unit area of the plane. This quantity, which is a function of H_+ and H_- and is designated by $J(H_+,H_-)$, is the 3-dimensional distribution function which characterizes a magnetic recording tape. The magnitude of J is measured along an axis perpendicular to the $H_+ - H_-$ plane. Because of the symmetry of the bulk magnetic properties of the tape it is reasonable to expect $J(H_+,H_-)$ to be symmetrical about the H_-' axis of Fig. 2. This symmetry is verified by measurements.

III. DEMAGNETIZATION PROCESS

Recording tapes are usually demagnetized by applying a strong ac field which is then gradually reduced to zero. The demagnetizing field as a function of time is illustrated in Fig. 3(a). The positive and negative peaks can be represented in the $H_+ - H_-$ plane as lines having the appropriate values of H_+ and H_-. For present purposes we will consider a distribution entirely contained in the first quadrant of the $H_+ - H_-$ plane as indicated by the dashed enclosure in Fig. 3(b). If the initial value of the demagnetizing field is sufficient to saturate the magnetic material, the demagnetizing process of Fig. 3(a) will leave the distribution of Fig. 3(b) divided in two equal parts separated by the heavy, step-shaped line. Above and to the left of this line the distribution

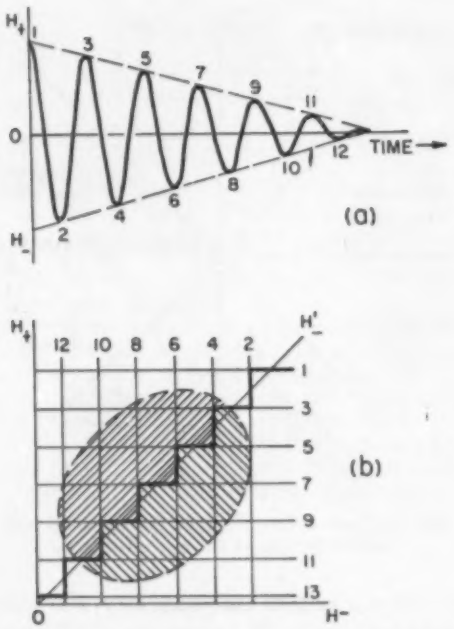

FIG. 3. (a) An alternating, demagnetizing field. (b) Remanent state of the distribution following demagnetization process of (a). Positive saturation below and negative saturation above the heavy line.

is saturated in negative polarity. Below and to the right of the line the distribution is saturated in positive polarity. The net magnetization of the distribution is zero. When the decay of the demagnetizing field is more gradual, the steps in the boundary line become smaller and, in the limit, the boundary between regions of positive and negative saturation in the distribution approaches the 45° line labeled H_-'.

The above procedure also may be used to show that any portion of the distribution extending into the third quadrant is likewise divided into regions of equal and opposite polarity by the H_-' line after ac demagnetization. Portions of the distribution in the second and fourth quadrants can never contribute to a net remanent magnetic moment in the distribution since, for zero field, particles whose point representations lie in these quadrants are spontaneously magnetized in a polarity which is independent of past magnetic treatment. Because of the symmetry of the distribution, the moment in the second quadrant is equal and opposite to that in the fourth quadrant.

IV. ANHYSTERETIC MAGNETIZATION

It should be evident from the nature of the distribution function that the net remanent magnetic moment in the distribution as a result of any dc magnetization process should be calculable by integration of the distribution function, $J(H_+,H_-)$, within the appropriate limits of H_+ and H_-. It is also possible to compute the net remanent magnetic moment resulting from anhysteretic magnetization processes, that is, those in which dc and ac fields are superimposed. This type of magnetization process has proved to be most useful in our experimental work.

Two forms of anhysteretic magnetization will be considered. In the first the ac and dc fields are applied together and are gradually decreased to zero, maintaining a constant ratio of dc to ac at all times. In the second the ac and dc fields are applied together, after which the ac field is decreased to zero while the dc field is held constant. Then the dc field is reduced to zero. The first form is illustrated in Fig. 4(a). The second is illustrated in Fig. 5(a). By using the procedure of the preceding section we find the distribution divided into regions of negative and positive polarity at the conclusion of both magnetization processes. In these cases, however, a net magnetic moment results. The results for the two forms of anhysteretic magnetization are illustrated in Figs. 4(b) and 5(b).

When the ac and dc decay together with a constant ratio of dc to ac, the line separating positive from negative polarity in the first quadrant of the H_+-H_- plane has a slope, in the limit for a large number of cycles of ac during the decay, of $H_{ac}+H_{dc}/H_{ac}-H_{dc}$, where H_{dc} and H_{ac} are the instantaneous values of the dc field and the envelope of the ac field, respectively. When the ac field decays while the dc field is held constant, the line separating the positive from the negative magnetic moment in the first quadrant of the H_+-H_- plane has unity slope and intersects the H_+ axis at $H_+=2H_{dc}$. In

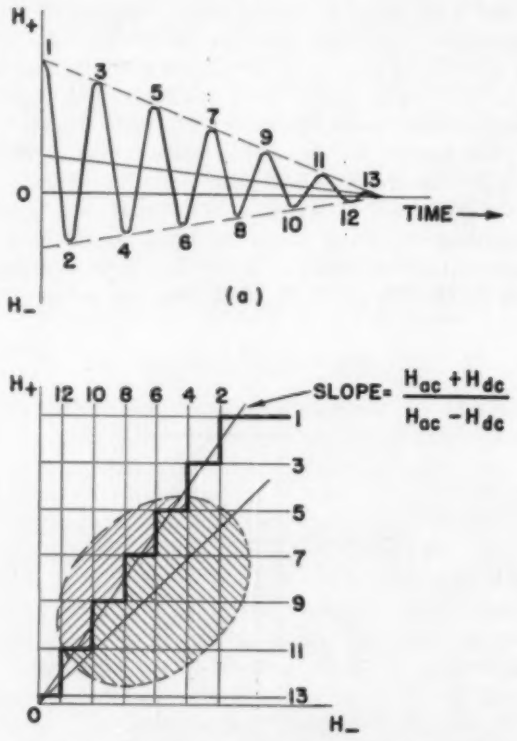

FIG. 4. Anhysteretic magnetization process in which ratio of dc field to ac field is held constant during decay of fields.

both cases the value of the net remanent magnetic moment may be obtained by integrating $J(H_+,H_-)$ in the H_+-H_- plane with the limits of the integration being the initial values of H_+ and H_-.

V. ROTATION OF AXES

A useful transformation results if the distribution function is referred to the $H_+'-H_-'$ axes, shown in Fig. 2, which are rotated 45° with respect to the H_+-H_- axes. The H_-' axis is the axis of symmetry of the distribution. This transformation of axes is made by the following relationships:

$$\left.\begin{aligned}\sqrt{2}H_+&=H_+'-H_-'\\ \sqrt{2}H_-&=H_+'+H_-'\end{aligned}\right\}. \tag{1}$$

When ac and dc fields are superimposed we may write

$$\left.\begin{aligned}H_+&=H_{ac}+H_{dc}\\ H_-&=H_{ac}-H_{dc}\end{aligned}\right\}. \tag{2}$$

Substitution of (2) in (1) gives the result

$$\left.\begin{aligned}H_+'&=\sqrt{2}H_{dc}\\ H_-'&=\sqrt{2}H_{ac}\end{aligned}\right\}. \tag{3}$$

We see that when the distribution function is referred to the $H_+'-H_-'$ axes, distances along the H_+' axis are proportional to H_{dc}, and distances along the H_-' axis are proportional to H_{ac}, the envelope of the ac field,

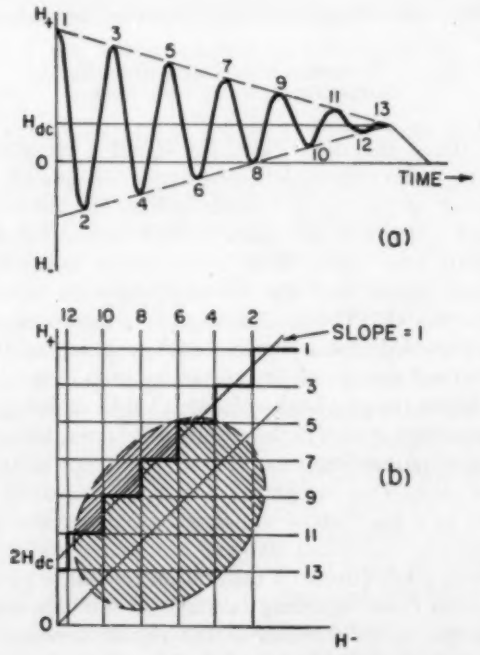

FIG. 5. Anhysteretic magnetization process in which ac field decays while dc field is held constant.

and we may designate the distribution function by $J(H_+,H_-)=J(H_{ac},H_{dc})$. It is convenient to use the $H_{ac}-H_{dc}$ axes when anhysteretic magnetization processes are being considered. It may be noted also that, except for a scale factor, distances along the H_{ac} axis correspond to the widths of the hysteresis loops of the tape particles, and distances along the H_{dc} axis correspond to the fields at the centers of the loops of the particles. Preisach[3] used these quantities as coordinates in his analysis.

VI. STABILITY OF THE DISTRIBUTION

Thus far we have assumed that the magnitude of the magnetic moment at each point in the H_+-H_- plane remains constant regardless of the state of magnetization of the distribution. Let us now attempt to judge the validity of this assumption. This is a crucial matter, for only if the function, $J(H_+H_-)$, remains unchanged as the applied fields are varied can simple integration procedures be used to compute the net magnetic moment of the distribution after magnetization.

We have supposed that the local fields of neighboring particles are responsible for the nonsymmetrical hysteresis loops which determine the distribution in the H_+-H_- plane. It follows that the polarity reversal of any particle will change the local fields surrounding its neighbors, will alter the asymmetry of their loops, and will cause their point representations to be relocated in the H_+-H_- plane. Hence, as a magnetization process progresses, the point representing any particle will move about in the H_+-H_- plane. It is evident, therefore, that the distribution function can be constant only in a statistical sense.

It is difficult to conceive and conduct experiments to test conclusively the statistical stability of the distribution function. However, certain deductions may be made which suggest a rather high degree of stability in the case of recording tapes. For example, let us suppose the distribution to be saturated in negative polarity. When a gradually increasing positive field is applied, a growing region of the distribution will switch from negative to positive polarity. If the reversal of a small portion of the distribution affects local fields in a manner which causes additional elements of the distribution to move toward or into the region already reversed, a regenerative process will ensue. In this case we expect a gradual decrease of negative net magnetic moment followed by a precipitous change to positive moment. Such a change might occur in one or more major steps. Behavior of this sort should make itself apparent in the bulk hysteresis curves of the material. Recording tapes give no noticeable indication of such an instability.

In the inverse example, as magnetization reversal proceeds, local fields may be altered in a way which drives elements of the distribution into regions more remote from the region already switched. This is a degenerative process which should result in a linearization

of the bulk dc demagnetization curve. It would be difficult to recognize this effect in bulk measurements unless it were present to a very marked degree.

When some initially demagnetized ferromagnetic materials are cycled around a minor hysteresis loop with equal negative and positive peak fields, several cycles may be required before the loop becomes stable and symmetrical. This phenomenon, sometimes called accommodation, may give information regarding the stability of the distribution function. This behavior may be interpreted as showing a dependence of $J(H_+,H_-)$ on the previously-applied fields. We have attempted to observe accommodation in a recording tape by cycling a sample of initially-demagnetized tape around a minor loop in a dc hysteresis-loop plotter. Because of the low permeability of the tape, measurements of this sort are difficult to make with high precision. However, the measurements showed that if there was a difference between the first loop and any subsequent loop, the difference as measured along the intensity axis of the loops was certainly less than 10% of the remanent intensity.

The above considerations give some basis for confidence that the distribution function for iron-oxide-coated recording tapes is sufficiently stable to be useful for present purposes. There is reason to suspect that the distribution functions of certain ferrites and ferromagmetic metals are less stable than the distribution functions of recording tapes. Consequently, until a more sophisticated treatment is developed to describe analytically the dynamic behavior of the distribution, the distribution-function approach for these other materials may have a restricted value.

VII. MEASUREMENTS

Three-dimensional distribution functions have been measured for two recording tapes having quite different characteristics. The measurements were made by means of an anhysteretic-magnetization method. We will assume that the distribution is contained entirely within the first quadrant of the H_+-H_- plane, for this is the only region of the H_+-H_- plane accessible for direct measurement by present techniques. It turns out that the assumption is reasonable for the two samples tested. Such a distribution is indicated by the enclosure in the $H_{ac}-H_{dc}$ plane in Fig. 6. When a dc field of initial magnitude, S_1, and an ac field of initial magnitude, B_1, are applied to demagnetized tape, the remanent magnetic moment, M_1, is twice that contained in the region bounded by OCB_1O. When the magnitudes of the dc and ac fields are S_1' and B_1, respectively, the remanent moment, M_1', is twice that contained in the region bounded by ODB_1O. Magnitudes S_2 and B_2 of dc and ac, respectively, give a net moment, M_2, corresponding to region OFB_2O. Magnitudes, S_2' and B_2, give a moment, M_2', corresponding to region OEB_2O. The remanent moment in the small region, $CDEF$, is therefore,

$$\Delta M=\tfrac{1}{2}(M_2'-M_2)-\tfrac{1}{2}(M_1'-M_1). \tag{4}$$

From the values of the magnitudes of the applied fields the area, ΔA, of $CDEF$ may be computed. The magnetic moment per unit area at ΔA is

$$J(H_{ac},H_{dc})=\Delta M/\Delta A. \tag{5}$$

By a systematic variation of H_{ac} and H_{dc}, the value of $J(H_B,H_S)$ may be measured over most of the region of the distribution.

Various techniques are available for achieving anhysteretic magnetization of recording tape and for measuring the remanent magnetization of the tape. In the work reported here magnetic tape recording equipment and techniques were employed. In the recording process, as a small, elementary length of tape leaves the recording head, the element of tape experiences a field in which a high-frequency bias and a low-frequency

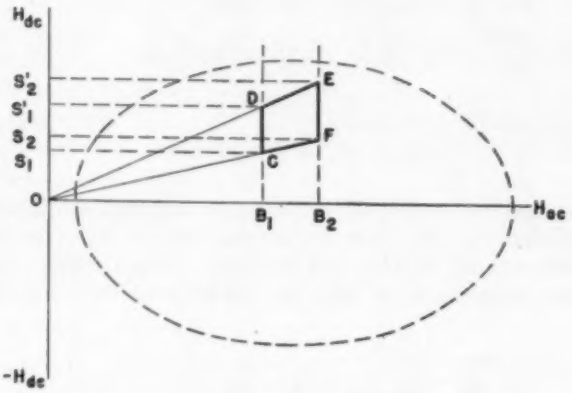

FIG. 6. Illustration of method of measuring the distribution in the $H_{ac}-H_{dc}$ plane.

signal decay together. Thus, the signal is recorded on the tape by an anhysteretic-magnetization process. The frequency of the signal is made sufficiently low so that for each element of tape passing the recording head, the phase of the signal does not change appreciably, and the signal for that element may be considered as being dc. The emf induced in a playback head as the recorded tape is reproduced is proportional to the time rate-of-change of the remanent induction on the tape. When the playback voltage is fed to an integrator and measured with a peak-reading voltmeter, the meter reading is proportional to the peak remanent induction on the tape. This integrated voltage is measured and plotted as a function of signal and bias currents in recording. The quantities involved in Eqs. (4) and (5) are read from these curves. A calibration technique permits conversion from recording currents in milliamperes to field strengths in oersteds in the region traversed by the tape at the recording head.

In order for the distribution-function discussion of the

preceding sections to be valid, the recording field must be uniform throughout the thickness of the tape coating and must be essentially longitudinal, i.e., parallel to the direction of motion of the tape. These requirements were met by using a recording gap length of 2 mils and spacing the front surface of the tape coating from the recording head by 3.2 mils. This latter dimension is considerably larger than the coating thickness of 0.5 mil or less. With these dimensions the perpendicular component of the recording field did not appear to influence the remanent induction on the tape until longitudinal field strengths sufficient to saturate the tape had been reached.

The length of the gap in the playback head was 0.06 mil, and the tape was in contact with the head during reproduction. Playback scanning losses were completely negligible for a tape speed of $1\frac{7}{8}$ in./sec and a signal frequency of 100 cps. A bias frequency of 30 kcs was used.

Using data obtained by the instrumentation and techniques described above, 3-dimensional plots of the distribution functions in the H_+-H_- plane were made for

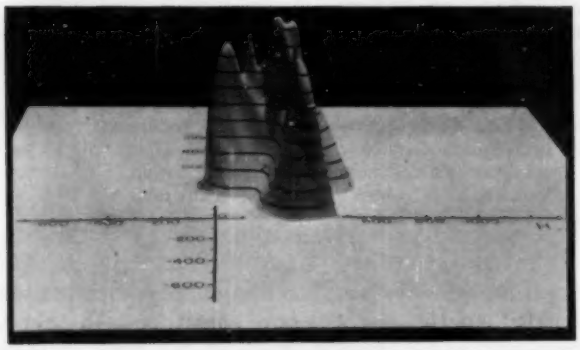

FIG. 7. Measured distribution function in the H_+-H_- plane for tape A.

two tapes, designated A and B. These plots are shown in Figs. 7 and 8. Tape A is a commercial product in which the magnetic material is acicular γ-iron-oxide, with some degree of particle alignment on the tape. Tape B is an experimental sample in which the magnetic material consists of irregularly-shaped particles having low anisotropy. We note that the distributions are not entirely contained in the first quadrant of the H_+-H_- plane. Hence, in order to complete the distributions as shown it was necessary to extrapolate from first-quadrant data. The extrapolation used to complete the plot of Fig. 8 for tape B is one of the possibilities on the basis of the data alone. However, the nature of the extrapolation required in this case is such that considerable uncertainty exists as to whether or not a portion of the distribution is contained in the third quadrant. Additional and more accurate data are needed to resolve this matter. That portion of the distribution, if any, which is contained in the third quadrant is a small fraction of the total. Hence, other conclusions based on the measured distribution for tape B are not invalidated.

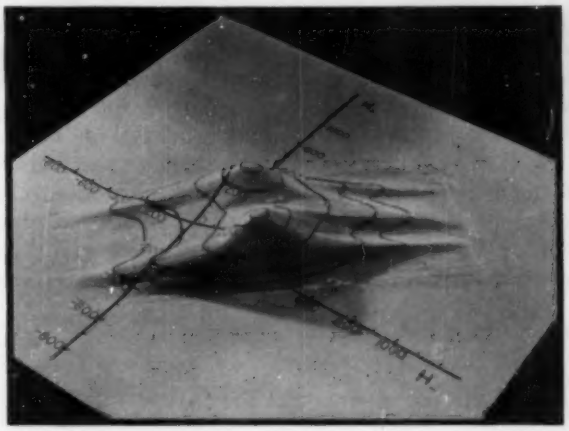

FIG. 8. Measured distribution function in the H_+-H_- plane for tape B. (Same horizontal and vertical scales as in Fig. 7.)

VIII. DISCUSSION

In Sec. II we saw that, in the absence of particle interaction, the distribution in the H_+-H_- plane would lie along a line of unity slope. The shape and the lateral extent of the distributions pictured in Figs. 7 and 8 show that particle interaction is highly significant in both tape A and B although the functions for the two tapes are markedly different in detail. We see that the effect of interaction is so marked and so complex that there is small likelihood of correctly describing the magnetic behavior of recording tapes in terms of the characteristics of noninteracting particles. In principle many of the bulk properties of recording tapes are derivable by integration of their 3-dimensional distribution functions. However, the analytical expressions required to describe the measured distribution functions are too complex to justify the effort involved in carrying out the integration at the present time. By inspection of the plots of the distribution functions certain qualitative and semiquantitative statements may be made regarding the coercivities, the relative slopes of the initial magnetization curves, the saturation fields, and the saturation inductions and remanences. These predictions were found to agree satisfactorily with bulk measurements of the magnetic properties of the two tapes. In the interests of economy of space these data have not been included here.

The measurements of the distribution functions give indications of fine structure in the distribution, and some fine structure is shown in Fig. 7. However, experimental techniques capable of considerably higher precision must be developed before fine structure can be measured and studied with any degree of confidence. When the distribution functions can be plotted with sufficient accuracy, useful quantitative information should be forthcoming on the effects of various tape-

coating materials and processes, of particle alignment, of particle shape and size distributions, of the degree of anisotropy of the coating material, and of methods which may be devised to control particle interaction.

Because of the strong particle interaction demonstrated to exist in recording tapes only a small fraction of the magnetic particles on the tape contribute to the remanent induction in conventional audio recording, which is an anhysteretic magnetization process. On the other hand it is easily shown that some particle interaction is necessary for this type of recording process to work at all. The shape of the 3-dimensional distribution function of a tape may also influence the high-frequency response and the pulse resolution capabilities of a recording system. These and other technical consequences of the nature of the distribution function are beyond the scope of this paper and will be discussed in more detail elsewhere.[6]

[6] J. G. Woodward and E. Della Torre, J. Audio Eng. Soc. **7**, 189–195, 222 (1959).

JOURNAL OF APPLIED PHYSICS VOLUME 31, NUMBER 1 JANUARY, 1960

Determination of Molecular Field Coefficients in Ferrimagnets

G. T. Rado and V. J. Folen
U. S. Naval Research Laboratory, Washington 25, D. C.

(Received July 24, 1959)

An improved method is presented for determining those three molecular field coefficients which yield essentially the best agreement between the Néel theory and the experimental curve of saturation moment per unit mass (σ) *versus* temperature (T) in a given ferrimagnetic material. This method is analytical, and for a given accuracy it is more rapid than previously used trial-and-error methods. Experimental data on σ *vs* T are presented for monocrystals of lithium ferrite and two compositions of magnesium-iron ferrite. One of the latter ferrites was measured in two states of ionic distribution which were obtained by varying the heat treatment. Application of the analytical method to these data shows that the agreement between the Néel theory and experiment is somewhat better than that expected on the basis of previous work. The present method is particularly useful for determining the temperature dependence of the sublattice magnetizations. Accurate values of these magnetizations are required, for example, in calculations of the temperature dependence of magnetocrystalline anisotropy by means of crystalline field theory.

I. INTRODUCTION

ALTHOUGH the Néel[1] theory of ferrites gives a remarkably good account of the temperature dependence of the spontaneous magnetization, it is generally surmised that the empirically determined parameters contained in the theory, known as molecular field coefficients, represent only an approximate measure of some average exchange interaction. Nevertheless, there are at least two reasons for attempting to determine the molecular field coefficients fairly accurately. The first is that the availability of reliable data on the molecular field coefficients of different ferrite types may conceivably provide some insight into the nature of the exchange problem. The second reason, and the one of more immediate interest, is connected with crystalline field calculations of the magnetocrystalline anisotropy of certain ferrites. It is this connection, described below, which was responsible for the work on molecular field coefficients reported in the present paper.

Recent experiments[2] on the anisotropy of certain magnesium-iron ferrite monocrystals led us to the following two conclusions: (1) The ionic anisotropies due to ferric ions are additive at low temperatures (even though a varying fraction of these ions may be situated on the two different sublattices) so that a "one-ion" model is applicable; (2) the signs of these anisotropies are different on the two sublattices, thus suggesting that these signs may be determined by the crystalline electric field. The same two conclusions were arrived at independently by Yosida and Tachiki[3] who introduced the use of the cubic crystalline field spin Hamiltonian into the calculation of ferrite anisotropies. In comparing their theory with experiments on the temperature dependence of anisotropy it is necessary to calculate the temperature dependence of the sublattice magnetizations as accurately as possible. This requirement is due to the fact that the anisotropy of a given sublattice depends on powers as high as the fourth of the argument of the Brillouin function which determines the magnetization of that sublattice. Furthermore, the anisotropies as well as the magnetizations of the two sublattices are, in many substances, opposite in sign, and it is only the measurements of the resultant magnetization and resultant anisotropy that are conveniently compared with theory.

Our calculations of the sublattice magnetizations are

[1] L. Néel, Ann. phys. **3**, 137 (1948). For a review of Néel's theory, see J. S. Smart, Am. J. Phys. **23**, 356 (1955).
[2] V. J. Folen and G. T. Rado, J. Appl. Phys. **29**, 438 (1958).
[3] K. Yosida and M. Tachiki, Progr. Theoret. Phys. (Kyoto) **17**, 331 (1957); W. P. Wolf, Phys. Rev. **108**, 1152 (1957).

based on an analytical method[4] for determining the "best-fitting" molecular field coefficients for a given ferrimagnetic substance. The present paper contains an explanation of this method and its application to our experimental results on the temperature dependence of the saturation magnetization of lithium ferrite and magnesium-iron ferrite monocrystals. In addition to providing a stringent test of the Néel theory, the combination of the new method and the magnetization experiments on monocrystals contributed significantly to the good agreement[2] between our anisotropy results and the Yosida-Tachiki theory.

II. BASIC EQUATIONS AND DEFINITIONS

We first outline the Néel[1] generalization of the molecular field theory for the case of two antiferromagnetically coupled sublattices A and B. It will be assumed, for simplicity, that these sublattices contain one kind of magnetic ion only. We denote Avogadro's number by N and the spontaneous magnetic moment per molecule by $\mathbf{M}_s/N$. The term "molecule" will be taken to mean "formula unit," such as $Li_{0.5}Fe_{2.5}O_4$ or $MgFe_2O_4$, in the case of the lithium and magnesium ferrites discussed later on. We define $\mathbf{M}_A/N$ and $\mathbf{M}_B/N$ as the contribution to $\mathbf{M}_s/N$ arising, respectively, from one magnetic ion per A site and one magnetic ion per B site. Thus $\mathbf{M}_s$ is given by[5]

$$\mathbf{M}_s=\mu\mathbf{M}_B+\lambda\mathbf{M}_A \tag{1}$$

where λ and μ denote the number of magnetic ions per molecule situated on A and B sites, respectively. The molecular field acting on each magnetic ion on an A site is

$$\mathbf{H}_A=n\alpha\lambda\mathbf{M}_A-n\mu\mathbf{M}_B, \tag{2a}$$

and that acting on each magnetic ion on a B site is

$$\mathbf{H}_B=-n\lambda\mathbf{M}_A+n\beta\mu\mathbf{M}_B. \tag{2b}$$

The positive quantities n, $n\alpha$, and $n\beta$ refer to the strengths of the AB, AA, and BB interactions, respectively. Since $\mathbf{M}_A$ and $\mathbf{H}_A$ are parallel to each other and antiparallel to $\mathbf{M}_B$ and $\mathbf{H}_B$, Eqs. (1) and (2) become

$$M_s=\mu M_B-\lambda M_A; \tag{3}$$

$$H_A=n\alpha\lambda M_A+n\mu M_B; \tag{4a}$$

$$H_B=n\lambda M_A+n\beta\mu M_B. \tag{4b}$$

The sublattice magnetizations are determined by

$$M_A=M_0B_J(u) \tag{5a}$$

and

$$M_B=M_0B_J(v) \tag{5b}$$

where $B_J(u)$ and $B_J(v)$ denote, respectively, the Brillouin function of $u=M_0H_A/RT$ and $v=M_0H_B/RT$. Use of Eqs. (4) yields

$$u=M_0n(\alpha\lambda M_A+\mu M_B)/RT \tag{6a}$$

and

$$v=M_0n(\lambda M_A+\beta\mu M_B)/RT, \tag{6b}$$

where R is the usual gas constant, T is the absolute temperature, and

$$M_0/N=gJ\mu_B \tag{7}$$

is the intrinsic moment of each magnetic ion in the type of molecule under consideration. Here g is the spectroscopic splitting factor, J is the total angular momentum quantum number, and μ_B is the Bohr magneton. If the constants g and J are known, and if the temperature-independent parameters λ, μ, n, α, and β can be deduced from suitable experimental results, then the Eqs. (3), (5), and (6) permit the calculation of M_A, M_B, and M_s as a function of T. The ratio of M_s to the molecular weight may be equated to σ, the saturation moment per unit mass, at temperatures where the experimentally applied magnetic field is negligible compared to the molecular fields.

III. CALCULATION OF THE MAGNETIZATION

Throughout the present section it will be assumed that α and β are known. Methods for determining α and β will be discussed in Sec. IV. The ionic distribution parameters λ and μ can be measured by X-ray or neutron diffraction, or determined magnetically. In the latter method, used for the present experiments,* it is assumed[6] that the Néel theory is valid at 0°K. Thus Eqs. (3), (5), and (7) yield

$$(n_B)_{T=0}=(\mu-\lambda)gJ, \tag{8}$$

where n_B is the spontaneous magnetic moment expressed in Bohr magnetons per molecule. The value of $(n_B)_{T=0}$ can be obtained by extrapolation of the experimental curve of n_B *vs* T. Since the quantity $(\mu+\lambda)$ is specified by the chemical formula of the molecule under consideration, Eq. (8) furnishes both μ and λ. As to the coefficient n, its value will be expressed below in terms of the Curie temperature, T_c.

Following Néel, we now introduce the ratios

$$\varphi=M_A/M_B \tag{9}$$

[4] G. T. Rado and V. J. Folen, Bull. Am. Phys. Soc. Ser. II, **2**, 263 (1957).

[5] The quantity M_s should not be confused with the spontaneous magnetic moment per gram-ion of magnetic ions. In stoichiometric lithium ferrite, for example, the value of the latter quantity is $M_s/(2.5)$.

* *Note added in proof.*—The magnetic method for determining μ and λ was used for the Mg-Fe ferrites only. In the case of Li ferrite we used the results of x-ray diffraction ($\lambda=1$) and chemical analysis ($\mu+\lambda=2.45$). Equation (8) then gives $(n_B)_{T=0}=2.58\mu_B$, whereas the measurements (Table I) yield $(n_B)_{T=0}=2.45\mu_B$. This discrepancy could be due to a combination of chemical and x-ray errors rather than to an inadequacy of the Néel theory.

[6] In magnesium ferrite this assumption is substantiated by the neutron diffraction experiments of G. E. Bacon and F. F. Roberts, Acta Cryst. **6**, 57 (1953), and Corliss, Hastings, and Brockman, Phys. Rev. **90**, 1013 (1953). Although no such experiments have been reported for lithium ferrite, the x-ray diffraction work of P. B. Braun, Nature **170**, 1123 (1952), shows that the Li^+ ions are on B sites only.

and

$$\psi = u/v, \tag{10}$$

so that Eqs. (5) and (6) lead to

$$\varphi = B_J(\psi v)/B_J(v), \tag{11}$$

$$\psi = (\alpha\lambda\varphi+\mu)/(\lambda\varphi+\beta\mu), \tag{12}$$

and

$$T = (nM_0^2/R)(\beta\mu+\lambda\varphi)B_J(v)/v, \tag{13}$$

and substitution of Eqs. (9) and (5b) into Eq. (3) yields

$$M_s = (\mu-\lambda\varphi)M_0 B_J(v). \tag{14}$$

Using the expansion

$$B_J(x)/x = (J+1)/(3J), \tag{15}$$

which is valid for $x \ll 1$, and denoting the value of φ at $T=T_c$ by φ_c, we combine Eqs. (9), (5), (10), and (12) to obtain

$$\varphi_c = (\alpha\lambda\varphi_c+\mu)/(\lambda\varphi_c+\beta\mu). \tag{16}$$

The solution of Eq. (16) is

$$\varphi_c = \{\alpha\lambda-\beta\mu+[(\alpha\lambda-\beta\mu)^2+4\lambda\mu]^{\frac{1}{2}}\}/(2\lambda) \tag{17}$$

where the negative square root was omitted because M_A and M_B (and hence φ) are defined to be positive. Finally, Eqs. (13) and (15) may be combined to give

$$n = \frac{3JRT_c}{(J+1)(\beta\mu+\lambda\varphi_c)M_0^2}. \tag{18}$$

Since λ and μ have been determined, and α and β are assumed to be known, the equations given above make it possible to calculate the values of M_s and T corresponding to any point on the magnetization curve. In the procedure to be described we used tables of the Brillouin function rather than the graphical method of Néel. The tables prepared by Schmid and Smart[7] were found to be very useful, especially in connection with Sec. IV of the present paper. Selected parts of these tables, relevant to the case $J=\frac{5}{2}$, are reproduced in the Appendix.

We start the calculation of M_s and T by using Eq. (17) to find φ_c. Since T_c is presumed to have been determined by an extrapolation of the experimental curve of n_B *vs* T, we then obtain n from Eq. (18). Next we note that at $T=0$ the value of φ is unity, as can be seen from Eqs. (5) and (9). Thus if we choose some value of φ in the range $1<\varphi<\varphi_c$, then this φ must correspond to some (as yet unknown) temperature in the range $0<T<T_c$. Equation (12) then yields the value of ψ corresponding to the chosen value of φ. The value of v may now be obtained by solving the implicit Eq. (11) with the use of the Brillouin function tables. This can usually be accomplished with considerable accuracy in two or three trials. Having determined v, we then calculate M_s from Eq. (14) and the corresponding T from Eq. (13). To obtain another point on the magnetization curve we choose a different value of φ and proceed as described above. It must be remembered, however, that the magnetization curve calculated in this way corresponds to *assumed* values of α and β. If the calculated curve is to agree with the experimental magnetization curve then it is necessary to use the best, or nearly best, values of α and β. Two methods for determining such values will now be discussed.

[7] L. P. Schmid and J. S. Smart, NAVORD Report 3640, U. S. Naval Ordnance Laboratory, May 4, 1954 (unpublished).

IV. DETERMINATION OF α AND β

In all previous work the best values of α and β were determined by a trial-and-error method. This method consists in choosing a set of α and β values from a certain permissible range and then calculating the M_s *vs* T relation via a graphical analog of the procedure described in Sec. III. As shown by Néel,[1] the permissible range of α and β values is restricted by the shape of the experimental magnetization curve of the material under consideration. If the calculated M_s *vs* T relation disagrees with experiment then the calculation must be repeated on the basis of another set of chosen α and β values. This process is continued until adequate agreement with experiment is obtained.

We have found that the trial-and-error method is very time-consuming in situations where the condition of "adequate" agreement requires a fairly "accurate" agreement. As mentioned in the Introduction, such a situation exists when the sublattice magnetizations are calculated for the purpose of predicting the temperature dependence of the magnetocrystalline anisotropy of certain ferrites by means of crystalline field theory. An especially discouraging aspect of the trial-and-error method is its slow "convergence." This means that at a given stage of the calculation it is difficult to decide whether still another choice of α and β would lead to a better agreement between the calculated and measured M_s *vs* T curves.

The analytical method developed below was found to be more rapid and reliable than the trial-and-error method. Although this new method involves certain first-order approximations, experience shows that it does provide an α and β which are so close to the best values that the residual disagreement between the calculted and measured M_s *vs* T curve is most probably due to the inherent approximations of the Néel theory.

The basic assumption of the analytical method is that the AB interactions are by far the strongest so that the AA and BB interactions may be regarded as small perturbations. This assumption is reasonably well fulfilled in many ferrites of interest. Thus we begin by choosing the values $\alpha=0$ and $\beta=0$ and using the procedure of Sec. III to calculate an "unperturbed" curve of M_s *vs* T. Next we introduce the notation

$$\bar{Q} \equiv (Q)_{\alpha=0,\beta=0}, \tag{19a}$$

$$Q_\alpha \equiv \partial Q/\partial\alpha \quad \text{and} \quad Q_\beta \equiv \partial Q/\partial\beta, \tag{19b}$$

where Q represents any quantity. By expanding M_s in a power series in α and β we thus obtain, to first order,

$$M_s=\bar{M}_s+\bar{M}_{s\alpha}\alpha+\bar{M}_{s\beta}\beta, \tag{20}$$

where $\bar{M}_s$ is, of course, the unperturbed value of M_s at some given temperature other than T_c or zero. Use of Eq. (3) yields

$$M_s-\bar{M}_s=F\alpha+G\beta, \tag{21}$$

where the temperature-dependent quantities F and G are defined by

$$F=\mu\bar{M}_{B\alpha}-\lambda\bar{M}_{A\alpha} \tag{22a}$$

and

$$G=\mu\bar{M}_{B\beta}-\lambda\bar{M}_{A\beta}. \tag{22b}$$

Since Eq. (21) may be rewritten in the form

$$(M_s-\bar{M}_s)/G=(F/G)\alpha+\beta, \tag{23}$$

it is seen that a graph of $(M_s-\bar{M}_s)/G$ *vs* (F/G) is a straight line whose slope and intercept determine the desired quantities α and β, respectively. Once α and β are known the procedure of Sec. III may be used to calculate the "perturbed" M_s *vs* T curve. It will be seen in Sec. V that this perturbed curve, which is correct to first approximation, agrees quite well with our experimental results.

It should be noted that each point on the straight line represented by Eq. (23) corresponds to a different temperature. Since the values of M_s used in Eq. (23) are taken from the experimental results and those of $\bar{M}_s$ have already been obtained, the only remaining task is the determination of F and G. In the calculation outlined below both F and G will be expressed in terms of quantities which are known from the calculation of the unperturbed magnetization curve.

Equations (22) show that F and G will be known once the quantities $\bar{M}_{A\alpha}$, $\bar{M}_{A\beta}$, $\bar{M}_{B\alpha}$, and $\bar{M}_{B\beta}$ are calculated. To do this, we use Eqs. (5) to obtain

$$\bar{M}_{A\alpha}=M_0\bar{B}_J'(u)\bar{u}_\alpha, \tag{24a}$$

$$\bar{M}_{A\beta}=M_0\bar{B}_J'(u)\bar{u}_\beta, \tag{24b}$$

$$\bar{M}_{B\alpha}=M_0\bar{B}_J'(v)\bar{v}_\alpha, \tag{24c}$$

and

$$\bar{M}_{B\beta}=M_0\bar{B}_J'(v)\bar{v}_\beta, \tag{24d}$$

where a prime affixed to a "dashed" Brillouin function indicates that it is the *derivative* of this function with respect to its argument which is to be evaluated at $\alpha=\beta=0$. Next we take appropriate partial derivatives of Eqs. (6), affix dashes, and then eliminate $\bar{M}_A$ and $\bar{M}_B$ by means of the dashed versions of Eqs. (5). Substitution of the resulting expressions for $\bar{u}_\alpha$, $\bar{u}_\beta$, $\bar{v}_\alpha$, and $\bar{v}_\beta$ into Eqs. (24) yields

$$\bar{M}_{A\alpha}=(M_0^2/RT)\times\bar{U}'[\bar{n}_\alpha\mu M_0\bar{V}+\bar{n}(\lambda M_0\bar{U}+\mu\bar{M}_{B\alpha})], \tag{25a}$$

$$\bar{M}_{A\beta}=(M_0^2/RT)\bar{U}'[\bar{n}_\beta\mu M_0\bar{V}+\bar{n}\mu\bar{M}_{B\beta}], \tag{25b}$$

$$\bar{M}_{B\alpha}=(M_0^2/RT)\bar{V}'[\bar{n}_\alpha\lambda M_0\bar{U}+\bar{n}\lambda\bar{M}_{A\alpha}], \tag{25c}$$

and

$$\bar{M}_{B\beta}=(M_0^2/RT)\times\bar{V}'[\bar{n}_\beta\lambda M_0\bar{U}+\bar{n}(\lambda\bar{M}_{A\beta}+\mu M_0\bar{V})], \tag{25d}$$

where we further simplified the notation by introducing the abbreviations

$$U\equiv B_J(u) \quad \text{and} \quad V\equiv B_J(v). \tag{26}$$

Before proceeding we must express $\bar{n}$, $\bar{n}_\alpha$, and $\bar{n}_\beta$ in terms of known quantities. Substitution of Eq. (16) into Eq. (18) yields an equation for n from which we obtain

$$\bar{n}=\frac{3JRT_c}{(J+1)M_0^2(\lambda\mu)^{\frac{1}{2}}}; \tag{27a}$$

$$\bar{n}_\alpha=-\frac{3JRT_c}{2(J+1)M_0^2\mu}; \tag{27b}$$

$$\bar{n}_\beta=-\frac{3JRT_c}{2(J+1)M_0^2\lambda}. \tag{27c}$$

Now we insert Eqs. (27) into Eqs. (25) and solve for the four unknowns $\bar{M}_{A\alpha}$, $\bar{M}_{A\beta}$, $\bar{M}_{B\alpha}$, and $\bar{M}_{B\beta}$. Equations (22) then yield the results

$$F=\frac{M_0\xi\lambda\{(\bar{V}-2r\bar{U})\bar{U}'-\bar{U}\bar{V}'+\xi[(2+r)\bar{U}-r^{-1}\bar{V}]\bar{U}'\bar{V}'\}}{2(1-\xi^2\bar{U}'\bar{V}')}, \tag{28a}$$

$$-G=\frac{M_0\xi\mu\{(\bar{U}-2r^{-1}\bar{V})\bar{V}'-\bar{V}\bar{U}'+\xi[(2+r^{-1})\bar{V}-r\bar{U}]\bar{U}'\bar{V}'\}}{2(1-\xi^2\bar{U}'\bar{V}')}, \tag{28b}$$

where the abbreviations ξ and r are defined by

$$\xi=[3J/(J+1)](T_c/T) \quad \text{and} \quad r=(\lambda/\mu)^{\frac{1}{2}}. \tag{29}$$

It may be noted that $(-G)$ can be obtained from F by interchanging μ with λ and u with r, and that the Eqs. (28) contain only constants or quantities which are known from the unperturbed calculation. The first derivative of the Brillouin function is listed in the Schmid-Smart[7] tables and also in the Appendix of the present paper.

V. MEASUREMENTS OF SATURATION MAGNETIZATION

A. Samples and Procedures

Measurements of saturation moment per unit mass (σ) *versus* temperature (T) were made on single crystals

TABLE I. Properties of the ferrite single crystals.

Compound	μ	μ_{eff}	λ	σ_0 (emu)	$(n_B)_{T=0}$ (μ_B)	T_c (°K)	n (moles/cc)	α	β
$Li_{0.55}^{+}\,Fe_{2.45}^{+++}\,O_4^{--}$	1.45	1.45	1.00	69.6	2.58	904	263	−0.54	−0.22
$Mg_{0.71}^{++}\,Fe_{2.15}^{+++}\,Fe_{0.06}^{++}\,O_4^{--}$	1.30	1.35	0.85	68.3	2.51	692	276	−0.72	−0.30
	1.24	1.29	0.91	51.1	1.87	701	256	−0.63	−0.27
$Mg_{0.72}^{++}\,Fe_{2.08}^{+++}\,Fe_{0.18}^{++}\,O_4^{--}$	1.14	1.29	0.92	49.7	1.84	715	263	−0.65	−0.27

λ, μ = actual number of ferric ions per molecule situated on A, B sites, respectively.
μ_{eff} = effective number of ferric ions per molecule situated on B sites.
σ_0 = saturation moment per unit mass at $T=0$°K.
$(n_B)_{T=0}$ = spontaneous magnetic moment, at $T=0$°K, in Bohr magnetons (μ_B) per molecule.
T_c = Curie temperature.
n = molecular field coefficient referring to the strengths of the AB interactions.
$n\alpha$, $n\beta$ = molecular field coefficients referring to the strengths of the AA, BB interactions, respectively.

of lithium ferrite and two compositions of magnesium-iron ferrite. Table I contains the chemical formulas and other data pertinent to the samples used. These formulas are based on chemical analyses[8] of all the cations listed. The lithium ferrite crystals, which were grown from a lead oxide flux, contain less than 0.2 weight percent PbO. The magnesium-iron ferrite crystals[9] were grown by means of a flame fusion method.

Spherical samples having diameters between 0.06 and 0.07 inch were ground by means of the air-jet technique[10] from single crystals of each of the three compounds listed in Table I. The magnetization measurements were performed by means of an inhomogeneous field method in which the field gradient throughout the sample was essentially constant. A torsion balance, previously calibrated with a nickel specimen, was used to measure the force exerted on the sample by the field. Since the single crystal spheres were free to rotate in the sample holder, the easy direction of magnetization was always parallel to the magnetic field. The temperatures used for the measurements ranged from 77°K to about 950°K, and the externally applied field was 7000 oersteds throughout this work. When corrected for the demagnetization arising from the spherical shape of the samples, this field is still considerably larger than either the anisotropy field[11] or the maximum internal demagnetizing field that could be caused by cavities.

The value of σ at $T=0$°K, to be denoted by σ_0, was determined by extrapolation of the experimental σ *vs* T curve. Since the measurements did not extend to very low temperatures the $T^{\frac{1}{2}}$ and T^2 laws were found to be equally adequate approximations for this purpose. Thus the resulting values of σ_0 obtained by the two methods were simply averaged. It should be noted that whereas the saturation magnetization is the quantity measured in the experiments, the spontaneous magnetization is the quantity occurring in the theory. However, the error arising from this difference is negligible except in the immediate vicinity of the Curie point. This statement may be illustrated, for example, by the Mg-Fe ferrite for which T_c is 692°K (Table I). At a temperature as high as 662°K the applied field (corrected for demagnetization) is only about 0.5% of the molecular field acting upon the B sites. Thus n_B is equated throughout this paper to the ratio $M_s/(N\mu_B)$, where M_s is the product of σ and the molecular weight. Data on σ_0, $(n_B)_{T=0}$ and T_c for the crystals investigated are given in Table I. The value of T_c was determined by graphically extrapolating the experimental curve of σ *vs* T to $\sigma=0$. It was found that a change of only about five degrees in the resulting value of T_c causes a significant deviation from linearity of the $(M_s-\bar{M}_s)/G$ *vs* (F/G) graph. Thus the straight line requirement contained in Eq. (23) may be regarded as a rather accurate operational method for determining an appropriately defined "experimental" Curie temperature.

Another point worth noting is that the theory described in the preceding sections deals with one kind of magnetic ion only. Thus the resulting equations are directly applicable to lithium ferrite, in which all the magnetic ions are ferric ions, but not to magnesium-iron ferrites, in which the magnetic ions are ferrous as well as ferric ions. Since an appropriate generalization of the theory would introduce undesirable complications, we proceed as if the material under study contained ferric ions only. To account for the magnetic effects of the ferrous ions, however, we use an "effective" rather than the actual number of ferric ions throughout the calculation. This approximation appears to be reasonable as long as the ferrous ion content of the material is fairly small.

Let λ and μ denote the actual number of ferric ions per molecule situated on A and B sites, respectively. If ν is the number of ferrous ions per molecule, and if it is assumed that these ions are located on B sites only, then the distribution of the effective number of ferric ions may be described by the parameters λ and μ_{eff}, where μ_{eff} is defined by

$$(5/2)\mu+2\nu=(5/2)\mu_{eff}. \tag{30}$$

In Eq. (30) and everywhere else in this section it is assumed that g has the value two and that J may be replaced by the spin quantum number, S. We note

[8] The chemical analyses were kindly performed by D. I. Walter of this Laboratory.

[9] These crystals were kindly supplied by Dr. W. H. Bauer of the Rutgers University School of Ceramics.

[10] W. L. Bond, Rev. Sci. Instr. **22**, 344 (1951).

[11] The first-order magnetocrystalline anisotropy constant and its temperature dependence were determined in reference 2 for the Mg-Fe ferrite crystals and by V. J. Folen (to be published) for the lithium ferrite crystal. The measured (and x-ray) density of the latter crystal is 4.76.

that Eq. (8), which now contains μ_{eff} instead of μ, can be combined with Eq. (30) and with the information given by the chemical formula to obtain μ as well as the desired quantities λ and μ_{eff}. The values of these three quantities for the compounds used are listed in Table I. Although the distribution of the Mg^{++} ions does not affect the molecular field coefficients directly, it is easily obtained from the above data if one makes the reasonable assumption that any existing cation vacancies occur on the B sites only.

B. Results and Discussion

The analytical method for determining molecular field coefficients reported in this paper was developed in conjunction with our experimental results on σ *vs* T for certain Mg-Fe ferrites.[4] However, the conditions for testing this method are more ideal in Li ferrite, a substance which contains only one kind of magnetic ion. Thus we present the Li ferrite results in somewhat greater detail even though the analytical method proves

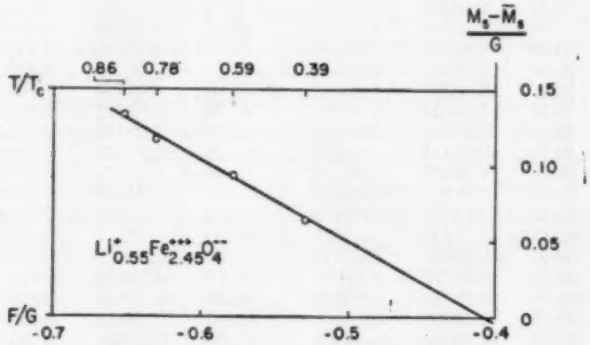

FIG. 1. Example of graph used for determining α and β by the method explained in connection with Eq. (23).

to be equally applicable to the Mg-Fe ferrites whose ferrous ion content is sufficiently low.

Figure 1 shows a graph of $(M_s-\bar{M}_s)/G$ *vs* F/G for the compound $Li_{0.55}^{+}\,Fe_{2.45}^{+++}\,O_4^{--}$ in a "disordered" state. Since the experimental points do lie on a straight line, as predicted on the basis of Eq. (23), the quantities α and β can now be determined (see Table I). It should also be noted that the data extend over a considerable range of temperatures, T/T_c varying from 0.39 to 0.86. Thus the linearity of the graph shown in Fig. 1 provides strong evidence for the combined validity of the Néel theory and the analytical method presented in this paper. Specifically, Fig. 1 indicates that our first order expansion in α and β (see Sec. IV) is apparently justified for the compound under study. This is rather fortunate because the actual value of $\alpha^2(\approx 0.29)$ is not really negligible compared to unity. The adequacy of the first-order expansion may be due to the fact that the signs of F and G are opposite whereas those of α and β are the same. According to Eq. (21), therefore, the correction arising from the AA interactions partially

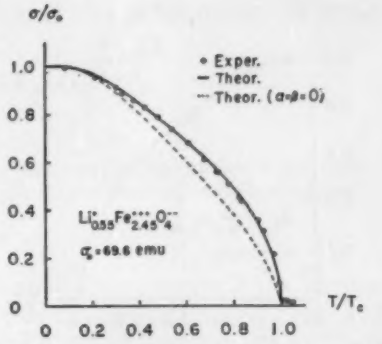

FIG. 2. Experimental data (circles) and theoretical curve (full line) for σ/σ_0 *vs* T/T_c in "disordered" $Li_{0.55}^{+}\,Fe_{2.45}^{+++}\,O_4^{--}$. The theoretical curve based on $\alpha=\beta=0$ (dashed line) is also shown.

cancels that arising from the BB interactions. Thus the requirement of a small α and β is not as restrictive as one might expect.

Figure 2 shows the experimental values of σ/σ_0 as a function of T/T_c for the Li ferrite mentioned above. The dashed line is the "unperturbed" theoretical curve corresponding to $\alpha=\beta=0$, whereas the full line is the best-fitting "perturbed" theoretical curve based on the values of α and β derived from Fig. 1 and Eq. (23). As expected from the remarks of the previous paragraph, the difference between these two curves is indeed relatively small. The most interesting aspect of Fig. 2, however, is the excellent agreement between the experimental data and the perturbed theoretical curve. Although this agreement is satisfying and perhaps better than expected, it should be noted that the straight line shown in Fig. 1 represents an even more stringent test of the theory.

The compound $Mg_{0.71}^{++}\,Fe_{2.15}^{+++}\,Fe_{0.06}^{++}\,O_4^{--}$ was measured in two states of ionic distribution obtained by using the method [12,13] of varying the heat treatment. Figures 3 and 4 show the experimental results corresponding to states in which σ_0 is relatively high and low, respectively. Similar results were also obtained for

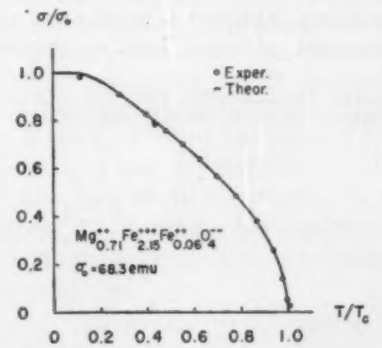

FIG. 3. Experimental data (circles) and theoretical curve (full line) for σ/σ_0 *vs* T/T_c in $Mg_{0.71}^{++}\,Fe_{2.15}^{+++}\,Fe_{0.06}^{++}\,O_4^{--}$. The value of σ_0 is 68.3 emu in this case.

[12] R. Pauthenet, Ann. phys. **7**, 710 (1952).
[13] C. J. Kriessman and S. E. Harrison, Phys. Rev. **103**, 857 (1956).

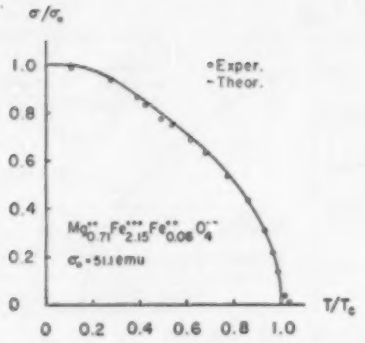

FIG. 4. Experimental data (circles) and theoretical curve (full line) for σ/σ_0 *vs* T/T_c in $Mg_{0.71}^{++}Fe_{2.15}^{+++}Fe_{0.06}^{++}O_4^{--}$. The value of σ_0 is 51.1 emu in this case.

one state of ionic distribution in the compound $Mg_{0.75}^{++}Fe_{2.06}^{+++}Fe_{0.18}^{++}O_4^{--}$. The molecular field coefficients and other pertinent data are listed in Table I. We find that in each of these compounds the correction arising from the AA interactions partially cancels that arising from the BB interactions, as in the case of Li ferrite. In addition, all the data obey the linear relation predicted by Eq. (23), and there is again good agreement between the perturbed theoretical curve of σ/σ_0 *vs* T/T_c and the corresponding experimental results.

In comparing our results with those of other workers we consider the observed magnetizations first. Gorter's[14] data on σ/σ_0 *vs* T/T_c for sintered $Li_{0.5}Fe_{2.5}O_4$ are consistent with the results given in Fig. 2. No corresponding measurements have been published for Mg-Fe ferrites having compositions and ionic distributions similar to those of our samples.

Values of the molecular field coefficients do not seem to exist in the literature either for the compounds which we studied or for related compounds. For other ferrites, however, Néel[1] and Pauthenet[13] have compared the measured curves of σ/σ_0 *vs* T/T_c with the molecular field theory. Their results show that the agreement between theory and experiment is not as good as that reported in the present paper. Although it is tempting to attribute the improvement obtained here to the use of the analytical method, it should be noted that our determination of molecular field coefficients differs from previous work in two additional respects. Firstly, our samples are crystallographically aligned monocrystals rather than sintered polycrystals, and secondly, their magnetizations are either entirely or almost entirely due to one kind of magnetic ion only. It is not impossible, therefore, that these two simplifications are partly responsible for the good agreement between theory and experiment.

[14] E. W. Gorter, thesis, Leyden, 1954. Reprinted in three parts in Philips Research Repts. **9**, 295, 321, 403 (1954).

APPENDIX

$B_{5/2}(x)$ and $B_{5/2}'(x)$. Reproduced from reference 7 with acknowledgment to Dr. J. S. Smart.

x	$B_{5/2}(x)$	$B_{5/2}'(x)$	x	$B_{5/2}(x)$	$B_{5/2}'(x)$
00.00	0.00000	0.46667	01.35	0.53917	0.29121
00.01	0.00467	0.46665	01.40	0.55351	0.28234
00.02	0.00933	0.46661	01.45	0.56741	0.27360
00.03	0.01400	0.46654	01.50	0.58087	0.26500
00.04	0.01866	0.46645	01.55	0.59391	0.25654
00.05	0.02333	0.46632	01.60	0.60653	0.24826
00.06	0.02799	0.46617	01.65	0.61874	0.24015
00.07	0.03265	0.46599	01.70	0.63055	0.23222
00.08	0.03731	0.46578	01.75	0.64196	0.22449
00.09	0.04197	0.46555	01.80	0.65300	0.21696
00.10	0.04662	0.46529	01.85	0.66366	0.20963
00.12	0.05592	0.46468	01.90	0.67397	0.20251
00.14	0.06521	0.46397	01.95	0.68392	0.19559
00.16	0.07448	0.46315	02.00	0.69353	0.18889
00.18	0.08373	0.46222	02.10	0.71177	0.17611
00.20	0.09297	0.46119	02.20	0.72878	0.16415
00.25	0.11595	0.45816	02.30	0.74463	0.15299
00.30	0.13877	0.45449	02.40	0.75940	0.14261
00.35	0.16139	0.45021	02.50	0.77317	0.13296
00.40	0.18378	0.44535	02.60	0.78602	0.12401
00.45	0.20592	0.43994	02.70	0.79800	0.11572
00.50	0.22777	0.43401	02.80	0.80918	0.10805
00.55	0.24931	0.42761	02.90	0.81963	0.10095
00.60	0.27052	0.42076	03.00	0.82939	0.09438
00.65	0.29138	0.41350	03.50	0.86962	0.06822
00.70	0.31187	0.40588	04.00	0.89897	0.05032
00.75	0.33196	0.39794	04.50	0.92084	0.03784
00.80	0.35165	0.38971	05.00	0.93741	0.02893
00.85	0.37093	0.38124	05.50	0.95016	0.02241
00.90	0.38978	0.37257	06.00	0.96009	0.01755
00.95	0.40818	0.36374	06.50	0.96791	0.01387
01.00	0.42615	0.35477	07.00	0.97410	0.01103
01.05	0.44366	0.34571	07.50	0.97904	0.00882
01.10	0.46072	0.33660	08.00	0.98300	0.00709
01.15	0.47732	0.32746	08.50	0.98619	0.00571
01.20	0.49346	0.31832	09.00	0.98876	0.00462
01.25	0.50915	0.30922	09.50	0.99085	0.00374
01.30	0.52439	0.30017	10.00	0.99254	0.00304

Explanation for the Low-Temperature Behavior of the Anisotropy of Iron

W. J. Carr, Jr.
Westinghouse Research Laboratories, Pittsburgh, Pennsylvania
(Received July 21, 1959)

The seemingly anomalous results obtained by Graham for the temperature dependence of magnetic anisotropy in iron are interpreted on the basis of Zener's theory, with the effect of thermal expansion included.

FROM experimental evidence available at the time Akulov[1] and Zener[2] concluded that the first crystalline anisotropy constant of iron decreased with temperature as the tenth power of the magnetization. Zener's theory[2,3] indicates the tenth power relationship should hold approximately over the entire ferromagnetic temperature range; various other calculations[1,4] also lead to such a dependence, at least in the low temperature region.

Paradoxically, Graham[5] recently reported precise measurements below room temperature which indicate in this range not a tenth power, but a fourth or fifth power dependence on magnetization. The new data (which agree with some unpublished values of Bozorth) along with the older results are plotted in Fig. 1.

The purpose of the present note is to point out that these data do not necessarily conflict with Zener's theory if the effect of thermal expansion on the anisotropy is considered. Let it be assumed, as Brenner[6] has done, that Zener's result is correct for constant volume, and in general the anisotropy constant is given by

$$K(T)=K_0(\omega)[\sigma(T)/\sigma_0]^{10}, \tag{1}$$

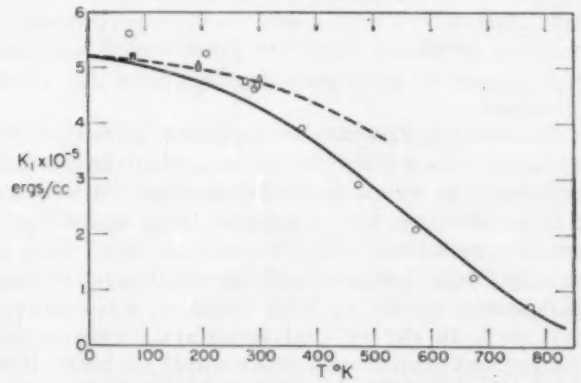

FIG. 1. Measured values of the first anisotropy constant of iron plotted against temperature. △—Recent measurements of Graham (reference 5). □—Measurements of Bozorth as given by Graham (reference 5). ○—Older values of Bozorth as calculated from magnetization curves of Honda, Masumoto, and Kaya. R. M. Bozorth, J. Appl. Phys. **8**, 575 (1937). – – – $5.2\times10^5\ (\sigma/\sigma_0)^8$; —— $5.2\times10^5\ (\sigma/\sigma_0)^{10}$.

where ω is the volume strain, T the temperature, and σ/σ_0 the reduced magnetization. From a Taylor expansion of $K_0(\omega)$ and from the law $\sigma(T)=\sigma_0(1-AT^{\frac{3}{2}})$ one obtains, for low temperature,

$$K(T)\simeq K_0(0)[1+\kappa\omega-10AT^{\frac{3}{2}}], \tag{2}$$

where κ is $(1/K_0)(dK_0/d\omega)$. Equation (2) may be written

$$K(T)=K_0(0)[1-(10-\kappa\omega T^{-\frac{3}{2}}A^{-1})AT^{\frac{3}{2}}]$$
$$\simeq K_0(0)[\sigma(T)/\sigma(0)]^n, \tag{3}$$

where $n=10-\kappa A^{-1}\omega T^{-\frac{3}{2}}$. The important thing to note is that empirically (Table I) $\omega T^{-\frac{3}{2}}$ over a wide range is nearly independent of temperature if the thermal expansion is substituted for ω. Thus, n is a constant given by $n\simeq10-0.38\kappa$ and (3) again gives a power law dependence on magnetization. Direct measurements of κ have not been reported; but from a thermodynamic argument Brenner obtained the value 4.7, for which $n=8.2$. Due to lack of accuracy in the experimental data, the value for κ can be considered only as an order of magnitude. To reproduce the experimental value, $n\simeq5$, κ would have to be three times the above estimate and of the same sign.

TABLE I. Measured values in iron of the volume strain ω [C. Nix and D. MacNair, Phys. Rev. **60**, 597 (1941)] multiplied by $T^{-\frac{3}{2}}$ for various temperatures.

T°K	$\omega T^{-\frac{3}{2}}\times10^6$
50	1.16 (est)
100	1.26
200	1.29
300	1.34
400	1.33
500	1.31
600	1.32
700	1.29
800	1.28
900	1.26

Near room temperature the $T^{\frac{3}{2}}$ expression for magnetization begins to break down and (2) no longer applies. As the temperature is increased further the variation of $K_0(\omega)$ becomes small compared with that of σ and thus by (1) the anisotropy approaches the tenth power law.

[1] N. S. Akulov, Z. Physik **100**, 197 (1936).
[2] C. Zener, Phys. Rev. **96**, 1335 (1954).
[3] W. J. Carr, Jr., Phys. Rev. **109**, 1971 (1958).
[4] F. Keffer, Phys. Rev. **100**, 1692 (1955).
[5] C. D. Graham, Jr., Phys. Rev. **112**, 1117 (1958).
[6] R. Brenner, Phys. Rev. **107**, 1539 (1957).

JOURNAL OF APPLIED PHYSICS VOLUME 31, NUMBER 1 JANUARY, 1960

Time-Dependent Electron Flow

M. C. PEASE
Sylvania Electric Products Inc., Special Tube Operations, Mountain View Components Laboratories, 500 Evelyn Avenue, Mountain View, California

(Received May 15, 1959)

The conditions of self-consistency for electron flow through arbitrary static or time-varying electric and magnetic fields are established assuming (a) nonrelativistic flow, (b) single streaming—i.e., the velocity has a single value and direction at every point, and (c) the electrons originate on a cathode not threaded by magnetic lines of force. In the case where the magnetic field is constant and uniform, a single-vector differential equation can be written which determines all possible solutions.

From this equation certain time-variant solutions are developed. These are fully self-consistent—that is, large signal—solutions which exhibit some of the nonlinear behavior that would be expected of such solutions.

Probably the most interesting of these solutions—since it offers an explanation of an observed phenomenon that does fit previous theory—is a radial oscillation of the cloud in a filamentary cathode smooth bore magnetron at $\omega/\sqrt{2}$.

The possible application of the other solutions to anomalous behavior in various magnetron type devices is also discussed.

I. INTRODUCTION

WE are concerned here with the self-consistent flow of electrons through an environment that may contain both electric and magnetic fields and which may be time variant, either as a perturbation or as a large signal disturbance.

The importance of this problem is obvious. Nearly all applications of electron beams do occur under time-variant conditions. In many of the more critical applications this variation is large, and a perturbation approach is, at best, questionable. Furthermore, it is often true that the electron density is high and space-charge effects cannot be ignored. Thus a complete theory of time-variant self-consistent beams would be most useful.

The intractability of the problem is equally obvious. It is demonstrated by the paucity of known solutions. Even for the much simpler case of static (i.e., the velocity field independent of time) two-dimensional flow under crossed-field conditions, where a uniform static magnetic field is perpendicular to the plane of flow, only a few self-consistent beams are known. There is the cylindrical and planar laminar flow of Brillouin,[1] the elliptical, hyperbolic, and parabolic laminar flows discovered by Kirstein,[2] the planar striated flow discussed by Slater,[3] and the "uniform" partially striated flow analyzed by Bartram and Pease.[4] No others are known to the author.

In view of the specialized nature of these known solutions (the laminar flow cases, for example, are all solenoidal, i.e., $\nabla \cdot \mathbf{v}=0$, which is a very strong restriction), we may wonder whether there may be important phenomena that will be suppressed by their specialization.

It has therefore seemed worthwhile to attempt a frontal attack on the problem and to see what results could be obtained without making restrictive assumptions.

While the general problem is still very far from being solved, it is possible to obtain solutions under some conditions. For the case where the magnetic field is constant and uniform, we can write a single vector equation in terms of $\partial/\partial t$ and of known spatial operators which must be satisfied by any suitable single streaming velocity field. From this, then, the known static solutions can be generalized into time-variant beams that are self-consistent under large signal conditions. At least one of these appears to be of importance in that it provides a mechanism for a type of operation that has been observed in a coaxial solid anode magnetron which had not previously been explained. Other solutions also appear to have possible significance for other phenomena.

We have specified that we are concerned with "self-consistent beams." By this we mean that the beam is established by its external conditions only. A velocity field is consistent with a possible beam under much broader conditions. (Gabor's condition only.) Such a velocity field may be used with the equations of motion to determine an electric field. However, in the general case, such an electric field requires the presence of charged ions or other such device within the beam. It is not consistent with Poisson's equation where the space charge is solely that of the beam itself. It is a much more stringent requirement to specify that the velocity field shall be consistent with an electric field that can be imposed externally to the beam without neutralization or enhancement of the space charge of the beam itself. By "self-consistent" we mean beams that meet this much more stringent condition.

Our attack will be based on the manipulation of the equation of motion, divergence equation, and equation of continuity in vector form. We shall assume only that

[1] J. C. Slater, *Microwave Electronics* (D. Van Nostrand Company, Inc., Princeton, New Jersey, 1950), Chap. 13.5.
[2] P. T. Kirstein, J. Electronics and Control 5, 425–433 (1958).
[3] See reference 1, Chap. 13.6.
[4] R. H. Bartram and M. C. Pease, Sylvania Technologist 11, No. 2, 59–65 (1958).

(a) the motion is nonrelativistic, (b) it is single streaming so that the velocity is a single valued vector function of position (although we could generalize to a finite number of streams), and (c) that the beam originates on a cathode that is not threaded by any magnetic lines of force. The last assumption allows us to use Gabor's[5] condition on the curl of the generalized momentum. We shall show that these equations can then be combined into a single nonlinear vector equation involving determined operators.

Having obtained this equation, we shall then apply to it various conditions of interest (crossed-field situations) to obtain specific time-variant beams.

Finally, we shall consider the application of these time-dependent solutions to various crossed-field devices.

II. GENERAL THEORY

We may take, as our variable describing the beam, the vector velocity $\mathbf{v}$. Then the equation of motion is

$$(\partial\mathbf{v}/\partial t)+(\mathbf{v}\cdot\nabla)\mathbf{v}=\mathbf{m}+\boldsymbol{\omega}\times\mathbf{v}, \tag{1}$$

where

$$\mathbf{m}=-\eta\mathbf{E}=-|e/m|\,\mathbf{E} \tag{2}$$

describes the electric field. $\boldsymbol{\omega}$ will normally be a constant vector of magnitude $|\boldsymbol{\omega}|=\eta B$, where $|\boldsymbol{\omega}|$ is the cyclotron frequency, in the z direction. In this section, however, we shall not so restrict it, but will consider $\boldsymbol{\omega}$ as a normalized vector B field.

The divergence equation is, then

$$K=\nabla\cdot\mathbf{m}, \tag{3}$$

where

$$K=-\eta\rho/\epsilon_0 \tag{4}$$

is the reduced space charge. This, of course, is a scalar function. The equation of continuity may be written

$$(\partial K/\partial t)+\nabla\cdot(K\mathbf{v})=0. \tag{5}$$

Added to this, we will also assume the condition that Gabor has shown to apply when there are no lines of magnetic flux that thread the cathode

$$\nabla\times\mathbf{v}=\boldsymbol{\omega}. \tag{6}$$

We may now solve these equations by the elimination of all variables except $\mathbf{v}$. Using (1) to find $\mathbf{m}$ and substituting in (3) we find

$$K=\nabla\cdot\{(\partial\mathbf{v}/\partial t)+(\mathbf{v}\cdot\nabla)\mathbf{v}-\boldsymbol{\omega}\times\mathbf{v}\}. \tag{7}$$

We have, now, the vector identity, which can be proven by its expansion in rectangular coordinates, that

$$\begin{aligned}(\mathbf{v}\cdot\nabla)\mathbf{v}&=\tfrac{1}{2}\nabla(\mathbf{v}\cdot\mathbf{v})-\mathbf{v}\times\nabla\times\mathbf{v}\\&=\tfrac{1}{2}\nabla(\mathbf{v}\cdot\mathbf{v})-\mathbf{v}\times\boldsymbol{\omega}\end{aligned} \tag{8}$$

from (6). Hence

$$K=\nabla\cdot\{(\partial\mathbf{v}/\partial t)+\tfrac{1}{2}\nabla(\mathbf{v}\cdot\mathbf{v})\}. \tag{9}$$

[5] D. Gabor, Proc. Inst. Radio Engrs. 33, 792–805 (1945).

Substituting in (5)

$$\nabla\cdot\left\{\frac{\partial^2\mathbf{v}}{\partial t^2}+\frac{1}{2}\frac{\partial}{\partial t}\nabla(\mathbf{v}\cdot\mathbf{v})+\mathbf{v}\frac{\partial}{\partial t}(\nabla\cdot\mathbf{v})+\tfrac{1}{2}\mathbf{v}\cdot\nabla^2(\mathbf{v}\cdot\mathbf{v})\right\}=0 \tag{10}$$

so that the bracketed expression must be a solenoidal vector function, thus giving the first integration of (10).

Equation (10) together with (6) are the conditions that any self-consistent beam must satisfy. It is very general, depending on no assumptions other than the nonrelativistic condition, Gabor's condition that no lines of B thread the cathode, and single streaming.

If we limit our attention to the situations of principal interest where the magnetic field may be taken as constant both in time and space, then we may put (10) in a more convenient form, in which the condition (6) is included. We do this by separating v into two parts

$$\mathbf{v}=\mathbf{A}+\nabla\phi, \tag{11}$$

where

$$\nabla\times\mathbf{A}=\boldsymbol{\omega},\quad \nabla\cdot\mathbf{A}=0 \tag{12}$$

so that $\mathbf{A}$ is the (normalized) vector potential. We may take $\mathbf{A}$ to be time independent, with the time dependence entirely contained in ϕ.

For flow confined to the (x,y) or (r,θ) plane

$$\mathbf{A}=\tfrac{1}{2}\omega(-y\mathbf{x}+x\mathbf{y})=\tfrac{1}{2}\omega r\boldsymbol{\theta} \tag{13}$$

is appropriate ($\mathbf{x}$ and $\mathbf{y}$ are the unit vectors in the x and y directions).

The assumption of such a form of $\mathbf{A}$ is not restrictive. For three-dimensional flow, for example, this simply adds additional terms to $\nabla\phi$, which may be inconvenient but is not limiting. Equation (10), then, becomes, after expanding the terms in $\nabla\cdot\mathbf{v}\nabla^2\phi$

$$\frac{\partial^2}{\partial t^2}\nabla^2\phi+\tfrac{1}{2}\nabla^2(\mathbf{v}\cdot\mathbf{v})+\nabla^2\phi\frac{\partial}{\partial t}\nabla^2\phi+\mathbf{v}\cdot\frac{\partial}{\partial t}\nabla\nabla^2\phi+\tfrac{1}{2}\mathbf{v}\cdot\nabla\nabla^2(\mathbf{v}\cdot\mathbf{v})+\tfrac{1}{2}\nabla^2\phi\nabla^2(\mathbf{v}\cdot\mathbf{v})=0. \tag{14}$$

Considering now the expression $\nabla^2(\mathbf{v}\cdot\mathbf{v})$, $\mathbf{A}$ as defined by (13), is such that $\mathbf{A}\cdot\mathbf{A}$ is $\omega r^2/4$ so that

$$\nabla^2(\mathbf{A}\cdot\mathbf{A})=\omega^2. \tag{15}$$

Also, since $\nabla\cdot\mathbf{A}=0$, we find that

$$\nabla^2(\mathbf{A}\cdot\nabla\phi)=(\mathbf{A}\cdot\nabla)\nabla^2\phi. \tag{16}$$

Hence

$$\begin{aligned}\nabla^2(\mathbf{v}\cdot\mathbf{v})&=\nabla^2(\mathbf{A}\cdot\mathbf{A}+2\mathbf{A}\cdot\nabla\phi+\nabla\phi\cdot\nabla\phi)\\&=\omega^2+2(\mathbf{A}\cdot\nabla)\nabla^2\phi+\nabla^2(\nabla\phi\cdot\nabla\phi)\end{aligned} \tag{17}$$

and (15) becomes

$$\frac{\partial^2}{\partial t^2}\nabla^2\phi+2(\mathbf{A}\cdot\nabla)\frac{\partial}{\partial t}\nabla^2\phi+\frac{1}{2}\frac{\partial}{\partial t}\nabla^2(\nabla\phi\cdot\nabla\phi)$$
$$+\nabla^2\phi\frac{\partial}{\partial t}\nabla^2\phi+\nabla\phi\cdot\frac{\partial}{\partial t}\nabla\nabla^2\phi$$
$$+\tfrac{1}{2}(\mathbf{A}+\nabla\phi)\cdot\nabla\{2(\mathbf{A}\cdot\nabla)\nabla^2\phi+\nabla^2(\nabla\phi\cdot\nabla\phi)\}$$
$$+\tfrac{1}{2}\nabla^2\phi\{\omega^2+2(\mathbf{A}\cdot\nabla)\nabla^2\phi+\nabla^2(\nabla\phi\cdot\nabla\phi)\}=0. \quad (18)$$

This equation, while it is complicated, is useful since it incorporates completely the conditions of self-consistency. It expresses $\nabla\phi$ as a partial differential equation with known, if involved, operators. It must contain all self-consistent beams satisfying the general assumptions we have made.

We may now consider various special cases in the following.

III. STATIC SOLENOIDAL FLOW

If the terms in $\partial/\partial t$ vanish and if $\nabla\cdot\mathbf{v}=0$ so that $\nabla^2\phi$ vanishes, then (18) becomes simply

$$(\mathbf{A}+\nabla\phi)\cdot\nabla\nabla^2(\nabla\phi\cdot\nabla\phi)=0. \quad (19)$$

This requires that $\nabla\nabla^2(\nabla\phi\cdot\nabla\phi)$ either vanish or be orthogonal to $\mathbf{v}$.

The problem for two-dimensional flow can be conveniently handled by the use of the polar harmonic functions (which are the separable solutions to Laplace's equation)

$$\begin{aligned} C_0&=1 & S_0&=0 \\ C_1&=r\cos\theta & S_1&=r\sin\theta \\ &\cdots & &\cdots \\ C_n&=r^n\cos n\theta & S_n&=r^n\sin n\theta \end{aligned} \quad (20)$$

some of the properties of which are listed in Appendix I. To this set of functions, we may also add

$$\begin{aligned} G_1&=\theta \\ G_2&=\ln r \\ G_3&=\theta\ln r \end{aligned} \quad (21)$$

which are also harmonic functions.

Then, as is shown in Appendix II, the only solutions of (19) of the first type, for which $\nabla\nabla^2(\nabla\phi\cdot\nabla\phi)$ vanishes, are

$$\phi=aC_1+bS_1+cC_2+dS_2. \quad (22)$$

These are the solutions found by Kirstein.[2] They represent flow along trajectories that, depending on the constants, are: (a) straight lines—planar laminar flow; (b) hyperbolas with common asymptotes; (c) ellipses with common eccentricity; (d) parabolas with common focal length; and (e) circles, representing flow around a filamentary cathode, but not around a finite cathode. In each case the space charge is constant throughout the beam.

The orthogonality condition allows one additional solution in two dimensions. If $\nabla\phi$ is a function of r only, however directed, then $\nabla\nabla^2(\nabla\phi\cdot\nabla\phi)$ will have only the $\mathbf{r}$ component. If this functional dependence of $\nabla\phi$ occurs only in the $\boldsymbol{\theta}$ component, then $\nabla\phi$ and hence, from (14) $\mathbf{v}$ will have only a $\boldsymbol{\theta}$ component. Hence the two vectors are orthogonal. The only ϕ's which satisfy these conditions are

$$\phi=-aG_1 \quad (23)$$

and the ϕ obtained by displacing the origin in space (see Appendix I). It may be readily shown that this corresponds to the usual beam around a cathode of radius $(2a/\omega)^{\frac{1}{2}}$. These, as Kirstein has suggested, are the only two-dimensional static solenoidal solutions possible.

IV. TIME-DEPENDENT SOLENOIDAL FLOW

If we again require that $\nabla^2\phi$ vanish, but no longer require the absence of time dependence, then (19) becomes

$$\frac{\partial}{\partial t}\nabla^2(\nabla\phi\cdot\nabla\phi)+(\mathbf{A}+\nabla\phi)\cdot\nabla\nabla^2(\nabla\phi\cdot\nabla\phi)=0. \quad (24)$$

If, now, the second term of this is zero—so that the instantaneous solution at any time is a solution of the static equation—then $\nabla^2(\nabla\phi\cdot\nabla\phi)$ must be a constant independent of time. In the case of solutions of the form of (21), the methods of Appendix I show that this requires only that (c^2+d^2) be independent of time. It can be seen that this allows a completely arbitrary time dependence of the center of the family of trajectories. Their shape and orientation, however, are fixed. This is, of course, a trivial case in a device whose boundary conditions do not permit such a variation. It may be significant in problems involving less rigid boundary conditions such as a pinched beam or the like. It may be a factor in the observed instability of such beams.

A similar instability of the center can be obtained for solutions of the form of (22). Again, it appears trivial except under conditions of loose restraint by the boundaries.

If the second term is not zero then other solutions may be possible. We note that their time dependence is of exponential rather than oscillatory character. Such solutions may be of interest in developing a starting transient. However, we can also show that there is no such solution which has complete cylindrical symmetry. Hence they appear to be of marginal interest. We shall not here consider them further.

V. TIME-DEPENDENT DISTORTION OF SOLENOIDAL FLOW

Let us now consider a flow which is made up of two parts, $\phi=\phi_0+\psi$ of which ϕ_0 is a solenoidal, static solution of the form of (22). For ψ we shall assume the

simplest case leading to nonsolenoidal flow:

$$\nabla^2\psi = f(t)$$

so that ψ is the sum of $\frac{1}{4}fr^2$ and harmonic functions.

If we confine our attention to the first two orders of functions, and let

$$\psi = \tfrac{1}{4}fr^2 + \alpha C_1 + \beta S_1 + \gamma C_2 + \delta S_2 \tag{25}$$

where f, α, β, γ, δ are time-dependent functions, and if we require that

$$c\gamma + d\delta = 0 \tag{26}$$

then we find that

$$\nabla^2(\nabla\psi\cdot\nabla\phi_0) = 0 \tag{27}$$

which simplifies the situation. Then

$$\begin{aligned}\nabla^2(\nabla\phi\cdot\nabla\phi) &= f^2 + (c+\gamma)^2 + (d+\delta)^2 \\ &= f^2 + (c^2+d^2) + (\gamma^2+\delta^2).\end{aligned} \tag{28}$$

Substituting (24) and (28) in (18) (realizing that all space derivatives vanish)

$$f'' + 2ff' + \tfrac{1}{2}f^3 + \tfrac{1}{2}(\omega^2+c^2+d^2)f + \frac{1}{2}\frac{d}{dt}(\gamma^2+\delta^2) + \tfrac{1}{2}f(\gamma^2+\delta^2) = 0. \tag{29}$$

Solutions of the type of (22) can, therefore, be distorted by the addition of a time-dependent function of the form of (25) to the velocity potential, where the time-dependent variables f and $(\gamma^2+\delta^2)$ are related by (29). [The relation between γ and δ are given by (26).] The lack of any conditions on α and β allows them to vary arbitrarily. This can be seen to correspond to an arbitrary motion of the center of the beam such as we have already noted in Sec. IV.

If, now, δ and γ are zero, then (29) simply determines the form of $f(t)$. If f is small, (29) is seen to have an oscillatory behavior at the frequency $\omega\{\frac{1}{2}+\frac{1}{2}(c^2+d^2)/\omega^2\}^{\frac{1}{2}}$. If f is not small, the nonlinear terms of (29) distort this somewhat, leading to the addition of terms that are the higher harmonics of this frequency. We shall discuss in some detail later the physical interpretation of this solution.

If γ and δ are not zero, then they vary in a nonlinear oscillatory manner that is coupled to f with fundamental frequency half that of f (which, however, need no longer be exactly that given above). This represents a periodic variation of the character of the beam. If, for example, $c=d=0$, and the beam is terminated on an outer trajectory, so that the static beam corresponds to a cylindrical magnetron with filamentary cathode, then an oscillation of γ and δ represents the periodic appearance of "bumps" on the periphery of the beam. At a given instant, the beam is distorted into an ellipse oriented along, say the x axis (the orientation in general depends on the relative weight of γ and δ). The ellipse then collapses back into a circle and, a half-cycle after the first instant, reappears, but now oriented along the y axis. Coupled with this, as mentioned, is an f dependence which represents a "breathing" of the beam as a whole.

It may be questioned whether such solutions are actually possible since (29) relates a function $(\gamma^2+\delta^2)$ which must be positive, to an involved function of f. However, we can write a general solution to (29) as

$$\gamma^2+\delta^2 = \epsilon^{-s(t)}\left[C - \int_0^t H(\tau)\epsilon^{-s(\tau)}d\tau\right] \tag{30}$$

where

$$s(t) = \int_0^t f(\tau)d\tau$$

$$H(t) = 2f'' + 4ff' + f^3 + (\omega^2+c^2+d^2)f$$

and C is an arbitrary constant.

If f is periodic, so is the integral. A lower bound of C therefore exists such that any larger C results in $(\gamma^2+\delta^2)$ being never negative. Hence, for f any periodic function, there exists a class of possible solutions for γ and δ.

One is tempted, now, to proceed with other forms of ψ which contain the higher harmonic functions. While such solutions almost certainly exist, they are difficult to handle. The analog of (29) then contains terms in the various powers of r and with various θ dependencies, thus leading to a set of simultaneous equations, for the various components. The situation thus becomes much more difficult than the case considered above.

If we attempt to apply the same method to the static solution of (23), we also run into difficulty in that the r dependence does not disappear. There is no possible time distortion of this type for solenoidal flow around a finite cathode.

VI. TIME-DEPENDENT DISTORTION OF TIME-VARIANT SOLENOIDAL FLOW

We do obtain a possible disturbance of the solenoidal flow about a finite cathode if we let ϕ have the form of (23), but with $a=\alpha(t)$, a function of time, so that we combine a time-dependent solenoidal solution with a nonsolenoidal disturbance of the form considered above.

We then still have

$$\nabla^2(\nabla\phi\cdot\nabla\phi) = f^2 + 4\alpha^2/r^4. \tag{31}$$

Equation (18) now yields

$$f'' + 2ff' + \tfrac{1}{2}f^3 + \tfrac{1}{2}\omega^2 f + \frac{2}{r^4}\left(\frac{d\alpha^2}{dt} - \alpha^2 f\right) = 0. \tag{32}$$

Equating the coefficients independently to zero

$$\frac{d\alpha^2}{dt} - \alpha^2 f = 0 \tag{33}$$

and

$$f'' + 2ff' + \tfrac{1}{2}f^3 + \tfrac{1}{2}\omega^2 f = 0. \tag{34}$$

The appropriate solution of (34) may be substituted into (33) and the latter solved for $\alpha(t)$.

This time-dependent solution generates an oscillation of the effective cathode radius according to (33), but is otherwise consistent with normal boundary conditions.

VII. PHYSICAL INTERPRETATION

We may now ask whether these time-dependent solutions do appear in any device. We may consider several situations as follows.

(a) Smooth Bore Cylindrical Magnetron with Filamentary Cathode

One case of particular interest is that of Eq. (29) when the static solution corresponds to (22) with $c=d=0$. The boundary conditions then correspond to a cylindrical magnetron with a filamentary cathode. These boundary conditions are not upset by the time dependence of (29). Equation (29) therefore indicates the possibility of a nonharmonic oscillation whose fundamental is at $\omega/\sqrt{2}$.

This oscillation, being wholly contained within a unipotential boundary will not of itself couple to the boundary. Hence it will neither be driven by the applied power, nor coupled to any detector outside the beam.

If, however, we superimpose on the conditions considered a z-axis distortion then we might expect to obtain effective coupling both to the power source and to a load. If this coupling is properly phased, we should then expect these oscillations to occur and to be detectable as a signal between the anode and cathode which are also the terminals of the power source.

Alternatively, the coupling might be obtained through the γ and δ terms of (29), arising as a result of a slight asymmetry either within the tube, or in the magnetic field.

Given the proper magnitude and phase of the coupling, there does not appear to be any condition present that would lead to a sharp start-oscillation requirement. We would expect that the power obtained from the mode would be proportional to the power coupled into it. The latter might well fall off rapidly with current so that the signal obtained would disappear into the noise level, but without the sharp cutoff characteristic normally found in magnetrons and other devices which use different coupling mechanisms for the source-to-mode and mode-to-output transduction.

Oscillations with precisely these characteristics have, in fact, been observed by Hill and Olson[6] using a smooth bore magnetron made part of a coaxial line. Qualitative agreement of their observations with this theory (and quantitative in so far as the fundamental frequency is concerned) is very good. Since the performance they found does not fit the usual magnetron mechanism, this agreement appears to be significant.

(b) General Magnetron with Filamentary Cathode

The more general disturbance of (29) may correspond to an oscillation of a magnetron with filamentary cathode in the $N=2$ mode. The coupling considerations of the previous section do not apply here because we no longer have the space charge enclosed in a unipotential envelope, so that Gauss' theorem does not apply. Such an oscillation will, in fact, couple to the anode segments in the $N=2$ mode.

This is not to say that this beam is the full description of the $N=2$ mode of a conventional magnetron. It is not, in fact, since it implies an incorrect frequency. It simply says that it is one possible state of the beam. We may, in fact, suggest that the possibility of such states, either as competitive oscillations or as damping mechanisms, may be an additional reason against the use of a filamentary cathode. The collapse of such modes as the cathode diameter is increased may have an important bearing on the successful operation of practical magnetrons.

(c) Cylindrical Magnetron with Finite Cathode

The radial oscillatory mechanism at $\omega/\sqrt{2}$ cited above would not apply directly to a tube with a finite cathode since, in this case, its boundary conditions require an oscillating cathodic potential surface. It is probably significant that efforts by Hill and Olson to extend their observations to such tubes were unsuccessful.

However, we may suggest that the time-dependent effect described by Eqs. (33) and (34) is significant in the "efficiency valley" effect in "rising-sun" magnetrons. This effect is generally interpreted as the effect of interaction between the zero harmonic contamination of the π space harmonic (which is always present in a "rising-sun" type anode) and a cyclotronic electron motion. It has been observed, however,[7] that the minimum efficiency occurs at a higher magnetic field than this would indicate. The available data, in fact, indicate that it involves a broad spectrum interaction centered, not at ω, but at some value closer to $\omega/\sqrt{2}$.

The velocity field indicated by (33) and (34) involves principally a time variation of the angular velocity in a manner dependent only on r and not on θ. Hence it would, in fact, couple to a zero-harmonic contamination.

Since the variation of α, which requires variation of the radius of the zero potential surface, would, during part of its cycle, drive electrons back into the cathode, the energy coupled into the mode through the zero-harmonic contamination would be transferred ultimately to the cathode.

[6] R. M. Hill and F. A. Olson, "Electronically tunable microwave oscillations and detection and mixing properties of a coaxial magnetron," Sylvania Microwave Physics Laboratory, Tech. Rept. No. MPL-7 (June 30, 1957). See also, reports on Signal Corps Contracts DA 36-039-sc-71053 and DA 36-039-sc-73188.

[7] G. B. Collins, *Microwave Magnetron* (McGraw-Hill Book Company, Inc., New York, 1948), Vol. 6, Radiation Laboratory Series, pp. 437–439.

The observed effect, therefore, appears to be in qualitative agreement with the theory.

We may also suggest that the type of behavior indicated by Eq. (30) could indicate a transient instability. It may be of significance in the generation of noise in such devices.

(d) Beam Type Tubes

Additional possibilities are present in beam type tubes where the physical surface of the cathode is no longer in direct contact with the bottom of the beam. In this case the oscillations indicated by (33) and (34) are no longer damped out. As in the filamentary case, such oscillations would not be coupled to the structure expect through a z-axis distortion. Although such distortion is always present, it is generally introduced from the negative voltage side (through the "end hats") and hence will load down the mode, rather than driving it. In consequence such oscillations are not "per se" an immediate problem. One may suspect, however, that, under suitable conditions, they will couple effectively to the energy in the growing wave, and will therefore contribute both to noise and to the generation of "spurious" sidebands on the operating frequency.

While we cannot in this case, point to specific correlation with experimental observation, there nevertheless appears to be sufficient possibility of significance in this area to justify further consideration.

VIII. SUMMARY

We have undertaken the analysis of single streaming self-consistent time-dependent electron beams. Our general analysis is valid for three-dimensional flow in the presence of a magnetic field that may or may not be uniform and that may, conceivably, be itself time-dependent. In the case of a constant magnetic field, we have been able to write a single vector equation that any such (nonrelativistic) beam must satisfy.

We have then specialized this equation in various ways so as to obtain some time-dependent solutions which are of interest under crossed-field conditions—that is, where the flow is confined to one plane and the magnetic field is uniform and constant and transverse to this plane.

Finally, we have discussed in a qualitative manner the possible significance of these solutions in existing devices. We have been able to suggest that the modes found here may be significant in accounting for some of the anomolous behavior of magnetrons and other devices. The theory also offers a mechanism for the operation observed in a new type of smooth bore coaxial magnetron which has several properties which do not appear to fit conventional magnetron theory.

APPENDIX I: PROPERTIES OF THE POLAR HARMONIC FUNCTIONS

The functions of (20) have several properties that make them useful for this investigation. We will simply tabulate these properties since, in each case, they may be verified directly from the functions themselves.

The defining relation for a "harmonic" function is that

$$\nabla^2 C_n = \nabla^2 S_n = 0.$$

If $n > m$, the product of the divergences of two such functions is

$$\nabla C_n \cdot \nabla C_m = \nabla S_n \cdot \nabla S_m = nmr^{2(m-1)} C_{n-m}$$
$$\nabla S_n \cdot \nabla C_m = -\nabla C_n \cdot \nabla S_m = nmr^{2(m-1)} S_{n-m}.$$

These, it will be noted, become particularly simple if either $n = m$ or $m = 1$.

The Laplacian of these quantities is also simple

$$\nabla^2(\nabla C_n \cdot \nabla C_m) = \nabla^2(\nabla S_n \cdot \nabla S_m) = 4(m-1)(n-1)r^{2(m-2)} C_{n-m}$$
$$\nabla^2(\nabla S_n \cdot \nabla C_m) = -\nabla^2(\nabla C_n \cdot \nabla S_m) = 4(m-1)(n-1)r^{2(m-2)} S_{n-m}.$$

We are also interested in the product of the divergence of S_n or C_n times a vector whose magnitude is proportional to r. We find that

$$r\mathbf{r} \cdot \nabla C_n = nC_n$$
$$r\mathbf{r} \cdot \nabla S_n = nS_n$$
$$r\boldsymbol{\theta} \cdot \nabla C_n = -nS_n$$
$$r\boldsymbol{\theta} \cdot \nabla S_n = nC_n$$

so that the Laplacian of all these terms vanish.

These relations are useful in the manipulation of functions of the types discussed in the paper.

Of minor interest also (principally in Appendix II) are the following relations:

$$\nabla^2(\nabla G_1 \cdot \nabla C_n) = 4n(n-1)r^{-4} S_n$$
$$\nabla^2(\nabla G_1 \cdot \nabla S_n) = -4n(n-1)r^{-4} C_n$$
$$\nabla^2(\nabla G_2 \cdot \nabla C_n) = -4n(n-1)r^{-4} C_n$$
$$\nabla^2(\nabla G_2 \cdot \nabla S_n) = -4n(n-1)r^{-4} S_n$$
$$\nabla^2(\nabla G_3 \cdot \nabla C_n) = 4n(n-1)r^{-4}(-G_1 C_n + G_2 S_n - S_n)$$
$$\nabla^2(\nabla G_3 \cdot \nabla S_n) = 4n(n-1)r^{-4}(-G_1 S_n - G_2 C_n + C_n).$$

APPENDIX II: POSSIBLE SOLUTIONS OF THE STATIC SOLENOIDAL CASE

We have seen that the solution of the static solenoidal case depends on the solution of (19). Two types of solutions are possible—those in which $\nabla^2(\nabla\phi \cdot \nabla\phi)$ is constant and those where $\nabla\nabla^2(\nabla\phi \cdot \nabla\phi)$ is orthogonal to v. Kirstein has given these solutions in two dimensions. However, he does not prove that they are the only possible solutions (although it seems likely from his equation), nor does he draw a clear distinction between the two types. Furthermore, the proof is of interest in its own right as providing insight into the physical reasons why these are the only solutions.

Any static two-dimensional solenoidal solution can be written

$$\phi = aG_1 + bG_2 + cG_3 + \sum h_n C_n + \sum k_n S_n.$$

We now ask what is the nature of $\nabla^2(\nabla\phi \cdot \nabla\phi)$. It will be seen from the relations of Appendix I that the only combinations for which the Laplacian either vanishes or is constant are those involving C_1, S_1, C_2, S_2. (Cross products of, for example C_n and S_n may vanish, but the diagonal terms do not for $n>2$.) Furthermore, since this functional relation is clearly a positive definite one, there is no possibility of the higher functional relations cancelling out. Consequently, the most general form of the first type of solution in two dimensions is that given by (22).

For the second type of solution, we note, by similar arguments, although the form becomes much more elaborate, that ϕ cannot contain any C_n or S_n with $n>2$.

A similar argument applies if ϕ contains G_2 or G_3. So ϕ can contain only G_1, S_1, C_1, S_2, and C_2. But we also see that the cross terms of the G's and S_n or C_n involve factors in $(n-1)r^{-4}$ which do not vanish unless $n=1$. Hence ϕ can contain only G_1, S_1 and C_1, which is the solution indicated.

Hence the given solutions are, in fact, the only two-dimensional static solenoidal solutions possible.

JOURNAL OF APPLIED PHYSICS VOLUME 31, NUMBER 1 JANUARY, 1960

Formation of Cesium Antimonide. I. Electrical Resistivity of the Film of Cesium-Antimony System

KIYOSHI MIYAKE
Electrical Communication Laboratory, Nippon Telegraph and Telephone Public Corporation, Tokyo, Japan
(Received June 24, 1959)

The films of Cs-Sb alloys whose compositions were determined by the weighing method, were prepared at the temperature ranged from 70°C to 100°C. The electrical resistance and its temperature dependency of the samples, of which atomic ratio of Cs to Sb was ranged from 0.91 to 4.86, were measured. The reproducibility of electrical resistance was obtained for all the samples, except for $Cs_{3.26}Sb$, and the temperature coefficients of resistance of the samples, except for $Cs_{0.91}Sb$, were all negative. It was found that three compounds, CsSb, Cs_3Sb_2, and Cs_2Sb in addition to Cs_3Sb, having a remarkably high resistance, could be formed. The observed values of the electrical resistivity at 0°C and the thermal activation energy associated with conductivity were 1.84×10^3 ohm-cm, 0.61 ev for $Cs_{1.02}Sb$; 1.82×10^3 ohm-cm, 0.76 ev for $Cs_{3.03}Sb_2$; 2.85×10^3 ohm-cm, 0.62 ev for $Cs_{2.02}Sb$; and 1.95×10^3 ohm-cm, 0.77 ev for $Cs_{3.33}Sb$. The alloys with atomic ratio above 4 looked gold in reflected light, and those with atomic ratio above 5 were not formed.

INTRODUCTION

MANY investigations of the cesium-antimony film with a remarkable photosensitivity have been carried on since Görlich's development[1]; it was found by several investigators, Lukýanov and Mazover,[2] Zaitev,[3] Sommer,[4] Khlebnikov,[5] and Miyazawa,[6] that the composition of the material with the highest photoelectric response corresponded to the formula Cs_3Sb. However, there are some discrepancies in the reported values of its electrical conductivity and thermal activation energy associated with conductivity, even in the values reported recently by Harper and Choyke[7] and Wallis.[8] Indeed, it is very difficult to prepare the samples of Cs_3Sb having definite character, and the reasons why they do not exhibit definite character in the measurements of their electrical properties are supposed to be as follows. (i) The reaction rate of cesium on antimony is too fast because of high preparation temperature (usually 150°C); (ii) the photoresponse of a cathode with thick film shows a round maximum in the final stage of its formation process, consequently, the films prepared by usual method have not always a definite composition; (iii) a material containing a larger amount of cesium than Cs_2Sb may be formed; (iv) when a film of Cs_2Sb is exposed to light, the magnitude of resistance is changed[7,9]; (v) the resistance of the films with a composition near Cs_3Sb depends on the current passing through them; (vi) the inhomogeneity in the composition of film in the direction normal to its surface, which is caused by the incomplete reaction of cesium on a thick antimony film; (vii) the nonuniformity of film thickness, which gives rise to the nonuniform composition of the film.

Schaetti and Baumgartner[10] investigated the spectral

[1] P. Görlich, Z. Physik **101**, 335 (1936).
[2] S. Y. Lukýanov and I. S. Mazover, Zhur. Eksptl. i Teoret. Fiz. **9**, 1459 (1939).
[3] N. S. Zaitev, Zhur. Tekh. Fiz. **9**, 661 (1939).
[4] A. Sommer, Proc. Phys. Soc. (London) **55**, 145 (1943).
[5] N. S. Khlebnikov, Zhur. Tech. Fiz. **17**, 333 (1947).
[6] H. Miyazawa *et al.*, J. Phys. Soc. Japan **7**, 647 (1952).
[7] W. J. Harper and W. J. Choyke, J. Appl. Phys. **27**, 1358 (1957).
[8] G. Wallis, Ann. Physik **17**, 401 (1956).
[9] W. Widmaier and R. W. Engstrom, RCA Rev. **16**, 109 (1955).
[10] N. Schaetti and W. Baumgartner, Helv. Phys. Acta **24**, 614 (1951).

photoresponse, electrical resistance, and those temperature dependencies of cesium antimony photocathode, and they classified the cathodes in four groups according to their characters. The fact that even the photocathodes, prepared by the same procedure, had different characters, has shown the difficulty of preparation of Cs_3Sb. We have experimented on the formation of Cs_3Sb under low constant cesium vapor pressure in order to obtain films having nearly stoichiometric composition, and found that the film with definite character could be obtained by stopping the reaction of cesium on sputtered antimony film when their electrical resistances attained to second maximum on the formation curve.[11]

At that time, however, we had no available data to interpret the phenomena mentioned above, and no information on the possibility of formation of the materials with the atomic ratio of cesium to antimony larger than three, except for Sommer's experiment. This work, therefore, was carried out in connection with the experiment of the formation of Cs_3Sb. It is the purpose of this paper to obtain information on the electrical resistivity and the thermal activation energy associated with conductivity of the cesium antimony system over an extended range of composition. Thus, in this work we adopted the simplest type of tube to avoid the inaccuracy mentioned previously in the composition of samples, and measured only their electrical properties.

EXPERIMENTAL ARRANGEMENTS

(a) Experimental Tube

It was necessary for maintaining the uniformity in the composition of sample during its formation process that the sputtered antimony film be uniform in thickness. Then, the sample used was prepared on a small square glass plate which corresponded to a very small part of spherical surface. Figure 1 (a) shows the used test tube. Antimony was evaporated with a tungsten filament W in the center of the spherical borosilicate glass envelope (5 cm or 7 cm in diam), and the electrical resistance of the film deposited on a square plate A was measured. Glass plate A [Fig. 1 (b)] has platinium foil leads P burned-in its two opposite edges, which were platinized over to obtain a good contact with the film to be deposited.

Preliminary tests were carried out, using four tubes with an opening of different type [cf., N in Fig. 1 (a)], in order to check whether a simultaneous reaction of cesium on antimony film takes place on all its surface. Then, the best result was obtained with a tube having the most simple type opening as shown in Fig. 1 (a). The tubes of large diameter were used for the samples whose atomic ratio was less than three to diminish the error in the thickness of the film due to the geometrical inaccuracy of spherical envelope and position of filament.

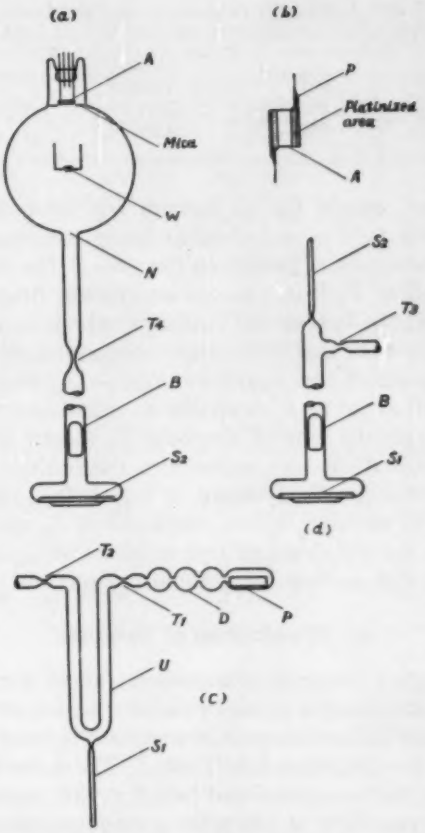

FIG. 1. Tubes used to prepare the samples and metallic cesium. (a) Test tube. (b) Glass plate on which the sample is prepared. (c) U-shaped trap used to prepare a glass ampoule containing metallic cesium. (d) T-shaped tube with a glass ampoule to be tipped off. The ampoule is shielded in the bottom of side tube of the test tube.

(b) Preparation of Metallic Cesium

Metallic cesium was made by reducing cesium chromate (guaranteed grade made by Kanto Chemical Company) with 99.99% silicon powder. Figure 1 (c) shows a U-shaped trap tube with an appendage, which is used to prepare a metallic cesium glass ampoule. The whole tube was evacuated and baked at 400°C for two hours, and trap U with ampoule was heated again by gas flame to secure outgassing. Reduced metallic cesium was distilled through condensing chambers D and trapped into U cooled by liquid nitrogen; then the appendage and the tube U containing metallic cesium were tipped off at T_1 and T_2 separately. The cesium in the U tube was evaporated by heating with gas flame and stored in ampoule S_1, and then it was tipped off at the bottom of U tube. The ampoule S_1 containing metallic cesium was weighed by a micro-balance and sealed into the end of T tube as shown in Fig. 1(d). The T tube was evacuated and baked at 350°C for three hours in an electric oven; then it was heated again by

[11] To be published in J. Appl. Phys.

TABLE I. Impurity contents in used antimony.

As	0.0007%
Cu	0.0002%
Fe	0.0004%
Pb	0.0003%

gas flame, except for its bottom end containing S_1, which was held at a somewhat lower temperature to avoid the attack of cesium on the glass.[12] The tube was tipped off at T_3 from evacuation system. Ampoule S_1 located in the bottom of T tube, was broken by dropping a glass-encased iron weight on it; released cesium was evaporated and stored in ampoule S_2, and S_2 was tipped off at its neck. Ampoule S_2 containing metallic cesium and the tips of ampoule S_1 (about 250 mg) were weighed; S_2 was sealed into the bottom of side tube of the test tube shown in Fig. 1 (a). The total amount of metallic cesium contained in S_2 was calculated as the difference of two weighing values of ampoule S_1 with cesium and without cesium.

(c) Preparation of Samples

A weighed fragment of antimony (about 5 mg) was fixed in the filament in the center of spherical envelope. The purity of antimony used was 99.99%, and its impurities were tabulated in Table I. The tube with its side arm was evacuated and baked at the temperature ranged from 300°C to 350°C for three hours, after which the side arm was heated again by gas flame. Then, antimony was evaporated from the filament; its evaporation rate was ranged from 0.01 to 0.002 mg per cm^2 per min to obtain a film of uniform thickness.[13] The structure of evaporated film of antimony has been studied by many investigators and it has been reported that the films thinner than 200 A are amorphous, and the films thicker than 200 A are recrystalized at room temperature.[14–17] We used, therefore, the films with about 500 A in thickness.

The initial resistance between two leads on glass plate was about ten ohms; the effective dimension of films was 10 mm in width and 4 mm in length. The film thickness of each sample was calculated from the weight of evaporated antimony and the dimension of spherical envelope, assuming that the resistivity of antimony in bulk is the same as that of an evaporated film.

After antimony was evaporated, the tube was tipped off from the evacuation system in a vacuum better than 3×10^{-8} mm Hg. Then, glass ampoule S_2 was broken by dropping a glass-encased iron weight on it; released cesium was evaporated and condensed near neck T_4 [Fig. 1(a)], and the lower part of side arm below T_4 was tipped off. The loss in the amount of cesium due to tip-off was estimated from repeating the weighing of glass ampoules with and without cesium; the mean loss in the weight of cesium for ten ampoules was 0.1 mg. The sensitivity of the micro-balance used was 10 micrograms.

The test tube with its side arm containing cesium, was heated and maintained at a definite temperature in an electric furnace. Although the character of samples is independent of the preparation temperature, the materials, whose atomic ratio are larger than 1.5, are decomposed by heating above 100°C.[18] The preparation of samples, therefore, was carried out at the temperature range of 70°C to 100°C; in some cases the temperature was risen to 130°C at the final stage of preparation in order to secure the completion of reaction. The both ends of the electric furnace used were enclosed, and so the maximum deviation in the temperature distribution along the spherical part of tube could be less than 0.5°C.

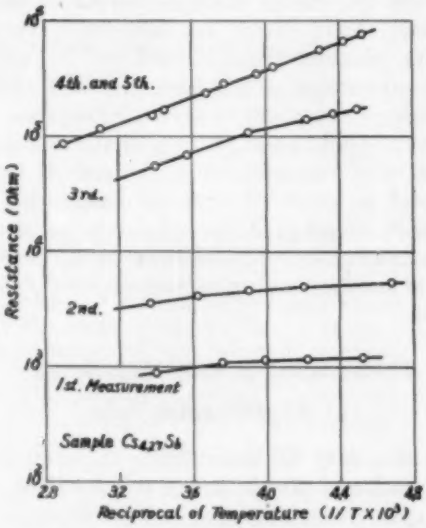

FIG. 2. Changes in the electrical resistance and its temperature dependency of the sample $Cs_{4.27}Sb$ produced by the reaction of cesium on antimony.

(d) Measurement of Electrical Resistivity

The electrical resistance of the specimen on glass plate A was measured by using a potentiometer, and its resistivity was calculated from the known thickness of the film. Generally the electrical resistance of most specimens is reduced by exposing them to light, remarkably for the specimens near Cs_3Sb. The measurement of resistance, therefore, was carried out after the

[12] J. B. Taylor and I. Langmuir, Phys. Rev. **51**, 753 (1937).
[13] R. B. Jones and A. M. Glover (to RCA) U. S. 2,401,735, June 11, 1946. The evaporation rate adopted by us was very much slower than that adopted by Jones and Glover.
[14] W. Latmer, Helv. Phys. Acta **18**, 232 (1945).
[15] A. I. Frimer, Doklady Akad. Nauk. (S.S.S.R.) **63**, 255 (1948).
[16] A. Götzberger, Z. Physik **142**, 182 (1955).
[17] L. T. Tatarinova, Trudy Inst. Krist. Akad. S.S.S.R. **11**, 104 (1955).
[18] According to our investigations on the thermal dissociation of Cs_3Sb, this phenomenon occurs appreciably at temperatures above 100°C.

tube had been stored in a copper cylinder placed in a Dewar vessel for sixteen hours or more.

The resistance and its temperature dependency of specimen were observed during the formation process, because it is a measure to deduce the end of the reaction of cesium on antimony film whether by further heating the electrical properties were changed or not. Furthermore, the electrical properties of specimens that attained a definite character were measured again after several months to see whether any change in their character was produced or not (cf. Fig. 2).

The measurement of electrical resistivity was carried out at the temperature range of 70° to −70°, considering that the samples would be decomposed at higher temperatures and that it was difficult to prevent a small leakage current at lower temperatures owing to the simple structure of the experimental tube.

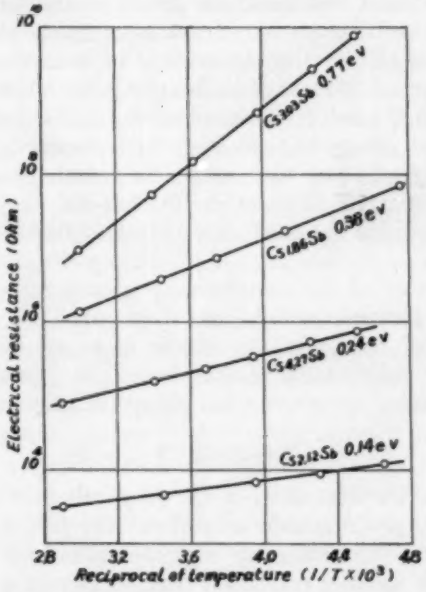

FIG. 3. Electrical resistance as a function of temperature for four samples with definite composition.

The voltage applied between the two leads of samples was usually 1.5 v. For three samples, however, with the composition, $Cs_{2.67}Sb$, $Cs_{2.76}Sb$, and $Cs_{3.30}Sb$, the applied voltage was lowered below 0.3 v to reduce a drift in their resistivities in the vicinity of room temperature, but it was still difficult to measure them without drift. The mean cooling rate of samples on the measurement of the temperature dependency of resistance was about 0.2°C per minute. Thus, the electrical resistance and its temperature dependency of all the samples in the experiment were reproducible except for those of $Cs_{3.30}Sb$.

RESULTS

Figure 3 shows the relations between the logarithm of electrical resistance and the reciprocal of absolute temperature on four samples. The electrical resistivity

TABLE II. Data for the electrical resistivity and thermal activation energy of used samples.

Composition of sample, Cs/Sb (atomic ratio)	Thickness of film (A)	Electrical resistivity (ohm-cm)	Thermal activation energy (ev)
0.91	584	9.27×10^{-6}	0
1.02	507	1.84×10^{3}	0.61
1.46	527	9.27×10^{2}	0.56
1.51	403	1.82×10^{3}	0.76
1.86	517	8.27×10	0.38
1.92	443	1.16×10^{3}	0.42
2.02	544	2.85×10^{3}	0.62
2.05	558	9.35×10^{2}	0.52
2.12	570	7.99×10^{-2}	0.14
2.24	532	1.10×10	0.17
2.67	551	2.34×10	0.66
2.75	511	3.83×10	0.68
3.03	431	1.95×10^{3}	0.77
3.14	540	2.05×10^{2}	0.71
3.30	549	8.24×10	0.57
4.04	551	3.30×10	0.29
4.27	532	2.93×10	0.24
4.86	416	5.41×10^{-2}	0.08

at 0°C and the thermal activation energy of all the samples were tabulated in Table II. Figure 4 shows the relation between the electrical resistivity at 0°C and the composition denoted with the atomic ratio of cesium to antimony. Figure 5 shows the relation of the thermal activation energy to the composition denoted with the same unit.

Samples with the atomic ratio 0.91 to 4.86 were used, and their temperature coefficients of resistance were negative, except for the sample with atomic ratio 0.91,

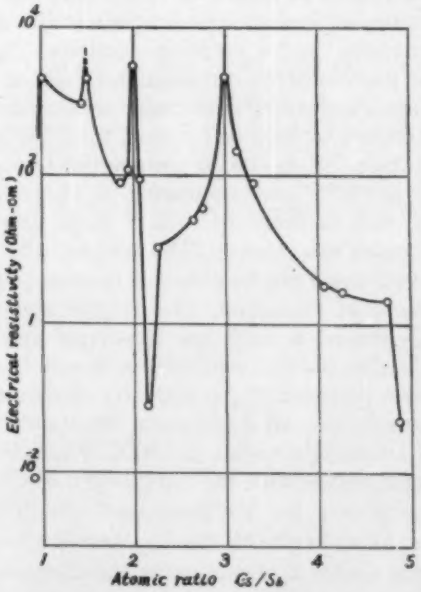

FIG. 4. Relation between the electrical resistivity at 0°C and the composition denoted by the atomic ratio of cesium to antimony. The resistivity of Cs_3Sb_2 is expected to be higher than that shown in this figure, considering the results of another experiment on the thermal decomposition of Cs_3Sb.

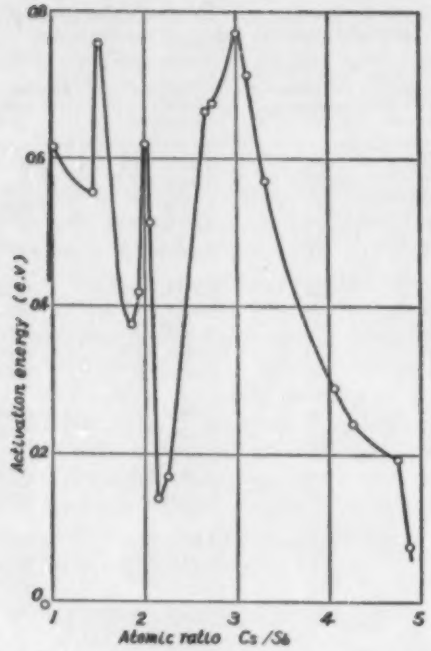

FIG. 5. Relation between the thermal activation energy associated with conductivity and the composition denoted by the atomic ratio of cesium to antimony.

of which the temperature coefficient of resistance is slightly positive. Comparing the sample of atomic ratio 0.91 with that of atomic ratio 1.02, the former had an extremely low resistivity, about 10^{-3} ohm-cm, while the latter had a very high resistivity, above 10^{3} ohm-cm, though there was no difference in the color of films by transmitted light. It should be noted that the former, whose content of cesium was deficient in the stoichiometric quantity, had a metallic character; the latter with near stoichiometric composition exhibited a character of semiconductor. The sample with atomic ratio 4.86 was formed by heating for more than 100 hours at a temperature 70° to 100°C; when the temperature was risen to 130°C after measuring its electrical characters, it was decomposed and a large amount of metallic cesium was released. The samples with atomic ratio above 5 could not be obtained because of melting in the course of formation. The sample with atomic ratio 2.12 showed a very low resistivity and had a small activation energy, compared with other samples.

Miyazawa prepared Cs_3Sb with the effusion method and measured the total electrical resistance of the sample of intermediate state at 150°C. Then, he found that the compounds with the composition of CsSb and Cs_3Sb were present, but the presence of Cs_3Sb_2 was not conclusive. According to his results, there is a minimum value of the electrical resistance at the composition of Cs_2Sb, but our result showed that a maximum value of the resistance was obtained at the same composition. Thus, Fig. 4 suggests the presence of the compounds of Cs_3Sb_2 and Cs_2Sb as well as CsSb and Cs_3Sb. Moreover, it was shown that the materials with a composition of atomic ratio above 3 were formed by prolonged heating, although the presence of such materials was not confirmed in Sommer's experiment. The resistance of Cs_3Sb_2 was remarkably higher than that of the samples near Cs_3Sb_2 and the activation energy of Cs_3Sb_2 was rather large, but those of the materials between CsSb and Cs_3Sb_2 had only a small variation in the magnitude.

The values of electrical resistivity of Cs_3Sb have been reported in a few papers and those values at room temperature were generally below 100 ohm-cm, except for Wallis's values. The resistivity of our sample with $Cs_{3.03}Sb$ was about 10^3 ohm-cm, and its thermal activation energy associated with conductivity was 0.77 ev, which corresponded to the values of Morgulis and Djatlowitzkaja[19] or Shuze *et al.*[20]

Wallis showed that the compositions of the sample at the maximum and minimum points on the formation curve, which showed the relation between the electrical resistance of film and the amount of reacted cesium, corresponded to those of CsSb and Cs_3Sb, respectively. Although the values of the resistivity and the thermal activation energy of CsSb and Cs_3Sb obtained by him were dispersed over some range, the resistivity of CsSb ranged from 10^3 ohm-cm to 10^4 ohm-cm, and agreed with the value obtained by us—1.84×10^3 ohm-cm for $Cs_{1.02}Sb$.

The color of the samples with atomic ratio above 2.67 by transmitted light was deep red. Then, as the content of cesium in the sample increased over this ratio, the color of film became deeper red. The samples with atomic ratio above 4 looked gold in reflected light.

DISCUSSION

One of the difficulties in the preparation of cesium antimony photocathode arises from the possibility of the formation of materials with atomic ratio above 3. Although Sommer concluded that no further reaction of cesium on Cs_3Sb occurred, it is evident, as shown in this experiment, that such materials can be obtained by prolonged heating even at a rather low temperature; for example, the sample with $Cs_{3.30}Sb$ was obtained by heating at 70°C for 70 hours. Therefore, it will not always be impossible that a material containing more cesium than Cs_3Sb is formed by heating for a comparatively short time at a usual preparation temperature, about 150°C.

By a usual method, there is a possibility that the samples would have a composition in a state arising from an equilibrium of the formation and decomposition of Cs_2Sb, in which case the composition of samples would not always attain Cs_3Sb, and would have a low resistivity and a small activation energy.

In all the compositions except for $Cs_{0.91}Sb$, the elec-

[19] N. D. Morgulis and B. T. Djatlowitzkaja, Izvest. Akad. Nauk. S.S.S.R. 12, 126 (1948).
[20] Shuze, Motzchan, and Ryvkin, Zhur. Tekh. Fiz. 18, 1494 (1948).

trical resistivity of samples was larger than that of both components and its temperature coefficient was negative. Then it was found that four compounds with stoichiometric composition—CsSb, Cs_3Sb_2, Cs_2Sb, and Cs_3Sb—were present as in the case of the cesium bismuth system.[21] The electrical resistivity and its activation energy associated with conductivity of the compounds having near stoichiometric composition were 1.84×10^3 ohm-cm, 0.61 ev for $Cs_{1.02}Sb$; 1.82×10^3 ohm-cm, 0.76 ev for $Cs_{3.02}Sb_2$; 2.85×10^3 ohm-cm, 0.62 ev for $Cs_{2.02}Sb$; and 1.95×10^3 ohm-cm, 0.77 ev for $Cs_{3.03}Sb$.

It is supposed that the electrical conductivity of these compounds is a result of the presence of impurity levels arising from the stoichiometric excess or deficiency of cesium atoms, and the thermal activation energy associated with conductivity represents the energy difference between the impurity level and filled band or conduction band. In fact, Wright[22] and Sakata[23,24] ascribed the conductivity of Cs_3Sb to the presence of an acceptor level, and Lukýanov and Mazover[2] to that of a donor level. According to our other experiments,[11] the photoresponse of cesium antimony film reached to a maximum just after the electrical resistance had passed through the maximum due to the formation of Cs_3Sb; in other words, cesium antimony film containing an excess of cesium showed a maximum photoresponse.

Provided that a material in an intermediate state consists of a layer of stoichiometric compound and another layer whose content of cesium is very excessive or deficient as compared with the compound, and the latter has a high conductivity and a small activation energy associated with conductivity, the electrical conductivity of the material at low temperatures may be characterized by the latter. Then, a small activation energy of Cs_3Sb at low temperatures, observed by a few investigators, may be a result of an impurity level produced by the presence of such a layer within specimens used by them. The activation energy of Cs_3Sb at low temperatures obtained by Suhrmann and Kangro[25] or Schaetti and Baumgartner[10] was about 0.15 ev and agreed with that of our sample $Cs_{2.12}Sb$.

The electrical resistance of the film $Cs_{0.91}Sb$ showed a metallic character. This suggests that the film consists of a thick CsSb layer with high resistivity and a thin layer of nonreacted antimony or dilute cesium-antimony alloy. Assuming that the thickness of the metallic layer is of the order of ten percent of the film, about 50 A, which is deduced from the atomic ratio of the sample, and neglecting the effect of CsSb layer because of its high resistivity, the calculated value of electrical resistivity of the metallic layer becomes 8×10^{-4} ohm-cm.

Thus, when the amount of cesium is insufficient to form CsSb, it seems that the reaction of cesium on antimony is stopped and a nonreacted antimony or dilute cesium-antimony alloy layer is left. This fact suggests a model for the mechanism of the reaction of cesium in vapor phase on solid antimony. In this work, it might be desirable to obtain the relation between composition and characteristics of optical absorption of the samples, and also to determine their crystal structure by x-ray crystal analysis. However, considerable changes in the shape of the glass envelope to be used were required to reduce a high background intensity in x-ray crystal analysis,[26,27] or to measure the optical property of the samples. Therefore, we gave up such studies.

[21] W. Klemnn, Angew. Chem. **66**, 148 (1954).
[22] D. A. Wright, *Semiconductors* (John Wiley & Sons, Inc., New York, 1955), second edition, p. 129.
[23] T. Sakata, J. Phys. Soc. Japan **8**, 125, 723, 793 (1953).
[24] T. Sakata and S. Munesue, J. Phys. Soc. Japan **9**, 141 (1954).
[25] R. Suhrmann and C. Kangro, Naturwissenschaften **40**, 137 (1953).
[26] K. H. Jack and M. M. Wachtel, Proc. Roy. Soc. (London) **A239**, 46 (1957).
[27] Private communication from M. Owaki. He has made an experiment to determine crystal structure of Cs_3Sb films by x-ray crystal analysis, and found that a extremely thin window was needed to reduce strong reflection and absorption of x-ray on and in the glass of the envelope, and a very thick film of the samples was necessary to obtain x-ray photographs with sharp diffraction pattern.

JOURNAL OF APPLIED PHYSICS VOLUME 31, NUMBER 1 JANUARY, 1960

Scattering by Nonspherical Particles*

J. MAYO GREENBERG
Department of Physics, Rensselaer Polytechnic Institute, Troy, New York
(Received August 15, 1957; revised manuscript received June 29, 1959)

The small angle scattering approximation of Schiff is applied to several nonspherical body shapes. Effects of orientation and elongation are discussed.

INTRODUCTION

SOLUTIONS for the scattering by nonspherical potentials are of interest in such diverse fields as astronomy and nuclear physics. However, there is not presently available an exact solution for the scattering by such a simple body as a refracting prolate spheroid although the equivalent sphere problem is one whose solution has been well known for a long time. The situation is further aggravated when the wavelength of the incident particles or radiation is comparable with the range or size of the scatterer. For such cases, even the spherical problems are at least tedious and one often is led to the use of approximations which yield reasonably simple analytical expressions. Some of these approximations are equally suitable to nonspherical particles. We may then gain valuable information by examining the results of approximate calculations and, in particular, we will gain some insight into the differences between the two types of scatterers. The scalar wave equation which is applicable to quantum-mechanical and acoustical problems will serve as the basis of the calculations. However, many of the qualitative features will be equally valid for the scattering of electromagnetic waves.

1. SUMMARY OF BASIC SCATTERING RELATIONSHIPS

The equation which governs the scattering process is

$$\nabla^2\psi+[k^2-U(\mathbf{r})]\psi=0 \tag{1.1}$$

where $k^2=2mE/\hbar^2=(2\pi/\lambda)^2$, E is the incident energy, $\lambda=$ wavelength, and $\hbar^2/2m\ U(\mathbf{r})=V(\mathbf{r})$ is the potential.

The wave function, ψ, is related to the scattering through its asymptotic form which we require to be given by

$$\psi(\mathbf{r})\rightarrow\psi_{\text{inc}}+\psi_{\text{scatt}} \tag{1.2}$$

where

$$\psi_{\text{inc}}=\exp(i\mathbf{k}_1\cdot\mathbf{r})$$
$$\psi_{\text{scatt}}=r^{-1}\exp(ikr)\,f(\mathbf{k}_1,\mathbf{k}_2)$$

and $\mathbf{k}_1$ and $\mathbf{k}_2$ are vectors along the incident and outgoing directions. The quantity $f(\mathbf{k}_1,\mathbf{k}_2)$ is the scattering amplitude from which the differential scattering cross section, $\sigma(\mathbf{k}_1,\mathbf{k}_2)$, may be obtained through

$$\sigma(\mathbf{k}_1,\mathbf{k}_2)=|f(\mathbf{k}_1,\mathbf{k}_2)|^2. \tag{1.3}$$

A fundamental and extremely useful relation[1] which connects the total scattering cross section and the imaginary part of the scattering amplitude in the forward direction is

$$\sigma_t=4\pi k^{-1}\,\text{Im}\{f(\mathbf{k}_1,\mathbf{k}_1)\}=\sigma_{\text{sc}}+\sigma_{\text{ab}} \tag{1.4}$$

where the scattering and absorption cross sections are given by

$$\sigma_{\text{sc}}=\int|f(\mathbf{k}_1,\mathbf{k}_2)|^2d\Omega_{\mathbf{k}_2} \tag{1.5a}$$

$$\sigma_{\text{ab}}=-k^{-1}\int|\psi|^2\,\text{Im}[U(\mathbf{r})]dr. \tag{1.5b}$$

An approximate solution[2] for the scattering amplitude, denoted here by $f_s(\mathbf{k}_1,\mathbf{k}_2)$, which is equally suitable for spheres and nonspheres is

$$f_s(\mathbf{k}_1,\mathbf{k}_2)=(ik/2\pi)\int_{-\infty}^{\infty}\int_{-\infty}^{\infty}\exp[i(q_xx+q_yy)]$$
$$\times\left\{1-\exp\left[(-i/2k)\int_{-\infty}^{\infty}U(\mathbf{r})dz\right]\right\}dxdy \tag{1.6a}$$

where $\mathbf{q}=\mathbf{k}_1-\mathbf{k}_2$. For problems with axial symmetry another integration may be carried out after trans-

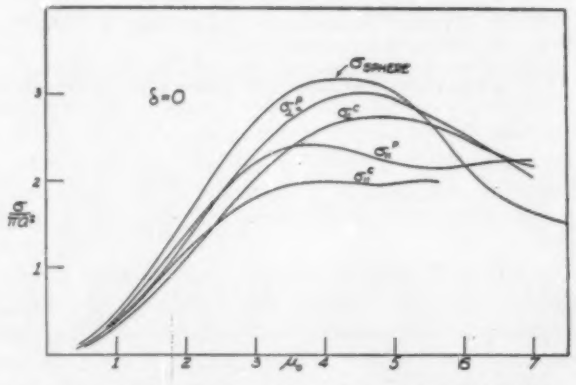

FIG. 1. Total cross sections for a sphere and paraboloidal and conical particles whose geometrical cross sections are equal as viewed parallel or perpendicular to their axes.

* This work was supported by a grant from the National Science Foundation.

[1] This relation has been derived by many authors. See, for example, R. Glauber and V. Schomaker, Phys. Rev. **89**, 667 (1953); L. I. Schiff, Progr. Theoret. Phys. (Kyoto) **11**, 288 (1954).
[2] L. I. Schiff, Phys. Rev. **103**, 443 (1956).

forming to cyclindrical coordinates and one obtains

$$f_s(\mathbf{k}_1,\mathbf{k}_2)=ik\int_0^\infty \rho d\rho J_0(q\rho)$$

$$\times\left\{1-\exp\left[(-i/2k)\int_{-\infty}^{\infty}U(\rho,z)dz\right]\right\}. \quad (1.6b)$$

2. NONSPHERICAL SCATTERERS

We will list here the results of applying Eqs. (1.4), (1.6a), and (1.6b) to several nonspherical scatterers.

For a potential $U(\mathbf{r})$, of ellipsoidal symmetry given by

$$U(\mathbf{r})=U[(x/A)^2+(y/B)^2+(z/C)^2]$$

the scattering amplitude becomes

$$f_s(\mathbf{k}_1,\mathbf{k}_2)=ikAB\int_0^\infty \rho d\rho J_0(q'\rho)$$

$$\times\left\{1-\exp\left[(-iC/2k)\int_{-\infty}^{\infty}U(\rho,\zeta)d\zeta\right]\right\}$$

where $\mathbf{k}_1$ is along the z axis and $q'=[(Aq_x)^2+(Bq_y)^2]^{\frac{1}{2}}$. This is of exactly the same form as the scattering amplitude from a spherically symmetric potential.

A potential with spheroidal symmetry which in a rotated coordinate system is represented by

$$U(\mathbf{r})=U[(x'/a)^2+(y'/a)^2+(z'/b)^2]$$

where the z' axis is in the x-z plane and makes an angle χ with respect to the z axis is equivalent to an ellipsoid defined by

$$A^2=b^2\sin^2\chi+a^2\cos^2\chi$$
$$B^2=a^2$$
$$C^2=(ab)^2/A^2.$$

We will consider complex square well potentials of the form

$$U=-U_0(1+i\delta) \quad \text{inside scatterer}$$
$$=0 \quad \text{outside scatterer}$$

Let us define the parameter μ by

$$\mu=U_0a(1+i\delta)/k=\mu_0(1+i\delta).$$

Then the total cross section for the spheroidal scatterer is given by

$$\sigma^s=4\pi AB\ \mathrm{Im}i\{\tfrac{1}{2}+(ia/C\mu)\exp(iC\mu/a)$$
$$+(a/C\mu)^2[1-\exp(iC\mu/a)]\} \quad (2.1)$$

where the superscript, s, denotes spheroidal.

For particles whose faces are paraboloids of revolution defined by $cz=a^2(1-\rho^2)$ we obtain

$$\sigma_{11}{}^p=4\pi a^2\ \mathrm{Im}i\{\tfrac{1}{2}+(c/2i\mu a)[1-\exp(i\mu a/c)]\} \quad (2.2a)$$

$$\sigma_\perp{}^p=(8\pi a^2/c)\ \mathrm{Im}\{(1/\mu)[J_2(\mu)+iH_2(\mu)]\}, \quad (2.2b)$$

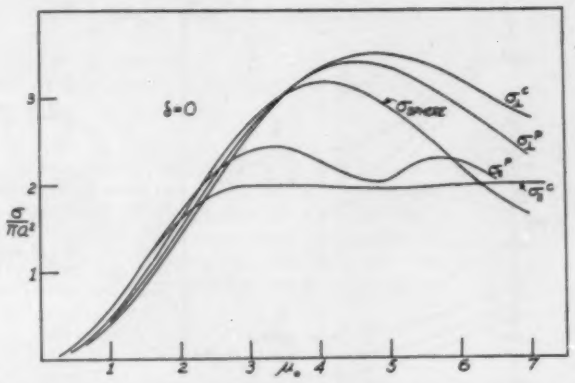

FIG. 2. Total cross sections of paraboloidal and conical particles whose volume is equal to that of the sphere.

where $J_2(\mu)$ is a Bessel function and $H_2(\mu)$ is a Struve function[3] and where p denotes paraboloidal and $\parallel$ and $\perp$ denote the orientation of the body axis relative to $\mathbf{k}_1$.

For a particle with conical faces of height b and radius a we obtain

$$\sigma_{11}{}^c=4\pi a^2\ \mathrm{Im}i\{\tfrac{1}{2}-(ia/\mu b)$$
$$-(a/\mu b)^2[1-\exp(i\mu b/a)]\} \quad (2.3a)$$

$$\sigma_\perp{}^c=4\pi ab\ \mathrm{Im}\left\{i/\pi-(1/\mu)[J_0(\mu)+iH_0(\mu)]\right.$$
$$\left.+(1/\mu^2)\int_0^\mu[J_0(x)+iH_0(x)]dx\right\}. \quad (2.3b)$$

3. EFFECTS OF DEVIATIONS FROM SPHERICITY

In Fig. 1 there is a comparison with the sphere of the total cross sections for paraboloidal and conical particles whose geometrical cross section is the same as the sphere viewed in both the parallel and perpendicular directions. Thus, although all of these curves approach the same asymptote in the geometrical optics (classical)

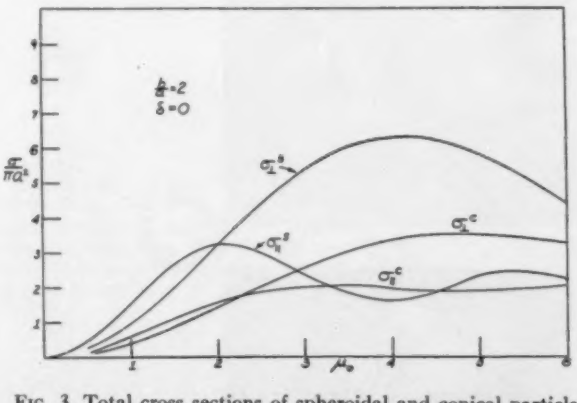

FIG. 3. Total cross sections of spheroidal and conical particles having the same elongation and the same axial geometric cross section.

[3] G. N. Watson, *Bessel Functions* (Cambridge University Press, New York, 1948), pp. 38, 328.

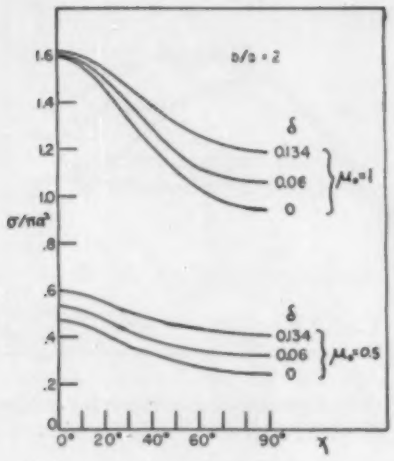

FIG. 4. Variation with orientation of the total cross section of a prolate spheroid with $b/a = 2$.

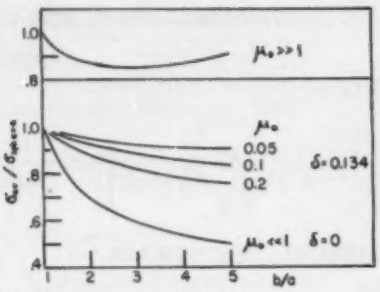

FIG. 5. Average cross sections for a uniform angular distribution of prolate spheroids as a function of elongation.

limit, there are obviously considerable variations among the group for small and intermediate values of μ.

The total cross section per unit volume is seen from Fig. 2 to differ by a considerable amount for the particles of different types although for the smaller values of μ the cross sections of axially oriented particles are essentially like that for the sphere. All of the particles considered in Fig. 2 have the same volume and axial geometric area, thus σ_{11}^{e}, σ_{11}^{p}, and σ sphere have the same asymptote.

Spheroidal and conical particles of the same elongation are compared in Fig. 3. It is interesting to note[4] that for $\mu<2$, $\sigma_{11}^{s}>\sigma_{\perp}^{s}$ and for $\mu>2$, $\sigma_{11}^{s}<\sigma_{\perp}^{s}$. Results very similar to those of Fig. 3 are obtained when one uses a value of $\delta=0.134$ which corresponds to the absorption by ice of visible light.

The continuous variation of σ with orientation has been derived only for spheroidal particles and some typical curves are given in Fig. 4. For $\mu\ll 1$ and $\mu\gg 1$ one may easily obtain the average cross section of a uniform distribution of elongated particles. These are compared with the equivalent sphere ($R^3=a^2b$) in Fig. 5.

[4] If the interstellar dust contains such elongated particles then the absorption by clouds of particles oriented normal to the line of sight (producing a relatively small degree of polarization) would be greater or less than the absorption by clouds of particles oriented along and perpendicular to the line of sight (large polarization) depending critically on the size of the particles.

JOURNAL OF APPLIED PHYSICS VOLUME 31, NUMBER 1 JANUARY, 1960

Rectangular Hysteresis Loop Ferrites with Large Barkhausen Steps

AARON P. GREIFER AND WILLIAM J. CROFT
Radio Corporation of America, Semiconductor and Materials Division, Needham Heights 94, Massachusetts
(Received June 15, 1959)

Observations have been made at low temperatures of large discontinuities (steps) in the 60-cycle hysteresis loops of polycrystalline ferrites containing copper. At the temperature for step formation, which is a function of copper content, the coercivity decreases and the loop squareness approaches unity. This behavior is attributed to the formation (in the toroidal specimens used) of circular 180° domain walls having different threshold fields. This domain wall configuration is probably brought on at low temperatures by a low effective magnetocrystalline anisotropy provided by the localized distortions exerted by divalent copper in the spinel lattice.

INTRODUCTION

IN the course of a search for rectangular hysteresis loops in ferrite systems containing copper,[1] some unusual discontinuities in the hysteresis loop were observed at low temperatures. These observations led to a somewhat more detailed study in order to gain some understanding of the factors responsible for the behavior. All the observations were made on sintered polycrystalline toroids in the copper ferrite-magnesium ferrite system. However, a cursory survey of other copper ferrite systems showed similar behavior. The cores were prepared by normal ceramic processing techniques.

OBSERVATIONS

When a toroid having a hysteresis loop of some measurable squareness at room temperature is subjected to moderate fields (about 10 oe) and then cooled while its 60-cycle hysteresis loop is displayed on an oscilloscope, it is found that the coercive force increases at first and then at some characteristic temperature starts to decrease. At this critical temperature, abrupt changes in the flux appear as "steps" in the loop, and the squareness ratio increases to unity (i.e., the top of the loop remains flat out to negative field values equal to or greater than one-half of the maximum positive field).* Figure 1(a) is a photograph of such a loop. Figure 2 shows the coercive force as a function of temperature for a toroid having a composition of 40% copper ferrite and 60% magnesium ferrite. Steps appear in the hysteresis loop for this toroid at approximately −70°C, with the maximum coercive force occurring between −60 and −70°C. As the temperature is lowered further, the steps become less pronounced. An increase in the field also tends to "erase" the steps [Fig. 1(b)], and at saturating fields the steps are usually reduced to "kinks" in the hysteresis loop. The characteristic temperature for step formation appears to be a function of the field and the toroid composition.

Figure 3 shows the copper content as a function of temperature of step formation at saturating fields. The relationship is almost linear for compositions in the center of the system. No steps in the hysteresis loops were observed down to −195°C for compositions approaching the end members. Figure 4 shows that for these compositions squareness ratios at −195°C had not attained values approaching unity. For the other compositions, comparison of Figs. 3 and 4 show that the high squareness ratios and step formation occur at the same temperature. Table I lists the maximum squareness ratios found across the system at −195°C.

The low ambient temperatures are obtained by placing the toroid in a dry nitrogen atmosphere that has been cooled by passage through a coil immersed in liquid nitrogen. The temperature can be controlled by adjusting the flow rate and by mixing the cooled nitrogen with warm nitrogen. Temperature measurements are made by means of a thermocouple in contact with the core. The temperature of liquid nitrogen (−195°C) is obtained by immersing the core in liquid nitrogen.

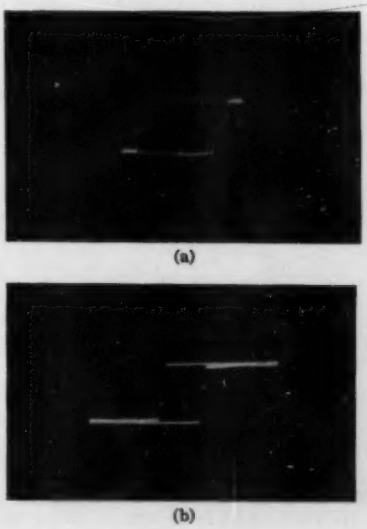

FIG. 1. 60-cps hysteresis loop for 40% copper ferrite-60% magnesium ferrite. (a) A minor loop at −195°C (b) Saturation loop at −110°C.

[1] A. P. Greifer and W. J. Croft, J. Appl. Phys. **30**, 34S (1959).

* For any hysteresis loop, the squareness ratio, R_s, is arbitrarily defined as the ratio of the flux density at half the negative applied field, $B_{(-H/2)}$, to the flux density at the positive applied field B_H: $R_S = B_{(-H/2)}/B_H$. For most materials the hysteresis loop having the maximum squareness ratio, $R_{S(\max)}$, is the loop for which the applied field is approximately equal to the saturation coercivity. However, for the materials discussed in this paper, all hysteresis loops are rectangular with squareness ratios approaching unity when the materials are subjected to sufficiently low temperatures (Fig. 1).

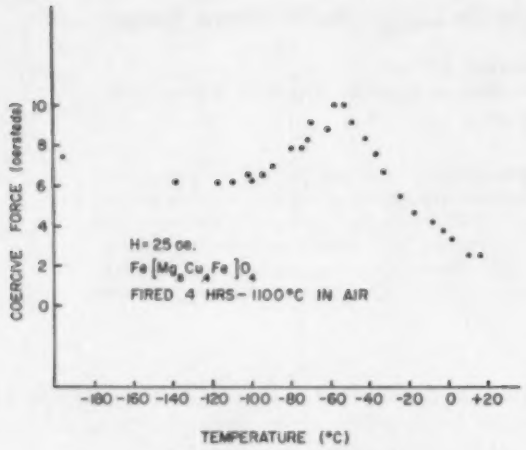

FIG. 2. Coercive force as a function of temperature for $Fe[Mg_{0.6}Cu_{0.4}Fe]O_4$.

If the toroid is subject to a low applied field (about 2 oe) and cooled from room temperature, the flux falls to zero at some particular temperature (i.e., the hysteresis loop collapses into a horizontal line). If the field is than increased while the core is kept at this temperature, a loop will eventually form. If the field is then reduced to its original value, a loop is retained at the low field. Only by warming up the core to about room temperature can the original behavior be duplicated.

The response to a square-wave voltage pulse shows some unusual characteristics. At room temperature the switching time is about 300 μsec at the field (about 3.5 oe) required for 2:1 coincidence. At liquid nitrogen temperature, fields of approximately 10 oe are required to initiate switching. The switching time under these conditions is about 8 μsec (voltage pulse) as compared to about 0.8 μsec with the same field applied at room temperature. At liquid nitrogen temperature there seems to be an initial delay before the core begins to switch.

Because cores in the system usually have large grains (as large as 20 mils in diameter), it was thought that the low temperature properties might be associated in some way with an assemblage of large grains. By changing the firing conditions, small-grained toroids having grains about 0.1 mil in diameter were prepared. These toroids also exhibited the "stepped" hysteresis loops, high values of squareness, and low coercive forces at low temperatures. These phenomena have been found to occur in all ferrite systems containing copper that have been examined. These systems have included combinations of copper ferrite with manganese ferrite, lithium ferrite, and nickel ferrite. This type of behavior was not observed in any other of the conventional ferrites. However, similar, but not identical, behavior has been observed in polycrystalline yttrium iron garnet[2,3] and in certain cobalt-bearing ferrites.[2] The phenomena cannot be associated with sequential switching of domains from the inner periphery of the cores to the outer because these same observations were made on cores having large variations in wall thickness.† It was also established that these effects are not introduced by any stresses imposed by the tightness of the windings of the primary and secondary coils around the core. The effects persist when the coils are loosely wound around the core.

TABLE I. Squareness *vs* composition at −195°C system: $Mg_{(1-x)}Cu_xFe_2O_4$.

X	R_s
0	No loop at 80 oe
0.1	0.82
0.2	0.89
0.3	0.99
0.4	0.97
0.5	1.0
0.6	1.0
0.7	1.0
0.9	0.70
1.0	No loop at 80 oe

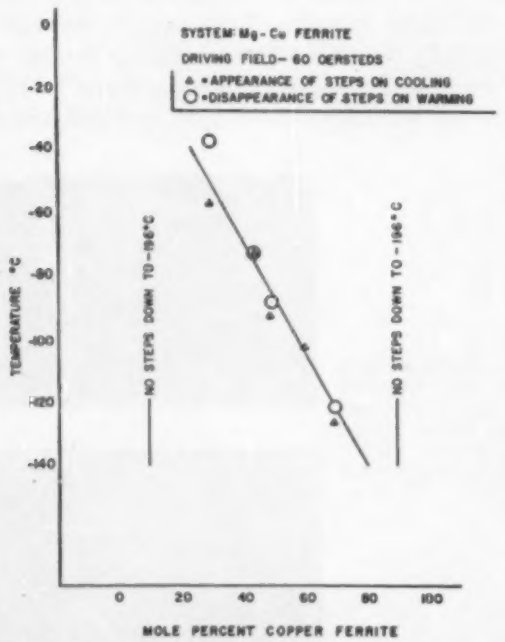

FIG. 3. Temperature of step appearance as a function of copper ferrite content in the system copper ferrite-magnesium ferrite.

It was first suspected that the low temperature

[2] P. K. Baltzer and C. Wentworth (private communication).
[3] B. A. Calhoun;, J. Appl. Phys. **30**, 293S (1959).

† These studies were made on toroids varying in size from 0.080 in. o.d. by .050 in. i.d. to .200 in. o.d. by .100 in. i.d. The materials were prepared by grinding together ferric oxide and the carbonates of the other metals, drying, calcining at 750 to 850°C, adding binders such as polyvinyl alcohol or Flexalin, pressing at about 20 000 psi and firing in air or oxygen at 1000 to 1200°C. However, the phenomena described do not depend in any way upon following any specific preparative scheme. In order to obtain the highest squareness ratio at room temperature, the magnesium-copper ferrites are fired in air at 1100°C for 4 hr. (see reference 1).

properties involved a phase change. Because pure copper ferrite itself is tetragonal unless quenched from high temperature, it seemed reasonable to expect that copper-bearing ferrites might revert to a tetragonal phase at low temperatures.[1] The tetragonal distortions at low temperatures then would force a change in the easy direction of magnetization, making the crystal magnetically isotropic when all the crystal axes were energetically equivalent to magnetization. Such conditions would, at least, explain the high squareness values found across the system on the basis of the criterion of zero effective magnetocrystalline domain anisotropy as put forth by Baltzer.[4] However, x-ray diffraction showed that the crystal lattice remains cubic down to −195°C. The possibility of a cubic to cubic transformation was then considered. Careful measurement of the unit cell dimension as a function of temperature did not give any data that could be taken as evidence of a discontinuity. Figure 5 shows a curve obtained for the 40% copper ferrite composition. A similar curve displaced downward was obtained for pure magnesium ferrite. Finally, diffraction studies were made at low temperatures in the presence of magnetic fields to examine the possibility of a field-induced phase transition. The results were negative.

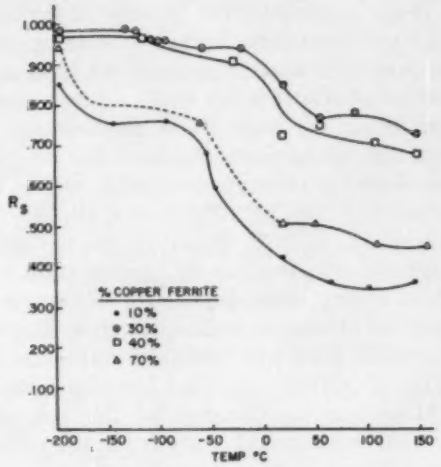

FIG. 4. Squareness ratio (Rs) as a function of temperature for several compositions in the system copper ferrite-magnesium ferrite.

INTERPRETATION

Rectangular hysteresis loops with vertical sides have been induced in metal wires under tension,[5] from metals that have been heat treated in a magnetic field[6,7] from "window frames" cut from oriented single metal and ferrite crystals[8–10] and from stressed polycrystalline ferrites.[11] In all these cases, the particular treatments mentioned have created or made use of a preferred orientation. The magnetization change, which occurs almost entirely along the vertical portion of the loop when such samples are properly prepared, is attributed to the motion of a single 180° domain wall sweeping through the material.‡ In each case, the magnetization reversal may be considered to be propagated by one large Barkhausen jump. Large discontinuities of this sort were first observed by Forrer[12] and later by Preisach[5] and Sixtus and Tonks.[13] Preisach found that the Barkhausen jumps increased in size as greater tension was applied to a Permalloy wire. As the elastic limit of the wire was approached, a rectangular loop formed that contained 97% of the net magnetization change between positive and negative saturation in the vertical discontinuity.

An ideal rectangular loop would have 90° corners and vertical sides. The induction would remain constant from maximum positive applied field to a negative field of equal magnitude. (Any loop less than ideal is approximately a parallelogram rather than a rectangle.) Furthermore, for complete idealization these conditions would hold for all loops having maximum fields ranging from the coercive field to the saturating field. For such an ideal loop it is evident that a squareness ratio of unity is maintained to the limiting condition of 1:1 coincident field.

The existence of rectangular loops having vertical sides has not been reported, as far as can be determined, for polycrystalline ferrites not subject to external

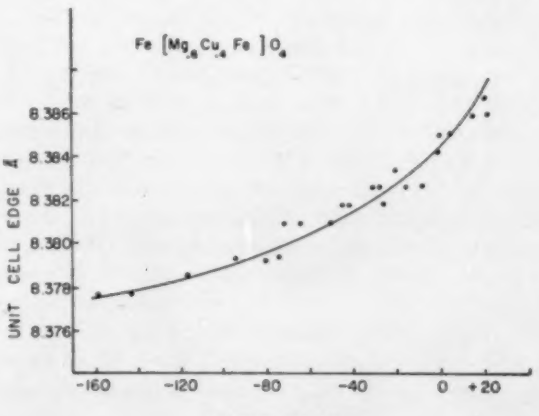

FIG. 5. Unit cell dimension as a function of temperature for the composition $Fe[Mg_{0.6}Cu_{0.4}Fe]O_4$.

[4] P. K. Baltzer, *Proceedings of the Conference on Magnetism and Magnetic Materials*, Pittsburgh, 1955 (American Institute of Electrical Engineers, New York, 1955), AIEE Spec. Publ. T-78.
[5] F. Preisach, Ann. Physik **5**, 737 (1929).
[6] Bozorth, Dillinger and Kelsall, Phys. Rev. **45**, 742 (1934).
[7] H. J. Williams and M. Goetz, J. Appl. Phys. **23**, 316 (1952).
[8] J. H. Williams and W. Shockley, Phys. Rev. **75**, 178 (1949).
[9] Galt, Andrus, and Hopper, Revs. Modern Phys. **25**, 93 (1953).
[10] J. F. Dillon, Jr., and H. E. Earl, Jr., J. Appl. Phys. **30**, 202 (1959).
[11] Williams, Sherwood, Goetz, and Schnettler, Communications and Electronics **9**, 531 (1953).
‡ In polycrystalline Perminvar heat treated in a magnetic field, several 180° walls are usually responsible for magnetization reversal. (See reference 7.).
[12] R. Forrer, J. phys. radium **67**, 109 (1926).
[13] K. J. Sixtus and L. Tonks, Phys. Rev. **37**, 930 (1931); K. J. Sixtus, *ibid.* **35**, 1441 (1929); K. J. Sixtus, *ibid.* **48**, 425 (1935).

stress. If the steps were not present in the hysteresis loop, the polycrystalline ferrites containing copper at low temperatures would approach the ideal condition as described above. It is felt that the steps observed in these materials are basically a manifestation of the same type of phenomena observed for the materials mentioned above, although the specific physical factors responsible have not actually been established. It appears necessary, at least, to accept the statement that the magnetic domains in the polycrystals must be aligned to a very great degree. At low temperatures, the top of the 60 cps saturation hysteresis loop remains flat for applied fields five times as large as the coercive field [Fig. 1(b)] indicating that the alignment is complete. Magnetization changes by the movement of circular 180° walls would account for the existence of rectangular loops at all applied fields.

The conditions responsible for the creation of 180° domain walls are believed to be the following. At low temperatures, the effective magnetocrystalline domain anisotropy may be reduced to very low values by means of the local Jahn-Teller distortions that divalent copper is known to impose on the spinel lattice.[14,1] Easy directions are then created in the field direction similar to the situation that prevails in magnetically annealed polycrystalline Perminvar having a composition of low anisotropy (43% Ni, 34% Fe, and 23% Co). Williams and Goetz[7] found that in a toroid of this material, flux reversal is achieved by the motion of a few circular 180° domain walls that are concentric with the toroid. Such a wall, as they have shown through use of the Bitter technique, cuts through grains indiscriminately. Domain theory predicts that even though the crystalline anisotropy may be zero, domain walls will still exist as long as the magnetostriction is not zero. It is believed that in the copper magnesium ferrites, the magnetostriction is not zero and, as in the Perminvar described above, responsible for the 180° walls.

[14] J. Ó. Dunitz and L. E. Orgel, Phys. and Chem. Solids **3**, 20 (1957).

The interpretation that relatively few 180° walls reverse the magnetization is in accord with the long switching times at low fields ($\approx 300\ \mu$sec) and the large values of low field switching coefficient (as high as 15 μsec-oe). According to this interpretation, all domain walls do not move at the same threshold field; since different threshold fields, then, are required to completely reverse the magnetization, abrupt flux changes occur in the hysteresis loop. Under these conditions, the 60 cps unintegrated voltage output should have a number of discrete pips on the oscilloscope which correspond to the number of steps. This has been observed.

Bray and Silverman[15] have artificially created stepped loops and suggest their possible applications.

CONCLUSION

Rectangular hysteresis loops with large vertical discontinuities and square corners have been found at low temperatures in polycrystalline ferrites containing copper. The coercivity goes through a maximum at the temperature for the step formation. This characteristic temperature is a function of the copper content. This unusual behavior may result from a decrease in the effective magnetocrystalline anisotropy to a near zero value by an increase in the short range tetragonal distortions exerted on the spinel structure by divalent copper at the lower temperatures. A small number of circular 180° domain walls having different threshold fields are probably created.

ACKNOWLEDGMENTS

The authors wish to thank Mr. Roy Buck for the preparation of the samples and Mr. David MacDonald for making the measurements, and Mr. Joseph McCusker and Mr. P. K. Baltzer for their invaluable technical discussions with us.

[15] T. E. Bray and B. Silverman, *Proceedings of Special Technical Conference on Solid State Dielectric and Magnetic Devices* (Catholic University, Washington, D. C., April, 1957).

JOURNAL OF APPLIED PHYSICS VOLUME 31, NUMBER 1 JANUARY, 1960

Interaction between Arsenic and Aluminum in Germanium

J. O. McCaldin
Hughes Semiconductors, Newport Beach, California

(Received May 28, 1959)

The behavior of As in Ge containing regions doped with $\sim 5\times10^{20}$/cc Al was studied. The solubility of As is enhanced tenfold or more by the heavy Al doping, on the basis of (1) measurements of conductivity type and (2) the negative results of a search for compounds by x-ray diffraction. The behavior of As diffusion fronts was studied by observing the progress of the *p-n* junction formed in Ge containing 10^{17}/cc In. When a region of heavy Al doping was added, the *p-n* junction was displaced. The displacements indicate that the diffusing As is attracted to regions of heavy Al doping. These results are similar to those of Reiss, Fuller, and others for Li in Si, though a detailed understanding is not yet available in the present case.

INTRODUCTION

THE simplest treatment of impurity diffusion in a solid assumes that the only driving force for diffusion is the gradient in the impurity concentration. This assumption, which is formulated in Fick's law, is adequate for most cases of diffusion doping of silicon and germanium with impurities from columns III and V. At sufficiently high doping concentrations, however, other driving forces may be expected to become important. For example, in the so-called "double *D*" effect, for which some evidence has been presented,[1] the charge interaction in extrinsic regions of a semiconductor provides an additional driving force. Furthermore, an effect corresponding to more than a doubling in the diffusivity might be expected at the junction between two extrinsic regions of opposite type.

The behavior of a semiconducting medium in which two impurities interact has been studied in detail for the case of lithium in doped silicon. These studies, which are most recently described in articles by Fuller and Reiss,[2] provide a relatively complete and quantitative picture of the system. Perhaps analogous behavior occurs for elements from columns III and V under suitable conditions. The purpose of the present study is to explore this possibility.

I. SYSTEM Ge-Al-As

The system Ge-Al-As, which was selected for experiment, offers some distinct advantages for diffusion measurements. The principal advantage is that the diffusivity of As is 100 times or more the diffusivity of Al in Ge. Thus, to a first approximation, the Al stands still while the As diffuses. This approximation is basic to the experimental arrangements to be described. A second advantage derives from the high solubilities[3,4] of both diffusants. Interaction of diffusants is more likely at high concentrations, and this is particularly important in view of the high temperature needed for measurable diffusion in this system.

The impurities are easily introduced into Ge. Aluminum was alloyed[5] in by the well-known evaporative-fusion process. The Ge was held at about 600°C during fusion, so that approximately 5×10^{20}/cc Al was present in all the regrowth layers to be described. Arsenic was introduced from the vapor established by a doping source consisting of 10^{19}/cc As in Ge. The Ge used in the experiments was indium doped with $C_b=10^{17}$/cc.

II. SOLUBILITY EFFECTS

Indications of an interaction between As and Al impurities in Ge were first obtained in solubility measurements. A mutual solubility effect of the two impurities is closely related to a diffusion effect. Suppose, for example, that the solubility of As is greater in heavily doped regions of Ge than in intrinsic regions. An As concentration gradient is present in an equilibrium situation. Fick's law is inadequate in this case, and the heavy doping must be taken into account to describe the diffusion of As.

The starting material in the solubility study was a slice of Ge about $\frac{1}{2}\times1\times0.030$ in. Aluminum was evaporated onto the heated slice to form an Al-Ge eutectic structure and an Al regrowth layer. The eutectic structure had to be completely removed to avoid later complications, and this requirement was met by alternately boiling the slice in HCl and rubbing the surface to break off the dendrites of the eutectic structure. The regrowth layer which remained was about 15×10^{-4} cm thick. The slice was cut into dice $0.3\times0.3\times0.07$ cm. Each die was placed with two doping dice, containing 10^{19}/cc As, in an evacuated quartz capsule. The capsule was held at 800°C for a selected time and then cooled rapidly. Type measurements were made on the regrowth surface with a thermoelectric probe.

Typically the regrowth surface would remain *p* type for about 15 hr of the treatment. At this time *n*-type areas developed at various spots on the surface. After

[1] A. D. Kurtz and C. L. Gravel, J. Appl. Phys. **29**, 1456 (1958). Also F. M. Smits, Proc. Inst. Radio Engrs. **46**, 1049 (1958).
[2] C. S. Fuller and H. Reiss in *Semiconductors*, edited by N. B. Hannay (Reinhold Publishing Corporation, New York, 1959), Chaps. 5 and 6.
[3] Thurmond, Trumbore, and Kowalchik, J. Chem. Phys. **25**, 799 (1956).
[4] F. A. Trumbore and A. A. Tartaglia, J. Appl. Phys. **29**, 1511 (1958).
[5] R. A. Gudmundsen and J. Maserjian, Jr., J. Appl. Phys. **28**, 1308 (1957).

some 30 to 60 hr the whole regrowth surface would be n type. The conversion to n type was limited to a thin surface layer at this stage, however, since the lightest polishing of this surface would expose p-type material. Conversion of the entire regrowth layer to n type occurred after 200 to 400 hr at 800°C. At this time an As diffusion front appeared in the bulk Ge just inside the regrowth layer.

This result could not have been anticipated from the solubilities of the individual impurities in Ge. The concentration of As in the doping source used in the present experiments was only ~6% the concentration of Al in the regrowth layer. Evidently the As solubility is enhanced some tenfold or more by the presence of the high Al concentration. The over-doping effect is reversible, as can be observed by substituting a getter for the As doping source. Under these conditions the regrowth surface returns to p type.

X-ray diffraction methods were used to examine the completely converted regrowth layer by Dr. John Bryden of this laboratory, who could find no indication of a second phase. Thus it seems likely that aggregation of the As and Al impurities, if it occurred, was limited to small clusters, perhaps pairs.

III. DIFFUSION OF Al AND As AT A CORNER

The behavior of the two impurities during diffusion was first studied with the procedures indicated in Fig. 1. The specimens were Ge dice 0.3×0.3×0.07 cm. An Al regrowth layer had been provided on one face of each die, as described in Sec. II, except that the regrowth layer in this case was 100×10^{-4} cm or more in thickness. The regrowth layer, which is labeled P^+ in the figure, was doped about 5000 times more heavily than the bulk Ge, which is labeled P. Five dice were sealed in an evacuated quartz capsule together with an equal number of doping dice (Ge with 10^{19}/cc As). The capsule was held at 850°C for the initial doping period, $\tau\cong20$ hr. The As atmosphere provided by the doping dice produced a diffused As layer in the specimen dice. On the P^+ side of a specimen die the diffused As caused a spotty surface conversion of type, as indicated in Sec. II. Resistivity profiles made on the P side showed that As was distributed according to a complementary error function with $5\times10^{18}\leq C_0\leq10^{19}$/cc. The face of the (lightly doped) P side of the die was polished to remove the As diffusion front there. Arsenic remained around the edge of the die as shown in Fig. 1.

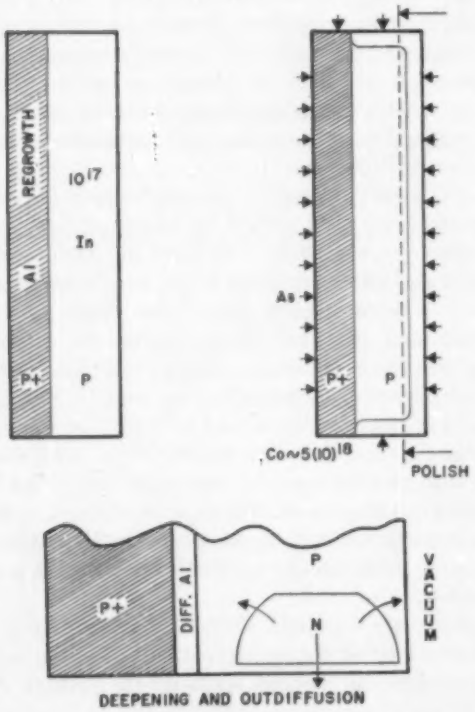

FIG. 1. Preparation of specimens for the corner diffusion experiment. The specimens are shown in cross section.

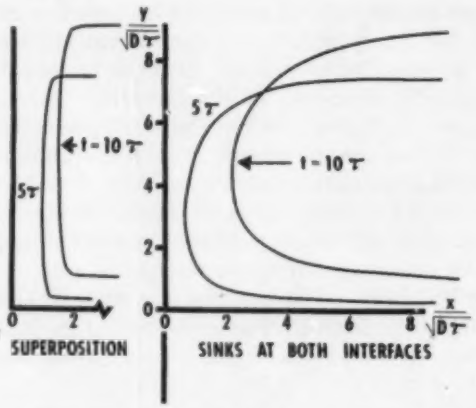

FIG. 2. Junction shapes calculated for corner diffusion. For the right-hand curves, a perfect sink for As is assumed along both coordinate axes. For the left-hand curves, a sink is assumed only along $y=0$, but the spreading out of an Al diffusion front from $x=0$ is allowed for.

The point of interest is the behavior of the diffused As near the $P-P+$ interface. The situation at the edge of a die is shown in the last part of Fig. 1. Neglecting for the moment the diffusion of Al from the $P+$ region, the p-n junction between the diffused arsenic and the remainder of the die is a contour of equal As concentration, $N_D=10^{17}$/cc. Assuming that Fick's law applies to regions of this order of concentration, the flow of As will be everywhere perpendicular to the junction line. Thus, if the junction curves near the $P-P+$ interface as shown in the figure, As flows preferentially toward the $P+$ regions as indicated. Similarly the vacuum interface on the right operates as a sink for diffusing As. Thus the relative attractions of a vacuum and of a $P+$ region for diffusing As can be compared in the experiment.

The junction curvature that is being sought in the experiment is enhanced if the initial doping period, τ,

is followed by a deepening period during which sinks for As are effective. During the deepening period the die should be surrounded by vacuum so that outdiffusion occurs at all surfaces of the specimen. Thus the lower right-hand corner of the die shown in Fig. 1 would have sinks for As along both vertical and horizontal boundaries. A similar corner would occur at the left side of the As-rich region if the $P-P+$ interface were as effective a sink for As as the vacuum interface.

The junction shape expected when a perfect sink for As operates along both surfaces at a corner may be calculated. The concentration, C, of As at any time, t, and place is given by

$$\frac{C}{C_0}=\left(\operatorname{erfc}\frac{y}{2(Dt)^{\frac{1}{2}}}-\operatorname{erfc}\frac{y}{2D^{\frac{1}{2}}(t-\tau)^{\frac{1}{2}}}\right)\operatorname{erf}\frac{x}{2(Dt)^{\frac{1}{2}}},$$

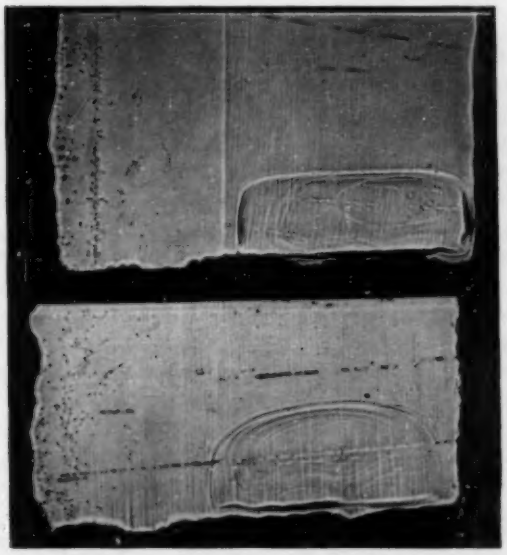

FIG. 3. Actual junction shapes developed during corner diffusion. The upper photomicrograph is for a total time at 850°C of $t=4\tau$. The lower photomicrograph is for $t=11\tau$. Total width of specimens is about 0.07 cm.

where D is the As diffusivity and C_0 is the surface concentration at the end of the initial doping time, τ. To obtain the junction contour the concentration C is set equal to the bulk doping, $N_A=10^{17}$/cc, and a family of curves plotted for various times, t. Some typical results of the calculations are shown on the right-hand side of Fig. 2. After deepening times of the order of 10τ, the junction becomes markedly curved.

For comparison, the junction shape expected under the usual assumptions, which neglect an attractive force between As and Al, is shown on the left-hand side of Fig. 2. In this case the spreading out of Al from the $P+$ region due to diffusion is taken into account, and the only sink for As is the vacuum interface at $y=0$. Since $D_{As}\geq 100D_{Al}$, the arsenic concentration falls off roughly 10 times more slowly than the Al concentration, so that

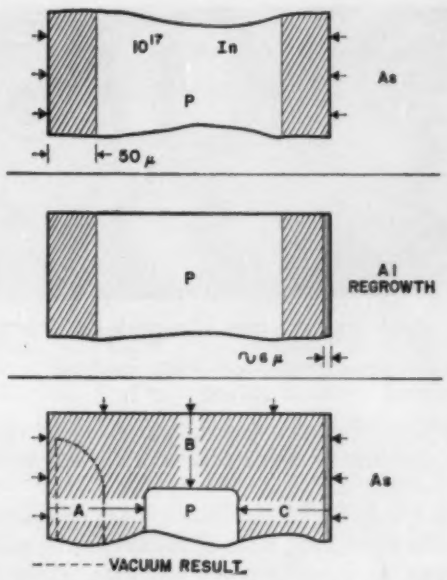

FIG. 4. Preparation of specimens for parallel diffusion experiment. The specimens are shown in cross section.

either one or the other diffusant dominates the junction shape in most regions. The result is an almost rectangular junction shape.

The purpose of the experiment was to decide which of the two calculated junction shapes* actually would develop. Typical metallographic sections obtained under the conditions described are shown in Fig. 3. Early in the deepening period the actual junction shape is hard to classify between the two calculated shapes, though close inspection suggests the interaction assumption is the better of the two. Also note the symmetry in the junction shape between the $P-P+$ interface side and the vacuum interface side. At later stages in the deepening, the junction clearly develops the shape predicted by the interaction hypothesis.

IV. DIFFUSION WITH Al AND As FRONTS PARALLEL

Other observations of the two impurities during diffusion were made in an essentially one-dimensional situation. The experimental procedure is illustrated in in Fig. 4. Again the starting material was a Ge slice doped with 10^{17}/cc of In. In this case, the As doping was performed first, followed by the formation of an Al regrowth layer. The techniques for carrying out the two processes were very similar to those described in Sec. III, except that a diffusion temperature of 800°C and an initial doping time, τ, of about 50 hr were used. The regrowth layer was 10% to 15% the thickness of the As layer in which it was formed. After formation of the

* The actual outdiffusion probably is not to a perfect sink as assumed in the calculations. See, for example, R. C. Miller and F. M. Smits [Phys. Rev. 107, 65 (1957)], who studied surface rate limitations on out-diffusion. The junction shape might then be expected to develop more slowly than calculated.

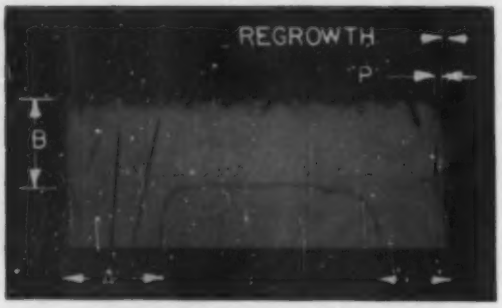

FIG. 5. Metallographic section of a specimen in the parallel diffusion experiment. The dimensions A, B, and C are penetrations of As diffusion fronts for various boundary conditions.

regrowth layer, the slice was cut into dice, 0.3 cm×0.3 cm. The appearance of the edge of a die was as shown in part 2 of Fig. 4.

The final step in the experiment was a deepening of the As diffusion fronts. Most of the deepening was performed with As vapor over the specimen. Three specimen dice and one doping die were sealed in an evacuated quartz tube, which was heated at 800°C for the deepening time. The additional doping source was approximately sufficient to make up for As losses in the system, so that the amount of As in each specimen die, exclusive of the regrowth region, remained roughly constant during deepening. Sheet conductance measurements[6] made on the die surface with a four-point probe confirmed that the amount of As in the region of interest was constant within ±30% in every case and within ±15% in most cases.

The penetration of As that occurred under these conditions is shown schematically in the last part of Fig. 4. The dimension A is the depth of As diffusion through the left-hand surface in the figure. A Gaussian distribution would be expected for this As front. The dimension B is the depth of penetration of As through the freshly cut edge of the die, and for long deepening times is very nearly the same as A. The dimension C is the penetration that occurs when a regrowth layer overlying an As diffusion front imposes a boundary condition on it. If C were to lag behind A and B, the imposed boundary condition would evidently result in a loss of As from the diffusion front to the regrowth layer.

Figure 5 is a metallographic section showing the experimental result obtained. In this example, the deepening time was about 15τ, i.e., some 780 hr, and the deepening temperature was the same as in the initial doping, i.e., 800°C. The dimensions A and B are nearly equal, as would be expected if these regions were in good contact through a vapor phase. The dimension C, however, is only some 70% as large as A or B. Evidently the diffusion front associated with C was weakened by loss of As.

An interesting detail in Fig. 5 is the curvature of the junction at the interior corners. The junction near the weak As front on the right exhibits the greater rounding of the two. A simple argument provides a comparison of the strengths of the As fronts on the basis of the rounding of the junction line. Suppose that one tries to superpose the junction shapes at the two interior corners by a suitable mirror reflection. The discrepancy between the two curves can be ascribed mostly to different As gradients in the horizontal direction. The reasons for this are (1) that superposition of a vertical and a horizontal component of As concentration is a reasonable approximation near the junction, and (2) that the vertical component of As concentration is roughly the same at both interior corners. The validity of the superposition assumption can be judged for the left corner, where the equation of the junction line is

$$\frac{C}{C_0}=\frac{10^{17}}{10^{19}}=\operatorname{erfc}\frac{x}{2(Dt)^{\frac{1}{2}}}+\operatorname{erfc}\frac{y}{2(Dt)^{\frac{1}{2}}}-\operatorname{erfc}\frac{x}{2(Dt)^{\frac{1}{2}}}\operatorname{erfc}\frac{y}{2(Dt)^{\frac{1}{2}}}$$

and the higher order term is less than one percent of the linear terms. The second assumption can be judged in terms of the results obtained in Sec. III. On these assumptions, the gradient in As concentration at the junction is two or three times greater for front A than for front C.

In some cases the deepening step in this experiment was performed with the specimen in vacuum. The specimen was sealed in an evacuated quartz capsule together with a getter consisting of pure Al supported on a body of pure Ge. The capsule was heated at 800°C for the deepening time. Some of the As penetration distances shown in Fig. 4 were strongly affected by the substitution of vacuum for As vapor. The diffusion front associated with dimension B never formed, and the front A was weakened by loss of As at the surface. Front C was imperceptibly affected.

The progress of the diffusion fronts for the various boundary conditions is shown in Fig. 6. For comparison, the penetration distances for a complementary error function distribution and a Gaussian distribution are also shown.† The erfc distribution corresponds to a small influx of As at the surface, while the Gaussian distribution corresponds to zero As transfer at the surface. Figure 6 shows that the normal diffusion fronts A and B behave appropriately for a Gaussian or erfc distribution, whereas the diffusion fronts subjected to the boundary condition of a vacuum or an Al regrowth become weakened.

DISCUSSION

The solubility and diffusion experiments showed an attractive force to exist between two common dopants of opposite conductivity type, under suitable conditions.

[6] G. Backenstoss, Bell System Tech. J. 37, 699 (1958).

† A curve for the case of outdiffusion to a perfect sink can be made to fit the experimental points for the vacuum boundary condition, provided suitable values of C_0 and C_b are chosen. In the absence of an accurate value for C_0, however, the curve is not shown.

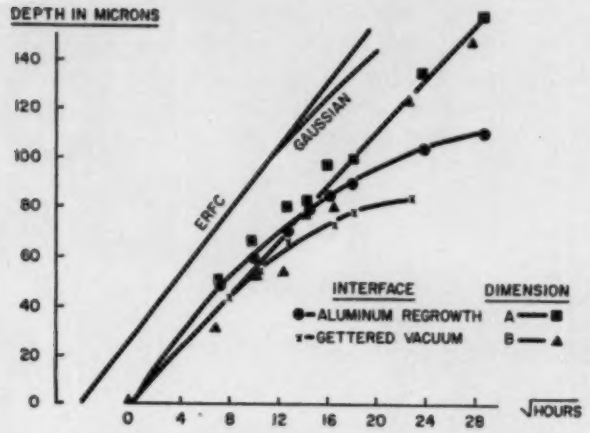

FIG. 6. Penetration of As diffusion fronts for various boundary conditions.

A possible explanation for the attraction is the existence of a macroscopic compound, i.e., second phase, in the ternary system at the compositions and pressures used. The search for such a compound by x-ray diffraction techniques yielded negative results. Furthermore, the diagrams of related binary systems[7] for which detailed information is available suggest that most III-V compounds probably are not stable at the compositions and relatively low pressures used in the present study. In the absence of an equilibrium diagram for this ternary system, however, the existance of the compound AlAs in the range of composition, temperature, and pressure studied is not altogether ruled out.

Another possibility is the formation of substitutional AlAs pairs, as suggested by Reiss[8] *et al.* Such pairs might aggregate to form a macroscopic second phase only after prolonged heating at high temperature, if at all. In support of this possibility, the solubility measurements showed As and Al to be present in a ratio only slightly greater than 1:1. Also, diffusing As was observed to permeate a thin Al-rich region relatively slowly. This last observation can be interpreted in terms of a reduced diffusivity, D', due to a pairing reaction. For the present experimental values, the reduced value, D', is about 0.1 of the normal diffusivity, D, for unpaired As. According to the simple theory[2] for diffusion in the presence of pairing, this result means that most ($\sim$90%) As atoms are paired, and only the relatively few unpaired atoms are free to diffuse.

A similar experiment has been reported by Fuller.[2] Radioactive As was the diffusant and heavy doping was obtained with Ga concentrations up to 10^{19}/cc, instead of Al doping. No change in As diffusivity due to Ga doping was detected. This negative result probably is due to the use of an acceptor doping some 50 times less than in the present work. If the same equilibrium pairing constant, Ωp, is applied to the Al and Ga cases, the simple theory predicts that D' would be about $0.8 \times D$, when N_A is 10^{19}/cc. This small a change in diffusivity would be difficult to detect.

An alternative interpretation of the present results is that the region of heavy Al doping remains extrinsic at higher temperatures. Evidence for extrinsic behavior of heavily doped Ge at elevated temperatures has been given by Valenta and Ramasastry[9] in their study of Ge self-diffusion. Data[10] on the hole concentration, p_i, in intrinsic Ge suggest an extrapolated value at 850°C of $p_i \sim 10^{19}$/cc. The Al concentration is some 50 times larger, and room temperature measurements[4] have shown that each acceptor atom gives rise to one hole. Thus the hole concentration is estimated to be $\sim$50 times larger in the Al-rich region than in the intrinsic region. In terms of the mass action law for the hole-electron equilibrium, the equilibrium concentration of the ionized donor, As^+, would also be $\sim$50 times larger in the Al-rich region. (Actually the mass action law is only an approximation[2] at these high concentrations.) This distribution of As between the two regions is in qualitative agreeement with the experimental results for solubility and diffusion. The enhanced solubility observed is the right order of magnitude, and the attraction between As and Al during diffusion follows directly from the enhanced solubility. The relatively long time required for As to "penetrate" a thin Al-rich region would be due, in this interpretation, to the distribution coefficient of $\sim$50:1 in effect at the junction between extrinsic and intrinsic regions.

One way to distinguish between the two interpretations presented is to measure As diffusivity within the Al-rich region, rather than an over-all time for As to penetrate the whole region. The techniques of metallography and resistivity profiling used in the present investigation are not well suited to this purpose. Some profiling measurements were made and inconclusive results obtained, though some slight preference might be given to the substitutional pairing hypotheses on this basis. Other experimental techniques appear more promising, such as the use of tracers and the application of the electron probe microanalyzer[11] to impurity profiling. The latter technique is being used in this laboratory for further study of the problem.

CONCLUSIONS

The experiments indicate that arsenic diffusing in germanium at $\sim$800°C is attracted to regions of heavy aluminum doping. These regions also exhibit an en-

[7] J. van den Boomgaard and K. Schol, Philips Research Repts. **12**, 127 (1957).
[8] Reiss, Fuller, and Morin, Bell System Tech. J. **35**, 535 (1956), Sec. XV.
[9] M. W. Valenta and C. Ramasastry, Phys. Rev. **106**, 73 (1957).
[10] F. J. Morin and J. P. Maita, Phys. Rev. **94**, 1525 (1954).
[11] D. B. Wittry, J. Appl. Phys. **29**, 1543 (1958).

hanced solubility for arsenic. No evidence for the presence of a macroscopic second phase was found; however, other explanations of the observed effects are possible, including: (1) formation of substitutional AlAs pairs; and (2) the persistence of extrinsic behavior to high temperature.

ACKNOWLEDGMENTS

The author wishes to thank T. W. Griswold and H. Winston for helpful suggestions and R. D. Mathis, J. Healy, H. Ross, and J. Blackmon for assistance with the experiments. Thanks are due to J. Bryden, who made the x-ray diffraction examinations.

JOURNAL OF APPLIED PHYSICS VOLUME 31, NUMBER 1 JANUARY, 1960

Dislocations in Two Types of CdS Crystals*

D. C. REYNOLDS, *Aeronautical Research Laboratory, Wright Patterson Air Force Base, Ohio*

AND

S. J. CZYZAK, *Physics Department, University of Detroit, Detroit 21, Michigan*

(Received July 21, 1959)

Dislocation densities in CdS crystals (types I and II) have been investigated employing chemical etching techniques. There is very little difference in the dislocation densities in the two types of CdS crystals. The dislocation density in both types of growth varies over a range from $10^7/cm^3$ to $10^1/cm^3$. However, type I crystals have a greater tendency to twin and low angle boundaries are generally present in the twinned crystal.

INTRODUCTION

TWO types of crystals are formed from the vapor phase growth of cadmium sulfide.[1]

(a) Type I crystals are those which grow directly on the powder charge with the growth plane parallel to the growth surface.

(b) Type II crystals are those which grow on a seed plate with the growth plane making an angle of approximately 14° with the growth surface.

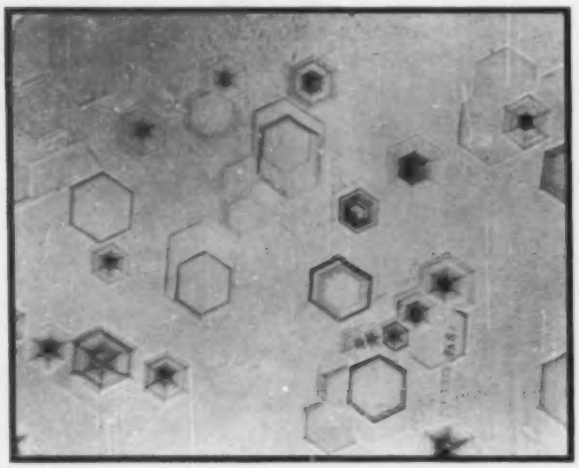

FIG. 1. Typical etch pattern showing the direction of preferential etching (*c* axis). Magnification 132×.

In both types of growth, the growth plane is the 0001 plane. Dislocation studies have been made on both types of growth using chemical etching techniques.

HYDROCHLORIC ACID ETCHING

The etching is accomplished by exposing the crystal to hydrochloric acid vapor. In these experiments boiling concentrated hydrochloric acid was used and the crystal was held in the vapor 1 to 2 in. above the boiling acid for a period of 5 to 10 sec. The etch products are easily removed from the crystal, hydrogen sulfide going off as a gas and cadmium chloride being water soluble. The etch is preferential in the direction of the "*a*" axis and

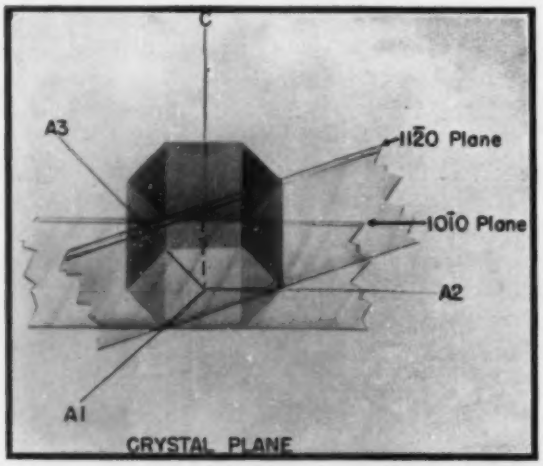

FIG. 2. A pictorial view of CdS structure. (Consider the light colored spheres to be sulfur and the darker colored spheres to be cadmium.) Magnification 132×.

* The research effort at the University of Detroit, Physics Department is supported by the Physics Branch ONR Contract No. Nonr 1511 (01) NR 015-218.

[1] Greene, Reynolds, Czyzak, and Baker, J. Chem. Phys. **29**, 1375 (1958).

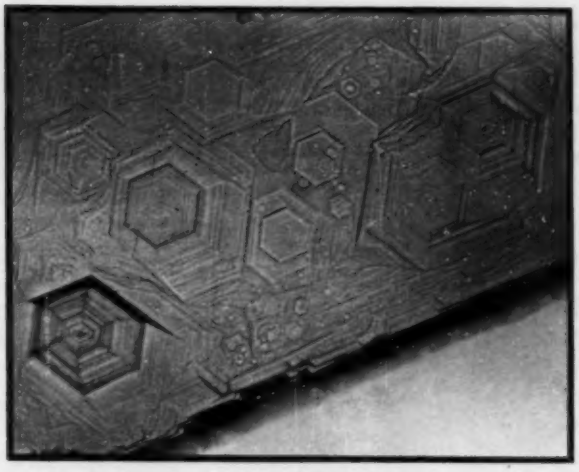

FIG. 3. Type I crystal showing $10\bar{1}0$ boundary plane. Magnification 132×.

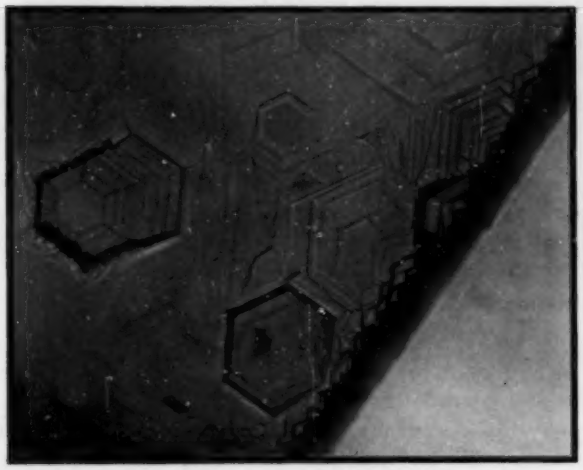

FIG. 4. Type I crystal showing $11\bar{2}0$ boundary plane. Magnification 132×.

has little effect in the direction of the "c" axis unless there is some disturbance in the planes normal to the c axis. This shows up dislocations by etching down the core of the dislocations. A typical etch pattern is shown in Fig. 1. Here the etch pits occur in the direction of the c axis, as the hexagonal geometry of the patterns indicates. X-ray investigations have shown that the etch pits are bounded by crystalline planes. A pictorial view of the cadmium sulfide structure is shown in Fig. 2. The two planes ($10\bar{1}0$ and $11\bar{2}0$) inscribed within the hexagon are the bounding planes of the etch pits. In the great majority of cases, the etch pit is completely bounded by the lower index, $10\bar{1}0$ planes.

Crystals of type I growth are bounded by the same two planes. The $10\bar{1}0$ plane is shown in Fig. 3 and the $11\bar{2}0$ plane is shown in Fig. 4. These planes are obvious from the etch pit geometry.

As long as the etch pits observed in Fig. 1 remain pyramidal in shape a continued disturbance in the axial direction of the etch is indicated and these disturbances are believed to be dislocations. When the pyramidal etch pit develops into a plateau, the dislocation has then disappeared. One might expect that if there were emergent screw dislocations on the growing surface of a crystal then at low supersaturations growth peaks would be observed at these sites. It would also be expected since the supersaturation is low that the growth peaks would consist of an oriented growth. This has been observed and is shown in Fig. 5. The growth may result from the spiral step being held up by an absorbed impurity as suggested by Amelinckx[2] in explaining dendritic growth. The growth appears as the beginning of a whisker. If this is growth resulting from emergent screw dislocations, then on etching the growth peaks should be the sites of etch pits. The results of a two second etch are shown in Fig. 6. It is seen that the

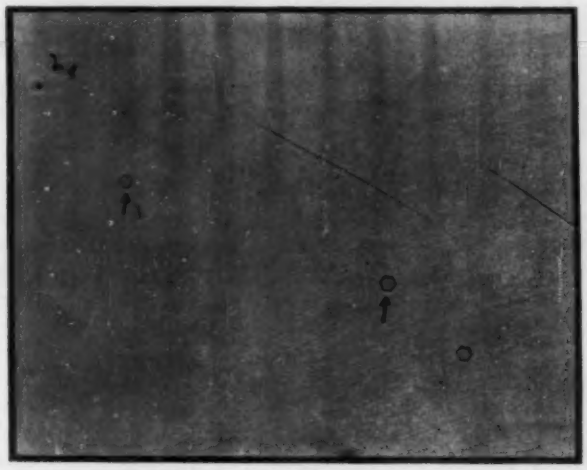

FIG. 5. Oriented growth peaks at low supersaturations. Magnification 132×.

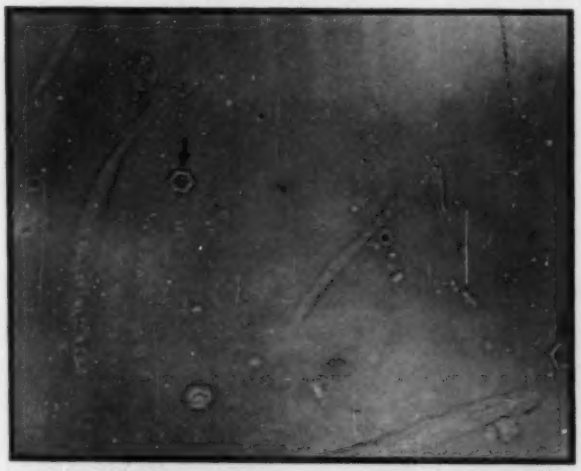

FIG. 6. Etch pits resulting from a 2 sec etch of the growth peaks in Fig. 5. Magnification 200×.

[2] S. Amelinckx, *Conference on Dislocation and Mechanical Properties of Crystals*, edited by J. C. Fisher (John Wiley & Sons, Inc., New York, 1957).

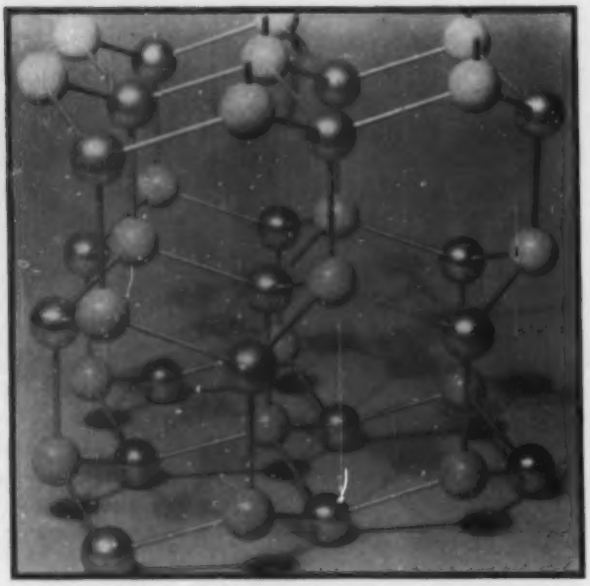

FIG. 7. Structure of CdS. (Consider the light colored spheres as sulfur atoms and the darker colored spheres as cadmium atoms.)

growth peaks are the beginnings of etch pits. This strongly suggests that both the growth peaks and the corresponding etch pits occur at sites characterized by emergent screw dislocations. (The etch peaks of Fig. 5 marked by arrows correspond to the etch pits marked by arrows in Fig. 6.)

ANISOTROPY OF ETCH

It has been observed by Lavine, Rosenberg, and Gates[3] that the two faces of indium antimonide crystals resulting from a cut normal to the ⟨111⟩ direction show different etching characteristics. They point out that the two faces, arbitrarily designated as {111} and {$\bar{1}\bar{1}\bar{1}$}, are structurally indistinguishable but that chemical differences would be expected in view of the different bonding relationships. The bonding along the direction of the c axis in cadmium sulfide is very similar to the bonding in ⟨111⟩ direction in the zinc-blende structure. The wurtzite structure of cadmium sulfide is shown in Fig. 7. When looking from the top of the figure down, which is along the c axis, each sulfur atom is triply bonded and each cadmium atom is singly bonded. Reversing the direction of observation it is seen that the bonding scheme is also reversed, each cadmium atom being triply bonded and each sulfur atom singly bonded. In this structure, as in the indium antimonide structure, differences in chemical etching on these two surfaces would be expected. The etch pattern, shown in Fig. 1 occurs on one of these faces. The etch pattern shown in Fig. 8 is characteristic of the opposite face. On one face hexagonal shaped etch pits form, on the opposite face a velvet-like appearance results from the identical etch.

Assuming the cadmium atoms have a positive charge and the sulfur atoms a negative charge, it has been determined from the sign of the piezoelectric voltage that the hexagonal shaped etch pits form on the crystal surface on which sulfur is exposed. It has been found that in all cases this is the growing surface on type I crystals. In type II crystals this plane makes an angle with the growth surface and there appears to be no preference with respect to the 0001 or 000$\bar{1}$ plane for this type of growth.

FIG. 8. Etch pattern of the opposite face of that of Fig. 1. Magnification 132×.

[3] Lavine, Rosenberg, and Gates, J. Appl. Phys. **29**, 1131 (1958).

CRYSTAL IMPERFECTIONS

Etching studies by many investigators on many different materials have shown that dislocations are exposed by selected and controlled etches. The fact that growth peaks and etch pits form at the same site on the crystal surface as described above indicates strongly that hydrochloric acid etch employed on cadmium sulfide exposes screw dislocations. It is, therefore, reasonable to assume that it will also show up edge dislocations. Etching studies have been made on the two types of growth described herein to determine if there is a significant difference in the "as grown" crystalline perfection of the two types of growth. In these studies the surface investigated was always the surface on which hexagonal etch pits formed. A typical etch pattern for a crystal of growth type I is shown in Fig. 9(a), (b), and (c). Fig. 9(a) shows a pattern near the edge of the crystal whereas Fig. 9(b) shows one that is approximately halfway between the edge and center of the crystal and in Fig. 9(c) a pattern at the center of the crystal is shown.

Near the edge of the crystal a large concentration of randomly distributed dislocations is observed. These [Fig. 9(a)] are believed to result from stresses set up by more rapid cooling of the surface which would both create a larger concentration of dislocations and provide a shorter time for any rearrangement of the dislocations.

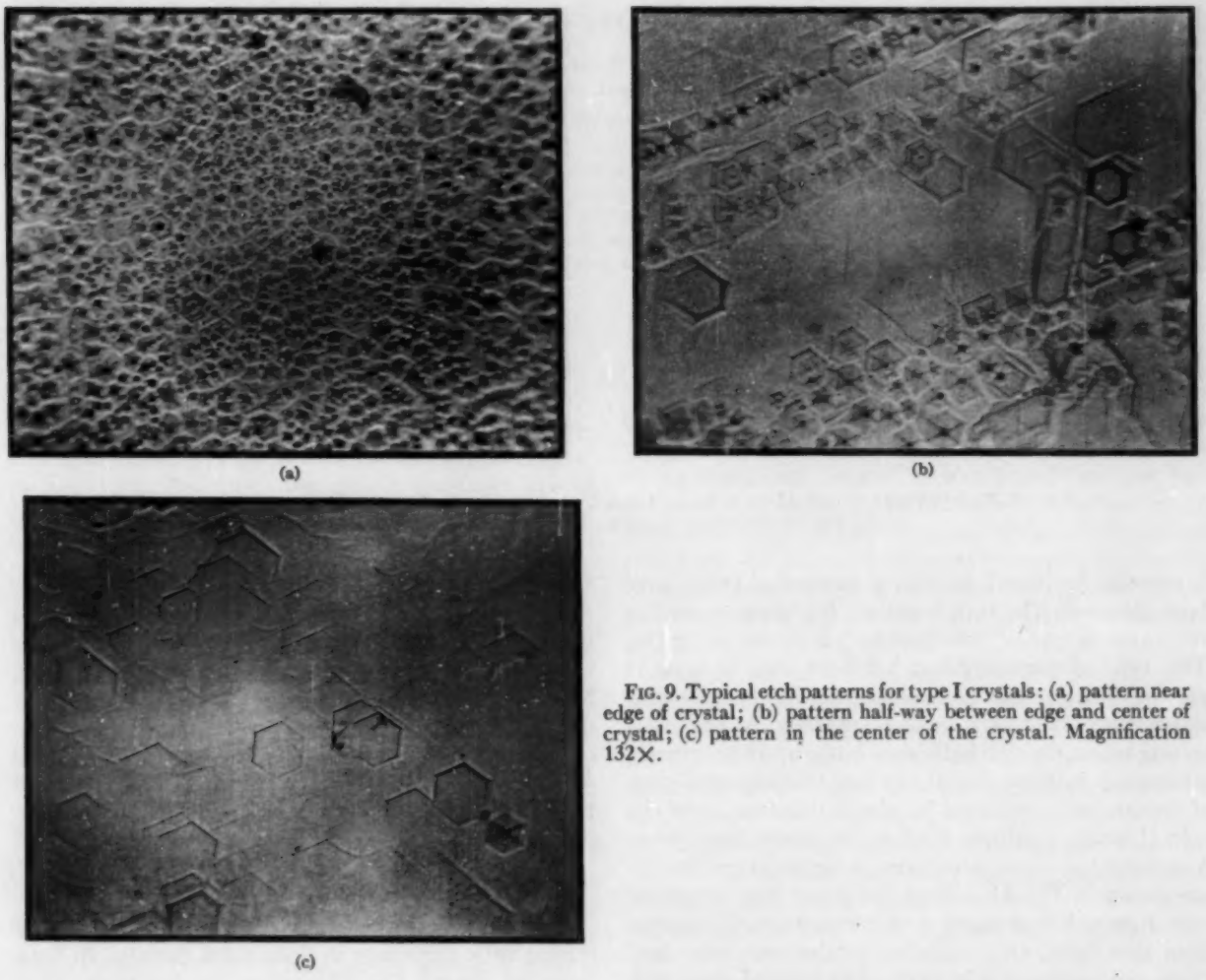

(a) (b) (c)

FIG. 9. Typical etch patterns for type I crystals: (a) pattern near edge of crystal; (b) pattern half-way between edge and center of crystal; (c) pattern in the center of the crystal. Magnification 132×.

The region shown in Fig. 9(b) would tend to cool more slowly resulting in smaller stresses creating fewer dislocations and allowing more time for rearrangement. Here, well-developed glide bands are observed. At the center of the crystal the dislocation concentration is low. In Fig. 9(c), it is seen that only one active dislocation

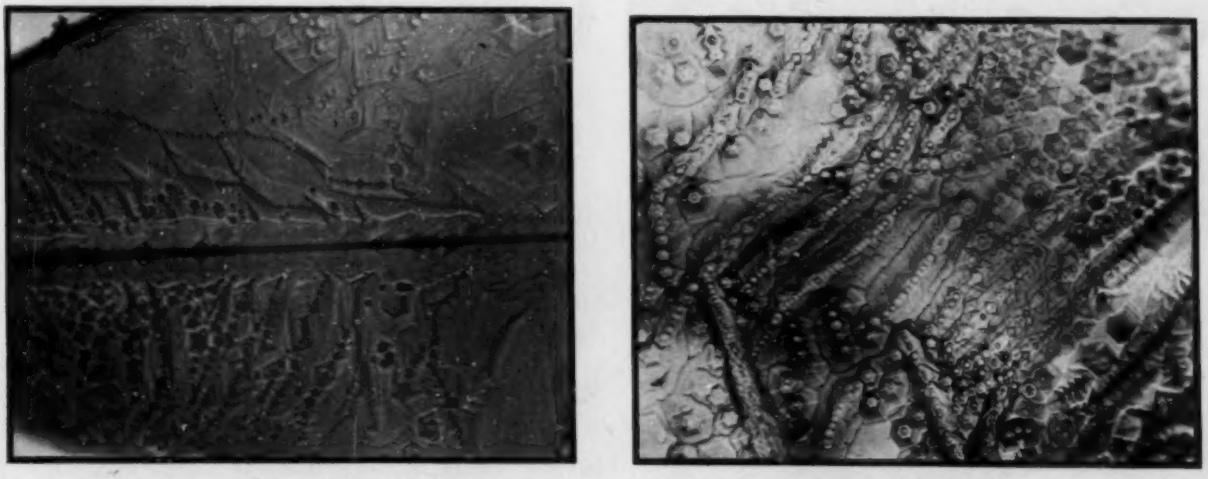

FIG. 10. A type I crystal in which a twin boundary is observed. Magnification 132×.

FIG. 11. A series of low angle boundaries in twinned crystal. Magnification 132×.

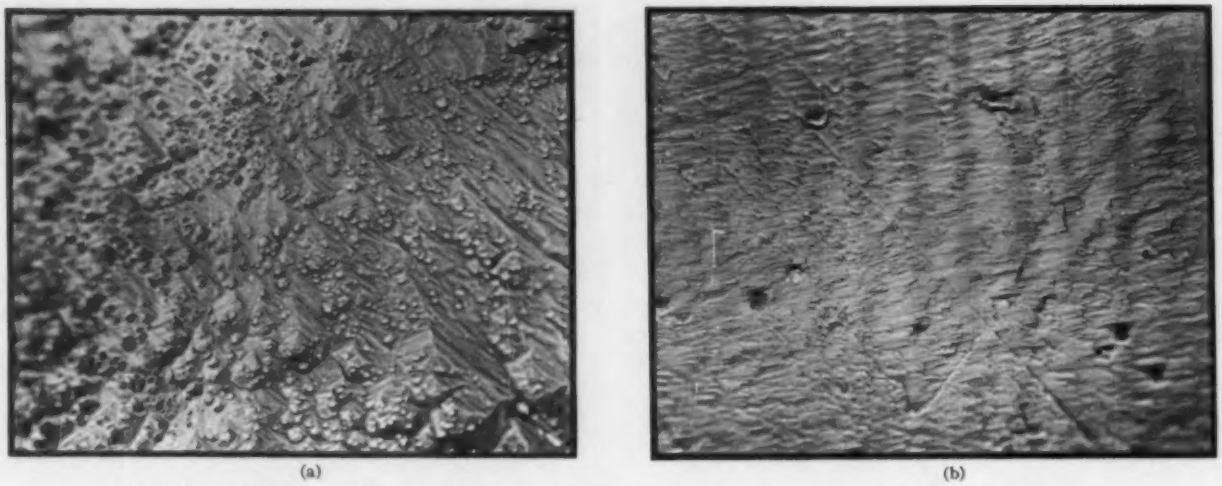

(a) (b)

FIG. 12. Etch patterns of type II crystals. (a) Large concentration of randomly distributed dislocations; (b) low concentration of dislocations. Magnification 132×.

is present. In type I growth, a number of twins have been observed. The twin boundary is a plane parallel to the c axis. A typical twin boundary is shown in Fig. 10. This type of boundary has not been seen in type II growth. The surface of the specimen has been etched, showing up several low angle boundaries. At the intersecting plane, the two individual lattices will be severely strained. It is likely that at elevated temperatures some of the strains are relieved by plastic deformation of the crystal which manifests itself as low angle boundaries. A series of low angle boundaries at higher magnification are shown in Fig. 11. These also occur in a crystal of type I growth containing a twin boundary. It appears from this figure that a distinction between edge and screw dislocations can be made. The rows of small etch pits correspond to edge dislocations, the larger more randomly distributed pits correspond to screw dislocations.

Etch patterns for type II growth are shown in Fig. 12(a) and Fig. 12(b). In this type of growth the 0001 plane makes an angle with the growth surface; therefore, it is necessary to use cleaved surfaces as etching surfaces and these are never as smooth as a grown surface. For this reason, the etching field will be more irregular than that for the type I growth. Section (a) shows a large concentration of randomly distributed dislocations. Section (b) shows a low concentration of dislocations. These patterns are typical of a number of etch patterns made on type II growth tending to bracket the upper and lower dislocation densities that have been observed in this type of growth.

CONCLUSION

The two types of crystal growth investigated above exhibit little difference in dislocation density. In both types of growth the dislocation density varies considerably, extending over a range from $10^7/cm^2$ to $10^1/cm^2$. The most striking structural difference between the two is the formation of twins in type I growth and the lack of such twinning in type II growth. In general, there are a series of low angle boundaries accompanying the twin boundaries in type I growth.

JOURNAL OF APPLIED PHYSICS VOLUME 31, NUMBER 1 JANUARY, 1960

Elastic Constants of Single Crystal Beryllium*

J. F. SMITH AND C. L. ARBOGAST
Institute for Atomic Research and Department of Chemistry, Iowa State University of Science and Technology, Ames, Iowa
(Received June 4, 1959)

The five independent elastic constants of beryllium have been determined with the pulse echo technique at a frequency of 10 Mc/sec. The values extrapolated to 0°K are $C_{11}=29.94\pm0.06$, $C_{33}=34.22\pm0.12$, $C_{44}=16.62\pm0.05$, $C_{12}=2.76\pm0.08$, $C_{13}=1.1\pm0.5$ in units of 10^{11} dyne/cm². Voigt averaging and Reuss averaging of the single crystal elastic constants give excellent agreement because of the small magnitude of the nondiagonal elements, C_{12} and C_{13}. The averaged values compare favorably with previous data from polycrystalline beryllium.

INTRODUCTION

SINGLE crystal elastic constants have been determined for only a small percentage of the metallic elements which crystallize with the hexagonal closest-packed structure. Since the elastic constants are of fundamental interest in connection with theories of lattice dynamics, metallic binding, and mechanical properties, it is desirable to increase the number of measurements of the elastic parameters to include representative elements from various portions of the periodic chart. The five independent elastic constants of single crystals of metallic beryllium were determined in the present investigation.

Evaluation of elastic constants from theory has so far been done without including the vibrational energy contributions; therefore, comparison of theoretical and experimental values should be made for 0°K. On this basis, experimental determination of elastic constants should be carried to sufficiently low temperatures so that valid extrapolation to 0°K may be made. In the case of beryllium, which has a relatively high Debye temperature,[1] the vibrational modes approach ground state at relatively high temperatures, and the curves representing the temperature dependence of the elastic parameters are essentially flat at the temperature of liquid nitrogen and below. This fact was verified by measuring C_{11} to 4.2°K on the beryllium crystal in the original strained condition, and subsequent measurements were not made below liquid nitrogen temperature.

Preliminary results of the present investigation have been included in the recent compilation of Huntington.[2] It has been found necessary to revise these preliminary values upward by about 4% on the average. Two factors necessitated this revision. First and most serious, an inadvertent computational error changed the sign of the transit time correction so that the calculated elastic constants were too low; the responsibility for this error rests entirely on the present authors and in no way reflects on Professor Huntington. Subsequent modification of the experimental apparatus to display an unrectified echo pattern has eliminated the need for a transit time correction[3] in the current evaluation of the elastic constants. Second, it was found that the preliminary measurements were made on crystals which retained a finite amount of residual strain. This residual strain was satisfactorily removed by annealing. Finally, it should be noted that in the process of reproducing the compilation the sign of C_{12} was changed from positive to negative.

Another set of values for the elastic constants of beryllium at room temperature has previously been reported by Gold.[4] The present values and Gold's values for C_{11} and C_{33} agree within 5% and, in view of the extrapolation technique used by Gold, the agreement is considered to be satisfactory. However, in solving for the three additional constants, C_{12}, C_{13}, and C_{44}, Gold utilized a measured value for the polycrystalline shear modulus, and in so doing he introduced the two following approximations. Gold assumed that beryllium was sufficiently isotropic so that he could equate the independently averaged velocities of each of the two quasi-transverse shear modes taken over a solid angle and, in turn, set these average values equal to the velocity of a shear wave propagated in a polycrystalline sample. This procedure is highly questionable since the velocity of one shear mode is everywhere greater than the other, except parallel to the c axis, in which direction the shear velocities are degenerate. On the basis of the present values for the shear constants, Gold's equating of the average values of the two shear velocities is likely to be in error by the order of 10%, and this would introduce a disproportionately large error in the calculated shear constants. The further assumption that the average shear velocity in a single crystal is equal to the shear velocity in a polycrystal corresponds to Voigt averaging[2,5,6] and is equivalent to assuming that an applied stress is distributed uniformly in a randomly oriented polycrystal. The degree of validity of this assumption for beryllium is likely to be high since a

* Contribution No. 769. Work was performed in the Ames Laboratory of the U. S. Atomic Energy Commission.

[1] C. Kittel, *Introduction to Solid State Physics* (John Wiley & Sons, Inc., New York, 1953), p. 77.

[2] H. B. Huntington in *Solid State Physics*, edited by F. Seitz and D. Turnbull (Academic Press, Inc., New York, 1958), Vol. 7, p. 213.

[3] S. Eros and J. R. Reitz, J. Appl. Phys. **29**, 683 (1958).

[4] L. Gold, Phys. Rev. **77**, 390 (1950).

[5] W. Voigt, *Lehrbuch der Kristallphysik* (B. G. Teubner, Leipzig, Germany, 1928), p. 956.

[6] A. Reuss, Z. angew. Math. u. Mech. **9**, 49 (1929).

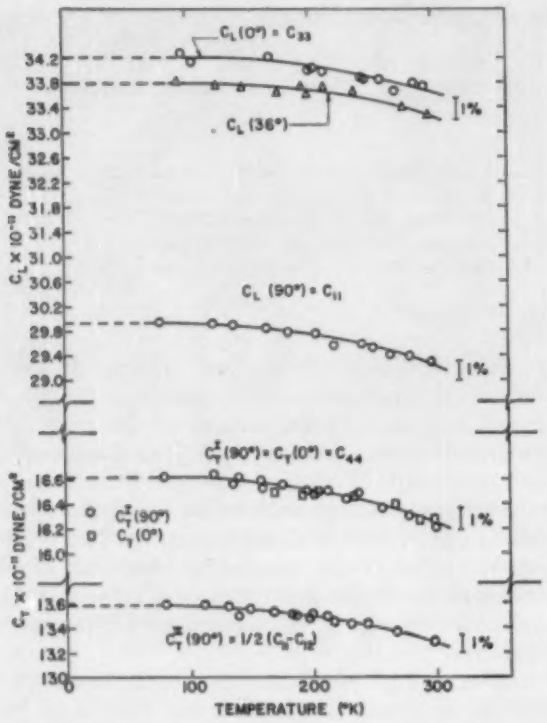

FIG. 1. Adiabatic elastic moduli of single crystalline beryllium as a function of temperature.

comparison of Voigt and Reuss averaging in the discussion section shows excellent agreement. On this basis, the lack of agreement between the present values and Gold's values for C_{12}, C_{13}, and C_{44} is attributable to his assumption that the average velocity of each of the quasi-transverse modes is equal one to the other.

EXPERIMENTAL PROCEDURE AND RESULTS

Two beryllium crystals were used in the present investigation. Both of these crystals were cut from the same large-grained casting of metal. One of these crystals was cut with a rectangular cross section and with the c axis parallel to one edge of the rectangle. Opposite faces were ground closely parallel and worked surface metal was removed by successive etching and polishing. The sample dimensions were 1.2804 ± 0.0003 cm parallel to the c axis and 2.6307 ± 0.0005 cm perpendicular to the c axis. A second crystal was cut with a thickness of 2.5171 ± 0.0005 cm measured in a direction making an angle of 36° with the c axis. Again, the thickness measurement was made after opposite faces had been ground parallel and the worked surface metal had been etched away. All orientations were determined by x-ray diffraction with a precision of 0.5 degree. The purity of the beryllium metal was specified as >99.5%, and spectroscopic analysis showed traces of Al, Ca, Cr, Cu, Fe, Mg, Mn, Ni, and Si.

For any given crystallographic direction three plane elastic wave velocities may be measured, and the pulse echo technique was used to measure these velocities for 10 Mc/sec pulses. The apparatus has previously been described.[7] X-cut quartz transducers were used to initiate longitudinal waves, and Y-cut quartz transducers were used to initiate transverse waves. An elastic constant,

$$C=\rho v^2, \tag{1}$$

may be calculated from the crystal density, ρ, for each velocity, v, corresponding to a given mode and direction of wave propagation. The problem of plane wave propagation in hexagonal crystals has been discussed by Musgrave[8] and by Neighbours.[9] In the hexagonal case the elastic properties are cylindrically symmetric, and the only directional coordinate which must be specified is the angle θ between the direction of the propagation and the c axis. The three constants associated with the three modes of wave propagation at a given angle θ are related to the five independent elastic constants in the following way:

$$C_L=(1/2)[(C_{11}-C_{33})\sin^2\theta+C_{33}+C_{44}+\phi(C_{ij},\theta)], \tag{2a}$$

$$C_T^I=(1/2)[(C_{11}-C_{33})\sin^2\theta+C_{33}+C_{44}-\phi(C_{ij},\theta)], \tag{2b}$$

$$C_T^{II}=(1/2)(C_{11}-C_{12}-2C_{44})\sin^2\theta+C_{44}, \tag{2c}$$

with

$$\phi=\{\sin^4\theta[(C_{11}+C_{33}-2C_{44})^2-4(C_{13}+C_{44})^2]-2\sin^2\theta[(C_{33}-C_{44})(C_{11}+C_{33}-2C_{44})-2(C_{13}+C_{44})^2]+(C_{33}-C_{44})^2\}^{\frac{1}{2}}.$$

In these equations C_L is associated with the longitudinal mode and C_T^I and C_T^{II} are associated with the two transverse modes. The polarization vector for C_T^{II} always has a zero projection on the c axis while the polarization vector for C_T^I has a finite projection on the c axis except in the case that $\sin\theta=0$. The orientation of the first beryllium crystal was such that the waves were propagated as normal modes along simple crystallographic directions, and the following simplifications of the elastic constants were made: parallel to the c axis, $C_L=C_{33}$ and $C_T^I=C_T^{II}=C_{44}$; perpendicular to the c axis, $C_L=C_{11}$, $C_T^I=C_{44}$, and $C_T^{II}=1/2(C_{11}-C_{12})$.

The experimentally determined elastic constants are shown graphically in Fig. 1. The points which are plotted in the graph were calculated using the x-ray density,[10] $\rho=1.8477$ g/cm^3. Corrections for dimensional changes resulting from thermal expansion[11,12] have been neglected since a computation showed that such

[7] Armstrong, Carlson, and Smith, J. Appl. Phys. **30**, 36 (1959).
[8] M. J. P. Musgrave, Proc. Roy. Soc. (London) **A226**, 339 (1954).
[9] J. R. Neighbours, J. Acoust. Soc. Am. **26**, 865 (1954).
[10] J. T. Stacy, "The Reactor Handbook," U. S. Atomic Energy Commission Rept. No. AECD-3647 (1955), Vol. 3, p. 55.
[11] H. D. Erfling, Ann. Physik **34**, 136 (1939).
[12] R. W. Meyerhoff, Iowa State University (1959) (unpublished research).

corrections would in all cases change the elastic constants by 0.1% or less and, hence, would not be significant since the experimental precision in the determination of the elastic constants varies between 0.2% and 0.4%.

The internal consistency of the data may be evaluated by comparing values for C_{44} calculated from velocity measurements for shear waves independently propagated parallel and perpendicular to the c axis. It can be seen from Fig. 1 that values for C_{44} computed from these two independent sets of measurements scatter about the mean line by an amount which is comparable with the estimated precision of measurement.

It may be noted that lack of consistency between values for C_{44} obtained from wave propagation parallel to and perpendicular to the c axis led to the discovery of the presence of residual strains in the "as prepared" condition of the crystals. Annealing of the crystals at 975°C for 70 hr brought the two independent measurements of C_{44} into agreement. This result supports Huntington's view[13] that in materials devoid of permanent polarization or magnetization, first-order torques are absent but, as in the present case, residual strain may modify the elastic parameters in a manner which could be misconstrued to indicate the presence of nonvanishing torques.

After annealing, further checks on consistency were made by measuring the propagation velocities of the two shear-induced modes propagated at room temperature with $\theta=36°$. The value of $C_T^{II}(36°)$ obtained from the direct measurement was 15.10×10^{11} dyne/cm² while a value of 15.23×10^{11} dyne/cm² was computed from Eq. (2c) using the measured values of $1/2(C_{11}-C_{12})$ and C_{44}. The measured value for $C_T^{I}(36°)$ was added to the measured value for $C_L(36°)$ to obtain 48.66×10^{11} dyne/cm²; this value can be compared with a value of 48.41×10^{11} dyne/cm² computed from the sum of Eqs. (2a) and (2b) using values of C_{11}, C_{33}, and C_{44}. In both cases the agreement is satisfactory and the deviation is of the order of the precision of the experimental measurements.

Values for C_{12} and C_{13} were calculated as a function of temperature from interpolated values taken from the smoothed curves shown in Fig. 1. Since Eq. (2a) is quadratic in C_{13}, the stability conditions of Alers and Neighbours[14] were used to decide the correct choice for C_{13}. A tabulation of both the smoothed experimental constants and the calculated constants is shown in Table I. The precision of the experimental measurements reflects an uncertainty of about 0.08×10^{11} dyne/cm² in C_{12} and 0.5×10^{11} dyne/cm² in C_{13}, and in view of the uncertainties the temperature dependence of these quantities indicated in Table I is of questionable significance. This is particularly true of C_{13} since a value of $C_{13}=0.7\times10^{11}$ dyne/cm² was computed from measurement of the quasi-transverse mode, $C_T^{I}(36°)$, at room temperature. The deviation of this value for C_{13} from the value listed in Table I is only marginally greater than the estimated precision of the tabulated value, and the average of the two independent room temperature values is about equal to the tabulated 0°K value.

TABLE I. Adiabatic elastic constants of beryllium in units of 10^{11} dyne/cm².

Temp (°K)	C_{11}	$1/2(C_{11}-C_{12})$	C_{33}	C_{44}	$C_L(36°)$	C_{12}	C_{13}
0	29.94	13.59	34.22	16.62	33.80	2.76	1.1
75	29.94	13.59	34.22	16.62	33.80	2.76	1.1
100	29.92	13.58	34.21	16.62	33.80	2.76	1.1
125	29.90	13.57	34.20	16.61	33.79	2.76	1.2
150	29.87	13.55	34.18	16.58	33.77	2.77	1.2
175	29.81	13.53	34.14	16.55	33.73	2.75	1.2
200	29.75	13.49	34.08	16.50	33.68	2.77	1.3
225	29.64	13.45	34.04	16.46	33.64	2.74	1.3
250	29.53	13.41	33.90	16.40	33.52	2.71	1.4
275	29.39	13.35	33.78	16.33	33.41	2.69	1.4
300	29.23	13.28	33.64	16.25	33.26	2.67	1.4

DISCUSSION

Some measure of the degree of elastic anisotropy of beryllium may be made by comparing the ratios C_{33}/C_{11}, $2C_{44}/(C_{11}-C_{12})$, and C_{12}/C_{13}. At room temperature the values are, respectively, 1.15, 1.22, and 1.9. Averaging of the single crystalline elastic constants in the manner of Voigt[5] and in the manner of Reuss[6] shows excellent agreement which is attributable to the small magnitude of the nondiagonal elements, C_{12} and C_{13}. Values computed by the two methods of averaging are, respectively, compressibility, 8.56 and 8.58×10^{-7} cm²/kg; shear modulus, 21.6 and 21.4×10^{6} psi; Young's modulus, 45.3 and 45.0×10^{6} psi; and Poisson's ratio, 0.05 and 0.05. The averaged values are in good agreement with typical dynamic values for polycrystalline beryllium which are listed by Stacy[10] as $21.2–21.3\times10^{6}$ psi for the shear modulus, $43–45\times10^{6}$ psi for Young's modulus, and 0.01–0.05 for Poisson's ratio. The compressibility values agree closely with the earliest value of 8.55×10^{-7} cm²/kg reported by Bridgman[15] but are in considerably poorer agreement with his more recent value[16] of 7.84×10^{-7} cm²/kg. This latter value was based upon linear compressibility measurements made on single crystals: 2.20×10^{-7} cm²/kg parallel to the c axis and 2.82×10^{-7} cm²/kg perpendicular to the c axis. Corresponding values of 2.67×10^{-7} cm²/kg for the parallel direction and 2.95×10^{-7} cm²/kg for the perpendicular direction were computed from the elastic constant values determined in the present investigation. The disagreement in the perpendicular direction is only 4% but in the parallel direction is of the order of 20%. It may be significant to note that Bridgman observed an appreciable temperature dependence in the linear compressibility parallel to the c axis but did not observe such a

[13] H. B. Huntington, reference 2, pp. 230–233.
[14] G. A. Alers and J. R. Neighbours, J. Appl. Phys. 28, 1514 (1957).
[15] P. W. Bridgman, Proc. Am. Acad. Arts Sci. 62, 224 (1927).
[16] P. W. Bridgman, Proc. Am. Acad. Arts Sci. 68, 27 (1933).

dependence in the perpendicular direction nor in the volume compressibility of the original polycrystalline sample. The present determination does not indicate a strong temperature dependence in any of these three quantities.

The Cauchy relations[17] for a hexagonal crystal with D_{6h} symmetry are $C_{13}=C_{44}$ and $1/2(C_{11}-C_{12})=C_{12}$. Since the atoms in the hcp structure are not at centers of symmetry, beryllium on this basis alone need not satisfy the Cauchy relations. Nonetheless, the degree of failure of beryllium to satisfy the Cauchy relations may reasonably be interpreted to indicate an appreciable contribution from noncentral force interactions in the metal.

Note added in proof.—G. A. Alers and J. R. Neighbours of the Ford Motor Company have recently utilized the values of the elastic constants for beryllium obtained by extrapolation to 0°K to calculate a value for the Debye parameter. They obtained $\theta_0=1462$°K. In comparison the value obtained from low temperature heat capacity measurements [R. W. Hill and P. L. Smith, Phil. Mag. **44**, 636 (1953)] is $\theta_0=1160$°K. The agreement between values for θ_0 determined from elastic constants and from calorimetry is generally poorer for hexagonal metals than for cubic metals, but the discrepancy in the case of beryllium is exceptionally large. An adequate explanation for this discrepancy is not available at the present time.

[17] C. Zener, *Elasticity and Anelasticity of Metals* (University of Chicago Press, Chicago, 1948), p. 19.

ACKNOWLEDGMENTS

The authors wish to express their appreciation to Mr. W. B. Whitten and Mr. J. A. Gjevre for their assistance in the experimental work and to Dr. V. A. Fassel and his group for performing the spectrographic analysis.

JOURNAL OF APPLIED PHYSICS VOLUME 31, NUMBER 1 JANUARY, 1960

Field Dependence of Photoelectric Emission from Tantalum*

J. L. Gumnick† and D. W. Juenker
Department of Physics, University of Notre Dame, Notre Dame, Indiana

(Received July 23, 1959)

An experimental study is made of the photoelectric emission from tantalum as it depends directly on accelerating electric field. Observations cover a range of fields from 0 to 90 kv/cm and illumination wavelengths from 248 to 300 mμ. The results are in agreement with the Fowler photoelectric theory modified by a Schottky lowering of the surface barrier. No evidence is found for a periodic deviation from this regular behavior such as exists in its thermionic counterpart, but experimental conditions may have been inadequate for the observation of such a deviation. A new method of threshold measurement at high fields is described and applied to drawn tantalum filaments of circular cross section. The resulting value is 4.16 ev for freshly flashed specimens and it is suggested that this is slightly greater than the lowest work function present in the surface. A Fowler determination in the same field range yields 4.13 ev. The influence of nonuniformity of the surface work function on the field dependence of photoemission and on threshold measurements is discussed.

INTRODUCTION

RELATIVELY little research has been devoted to examining the influence of an accelerating electric field on the external photoelectric effect. Lawrence and Linford[1] studied the variation in threshold energy for a potassium film deposited on a tungsten filament and found it to be a decrease approximately proportional to the square-root of the applied field, indicating a simple lowering of the mirror-image surface barrier. Guth and Mullin[2] suggested the combination of Schottky's mirror-image theory[3] with the Fowler model[4] for the photoelectric effect as the simplest starting point for the extension to photoemission of their theory for the periodic Schottky deviation. The same basis was used later by Juenker[5] in a revision of that theory. Weber and associates[6] have reported experimental evidence for the second-order periodic deviation from the photoelectric Schottky effect for tungsten; the character of the experimental first-order effect itself was not discussed explicitly or compared with the Fowler-Schottky theory, however.

Herring and Nichols[7] have discussed the usefulness of the photoelectric Schottky effect in the study of

* Partially supported by the U. S. Atomic Energy Commission.
† Presently at RIAS Division of the Martin Company and Loyola College, Baltimore, Maryland.
[1] E. O. Lawrence and L. B. Linford, Phys. Rev. **36**, 482 (1930).
[2] E. Guth and C. J. Mullin, Phys. Rev. **59**, 867 (1941).
[3] W. Schottky, Physik. Z. **15**, 872 (1914).
[4] R. H. Fowler, Phys. Rev. **38**, 45 (1931).
[5] D. W. Juenker, Phys. Rev. **99**, 1155 (1955).
[6] Buder, Ruddick, and Weber, Phys. Rev. **91**, 561 (1953); Stafford, Weber, and Zepf, Bull. Am. Phys. Soc. Ser. II, **3**, 322 (1959).
[7] C. Herring and M. H. Nichols, Revs. Modern Phys. **21**, 185 (1949), Sec. II. 12.

emitters and have referred to some precedent experiments[8] but, in point of fact, direct observation of photoemission as it depends on a continuously varied accelerating field practically never is carried out. In the course of experiments on semiconducting emitters over probably short ranges of low fields, Apker *et al.*[9] and Carroll[10] found the photoemission to vary approximately linearly with the square-root of the field, and Carroll applied an approximate form of the Fowler-Schottky theory to the results in order to evaluate the work function (*sic*) of the emitter. More recently, one of the present authors[11] reported preliminary data taken from polycrystalline tantalum at fields up to about 40 kv/cm; besides displaying an interesting structure at low fields which was interpreted as a patch effect, these data had a high-field shape which agreed qualitatively with Fowler-Schottky theory, and from which presumably the threshold could be determined. These findings encouraged the work reported here, which was designed to study experimentally the photoemission from a clean metal under monochromatic illumination as the collecting field is varied over a broad range.

For the sake of cleanliness, the choice of subject materials was limited to the family of highly refractory metals. In order to enhance the range of illumination wavelengths which could be used, it was desirable to narrow the choice further to the material of lowest threshold energy. In this respect, values given in the literature[12] favored tantalum slightly over molybdenum. Another point favoring tantalum for the present study was its history[11] of displaying an easily recognizable patch effect in thermionic Schottky measurements, which characteristic should also appear in the photoelectric case and eliminate confusion between the basic field dependence of the emission and behavior peculiar to the particular emitter specimen.

The tantalum sample was in the form conventional for thermionic work at equivalent collecting fields, *viz.*, a long filament of circular cross section. A 0.010-inch diameter was chosen in order to have convenient emission yields without sacrificing a wide field range. No effort was made to obtain a single-crystal filament. To benefit from such a refinement would have required a multiplication of the complexity of the experimental structure and a drastic reduction in the currents to be measured. For this exploratory study, it was felt that simplicity of apparatus should take precedence.

EXPERIMENTAL PROCEDURE

Three sample filaments of Fansteel tantalum were studied. Each was mounted in a tube differing only in minor modifications from that shown in Fig. 1. The body of the envelope was 35-mm Pyrex tubing, with a central section, 7.5 cm long, of ultraviolet-transmitting glass (Corning #9741) graded to the Pyrex to act as a window. The inside of this window section, over a length of 6.5 cm, was given a conductive coating to serve as the current collecting element. The coating was effected either with fuming stannic chloride or with Aquadag. In the latter case a small window area was left bare. The ultraviolet transmission, conducting properties, and method of deposition of the stannic chloride coating are discussed elsewhere[13]; in the present application the lightest possible coatings were used. Since the illuminated portion of the filament was only about 2 cm in length there was no need for a system of guard rings to provide a uniform field at the emitting surface. However, to prevent the electrical leakage brought about by evaporation of tantalum from the filament during outgassing, a ring of the conducting coating was applied to the tube interior on either side of the collector. The rings were about 1 cm in breadth and were separated from the collector by about 1 cm; by external connections, they were kept at a potential near that of the collector during measurements. Further to promote a long leakage path between collector and emitter, cowls were blown in the Pyrex envelope on either side of the anode-guard ring system. A movable molybdenum can, 10 cm long, 2.5 cm in diameter, and 0.007 in. in wall thickness, was introduced to act as an evaporation shield during tube processing. The can rested at the bottom of the tube during measurements; the tube was inverted during pumping or flashing of the

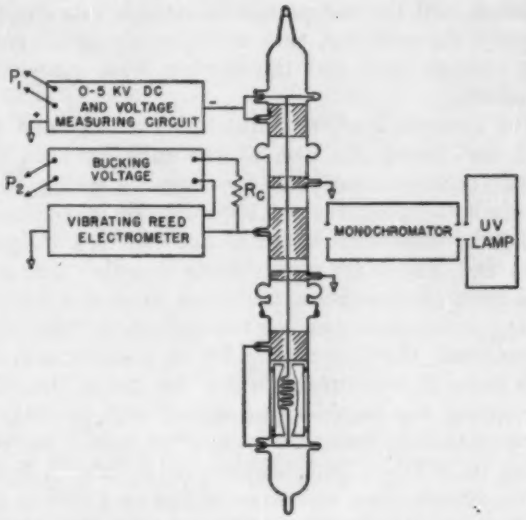

FIG. 1. The experimental phototube in operating position. Its situation with respect to other apparatus is shown schematically. Shaded areas represent internal conducting coatings on the glass tube walls. The molybdenum can at the bottom of the tube is cut away to show the filament spring.

[8] For example, cf. R. C. L. Bosworth, Trans. Faraday Soc. **33**, 590 (1937); A. L. King, Phys. Rev. **53**, 570 (1938).
[9] Apker, Taft, and Dickey, Phys. Rev. **74**, 1462 (1948).
[10] P. E. Carroll, Phys. Rev. **104**, 660 (1956).
[11] D. W. Juenker, J. Appl. Phys. **28**, 1398 (1957).
[12] C. Herring and M. H. Nichols, reference 7, Table IV; G. L. Weissler, *Handbuch der Physik* (Springer-Verlag, Berlin, Germany, 1956), Vol. XXI, p. 304, Table 3.
[13] D. W. Juenker and E. W. Parsons, J. Opt. Soc. Am. **48**, 857 (1958).

filament, and the can permitted to slide into position opposite the collector, thus shielding the anode-guard ring leakage path and the window from evaporated tantalum.

The filament itself was about 43 cm long, and was held taut along the axis of the tube between two cantilever suspension leads by a zig-zag spring. Each cantilever support was a 0.100-in. nickel rod situated on a tube diameter, welded at one end to a tungsten press lead, and at the other resting in a glass side arm. This form of suspension facilitated mounting and reloading operations, since the two ends of the tube could be removed, the filament welded in position, and the ends resealed, without disturbing the rest of the tube. The spring was empirically designed with the help of the recommendations of Tawney.[14] It was a 10-cycle zigzag of 0.007-in. molybdenum sheet, with a 5-mm width, 10-mm span, and inner radius of 1 mm at the bends. After forming, the spring was treated in hydrogen at 900°C for 30–60 min. To prevent field emission from structural projections at the ends of the filament, these were separated from the collector by equipotential regions formed by conducting coatings of 5-cm length within the tube, but connected externally to cathode potential.

The tube had an over-all length of about 80 cm, the drawing in Fig. 1 being somewhat distorted for the sake of clarity. Electrical access to the internal coatings was provided in each case by a 0.015-in. press lead connected with the coatings by silver paste. Two side arms situated just below the lower cowl lead to a getter tube and an ion gauge, not shown in Fig. 1. The getter was a spiral of 0.010-in. molybdenum wire, and the gauge was of the Bayard-Alpert type. The pump lead and seal-off constriction are at the upper end of the tube as it is shown in the figure.

All elementary vacuum processing was carried out on a 3-stage Octoil diffusion pump with a liquid nitrogen trap. Metal parts were outgassed before mounting and again in the assembled phototube. The tantalum filament was heated by the passage of alternating current for repeated short periods until the pressure remained at 10^{-8} mm Hg with the filament at 2550°K. With the tube sealed off from the pump, gettering and ion pumping maintained pressures below 5×10^{-10} mm Hg, except when the filament was heated for extended periods and gas was evolved from the tube walls.

A mercury arc (General Electric UA-2 Uviarc) was used as the light source in the experiment. For stability, it was mounted in a convection-cooled chimney and powered through a Stabiline electronic voltage regulator. A bank of capacitors also was connected across the regulator output to compensate for the lagging load of the lamp ballast. The intensity of the lamp output under these conditions was stable to within 0.2%. A Gaertner Model L-234-150 quartz monochromator was

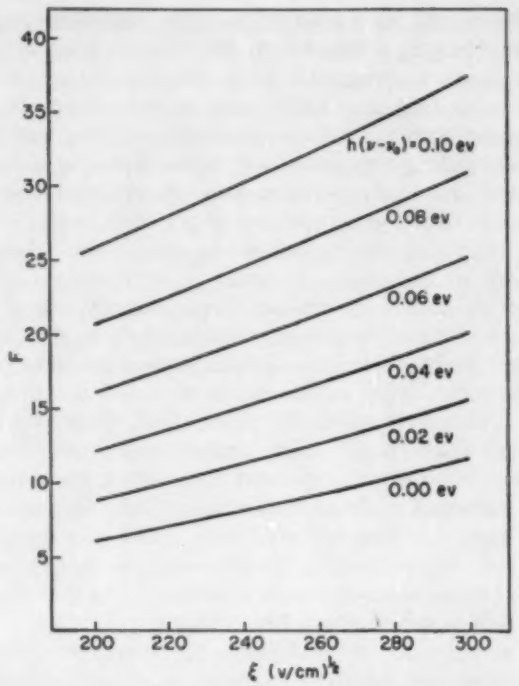

FIG. 2. Some typical plots of the theoretical Fowler-Schottky function F, or photocurrent in arbitrary units, *versus* the square-root of field.

used to purify the illumination. The normal slit opening was 0.2 mm as a compromise between spectral purity and useful output intensity. The exit slit was situated as close to the phototube as possible without actual contact, hence about 2 cm from the cathode; entrance slit and lamp were separated by about 5 cm. Calibrations of intensity *vs* wavelength were carried out with a Farrand-Hornig compensated vacuum thermocouple.

The electrical circuitry for the photoelectric measurements was essentially identical with that used by Munick, LaBerge, and Coomes[15] in thermionic work, except of course for the absence of a special heating supply for the cathode. Collecting fields were supplied by a full wave rectifier with a bank of 48 voltage regulator (VR 105) or voltage reference (5651) tubes in series across the output. Coarse adjustment of the applied voltage was achieved at the high (negative) voltage end by a simple arrangement of a probe and insulated porcelain switches with which positions along the VR-tube bank could be selected. Fine adjustment was provided for at the ground (positive) side by means of a 135-v battery of dry cells across a voltage divider in series with the VR-tubes. A fixed fraction of the total applied voltage was delivered by another voltage divider to the potentiometer P_1 for measurement. The voltage source was connected between the cathode of the phototube and either ground or the low-impedance terminal of the null-reading electrometer; since only the high-field measurements required quantitative ac-

[14] G. L. Tawney, Rev. Sci. Instr. **10**, 152 (1939).

[15] Munick, LaBerge, and Coomes, Phys. Rev. **80**, 887 (1950).

curacy, the ground connection was used normally, the potential difference between ground and the collector and the contact potential difference between collector and emitter being considered negligible. Emission current was measured by passing it through a high resistance $R_e(10^{10}$ ohms), the voltage drop in which was bucked out by a continuously variable low-voltage source. The null adjustment was determined with a Cary vibrating reed electrometer and the bucking voltage, corresponding to the product of the emission current and R_e, was measured with a potentiometer P_2.

All data were taken with the tube and the preamplifier unit of the vibrating reed enclosed in a copper shield box, into which the exit slit structure of the monochromator was intruded. Tube and monochromator were adjusted so that an approximate 2 cm of the filament was bathed in the desired illumination over half its circumference. The applied voltage was varied in steps over the range of interest, and the potentiometer readings P_1 and P_2 were recorded. The reading P_1 was translated into terms of the field at the emitter by application of the numerical factors appropriate for the geometry of the tube and the characteristics of the voltage divider; in the case of the tube geometry used here, the field in v/cm is approximately 16 times the applied voltage. The reading at P_2 is the bucking voltage in millivolts; where this reading occurs, as in Fig. 3, it can be converted approximately to emission current in amperes by multiplying by 10^{-13}. Current levels were in the orders 10^{-12} and 10^{-13} amp.

DATA PROCESSING

The simple theory for the photoelectric Schottky effect has been discussed elsewhere.[2,11] A uniform metal surface of zero-field threshold $h\nu_0$, subjected to illumination of photon energy $h\nu$ and to an accelerating electric field E, is expected to yield photoelectric emission current in the amount

$$I=B(kT)^2F(\delta) \tag{1}$$

where for a given metal and the range of illumination frequencies of present interest B may be considered independent of $h\nu$ and E, and where F is a universal function[4] of the quantity

$$\delta=[h(\nu-\nu_0)+e^{\frac{1}{2}}E^{\frac{1}{2}}]/kT$$

here written in cgs units. For the useful case $\delta \gtrsim 0$, F has the form

$$F(\delta)=\pi^2/6+\delta^2/2+\sum_{n=1}^{\infty}(-1)^n e^{-n\delta}/n^2. \tag{2}$$

This function has been tabulated[11] for $T=293°$K, values of $h(\nu-\nu_0)$ from 0 to 1 ev in 0.02-ev steps, and values of $E^{\frac{1}{2}}$ from 0 to 500 $(\text{v/cm})^{\frac{1}{2}}$ in steps of 20 $(\text{v/cm})^{\frac{1}{2}}$. Typical plots are shown in Fig. 2 for a field range applicable to the present experiment. The curves are nearly linear, but have a slight upward curvature.

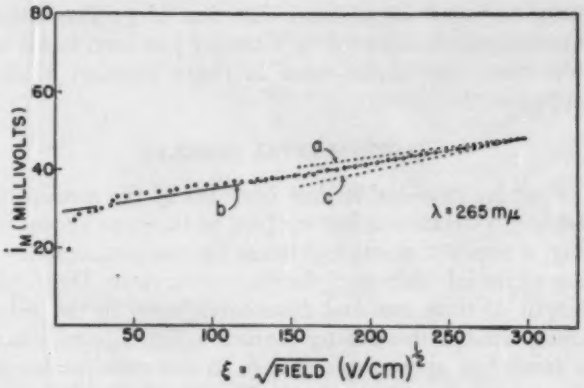

FIG. 3. A photoelectric Schottky plot taken from slightly contaminated tantalum to illustrate general features of the field dependence of the photocurrent (i_m) and the curve-fitting method used to determine the threshold. The circles are data points, and the solid and dashed curves are theoretical lines normalized to the data at $\xi=300$ $(\text{v/cm})^{\frac{1}{2}}$. Curves a, b, and c are for $h(\nu-\nu_0)=0.46$, 0.38, and 0.32 ev, respectively.

The average slopes are greater for greater $h(\nu-\nu_0)$, but normalized to a common value at some value of the field, the curves appear less steep for illumination farther from the threshold. In Fig. 3, for example, curves a, b, and c represent the function F for $h(\nu-\nu_0)=0.46$, 0.38, and 0.32 ev, respectively, all adjusted to the same value at $\xi=E^{\frac{1}{2}}=300$ $(\text{v/cm})^{\frac{1}{2}}$.

This dependence of the character of the Schottky curves on $h(\nu-\nu_0)$ should in theory permit the measurement of the threshold by comparing an experimental plot with curves such as those in Fig. 2. In practice, however, Schottky plots of appreciable length are incompatible with uniform single crystal surfaces, and the result of such a comparison is an "apparent" threshold which will be symbolized by $h\nu_0^{**}$, to correspond to the nomenclature adopted by Herring and Nichols,[16] Smith,[17] and others for the measured value of the thermionic work function for a nonuniform surface. Thus, in Fig. 3, the theoretical curve of closest fit to the data at high fields is that for $h(\nu-\nu_0)=0.38$ ev; the illumination energy used to obtain the data was $h\nu=4.68$ ev; the apparent threshold is, therefore, $h\nu_0^{**}=4.30$ ev.

Over an abbreviated range of fields, the photocurrent varies in nearly linear fashion with $\xi=E^{\frac{1}{2}}$. It proved convenient to fit a least-squares straight line to the data from a given experimental run lying between, say, $\xi=200$ and 300 $(\text{v/cm})^{\frac{1}{2}}$. The tabulated values of F at 300 $(\text{v/cm})^{\frac{1}{2}}$ for various values of $h(\nu-\nu_0)$ were normalized to the ordinate of the fitted line at 300 $(\text{v/cm})^{\frac{1}{2}}$. The normalized values of F at 200 $(\text{v/cm})^{\frac{1}{2}}$ were then compared with the ordinate of the fitted line at the same field. Only a few such trial-and-error steps are necessary to establish the most appropriate $h(\nu-\nu_0)$ to within 0.02 ev. This procedure is not equivalent to ap-

[16] See reference 7, Sec. II. 7.
[17] G. F. Smith, Phys. Rev. 94, 295 (1954).

proximating F as a linear function of ξ. The latter approximation, adopted by Carroll,[10] has been found to introduce appreciable error in the evaluation of the apparent threshold.

EXPERIMENTAL RESULTS

Due to the sizeable time constant of the measuring circuit, a detailed Schottky plot of the type shown in Fig. 3 required about five hours for completion following an initial flashing of the emitter filament. Over this length of time, residual adsorbable gases in the tube contaminated the emitter surface sufficiently to effect a small but appreciable change in the emission level. Comprehensive plots of this sort usually were made about a day after cleanup, and then only to map the general features of the field dependence and to note the approximate location of irregularities due to patch effects. Since such irregularities were not noticeable above about $\xi=150$ (v/cm)$^{\frac{1}{2}}$ in any of the three experimental diodes, the region $175<\xi<285$ (v/cm)$^{\frac{1}{2}}$ was singled out for closer examination. Following flashing of the emitter at 2550°K, data points in this region were obtained in random order over about one hour, and these were processed in the manner described in the previous section. The results from tube No. 1 for four illumination wavelengths are shown in Fig. 4. Despite an expected possible error of 0.02 ev for the shorter wavelengths, the results from tubes No. 2 and No. 3 yielded identical values of the apparent threshold, ranging from 4.24 ev for $\lambda=255$ mμ down to 4.16 ev for $\lambda=297$ mμ. For the sake of graphical convenience, a semilogarithmic scale was used for Fig. 4, with the experimental data normalized to the tabulated values of F.

In the course of the high field measurements, no evidence was found for periodic deviations from the Schottky curve. Whatever deviations were found seemed to be random, although estimated experimental precision should be adequate to distinguish the periodicities.[5] However, tantalum has proved inferior to tungsten and molybdenum as a subject for thermionic Schottky deviation studies,[11,15] possibly because of a proneness to contamination or surface disorder. Therefore, the present lack of evidence is not conclusive.

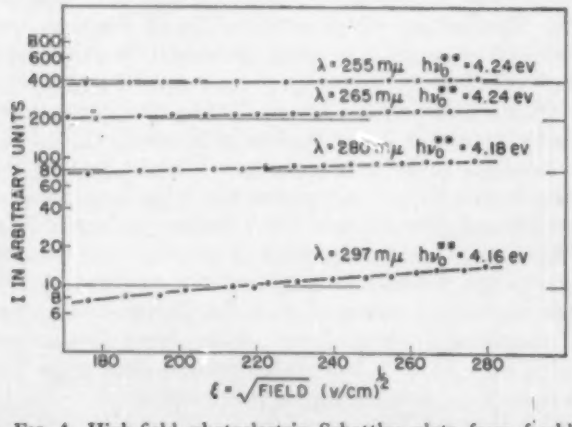

FIG. 4. High-field photoelectric Schottky plots from freshly flashed tantalum (Tube No. 1). The lines represent fitted theoretical curves from which were found the apparent threshold values $h\nu_0^{**}$. Note the semilogarithmic scale.

In tube No. 3, an independent threshold determination was made by the Fowler method with the emitter subjected to an accelerating field of 40 kv/cm ($\xi=200$). The data are shown in Fig. 5. No single theoretical Fowler curve could be made to match the data over the entire spectral range. The two dashed curves shown are those which gave the best fit at the two extremities. A vertical index line represents the position of the origin ($h\nu_0^{**}=h\nu+e^{\frac{1}{2}}E^{\frac{1}{2}}$) for each of the theoretical curves. Since these curves already contain the correction for accelerating field, the values of $h\nu_0^{**}$ obtained from the Fowler plots, like those from the Schottky plots, are to be understood as having been adjusted to zero field. In good agreement with the Schottky measurements, the

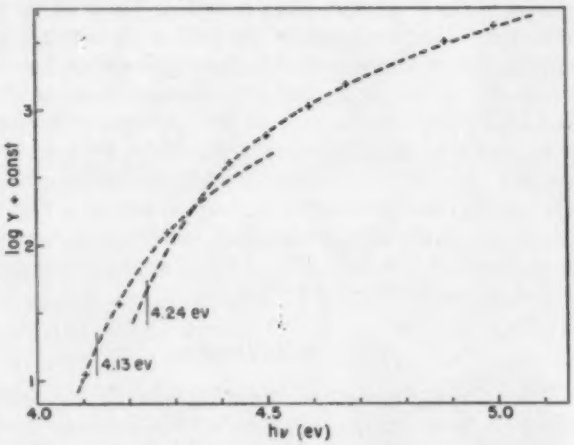

FIG. 5. Fowler plot for clean tantalum at 293°K and a field of 40 kv/cm. Y is the photoelectric yield in electrons per photon (arbitrary scale). The dashed curves are the Fowler function corrected for field and suitably displaced to fit the data at the extremes of energy. The number on each curve is the resulting apparent threshold.

extreme values for $h\nu_0^{**}$ are 4.24 ev for illumination much more energetic than the threshold and 4.13 ev close to the threshold.

To illustrate the sensitivity of the Schottky threshold determination and the effect of surface contamination on the photoemission from tantalum, short Schottky plots are shown in Fig. 6. These data were taken in succession at times 1, 2, 10, 20, and 100 hours, respectively, after the emitter filament had been flashed at 2550°K. It is seen that $h\nu_0^{**}$ rises from 4.24 ev to a fairly stable condition near 4.30 ev in about ten hours. This probably corresponds to the development of something like a monolayer coverage of gaseous contamination on the more active exposed crystal planes. All five of the plots in Fig. 6 were made with illumination of wavelength 265 mμ.

Some examination of the interesting patch irregu-

larities at low fields was carried out. It is not surprising that this structure varied from specimen to specimen, since one could not hope to reproduce the surface nonuniformities which bring it about. At least one major sigmoidal patch break seems to occur in the vicinity of $\xi=50$ (v/cm)$^{\frac{1}{2}}$ for each of the specimens studied in the present work. This break appears in Fig. 3. Other patch anomalies of lesser magnitude but similar sigmoidal shape were observed throughout the region $5<\xi<150$ (v/cm)$^{\frac{1}{2}}$. The percentage current increase at each break was found to be less pronounced for more energetic illumination, hence the breaks are more clearly observed closer to the threshold. Under such conditions, the emission currents were so minute that a detailed investigation of the fine structure occupied a time comparable to that needed for the accumulation of appreciable contamination and the consequent alteration of the patch behavior itself. As a result, it was impossible to verify unambiguously a secondary observation, that some of the minor patch breaks disappeared completely as the illumination wavelength was increased toward the long-wave limit. Such an effect would not be contradictory to the previous statement that the breaks become stronger with increasing wavelength.

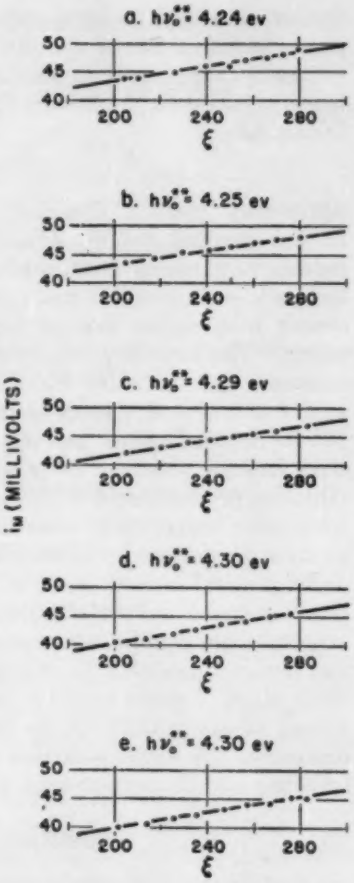

FIG. 6. High-field photoelectric Schottky plots showing the progress of contamination of a tantalum specimen by residual adsorbable gases. Plots *a*, *b*, *c*, *d*, and *e* were taken 1, 2, 10, 20, and 100 hours after flashing the filament at 2550° K. All measurements were made with an illumination wavelength of 265 mμ.

INTERPRETATION OF RESULTS

A proper interpretation of the apparent threshold values obtained here for tantalum requires a consideration of the photoemission from any nonuniform metal surface. Such a surface consists of a collection of subareas, or patches, of different work functions, a configuration whose behavior has been described amply by Herring and Nichols.[7] The point to be stressed is that any threshold determination by a "saturation" current technique such as the Fowler isotherm, the DuBridge isochromat, or the method introduced in the present work, yields a result which is a more or less complicated average depending on the sizes, shapes, work functions, photoelectric efficiencies, and arrangement of the various patches; moreover, this weighted average varies as the illumination wavelength and applied field are altered. The situation is not completely hopeless, however. Near the long-wave limit, where the accuracy is greatest for all three methods of threshold measurement, the emission from high work function patches is minimized, and a less ambiguous result emerges. With respect to the average $\bar{E}_p$ of the local interpatch fields on which the applied field E is superimposed, two cases can be distinguished as the illumination wavelength is increased toward its limit:

Case 1: When $E\gg\bar{E}_p$, the apparent threshold should approach that of the patch of lowest work function;

$$h\nu_0^{**}\rightarrow e\phi_{i\,\min}.$$

Case 2: When $E\ll\bar{E}_p$, the apparent threshold should approach the average work function of the illuminated surface;

$$h\nu_0^{**}\rightarrow e\bar{\phi}\equiv e\sum f_i\phi_i.$$

When the patches are numerous and varied in nature, E_p varies over the surface from zero to very large values. At first, one hesitates at accepting the validity of the inequalities characterizing the two cases cited above for any real surface. However, there is an upper limit to the work function difference between nearby patches and the regions of very high E_p are bound to be localized. Therefore, one can suppose that by applying a moderate collecting field to a coarse-grained surface it is possible to have the Case 1 inequality prevail over all but a negligible portion of the surface. This is taken to be the state of affairs in the region of fields at which threshold determinations were made in the present work. As such, the lowest observed threshold value from Schottky measurements, *viz.*, 4.16 ev, should be slightly greater than the lowest work function represented as an appreciable fraction f_i of the illuminated surface; the value 4.13 ev yielded by the Fowler method probably is an even better measure of this minimum. Since the specimens studied were round drawn filaments, and since tantalum and tungsten show qualitatively similar emission characteristics with respect to crystalline di-

rection, the regions in question are possibly (*hhk*) planes on either side of the (001).[17]‡

Case 2 collecting fields should be harder to achieve unless patches of a single work function ϕ_j predominate. In this case

$$h\nu_0^{**} \rightarrow e\bar{\phi} \simeq e\phi_j.$$

Apparently such a situation occurred in tungsten ribbons investigated by Apker, Taft, and Dickey[18]; patches neighboring (100) predominated, and the photoelectric work function was found to be 4.49 ev, consistent with values derived from thermionic experiments.[17] The same is probably true of the early measurements on tantalum by Cardwell.[19] The latter's values of 4.13 and 4.16 ev were obtained by low-field Fowler determinations, and in the light of the present work indicate that the lower work function planes of tantalum predominated in the surfaces of his well-aged specimen ribbons. Aside from scattered instances such as these, photoelectric threshold measurements for nonuniform metal surfaces made in the past with "saturation" emission currents share an ambiguity which cannot be resolved by refinement of vacuum technique and surface cleanliness. To this ambiguity can be traced much of the diversity extant in tabulated work function values, to say nothing of the long-standing confusion concerning the identity or lack of same between photoelectric and thermionic work functions.

SUMMARY

In confirmation of previous evidence, present results show that the photoemission from a metal surface varies with applied accelerating field in complete agreement with the simple theory compounded of the Fowler photoelectric model and a Schottky lowering of the surface barrier. Furthermore, the use of the photoelectric Schottky plot to evaluate the photoelectric threshold is shown to be a legitimate substitute for the more conventional Fowler determination made at comparable fields. Although this new method requires an uncommon phototube geometry, it circumvents the difficulties of light calibration and temperature measurement encountered in the Fowler and DuBridge methods, and uses a filament emitter form which in some instances lends itself to vacuum processing and ease of handling. It is understood that with such a cylindrical emitter the angle of incidence of the excitation varied between 0 and 90° in the present experiment. While this may be equivalent practically to a varying radiant flux and a simultaneously varying photo-sensitivity over the illuminated surface, it has no influence on the interpretation of the results.

The apparent threshold for photoelectric emission from tantalum has been obtained by this method at collecting fields of the "Case 1" type described by Herring and Nichols. The result varied with illumination frequency, the lowest value, 4.16 ev, being obtained for the longest usable wavelength. The lowest work function represented in the surface must be somewhat less than 4.16 ev, probably closer to the value 4.13 ev found by a Fowler plot, also at Case 1 fields. It is felt that the high-field measurement yields a more unequivocal answer than does the conventional low-field approach.

Patch anomalies in the low-field behavior of emission current become increasingly complex with decreasing field, and in general vary from specimen to specimen. One such anomaly of sigmoidal shape was particularly noticeable in all three tantalum wires examined. Although not exactly at the same place for all specimens, it always occurred in the 1-kv/cm field range. No effort was made to establish its origin.

ACKNOWLEDGMENTS

We are indebted to Mr. R. C. Jaklevic for checking the high-field measurements described here, and for taking the data necessary for the Fowler plot, and to Mr. E. W. Parsons for his invaluable technical assistance.

‡ Unfortunately, the major dissimilarities between W and Mo on the one hand, and Ta and Nb on the other, seem to lie in the very region proposed here; cf. R. H. Good, Jr., and E. W. Muller, *Handbuch der Physik* (Springer-Verlag, Berlin, Germany, 1956), Vol. XXI, p. 208.

[18] Apker, Taft, and Dickey, Phys. Rev. 73, 46 (1948).

[19] A, B. Cardwell, Phys. Rev. 38, 2041 (1931); 47, 628 (1935).

Shapes of Etch Hillocks and Pits and Their Correlation with Measured Etch Rates

B. A. IRVING
Research Laboratory, Associated Electrical Industries, Ltd., Aldermaston Court, Aldermaston, Berkshire, England
(Received June 5, 1959)

The factors which govern the occurrence and stability of etch hillocks and pits have been examined. Batterman's original analysis has been reconsidered and extended to account for all the crystallographic facets of etch hillocks and pits produced by a dilute hydrogen peroxide-hydrofluoric acid etchant on germanium surfaces. The treatment should be valid for other etchants and materials but suitable data are not available.

THE high purity and perfection of semiconductor crystals make them especially suitable for studies of the etching process. Batterman, in one such study[1] observed etch hillocks on germanium surfaces attacked by a dilute mixture of hydrogen peroxide and hydrofluoric acid (superoxol etchant) and measured etch rates for a range of surface orientations. He derived two conditions, one from the geometry of etch hillocks and the other from the etch rate-curvature reciprocity relation which are necessary for hillock stability. One set of observed hillock planes, {322}, fulfill these conditions but others, {310}, do not. The present work gives a further analysis of Batterman's data and presents a third condition for etch hillock stability. All the etch hillock planes observed by Batterman conform to the new set of conditions, which also satisfactorily explain the occurrence and shape of dislocation etch pits. The conditions enable the stable hillock faces to be predicted from a knowledge of the etch rate distribution. Detailed molecular etching mechanisms are not considered but as in Batterman's work, the etch rate is regarded as a vector property of a macroscopic surface.

Batterman's conditions are that a hillock plane h, inclined at an angle θ to a ground plane g, must be such that $R_h \sec\theta_{(h,g)}$ is less than R_g (R is the etch rate of the surface indicated by subscript), and that no other plane between g and h has an etch rate lower than h. The latter is a result of the etch rate-curvature reciprocity condition, expressed in Batterman's words, "Convex surfaces will, upon dissolution, limit on fast etching planes, while slow etching planes will bound on concave surfaces." The application of this relation to the intersections of the hillock faces themselves has enabled the other stability condition to be derived.

Only the etch rates of planes about the zone axis of the intersection need be considered in applying the reciprocity condition to an intersection. These planes can be thought of as exposed in the small region of curvature between one face and the next, and will be developed if of suitable etch rate.

ETCH HILLOCKS

For hillocks on (110) almost any other plane obeys the reciprocity condition because (110) has a maximum etch rate. However, the $R_h \sec\theta_{(h,g)} < R_g$ condition restricts considerably those surfaces which could be possible hillock faces.

If the intersection between the (322) and (232) faces of a hillock on the (110) surface of germanium is considered it is seen from Fig. 1, the section of the etch rate contour projection about the [$\bar{2}25$] axis [the intersection of (322) and (232)], that the (322) and (232) planes have maximum etch rates about the intersection, and obey the $R\sec\theta$ relation also indicated on the figure.

Therefore this is a stable convex intersection, in the same sense that Batterman showed the concave intersection between (322) and (110) to be stable.

If, however, the intersection between (322) and (32$\bar{2}$) is treated in a similar way, as in Fig. 2, the (322) and (32$\bar{2}$) planes now have minimum etch rates with a maximum, at (320) midway between.

This intersection is, therefore, unstable (and not observed). From the symmetry it is clear that the intersection will be replaced by a plane between (100) and (110). The (320) itself does not conform to the secθ

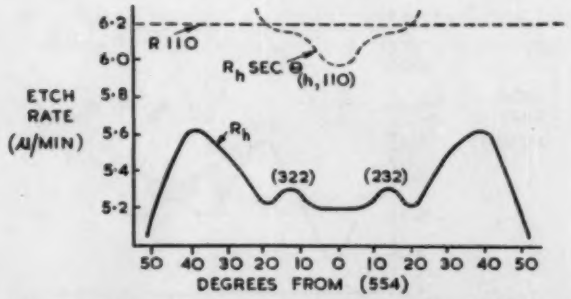

FIG. 1. Section of etch rate contour projection about [$\bar{2}25$] axis.

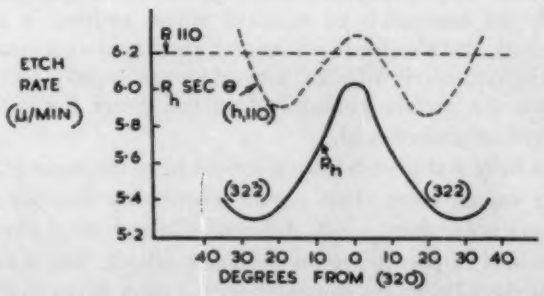

FIG. 2. Section of etch rate contour projection about [$\bar{2}30$] axis.

[1] B. W. Batterman, J. Appl. Phys. 28, 1236–1241 (1957).

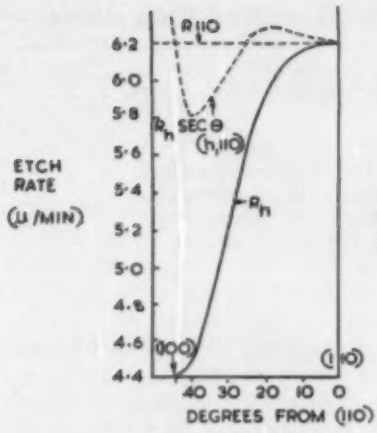

FIG. 3. Section of etch rate contour projection about [001] axis.

condition and therefore cannot form a stable etch hillock plane. The section of the etch rate contour projection between (100) and (110) is given, together with the secθ relation, in Fig. 3. This shows that only surfaces within about 20° of (100) could form a stable hillock face. These planes also obey the concave reciprocity condition, the etch rate curve rising smoothly to (110).

The introduction of such a plane within 20° of (100) introduces also the intersections between it and the {322} faces of the etch hillock. These intersections must also obey the reciprocity condition for convex surfaces. The section of the etch rate contour projection about $[2\bar{6}3]$, the intersection between (310) and (322), is shown in Fig. 4.

There are two maxima within the range of surfaces permitted by the $R_h\sec\theta$ condition and these correspond to (310) and (322) planes. Hence this is a stable intersection.

Examination of the etch rate contour projection shows that orientations closer to (100) do not give the double maxima and hence cannot form stable intersections with (322). [The section between (100) and (322) is shown in Fig. 10 of Batterman's paper.]

The apex of an etch hillock is also a convex region, and if the reciprocity relation is applied it is seen that the etch rate here should be a minimum (corresponding to corners of dissolution figures). For etch hillocks on (110) surface the apex lies in a *maximum* etch rate direction. This accounts for etch hillocks being formed only on contaminated surfaces where etching is inhibited, and also for the "complex and degenerate forms of the symmetric hillocks" formed by prolonged etching, when the surface contamination has either been dissolved or undermined.

A fully stable etch hillock should have the same etch rate on all faces. This occurs where only one set of planes is involved. Slight differences in etch rate, where two sets of planes are on the same hillock, will mean that the hillocks are elongated with a ridge between the faster etching planes.

PREDICTION OF ETCH HILLOCK PLANES

The above explanation has served to justify the {310} hillock faces. It has shown that planes not at saddle points on the etch rate contour projection can be expected to form the sides of etch hillocks. There remains the problem of how to decide, given an etch rate contour projection, what hillock faces will be stable on any given surface.

Batterman's data are shown in Fig. 5 replotted on (110) projection. Contours of the $R_{(110)}\cos\theta_{(h,110)}$ surface on this plot are circles centered on (110). These two etch rate surfaces intersect along the dotted lines. Within the center shaded region the etch rate surface is above the $R_{(110)}\cos\theta$ surface. Beyond this in the unshaded area the etch rate surface is below the $R_{(110)}\cos\theta$ surface and all stable hillock planes must lie within this region. It is seen that hillock faces {322} and {310} do not have maximum etch rates within this region as might be at first supposed. The (321) and (231) surfaces, for instance, have higher etch rates than {310} and {322} but are not at maxima along the zone circle defined by these planes. The intersection between (321) and (231) would be represented by this zone circle which traverses the prohibited $R\sec\theta > R_g$ region. The intersection is thus unstable. Stable intersections are represented by great circles completely outside the prohibited region. Hillock planes intersect two other faces apart from the ground plane and must lie at the point of intersection of two suitable great circles. This point of intersection must also be an etch rate maximum along both zone circles. The $[\bar{2}25]$ zone has etch rate maxima at (322) and (232) (Fig. 1); the $[2\bar{6}3]$ zone at (310) and (322) (Fig. 4). The plane common to both zones is (322), the hillock face. Similarly the $[\bar{2}63]$ zone and $[2\bar{6}3]$ zone have the (310) plane in common and it has maximum etch rate, and forms a stable hillock face. It is seen therefore that stable hillock planes occur where great circles intersect at their points of maximum etch rate, and lie within the $R_h < R_g\cos\theta$ region between the intersections, with no plane of lower etch rate between the point of intersection and the ground plane. These positions may be approximately described on a geographical analogy as the position on a spur below

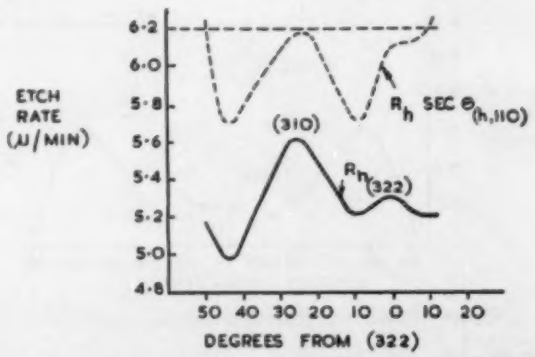

FIG. 4. Section of etch rate contour projection about $[2\bar{6}3]$ axis.

the $R\sec\theta = R_g$ "snow" line where an uninterrupted view to the corresponding position on the next spur may be obtained.

ETCH PITS

Certain of the above deductions can be applied, conversely, to etch pits. For a pit facet, f, the geometry of the intersection with the "ground" surface, g, indicates that $R_f \sec\theta_{(f,g)}$ must be greater than R_g. There must not be, because of the reciprocity relation, a plane between g, and f, with higher etch rate than f. Similarly the intersection of the facets within the pit must be directions of maximum etch rate.

These conditions are met by surfaces close to the minimum etch rate planes {111} and {100}. The pit facets will be comparatively slow etching planes and the intersections lie in directions of maximum etch rate. The base of a pit is also concave and should limit parallel to the slow etching ground planes. However, a dislocation can increase the local etching rate and prevent this condition applying. The shape of such a pit will depend on the enhancement of etch rate due to the dislocation and the shape of the etch rate contour projection. For a pit with flat facets, f, at angle θ to the ground plane, the apex of the pit etches at a rate $R_f \sec\theta$. If the dislocation is normal to the surface this could be described as a dislocation etch rate, but it is a characteristic of the etch rate distribution rather than of a dislocation.

On a surface s, at angle ϕ to a minimum etch rate plane, say (111), such that $R_s = R_{(111)}\sec\phi$, a pit once formed would neither enlarge nor diminish because (111) would be a stable facet of such a pit. Hence etch pits would be expected only on surfaces between (111) and s where a pit once formed could grow to observable size (and similarly for other minimum etch rate planes). This means that dislocations may locally affect the etch rate and yet not form dislocation etch pits.

In pits or hollows the reciprocity relation, as stated above, means that slow etching planes are developed. The etched spherical hollow pictured in Fig. 12 of Batterman's paper has not only {100} and {111} planes developing but has pairs of planes close to the {110} positions. This implies that there are two local minima of etch rate in the {110} region, toward {111} with corresponding maxima at the intersections. These may be too small to be shown on the etch rate contour projection but the maxima should lie somewhere near the {441} positions. Further etching of the hollow would be expected to reduce the size of these facets which would finally disappear as the {100} and {111} surfaces grow and apices are formed at the {110} positions. (The surface finally formed will be the inverse of the dodecahedron formed from dissolution of a sphere.)

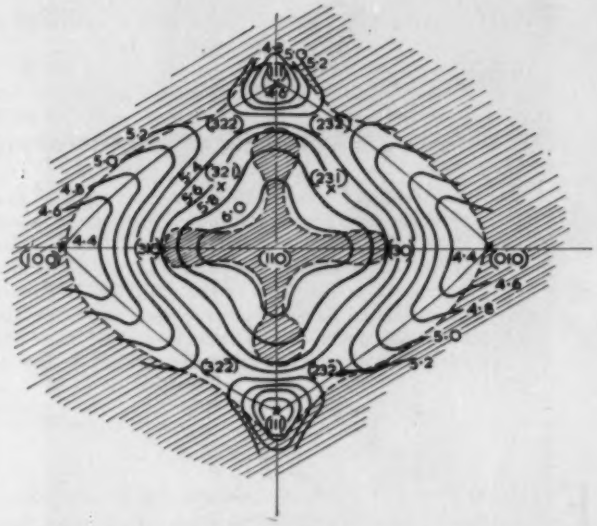

FIG. 5. Etch rate (μ/min) (110) projection Batterman's data $R\sec\theta \geq 6.2$ in shaded areas.

Dislocation etch pits are not, however, expected to form similar hollows. Although {100} surfaces have a minimum etch rate and obey the $\sec\theta$ condition they cannot form pit facets and stable intersections with {111} because there is a higher etch rate between these two planes. This higher etch rate is at {322} and these become the pit facets.

It is thus seen that the shapes and occurrence of etch hillocks and pits can be correlated with the etch rate measurements by the application of conditions derived from the geometry of the feature and the limiting etch plane curvature reciprocity relation.

ACKNOWLEDGMENTS

The author wishes to thank Dr. G. A. Geach for his interest in the work and Dr. T. E. Allibone, F.R.S., Director of this Laboratory, for permission to publish this paper.

Interferometric Determination of Twist and Polytype in Silicon Carbide Whiskers*

D. R. HAMILTON
Solid State Physics Department, Westinghouse Research Laboratories, Beulah Road, Churchill Borough, Pittsburgh 35, Pennsylvania

(Received June 25, 1959)

Whiskers of hexagonal SiC have been prepared in a graphite tube furnace. They are grown by sublimation of SiC in hydrogen, depositing at temperatures about 2000°C as acicular crystals of hexagonal section, with [0001] along the whisker length. The {1$\bar{1}$00} faces have been examined using optical interference techniques, and are found to exhibit a twist. The Eshelby formula for twist caused by a screw dislocation has been used to estimate the strength of the associated Burgers vector. It is found that, within the experimental error, the estimated Burgers vector is equal to, or is an integral multiple of the unit cell of the SiC polytype 4H. It is thus concluded that these twisted whiskers grow by means of a screw dislocation of integral strength parallel to the axis, and that they are of polytype 4H.

I. INTRODUCTION

ESHELBY[1] and Mann[2] have shown that a screw dislocation has a metastable position at or near the axis of a whisker, and that the presence of such a screw dislocation will introduce a shear stress, causing the whisker to develop a twist about its axis. These observations have prompted a number of investigators to look for evidence of axial screw dislocations in otherwise relatively perfect whisker structures. Webb[3] *et al.* have examined whiskers of a large number of materials for the predicted twist. In sapphire, Al_2O_3, they found twists, and were able to estimate the strength of the Burgers vector. In every instance, the vector was equal to, or a multiple of, the unit cell of sapphire, 13 A. Among the metals examined, only palladium and tin whiskers exhibited twist. Correlation was found between the unit cell of palladium and the Burgers vector, but only a residual twist was detected in tin, confirming earlier results of Trueting.[4] This result was thought to be caused by an off-axis screw of unit strength. Gomer[5] has shown, in a series of elegant experiments with a field emission microscope, that mercury whiskers contain an axial screw dislocation. Amelinckx[6] has demonstrated the presence of screw dislocations in sodium chloride whiskers grown from solution, using a gold decoration technique.

The present work is concerned with the twist of whiskers of silicon carbide. It will be shown that the twist is probably caused by a screw dislocation of strength equal to, or, in one instance, an integral multiple of the unit cell of polytype 4*H* SiC.

* This work was supported in part by the Air Force Cambridge Research Center, Bedford, Massachusetts, contract AF 19(604)-2174.

[1] J. D. Eshelby, J. Appl. Phys. **24**, 176 (1952); Phil. Mag. **3**, 440 (1958).

[2] E. H. Mann, Proc. Roy. Soc. (London) **A199**, 376 (1949).

[3] Webb, Dragsdorf, and Forgeng, Phys. Rev. **108**, 498 (1957); W. W. Webb and W. D. Forgeng, J. Appl. Phys. **29**, 817 (1958); W. W. Webb, *Growth and Perfection of Crystals* (John Wiley & Sons, Inc., New York, 1958), referred to as G.P.C. hereafter.

[4] R. G. Treuting, Acta Met. **5**, 173 (1957).

[5] R. Gomer, J. Chem. Phys. **28**, 457 (1958).

[6] S. Amelinckx, G.P.C.

II. PREPARATION AND MORPHOLOGY OF SILICON CARBIDE WHISKERS

Whiskers of silicon carbide were first grown accidentally in a graphite tube furnace used for the preparation of pure silicon carbide.[7] In this furnace, a charge of SiC is heated in graphite crucibles to temperatures about 2500°C in an argon or hydrogen atmosphere. Within the crucible grow thin hexagonal plates of SiC. It has been shown[7] that these plates are formed in a shallow temperature gradient, under conditions of low supersaturation. Such crystals grow to many square millimeters area in a five hour period.

During this process some of the vapor from the solid SiC escapes the crucibles and is carried upward by convection currents to cooler portions of the furnace. Here the vapor condenses. In argon, a mass grows which consists of conglomerate microcrystals and dendrites of hexagonal and cubic SiC. The surfaces of these crystals are clean. However, under certain conditions single crystal whiskers of hexagonal SiC form. This habit has been found only in an atmosphere of hydrogen and only if the depostion temperature is about 2000°C. It is felt that the supersaturation of the vapor with respect to SiC is probably high, since the gas moves through relatively steep temperature gradients before reaching the region of deposition. Whiskers deposited in this fashion in a hydrogen atmosphere are almost always heavily coated with a surface layer of carbon, in marked contrast with the behavior in argon. It is known from spectrographic analysis of the hydrogen atmosphere, after preparation of crystals, that an appreciable amount of methane is formed. Thermochemical data for methane show that the gas will not only form but will also dissociate at these elevated temperatures. Thus it is probable that free carbon will be available from this source. Considerable carbon does deposit within the furnace, and carbon particles are observed in the atmosphere during crystal growth, bearing out this assumption. It is not surprising that the crystals grown in hydrogen are covered with carbon. Since true whiskers have been

[7] D. R. Hamilton, J. Electrochem. Soc. **105**, 735 (1958).

found to grow only in hydrogen, it is possible that the considerable excesses of carbon promote whisker formation. Perhaps surface films of carbon inhibit growth of the $\{1\bar{1}00\}$ faces, poisoning them, in a manner similar to the poisoning of whiskers prepared in electrolytic cells.[8] In order to facilitate examination of the samples, this carbon was removed by brief oxidation in air at 800°C.

Some typical whiskers prepared in hydrogen are shown in Fig. 1. In the best examples the $\{1\bar{1}00\}$ prism faces are atomically plane, within an experimental error of two or three unit cells. In other instances, the faces have shallow depressions at the edges. These may be seen in later figures. The face widths range from fractions of a micron to some 50 microns, the lengths from a few millimeters to 2 centimeters. The sections of these crystals are rarely perfect hexagons. The typical variation of face width amounts to perhaps 20 or 30%, and at the worse, a factor of 2. In the present work, relatively symmetric samples were selected.

Accompanying the better samples, there are many crystals in which the face width, and crystal thickness, changes along the length. It is noted that this increase in thickness is symmetric above the axis, and also that samples very frequently will thin further along the length to their original thickness. This suggests that nucleation has simultaneously occurred, and later stopped, on all sides of the prism. In extreme cases, the increase and decrease in thickness may be as great as a factor of ten. In a few rare instances, the thickness changes continually along the length of the sample, giving rise to crystals that resemble miniature golf tees. Surprisingly, these crystals are frequently attached to the substrate by an exceedingly thin leader.

Silicon carbide whiskers prepared in this fashion are found to possess great mechanical strength. In bending, samples may be deformed to 1 or 2% strain before brittle fracture. Kinking or permanent elastic deformation has not been observed. This behavior suggests that the whiskers contain few mobile edge dislocations or micro-cracks. This observation at once prompted a search for evidence of screw dislocations along the prism axis.

The ends of the crystal have been examined for the characteristic pits that may form when a screw emerges upon a crystal face. These observations were often frustrated by the presence of a layer of cubic SiC on the free growth end. The cubic structure is widely held to be the low temperature phase of SiC, and deposits during the cooling cycle of the furnace. Those samples that were not covered with cubic SiC had, in general, complex topology. Many of the observed markings could well be interpreted as pits due to the emergence of a screw dislocation. The evidence is nevertheless felt to be inconclusive, since it was not possible to show that all whiskers had pits.

[8] Price, Vermilyea, and Webb (to be published).

FIG. 1. Whiskers of hexagonal SiC prepared from vapor at temperatures about 2000°C. The largest sample is about 4 mm long.

The samples were also examined for the presence of an axial pore, which might be formed if the strength of the screw vector were much greater than the unit cell. The refractive index of SiC is 2.6 and therefore cannot be conveniently matched by an immersion fluid, leading to considerable difficulty in transmission microscopy. Complex diffraction effects are also present. In three instances features were observed that could be interpreted as an axial pore.

Lithium decoration and fused salt etching were also attempted, with inconclusive results. A random group of whiskers of symmetric section were then selected and examined for twist.

III. MEASUREMENT OF TWIST

The twist of a whisker may be estimated by measuring the tilt of Laue spots formed when the sample is examined with a microfocused x-ray beam. The twist may also be detected by observing the concomitant twist of the habit faces by optical goniometric methods. The latter technique is not satisfactory for measurements upon the present whiskers, particularly those of small section. The prism faces of such samples are so narrow that the reflected beam in a conventional goniometer is greatly broadened by diffraction. The pattern is so broad that it is useless for even qualitative work. Since x-ray equipment suitable for the detection of twist was not available, whiskers were examined using optical interference techniques. This method has proven to be a convenient and powerful experimental tool.

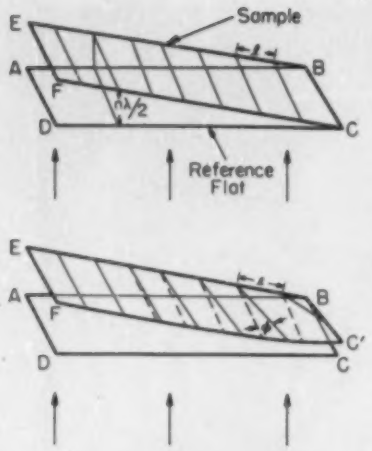

FIG. 2. The formation of multiple beam interference fringes, in transmission, between an optical flat and a flat sample face (upper diagram), and between a flat and a twisted sample face (lower diagram).

Quantitative measurements were made with a Leitz two-beam interference microscope. A conventional Leitz metallographic microscope was also adapted for use with a multiple beam interference cell. All quantitative data was taken with the former system.

The specimens were mounted by putting them on a common pin, normal to the pin axis. Fortunately, the whiskers always stuck to the pin without the deliberate use of an adhesive. Since no effort was made to clean the pin surface, the attachment was probably affected by residual oil or water contamination on the pin. Adhesives, such as glycerin or "Duco" cement, always induced severe bending strain in the whisker at the point of attachment.

The pin with the attached whisker was then placed on the interference microscope substage or moved close to a reference flat in the multiple beam interference cell. The whisker was oriented in a horizontal plane. The sample was thus free of external stress, except for bending due to its own weight. Subsequent interference measurements showed that the actual bending strain was less than about 10^{-8}, the experimental error.

The formation of interference fringes is shown schematically in Fig. 2, for convenience in the multiple beam case. ABCD, the reference flat, is illuminated from underneath with parallel monochromatic light. If the sample face, EBFC, is optically flat, as shown in the upper drawing, a set of parallel interference fringes will be formed in the wedge between the two surfaces. The spacing of the fringes, l, is determined by the angle of the wedge $\angle$FCD, and the wavelength of the light, λ. The fringes are observed through the sample. If, on the other hand, the sample face is twisted, as shown in the lower diagram, the fringes are no longer parallel. Although the fringe spacing along the line EB is unchanged, ($\angle$EAB is unchanged), the fringes near C have rotated through an angle ϕ from their previous positions. Figure 3 shows this effect for a whisker in the multiple beam interference cell. This sample had an extremely high twist, but was unfortunately lost, so the actual magnitude of the twist could not be determined. The photograph shows the exceptional resolution that is available with properly adjusted multiple beam interference fringes. Unfortunately, there are grave difficulties in the manipulation of samples prior to such examination. In order to obtain highest resolution, both the reference flat and the sample must be silvered to have about 95% reflectivity and 3% transmission. The silvered face of the whisker must then be maneuvered within a few microns of the reference flat, and yet not actually touch the flat. The angle of the whisker with respect to the reference flat must be adjusted so that a reasonable number of fringes are obtained along the sample length, without increasing the wedge spacing to the point where multiple beam interference effects can no longer be observed. These operations are extremely delicate. Should the whisker actually touch the reference flat, additional twist will be introduced, especially if the hexagonal end face lands on a corner, rather than on a side. Bending stresses will also alter the twist due to the screw dislocation. Although the use of high resolution multiple beam interference fringes could increase the accuracy of the twist measurements by a factor of about 5, the manipulations are too critical for any but qualitative observations.

Figure 4 shows typical fringes formed with a sample mounted in the Leitz two beam interference microscope. The fringes are broad. However, the sample does not have to be silvered. The fringes are observed in reflection, rather than in transmission through the sample, so that fringe position is not altered by refraction in the SiC.

To obtain quantitative data, the length of the whisker is traversed by moving the microscope substage. Fringe position and spacing is measured as a function of length with an eyepiece graticle. Prior to making these measurements, the residual twist of the substage was checked. A good optical flat was examined using the full stage traverse. The stage introduced measurable twist only at the very extremes of its motion. No fringe dis-

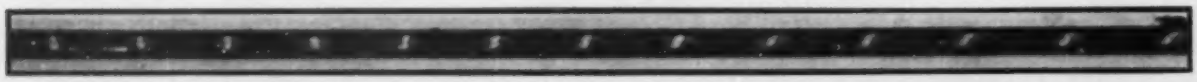

FIG. 3. Multiple beam interference fringes formed between a twisted SiC whisker and an optical flat. Both the flat and the sample are partly silvered to increase resolution. The illumination is from below, using parallel green light from a mercury arc. The fringes are viewed in transmission through the transparent upper face of the sample. The gradual rotation of the fringes is caused by the twist due to an axial screw dislocation.

placement whatsoever could be detected over the portion of the traverse used during measurement of whisker twists.

The actual twist of a whisker between two arbitrary points is given by the formula

$$\alpha=\frac{\lambda}{2l}(\tan\varphi_1-\tan\varphi_2) \qquad (1)$$

where α is the twist in radians, λ the wavelength of light employed, l the fringe spacing, and φ_1, φ_2 the displacement angles of the fringes from the normal at two different points on the whisker. Typical experimental data on two samples is shown in Fig. 5. In this figure, each of the three sets of points for W6 and W7 was taken on a separate traverse. The samples, and the point of mounting, were moved between each traverse. The experimental scatter of points depends principally upon the error in the determination of the center of gravity of the fringe. The effect of this scatter on α depends in turn upon l and the absolute magnitude of the angles. The scatter of total twist due to the original uncertainty in fringe angle is at best about ± 0.002 radian. These

TABLE I. Collected values of the length, L, and mean radius r, of whiskers of SiC. The measured twist in radians α is shown. From these data the strength of the Burgers vector of an axial screw dislocation, b, has been calculated.

	1	2	3	4	5	6	7a	7b
α rad	0.084	0.053	0.075	0.088	0.017	0.31	0.00	0.048
L cm	1.05	0.660	0.433	0.714	0.514	0.487	0.33	0.231
R μ	5.8	5.7	4.4	15.	10.	3.8	4.2	4.2
b A	8.4	8.1	10.7	8.7	10.3	29.	0.0	11.5

curves show that the measured magnitude of the twist is independent of the point of mounting, and of the handling involved in mounting samples. The twist of each of the six $(1\bar{1}00)$ prism faces was measured for several whiskers. The twist was the same for all faces, within experimental error. Other samples were examined after a period of several months had elapsed; it was found that the twist had not altered with time.

Collected data for seven samples is shown in Table I. Four of these exhibited right-hand twists, the other three, left-hand twists.

The Eshelby formula relating the twist per unit length of a cylindrical whisker of radius r, length L, to the strength of the Burgers vector, b, is

$$\frac{\alpha}{L}=\frac{b}{\pi r^2}\left(1-\frac{\epsilon^2}{r^2}\right) \qquad (2)$$

where ϵ/r is the displacement of the screw dislocation off the axis in reduced radial coordinates. Since the energy of a screw dislocation in a cylinder is a minimum if the screw is on the cylinder axis, we have assumed that $\epsilon/r=0$ in our samples. Should the dislocation be

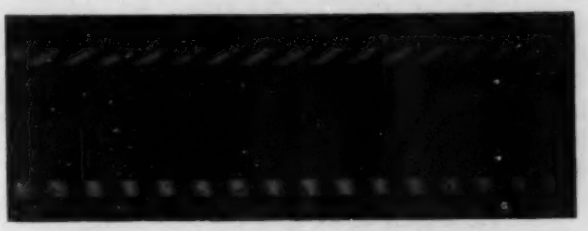

FIG. 4. Two portions of one whisker of SiC, showing the rotation of the two beam fringes formed in reflection from the twisted surface.

off axis, then the experimental twist will be less. In order to calculate b from the measured twist, it is necessary to determine the effective radii of each sample. To do this, the widths of the sample faces were measured on a traverse of their length, using the Leitz metallographic microscope, magnification about $\times 1200$. In some whiskers the faces were well-nigh indistinguishable; in these it is not certain that every face was measured. Average face widths were obtained, although it must be noted that a variation was detected in only one instance. Measurements were also made upon the ends of the samples. This information was then used to establish the true prism section. A value was then chosen for r so that πr^2 was equal to the section area. This choice of r is not strictly rigorous, particularly in samples of higher asymmetry. Fortunately, most of the samples employed were chosen for reasonable symmetry,

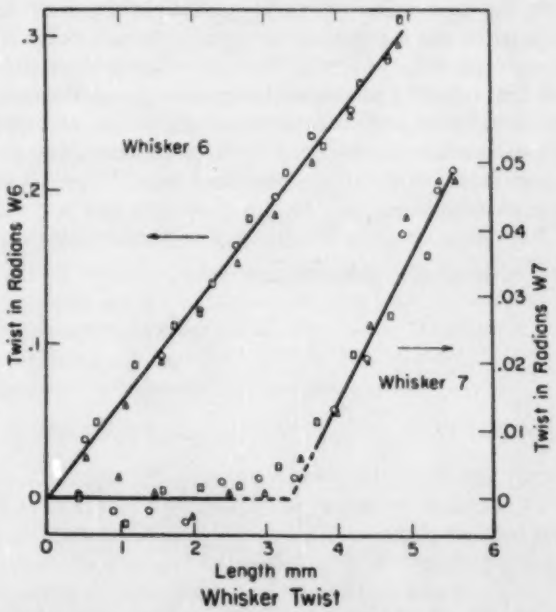

FIG. 5. Experimental data on two samples, W6 and W7. For each sample, three traverses were made of the sample length, using a Leitz two-beam interference microscope. From the rotation and spacing of the interference fringes, the twist caused by the screw dislocation along the length of the sample, was calculated in accordance with Eq. (1), and the points above plotted. From the average value of twist per unit length, the strength of the Burgers vector is calculated, and from this information, the polytype determined.

so that the error in this assignment of r is less than the experimental error from other sources. A correction of 1.5%, resulting from hexagonal, rather circular section, is also neglected. These values of r are collected together in Table I along with the values for L and α, and the estimates of b.

IV. DISCUSSION AND CONCLUSIONS

Hexagonal silicon carbide exhibits a structural phenomenon known as polytypism, which must, perforce, play an important role in the interpretation of the present results. The polytypes of hexagonal SiC are all derived from three basic unit cells, differing from each other in the number of carbon and silicon layers normal to the c axis and in the arrangement of the bonding between these layers. These basic unit cells have c dimensions of 10.053 A (polytype 4H), 12.69 A (15R, a rhombohedral unit cell), and 15.079 A (6H). The a dimensions are nearly constant. From these basic polytypes, others may be derived with larger unit cells. The formation of these latter polytypes may be accounted for by the presence of screw dislocations of various strengths in the three basic structures.[9] In general, the occurrence of such higher polytypes is very limited, at least under the conditions encountered in commerical silicon carbide furnaces. This is not necessarily true for the whiskers of SiC.

The values for the calculated Burgers vectors shown in Table I are in agreement, within experimental error, with the unit cell of the polytype 4H. In six cases, the strength of the Burgers vector equals the unit cell,while in one case, W6, the strength of the vector is three times this unit cell. The estimated Burgers vector in W6 could also arise from a dislocation of strength two unit cells in a 6H structure, or from a dislocation of non-integral strength in a 15R lattice, resulting in a 33R polytype. The rhombohedral cell of this polytype has a c axis 27.7 A. Since all the whiskers were prepared under very similar conditions, the simplest assumption is that they are all polytype 4H.

Specimen W7 deserves special mention. The data on this sample is shown in Fig. 5. This specimen is found to exhibit a twist over only part of its length. The dislocation strength in the twisted portion of the whisker lies between the 4H and 15R unit cells, but is somewhat closer to the 4H cell. The balance of the whisker apparently does not twist. The surface of the sample was examined carefully for singularities; none were seen. It is possible that the dislocation slipped out of the whisker after growth, but the probability of this is small in such a large sample.[10] The dislocation may have originated at this point but no other samples among many examined have been found free of twist. Furthermore, it is widely held that whiskers, prepared from the vapor phase, are unable to grow in the absence of a screw dislocation[11] parallel to the axis. The most likely explanation is that a second dislocation, of equal strength but opposite hand, started at this point, cancelling the twist of the original screw. Implicit in this is an assignment of the direction of sample growth, a factor that could not be determined experimentally.

It is concluded that silicon carbide whiskers do, indeed, grow with an axial screw dislocation. The twist induced by these dislocations is of the strength required by the Eshelby theory. On this basis it is found that the whisker lattice is of the 4H polytype.

Note:—W. W. Webb, of the Union Carbide Corporation, has been good enough to check the twists W2 and W3 by x-ray diffraction methods.[3] The data were generally within agreement to about 15%. The author is indebted to Dr. Webb for this confirmation.

ACKNOWLEDGMENTS

The author wishes to thank Dr. R. W. Keyes for calling his attention to the problem of twist in whiskers.

[9] R. S. Mitchell, Z. Krist. **108**, 341 (1957).

[10] J. P. Hirth and F. C. Frank, Phil. Mag. **3**, 1110 (1958).

[11] For example, see F. R. N. Nabarro and P. J. Jackson, G.P.C.

JOURNAL OF APPLIED PHYSICS VOLUME 31, NUMBER 1 JANUARY, 1960

Defects in Dislocations Produced by Focusing Collisions in f.c.c. Lattices

G. LEIBFRIED
Solid State Division, Oak Ridge National Laboratory, Oak Ridge, Tennessee*
(Received July 13, 1959)

It is assumed that a focusing collision of sufficiently high energy encountering a stacking fault area of an extended dislocation produces a Frenkel pair. This effect is thought to be important in radiation damage where primary knock-ons produce long range focusing collisions. The number of Frenkel pairs which are produced this way is calculated. Two effects are discussed in detail for Cu: (1) The enhancement of damage by enhanced production of Frenkel pairs if dislocations are present. It is shown that one can expect an appreciable enhancement of damage for heavily cold-worked material. (2) The pinning of dislocation motion. If one assumes that each Frenkel pair produced in a dislocation acts as a primary point, the theoretical result is in qualitative agreement with the experimental data on dislocation pinning by irradiation.

I. INTRODUCTION

IT has been pointed out by Silsbee[1] that focusing collisions may play an important role in radiation damage. These collisions transfer energy along close packed directions of the lattice by sort of head-on collisions, but there is no interstitial transport by a focusing collision.† The energy range in which focusing collisions can occur has an upper limit E_F which can be calculated by using an appropriate hard core potential between the atoms of the lattice. The range of these collisions depends strongly on the initial energy; it is limited by interaction with neighboring chains. The maximum range corresponds to a starting energy of E_F. In an ideal lattice a focusing collision travels along a close packed direction through a distance corresponding to its range or to its initial energy, loses its energy continuously and does not produce defects along its path. The initial energy is completely transformed into lattice vibrations or heat. However, if the focusing collision has to cross a region of lattice disorder a defect may be produced. Imagine that the collision would have to pass a stacking fault region. At the beginning of that region the close packed row is interrupted and shows through an open space in the lattice. The last atom in the close packed direction does not find a collision partner but leaves its lattice site, and is moved by a small distance to an interstitial position if it has sufficient energy. In this way a Frenkel pair is produced. We will assume that this process is the most important one when investigating the influence of dislocations on radiation damage. The stacking fault region corresponds then to the splitting separation of the dislocations. This process may help to explain two effects:

(1) the enhancement of the radiation damage rate by cold work through the enhanced production of Frenkel pairs;

(2) the pinning of dislocations by irradiation at low temperatures where we will assume that every Frenkel pair acts as a pinning point.

A focusing collision has many similarities with a particle because the collision energy is concentrated in a region of about one lattice distance along a close packed chain of atoms. In the following we will therefore call a focusing collision shortly a focuson.

II. THE RANGE DISTRIBUTION OF FOCUSING COLLISIONS

It can be shown† that for an exponential repulsion potential $V(r)=A\exp-r/a'$ the energy loss per hit $\epsilon(E)$ along the close packed direction for head-on collisions of initial energy E is given by

$$\epsilon(E)=\epsilon(E_F)E_F/E. \tag{1}$$

This formula is an approximation and holds only for about $E_F/3\leq E\leq E_F$. In the following (1) will only be used in this energy range. For a first approximation we will take the range R of such a focusing collision as

$$R=D/\epsilon(E)=R_mE/E_F \tag{2}$$

where D denotes the separation between neighboring atoms and R_m is the maximum range for E_F collisions. The numerical values for Cu are, using the parameters of Huntington[2] $A=2.1\times10^4$ ev and $a'=D/13$ in the expression for the interaction potential:

$$E_F=63\text{ ev},\quad \epsilon(E_F)=1.1\times10^{-2},\quad R_m=90D.$$

The relation (2) somewhat overestimates the range because the focusing collision generally does not start as a head-on collision. It is only eventually focused into such a collision and loses energy in the beginning stage where deviations from central collisions occur.

The number $Z(E_P,E)dE$ of focusons in the range (E,dE) produced by a primary knock on of energy $E_P\gtrsim E_F$ is given approximately as

$$Z(E_P,E)=\frac{2E_P}{E_F{}^2}\frac{12a'}{D}\ln E_F/E \quad\text{with}\quad E\leq E_F. \tag{3}$$

* Operated by Union Carbide Corporation for the U. S. Atomic Energy Commission, Oak Ridge, Tennessee.

[1] R. H. Silsbee, J. Appl. Phys. **28**, 1246 (1957).

† For a more detailed picture of the focusing effect the reader may be referred to G. Leibfried, "Correlated collisions in a displacement spike" (to be published).

[2] H. B. Huntington, Phys. Rev. **93**, 1414 (1954).

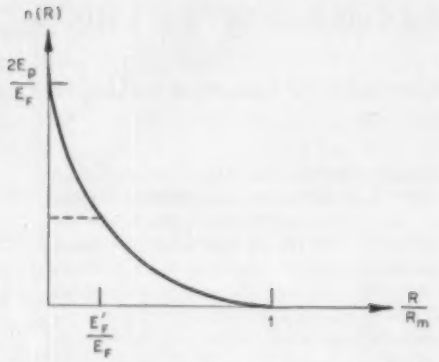

FIG. 1. Number of focusons $n(R)$ with range larger than R. The dotted line gives $n(R)$ if one neglects focusons with initial energy less than E_F'.

Since $a'/D=1/13$, one gets

$$Z(E_P,E)\cong\frac{2E_P}{E_F^2}\ln E_F/E. \tag{3a}$$

The corresponding number with range in (R,dR) is then

$$Z(E_P,R)=\frac{2E_P}{E_F R_m}\ln R_m/R. \tag{4}$$

From (4) one gets the number $n(E_P,R)$ with range larger than R

$$n(E_P,R)=\int_R^{R_m} Z(E_P,R')dR' =\frac{2E_P}{E_F}\left\{1-\frac{R}{R_m}(1+\ln R_m/R)\right\}. \tag{5}$$

Figure 1 shows a plot of *n versus* R/R_m. If one wants to exclude the low-energy collisions below an energy E_F' corresponding to the pair production threshold in a stacking fault, one cuts off the spectral distribution (3) at this energy or the range distribution (4) at a value $R'=R_m\cdot E_F'/E_F$. Then n is constant below this R value.

III. PRODUCTION OF DEFECTS IN DISLOCATIONS

Because the radiation effects are randomly distributed it does not matter whether or not one chooses a regular arrangement of the dislocations. For the purpose of simplification let us then assume that the dislocation lines are parallel to each other and arranged in a rectangular lattice with lattice distance λ (Fig. 2). The dislocation density ρ_D is then given by: $\rho_D=1/\lambda^2$. The production of focusing collisions by irradiation is randomly distributed in the crystal lattice. At first we take into regard only those effects caused by primaries of given energy E_P. Because of the random distribution of radiation effects one can treat one primary event as if the focusons all start at the same point $\mathbf{r}=(x,y,z)$ and have a range distribution according to Eqs. (4) and (5). Further one can treat the focusons as isotropically distributed though they only travel in close packed directions. The number of Frenkel pairs μ_D produced by the primary depends on the position $\mathbf{r}$ in the dislocation lattice and to get the average number produced one has to average $\mu_D(\mathbf{r})$ over all positions $\mathbf{r}$. Since the dislocation lines are parallel one can confine $\mathbf{r}$ to the x, z plane of Fig. 2, and because of the regular dislocation arrangement one has to take the average only over one periodic area in the x, z plane. So one gets the average value $\nu_D=\bar{\mu}_D$ as

$$\nu_D=\frac{1}{\lambda^2}\int_{-\lambda/2}^{\lambda/2}\int\mu_D(x,0,z)dxdz. \tag{6}$$

Let $f(x,z;x',z')$ be the production of Frenkel pairs for one dislocation, with x', z' being the position of the line center in the x, z plane; then f can only depend on the differences $x-x'$ and $z-z'$. The function μ_D contains contributions of all dislocation lines in the lattice. One can add the distributions due to the effect of single dislocations in μ_D if the screening effect due to the other dislocations is not important, i.e., if the dislocation-density is small enough. Then one has

$$\mu_D(x,z)=\sum_s f(x-x_s',z-z_s')$$

where x_s' and z_s' denote the dislocation positions in the lattice. In this case Eq. (6) simplifies to

$$\nu_D=\frac{1}{\lambda^2}\int_{-\infty}^{\infty}\int f(x,z)dxdz \tag{6a}$$

where now $f(x,z)$ denotes the production of Frenkel

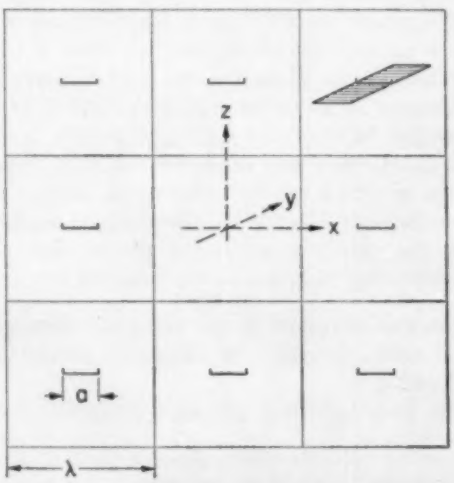

FIG. 2. Dislocations arranged in a lattice with lattice distance λ. The splitting separation of the dislocation is a. The dislocations are parallel to the y axis. The shadowed region of the dislocation in the upper right corner is the stacking fault area.

pairs for the dislocation in the origin of Fig. 2 and the focusons starting at (x,z).

From a small area of the stacking fault region $dx'dy'$ of the dislocation line at the origin of Fig. 2 one gets a contribution $df=(d\Omega/4\pi)n(|\mathbf{r}-\mathbf{r}'|)$ where $d\Omega$ means the solid angle of the small area $dx'dy'$ at $\mathbf{r}'=(x',y',0)$ seen from $\mathbf{r}=(x,0,z)$. One has $d\Omega=(|z|/|\mathbf{r}-\mathbf{r}'|^3)dx'dy'$. The final result is

$$\nu_D=\frac{1}{4\pi\lambda^2}\int_{-a/2}^{a/2}dx' \times\int\int\int_{-\infty}^{\infty}dxdy'dz\frac{|z|}{|\mathbf{r}-\mathbf{r}'|^3}n(|\mathbf{r}-\mathbf{r}'|) \quad (6b)$$

where the integral over x' and y' covers the whole stacking fault region of the dislocation line at the origin. The triple integral in (6b) does not depend on x' and changing the variables one gets

$$\nu_D=\frac{a}{4\pi\lambda^2}\int\int\int_{-\infty}^{\infty}\frac{|z|}{r^3}n(r)dxdydz. \quad (7)$$

Since $|z|$ averaged over the surface of a sphere r is $r/2$ one has eventually the simple result

$$\nu_D=\frac{a}{8\pi\lambda^2}\int\int\int_{-\infty}^{\infty}\frac{n(r)}{r^2}dxdydz=\frac{a}{2\lambda^2}\int_0^{\infty}n(r)dr. \quad (7a)$$

With the expression (5) for $n(r)$ one gets

$$\nu_D=\frac{2E_P}{E_F}\frac{aR_m}{2\lambda^2}\int_0^1\{1-\eta(1-\ln\eta)\}d\eta \quad (8)$$

$$\nu_D=\frac{2E_P}{E_F}\frac{aR_m}{8\lambda^2}. \quad (8a)$$

If one uses an energy cutoff E_F' for the pair production one has instead of (8)

$$\nu_D=\frac{2E_P}{E_F}\frac{aR_m}{8\lambda^2}\{1-\eta'^2+2\eta'^2\ln\eta'\} \quad (8b)$$

where $\eta'=E_F'/E_F$. For Cu the displacement threshold‡ energy E_d is about $E_d=22$ ev. One may take this as the cutoff energy for pair production though the production is easier in the process discussed here because the last atom in the close packed row is in a more favorable position for displacement than an atom in a normal lattice site where E_d refers to. This choice would compensate somewhat for other energy losses which we neglected in the foregoing calculation. Taking this value for the cutoff energy, η' is about $\frac{1}{3}$ and (8b) now reads

$$\nu_D=\frac{2E_P}{E_F}\frac{aR_m}{10\lambda^2}. \quad (8c)$$

‡ This value of E_d is consistent with the hard core potential used.

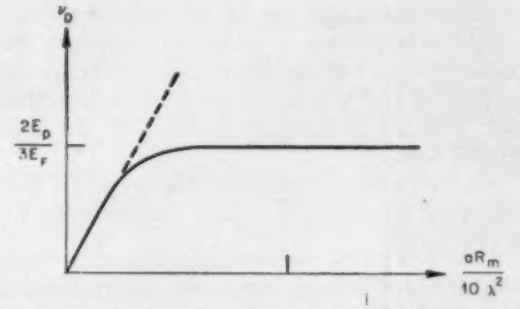

FIG. 3. Number of Frenkel pairs ν_D produced by a primary of energy E_P plotted *versus* dislocation density $1/\lambda^2$.

The number of Frenkel pairs produced is thus proportional to the dislocation density. This linear behavior can hold only as long as the dislocations do not screen each other. The maximum number which one reaches at very high densities is of course the total number of focusing collisions $n(R=0)$. Without cutoff $n(0)$ equals $2E_P/E_F$; with the above values of the cutoff energy $n(0)$ equals about $2E_P/3E_F$. So the factor $aR_m/10\lambda^2$ in (8c) cannot exceed $\frac{1}{3}$; if it approaches this value the production becomes constant independent of the dislocation density. This behavior is plotted in Fig. 3.

IV. ENHANCEMENT OF DAMAGE BY DISLOCATIONS

In the theory of radiation damage the effect of radiation is often expressed by the production of Frenkel pairs by primary knock ons. For the purpose of comparison we will use this picture also. In the simplest theory one gets for the number of Frenkel pairs $\nu(E_P)$ using a sharp displacement threshold E_d

$$\nu(E_P)=E_P/2E_d \quad \text{for} \quad E_P\gtrsim 2E_d. \quad (9)$$

In (9) ionization effects are not taken into account, which may be correct for Cu in pile- and deuteron-irradiation. Because in these irradiations the average value of E_P taken over the primary energy distribution is larger then $2E_d$ and E_F and the largest fraction of damage is caused by relatively fast primaries one can compare Equations (9) and (8c) directly. Then one gets for the total number ν_t of Frenkel pairs

$$\nu_t(E_P)=\nu(E_P)+\nu_D(E_P)=\nu(E_P)\left\{1+\frac{4E_d}{E_F}\frac{aR_m}{10\lambda^2}\right\}. \quad (10)$$

Using the values $E_F=63$ ev, $E_d=22$ ev, one has

$$\nu_t=\nu\left\{1+1.4\frac{aR_m}{10\lambda^2}\right\}. \quad (10a)$$

This means that a fraction $1.4\,aR_m/10\lambda^2$ of the damage in the ideal lattice has to be added to account for the dislocation contribution. The largest fraction occurs for $aR_m/10\lambda^2=\frac{1}{3}$ and this would mean an enhancement by about 50% for dislocation densities in the order of $1/\lambda^2\cong 10/3aR_m$.

For quantitative calculations one needs the value of the splitting separation a. Theoretical values for Cu are given by Seeger[3]:

$$a=4.5D=11\times10^{-8}\text{ cm} \quad \text{for screw dislocations} \quad (11a)$$

$$a=12D=30\times10^{-8}\text{ cm} \quad \text{for edge dislocations.} \quad (11b)$$

Let us take the lower value of the splitting separation; then the enhancement of damage rate by cold work should be roughly proportional to the dislocation density up to densities of about $1/\lambda^2=10/3aR_m\cong10^{13}$ cm^{-2} where the enhancement is about 50%.

These figures may be somewhat misleading because of the underlying assumptions. First of all the theoretical damage in a lattice with low dislocation density is about one order of magnitude larger than the experimental data for pile neutrons. This may be due partly to self-annealing in the spikes with large primary energy and partly to the probability for displacement in the low energy range which is not likely to be a step-function with sharp threshold E_d. This means that the damage using (9) may be overestimated by a factor of about 10. Conversely the fraction of the dislocation contribution is underestimated by the same factor. On the other hand, one does not know if the contribution of a Frenkel pair, e.g., to the electrical resistivity, is independent of whether it is situated at a stacking fault or surrounded by a normal lattice. It may be mentioned that the calculation of ν_D is much more dependable that that of ν. Neither self-annealing nor varying displacement probability in the vicinity of E_d would influence the result much.

Recent measurements by Coltman, Blewitt, Klabunde, and Redman[4] show an enhancement of resistivity in heavily cold-worked Cu during pile irradiation by about 30%. This seems to be in agreement with the figure given in the foregoing. Nevertheless, the relative enhancements discussed in the foregoing can only be considered as order of magnitude results because the number ν is rather uncertain and because one does not have a dependable theory of resistivity for large spikes and for defects near dislocations.

V. DISLOCATION PINNING

If one assumes that a Frenkel pair produced in a dislocation line pins the dislocation, one can easily calculate the average number of pinning points α per unit length of dislocation line. The quantity α is the same as θt used in the paper of Thompson and Holmes[5] where t means the irradiation time. If one knows α and the distribution of the pinning points before irradiation, one can calculate the change of the elastic modulus with irradiation time. At low temperatures, where presumably no defects can diffuse, the pinning effected by focusing collisions is the only remaining one.§

The number of pinning points per unit volume ρ_P is given by

$$\rho_P=\int \nu_D(E_P)t\,dE_P\int\Sigma_s(E_n)\varphi(E_n)g(E_n;E_P)dE_n. \quad (12)$$

The meaning of the symbols is as follows: E_n neutron energy; E_P primary energy; $\varphi(E_n)$ neutron flux per unit energy; Σ_s macroscopic scattering cross section; $g(E_n;E_P)$ normalized distribution function for energy transfer to (E_P,dE_P) for scattering of neutrons of energy E_n; $\nu_D(E_P)$ is as before the average number of pinning points produced by a primary knock on of energy E_P; t is the irradiation time. The second integral in (12) $F(E_P)=\int\Sigma_s\varphi g dE_n$ is the number of primaries per unit volume, energy and time produced by irradiation.

For quantitative calculations one can assume an energy-independent macroscopic scattering cross given by Holmes[5] to 0.256 cm^{-1}. Further, one can assume a slowing-down distribution $\varphi(E_n)$ proportional to $1/E_n$ with a cutoff energy $E_{n,\max}$ of 1.5 Mev‖:

$$\varphi(E_n)=C/E_n \quad \text{for} \quad E_n\leq E_{n,\max}=1.5\text{ Mev}.$$

Then one gets for s scattering with $g=A/4E_n$ (for $E_P\leq 4E_n/A$ and with the atomic weight A of copper, $A\cong60$)

$$F(E_P)=\Sigma_s C\{1/E_P-1/E_{P,\max}\}$$

for

$$E_P\leq E_{P,\max}=4E_{n,\max}/A\cong10^3\text{ ev}. \quad (13)$$

The lower limit where displacement effects can occur at all is $E_{P,\min}\cong E_d$; as will be seen, the value of the lower limit is not very important. The average value of E_P averaged between the limits E_d and $E_{P,\max}$ is

$$\bar{E}_P=\int_{E_d}^{E_{P,\max}}E_P F(E_P)dE_P\Big/\int_{E_d}^{E_{P,\max}}F(E_P)dE_P \quad (14)$$

$$\bar{E}_P=\frac{E_{P,\max}-E_d-(E_{P,\max}^2-E_d^2)/2E_{P,\max}}{\ln E_{P,\max}/E_d-(E_{P,\max}-E_d)/E_{P,\max}}. \quad (14a)$$

Since $E_{P,\max}\ll E_d$ one gets approximately

$$\bar{E}_P\cong\frac{E_{P,\max}}{2\ln E_{P,\max}/eE_d}\cong6.5\times10^3\text{ ev}. \quad (14b)$$

[3] A. Seeger, *Encyclopedia of Physics* (Springer-Verlag, Berlin, Germany, 1955), Vol. VII, Part 1, p. 609.

[4] Blewitt, Coltman, Klabunde, and Redman, Bull. Am. Phys. Soc. Ser. II, 4, 135 (1959).

[5] D. O. Thompson and D. K. Holmes, J. Appl. Phys. 27, 713 (1956).

§ The range for the other effects due to a primary is much smaller than the focuson range. So one can neglect pinning by directly produced defects.

‖ D. K. Holmes has pointed out that this is a rather good approximation for the ORNL graphite reactor.

This shows that the average value of $\nu_D(E_P)$ may be taken as $\nu_D(\bar{E}_P)$

$$\bar{\nu}_D=\frac{2\bar{E}_P}{E_F}\frac{aR_m}{10\lambda^2} \tag{15}$$

because $\bar{E}_P$ is much larger than E_F, so the effects in the range $E_d\leq E_P\leq E_F$ where the formula (8c) for $\nu_D(E_P)$ would not hold are unimportant.

For the density ρ_P one gets

$$\rho_P=\bar{\nu}_D l\int_{E_d}^{E_{P,\max}} F dE_P\cong\bar{\nu}_D l\sum C\ln(E_{P,\max}/eE_d). \tag{16}$$

Usually the total flux is given by the epithermal flux ϕ

$$\phi=\int_{E_{th}}^{E_{n,\max}}\varphi dE_n=C\ln E_{n,\max}/E_{th}\cong 17C \tag{17}$$

where E_{th} is the average thermal neutron energy. This gives the final result as approximately

$$\rho_F\cong\bar{\nu}_D\sum_s\phi_s t/2 \tag{16a}$$

because $\ln E_{P,\max}/eE_d\cong 7.5$.

For a dislocation density of 10^8 cm^{-2} which is the order of magnitude for as-grown crystals, one gets, using the same data as before,

$$\bar{\nu}_D=5\times 10^{-4}. \tag{15a}$$

So the average number of pinning points per neutron hit is rather small.

Further, one can calculate the quantity α. Because the dislocation line length per cm^3 is also equal to $1/\lambda^2$ one has

$$\alpha=\rho_P\lambda^2=\frac{\bar{E}_P}{10E_F}aR_m\sum_s\phi_s t_s \tag{18}$$

and introducing the numerical values for Cu

$$\alpha\cong 6.5\times 10^{-13}\text{ cm}\times\phi t. \tag{18a}$$

If one looks up the experimental data[6] it appears that about one-half of the dislocation contribution to the elastic modulus is pinned down by irradiation of $\phi t\cong 2\times 10^{15}$. Here it is assumed that after the final warmup after irradiation the dislocation contribution has totally disappeared. In the theory of the dislocation pinning an exponential distribution of pinned dislocation lengths before irradiation is assumed where l_0 is the average length. In this theory α only enters in the form αl_0. Then under the above-given assumptions $(1+\alpha l_0)^2$ should be about 2 (or $\alpha l_0\cong 0.4$) for $\phi t\cong 2\times 10^{15}$ cm^{-1}. With (18a) one gets $\alpha=1.3\times 10^{+3}$/cm or for the average length $l_0\cong 3\times 10^{-4}$ cm, which is well within an order of magnitude of the results given in reference 5.

[6] Thompson, Blewitt, and Holmes, J. Appl. Phys. 28, 742 (1957).

VI. CONCLUSIONS

The last result shows that dislocation pinning by focusons can explain the effect of irradiation on the elastic behavior of Cu. The enhancement of damage in heavily cold-worked materials is just in the limit of experimental possibilities and has also been demonstrated in Cu[4]. It may be mentioned that the focuson model is only likely to hold for the noble metals and here the quantitative results are very sensitive to the potential between the atoms determining R_m and the dislocation splitting. In particular this theory would predict much smaller effects in a metal like aluminum where the extension of dislocations is small and where the focusing effect may also be reduced. It would be valuable to check this prediction.

The calculations made here are only approximate. Better approximations could be made, for instance in the calculation of $n(r)$ defined by Eq. (5). Here one should first calculate the distribution $Z(E,r)dE$ after the focuson has traveled by a distance r. Then one has a better approximation by $n(r)=\int_{E_d'}^{E_F}Z(E,r)dE$ where E_d' is the displacement threshold in a stacking fault. The range defined by (2) is that distance where the initial energy E is decreased roughly by a factor of e. Taking E_d' as E_d then the range for $E=E_F$ would correspond to the desired range for pair production. Presumably E_d' is smaller than E_d, say by a factor of two. Then the range for E_F collisions would be larger than the value corresponding to (2) and that for E_d collisions would be smaller. If one defines $n(r)$ in the above way one can treat the problem as before, and gets

$$\int_0^\infty n(r)dr=R_m\int_{E_d'}^{E_F}\frac{E}{E_F}\ln\frac{E}{E_d'}Z(E)dE$$

where R_m is as before $D/\epsilon(E_F)$ and $Z(E)$ is the distribution of initial energies. Using the distribution (3a) one gets for $E_d'\cong E_d/2\cong 10$ ev: $\int n dr=(2E_P/E_F)(R_m/5)$ which is about the result of Eq. (8c). The result depends very sensitively on the value of E_d' if E_d' approaches E_d.

Further, one must keep in mind that the relation between energy and distance also depends on the initial collision angle. For the limiting angle where focusing is just possible the collision loss due to change of collision angle is about the same as due to interaction with neighboring chains. This would mean that one gets a lower limit for the effect by replacing R_m through $R_m/2$.

It is improbable that this procedure would change the results essentially, and since the numerical values anyhow have only a qualitative meaning, it does not seem worth while at present to do more exact calculations.

ACKNOWLEDGMENTS

The author would like to express his appreciation to T. H. Blewitt, R. R. Coltman, D. O. Thompson, and especially D. K. Holmes for many helpful discussions.

Impurity Effects upon Mobility in Silicon

R. A. LOGAN AND A. J. PETERS
Bell Telephone Laboratories, Incorporated, Murray Hill, New Jersey
(Received July 15, 1959)

In sufficiently pure n-type silicon, the carrier mobility follows a $T^{-1.5}$ law at low temperature and agrees well with Herring's theory of lattice scattering mobility. Similar results for p-type silicon give a T^{-2} law for the temperature dependence and is in disagreement with theory. In less pure samples, scattering is by ionized impurities and the magnitude of the mobility reduction agrees well with the theory of Herring and Brooks. Scattering by large concentrations ($\sim 10^{18}$ cm^{-3}) of dissolved neutral oxygen is negligible compared to that by other mechanisms.

INTRODUCTION

BY measurement of electrical conductivity and Hall effect, extensive studies have been made of the electrical properties of silicon. The first studies by Pearson and Bardeen[1] were performed on multicrystalline material. Morin and Maita[2] extended these studies using pulled single crystals of higher purity. As a result, considerable knowledge has been gained on subjects such as carrier ionization energy, effective mass, intrinsic conductivity, etc. One important problem that was not understood was the nature of the various scattering mechanisms that reduced the mobility. Recently the development of floating-zone crystal pulling techniques has extended the degree of purity of readily available crystals. In addition, these crystals are relatively free of the large oxygen concentrations now known[3] to be present in pulled crystals. It therefore seemed appropriate to examine once again the electrical properties of silicon using Hall effect techniques primarily to observe the scattering mechanisms in the presence of a reduced contribution from impurities.

PROCEDURE

The silicon crystals were prepared by both the conventional pulling technique and the floating zone method. The Hall effect apparatus used to make the electrical measurements has already been described.[4] Measurements were made over the temperature range from liquid hydrogen to room temperature. The lower temperature limit was generally dictated by the high sample impedance ($\sim 10^{10}$ ohms) which developed near 20°K. From the measured Hall coefficient, R, the carrier concentration, n, was determined from

$$n=\frac{3\pi}{8Re}. \tag{1}$$

This expression is valid for the simple semiconductor model in which the conduction (or valence) band has a single valley with spherical surfaces of constant energy in which the ratio of Hall mobility to drift mobility is $3\pi/8$. Silicon is more accurately described by a many-valley model with ellipsoidal surfaces of constant energy. According to Herring's theory for this model, the assumed mobility ratio may be a fairly good approximation since at temperatures >100°K, theory predicts a value near $3\pi/8$ in many cases.[5]

The donor and acceptor concentrations, N_D and N_A, were determined from the curves of n *vs* $1/T$°K with the conventional curve fitting techniques.[2] In this method one uses the known ionization energy of the majority impurities[6] and the density of states obtained with the mass ratios m^*/m_0 of 1.0 and 0.4 in n- and p-type silicon, respectively. These mass ratios were determined empirically[2] to obtain a best fit to the curves of carrier concentration as a function of the reciprocal of the temperature. It is of interest to note that the density of states obtained in this way is the same as that calculated from the known band structure,[7] state degeneracy,[7] and the effective mass ratios of 0.33 and 0.6 determined with cyclotron resonance experiments[8,9] in n- and p-type silicon, respectively.

The carrier mobility, μ, was determined from the relationship

$$\sigma=ne\mu, \tag{2}$$

where σ is the sample conductivity. With the assumed ratio of Hall mobility to drift mobility equal to $3\pi/8$, the mobility defined in Eq. (2) then equal to $(8/3\pi)\mu_H$.

RESULTS

In Fig. 1 a log-log plot is made of mobility *versus* temperature for floating zone crystals in which $N_A=3.4\times10^{14}$ cm^{-3}, $N_D=2.0\times10^{12}$ cm^{-3} for the boron doped crystal and $N_D=1.14\times10^{14}$ cm^{-3}, $N_A=4.0\times10^{12}$ cm^{-3} for the phosphorous doped crystal. At low temperatures the mobility follows a $T^{-1.5}$ law in n-type and a T^{-2} law in p-type silicon. These temperature dependences were also observed[10] in germanium crystals where

[1] G. L. Pearson and J. Bardeen, Phys. Rev. **75**, 865 (1949).
[2] F. J. Morin and J. P. Maita, Phys. Rev. **96**, 28 (1954).
[3] Kaiser, Keck, and Lange, Phys. Rev. **101**, 1264 (1956).
[4] Logan, Pearson, and Kleinman, J. Appl. Phys. **30**, 885 (1959).
[5] C. Herring, Bell System Tech. J. **34**, 237 (1955).
[6] Morin, Maita, Schulman, and Hannay, Phys. Rev. **96**, 833 (1954). The value for P is misprinted there and should read 0.044 ev.
[7] W. Kohn, *Solid State Physics*, edited by F. Seitz and D. Turnbull (Academic Press, Inc., New York, 1957), Vol. 5, pp. 257–320.
[8] Dexter, Lax, Kip, and Dresselhaus, Phys. Rev. **96**, 1222 (1954).
[9] Dexter, Lax, and Zeiger, Phys. Rev. **104**, 637 (1956).
[10] F. J. Morin and J. P. Maita, Phys. Rev. **94**, 1525 (1954).

they were assumed to be characteristic of lattice scattering.

The curve drawn for the n-type sample in Fig. 1 was obtained using Herring's theory[5] for lattice scattering mobility, with the parameters $(\omega_2/\omega_1)=0.5$ and $(m^*\|/m^*\perp)=1$. The quantities ω_1 and ω_2 measure the strength of the coupling of the carriers to intravalley and intervalley modes, respectively. $m^*\|$ and $m^*\perp$ are the effective masses in the direction of the major and minor axis, respectively, of the energy band surface. The results are not sensitive to the effective mass ratio which is used only in transposing the calculated drift mobility to Hall mobility. For mass ratios between 0.5 and 2, the mobility changes by only 5%. The departure from the $T^{-1.5}$ law at temperatures above 100°K is due to scattering by optical modes, in addition to that by acoustical modes. The optical mode temperature varies from 570° to 730°K with position in the energy band.[11] The calculated mobility does not depend strongly on the choice of this temperature and the intermediate value of 650°K was used.

Herring's theory does not describe our results for p-type silicon due to the T^{-2} dependence at low temperature. The mobility, μ_{ac}, for scattering by acoustical modes should obey the equation[12]

$$\mu_{ac}=AT^{-1.5}, \tag{3}$$

where A is a constant. For lattice scattering by optical modes, theory[12] predicts

$$\mu_{op}=B(e^{\theta/T}-1), \tag{4}$$

where B is a constant and θ is the optical mode temperature which has been observed[11] to be ~650°K for silicon. Lattice scattering mobility, μ_L, may be approximated by the relation

$$\frac{1}{\mu_L}=\frac{1}{\mu_{ac}}+\frac{1}{\mu_{op}}. \tag{5}$$

It was possible to describe the observed lattice scattering mobility in germanium[10] by using these relations, with the acoustical mode temperature dependence modified to a T^{-2} law for the p-type samples as suggested by the experimental results. However, attempts to describe our data in silicon in this way were not successful.

In samples of less purity, the mobility at low temperatures is reduced. This effect is demonstrated in Fig. 2 where a log-log plot of mobility *versus* temperature is made for five different n-type crystals. The donor and acceptor concentration observed in each crystal is also listed in Fig. 2. In addition, the oxygen concentration, measured[13] from the absorption coefficient at 9 μ, is also listed. Samples A and B were grown

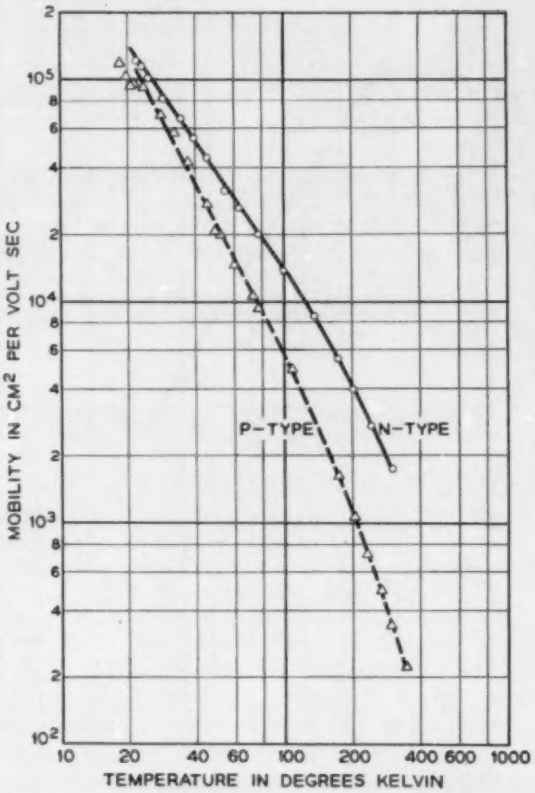

FIG. 1. A log-log plot of mobility *versus* temperature for n- and p-type silicon of sufficient purity that lattice scattering is the dominant mechanism.

by the floating zone technique where the oxygen concentrations is below the limit of detection (~10^{16} cm^{-3}). Samples C, D, and E were obtained from pulled crystals. It is evident that the mobility does not correlate with either the oxygen or donor concentration. However, the reduction in magnitude of the mobility at low temperatures correlates with the acceptor concentration in the samples. At low temperature, the acceptor concentration is one-half of the ionized impurity concentration since the uncompensated donors are neutral.

The mobility μ_I due to scattering by a density of N_I ionized impurity centers at temperature T is given by the Brooks-Herring formula[14] as

$$\frac{1}{\mu_I}=\frac{\pi^{\frac{1}{2}}m^{\frac{1}{2}}e^3N_I}{2^{\frac{3}{2}}D^2(kT)^{\frac{3}{2}}}\log\left[(1+b)-\frac{b}{1+b}\right], \tag{6}$$

where D is the dielectric constant, m is the effective electron mass, e is the electronic charge, and κ is Boltzman's constant and

$$b=\frac{24\pi mD(kT)^2}{e^2h^2N_I},$$

where h is Planck's constant.

[11] B. M. Brockhouse, Phys. Rev. Letters **2**, 256 (1959).

[12] For example, the review article by M. S. Sodha in *Progress in Semiconductors* (John Wiley & Sons, Inc., New York, 1958), Vol. 3.

[13] W. Kaiser and P. H. Keck, J. Appl. Phys. **28**, 882 (1957).

[14] H. Brooks, Phys. Rev. **83**, 879 (1951). This result was obtained independently by C. Herring (unpublished).

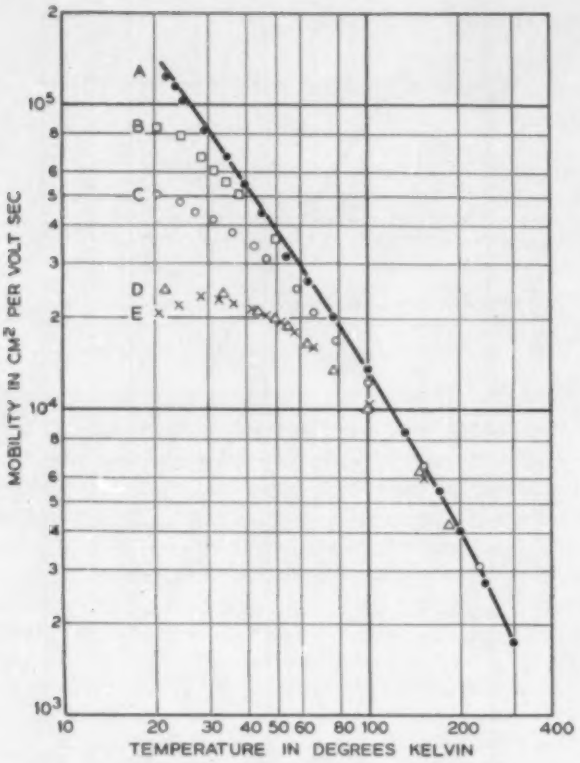

FIG. 2. A log-log plot of mobility *versus* temperature for five samples of *n*-type silicon containing the following impurities:

	N_D(cm^{-3})	N_A(cm^{-3})	Oxygen (cm^{-3})
A	1.14×10^{14}	4.0×10^{12}	$\sim10^{16}$
B	9.0×10^{13}	2.0×10^{12}	$\sim10^{16}$
C	2.5×10^{14}	5.5×10^{12}	$\sim10^{18}$
D	4.9×10^{14}	2.1×10^{14}	5.0×10^{17}
E	3.3×10^{14}	2.3×10^{14}	7.7×10^{17}

One may assume that the mobility μ_T observed in the presence of ionized impurity scattering is given by the relationship

$$\frac{1}{\mu_T}=\frac{1}{\mu_I}+\frac{1}{\mu_L}. \tag{7}$$

Using the value of μ_L observed in sample *A* where the mobility follows the $T^{-1.5}$ law characteristic of lattice scattering, the contribution to mobility due to ionized impurity scattering may be calculated from Eq. (7). From the data presented in Fig. 2 and other similar data, a plot of $10^5/\mu_I$ at 25°K *versus* $2N_A$ is shown in Fig. 3. The curve drawn there was computed from theory [Eq. (6)] using the electronic mass 0.33 that of the free electron.[8] The excellent agreement between theory and experiment confirms the identification of the scattering mechansim as ionized impurity scattering and rules out other scattering mechanisms.

DISCUSSION

In pure silicon crystals, below about 100°K, carrier mobilities follow the same temperature dependence as

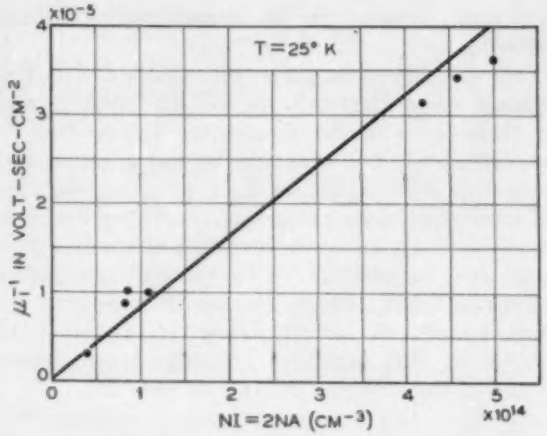

FIG. 3. The reciprocal of the mobility due to ionized impurity scattering plotted against the density of ionized impurities.

observed in germanium. This mobility, which is characteristic of the crystal lattice, has a $T^{-1.5}$ and T^{-2} dependence on temperatures in *n*- and *p*-type silicon, respectively. At temperatures above 100°K the mobility is further reduced presumably by optical mode scattering. This is in contrast to the results obtained by Morin and Maita[2] using less pure samples where the lattice scattering effects were obscured by impurity scattering. Herring's theory of lattice scattering mobility describes very well the results observed in *n*-type but not that observed in *p*-type silicon.

In samples of less purity, the mobility is reduced at low temperatures by ionized impurity scattering and the observed mobility reduction is in excellent agreement with the theory of Brooks and Herring so that other scattering mechanisms are negligible. According to Erginsoy's model,[15] contributions to the mobility reduction due to scattering by the neutral donors at this temperature would be less than 1% of that contributed by ionized impurities. It should be pointed out that some of our samples contained oxygen concentrations in the range 10^{17} to 10^{18} cm^{-3}. If these neutral impurities scattered according to Erginsoy's model, very significant reductions in mobility would have occurred. However, in passing, it may be remarked that Erginsoy's calculations were made with reference to neutral scattering sites which contained electrons in shallow levels, and would therefore not be expected to be a good description of neutral oxygen in silicon.

ACKNOWLEDGMENTS

The crystals were prepared by E. Buehler, H. C. Theuerer, and P. E. Freeland. The oxygen concentrations in these crystals were determined by W. Kaiser and W. G. Spitzer. We wish to thank D. A. Kleinman for many helpful discussions about this work.

[15] C. Erginsoy, Phys. Rev. **79**, 1013 (1950).

JOURNAL OF APPLIED PHYSICS VOLUME 31, NUMBER 1 JANUARY, 1960

Flow Rates Using Nuclear or Electron Paramagnetic Resonance Techniques with Applications to Biological and Chemical Processes

J. R. SINGER
University of California, Berkeley, California
(Received June 17, 1959)

The equations for measuring flow rates are derived using NMR and EPR relaxation time determinations. Several experimental procedures are discussed. One method of measurement depends upon the difference between static relaxation times and the apparent relaxation time of materials flowing through the observation region. Another procedure utilizes saturated or inverted spins as a "tracer" to measure flow rates. These schemes may readily be applied to blood flow velocity measurements in humans or animals, or to mineral and chemical flow rate determinations. The advantage of this spin resonance flowmeter is that the flow channel is not disturbed. Thus blood flow velocities are readily measured without the necessity of breaking the skin.

INTRODUCTION

THIS paper discusses a new method of flow rate measurement using either (or both) electron paramagnetic resonance (EPR) and nuclear magnetic resonance (NMR). We are especially interested in determining: (1) the transport rates for certain fluids, (2) the diffusion rates for tracer materials, and (3) the transport and diffusion rates for biological processes. As very practical instances for the use of such measurements, one may measure oil or water flow rates in a pipe line without opening the line, or detect the degree of completion of a chemical process while the liquid continues flowing through its normal pathway. Another interesting and useful application is the measurement of blood flow and other biological fluid flow rates in humans or animals without breaking the skin.

In the first method we will discuss, the measurement depends upon a determination of the real and apparent relaxation time. The method of measurement for this time is not important. One may use a saturation scheme,[1] an adiabatic fast passage,[2] or a 180° pulse.[3] For purposes of illustration consider the NMR saturation method. A given region of the transport tube is in a static magnetic field (for some materials, the earth's field may be satisfactory). Sufficient rf intensities at the resonant frequency of the transported nuclei will equalize the energy levels (cause saturation). The resonance signal is now observed, and in a time $(T_1)'$, it is found that resonance absorption is within $1/e$ of the original signal strength. We suppose that the nuclei replacing the transported saturated nuclei are observed in an equilibrium magnetized state. This may be achieved by permitting these nuclei to flow through a magnetic field for a time greater than T_1. If the replacement nuclei are not in equilibrium, some sensitivity is lost. The equation governing the rate of change of volume magnetization must account for the magnetization change due to the relaxation process and the change due to flow of magnetic nuclei.

[1] Bloembergen, Purcell, and Pound, Phys. Rev. **73**, 697 (1948).
[2] F. Bloch, Phys. Rev. **70**, 460 (1946), and Bloch, Hansen, and Packard, *ibid.* **70**, 474 (1946).
[3] E. Hahn, Phys. Rev. **80**, 580 (1950).

THEORETICAL DERIVATION OF FLOW RATE EQUATIONS

Considering the thermal spin-lattice relaxation alone, the rate of change of volume magnetization M_z *in the volume under observation* is given by[2]

$$(dM_z/dt)=(M_0-M_z)/T_1, \tag{1}$$

where M_0 is the equilibrium volume magnetization value, M_z is the instantaneous value, and T_1 is the spin-lattice or longitudinal relaxation time characteristic of the material. We wish to consider an added effect; that of replacing some of the material having magnetization M_z by material having magnetization M_0. Assume that the entering nuclei have passed through the static magnetic field for a sufficient time (i.e., a time longer than T_1) to reach their equilibrium magnetization M_0. This assumption is valid so long as the static magnetic field expanse is large enough to result in a longer flow time in that field than T_1. Using this assumption we may express the magnetization change due to flow as

$$(h/V_0)(M_0-M_z), \tag{2}$$

where we denote the average volume flow per second by h, and let V_0 be the volume enclosed by the effective rf field in the measurement region.

The complete expression for the magnetization change is then

$$(dM_z/dt)=[(M_0-M_z)/T_1]+[h(M_0-M_z)/V_0]. \tag{3}$$

This is readily soluble to obtain the instantaneous magnetization at time t after saturating the system when $t=0$. The solution is

$$M_z=M_0\left[1-\exp-\left(\frac{t}{T_1}+\frac{ht}{V_0}\right)\right]. \tag{4}$$

The significance of this equation is that a measurement of relaxation time of a flowing material will result in a value different from that found for the same material in a static state. We derive the apparent relaxation time

$(T_1)'$ of the flowing material by using (4) as

$$(T_1)'=T_1V_0/(V_0+hT_1), \tag{5}$$

with T_1 being the "true" relaxation time for the non-flowing substance as before.

A method of measuring flow rate will next be described. First the true relaxation time of the material is measured. Next the apparent relaxation time of the *flowing* material is measured. The difference between the two may be expressed as

$$T_1-(T_1)'=T_1[1+(V_0/hT_1)]^{-1}. \tag{6}$$

The limitations of this method are most readily considered for two limiting cases. The first case is when $h\gg V_0/T_1$. Here the measurement will have low precision. Hence for large flow rate measurements, one may increase the volume enclosed by the detection system, or if conditions permit, T_1 may be decreased by the addition of chemical agents (for examples, see reference 1).

The second case is the limitation occurring when h is very small relative to V_0/T_1. Here the measurement is limited by the precision with which relaxation times may be measured. In this instance, one may decrease the measurement volume, but there is no way to *increase* T_1.

The measurement system may achieve reasonable precisions dependent upon the degree of elaboration used to measure relaxation times, and providing that the measurement utilizes, where possible, measurement volumes of materials having relaxation times such that h is about the same magnitude as V_0/T_1. In this case, the real and apparent relaxation times are different by about a factor of two.

The analysis is applicable to both NMR and EPR methods, and they are certainly complementary since some materials readily exhibit electron microwave absorption with very short relaxation times, while other substances lend themselves to NMR methods where relaxation times are often quite long.

The use of electron resonance is necessarily restricted to substances possessing unpaired electrons. Thus a more limited class of materials are subject to flow rate measurements by EPR than NMR. The method of measuring flow rate is practically identical with the NMR scheme, that is, a comparison of the static relaxation time T_1 with $(T_1)'$ the apparent relaxation time of the flowing material. In general, T_1 for electron resonance is less than nuclear relaxation times, hence an additional limitation appears.

Despite these limitations, there are some counteracting advantages to the use of EPR for flow rate measurements. One important point is that the measurement requires fewer molecules—even one billionth of a gram of material is detectable. Further, it is often possible to use very small magnetic fields for measurements. The use of low fields reduces the sensitivity of the EPR measurements, however, and considerably more than a billionth of a gram of paramagnetic substance would then be needed. One possibility is the use of tracer materials in the "inert" fluid whose flow rate is to be measured. Thus EPR methods present an alternative measurement scheme which complements NMR methods in flow rate measurements.

A less direct method than relaxation time measurement was also used by the author. This may be termed the saturation factor method, and depends upon the fact that the signal for adjoining level transitions is reduced due to partial saturation by the factor

$$[1+\tfrac{1}{2}\gamma^2H_1^2T_1g(\nu)]^{-1}, \tag{7}$$

where γ is the nuclear gyromagnetic ratio, H_1 is the rf magnetic field intensity, T_1 is the thermal relaxation time, and $g(\nu)$ is the normalized shape function for the resonance line. For simplicity of notation we define (7) as identically equal to $1/(1+s)$. If a resonance absorption signal from static material is measured, the amplitude is proportional to (7), however if the sample is flowing and partially saturated material is replaced by completely unsaturated material having an equilibrium magnetization, then the signal amplitude is proportional to

$$\left[1+\frac{sV_0}{V_0+hT_1}\right]^{-1}. \tag{8}$$

Therefore, if the resonance absorption signal amplitude when flow is stopped is denoted by A, and the amplitude with flow is called A_f, a readily derived relation is

$$\frac{A_f-A}{A}=\frac{s\{1-[V_0/(V_0+hT_1)]\}}{1+[sV_0/(V_0+hT_1)]}. \tag{9}$$

This is a simple equation to use if $sV_0/(V_0+hT_1)\gg 1$, since in this case of notable saturation,

$$(A_f-A)/A\approx hT_1/V_0. \tag{10}$$

The flow rate is now found to be

$$h\approx(V_0/T_1)[(A_f-A)/A], \tag{11}$$

which implies that one must know the volume of the region under measurement in order to obtain the volume flow rate.

Since we are usually interested in channels of constant cross sectional area, Eq. (11) may be simplified to

$$v=(L_0/T_1)[(A_f-A)/A], \tag{12}$$

where L_0 is the length of tube in the effective rf field, and v is the average linear velocity of flow.

One advantage of this measurement procedure is that the time needed for an observation of amplitude is much less than the time required for a relaxation time measurement. Thus it is possible to determine flow rates rather rapidly. Another point of interest is that a change in flow is readily apparent by a change in the resonance

absorption amplitude. Flow rate readings may be taken every period of the magnetic sweep rate. Since the sweep period may be set for a millisecond or less, blood flow rates can be determined both at the instant of heart pumping, and during the intermediate "coasting time" between heart impulses. Furthermore, this is a particularly sensitive method for quickly estimating relative flow since one need only observe the amplitude of the signal with zero flow rate and the increased amplitude with flow. Even if T_1 were not measured, it is quite simple to observe changes in flow rate. We mostly utilized this scheme to detect blood flow in mouse tails. By observing the signal amplitude with and without a tourniquet and measuring T_1, the flow rate was estimated.

There is one disadvantage to this method as an absolute measurement of blood flow rate. This is due to the fact that body tissues often contain enough nonflowing fluid to provide a constant contribution to both A and A_f in Eq. (12). Such a contribution cancels in the numerator, but remains in the denominator. Therefore this method is best for relative blood flow rates or may readily be used for absolute measurements with inorganic systems.

An additional technique which is very practicable but has not been experimentally utilized by us is the successive saturation method.[1] Here the rf intensity to obtain the same amplitude of absorption is found for both a flowing and static liquid. The relative ratio of static and flowing relaxation times are then obtained from the ratios of the respective $(H_1)^2$ (e.g., see Andrew[4] for an exposition of the T_1 measurement technique).

SEPARATED COIL FLOW METER

A method of observing flow rates which appears to be especially applicable to materials with long relaxation times would be as follows. A region of observation A is chosen for a resonance observation somewhere along the flow channel. A second point B is surrounded by a transmitter coil. First the signal at A is observed in a normal manner on an oscilloscope which is triggered periodically. A number of resonance peaks may be observed due to a rapid field sweep. The resonance signals are constant in amplitude or may vary with a periodic flow rate in the case of a periodic pump (as with blood driven by the heart). Next, at some predetermined instant, the trigger signal sets off a saturation signal (or a 180° pulse or adiabatic fast passage magnetization reversal). The time at which the magnetically saturated (or inverted) spins enter the observation region is then indicated by the decrease (or increase) of amplitude of one or more resonance absorption signals. The time is given by the time base of the oscilloscope and the distance is given by the spacing between A and B, hence the linear velocity of flow is directly calculable.

We are presently constructing a system based on these ideas to measure human blood flow rates. In addition to the simplicity of measurement, this system will have the advantage of measuring either arterial flow or venous flow since it is unidirectional. The method may be best summarized as a magnetization tracer scheme. The saturated or inverted spins are detected a given distance from their origin, and the time taken to move that distance gives the velocity of flow.

CONCLUSIONS

We have derived the equations for NMR measurement of linear flow; volume flow rates are obtainable if the channel area is known. There are several important applications for such measurements. Body processes—particularly relative blood flow studies for drug testing, hypertension diagnostic procedures, and arterial flow studies appear to be promising areas. Industrial applications where flow and process monitoring procedures are necessary present additional possibilities. Most fluids will possess protons having a relatively long relaxation time, and are compatible with NMR flow rate measurements. EPR probably has somewhat more limited application for flow measurements.

We have performed some initial experiments to measure water flow in glass tubes and blood flow velocity in mice tails. This work is continuing and being extended to human blood flow measurement. These experiments will be the topic of a later communication. It may be well to mention, however, that the relaxation time of mouse blood is about 0.4 sec. The T_1 of human blood *in vivo* is about the same order of magnitude.

ACKNOWLEDGMENTS

It is a pleasure to thank Dr. Enoch Callaway and Dr. Robert E. Harris for stimulating my interest in biological measurements.

[4] E. R. Andrew, *Nuclear Magnetic Resonance* (Cambridge University Press, New York, 1955), p. 111.

Interaction of Atomic Hydrogen with Glass*

T. W. Hickmott
General Electric Research Laboratory, Schenectady, New York
(Received July 8, 1959)

An omegatron ion resonance mass spectrometer has been used to study residual gases in an ultra-high vacuum system. Atomic hydrogen, produced from molecular hydrogen by an incandescent tungsten filament, reacts with glass to produce contaminant molecules, CO, H_2O, and CH_4, whose presence seriously interferes with studies of surface phenomena. Such spurious effects are substantially reduced by substituting a lanthanum boride-coated tantalum filament for the tungsten electron source of an ionization gauge used to measure pressures of hydrogen. Quantitative measurements of the binding of atomic hydrogen by glass show the existence of two distinct binding sites of nearly equal population that are occupied simultaneously at low surface coverages and low temperatures. The rate of recombination of atomic hydrogen bound to glass is proportional to the number adsorbed and is much smaller than the rate of recombination of atomic hydrogen impinging on a glass surface from the vapor phase.

INTRODUCTION

ALTHOUGH glass is of primary importance as a construction material for vacuum systems used in studying such diverse phenomena as surface reactions, gas discharges, or electron emission, its effect on such measurements is by no means well defined. Fortunately, in many uses the glass is inert under the experimental conditions but in certain cases its presence may seriously obscure the phenomena being studied unless suitable precautions are taken. If such spurious effects occur they are usually difficult to detect. Two main types of interference may be distinguished; the glass walls of the vacuum system are the source of some contamination which interferes with measurements of the phenomena under study[1–5] or the glass may serve to remove species whose properties are being determined.[6] Some of the complexities of both types of interference are illustrated in the present work in which formation of contaminant species by reaction of atomic hydrogen with glass under well-defined ultra-high vacuum conditions and the recombination and binding of atomic hydrogen by glass have been examined.

EXPERIMENTAL METHODS

Vacuum Techniques

The vacuum system used in this work is shown schematically in Fig. 1. A 0.010-in. tungsten filament, 16 cm long, mounted on 0.150-in. Mo leads in a 2¼-in. o.d. Pyrex bulb which was thermostatted when necessary, served as a source of atomic hydrogen and also provided a reproducible clean surface for adsorption experiments. The geometric surface area of the sample bulb was 255 cm^2. Gas partial pressures as low as 2×10^{-10} mm could be measured by the omegatron ion-resonance mass spectrometer[7] while total pressures were determined by a Bayard-Alpert[8] inverted ionization gauge modified by substituting a lanthanum boride-coated tantalum filament for one of the tungsten gauge filaments. The low work function[9] and low operating temperature of this emitter were essential in reducing contaminant effects due to atomic hydrogen as well as minimizing excessive pumping of hydrogen by the conventional gauge. Analyzed reagent grade gases were obtained from the Air Reduction Company in liter flasks and were used as received. Gas flow into the system from the high pressure reservoir was controlled by a Granville-Phillips Type C valve while the ground glass valve, operated by an external magnet, served to control gas flow and to define the total system volume of 950 cc. Standard procedures for obtaining and measuring ultra-high vacua[9,10] were used. In all cases, before admission

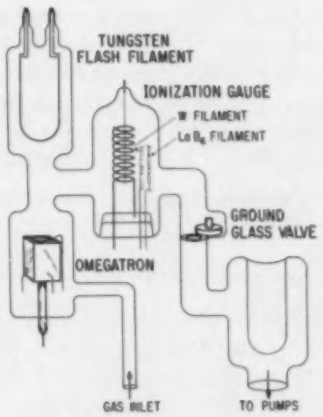

FIG. 1. Schematic of the vacuum system and omegatron.

* Presented in part at the American Physical Society Meeting, Ithaca, New York, June, 1958.
[1] I. Langmuir, Trans. Am. Inst. Elec. Engrs. **32**, 1913 (1913), see S. Dushman, *Vacuum Techniques* (John Wiley & Sons, Inc., New York, 1949), p. 679.
[2] K. B. Blodgett and I. Langmuir, Phys. Rev. **40**, 78 (1932).
[3] T. W. Hickmott and G. Ehrlich, J. Phys. Chem. Solids **5**, 47 (1958); J. Chem. Phys. **24**, 1263 (1956).
[4] Farnsworth, Schlier, and Tuul, J. Phys. Chem. Solids **9**, 57 (1959).
[5] D. G. Bills and A. A. Evett, J. Appl. Phys. **30**, 564 (1959).
[6] G. Glockler and S. C. Lind, *The Electrochemistry of Gases and Other Dielectrics* (John Wiley & Sons, Inc., New York, 1939), p. 115.
[7] Sommer, Thomas, and Hipple, Phys. Rev. **82**, 697 (1951).
[8] D. Alpert, J. Appl. Phys. **24**, 860 (1958).
[9] J. M. Lafferty, J. Appl. Phys. **22**, 299 (1951).
[10] G. Ehrlich, J. Phys. Chem. **60**, 1388 (1956).

of hydrogen, residual pressures of $\sim 1\times 10^{-10}$ mm were obtained with ionization gauge and omegatron operating. Ion currents from the gauge were measured on a Keithley Model 301 amplifier. Pressure corrections for differences in temperature of ionization gauge and adsorption samples were made where necessary. The gauge constant of 4.4 (mm Hg)$^{-1}$ was obtained by calibration against a sensitive McLeod gauge. Filament temperatures were determined from the tables of Jones and Langmuir.[11]

Quantitative measurements of the binding of atomic hydrogen by glass require knowledge of the pumping speed of the system for molecular hydrogen. The pressure, p_c mm, in a vacuum system of volume V cc at temperature T_c is determined at any instant by the rate of supply of molecules to the system and their rate of removal,[10]

$$\frac{V}{kT_c}\frac{dp_c}{dt}=F_M+F_F-F_W-\alpha F_H \text{ molecules/sec.} \quad (1)$$

F_M, the flow of gas into the system from the reservoir at pressure p_m is controlled by the high vacuum valve and is constant in any series of measurements since $p_m \gg p_c$. F_W, the flow of hydrogen from the system, is controlled by the ground glass valve. F_W also includes the adsorption of molecular hydrogen on the glass walls since this is negligible even at liquid nitrogen temperature. It may be expressed as

$$F_W=\frac{S_W}{kT_c}(p_c-p_u)\cong\frac{S_W}{kT_c}p_c, \quad (2)$$

where S_W is the effective pumping speed due to gauge, walls and exit port, p_u is the ultimate pressure in the vacuum system ($\sim 10^{-10}$ mm), and $p_c \gg p_u$. F_F gives the effect of the filament on molecular flow; its sign will depend on whether the filament is adsorbing or desorbing gas but for a saturated filament or one maintained at constant temperature, $F_F=0$. αF_H is the rate of removal of molecular hydrogen from the system after dissociation on a hot filament and subsequent adsorption on the glass walls. F_H, the rate of dissociation of molecular hydrogen, depends on filament temperature and hydrogen pressure while α, the fraction of atomic hydrogen adsorbed by the glass, is primarily a function of the amount of atomic hydrogen previously adsorbed and also of the glass surface temperature and filament temperature.

To measure S_W, the effective pumping speed, a flow of H_2 is established with the exit port open, the filament saturated, and no atomic hydrogen being produced; $F_F=F_H=0$. When the ground glass port is closed S_W is reduced, p_c rises rapidly and

$$\frac{V}{kT_c}\frac{dp_c}{dt}=F_M-\frac{S_W p_c}{kT_c}. \quad (3)$$

A new steady state will then be established, $dp_c/dt=0$ when $p_c=p_0$, and

$$F_M=\frac{S_W p_0}{kT_c}. \quad (4)$$

S_W is thus determined experimentally from the rate of pressure increase on closing the port

$$S_W=-V\frac{d\ln(p_0-p_c)}{dt}. \quad (5)$$

Once S_W is known, αF_H can be measured by raising the filament temperature, T, above 1100°K. p_c will drop due to production of atomic hydrogen and its pumping by glass, whether the bulb is at room temperature or immersed in liquid nitrogen, and

$$\alpha F_H=\frac{S_W}{kT_c}(p_0-p_c) \text{ molecules/sec.} \quad (6)$$

Omegatron Ion-Resonance Mass Spectrometer

The omegatron used, of conventional design,[7,12,13] was constructed of 0.010-in. Mo sheet and could be thoroughly outgassed by induction heating.† The magnetic field of 3200 oersted was provided by a permanent magnet, a Hewlett-Packard Model 650A oscillator supplied the variable radio-frequency field and ion currents were measured by an Applied Physics Model 30 vibrating reed electrometer. A regulated electron current of 1 μamp was used. Mass spectra were calibrated by admission of reagent grade N_2, O_2, H_2, and CO. Resolution was adequate to separate up to masses 17 and 18 completely as well as masses 28 and 30 while higher adjacent masses to mass 50 were distinguishable but not completely resolved. No attempt was made to calibrate the omegatron to measure pressures quantitatively, but measurements of the changes or relative amounts of any gas species were reproducible. The noise level of the vibrating reed electrometer and mass spectrometer was $\sim 3\times 10^{-16}$ amp on the lowest scale used, corresponding to gas partial pressures of $\sim 1\times 10^{-10}$ mm. Since this represents the lowest detectable mass signal, mass spectra are reported as multiples of this value or as fractions of some standard signal. The omegatron was used primarily to determine residual gases and contaminant species due to atomic hydrogen, and to make qualitative measurements of the interaction of atomic hydrogen with glass. All quantitative measurements

[11] H. A. Jones and I. Langmuir, General Elec. Rev. **30**, 310, 354, 408 (1927).

[12] D. Alpert and R. S. Buritz, J. Appl. Phys. **25**, 202 (1954).

[13] J. S. Wagener and P. T. Marth, J. Appl. Phys. **28**, 1027 (1957).

† The omegatron was a modified version of a design developed by J. L. Taylor.

were made with the omegatron turned off since dissociation of hydrogen by its hot electron source interfered with accurate determination of the pumping speed of the vacuum system.

EXPERIMENTAL RESULTS

Residual Gases in a Pyrex Vacuum System

The residual gases in a glass vacuum system, those formed when the glass is heated and slowly evolved after a bakeout, are also those which are likely to interfere with studies of surface phenomena, particularly surface reactions occurring on samples of small area. Although the use of ultra-high vacuum techniques to achieve very low pressures is widespread, little information is found on the residual gases in a Pyrex vacuum system after bakeout at various temperatures.[14] New glassware and a new ionization gauge and omegatron were sealed onto the vacuum system which was then pumped for two weeks. Table I shows the principal mass peaks for the unbaked system, for the system baked four hours at 125°C, and for the system plus traps and manifold baked for 12 hr at 225°C. The principal residual gases are CO, H_2O, and CO_2; no O_2 was detected, possibly because of conversion to CO by the omegatron electron source.[13,15] Hg is removed by baking traps and manifold while the system is baked. The H_2 peak was readily reduced by outgassing the omegatron and was not evolved from the glass. The presence of CO rather than N_2 was identified by the large mass 12 peak and the absence of a peak at mass 7. The ionization gauge was found to be a source of CO rather than a pump when operated prior to being baked out and outgassed. Existence of such an effect is indicated if the measured pressure appears to increase as the electron current of the gauge is increased. Thus operation of an ionization gauge at as low an electron current as possible gives more accurate pressure measurements than use of a high current, particularly in a poorly baked system.

TABLE I. Change in residual gases in a Pyrex vacuum system with bakeout. (Omegatron ion currents in units of 3×10^{-10} amp.)

Gas	Mass peak	Unbaked system	Baked at 125°C	Baked at 225°C	Baked at 425°C: metal outgassed
Hg	100	1280	530	...	...
CO_2	44	790	69	24	...
CO	28	2580	570	152	2
H_2O	18	6100	430	36	1
CH_4 or O	16	300	33	7	...
H_2	2	860	240	64	...
Total pressure (mm eq. N_2)		8×10^{-7}	4×10^{-7}	5×10^{-9}	2×10^{-10}

[14] J. Blears, J. Sci. Inst. Suppl. **1**, 36 (1950).
[15] R. E. Schlier, J. Appl. Phys. **29**, 1162 (1958); H. D. Hagstrum and J. T. Tate, Phys. Rev. **59**, 509 (1941).

By repeated baking at 425°C and outgassing of all metal parts, pressures of $\sim1\times10^{-10}$ mm were obtained with the omegatron operating; traces of residual CO and H_2O were just barely detectable before the gas being studied was introduced from the reservoir. In general, CO, one of the gases most rapidly adsorbed by metals, is the most common residual gas in well baked Pyrex systems. However H_2O, if present, is tightly bound to glass and only slowly removed by the pumps.

Atomic Hydrogen and Contaminant Effects

Studies of the chemisorption of H_2 and O_2 on tungsten have shown that operation of an ionization gauge to measure pressures has a marked effect on chemisorption of these easily dissociated gases.[3] For H_2 on W two apparently distinct states of binding were found, one of which desorbed below 600°K while the second evaporated above 1100°K. However, the size of the peak associated with the more tightly bound state depended directly on operation of the hot filament of the ionization gauge. It was recognized that production of atomic hydrogen by the hot tungsten filament was responsible for spurious effects but flash filament measurements could not distinguish whether direct adsorption of atomic hydrogen occurred or whether some more complicated contaminant effect was present. Using the omegatron to identify residual gases, we have been able to isolate reactions between atomic hydrogen and the container walls which occur under ultra-high vacuum conditions and result in the production of contaminant gas species, primarily CO, H_2O, and CH_4.

TABLE II. Comparison of tungsten and lanthanum boride as electron sources for ionization gauges.

Gas	f_m, omegatron only	f_m, LaB_6 filament	f_m, W filament
CO	3.8×10^{-3}	5.1×10^{-3}	26×10^{-3}
H_2O	3.1×10^{-3}	6.8×10^{-3}	3.4×10^{-3}
CH_4	5.4×10^{-3}	5.1×10^{-3}	15×10^{-3}
H_2	1.0	0.98	0.82
Total pressure (mm)		3.7×10^{-6}	3.2×10^{-6}
		$i_e=5.00\times10^{-4}$ amp	

To minimize atomic hydrogen formation during pressure measurements with the ionization gauge one of the two tungsten electron sources was replaced by a lanthanum boride-coated tantalum filament which gave emission of 5–50 μamp at $\sim$1100°K. Table II shows changes in gas composition in one particular vacuum system with a constant flow of hydrogen but with pressures measured by the conventional and by the modified gauge. $f_m=i_m/i^0_{H_2}$ is the ratio of i_m, the positive ion current at mass m, to the H_2 ion current with only the omegatron in operation. Both the CO and CH_4 peaks increase substantially when the tungsten gauge fila-

ment is used while the H_2O peak changes only slightly. The H_2 peak decreases because molecular hydrogen is dissociated by the incandescent tungsten filament but not by the lanthanum boride electron source. The magnitude of pumping of H_2 depends primarily on how extensively the glass walls are saturated with atomic hydrogen. At high saturations most of the atomic hydrogen will recombine at the walls and the apparent pumping by the hot filament will appear to be small. Copious amounts of CO are produced in outgassing the LaB_6 filament but if outgassing is done at temperatures higher than needed for operating the gauge, pressures of $\sim 2\times10^{-10}$ mm are readily obtained. The modified ionization gauge has been operated with electron currents of 50 μamp or less to minimize contamination.

To show the dependence of contaminant on filament temperature a flow of hydrogen sufficient to maintain a pressure of 4.0×10^{-7} mm, as indicated by the modified ionization gauge, was established with the omegatron operating. The tungsten flash filament was then held at different temperatures until steady state conditions were reached. Table III shows the major components of the gas in the system, expressed as the fraction $f_m = i_m/i^0_{H_2}$, for different tungsten filament temperatures where $i^0_{H_2}$ is now the H_2 current with tungsten filament cold. Carbon monoxide, identified by separate C and O peaks and initially negligible in amount, becomes a major constituent with rising filament temperature; under normal operating temperatures of a tungsten gauge filament (1900°–2200°K) it may exceed in amount the hydrogen present. H_2O_2, H_2O, and CH_4 are found in smaller but significant quantities. Exceptional behavior was observed if H_2 was used in a vacuum system after O_2 had been studied. In this case a water peak larger than the CO peak was produced by operating the omegatron filament; this peak diminished to negligible size after three or four days, and was probably due to atomic hydrogen reacting with oxygen chemisorbed on the Mo plates of the omegatron.

Examination of the desorption peaks for H_2 on W under experimental conditions comparable to those reported previously[3] shows that the low temperature peak, desorbed below 600°K, is H_2. However, the high temperature peak which desorbs above 1100°K and *does* depend on the presence of a hot tungsten filament, is found to be CO and is *not* characteristic of the interaction of molecular hydrogen or atomic hydrogen with the surface. In fact, observation of a pressure *rise* when the filament is heated above 1100°K shows a large amount of adsorbed contaminant since a marked *decrease* should be observed due to formation of atomic hydrogen by flash filament and gauge filament followed by adsorption on the glass.

The question arises as to the origin of the contaminant species. Although molecular hydrogen reacts with hot tungsten to produce atomic hydrogen, Tables II and III show that the tungsten omegatron cathode produces little contaminant compared to the hot tungsten filament in the gauge. The omegatron filament, however, is almost completely surrounded by molybdenum electrodes which can efficiently recombine any H atoms evolved. Atoms formed at the gauge filament on the other hand have unimpeded access to the glass walls and the difference in the amounts of CO observed suggests that such contamination is formed by the interaction of H atoms with the glass walls. This interpretation‡ is supported by the fact that identical contact potentials for H_2 on W have been obtained both in the presence and absence of atoms if the glass walls were shielded by a metal film.[16] In contrast, thermionic measurements without a protecting film have yielded anomalously high values.[17]

TABLE III. Gases in system containing H_2 and hot W filament

Filament Temperature	H_2O_2 f_{34}	CO f_{28}	H_2O f_{18}	CH_4 f_{16}	H_2 f_2
300°K	2.6×10^{-3}	5.6×10^{-3}	3.3×10^{-3}	0.2×10^{-3}	1.0
1010°	2.7×10^{-3}	7.0×10^{-3}	3.0×10^{-3}	0.1×10^{-3}	1.07
1550°	4.4×10^{-3}	8.2×10^{-3}	4.4×10^{-3}	0.4×10^{-3}	0.99
1840°	6.7×10^{-3}	27×10^{-3}	8.2×10^{-3}	4.0×10^{-3}	0.86
1975°	7.3×10^{-3}	125×10^{-3}	7.1×10^{-3}	27×10^{-3}	1.1

The source of carbon in contaminant molecules is either the tungsten filament or the glass walls themselves; the oxygen in CO and H_2O must come from the glass. In the first case a modified water cycle[1,2] may be involved in which H atoms react with oxides of the glass to form H_2O molecules. The H_2O in turn decomposes on tungsten and reduces surface carbon to CO which then evaporates. Three tungsten filaments with different carbon content have been examined. Filament 1 was 0.010 in prewar 218 tungsten, aged by heating in vacuum,[10] for which analysis showed 0.006% carbon. Filament 2 was obtained by electrolytically etching such a 0.010 in. filament down to 0.009 in. in 1*N* NaOH before aging, a procedure that reduces surface contamination. Filament 3 was 0.010 in. tungsten obtained from the Kulite Company for which analysis showed 0.003% carbon. This filament was very lightly etched electrolytically in NaOH before aging. Although the percentage of carbon is small, the total amount present would be large enough to account for the observed quantities of contaminant molecules, particularly if the carbon were concentrated at the surface or diffused readily to the surface.[15] For all three filaments contaminant effects were qualitatively the same, CO and CH_4 being produced in substantial amounts by the incandescent filament while H_2O was present to a much lesser extent. Table III shows that the amount of contaminant CO increases substantially for a filament at 1840°K compared to one at 1550°K and yet measurements of the rate of formation of atomic hydrogen at pressures of 4×10^{-7} show

‡ The significance of these observations was first pointed out by Dr. Gert Ehrlich.

[16] J. C. P. Mignolet, Rec. trav. chim. **74**, 685 (1955).

[17] R. C. L. Bosworth, Proc. Camb. Phil. Soc. **33**, 394 (1937).

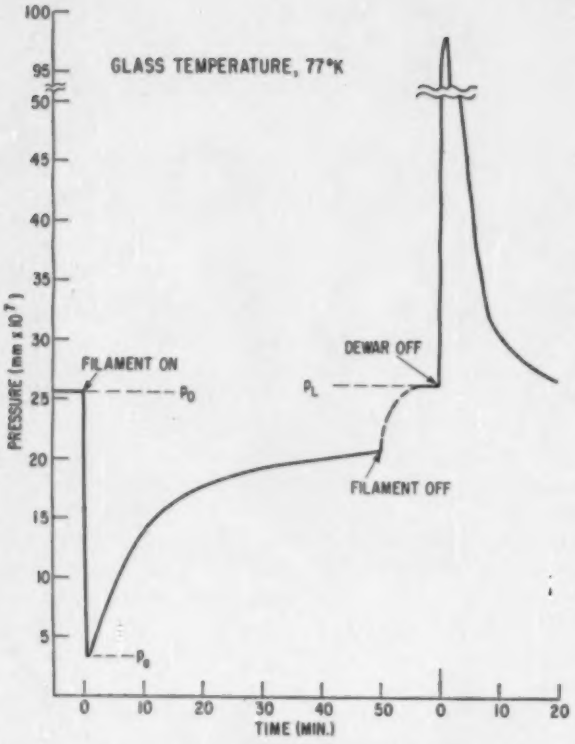

FIG. 2. Pressure changes due to interaction of atomic hydrogen glass. Glass temperature, 77°K. Filament temperature, 1325°K. Constant flow of hydrogen, 2.5×10^{13} molecules/sec.

nearly identical rates for these two filament temperatures. Thus it is possible that the filament needs to run at about 1800°K or higher to diffuse carbon to the surface or to have proper conditions for surface reaction of carbon to form CO. On the other hand, operation of a tungsten filament at 2200°K for five days in a pressure of 5×10^{-6} mm H_2 failed to reduce the amount of contaminant gases.

Even after repeated bakeouts of the glass, CO remains the important constituent of residual gases in Pyrex vacuum systems. It is quite possible that highly reactive atomic hydrogen can release CO from the glass as efficiently as heating. Cleaning of the glass with HF before use increased the ratio of CH_4 to CO but did not appreciably reduce the amount of contaminant. In general, the observations of contaminant were not quantitatively reproducible either for different systems or for the same system at different times; only qualitative observations of contaminant species remained the same. Although the source of carbon, whether glass walls or hot tungsten filament, is uncertain, reaction of atomic hydrogen with the walls is essential as a source of oxygen and is the primary step in the production of contaminant molecules.

Anomalous effects due to operation of hot electron sources have likewise been observed in adsorption studies involving oxygen.[3,13,15] Mass spectrometric examination of the gas composition in our system upon introducing O_2 have confirmed earlier reports on the conversion of oxygen to CO and CO_2. Flash filament studies of the adsorption of oxygen on tungsten show that CO is the major gas isolated in the bursts with O_2 present to less than 10% of the total; in the lower state of binding previously reported,[3] only contaminant CO can be detected. Here too, the origin of carbon in CO and CO_2 is either the incandescent filament or the glass walls of the vacuum system though the evidence is not conclusive for either mechanism. The tungsten omegatron cathode, in close proximity to metal electrodes, produces considerably less contaminant than the ionization gauge filament, but the difference in contaminant production for gauge filament and for omegatron filament is less than with atomic hydrogen.

The ubiquity of contaminant effects due to atomic hydrogen is shown in several recent papers. Observations[3] of two states of binding for H_2 on W in flash filament studies using a conventional ionization gauge to measure pressures have been confirmed though both states have been considered characteristic of the interaction of hydrogen with tungsten.[18] Increased adsorption of hydrogen on silicon in the presence of hot filaments has been attributed to direct adsorption of atomic hydrogen,[19] while water vapor produced by a hot filament has been found to cause anomalies in studies of the diffraction of low energy electrons by hydrogen adsorbed on nickel.[4] Poisoning of the recombination of atomic hydrogen by metal surfaces has been attributed to contaminant species produced by reactive hydrogen atoms.[20] The present work indicates appreciable variation in the qualitative and quantitative contaminant effects due to the presence of an incandescent filament in a low pressure of hydrogen but some such effects have always been found. Use of a low work function electron source such as lanthanum boride or shielding of the hot

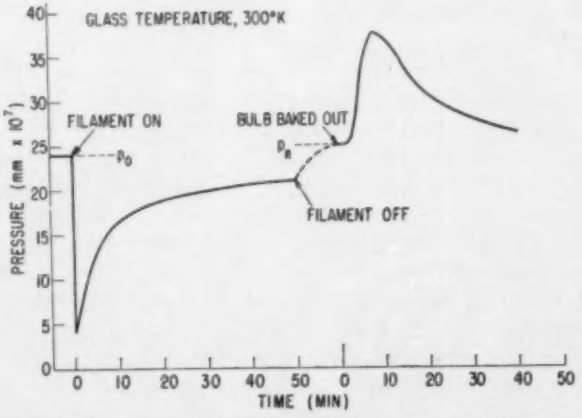

FIG. 3. Pressure changes due to interaction of atomic hydrogen with glass. Glass temperature, 300°K. Filament temperature, 1325°K. Constant flow of hydrogen, 2.4×10^{13} molecules/sec.

[18] J. Eisinger, J. Chem. Phys. **29**, 1154 (1958).
[19] J. T. Law, J. Chem. Phys. **28**, 511 (1958); **30**, 1568 (1959).
[20] Fox, Smith, and Smith, Proc. Phys. Soc. (London) **73**, 533 (1959).

filament with metal that recombines free radicals and prevents their reaching the glass walls, as in the omegatron, can reduce these effects to negligible amounts for adsorption and surface studies involving hydrogen. Regardless of the mechanism of formation of contaminant molecules when reactive species are produced by the gauge, it is apparent that great caution must be exercised in interpreting surface phenomena observed when pressures of easily dissociable gases, for example, H_2, O_2, H_2O, or C_2H_4, are measured by conventional ionization gauges or in the presence of incandescent filaments.

Adsorption and Recombination of Atomic Hydrogen by Glass

Langmuir's[21] early studies of the production and properties of atomic hydrogen showed it to be strongly bound by glass. Coverages of 1.5×10^{15} atoms/cm^2 were found for glass surfaces saturated at 80°K but fatigue effects when glass was used to trap the free radicals formed made measurements of the rate of formation of atomic hydrogen uncertain. When glass cooled in liquid air was warmed to room temperature, about half of the atomic hydrogen adsorbed recombined as molecular hydrogen, "nonrecondensable gas," while the rest was evolved on further heating. Subsequent work on the interaction of atomic hydrogen with glass has confirmed and extended Langmuir's observations.[22–24]

Observations of contaminant effects due to the interaction of atomic hydrogen with glass have been made in systems whose walls were nearly saturated with atomic hydrogen. By baking out the glass bulb containing the adsorption sample at 250°C, a reproducible surface for studies of the binding of atomic hydrogen by glass is obtained. Figures 2 and 3 show the variation in pressure in a vacuum system with a constant flow of hydrogen when a tungsten filament is held at 1325°K for 50 min and the baked out glass bulb is at 77° and 300°K, respectively. p_0, the steady state pressure when no atomic hydrogen is being produced, is established by adjusting F_M, the flow of molecular hydrogen into the system, and S_W, the pumping speed of the ground glass valve. Qualitatively, the results for the two bulb temperatures are similar. A rapid pressure drop is followed by a gradual return to pressures about 0.7–0.9 p_0. For the glass at 77°K, a minimum pressure, p_a, is maintained for about 30 sec before the pressure rise begins. For the glass at 300°K the minimum pressure reached is greater than p_a and the pressure rise is more rapid. Integration of Figs. 2 or 3 gives N_{77} and N_{300}, the total surface coverages of absorbed hydrogen molecules for the glass at 77° and 300°K, respectively. (Table IV summarizes definitions of quantities discussed in this section.) αF_H, the rate of adsorption of atomic hydrogen, can be calculated from Eq. (6). To measure F_H, the rate of formation of atomic hydrogen,‖ the value of α for $p_c=p_a$, α_0, has been assumed to be unity. With this assumption F_H is directly proportional to pressure for pressures less than 10^{-6} mm.[25,26] α, the fraction of hydrogen atoms adsorbed by the glass, depends primarily on glass temperature and surface coverage although for filament temperatures greater than 1400°K and glass at 77°K it also depends on filament temperature. Since F_H is proportional to pressure,

$$\frac{\alpha}{\alpha_0}=\frac{(p_0-p_c)}{(p_0-p_a)}\left(\frac{p_a}{p_c}\right). \tag{7}$$

Figure 4 shows this ratio as a function of the total number of molecules of hydrogen adsorbed as atoms by the glass at 77°K, N_{77}, for different values of filament temperature. If α_r is the value of α corresponding to the minimum pressure reached when the filament produces atomic hydrogen and the bulb is at 300°K, $\alpha_r<\alpha_0\leq1$ and α/α_r may be similarly calculated as a function of surface coverage as shown in Fig. 5. α/α_0 and α/α_r as functions of coverage are independent of F_H for filament temperatures, $1100°<T<1400°$K, but at higher values of T they diminish less rapidly as functions of glass surface coverage. The agreement for different values of F_H shows the reproducibility of the glass surface.

For a glass temperature of 77°K, α/α_0 decreases

TABLE IV. Symbols used in discussing the adsorption and recombination of atomic hydrogen by glass.

F_m	Flow of molecular hydrogen into system from the reservoir (molecules/sec).
F_H	Rate of formation of atomic hydrogen by the tungsten filament (molecules/sec).
α	Fraction of atomic hydrogen produced by the filament that is adsorbed by the glass.
α_0	Maximum value of α when the glass temperature is 77°K.
α_r	Maximum value of α when the glass temperature is 300°K.
N_{77}	Total number of molecules of hydrogen adsorbed as atoms by the glass at 77°K.
N_{300}	Total number of molecules of hydrogen adsorbed as atoms by the glass at 300°K.
N_L	Number of molecules of adsorbed hydrogen evolved when glass is warmed from 77° to 300°K.
N_R	Number of molecules of adsorbed hydrogen evolved when glass is heated from 300° to 525°K.
F_L	Rate of recombination of hydrogen adatoms after deposition on glass at 77°K (molecules/sec).
F_R	Rate of recombination of hydrogen adatoms after deposition on glass at 300°K (molecules/sec).
F_H'	Rate of formation of atomic hydrogen just before filament is turned off after depositing N_{77} or N_{300} molecules of atomic hydrogen on the glass (molecules/sec).

[21] I. Langmuir, J. Am. Chem. Soc. **34**, 1310 (1912); **37**, 417 (1915).
[22] M. C. Johnson, Proc. Roy. Soc. (London) **A123**, 603 (1929); **A132**, 67 (1931).
[23] J. H. deBoer and J. J. Lehr, Z. Physik. Chem. **B22**, 423 (1933).
[24] J. H. deBoer and J. van Steenis, Koninkl. Ned. Akad. Wetenschap. Proc. **B55**, 578, 587 (1952).

‖ Measurements of the rate of formation of atomic hydrogen will be discussed in a separate paper.
[25] D. Brennan and P. C. Fletcher, Proc. Roy. Soc. (London) **A250**, 389 (1959).
[26] G. Ehrlich, J. Chem. Phys. **31**, 1111 (1959).

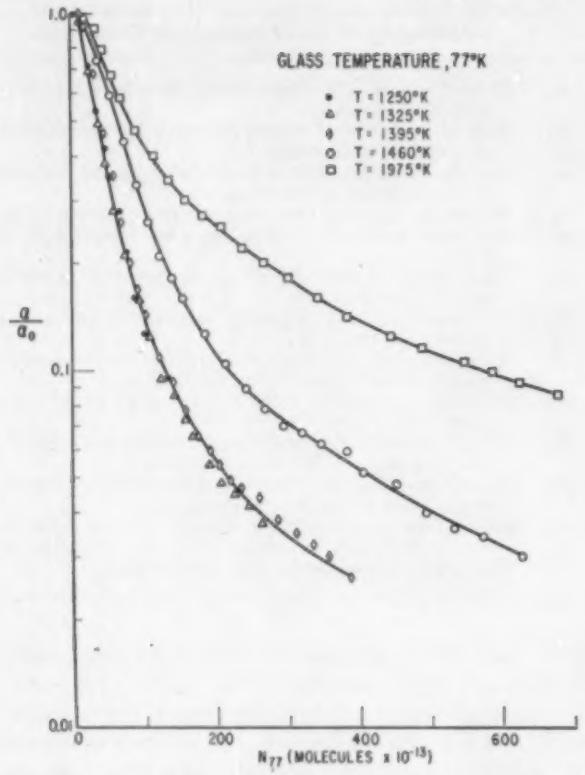

FIG. 4. Change in the fraction of atomic hydrogen adsorbed by glass with increasing amounts of adsorbed hydrogen for different rates of formation of atomic hydrogen. Glass temperature, 77°K.

rapidly with increasing surface coverage and, correspondingly, the fraction of atomic hydrogen recombined by the glass, $(1-\alpha/\alpha_0)$, increases until at saturation of the surface all the atoms are recombined on striking the surface. The magnitude of recombination of atoms bound to the glass can be determined experimentally by stopping production of atomic hydrogen. When the tungsten filament is turned off and saturated after N_{77} molecules of hydrogen have been deposited on the glass at 77°K, the pressure in a constant flow system will return to some steady-state value $p_L > p_0$, as shown in Fig. 2. This increase in pressure is due to the flow, F_L, from a source of hydrogen molecules in addition to flow from the reservoir, F_M, and is the result of recombination of adatoms deposited on the glass bulb, $F_L = S_W/kT_c(p_L - p_0)$ molecules/sec.

Evolution of adsorbed hydrogen atoms from glass at 77°K occurs in two distinct stages. If the Dewar of liquid nitrogen is removed from around the sample bulb, a large, rapid pressure rise is observed, the maximum pressure being reached in about one minute as shown in Fig. 2. Molecular hydrogen is evolved, Langmuir's "nonrecondensable gas."[21] Integration of the pressure burst gives N_L, the number of molecules in this lower state of binding of atomic hydrogen by glass. Further heating of the bulb to 250°C results in nearly quantitative recovery of the remainder of the adsorbed hydrogen. N_R, the number of molecules evolved on heating the glass above 300°K is less accurately determined than N_L but $(N_{77}-N_L)$ and experimental values of N_R agree reasonably well. Table V shows N_L, F_L, N_R, and $F_H{}'$ for values of N_{77} obtained by running the tungsten filament at the temperature indicated for 50 min in a constant flow of hydrogen. $F_H{}'$ is the rate of formation of atomic hydrogen just before the filament is turned off. N_L is 0.56 N_{77} while comparison of $F_H{}'$ with F_L shows that F_L, proportional to N_L but not to $N_L{}^2$, is too small by at least a factor of 500 to account for observed recombination rates when the filament is operating.

Recombination of atomic hydrogen bound to the glass does not occur by surface diffusion followed by reaction of adatoms since this process would be second order in the number of adatoms.[26] The slow step leading to F_L appears to be evaporation of adatoms since F_L is first order in the number of adatoms. Figure 4 shows that at surface coverages, $N_{77} > 130\times10^{13}$ molecules, more than 90% of all atoms produced by the incandescent filament are recombined indicating that efficiency of recombination of hydrogen atoms from the vapor phase is high under the experimental conditions. Once an atom bound to the glass evaporates the probability of recombination is nearly unity and is insensitive to an increase in the total number of molecules adsorbed by the glass. For a simple first-order rate law, $F_L = N_L\nu_L \exp(-\Delta H_L/RT)$, if $\nu_L \approx 1\times10^{13}$ sec^{-1}, the heat of recombination of adatoms in the lower binding state, i.e., the heat of evaporation of atoms, can be estimated as $\Delta H_L = 6600$ cal/mole.

When the freshly baked glass surface is maintained at 300°K instead of 77°K during the production of atomic hydrogen, curves of α/α_r *versus* N_{300} are qualitatively similar to those of α/α_0 as a function of surface coverage. Quantitatively they differ since the lower binding state, N_L, remains unpopulated. Here, too, recombination of adatoms after formation of atomic hydrogen ceases is insufficient to account for the observed recombination rates when the filament is producing atomic hydrogen. Table VI shows F_R, the molecular flow due to adatom recombination at 300°K when production of atomic hydrogen ceases, and a minimum value of $F_H{}'$, the rate of formation of atomic hydrogen just before deposition of N_{300} molecules of hydrogen is complete. For a first-order evaporation,

TABLE V. Binding of atomic hydrogen by glass at 77°K.

Filament temperature	N_{77} (molecules)	N_L (molecules)	N_R (molecules)	F_L (molecules/sec)	$F_H{}'$ (molecules/sec)
1250°K	135×10^{13}	100×10^{13}	84×10^{13}	4×10^{9}	2.3×10^{12}
1325°K	260×10^{13}	150×10^{13}	130×10^{13}	6.5×10^{9}	13.4×10^{12}
1395°K	390×10^{13}	210×10^{13}	150×10^{13}	8.4×10^{9}	21×10^{12}
1460°K	630×10^{13}	370×10^{13}	250×10^{13}	13×10^{9}	64×10^{12}
100 min at 1975°K	1000×10^{13}	550×10^{13}	190×10^{13}		
5 hr at 2100°K	430×10^{13}	165×10^{13}	150×10^{13}		

$F_R = N_{300}\nu_R \exp(-\Delta H_R/RT)$, $\Delta H_R \simeq 25$ kcal/mole for $\nu_R \approx 1\times10^{13}$ sec^{-1}, in close agreement with earlier values.[24]

Our results again[21] show the existence of two distinct states for atomic hydrogen bound by glass, an L state and an R state with populations N_L and N_R, respectively. de Boer has suggested that the L state is atomic hydrogen adsorbed as a second layer on top of a first saturated layer of hydrogen atoms.[24] Determination of the exact amount in the L state depends on a knowledge of the interaction and relation of both states which is not available. For total surface coverages at least up to $N_{77}=1000\times10^{13}$ molecules, Table V shows that $N_L/N_{77}=0.56$, while in saturating the glass a total coverage, $N_{77}=430\times10^{15}$ molecules in a bulb of 255 cm^2 area, was obtained. Thus formation of the L state does not require a saturated first layer. If the two states are completely independent, evolution of molecular hydrogen when the glass temperature increases from 77° to 300°K involves recombination of atoms in the L state only and $N_L=0.56\,N_{77}$. It is more probable that formation of "nonrecondensable gas" results from reaction of atomic hydrogen in the L state with atoms in either state and thus $0.28\,N_{77}<N_L<0.56\,N_{77}$. In any case for glass at 77°K both states are present in roughly equal amounts at surface coverages that are a small fraction of a monolayer. Thus at least two distinct binding sites for atomic hydrogen are present on a glass surface and both states form simultaneously at low coverages when atomic hydrogen is deposited on glass at 77°K.

The increase in rate of recombination with increased surface coverage is qualitatively similar for glass at 77° and 300°K; for both, recombination of atomic hydrogen becomes significant at relatively low surface coverages. Quantitative differences for the two temperatures depend on the occupation of the lowest state of binding of atomic hydrogen by glass at 77°K. Recombination of atomic hydrogen produced by the filament can occur either by reaction between two atoms after being bound to the surface or by collision of an atom from the gas phase with an atom on the surface.[26–28] F_L and F_R in Tables V and VI are experimental measurements of the first process and indicate that such a mechanism does not account for observed recombination rates when the filament is producing atomic hydrogen. The opening from the sample bulb, of area ~5 cm^2, is small compared to the total bulb area of 255 cm^2. Even though the probability of recombination may be small for a single collision ($\gamma=7.5\times10^{-4}$ for Pyrex at 300°K),[27,29] any atom will suffer many collisions with the wall before it can escape from the reaction bulb. Therefore the total probability for recombination of those atoms not adsorbed by glass is high; recombination of atomic hydrogen by collision from the gas phase has an efficiency of nearly unity at small fractions of saturation of the glass surface under the experimental conditions. Nearly quantitative recovery of the atomic hydrogen produced indicates that little diffusion from the reaction vessel occurs, and the detailed shape of the pressure-time curves such as in Fig. 2 and 3 depends primarily on the number of binding sites unfilled.

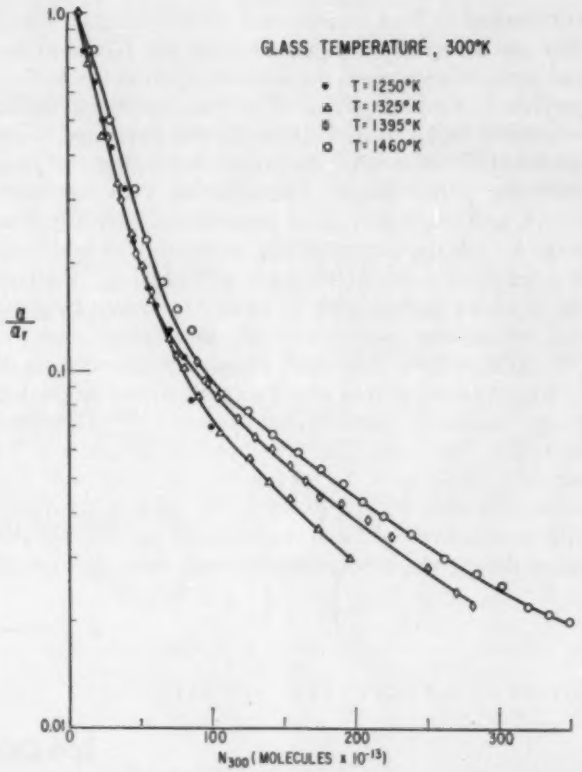

FIG. 5. Change in the fraction of atomic hydrogen adsorbed by glass with increasing amounts of adsorbed hydrogen for different rates of formation of atomic hydrogen. Glass temperature, 300°K.

TABLE VI. Binding of atomic hydrogen by glass at 300°K.

Filament temperature	N_{300} (molecules)	N_R (molecules)	F_R (molecules/sec)	F_R' (molecules/sec)
1250°K	105×10^{13}	97×10^{13}	2.9×10^{9}	2.4×10^{12}
1325°K	195×10^{13}	155×10^{13}	9.5×10^{9}	11×10^{12}
1395°K	280×10^{13}	210×10^{13}	12×10^{9}	26×10^{12}
1460°K	360×10^{13}	230×10^{13}	13×10^{9}	36×10^{12}

CONCLUSION

Studies of adsorption and reactions on glass are inconclusive by the very nature of the material since the structure of bulk glass is poorly understood and even less is known of the nature of the surface. However, we find that reproducible surfaces may be obtained by baking Pyrex at 250°C. Quantitative examination of the binding of atomic hydrogen by glass has shown the

[27] W. V. Smith, J. Chem. Phys. **11**, 110 (1943).
[28] K. E. Shuler and K. J. Laidler, J. Chem. Phys. **17**, 1212 (1949).
[29] B. J. Wood and H. Wise, J. Chem. Phys. **29**, 1416 (1958).

existence of at least two distinct binding sites on Pyrex that are occupied simultaneously at low temperatures and have roughly equal populations, even at low surface coverages. Recombination of atomic hydrogen bound to glass is found to be very inefficient compared to recombination of atomic hydrogen impinging on glass from the vapor phase. Complicating such measurements, and important as an experimental artifact that may obscure the nature of the interaction of hydrogen or other readily dissociable gases with surfaces, is pumping of active species such as atomic hydrogen by glass and subsequent production of contaminant species, CO, H_2O, or CH_4. Any flash filament measurements of hydrogen adsorption in which a conventional ionization gauge measures pressure are suspect.[3,18,19] Desorbed molecular hydrogen that reaches the gauge will be partially dissociated by the gauge filament and the atoms adsorbed by the glass. If the glass is saturated with atomic hydrogen due to continued operation of the gauge during the adsorption interval, some fraction of the atoms produced by the gauge filament will be recombined on the glass and recorded by the gauge as molecular hydrogen. However, constant gauge operation may produce serious contamination of the adsorbing surface. If gauge operation is discontinued during the adsorption interval,[3,19] contamination is minimized; the glass remains unsaturated and the pressure bursts will be reduced an uncertain amount due to adsorption of atomic hydrogen on glass. Once recognized, these difficulties may be markedly reduced or eliminated by using gauges with low work function electron sources and producing as little atomic hydrogen as possible, or by avoiding hot filaments altogether.

ACKNOWLEDGMENT

Both experiments and interpretation have benefited from many conversations with Dr. Gert Ehrlich who first appreciated the subtlety of the contaminant effects due to the presence of atomic hydrogen.

JOURNAL OF APPLIED PHYSICS VOLUME 31, NUMBER 1 JANUARY, 1960

Ion Drag Pumps

OTMAR M. STUETZER
Mechanical Division of General Mills, Incorporated, Minneapolis, Minnesota
(Received June 11, 1959)

The behavior and the efficiency of a simplified model of an ion drag pump for insulating fluids is discussed theoretically. Supporting measurements on real pumps are reported. Cascading and paralleling of pumping stages is investigated.

1. INTRODUCTION

IN a recent publication[1] it was demonstrated that high electrical fields in fluids with preferably unipolar ion conduction can create substantial pressures. For insulating liquids, rather simple arrangements yield pressures of the order of 0.1 atmos. A first-order approximation theory gave good agreement with the experiments but was limited to the static case, i.e., a nonmoving fluid.

If we want to use an ion drag configuration as a pump, the carrier has to move. In insulating liquids the carrier mobility is such that the velocity of the ions with respect to the liquid is of the same order of magnitude as the velocity the liquid can obtain relative to the electrodes. The simple theory for the static case is then no longer applicable, mainly because the electrical current drawn is now much higher. It has been shown[2] that for a linear model the system of differential equations describing ion drag under dynamic conditions can be integrated and, for certain boundary conditions, yields simple explicit expressions. The purpose of this paper is to adapt this solution to the specific problems of interest for ion drag pumping; we shall compute the efficiency of pumps, discuss their optimum dimensions, and investigate paralleling and cascading of single stages. The mathematical considerations will be limited to a linear model. Experimentally it will be shown, however, that the predictions of our model hold, at least qualitatively, for the much more complicated two-electrode devices where the emitter is a corona point. The experiments will be restricted to insulating liquids where the pumping efficiency is highest.

The nomenclature we use will be very closely related to that in reference 1 which contains literature references on previous work. mks units will be used throughout the paper.

2. THEORETICAL MODEL AND BASIC EQUATIONS

We shall first briefly summarize and modify the development of the equations[1,2] that describe a simple one-dimensional pumping system as sketched in Fig. 1(a).

[1] O. M. Stuetzer, J. Appl. Phys. 30, 984 (1959).
[2] O. M. Stuetzer, Phys. Fluids 2, 642 (1959).

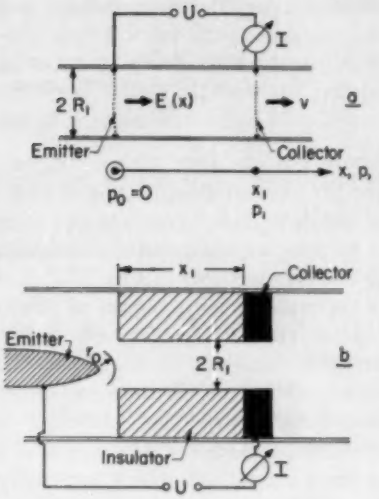

FIG. 1. Theoretical model arrangement (a) and a practical pump stage (b).

The fluid to be moved is contained in a tube of cylindrical cross section with radius R_1(m). At $x=0$ a planar emitter arrangement supplies ions; the electric field E (v/m) attracts them to a collector grid at $x=x_1$. Collector and emitter shall present only negligible hydrodynamic resistance. The walls of the confining vessel shall not influence the electrical field distribution, i.e., they shall not charge up. Turbulence in the fluid shall be neglected for computation of the field distribution.

The ions move under the influence of the electric field with an average velocity bE with respect to the fluid where b is the mobility measured in m²/v·sec. Through friction they exchange momentum with the fluid building up a pressure p which varies along the coordinate x. The pressure p is measured in newton/m² where 1 newton/m²≈0.1 mm water. Energy losses due to turbulence and viscosity cause a superimposed pressure drop p' along the system. This we shall take into account later.

The gradient of the ion drag pressure p has to balance the force which our field $E(x)$ exerts on the unit volume space charge $\rho(x)$(amp·sec/m³), yielding for our one-dimensional case

$$dp/dx=\rho E \quad \text{(newton/m}^3\text{)}. \tag{1}$$

As in the static case, field and space charge are linked by Poisson's equation

$$\rho/\epsilon=dE/dx \quad \text{(v/m)}. \tag{2}$$

ϵ is the absolute dielectric constant of the fluid. Of course we have $E=-dV/dx$ where V is the potential. The transport equation has to take into account that the current producing motion of the space charge ρ occurs with a velocity of $bE+v$, where v is the velocity of the carrier liquid with respect to the electrode system. We thus obtain for the current density $j=I/R_1^2\pi$ in the system, neglecting diffusion currents,

$$j=\rho(bE+v) \quad \text{(amp/m}^2\text{)}. \tag{3}$$

Integration and combination of Eqs. (1) to (3) is simple.[2] The Appendix describes the mathematical steps necessary for our purpose. We obtain the following expression for the pressure p_1 generated between emitter and collector:

$$p_1=\frac{\epsilon}{2}\left[\frac{2jx_1}{\epsilon b}-2\frac{v}{b}\left\{\left[\frac{2jx_1}{\epsilon b}+\left(E_0+\frac{v}{b}\right)^2\right]^{\frac{1}{2}}-\left(E_0+\frac{v}{b}\right)\right\}\right] \quad \text{(newton/m}^2\text{)}. \tag{4}$$

E_0, here, is the field strength at the emitter; the pressure is expressed as a function of the current density j, the flow velocity v, and the constants of the system. j itself is linked to the applied voltage U and the flow velocity through

$$\frac{U-U^*}{(2/3)x_1}=\frac{\left[\frac{2jx_1}{\epsilon b}+\left(E_0+\frac{v}{b}\right)^2\right]^{\frac{3}{2}}-\left(E_0+\frac{v}{b}\right)^3}{2jx_1/\epsilon b}-\frac{3}{2}\frac{v}{b} \quad \text{(v/m)}. \tag{5}$$

U^*, here, is the voltage at which space charge limited conduction starts in our system. For most cases of interest it is small *versus* the applied voltage U.

3. APPROXIMATE RELATIONS FOR FORWARD FLOW

When pumping, the flow in our system $i=R_1^2\pi v$ (m³/sec) will be caused by the generated pressure p_1. This means that the liquid moves in the same direction as the ions, i.e., v is a positive quantity. If our emitter is a good supplier of ions, the field strength E_0 at the emitter is small.[2] We shall neglect it for the purpose of this paper.

For $E_0=0$, Eqs. (4) and (5) permit us to express the electrical quantities of our systems as functions of the generated pressure p_1 and the flow velocity v (see Appendix)

$$j=\frac{\epsilon b}{2x_1}\cdot\left(\frac{2p_1}{\epsilon}\right)^{\frac{1}{2}}\left[\left(\frac{2p_1}{\epsilon}\right)^{\frac{1}{2}}+2\frac{v}{b}\right] \quad \text{(amp/m}^2\text{)} \tag{6}$$

$$U-U^*=\frac{2}{3}x_1\cdot\left(\frac{2p_1}{\epsilon}\right)^{\frac{1}{2}}\cdot\frac{(2p_1/\epsilon)^{\frac{1}{2}}+(3/2)\cdot(v/b)}{(2p_1/\epsilon)^{\frac{1}{2}}+(4/2)\cdot(v/b)} \quad \text{(v)}. \tag{7}$$

The electrical input power into our system is $P=U\cdot I=R_1^2\pi jU$. Only a part of this, $P^*=kP=(U-U^*)I$, is available for the pumping process, the part $(1-k)P$ being, in our technical arrangement discussed below, used for creating the necessary ions. By multiplying

Eqs. (6) and (7) we obtain

$$P^*=kP=\frac{1}{3}R_1^2\pi\epsilon b\cdot\frac{2p_1}{\epsilon}\left[\left(\frac{2p_1}{\epsilon}\right)^{\frac{1}{2}}+\frac{3}{2}\frac{v}{b}\right] \quad \text{(w)} \quad (8)$$

with k being defined as

$$k=\frac{U-U^*}{U}. \quad (9)$$

The foregoing equations permit, without specific assumptions on the properties of the hydrodynamic arrangements (which link p_1 and v), a description of the general behavior of an ion drag pump: For $v=0$ the current is proportional to the pressure p_1 [Eq. (6)]. If the medium starts to flow and the pressure stays constant, the current has to rise proportionally to v. If the current is kept constant (atomic battery) the pressure drops when the velocity increases. It is easy to see that in this case our arrangement is a stable source of pressure.

From Eq. (7) we see that for $v=0$ the pressure developed, p_1, is proportional to the square of the voltage $U-U^*$. With increasing flow and the generated pressure kept constant, this voltage drops, reaching asymptotically 3/4 of the original value. Conversely, if we operate our system from a constant voltage power supply set, the pressure p_1 increases with increasing flow velocity approaching asymptotically 16/9 of the static pressure. It has been pointed out[2] that this leads to instability in our system. As, however, the flow velocity in practical arrangements is usually limited by hydrodynamic resistance, this increase of the dynamic pressure over its static value is usually much less than the asymptotic factor 16/9. The phenomenon lies, for pumps, within the accuracy limits of measurements ($\sim 10\%$) and expresses itself mainly in annoying nonlinear oscillations of pressure, accompanied by fluctuations of current $I=R_1^2\pi j$ according to Eq. (6).

The hydrodynamic power output of our system will be proportional to $R_1^2\pi v\cdot p_1$. The electrical input power required, however, increases faster than this value according to Eq. (8). This fact limits the efficiency of our pump. As demonstrated below for a more specific case, this influence is significant. It is mainly for this reason that the dynamic equations had to be developed.

4. FLOW LOSSES IN THE SYSTEM

Above we have discussed the pressure p_1 generated along the length x_1 of our pumping stage and its depencence on flow velocity v, input current I, and accelerating voltage $U-U^*$. The velocity v is in our case generated by p_1 and depends on the hydrodynamic resistance of the system. Of special interest to us is the internal hydrodynamic resistance of our pump stage which we may define in analogy to the electrical case as

$$S_1=\frac{p_1'}{i} \quad \text{(newton·sec/m}^5\text{)}, \quad (10)$$

where i is the flow rate, $i=R_1^2\pi v$ (m³/sec) and p_1' is the pressure drop across the system under the influence of the flow. S_1 is a function of i except for viscous flow.

In practice the pumps we wish to discuss are similar to the arrangement in Fig. 1(b). A corona point emitter is surrounded by a region of effective radius r_0 where bipolar conduction prevails; its contribution to the pressure buildup is neglected. Unipolar conduction occurs along the distance x_1, often surrounded by an insulating sleeve. The collector is a ring with an opening of diameter $2R_1$. (x_1 and R_1 are of the same order of magnitude which is roughly 1 mm for many of the experiments to be reported.)

Due to the properties of the corona emitter, the flow in our pump stage is always highly turbulent even for velocities where Reynolds numbers would permit laminar flow. For liquids this can be easily shown experimentally by adding small amounts of an optically different material to our pumping fluid.

If there were no friction losses in our system, the energy law would link the pressure drop p_1' with the flow rate i through the well-known equation

$$i=R_1^2\pi\left(\frac{2p_1'}{\delta}\right)^{\frac{1}{2}} \quad \text{(m}^3\text{/sec)}$$

where δ is the density of the liquid in kg/m³. Von Karman and Prandtl[3] have developed a theory which takes small losses into account: With our designations the improved equation above reads

$$i=R_1^2\pi\cdot\gamma'\cdot\left(\frac{2p_1'}{\delta}\cdot\frac{R_1}{x_1}\right)^{\frac{1}{2}} \quad \text{(m}^3\text{/sec)}.$$

γ', here, is a dimensionless parameter which depends logarithmically on the Reynolds number of the flow, i.e., it depends on i. For variations in Reynolds numbers from 10^3 to 10^8 it varies only by a factor of 3 in smooth pipes.[4] R_1 and x_1 are of the same order of magnitude, and for many technical arrangements derived, assume the character of effective quantities, only approximated by their geometric values. Usually R_1/x_1 is about 0.3 to 0.5. For the purpose of this investigation we may combine the little varying quantities $\gamma'(R_1/x_1)^{\frac{1}{2}}$ into a parameter

$$\gamma=\gamma'\left(\frac{R_1}{x_1}\right)^{\frac{1}{2}}$$

[3] Summarized in L. Prandtl, *Essentials of Fluid Dynamics* (Hafner Publishing Company, New York, 1952), p. 121f, English translation.

[4] J. Kozeny, *Hydraulik* (Springer-Verlag, Berlin, Germany, 1952), p. 114.

which we may assume constant with respect to i. Its value lies between 0.5 and 0.9 for insulating liquids like kerosene or transformer oil which have a reasonably low viscosity. It can be seen that for efficient pumps this mathematical simplification has very little effect on our results.

We shall therefore use, as a good approximation, the relationship

$$i=R_1^2\pi\cdot\gamma\cdot\left(\frac{2p_1'}{\delta}\right)^{\frac{1}{2}} \quad (\mathrm{m^3/sec}) \tag{11}$$

for the generator space in our pump. Inserting Eq. (11) into Eq. (10) we see that the hydrodynamic resistance S_1 is proportional to i. In other parts of our system laminar flow may occur where the pressure drop and the flow rate are related by the well-known Poiseuille equation.

5. DYNAMIC BEHAVIOR OF TWO IRIS SYSTEM

In this section we shall combine the results developed in Secs. 3 and 4 and study a pump which works into a load. The flow rate into the load is of course the same as that through the pump, i. As the flow velocity in the two parts will in general be different, we will distinguish the values by subscripts, calling the velocity in the pump stage v_1. If the pressure drop across the work stage is p_2' (newton/m²), the power delivered to it is $P_2=ip_2'$ (w).

For calculating purposes we shall assume an arrangement as sketched in Fig. 2. The load pressure drop p_2' is created by a constriction of radius R_2 similar to the one of the pump stage. The system is closed and its diameter away from the constrictions is so large that pressure drops can be neglected. Calling the pressure in front of the pump (and behind the load) $p_0=0$, we see that the pressure drops p_1' and p_2' must add up to the generated pressure created by the pump, p_1. The pressure drop across the load p_2' obeys an equation equivalent to Eq. (11). The respective quantity γ, depending on the Reynolds number (i.e., on R_2 for constant i) will be slightly different if R_2 is not equal to R_1 but we shall neglect this small correction. We obtain then

$$p_1=p_1'+p_2'\approx\frac{\delta}{2}\frac{i^2}{(R_1^2\pi\gamma)^2}[1+(R_1/R_2)^4] \quad (\mathrm{newton/m^2}). \tag{12}$$

This equation now links the flow rate i or the flow velocity $v_1=i/R_1^2\pi$ to the generated pressure p_1 and the dimensions of the system. p_1 itself is a function of v_1 according to Eqs. (4) and (5). Combining Eq. (12) with these equations, we can now compute the actual pressure and the actual flow rate occurring for an applied voltage U or an enforced current I. We shall restrict ourselves to the case of constant voltage which occurs more often in practice; the efficiency computed is the same for other energizing electrical circuits.

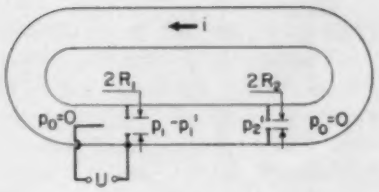

FIG. 2. Closed system with pump stage (subscript 1) and work stage (subscript 2).

From Eqs. (12) and (5) we obtain after some manipulation for the flow velocity

$$\frac{v_1}{b}\approx\frac{U-U^*}{(2/3)x_1}\cdot\frac{1}{(b/\gamma)(\delta/\epsilon)^{\frac{1}{2}}[1+(R_1^4/R_2^4)]^{\frac{1}{2}}}\cdot\frac{2+(b/\gamma)(\delta/\epsilon)^{\frac{1}{2}}[1+(R_1^4/R_2^4)]^{\frac{1}{2}}}{(3/2)+(b/\gamma)(\delta/\epsilon)^{\frac{1}{2}}[1+(R_1^4/R_2^4)]^{\frac{1}{2}}} \quad (\mathrm{v/m}). \tag{13}$$

Abbreviating the material dependent expression

$$(b/\gamma)(\delta/\epsilon)^{\frac{1}{2}}=a \tag{14}$$

and the geometry parameter

$$\left[1+\left(\frac{R_1^4}{R_2^4}\right)\right]^{\frac{1}{2}}=s, \tag{15}$$

Eq. (13) reads

$$\frac{v_1}{b}\approx\frac{U-U^*}{(2/3)x_1}\cdot\frac{1}{a\cdot s}\cdot\frac{2+as}{(3/2)+as} \quad (\mathrm{v/m}). \tag{13*}$$

Inserting this into Eq. (12) we obtain for the dynamic pressure generated in the system

$$p_1\approx\frac{\epsilon}{2}\left[\frac{U-U^*}{(2/3)x_1}\right]^2\left[\frac{2+as}{(3/2)+as}\right]^2 \quad (\mathrm{newton/m^2}). \tag{16}$$

The pressure measured behind the pump, p_1-p_1', which is also the pressure available for work p_2', is

$$p_2'=p_1\frac{s^2-1}{s^2} \quad (\mathrm{newton/m^2}). \tag{17}$$

Finally, combining Eqs. (16), (13*), and (6), we obtain for the electrical current drawn

$$I=\frac{R_1^2\pi\epsilon b}{2x_1}\left[\frac{U-U^*}{(2/3)x_1}\right]^2\left[\frac{2+as}{(3/2)+as}\right]^2\left(1+\frac{2}{as}\right) \quad (\mathrm{amp}). \tag{18}$$

Multiplying Eq. (18) by U we obtain the input power P of the system. As the output power is $i\cdot p_2'=R_1^2\pi v\cdot p_2'$, we can easily calculate the pumping efficiency η, and get

$$\eta=\frac{k}{1+(2/3)a\cdot s}\cdot\frac{s^2-1}{s^2}=\frac{k}{1+(2/3)a(p_1/p_1')^{\frac{1}{2}}}\left(1-\frac{p_1'}{p_1}\right) \tag{19}$$

where k is defined in Eq. (9).

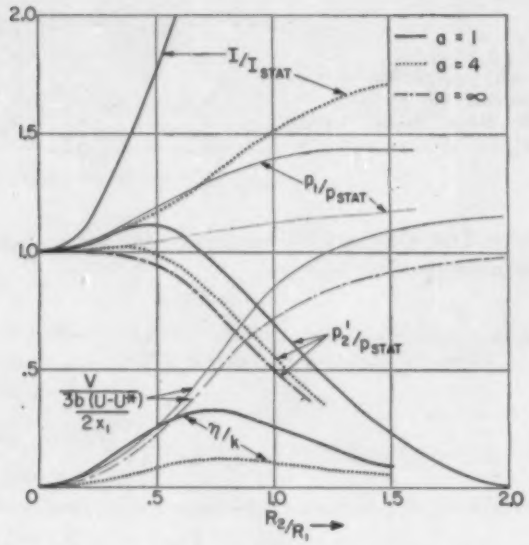

FIG. 3. Dynamic to static value ratios for current I, generated pressure p_1, working pressure p_2', and internal efficiency η/k, plotted *versus* effective radii ratio R_2/R_1.

The relations computed above are illustrated graphically in Fig. 3, plotted *versus* increasing ratios of R_2/R_1. For $R_2=0$, or $s=\infty$, we obtain the static values of pressure and current against which our dynamic values are normalized.

Our results depend on the properties of the pumping fluid represented in the equation by the dimensionless parameter $a=(b^2\delta/\gamma^2\epsilon)^{\frac{1}{3}}$. a is sensitive to the mobility b which depends on impurities in our pumping fluid. In our Fig. 3 two values for a are used, $a=1$ and $a=4$. (Values for commercial grade insulating oils lie in the neighborhood of $a=4$, for very clean kerosene $a\approx 1.5$.)

We see from Fig. 3 and Eq. (16) that the generated pressure p_1 increases when we increase R_2, i.e., open a valve to this effective radius. For $R_2 \gg R_1$, s tends towards unity and the pressure p_1 reaches asymptotically a value which is by a factor $[(2+a)/(\frac{3}{2}+a)]^2$ higher than the static one. This value is smaller than the figure 16/9 quoted in the preceding section. The reason is that the flow velocity is now limited by R_1. For $a=4$ the maximum dynamic increase of p_1 is 20%.

The dynamic pressure increase with flow rate is, for low enough values of a, sufficient to create a working pressure $p_2'=p_1-p_1'$ which is higher than the static pressure. For $a=4$ this is only a few percent (see Fig. 3, dotted curve).

The electrical current I can be seen to increase strongly with increasing flow rate as long as a is small. It reaches a value for maximum flow which is by $(2+a)^3/a\cdot(1.5+a)^2$ larger than the static figure.

The increase in flow velocity v_1 with increasing R_2 plotted in Fig. 3, normalized to the velocity is $3b\cdot(U-U^*)/2x_1$. Dash-dotted curves show the behavior of flow velocity v_1 and working pressure p_2' for no dynamic effects present, i.e., the pressure generated by conventional hydrostatic means ($a\to\infty$).

The quantity η/k, which is the internal efficiency of our system, is also plotted in Fig. 3. The maximum value of η/k can be computed from a cubic equation. For large values of a the maximum occurs at $R_1:R_2=\sqrt[4]{2}$.

6. POWER OUTPUT OPTIMIZATION

We shall now investigate for what external flow resistance a given ion drag pump will deliver the maximum power. With the results we shall compute the efficiency $\bar{\eta}$ for this case.

From Eqs. (13) and (17) we get for the power output

$$P_2=i\cdot p_2'=\frac{R_1^2\pi\gamma\cdot\epsilon}{2}\left(\frac{\epsilon}{\delta}\right)^{\frac{1}{3}}\cdot\left[\frac{U-U^*}{(2/3)x_1}\right]^3\left[\frac{2+as}{(3/2)+as}\right]^3 \times\frac{s^2-1}{s^3}\ \text{(w)}. \quad (19^*)$$

We wish to determine the value of the geometric parameter s which maximizes this expression. To simplify our computations, we may assume the little changing factor $(2+as/\frac{3}{2}+as)$ a constant for this purpose. Simple analysis shows then that the maximum of the expression $(s^2-1)/s^3$ occurs for $s_0=\sqrt{3}$. We obtain

$$P_{2_{\max}}\approx\frac{R_1^2\pi\gamma\epsilon}{3\sqrt{3}}\left(\frac{\epsilon}{\delta}\right)^{\frac{1}{3}}\cdot\left[\frac{U-U^*}{(2/3)x_1}\right]^3\left[\frac{2+a\sqrt{3}}{(3/2)+a\sqrt{3}}\right]^3 \text{(w)} \quad (20)$$

for $s_0^2=3$ or $R_2/R_1=1/\sqrt[4]{2}$. For $s_0=\sqrt{3}$ we see from Eq. (17) that for optimum power output design one-third of the generated pressure is lost in the pump stage and two-thirds are available for work.

Now the efficiency $\bar{\eta}$ for optimum power output operation becomes

$$\bar{\eta}\approx\frac{(2/3)k}{1+[2a/(3)^{\frac{1}{3}}]}=\frac{(2/3)k}{1+2(b/\gamma)(\delta/3\epsilon)^{\frac{1}{3}}}. \quad (21)$$

This equation contains the ionization efficiency k which for high values of applied voltage nears unity. If a is very small our equation predicts 66% maximum obtainable efficiency for optimum match of pump stage to work stage.

7. GENERALIZATION OF RESULTS

The foregoing derivations were made for quadratic dependence of pressure drop p_1' and p_2' on the flow rate i [Eq. (11)]. The theory can be straightforwardly extended to include the case where p_1' and p_2' depend linearly on i (laminar flow) or where the relationship is a combination of both assumptions

$$p'=Ai^2+Bi. \quad (22)$$

B, here, is proportional to the viscosity of the liquid

and the fourth power of the pump radius R. If we exclude extremely viscous liquids like castor oil and very narrow pumping arrangements, Ai^2 is always much larger than Bi for reasonably high flow rates i. We can thus design our pumping stages so that the quadratic approximation, Eq. (11), holds very well.

For the load this may not be the case, i.e., we may want to pump through a long capillary tube. Then our result obtained above for the optimum dimensioning of R_2 does, of course, no longer hold. The equation [Eq. (21)] for the efficiency at maximum power output can be seen to be still valid, however: It depends only on the pressure losses in the generator stage and not at all on any assumption on how the power delivered is put to work.

Our pump stages deliver only very small power of the order of a few milliwatts. Therefore parallel and series arrangements of single stages are of interest.

If we assume that the stages do not influence each other, the parallel arrangement of n pumps, operated with the same voltage U, will just increase the flow rate i and the electrical current drawn by the factor n. The efficiency η does not change. For our example in the preceding section the optimum dimensions of the "load" radius R_2 would now be given by $R_2:R_1=(n/2)^{\frac{1}{2}}$.

Cascading of n pump stages is not so easy to understand immediately on account of the nonlinear pressure-flow rate relationship. A simple mathematical investigation shows, however, that this arrangement behaves equivalently to the series connection of electrical batteries. The theoretical efficiency is the same as for the single pump stage and the optimum dimensioning for R_2 is now $R_2:R_1=(1/2n)^{\frac{1}{2}}$.

Our derivation of the basic dynamic equations has been made for a rather simplified linear model. It is known[1] that, e.g., through constriction of the current path higher pressures p_1 can be built up than are predicted by Eq. (4). But this constriction will now increase the pressure drop loss p_1' in the stage, too. The mathematical evaluation of this and similar cases is complex. No simple explicit solution corresponding to Eqs. (6) through (8) could be found. Approximations lead to formulations for the efficiency $\bar{\eta}$ which differ only in the constant factor in front of the quantity a in the denominator. Many assumptions and simplifications are needed for this mathematical exercise; they make it unclear to what degree the results improve our Eq. (21). We wish to present instead a physical argument to demonstrate that our efficiency equation is usable above and beyond the restricted model for which it was derived. As the equation does not contain any geometric parameters, it is *a priori* likely not to be sensitive to small variations of geometric boundary conditions.

The factor k, as stated, represents the ratio of energy available for pumping to the energy furnished from the outside. It was introduced solely to take our special experimental conditions into account, i.e., corona point emitters for generation of the necessary ions. k is therefore a property of the emitter, almost completely uninfluenced by the geometric shape of the pump electrode system. (As said before, k becomes almost unity when the voltages can be made high enough. In other cases it has to be determined experimentally.)

The factor 2/3 in the numerator is the matching efficiency to the load. It is a direct consequence of our assumption, Eq. (11), of the quadratic dependence of flow i on pressure p'. It holds for all arrangements for which this assumption is true, which is the large majority of cases involving liquids of medium and low viscosity.

The denominator of our Eq. (21) signifies the inverse efficiency of energy transfer from accelerator ion to host liquid. For extremely low mobility b it would be near unity, and of course independent of the arrangement. For higher values of b the denominator should stay unaffected by our geometric arrangement if we prevent ions from traveling paths where they do not contribute fully to dynamic pressure generation. (If we, e.g., remove the insulating insert from our arrangement in Fig. 1(b) the ions traveling to the outer parts of the metal disc collector do not add to the pressure buildup in front of the hole which we utilize. They draw electric current, however, thus decreasing the efficiency.)

Our efficiency equation [(21)] is therefore rather generally applicable. It suffers from the fact that the mobility b which turns out to be the dominant parameter in practical cases depends strongly on impurities. It may also depend on transit time and field strength in certain cases. It is therefore a parameter which has to be determined experimentally.

Our equations have been derived for dc operation. If we operate the pumps with ac and make sure that the transit time between emitter and collector is short compared to the duration of a cycle, our equations for pressure and flow rate dependence on voltage can be seen to apply approximately. The input power required, however, is not easy to compute. One of the reasons is that the high lifetime of ions in insulating liquids provides for the presence of a not negligible amount of ions from the previous cycle. This leads to a lowering of U^* because ionization and current flow is now easier. This favorable effect is more than counterbalanced by a higher current drain, however. (Additional sizeable capacitive currents drawn do not, of course, influence our input power.) The efficiency expression, Eq. (21), can therefore only be used as an upper limit for ac operation.

8. EXPERIMENTAL DIFFICULTIES

As already partly reported,[1,2] measurements are made difficult by a number of effects. As stated, the increase of p_1 with increasing flow rate i at constant voltage operation leads to instability and oscillations of pressure and current. This affects measurements especially when the flow rate is low. For higher flow

rates the effects are observed to become less and less pronounced; this is explainable (see reference 2 and Fig. 2).

Static charges on insulating parts of the system are a major source of errors. Unfortunately very little information is obtainable on the surface properties of good insulating materials in contact with insulating liquids. Quartz and glass always charge up rather highly; occasionally pieces of Plexiglas and Teflon are found which for unknown reasons show little charging effects. When ac is used to operate the pumps, only very small charging effects are observed, as the charges furnished in subsequent cycles tend to cancel. But then measurement of the electrical power absorbed by the system is difficult, as the ohmic part of the current is smaller than the capacitive current in the system.

The mobility, b, as mentioned, depends on impurities in the fluid. Sometimes particles and gas bubbles, charged up by the emitter, act as impurities with low mobility, leading to very favorable efficiency of the system. In the measurements to be reported it was attempted to eliminate this phenomenon by always operating the pumps for several hours after changing liquids before readings were taken. During this time particulate matter was removed by the Cottrell effect.

High fields and an occasional sparkover can produce chemical changes in insulating liquids.[5] For kerosene, transformer oil, and freon this appears to be of no noticeable influence on pumping properties. Light mineral oil, however, seems to undergo severe polymerization leading to occurrence of unsoluble filament-like fibers which tend to clog small pumping holes. CCl_4 on occasion attacks plastics.

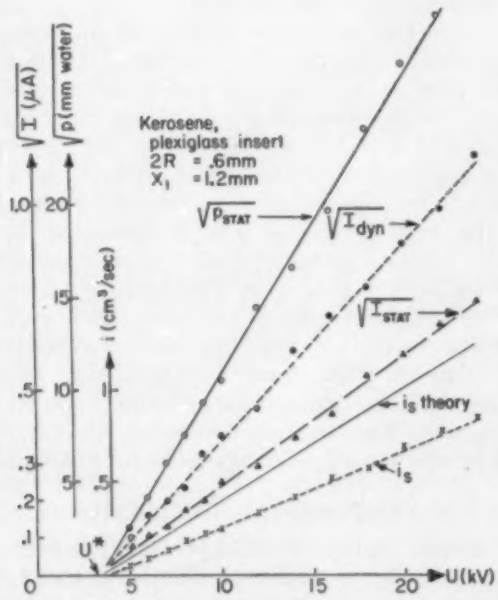

FIG. 4. Example of performance characteristics for dc operation

[5] A. Gemant, *Liquid Dielectrics* (John Wiley & Sons, Inc., New York, 1933), p. 111 ff.

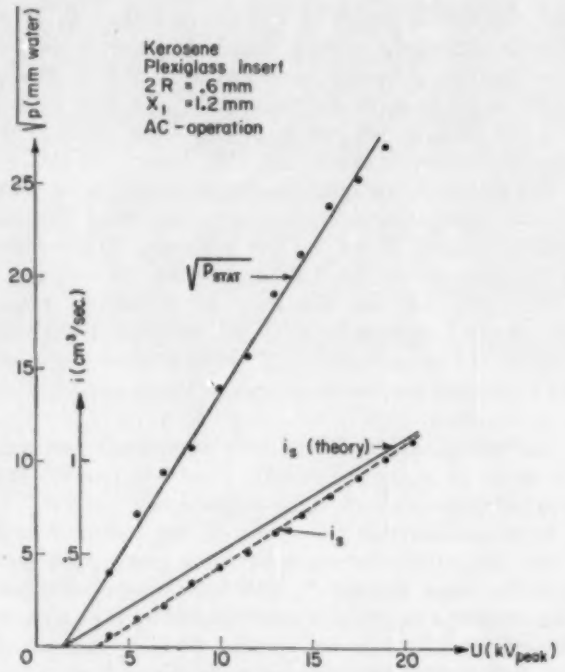

FIG. 5. Example of performance characteristics for ac operation corresponding to Fig. 4.

In the light of the above comments it will be seen that the accuracy and reproducibility of our measurements cannot be expected to be very high. With some experimental precautions, reproducibility of pressure and flow rate within 10%, and efficiency measurements within ±25% can be obtained. Within these limitations the general operational behavior of ion drag pumps appears to be well explained by the theory presented above.

9. MEASUREMENT PROCEDURES

Before efficiency measurements were taken it was assured that the pump system was adequately described by the equations developed. Equations (16), (17), and (18), respectively, let us expect that a plot of $(p_2')^{\frac{1}{2}}$ and of $\sqrt{I}$ *versus* applied voltage U is a straight line if the geometry of the system and the properties of the liquid are constant.

That this is true in the majority of arrangements has already been reported for the static[1] and the dynamic[2] cases. When deviations from the functional dependence show up, they indicate strong impurity contamination or high turbulence and circulation losses; then it is not surprising that the efficiencies will be low. Such cases were found on occasion but will not be reported. Strong long-time fluctuations of pressure or current, after the introduction of sufficient artificial damping to eliminate instability phenomena, indicated undesirable charging up properties of insulators in the apparatus; readings on such arrangements were discarded.

Equation (13) predicts that the flow rate, $i=R_1^2\pi v_1$, is proportional to the driving voltage $U-U^*$. Experiments show that this functional dependence is very accurately fulfilled.

To illustrate the above statements and to give an idea of the order of magnitude of the quantities involved, we have plotted some measurements in Fig. 4. They were made with the arrangement of Fig. 1(b). The curves for $(P_{stat})^{\frac{1}{2}}$, the static pressure, and for $(I_{stat})^{\frac{1}{2}}$, the current drawn under static pressure operation, are self-explanatory. $(I_{dyn})^{\frac{1}{2}}$ is the measurement for very large R_2, i.e., maximum flow rate i_s. The latter is also plotted.

Figure 4 is presented for an additional purpose, which is, to show how we can draw conclusions on the charging up properties of the constricting sleeve material used, which may force us to adjust the quantity R_1: From our static pressure value p_{stat} and from Eq. (11) we can compute theoretical minimum values for i_s if we assume for the moment that $\gamma=0.9$. Dynamic effects should make the values slightly higher. The curve is entered into the graph; our actual values are considerably lower. This could be due to the wrong estimate of our somewhat vaguely defined parameter γ. Figure 5 shows, however, corresponding pressure and flow rate measurements with ac on the same device. Here our measurements approach very closely the semitheoretical values for i_s. We have to conclude that it is not the wrong choice of γ, but surface charges on the insulator, which produce the phenomenon. We may attribute a $\gamma\approx0.9$ to the ac arrangement also. Then we obtain compatibility with the dc case if we replace the geometric value of R_1 by an effective value which (taking dynamic effects into account) turns out to be about $0.8\,R_1$.

By building up pressure hydrostatically and measuring the flow rate i_s, we can assure ourselves that the value $\gamma\approx0.9$ is reasonable.

From plots of the square root of current I *versus* the applied voltage U [see Eq. (18)] we can obtain the quantity U^* as the "cut-in" voltage (see Fig. 4). For the static case, $s\rightarrow\infty$, the slope of the straight line permits us to determine our quantity b. If charges appear to be present, an evaluation like the one

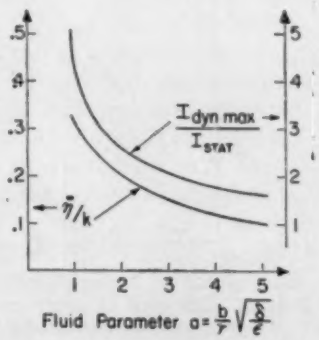

FIG. 6. Internal maximum power output efficiency $\bar{\eta}/k$ and electrical current ratio for maximum flow to no flow *versus* characteristic parameter a.

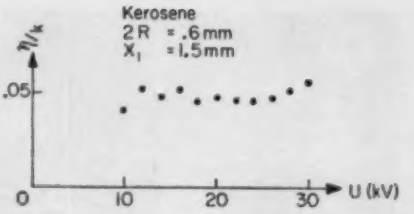

FIG. 7. Example of η/k *versus* applied voltage measurement.

presented above will furnish an effective value for the radius R_1 in Eq. (18). With these parameters we can obtain η and $\bar{\eta}$.

The results can be independently checked; a plot of $\sqrt{p}$ over U should furnish the same value of U^*. The ratio of highest dynamic value of the current I_{dyn}, obtained for $R_2\gg R_1$ ($s=1$), over the static value is according to Eq. (18)

$$\frac{I_{dyn}}{I_{stat}}=\frac{[1+(2/a)](2+a)^2}{(1.5+a)^2} \tag{23}$$

and gives us an opportunity to obtain a and $\bar{\eta}$ independently of the numerical value determination for b. In Fig. 6 the theoretical relationship of the above quantities is plotted.

After the general properties of the pump have been checked and possible effective values of the parameter R_1 determined, a desired pressure drop ratio (or ratio of R_2/R_1) is introduced into the system. Then the value of p_2' and the flow rate i is measured. $p_2'\cdot i$ is then our power output. As we know the power input $U\cdot I$, comparison of our measurements with theory is easy.

10. MEASUREMENTS

The liquids pumped most often were industrial grade kerosene and transformer oil, and on occasion, freon, CCl_4 and light mineral oil. Measurements on one-stage pumps were generally made with arrangements similar to the schematic of Fig. 1b, with and without insulating insert. R varied from 0.3 to 5 mm, x_1 from 0.6 to 10 mm.

With insulating inserts whose function it is to force the ion current into paths where it has to do useful work, the measurements are in good agreement with the theory presented.

Our theory predicts that the inner efficiency η/k is independent of the driving voltage U. A measurement which demonstrates this is shown in Fig. 7. The power output between 10 and 30 kv varies by a factor of about 60. (The outside load in this case was not such that optimum power output efficiency was obtained.)

Equation (19) expresses the efficiency as a function of a and the flow resistance parameter s. The latter quantity can be written in terms of the ratio p_1/p_1', as has been done in the second expression of Eq. (19). For not too low a value of a we may, thus neglecting

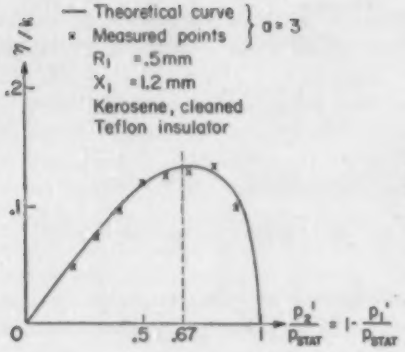

FIG. 8. Internal efficiency *versus* pressure drop ratio for $a=3$.

dynamic effects, replace p_1 by the static value p_{stat}. The resulting theoretical approximative curve is plotted in Fig. 8 for $a=3$ and $k=0.9$. Measured values are entered; hereby $p_1'=p_1-p_2'$ was replaced by the approximative value $p_1'\approx p_{stat}-p_2'$, which can be easily obtained. The result demonstrates also that the maximum efficiency is obtained in the neighborhood of the maximum power output operation which occurs for $p_2'=2p_1/3$.

One of the essential results of our theoretical analysis is Eq. (21), linking the maximum efficiency to properties of the liquid. Its approximate validity was checked for many cases. As an example the figures may be given here which relate to the characteristics in Fig. 4. From the slope of the curve for the static current we obtain with the dimensions given on the graph (but an effective value of 0.8 R_1 as derived above) a mobility value $b=2.4\cdot10^{-7}$ m²/v·sec. This makes our parameter a (with $\gamma=0.9$ and $\epsilon=20\cdot10^{-12}$ amp·sec/v·m) assume the value 1.65. The value $\bar{\eta}/k$, Eq. (21) would thus be 23%. From the value for $I_{dyn}/I_{stat}=2.4$ we obtain from Fig. 6 a value $a=2.4$ and $\bar{\eta}/k=18\%$. With k at 18 000 v being about 0.8, we should expect a maximum power output efficiency of 18.5% and 14.5%, respectively. The observed value is 15%.

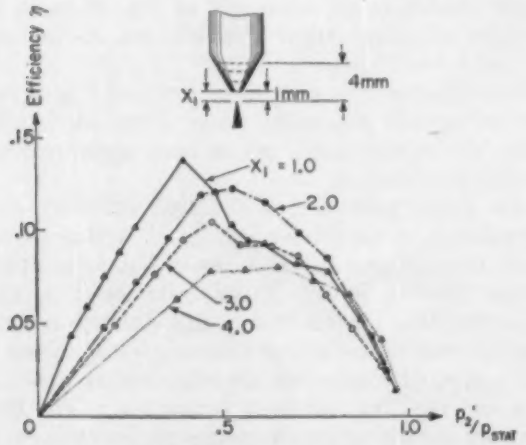

FIG. 9. Efficiency of practical all-metal pump stage *versus* pressure drop ratio.

The following observation was made regularly on devices similar to the one in Fig. 1(b) with insulating insert and operated with kerosene: After about 3 hr of cleaning the values of current, pressure and flow rate became stable. The efficiency of the pumps was of the order of 10%. After some time of operation the efficiency as well as the ratio I_{dyn}/I_{stat} became higher and the effective mobility b decreased. After about a day of operation the efficiency of pumping $\bar{\eta}$ was roughly 20%. Twenty-five percent efficiency can be reproducibly reached, and occasionally values as high as 30% have been obtained.

For devices without insulating insert two effects tend to decrease the efficiency. Not all of the ion current contributes to pressure build up, and the flow can "break out" into eddies on the side. For very close spacing between emitter and collector these two detrimental phenomena are minimized; we can expect, and actually obtain, almost the same efficiencies as reported above. Of the many possible configurations, one is sketched in Fig. 9: A system of four conical arrangements with constant opening angle, and varying radius R_1 of the collector were compared. (Large values of R_1 are of interest for higher flow rates.) The plot of efficiency *versus* pressure ratio shows that for increasing distance of the emitter from the collector the efficiency drops. When we compare the shape of the measured curves with that of our Fig. 8, we see that maximum power output no longer occurs for $p_2'/p_{stat}\approx\frac{2}{3}$. The reason is probably that for the low flow rates corresponding to the high pressure ratios at the right side of the plot, both the dynamic ion current carried to the side and the eddy losses become more pronounced.

For devices without insert the internal flow creates an always present dynamic ion current. Therefore, the current measured at no outside flow is not our static

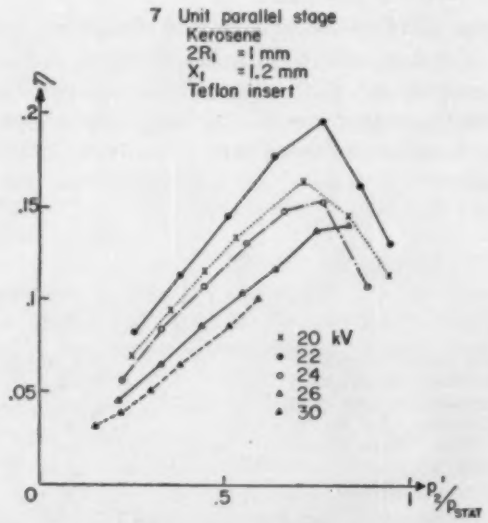

FIG. 10. Efficiency of seven-unit parallel arrangement *versus* pressure drop with driving voltage U as parameter.

current, and Eq. (23) is no longer applicable for estimating the efficiency.

For transformer oil and silicone oil (Dow "550" fluid) the measurements show results very similar to the ones reported above for kerosene, the efficiencies being roughly $\frac{1}{2}$ and $\frac{1}{3}$, respectively. (The viscosity between kerosene and silicone oil varies about as 1:60.) For other liquids used on occasion no contradiction to the theory became apparent; Freon "TE" generally gave efficiencies slightly higher than kerosene.

For gases, our parameter a [see Eq. (14)] is high; for standard air ($b=1.4\cdot10^{-4}$ m²/v·sec, $\gamma\approx0.6$, $\delta=1.29$ kg/m³, $\epsilon=8.86\cdot10^{-12}$ amp·sec/v·m), a is about 90. The efficiency for optimum power output would thus be less than 1%. This has been roughly checked experimentally. While other gases (SF_6) are somewhat more favorable and pressurizing of the system is helpful, the efficiencies obtained for pumping gases are disappointingly low.

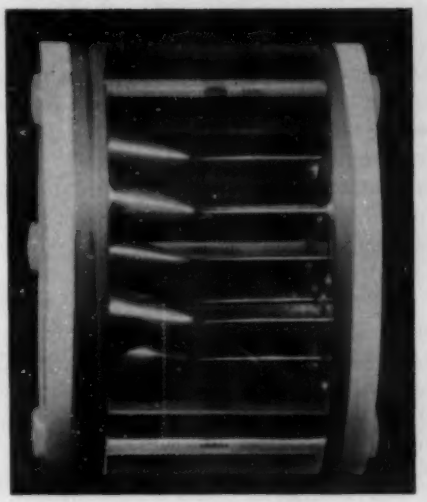

FIG. 11. Seven-unit pump stage. (Diam: 6 cm).

11. PRACTICAL PUMPS

In practical cases, aside from the efficiency, the amount of the power output P_2 which can be obtained is of interest. From Eq. (20) we can see, if we disregard the little-varying quantities γ, ϵ, δ, and $(2+a\sqrt{3})^3/(1.5+a\sqrt{3})^3$, that

$$P_{2\max}\sim R_1^2\cdot\left(\frac{(U-U^*)}{(2/3)x_1}\right)^3=R_1^2E_{\max}^2. \qquad (24)$$

The second factor in this expression is the maximum field strength in the system.[1] Unfortunately, the maximum field strength tolerated by a liquid is the smaller, the larger the field filled volume is,[6] that is, the two factors in Eq. (24) work against each other. The output power obtainable, as experiments prove, does not depend on R_1 very much; it turns out to be somewhat advantageous to choose R_1 as small as the desired flow rate will allow. Several milliwatts output is reached in practice for industrial grade liquids. The highest value obtained for one stage was 20 mw. As one milliwatt hydrodynamic output corresponds to a flow rate of 1 cm³/sec against a pressure of 100 mm water, multistage devices will be required for many applications.

In our theoretical discussion of paralleling of pumps we have made the assumption that parallel stages do not influence each other. In practice they do, however, if the units are not completely equal in performance. Let us assume for the moment two parallel stages, one having a lower U^* than the other one. Operated with the same driving voltage U, the better unit will create a higher pressure, pumping part of its flow back into the second unit. This, on account of our dynamic dependence of generated pressure on flow rate, will further decrease the generated pressure in the second unit. The phenomenon is more pronounced the lower the parameter a of the liquid is.

Paralleling of pumps, therefore, requires high mechanical precision units to guarantee the necessary uniformity. Fortunately it has been observed that small differences in unit performance tend to decrease if the system is deliberately operated at too high a voltage; the better units spark and thus decrease the sharpness of their emitter points.

Nevertheless, the efficiency reached with parallel systems has never been quite as high as that of single stage pumps using the same liquid. As uniformity of pressure generation cannot be completely reached for each operating voltage, we cannot be disappointed now, if the efficiency depends on the applied voltage to a higher degree than predicted by the factor k, especially for clean fluids. The voltage effect is discernible in Fig. 10, a pressure ratio diagram for a seven-unit pump. A picture of the pump (with insulators around the collector removed) is presented in Fig. 11.

Cascading of single units or of well equalized parallel systems does not present a practical problem. Figure 12 shows an experimental pump consisting of three of the

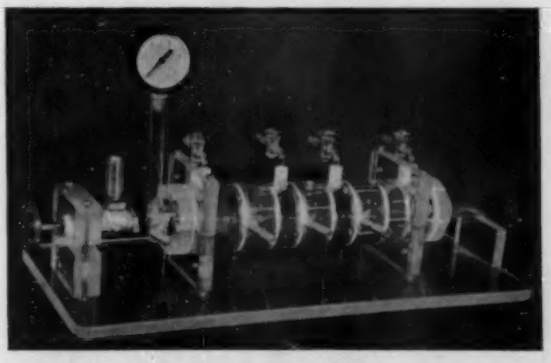

FIG. 12. Experimental pump.

[6] W. R. Wilson, Trans. Am. Inst. Elec. Engrs. **72**, 878 (1953).

systems of Fig. 11 in series. It pumps 8 cc of kerosene per second 1 m high with an efficiency of 10%.

Ion drag pumps have applications where high voltages are easily available (mechanical work from nuclear batteries; circulation cooling of high-voltage transformers). They recommend themselves where lack of mechanical movement or gyroscopic properties (satellites), noiselessness, and extreme simplicity and ruggedness are desired.

12. CONCLUSION

Extending previous investigations for static conditions, we have presented above a theoretical model which describes the dynamic behavior of an ion drag pumping arrangement for unipolar ion conduction. For us, the essential feature of the model is the strong increase of electric current with hydrodynamic flow rate for liquids with very low ion mobility. This increases the electrical power consumed and influences adversely the efficiency of the pumping arrangement.

It has been shown that the maximum power output efficiency of the system depends on the properties of the pumping fluid only for our linear model. A physical argument and measurements were presented which demonstrate that this result is a useful approximation for the more complicated technical arrangements that use a corona point emitter as ion source. Coordination can be obtained between the impurity dependent mobility in liquids and the measured pumping efficiency.

The efficiencies that have been reached with suitable liquids (kerosene, freon) are somewhat better than 20%. The power output obtainable per single unit is several milliwatts for the investigated industrial grade insulating liquids and about 20 mw for very clean liquids. Paralleling and cascading of units was investigated.

ACKNOWLEDGMENTS

The author is indebted to Mr. Herbert Loeckenhoff for many suggestions and the careful performance of many hundreds of measurements, to Mr. Gerhard Voll for the construction of the pumps, and to Mr. Emil Benz for technological advice.

APPENDIX: INTEGRATION OF INTERACTION EQUATIONS

Elimination of ρ from Eq. (3) by substituting Eq. (2) gives

$$\frac{j}{\epsilon b}=\left(E+\frac{v}{b}\right)\frac{dE}{dx} \quad (\mathrm{v^2/m^3}). \tag{1A}$$

Integration between $x=0$ and x gives the field strength $E(x)$ as a function of location x with the impressed current density j as a parameter:

$$E(x)=\left[\frac{2jx}{\epsilon b}+\left(E_0+\frac{v}{b}\right)^2\right]^{\frac{1}{2}}-\frac{v}{b} \quad (\mathrm{v/m}). \tag{2A}$$

E_0 is the field strength at the emitter. Differentiation according to Eq. (2) gives the space charge distribution

$$\rho=\frac{j/b}{\{(2jx/\epsilon b)+[E_0+(v/b)]^2\}^{\frac{1}{2}}} \quad (\mathrm{amp\cdot sec/m^3}). \tag{3A}$$

Combining Eqs. (3A) and (1) we obtain the field gradient

$$\frac{dp}{dx}=\frac{j}{b}-\frac{v/b}{\{(2jx/\epsilon b)+[E_0+(v/b)]^2\}^{\frac{1}{2}}} \quad (\mathrm{newton/m^3}). \tag{4A}$$

Integration of (4A) between $x=0$ and $x=x_1$ yields Eq. (4).

Integration of Eq. (2A) for $E=-dV/dx$ gives the potential distribution $V(x)$. If we call $-V(x_1)=U$ and introduce the parameter U^* in line with the reasoning in paragraph 2 of reference 1, we obtain Eq. (5).

If we neglect E_0, as we do in paragraph 3, we can write Eq. (4)

$$\frac{2p_1}{\epsilon}=\left[\left(\frac{2jx_1}{\epsilon b}+\frac{v^2}{b^2}\right)^{\frac{1}{2}}-\frac{v}{b}\right]^2 \quad (\mathrm{v/m})^2. \tag{5A}$$

This leads through simple substitutions to our Eqs. (6) and (7).

JOURNAL OF APPLIED PHYSICS VOLUME 31, NUMBER 1 JANUARY, 1960

X-Ray Study of Ferromagnetic Domains in Cobalt Zinc Ferrite*†

KENNETH M. MERZ‡
Rutgers, The State University, New Brunswick, New Jersey
(Received January 27, 1959)

Double crystal diffractometer and x-ray micrograph techniques were used to study ferromagnetic domains in cobalt zinc ferrite single crystals. Diffraction curves of the (400) reflection were observed to broaden when a magnetic field was applied to the crystal. Berg-Barrett x-ray micrographs showed there was a "d" spacing shift in the crystal during the magnetization process.

INTRODUCTION

THE first attempt to influence the diffraction of x-rays by applying a field to a magnetic material was made in 1913 by de Broglie[1] only one year after the discovery of x-ray diffraction. Since then several workers[2–7] have made similar studies, also without success. In this investigation the double crystal x-ray diffractometer and x-ray micrograph techniques were used to detect changes in interplanar spacing and lattice strain associated with a large magnetostriction.

The use of a material with a large magnetostriction, such as cobalt zinc ferrite, was of fundamental importance since the larger the magnetostriction, the larger must be the difference in "d" spacing between the direction of spontaneous magnetization within a domain and the directions at right angles to it. If an x-ray beam was diffracted at the Bragg angle of an oriented crystal cube, domains magnetized parallel to the surface would present a slightly different "d" spacing to the x-ray beam than domains magnetized perpendicular to the surface. Consequently, if one type of domain was reflecting, a small rotation would be necessary to bring the other type into reflecting position. Since cobalt zinc ferrite has a negative magnetostriction, theory predicts that domains magnetized perpendicular to the crystal surface would present a smaller "d" spacing to the x-ray beam and therefore reflect at a slightly higher Bragg angle than domains magnetized parallel to the surface. This relationship, much exaggerated, can be seen from Fig. 1 (C) or (D). The blocks are considered to rotate around an axis perpendicular to the plane of the paper. It should be noted that domains magnetized 180° to each other cannot be differentiated by this method nor can 90° domains aligned parallel to the easy directions of a cube surface.

From a knowledge of the magnitude of the magnetostriction and Bragg's law, it is possible to calculate the difference in reflecting angle for the two types of domains. For the (400) plane of cobalt zinc ferrite, a difference of 9 seconds of arc for each -100×10^{-6} $\Delta l/l$ was computed. A crystal with a maximum magnetostriction of -335×10^{-6} would therefore require a rotation of about 30 sec of arc to move from the diffraction peak associated with one domain to the other.

Associated with the change in "d" spacing due to magnetostriction, the crystal must undergo an elastic strain. Studies of heterogeneous elastic strain due to mechanical bending,[8–10] piezoelectric oscillation,[11–14] or ferroelectric domain formation[15,16] have been observed to increase the x-ray reflecting power of crystals. The integrated intensity (area under the x-ray diffraction curve) as well as the half-width or perfection (width of the diffraction curve at one-half maximum intensity) were increased by strain.

To sum up, theory predicts that a large magnetostriction would have two effects on x-ray diffraction from a crystal undergoing magnetization; first, a diffraction peak shift due to "d" spacing change, and second, an increase in integrated intensity due to strain.

EXPERIMENTAL PROCEDURE

In order to detect very small changes in "d" spacing, with high precision and resolution, a double crystal x-ray diffractometer similar to the one described by Intrater and Weissmann[17] was used. The instrument was especially built of nonmagnetic materials so that no movement would result from the application of a magnetic field to the ferrite crystal held in the second crystal position. The instrument was used in the (1-1)

* This study was supported by Project No. N-ONR-404(02) of the Office of Naval Research.
† Based upon a thesis submitted to the Graduate School of Rutgers, The State University, in partial fulfillment of the requirements for the degree of Doctor of Philosophy in November, 1956.
‡ Now at Cornell Aeronautical Laboratory, Buffalo, New York.
[1] M. de Broglie, Le Radium **10**, 186 (1913).
[2] K. T. Compton and E. A. Trousdale, Phys. Rev. **5**, 315 (1915).
[3] A. H. Compton and O. Rognley, Phys. Rev. **16**, 464 (1920).
[4] T. D. Yensen, Phys. Rev. **31**, 714 (1928).
[5] J. C. Stearns, Phys. Rev. **35**, 1 (1930).
[6] J. A. Becker, Phys. Rev. **20**, 134 (1922).
[7] E. Rodgers, Phys. Rev. **61**, 35–38 (1942).
[8] S. Miyake, J. Phys. Soc. Japan **2**, 98 (1947).
[9] J. E. White, J. Appl. Phys. **21**, 855 (1950).
[10] T. Sun and S. Ch'u, Acta Cryst. **1**, 135 (1948).
[11] C. S. Barrett, Phys. Rev. **38**, 832 (1931).
[12] C. S. Barrett and C. E. Howe, Phys. Rev. **39**, 889 (1932).
[13] G. W. Fox and J. R. Frederick, Phys. Rev. **53**, 135 (1938).
[14] J. Guillaume, Compt. rend. **234**, 1071 (1952).
[15] H. Hulubei, Compt. rend. **200**, 1530 (1935).
[16] S. Miyake, Acta Cryst. **2**, 192 (1949).
[17] J. Intrater and S. Weissmann, Acta Cryst. **7**, 729 (1954).

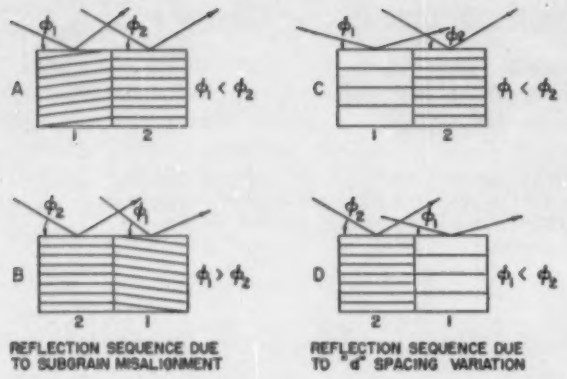

FIG. 1. Method for differentiating between misalignment and "d" spacing variations.

or parallel arrangement.[18] The $K\alpha_2$ component was removed with a collimator 50 cm long to decrease the loss in resolution resulting from the use of different materials in the two crystal positions. Cobalt radiation was used throughout to avoid fluorescence. The first crystal was prepared from a freshly cleaved calcite crystal and found to have a perfection of 18 sec of arc by checking against a quartz crystal of known perfection.

The electromagnet used in the investigation was of the rectangular yoke type and made of cold-rolled steel. Because of the required Bragg relation between the x-ray beam, specimen and Geiger tube, the magnet pole pieces were limited to a diameter of 2.5 cm and a gap of 4.16 cm. With these pole pieces, the maximum obtainable field intensity was 5000 oe. The magnet was supported above the diffractometer table by a heavy aluminum frame so constructed that the relationship between the specimen and field direction could be easily adjusted.

The major apparatus problem of the investigation centered around the movement of the ferrite specimen when a magnetic field was applied. This movement made measurement of a "d" spacing change impossible. Specimen motion was detected by diffracting an x-ray beam from a calcite crystal placed in front of the ferrite specimen while turning the magnet current on and off and observing any movement of the recorder pen connected to the Geiger counter. A specimen motion corresponding to a few seconds of arc was easily detected by this method. In order to eliminate the motion problem, locking devices were put on the specimen goniometer and a 14-in. goniometer on which the whole spectrometer table could be mounted and locked was built.

In practice the following procedure was used. The x-ray beam was diffracted from the (400) plane ($\theta = 25.25°$) of the ferrite crystal ($a_0 = 8.38$ A). The specimen was brought into peak reflecting position by adjustment of the specimen and table goniometers which were then locked. Diffraction curves were obtained by rotating the crystal through the diffraction peak first without a field and then with the magnetic field applied in the [100] direction.

Various film techniques were employed to supplement the information obtained from the rocking curves.[17,19] Berg-Barrett[20] x-ray pictures were taken by exposing a Kodak V-O spectographic plate to the beam diffracted from the stationary crystal. The film was placed as close to the specimen as possible so that little distortion and spreading of the reflection took place. By rotating the crystal stepwise through the diffraction curve and exposing a fresh portion of film at each setting, a series of pictures was obtained which showed which areas of the crystal were contributing to the diffraction curve at any particular position.

Because the x-ray beam of the double crystal diffractometer irradiated a very small (0.2×2 mm) area of the specimen, the results were often difficult to interpret. To obtain an over-all picture of the crystal surface, a simple form of x-ray microscopy developed by Barrett[20] was employed. A resolution of about 16 microns was obtained by using an x-ray source to specimen distance of 36 cm and a specimen to film distance of 2 mm with filtered cobalt radiation.

Cobalt zinc ferrite single crystals were grown by the flame-fusion method as described by Bauer, Gordon,[21] and Moore[22] in connection with the growth of various silicates. Feed materials for the flame fusion furnace were prepared from reagent grade chemicals by precipitating a mixture of the oxalates from a chloride solution of the metal ions with sodium hydroxide. After washing and drying, the mixed oxalates were decomposed to an open-structured ferrite powder by calcination.

Since the ferrite single crystals usually grew without the formation of any natural faces, the Laue back-reflection technique[23] was used to orient the crystals. After orientation, the crystals were cut with a small diamond wheel so as to form several cube faces and

TABLE I. Magneto-thermal anneal history of ferrite specimen.

Anneal number	Magnetic field direction	Temperature of anneal (°C)	Time of anneal (hr)	Field strength (oe)
I	[001]	204	12	1750
II	[010]	208	14	1750
III	[001]	210	13	1750
IV	...	580	2	0
V	[001]	210	14	1750
VI	[100]	200	13	1750

[18] A. H. Compton and S. K. Allison, *X-Rays in Theory and Experiment* (D. Van Nostrand Company, Inc., Princeton, New Jersey, 1935).

[19] W. L. Bond and J. Andrus, Am. Mineralogist **37**, 622 (1952).

[20] C. S. Barrett, Trans. AIME **161**, 15 (1945).

[21] W. H. Bauer and I. Gordon, J. Am. Ceram. Soc. **34**, 250 (1951).

[22] Bauer, Gordon, and Moore, J. Am. Ceram. Soc. **33**, 140 (1950).

[23] C. S. Barrett, *Structure of Metals*, (McGraw-Hill Book Company, Inc., New York, 1952), second edition.

TABLE II. Variation of perfection in a cobalt zinc ferrite crystal grown by the flame-fusion technique.

Curve number	Half width (W) (seconds of arc)	Integrated intensity (R_c) (sq cm)	Peak intensity (I) (cm)	Laue integral breadth (B) (seconds of arc)
1	83	21.0	9.2	97
2	103	23.1	10.0	99
3	88	37.2	17.0	94
4	98	44.8	18.8	102
5	120	48.0	16.1	127
6	73	38.0	19.9	83
7	66	37.0	19.6	81
8	101	40.5	17.4	102
9	118	49.5	16.3	129
10	245	57.0	12.2	200
11	74	35.5	14.7	103
12	83	32.5	13.8	100
13	101	33.0	14.0	101
14	164	37.0	11.0	144

define the cube directions. The cube face to be studied was then polished with emery polishing papers and etched for 20 min at 110°C with an etchant containing 50% H_2SO_4 and 50% saturated oxalic acid solution.

Cobalt-containing ferrites respond to heat treatment in a magnetic field so that domains are permanently oriented in the field direction after the specimen is cooled to room temperature and the field removed. This magneto-thermal anneal effect was used to obtain a simple, known domain configuration so as to make possible a clear interpretation of the x-ray results. The magneto-thermal anneal conditions used in the investigation were 1750 oe at 200°C for 12 hr. Bozorth, Tilden, and Williams[24] have shown that these conditions give a large amount of domain alignment as measured by the increase in maximum magnetostriction. In order to check the domain configuration resulting from each magneto-thermal anneal, the magnetite colloid of Elmore[25] was used to form Bitter patterns.

An SR-4 type "L" portable strain indicator was used to measure the variation of magnetostriction with the field strength and also to check on the effectiveness of the magneto-thermal anneal in the three cube directions of the ferrite crystal.

As far as possible, the experimental results were obtained from one specimen so as to avoid possible complications due to a compositional variable. The dimensions of this crystal and the reference axes used in the discussion corresponding to these dimensions are as follows. The crystal was 2.2 mm thick, [100] direction; 3.5 mm wide, [010] direction; 3.5 mm high on one side and 6.0 on the other, [001] direction. These dimensions result in the crystal surfaces corresponding to five cube faces and the $(01\bar{1})$. Chemical analysis of part of the crystal indicated the composition to be $Co_{0.23}Zn_{0.04}Fe_{0.29}^{II}Fe_{2.36}^{III}O_4$.

[24] Bozorth, Tilden, and Williams, Phys. Rev. **99**, 1788 (1955).
[25] W. C. Elmore, Phys. Rev. **54**, 309 (1938).

EXPERIMENTAL RESULTS

To avoid repetition, the following conventions are used in discussing the figures. The specimen is always oriented so that the [100] direction is perpendicular to the page. This is also the direction of the applied magnetic field (H_A) except for Fig. 10. The rocking curves were taken in a series from right to left with increasing field (H in oersted). The last curve was a repeat of the first. The magneto-thermal anneal history of the specimen is given in Table I.

A series of rocking curves was made from different parts of the crystal surface before the crystal was given any magnetic treatment. In Table II, the half-width, integrated intensity, peak intensity, and Laue integral breadth (ratio of integrated intensity to peak intensity) values are given for each of the fourteen rocking curves obtained. It can be seen that there is a large variation of perfection in different regions of the crystal. The half width of 245 sec was obtained from an area which was more deeply etched than the rest of the surface. This probably represented a region in which there was an abrupt change in conditions during crystal growth. The Laue integral breadth takes a smaller range of values than the half-width since the effect of curve shape is eliminated.

It was found that when a magnetic field was applied to the ferrite crystal, the rocking curve broadened. Referring to Fig. 2(A) it can be seen that as the field

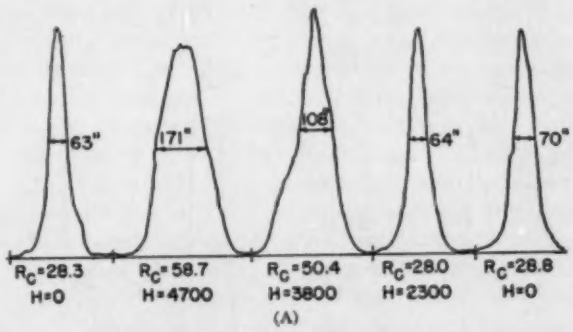

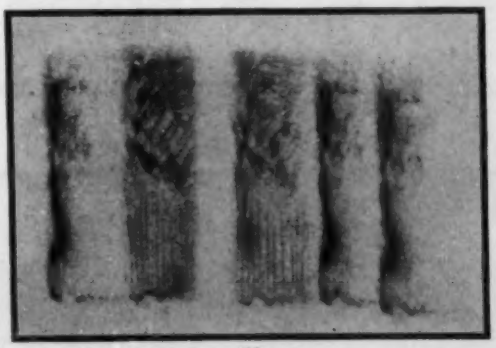

FIG. 2. (A) Rocking curves after anneal IV. Heated above Curie temperature without applied field. (B) Berg-Barrett pictures of corresponding rocking curve peaks. 17½×.

strength was increased, the broadening was first accompanied by a small increase in peak intensity and then by a decrease at the highest field strength (4700 oe). This specimen, with a random domain orientation, exhibited a maximum increase in half-width of 144% and an increase of 104% in integrated intensity (R_C). As would be expected, the amount of broadening varied from one part of the crystal to another because of the large variations in perfection of the unmagnetized crystal.

Since various domain configurations might produce different amounts of rocking curve broadening, a series of magneto-thermal anneals was made along the [100], [010] and [001] directions. In the case of an anneal in the [001] direction, the series of rocking curves in Fig. 3(A) was obtained with increasing field. The half-width increased by 49.2% and the integrated intensity by 87.2% at 4700 oe. When the crystal was rotated 90° around an axis perpendicular to the reflecting planes, the same directional relationships were obtained as if the crystal were annealed in the [010] direction. In this case [Fig. 4(A)] the half-width increased 119% and the integrated intensity 78.5% at 4700 oe. After a magneto-thermal anneal in the [100] direction, a maximum increase of only 20.7% in half-width and 25% in integrated intensity was observed with the same applied field.

Berg-Barrett pictures were taken at various points along the rocking curves in order to gain an insight into the cause of the rocking curve broadening. These pictures show the position and relative intensity of reflection of those areas of the crystal which are in reflecting position at a particular setting along the rocking curve. Referring to Figs. 2(B), 3(B), and 4(B), we see Berg-Barrett photographs taken at the peak positions of the corresponding rocking curves of Figs. 2(A), 3(A), and 4(A). The first pictures on the right, show the areas which are normally reflecting. The second and third pictures show the changes which have taken place after applying a field of 3800 and 4700 oe respectively. The last pictures on the left, taken after demagnetizing the magnet, usually cannot be distinguished from the first pictures. This indicates the effects are reversible as would be expected from the evidence of the corresponding rocking curves.

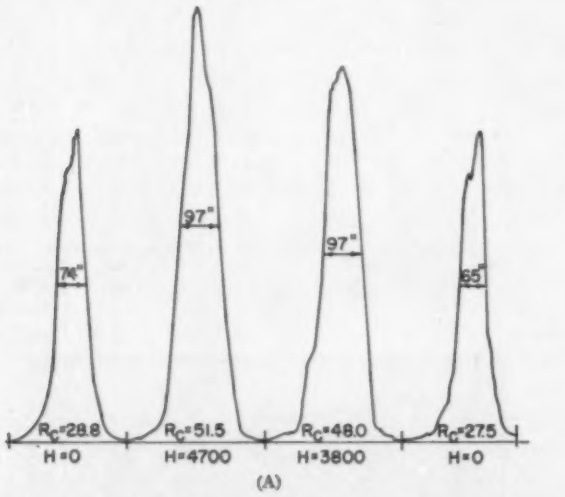

FIG. 3. (A) Rocking curves after anneal I. H_T parallel to [001] direction. (B) Berg-Barrett pictures of corresponding rocking curve peaks. 6½×.

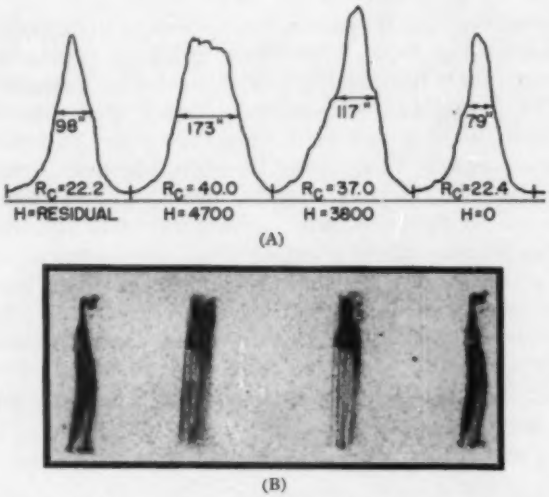

FIG. 4. (A) Rocking curves after anneal I. Crystal was rotated 90° from Fig. 3(A) position around an axis perpendicular to the page [(400) plane]. (B) Berg-Barrett pictures of corresponding rocking curve peaks. 7×.

The Berg-Barrett pictures taken with an applied field, show a breakup of the original image into a series of regularly arranged black and white lines. These lines clearly represent regions of the crystal which have come into or gone out of reflecting position because of the applied field. There are two mechansims which can satisfactorily explain the appearance of these lines. Either they represent regions of altered "d" spacing or an ordered arrangement of the normal subgrain misalignment has taken place. Since a large magnetostriction could conceivably cause changes in misalignment of subgrains or in "d" spacing, some method for differentiating these effects is needed. Such a method, first proposed by Berg,[26] can be understood from a consideration of Fig. 1. In (A) two misaligned regions are shown reflecting. If the crystal is now rotated

[26] W. Berg, Naturwissenschaften **19**, 391 (1931). Z. Krist. **89**, 286 (1934).

180° around the normal to the diffracting planes as in (B), it will be seen that the reflecting order has been reversed. In (C) two regions with differing "d" spacing are reflecting at their characteristic Bragg angles. A 180° rotation as in (D) now has no effect on the reflecting order of the two regions. The major problem in using this criterion is the difficulty of irradiating the same area of the crystal after the 180° rotation.

An attempt was made to apply the Berg criterion to the black and white lines observed in the Berg-Barrett photographs. A series of pictures was taken at intervals along the rocking curve while a field of 3800 oe was applied [Fig. 5(A)]. The pictures are arranged so that higher θ angles are in sequence from left to right. It

(A)

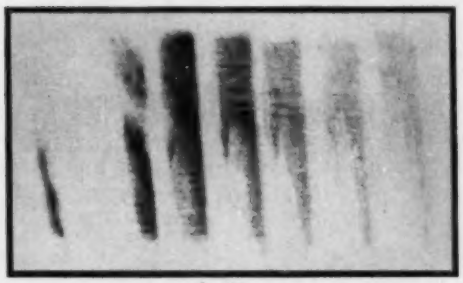

(B)

FIG. 5. (A) "d" spacing shift due to magnetization. Pictures taken at intervals along rocking curve. Increasing angle left to right. Anneal III. H_A–3800. 8½×. (B) Same as 5(A) except crystal was rotated 180° around an axis perpendicular to the reflecting planes.

can be seen that wherever a white line exists, movement to the right brings into reflection a corresponding black line. The center image has both black and white lines; observation of the image to the right shows that the white lines change to black and the image to the left shows that the black lines are preceded by white. After rotating the crystal 180° around an axis perpendicular to the reflecting planes, the pictures of Fig. 5(B) were taken. As can be seen from the figure, the black lines still come into reflecting position at higher θ values. This demonstrates that the black lines are due to differences in "d" spacing and not lattice misalignment. The fact that reflection occurs at higher angles indicates that the "d" spacing is smaller in a black line than in other parts of the crystal.

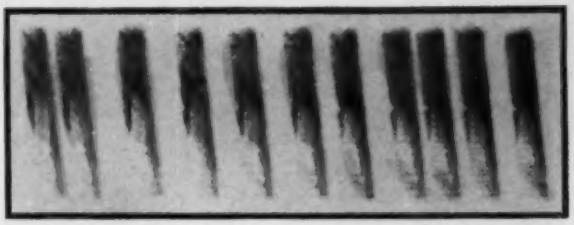

FIG. 6. Berg-Barrett pictures after anneal III. Left to right, effect of increasing field from 2800 to 4800 oe by 200 oe intervals. 8×.

Additional evidence of the fact that reflection occurs at higher angles when a field is applied can be seen from the rocking curves of Figs. 2(A), 3(A), and 4(A). With increasing field strength, the rocking curves broaden mainly on the high θ side of the curves (left-hand side).

Since cobalt zinc ferrite has a negative magnetostriction, a decrease in "d" spacing would be expected for ferromagnetic domains magnetized parallel to the applied field and perpendicular to the original domain alignment as determined by magneto-thermal annealing. This was the actual arrangement of domains and applied field in the crystal when the Berg-Barrett pictures of Fig. 5 were taken. All of the above considerations indicate that the black lines observed on the Berg-Barrett pictures represent ferromagnetic domains and we shall henceforth refer to them as domain lines.

A calculation of the magnitude of the rocking curve displacement expected from the "d" spacing change associated with magnetostriction was made as described previously. Since strain gauge measurements indicated that the specimens had a maximum magnetostriction of -335×10^{-6} $\Delta l/l$, a rocking curve displacement of about 30 sec of arc was expected. To check this calculation a series of Berg-Barrett pictures was made by rotating the crystal 12 sec of arc between each exposure with an applied field of 3650 oe. By counting the number of images in which white lines appear corresponding to a definite black line, it was possible to obtain an approximation of the amount of rotation necessary to bring a domain line into reflecting position. The white lines could be traced in three or four of the images before black lines appeared. This corresponds to a shift of 36 or 48 sec of arc which compares favorably with the calculated value of 30 sec considering the coarseness of the measurement.

In Fig. 6 are shown Berg-Barrett pictures taken as the applied field was increased by 200 oe intervals from 2800 to 4800 oe. Domain lines first appear in the fourth image at a field strength of 3400 oe. In the next few pictures, the number of domain lines increases rapidly but they broaden only slightly if at all. The last pictures show that the crystal is reflecting more intensely and areas which were initially out of reflecting position entirely have begun to reflect weakly.

The techniques described to this point involved only a small area of the crystal and it was impossible to

FIG. 7. X-ray micrograph after anneal II. H_T parallel to [010] direction. H_A=0. 10×.

determine whether the effects observed were localized or extended from one end of the crystal to the other. By taking x-ray micrographs with and without an applied magnetic field, it was possible to show that the domain lines extended over the crystal in characteristic patterns depending on the direction of the magneto-thermal anneal.

Figures 7 and 8 are x-ray micrographs of the crystal after anneal II. Figure 7 shows the image obtained without an applied magnetic field. The density of the image is relatively uniform with hundreds of small dark dots scattered over the picture. The origin of these dots is unknown and they disappeared after several additional anneals. In Fig. 8 the domain lines previously described clearly extend over the entire crystal at right angles to the direction of the magneto-thermal anneal. The lines are weaker along the edges due to demagnetizing effects. At higher field strengths, the domain lines begin to blend into one another due to the general diffuseness of the reflection.

Figure 9 shows the image obtained when the crystal was placed near the edge of the gap of the electromagnet where the field was inhomogeneous after magneto-thermal anneal III. The field strength was 3650 oe at the center of the gap where the lower part of the crystal was situated. At the top of the crystal, the field was much smaller. It can be seen that at the bottom of the crystal the domain lines are continuous and at right angles to the anneal direction. In the upper part of the crystal the number of domain lines decreases and they do not extend completely across the crystal. This indicates that domain growth occurs mainly at the ends of the domain lines. Again very little broadening is observed.

Since the crystal was in the form of a thin plate, demagnetizing effects caused a magneto-thermal anneal in the [100] direction to be less effective than anneal in the other two cube directions. This was evidenced by the fact that when the crystal was annealed first in the [001] and then in the [100] directions, dark bands running in the [001] direction were observed on the micrographs. If the anneal sequence was first in the [010] and then in the [100] directions, the dark bands ran in the [010]. When a magnetic field was applied, domain lines perpendicular to the direction of the first anneal of either sequence appeared. Strain gauge measurements also showed that the magneto-thermal anneal in the [100] direction was not very effective.

In order to obtain a random domain orientation, the crystal was heated at 580°C for two hours. This is well above the Curie temperature of 520°C for cobalt ferrite. With an applied field of 3600 oe both vertical and horizontal domain lines could be observed in the micrographs, corresponding to an original domain alignment perpendicular to these directions. This fact was checked by observing the domain structure by the colloid technique. Evidence of this can also be seen in Fig. 2(B).

To determine whether the domain lines represented long rods or flat sheets, it was necessary to examine another face of the crystal or change the direction of the field. Because of the geometry of the apparatus, it was not possible to alter the field direction and still diffract the x-ray beam from the (400) plane. However, the beam could be diffracted at the θ angle of 58.6° corresponding to the (800) reflection, with the applied field in the [010] direction rather than the [100]. The crystal was magneto-thermally annealed in the [001] direction and x-ray micrographs were taken of the (800) with a field in the [010] direction. No change was observed. The crystal was then annealed in the [100] direction and the micrograph of Fig. 10 was obtained with a field of 3800 oersted. In this figure, domain lines extend along a [110] direction. This anneal procedure was followed twice with the same results. It is not known why the (110) domain lines appear only after this particular anneal sequence and not after an anneal in the [001] direction alone. It was also ob-

FIG. 8. Same as Fig. 7 except H_A=3800 oe.

served that a reversal of the field direction did not alter the direction of the domain lines.

DISCUSSION

That the black domain lines observed on the Berg-Barrett pictures and x-ray micrographs actually correspond to ferromagnetic domains is shown by the fact that there is a "d" spacing shift to a higher diffraction angle within the domain lines. The higher diffraction angle indicates a contraction or decrease in "d" spacing. This agrees in sign with the result expected from the negative magnetostriction of the cobalt zinc ferrite specimen. The magnitude of the "d" spacing shift (30 sec of arc) calculated from the known magnetostriction agrees roughly with the shift observed in the series of Berg-Barrett pictures taken at 12-sec intervals (36–48 sec of arc).

One of the most striking features of the x-ray micrographs is that the black domain lines which appear when a magnetic field is applied are always perpendicular to the original domain alignment as determined by the direction of magneto-thermal anneal. This fact makes it possible to determine the magnetization directions of domains in crystals with an unknown domain alignment.

In order to determine whether the domain lines were long rods or sheets, the (800) reflection was examined with the applied field in the [010] direction. This is equivalent to examining the (010) face rather than the usual (100) face. In Fig. 10 it can be seen that black domain lines running in a [110] direction are observed. This indicates that the domain lines are actually sheets parallel to a (110) plane since rods would be expected to show a pattern of black dots perhaps similar to the colloid patterns observed on hexagonal faces of cobalt crystals.[27] It should also be noted that if the domain lines were in the form of cylindrical rods, the direction of magnetization would correspond to a diameter of the cylinder. This would give rise to a very high shape anisotropy.

FIG. 9. X-ray micrograph after anneal III. H_T parallel to [001] direction. H_A 3650 oe. 10×.

FIG. 10. X-ray micrograph after anneal sequence V and VI. H_A=3800 oe parallel to [010] direction. Reflecting planes are the (800). 8½×.

The fact that the domain lines were in a [110] direction was expected since the usual condition for no internal free poles through a domain wall is that the components of magnetization normal to the wall must be continuous from one domain to the other. From this requirement, it follows that a reversal of the magnetic field direction should cause a 90° change in the direction of the domain, in this case from the [011] to the [01$\bar{1}$] direction. No such change was observed. Although an explanation for this behavior cannot be readily advanced, it is probably connected with the direction of previous magneto-thermal anneal.

It is not possible to equate the width of a domain line observed on an x-ray micrograph to the width of a ferromagnetic domain since strain within the domain produces an unknown amount of line broadening. The line broadening would cause the observed domain line to appear wider than the corresponding ferromagnetic domain. An estimate of the actual domain width can be obtained however, by measuring not only the black domain line but also the white line which precedes it in the series of micrographs in Fig. 5. The width of the domain would be expected to lie between the width of the white and black lines. This is observed to be approximately 20 microns.

The experimental results indicate that domain growth in cobalt zinc ferrite does not occur by the process of domain boundary displacement. This is ruled out since in all the Berg-Barrett pictures and x-ray micrographs, the domain lines are seen to widen very little if at all with increasing field. Instead, higher field strengths cause the domain lines to increase in length, Fig. 9, or increase in number, Fig. 6.

The experimental results suggest that during magnetization domains magnetized in the field direction form within the crystal, perhaps in the domain walls as small disks. Domain growth then occurs at the circumference of the disk until the domain intersects the crystal boundaries. Further increases in the applied field

[27] R. M. Bozorth, *Ferromagnetism* (D. Van Nostrand Company, Inc., Princeton, New Jersey, 1951).

increase the number of properly oriented domains without widening them to any extent. This mechanims of domain growth is similar to the model proposed by W. J. Merz[28] for ferroelectric domains in barium titanate. Merz showed that a process of nucleation and growth of very thin antiparallel domains occurred in barium titanate when subjected to an electric field.

Because of the large magnetostriction of cobalt zinc ferrite, magnetization produces large strains in the crystal. Many studies have shown that strains cause an increase in angular misalignment and therefore an increase in the half-width and integrated intensity of reflection of x-rays.[8-16] The increase in angular misalignment is most apparent in those lattice regions where the strains are largest and which correspond to the domain lines. The strains in the crystal produced by magnetostriction also become manifest by a corresponding increase in the density of the x-ray micrographs. Furthermore, with an increase in applied field there is a general loss of detail in the images of the micrographs (Fig. 6).

It should be noted that the difference between the rocking curves of Figs. 3 and 4 appears to indicate that the increase in strain is not the same in the directions parallel and perpendicular to the domain lines. Such a strain anisotropy is not unexpected since the negative magnetostriction of cobalt zinc ferrite results in a contraction in each domain line in the direction of applied field and an expansion in the direction of magnetization of the original domains (the [010] direction in Fig. 4). However, in a direction parallel to domain lines, there is no change in "d" spacing and therefore, no additional strain.

Because of the strain anisotropy, the half-widths and integrated intensities of the rocking curves depend on the direction of rotation of the specimen relative to the domain lines. When the crystal is rotated around an axis parallel to the domain lines (Fig. 4) every part of the increased crystalline misalignment due to strain perpendicular to the domain lines has a reflecting position at some point during the rotation. For this case a half-width of 173 sec of arc at 4700 oe is observed. When the crystal is rotated around an axis perpendicular to the domain lines, the same opportunity for reflection exists, but, owing to the smaller strain in the direction of rotation, a smaller half-width of 97 sec of arc is observed.

A quantitative measure of the effect of strain due to magnetization can be obtained by equating the square of the half-width W of the broadened curve to the sum of the squares of the half-widths of the component distribution curves. The distribution curves which contribute to the broadened curve are the rocking curve of the unmagnetized crystal w_1, the curve due to "d" spacing change w_2, and the curve due to the increased crystalline misalignment w_3:

$$W^2=w_1^2+w_2^2+w_3^2. \quad (1)$$

From the data of Fig. 3 (4700 oe) $W=97''$, $w_1=65''$, and $w_2=30''$ so that the half-width of the rocking curve due to increased crystalline misalignment w_3, is found to be $65''$ of arc. For the data of Fig. 4, $W=173''$, $w_1=79''$ and again $w_2=30''$ so that $w_3=151''$ of arc. The difference between these two values of the increased misalignment due to magnetization is a measure of the strain anisotropy between the two directions. It should be noted that if the change in w_2 is not independent of the change in w_3 a correction term would have to be introduced into Eq. (1).

By magneto-thermally annealing the crystal in a sequence first in the [010] or [001] direction and then in the [100] direction, it was possible to obtain x-ray micrographs which showed a mixed domain structure. These were obtained because the large demagnetizing factor due to the crystal dimensions decreased the effective field in the [100] direction during magneto-thermal anneal. The result was that the domain alignment in the field direction was not complete. This was shown by the fact that the magnetostriction measured in the [100] direction was not zero and also, application of a field caused domain lines to appear perpendicular to the [010] or [001] directions depending on the first magneto-thermal anneal of the sequence.

The most significant feature of these x-ray micrographs, is that broad light and dark bands occur which extend in the direction of the first magneto-thermal anneal of the sequence. These bands probably correspond to the domains remaining from the first anneal. This is supported by the fact that the bands are most prominent along the edges where the demagnetizing effects would be expected to be largest. These broad domains indicate that magneto-thermal anneal might be a process of domain growth by domain boundary displacement and domain fusion. This interpretation is also supported by the fact that when the crystal was heated above the Curie temperature for several hours, no change in the width of domain lines due to magnetization was observed except that they appeared in both the [010] and [001] directions as would be expected if the domains were now randomly distributed among the cube directions.

ACKNOWLEDGMENTS

I wish to express my appreciation to the members of my graduate committee, Dr. J. H. Koenig, Dr. H. T. Smyth, Dr. R. B. Sosman, Dr. S. Weissmann, and Dr. W. H. Bauer for their interest and suggestions. The author also wishes to extend his thanks to Dr. Roger Chang, Miss Doris Evans, Mr. Joseph Intrater, and Professor J. J. Slade, Jr. of the research staff for many stimulating discussions. Mrs. C. Barsky carried out the chemical analysis.

[28] W. J. Merz, Phys. Rev. **95**, 690 (1954).

Magnetization of the Compound TiFe†

M. V. Nevitt
Argonne National Laboratory, Lemont, Illinois
(Received June 17, 1959)

Magnetization curves were determined for the CsCl-type compound TiFe at six temperatures ranging from 9°K to 110°K. The curves show a saturation effect at high field strength but they are of a form that is not characteristic of ferromagnetism. A saturation magnetization of 3.30±0.07 cgs units per gram was derived from the high field data. This moment is tentatively interpreted as resulting from a small concentration of uncompensated spins produced by disorder in the CsCl-type lattice. The electrical resistance of samples of TiFe was measured over the temperature range from 10°K to room temperature. Magnetization measurements were attempted on the CsCl-type compounds TiCo and TiNi, but their magnetizations were too small to be detected.

INTRODUCTION

In papers by Beck, Darby, and Arora[1] and by Philip and Beck,[2] which dealt with CsCl-type phases in binary systems of metals of the first long period, the suggestion was made that this structure reflects a quasi-ionic bonding associated with an electron transfer between unlike atoms. Lattice parameter data and the occurrence of ordering were taken to indicate that there is a decreasing strength of the A−B bond as a shift is made from Ti to V to Cr in equi-atomic alloys with Fe, and that a diminution in the strength of the A−B bond also accompanies a shift from TiFe to TiCo to TiNi. It was suggested that the proposed electron transfer might affect the number of *d* electrons on the Fe, Co, or Ni atom. A search of the literature indicated that there were no quantitative data on the magnetic behavior of the compound TiFe, although a qualitative test indicated that it is not strongly magnetic at 78°K.[2] Data on TiCo and TiNi were also lacking. In the present work a somewhat detailed study of the saturation moment of TiFe was made, and TiCo and TiNi were examined briefly.

EXPERIMENTAL TECHNIQUE

Magnetic moments were measured by means of a modification of the widely used method in which a sample of the test material, in a uniform magnetic field, is withdrawn from an induction coil which is in series with a fluxmeter whose deflection has been calibrated in terms of magnetic moment. A schematic representation of the sample-actuating mechanism of the cryostat is shown in Fig. 1. The specimen is contained in the cylindrical copper sample holder *A* which is attached to the copper rod *B*. The phosphor bronze leaf springs C_1 and C_2 can be actuated remotely to move the rod and cause the sample cylinder to slide in the copper track *D*. In this way the sample cylinder is translated back and forth from one terminal position in which it is inserted in coil E_1 to the other terminal position in coil E_2. Buried in the copper track is a calibrated copper-constantan thermocouple which is used to determine the temperature of the sample. The coils, each containing 10 000 turns of copper wire, are connected in series opposition and are placed in series with a "trimmer" coil (outside the cryostat) and a ballistic galvanometer of high sensitivity. The coils and the copper track in which the sample cylinder slides are held in place by the heavy copper arms F_1 and F_2 which are attached to the bottom of the liquid helium container. Also attached to the liquid helium container is the rectangular copper radiation shield *G* which surrounds the mechanism just described. A second copper radiation shield *H* is attached to the liquid nitrogen vessel of the cryostat, and an outermost copper can *I* is connected to the outer vacuum wall of the cryostat. The complete assembly fits within the 2-in. gap of an A.D. Little electromagnet, one pole face of which is shown in the background of Fig. 1.

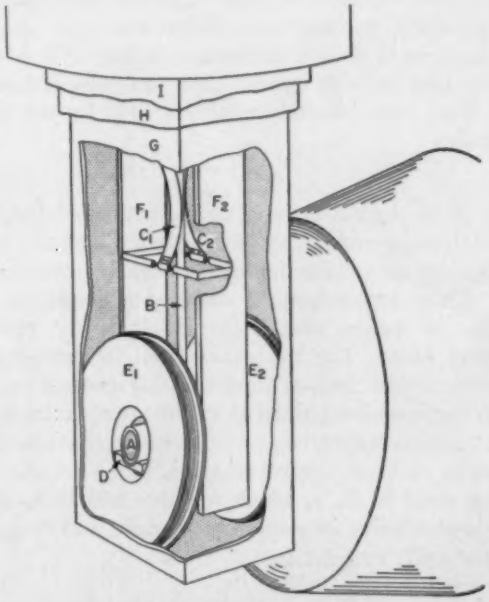

Fig. 1. Details of cryostat.

† Work performed under the auspices of the U. S. Atomic Energy Commission.

[1] Darby, Arora, and Beck, Trans. Am. Inst. Mining, Met. Petrol. Engrs. 206, 148 (1956).

[2] T. V. Philip and P. A. Beck, Trans. Am. Inst. Mining, Met. Petrol. Engrs. 209, 1269 (1957).

Although the thermal emf of a copper-constantan thermocouple is low in the temperature range below 20°K, the use of a potentiometer with a limit of error of 1 μv made it possible to measure temperature with an accuracy of ± 0.5°K at the lowest temperature that was achieved in this work. Because of the temperature gradient that existed between the liquid helium container and the specimen, the lowest specimen temperature that was obtained when the space surrounding the specimen was evacuated was several degrees above the normal boiling point of liquid helium. The specimen temperature could be reduced to as low as 4.5°K if a small quantity of helium gas was admitted to the space to serve as an exchange gas. In all of the tests described here the space surrounding the specimen was evacuated. Measurements at higher temperatures were made during slow warmup of the cryostat (heating rate not greater than 0.09°K per min).

The two induction coils were not in close enough electrical balance to give complete cancellation of the opposing voltages that were induced in them by spurious field changes of 1 part in 10^3. The result was an erratic drift of the galvanometer which reduced the reproducibility of the deflections. This defect was minimized by the "trimmer" coil which was mounted on pinions on the outside of the vacuum can and could be rotated in such a manner as to change its effective area normal to the field of the magnet. By the proper selection of its polarity and orientation it could be used to buck the spurious net voltage from the induction coils, so galvanometer drift was greatly reduced.

The calibrating sample consisted of 0.0447 g of carbonyl Ni powder evenly distributed in nonmagnetic dental plastic. The powder, which had an average particle size of 3 to 6μ and a minimum purity of 99.60%, constituted 0.3% of the volume of the sample. Using this standard, galvanometer deflections were observed as a function of field at temperatures from 7°K to room temperature in fields up to 12 kilo-oersteds. The deflections were extrapolated to infinite field by use of the expression

$$D_{H,T}=D_{\infty,T}[1-(b/H^2)], \qquad (1)$$

where D is the deflection per unit mass of magnetic material. Bean and Jacobs[3] have shown that this is the appropriate expression for the approach to saturation of a dilute ferromagnetic suspension in fields high enough to insure that magnetizing is by rotation processes alone. The calibration and its temperature dependence was derived from the extrapolated saturation deflections determined at various temperatures and the saturation magnetization of nickel at the same temperatures. A least squares analysis indicated that the random error in $D_{\infty,T}$, which was due mainly to slight nonreproducibility in sample movement and to galvanometer drift, was $\pm 1\%$.

[3] C. P. Bean and I. S. Jacobs, General Electric Research Laboratory Memo No. M179 (June, 1955).

The compound TiFe was prepared by arc melting in an inert atmosphere using electrolytic Fe and crystal-bar Ti, both having a purity better than 99.9%. The alloys were remelted several times to insure homogeneity and vacuum annealed for 72 hr at 1000°C. Extreme care was exerted to avoid contamination during annealing. Both metallographic and x-ray diffraction examination failed to reveal a trace of second phase in the structure. The brittle compound was then crushed to a fine powder and samples for magnetic moment measurements were prepared in the same way as the calibrating sample. Since the magnetization of TiFe was weaker than that of the carbonyl Ni it was necessary to employ a 7% volume concentration. Samples of TiCo were prepared in essentially the same way except that the volume concentration of the powder was increased, the highest being 17.5%. The phase TiNi was not brittle enough to be crushed to powder so a solid sample essentially spherical in shape with a diameter of 0.55 cm was used.

EXPERIMENTAL RESULTS

TiFe

In Fig. 2 the specific magnetization of TiFe is plotted as a function of field at various temperatures. The magnetization is small even at the lowest temperature and the curves have an unusual form. At 79°K and below the magnetization remains linear with field strength up to rather high fields and then there is a saturation effect. The slope of the linear portions of the magnetization curves is inversely proportional to temperature. Values of $\sigma_{\infty,T}$ were obtained by plotting the high-field data against $1/H^2$ and extrapolating to $1/H^2=0$, and the absolute saturation magnetization $\sigma_{\infty,0}$ was obtained by plotting $\sigma_{\infty,T}$ for the three lowest temperatures against T^2 and extrapolating to $T^2=0$.

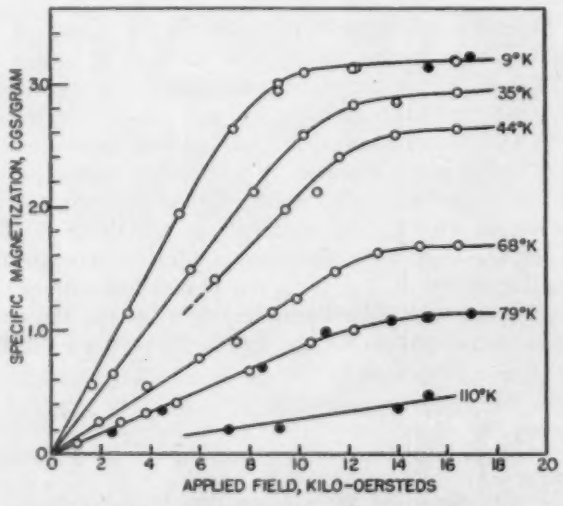

FIG. 2. Specific magnetization of TiFe *vs* field at various temperatures. Open and filled circles refer to two different samples.

This yielded a value of 3.30 cgs units per gram. When allowance is made for the uncertainty in the temperature measurements and in the calibration and for a random error (±1%, determined by a least squares analysis) in the determinations of $\sigma_{\infty,T}$, the uncertainty in $\sigma_{\infty,0}$ is ±0.07 cgs units per gram. The number of Bohr magnetons per unit cell of TiFe can be calculated from the expression

$$n_0=(\sigma_{\infty,0}\times M)/5585=(3.3\times 103.75)/5585=0.061, \quad (2)$$

where M is the molecular weight of TiFe. With the sensitivity of measurement employed in the tests described above, the remanent magnetization was below the level of detection. However, in a later test employing higher sensitivity, a residual magnetization amounting to less than 0.1 cgs unit per gram at 5°K was detected when the specimen was tested in zero field after having been magnetized at 17 kilo-oersteds.

In addition to the magnetization data, the electrical resistance of two polycrystalline solid specimens of TiFe were measured by the potential drop method as a function of temperature. The specimens were approximately 2 cm long, and, because of the brittle nature of the compound, had an irregular cross section. This fact prevented a calculation of the resistivity. The data exhibited a high degree of scatter probably because of internal cracks in the specimens. From 9°K to 38°K the specimens retained a constant residual resistance while above this temperature the resistance increased with temperature. The data are best fitted by a smooth curve without an inflection such as might be expected if a Curie point or a Néel point existed in this range. From 9°K to 115°K the resistance was measured in magnetic fields applied normal to the direction of current flow. No variation of resistance could be detected in fields up to 17 kilo-oersteds.

TiCo and TiNi

Negative results were obtained on TiCo and TiNi in that no consistently measurable deflections were observed at any field strength. TiCo was tested at 7°K and 79°K and TiNi was tested at 9°K and 79°K. If these compounds exhibit similar magnetic characteristics, their specific magnetizations are too small to be detected by the measuring system.

DISCUSSION

The significant features of the magnetization curves of TiFe are (a) a magnetization of very small magnitude, (b) an approach to saturation occurring at unusually high fields, and (c) a temperature effect at low field strength that does not seem to be characteristic of a process involving domain wall motion. These features indicate that TiFe is probably not ferromagnetic, and therefore the meaning of the observed saturation moment is open to question. One possible interpretation, for which the author is indebted to Dr. A. Arrott,[4] is that the moment arises from disorder in the CsCl-type lattice. The saturation moment of the structure with perfect long range order is assumed to be zero by the adoption of either a model in which electron transfer results in no net moment on either the iron or the titanium atom or a model in which there are moments on the Fe atoms but these are coupled antiferromagnetically by superexchange through the Ti atoms. However, in the real crystal some Fe-Fe nearest neighbors should occur because of imperfect ordering within an order domain and because of antiphase boundaries. In the first model this disorder should cause a perturbation of the normal electron transfer, while in the second model it should lead to localized partial uncoupling of the antiferromagnetic lattice. In either case the result is the same: The presence of a small concentration of uncompensated moments which can be aligned by a magnetic field, probably by purely rotational processes. From this point of view it appears that the saturation moment of TiFe may be a structure-dependent quantity that varies with the degree of order, rather than an intrinsic property. Until additional data are available it seems logical to assign the value of 0.061 Bohr magnetons per atom as its upper limit. The electrical resistance data suggest that if the antiferromagnetic model is the correct one, the Néel point is above room temperature. As has been suggested,[1,2] neutron diffraction work might help to clarify this point.

ACKNOWLEDGMENTS

The author wishes to thank Mr. R. A. Morris for assistance in all phases of the experimental work. Thanks are due Dr. D. W. Osborne and Dr. B. M. Abraham for advice in the construction of the cryostat and for supplying the liquid helium.

[4] A. Arrott (private communication).

JOURNAL OF APPLIED PHYSICS VOLUME 31, NUMBER 1 JANUARY, 1960

Asymmetrical Triple Probe Method for Determining Energy Distribution of Electron in Plasma

TAKAYOSHI OKUDA AND KENZO YAMAMOTO
Faculty of Engineering, Nagoya University, Nagoya, Japan
(Received June 26, 1959)

A new probe method is proposed. This method is an improvement of the floating triple probe method, which was proposed by us in a previous paper. In this method, the dimension of one operating probe is different from the other, so that the smaller probe behaves as the single probe. Thus, the measurable range of electron energy can be extended as much as that in the single probe method. The asymmetrical triple probe and double probe methods are verified experimentally. The asymmetrical triple probe method has a merit that a disturbance, which is inevitable in the single probe method, can be eliminated in this method. The electron energy distribution obtained by the new probe method is not always in accord with that obtained by the usual single probe method. The hump often observed at high energy range in the single probe method does not appear in the new method, illustrating that the latter is free from erroneous estimation due to the disturbance.

I. INTRODUCTION

THE electron energy distribution has been determined by either taking the second derivative of the single probe characteristic[1] or analyzing energy of the electron entering into an analyzing tube through the aperture on a plane probe.[2]

However, in those methods the probe should be held at the plasma potential by applying an appropriate voltage with respect to an electrode of the discharge. This can be realized in dc discharge plasma, but not in electrodeless discharge plasma.

We have proposed a triple probe method applicable to electrodeless discharge plasma,[3] in which the third probe held at the floating potential is inserted in order to establish a fixed reference potential, and a pair of probes with identical dimension are so operating that each probe current is equal and is limited by the positive ion current. Consequently, the electron current flowing into the probe with higher potential is limited by $2i_p$, where i_p is the positive ion current flowing into one probe. This electron current is smaller than the electron current which would be collected on the probe at the space potential in the single probe method, so that it is impossible to obtain a whole distribution of electron energy. In reality, the distribution curve obtained by the usual triple probe method is restricted within an energy range which extends from infinite energy to an energy corresponding to a potential slightly smaller than the floating potential.

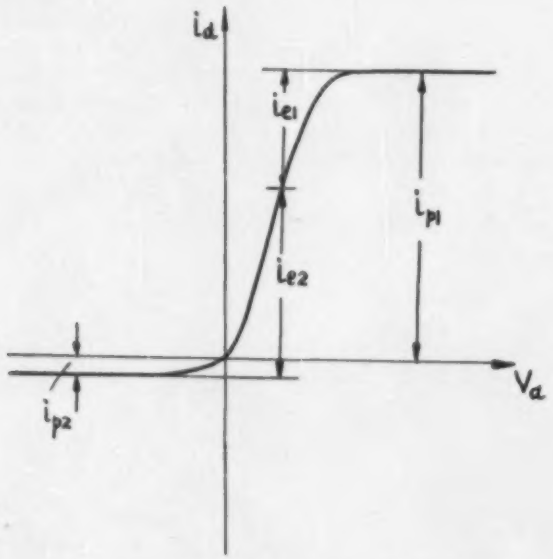

FIG. 1. Asymmetrical double probe characteristic.

In this paper, we propose an improved triple probe method, by which the whole energy distribution can be determined, using "asymmetrical double" probes and the third probe. The asymmetrical probes mean that the surface area of the one probe is quite different from that of the other; for example, in our case the ratio of those surface areas is taken by several hundreds to several thousands. Concerning the asymmetrical double probe method, Kojima, Takayama, and Simauchi[4] and Takayama and Kizaki[5] pointed out that the asymmetrical double probe characteristic should close to the single probe characteristic.

When the probe potential approaches the plasma potential by applying the voltage between one of the discharge electrodes and the probe in the single probe method, the probe characteristic may often be distorted by a disturbance owing to the fact that the current flowing into the probe circuit becomes large compared to the discharge current. We described such a disturbance in a previous paper.[6,7]

[1] M. J. Druyvesteyn, Z. Physik **64**, 790 (1930).
[2] C. Haith and T. Smith, Phil. Mag. **41**, 557 (1950).
[3] K. Yamamoto and T. Okuda, J. Phys. Soc. Japan **11**, 57 (1956).
[4] Kojima, Takayama, and Simauchi, Research Report on Gaseous Discharge, supported by National Science Foundation, No. 4047, 1952 (unpublished).
[5] K. Takayama and F. Kizaki, Session on Gaseous Discharge, Tokyo, Japan, 1955.
[6] T. Okuda and K. Yamamoto, J. Phys. Soc. Japan **13**, 1212 (1958).
[7] T. Okuda and K. Yamamoto, J. Phys. Soc. Japan **11**, 177 (1956).

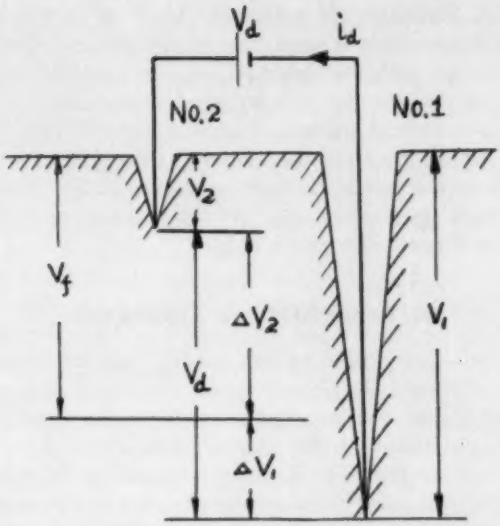

FIG. 2. Associated voltages of asymmetrical double probe method.

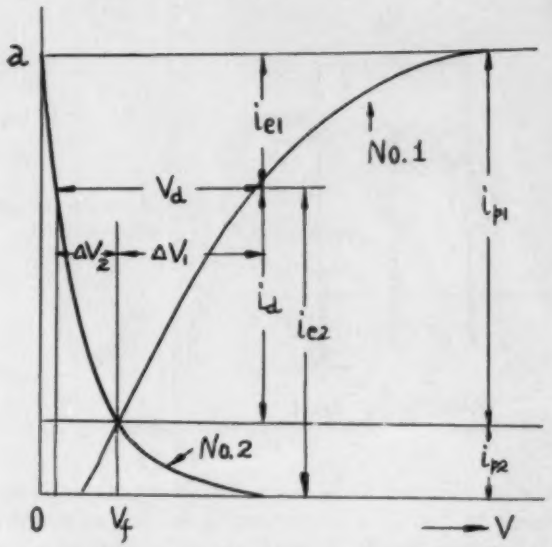

FIG. 3. Illustrating relation between double probe characteristic and electron or ion currents flowing into each probe.

The electron energy distribution curve obtained from such distorted characteristic should be different from that without the disturbance. Thus, a new method is performed without connection of the probe circuit with the reference electrode of the discharge tube, so that it has a merit that the distortion of probe characteristic due to such disturbance can be eliminated.

II. PRINCIPLE OF THE ASYMMETRICAL TRIPLE PROBE METHOD

First, we consider what happens when the surface area of one probe in the double probe method is different from the other.

Evidently, use of such dimensional asymmetry should result in an asymmetrical double probe characteristic, as shown in Fig. 1. Notations of the associated voltages of the asymmetrical double probe are shown in Figs. 1 and 2. The subscripts 1 and 2 refer to the larger probe No. 1 and the smaller probe No. 2, respectively.

Similar to the method of Johnson and Malter,[8] in which they analyzed for an ideal case, i.e., no slope at the saturated part of the double probe characteristic, the probe currents are expressed in terms of the associated voltages as follows:

$$i_d = i_{p1} - i_{e1} = i_{e2} - i_{p2} \tag{1}$$

$$i_{e1} = F_1 j_e \exp(-\phi V_1) \tag{2}$$

$$i_{e2} = F_2 j_e \exp(-\phi V_2) \tag{3}$$

$$V_1 = V_2 + V_d, \tag{4}$$

where i_p is positive ion current; i_e, electron current; j_e, random electron current density; i_d, probe current; F, surface area of probe; V, voltage applied across ion sheath; V_d voltage applied between two probes, No. 1 and No. 2; $\phi = e/kT_e = 11\,600/T$); T_e electron temperature (°K); ΔV, potential difference between the floating potential and the probe potential.

Figure 3 shows how the double probe characteristic relates to the electron current, ion current, and the probe potential. From this figure, it is seen that in order to obtain the whole curve of the electron energy distribution the electron current i_{e2} of the smaller probe must exceed the random electron current density times the surface area F_2 of No. 2 probe; i.e.,

$$i_{e2}(V=0) = i_{p1} + i_{p2} \geq F_2 j_e. \tag{5}$$

If we take a plane probe, Eq. (5) leads to

$$(F_1 + F_2) j_p \geq F_2 j_e, \tag{6}$$

where j_p is random ion current density. Setting $R = F_1/F_2$, Eq. (6) becomes

$$1 + R \geq j_e/j_p = (MT_e/mT_p)^{\frac{1}{2}}. \tag{7}$$

Considering Ar plasma as an example, the value of R must exceed 270 for $T_e/T_p = 1$. Since the value of T_e is usually greater than that of T_p, the value of R must be larger than 270 for Eq. (7) to be satisfied. However, the value of R measured is often smaller than this theoretical value owing to penetration effect in the ion sheath.[6] In a previous paper,[3] it was verified from the fact that the measured value of floating potential was always less than the theoretically deduced one.

Using asymmetrical double probe, we obtain an asymmetrical double probe characteristic, as shown in Fig. 2. As have been described in our other paper,[3] we can obtain a curve of i_{e2} *vs* negative voltage (or potential difference ΔV_2 between the potentials of the No. 2 probe and the floating potential V_f) from the double probe characteristic, with help of the third probe under a condition that the current i_3 flowing into the third

[8] E. O. Johnson and L. Malter, Phys. Rev. **80**, 58 (1950).

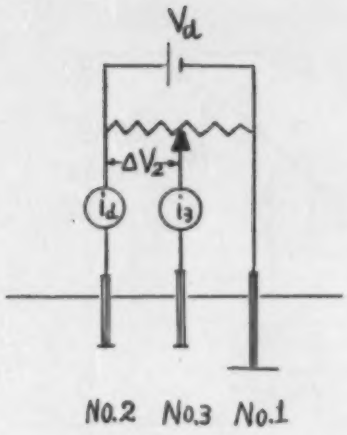

FIG. 4. Circuit of triple probe method.

probe is adjusted to be zero. The third probe makes possible to find ΔV_2 by measuring the potential difference between the No. 2 probe and the third probe (see Fig. 4).

The curve of i_{e2} *vs* ΔV_2 including the energy range from zero to the energy corresponding to the floating potential, can be obtained if V_d is positive. On the other hand, the curve of the energy range above an energy which corresponds to the floating potential, can be obtained by inversing the polarity of V_d.

Plasma potential is determined by computing the floating potential V_f through the theoretical expression,[3] or experimentally. For this purpose, we use the fact that at large R the double probe characteristic, in which ΔV_2 obtained by the triple probe is used instead of V_d, approaches the single probe characteristic of the smaller probe. Thus the plasma potential can be deduced from the bend of the corrected double characteristic in semi-log plot.

Next, we show that the characteristic of the asymmetrical double probe approaches that of the single probe, in other words, only slight or no change of the potential of the larger probe No. 1 occurs, when the ratio R of the surface areas of two probes is large. Change of potential δV_1 and δV_2 of probes No. 1 and No. 2 with changing V_d by δV_d are given by Eq. (1), provided that i_{p1} and i_{p2} are independent of V_d (or V). So we obtain

$$\delta i_d = -(di_{e1}/dV)\delta V_1 = (di_{e2}/dV)\delta V_2. \tag{8}$$

Substituting Eqs. (2) and (3) into Eq. (8), and using $F_1 = RF_2$, we obtain

$$|\delta V_1/\delta V_2| = R^{-1}\exp[-e(V_2-V_1)/kT_e] = R^{-1}\exp(eV_d/kT_e). \tag{9}$$

For example, if $eV_d/kT_e = 3$ and $R = 1000$, we obtain $\delta V_1/\delta V_2 = 1/50$. This means that the change of the potential of the probe No. 1 is quite small compared with that of the probe No. 2. Thus, for large R, the potential of the larger probe is in effect close to the floating potential. Therefore, if extremely large R as much as several thousands is used, the double probe characterisitc agrees with the single probe characteristic, except for large positive V_d. At a large positive value of V_d, in principle both characteristics should be different from each other, because the double probe characteristic under such a condition does not follow to the electron current flowing into probe No. 2 but to the positive ion current flowing into probe No. 1.

III. EXPERIMENTAL APPARATUS

In principle, three probes used in the triple probe method should be placed in the plasma of the same potential and density. If this requirement is not fulfilled, the double probe characteristic curve does not pass the point of $V_d = 0$, and consequently the associated voltages and the energy distribution are not exactly estimated. Also, in such a condition, it was found by Takayama and Kizaki[5] that a circulating current flowed in the probe circuit. For the foregoing requirement it is better to use a large discharge tube, where uniform plasma is formed extensively. Figure 5 shows a spherical tube with a diameter of 15 cm, in which three probes, an Ni anode, and an oxide-coated cathode are mounted. The larger probe No. 1 consists of six rings made of Ni. In order to obtain necessary surface area, some of those parts are connected together. The smaller probe No. 2 (Mo) and the third probe No. 3 (Mo) are plane probes with diameters of 0.2 mm.

The discharge tube is filled with Ar gas of pressure $1\sim10^{-3}$ mm Hg. The discharge currents are below 100 ma, and the tube voltage are several tens of volts.

IV. EXPERIMENTAL PROCEDURE AND RESULTS

(a) Double Probe Characteristic

When the voltage V_d is applied by connecting the larger probe No. 1 to the negative pole of the battery

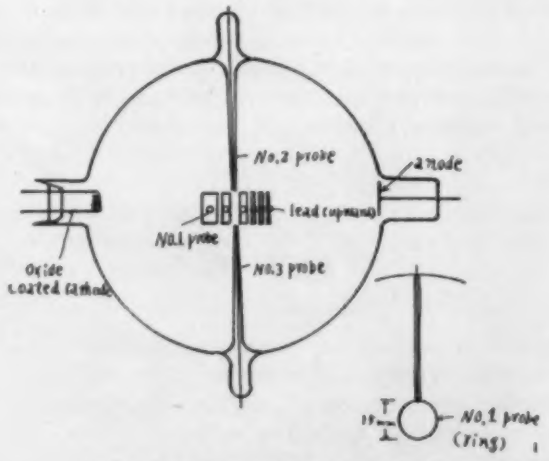

FIG. 5. Experimental discharge tube.

and the smaller probe No. 2 to the positive pole, the electron current i_{e2} flows in the smaller probe from plasma. The maximum value of i_{e2} is limited by the ion current flowing into probe No. 1. But, since the probe No. 1 is large enough to satisfy the condition $i_{e2} > F_2 j_e$, the double probe characteristic curve has a shape similar to the single probe characteristic curve, and with increasing R, the two characteristic curves become much closer.

Figure 6 shows the double probe characteristic curve with different values of R, comparing the single probe characteristic curve. For the large value of R above several hundreds, the current of the double probe unexpectedly exceeds that of the single probe. This discrepancy is explained by a characteristic disturbance in the single probe method, which is due to the fact that a part of the discharge current flows into the probe circuit.[6] Therefore, there is no such disturbance in the double probe method, in which the probe circuit is isolated from the discharge electrodes. Such disturbance was described in detail in previous papers.[6,7]

For larger value of R of several thousands, the double probe characteristics are the same with each other. Of course, the curves at large positive V_d do not agree with each other, because the ion current flowing into the No. 1 probe varies with varying R. Thus, the floating double probe with large value of R has an advantage that there is no such disturbance, as observed in the single probe method.

In Fig. 6, the result of the triple probe method, in which ΔV_2 is taken as the voltage scale in place of V_d, is also shown. The triple probe characteristic is plotted for $R=400$, showing that the curve is fairly in accord with the double probe characteristic with the value of R above several thousands.

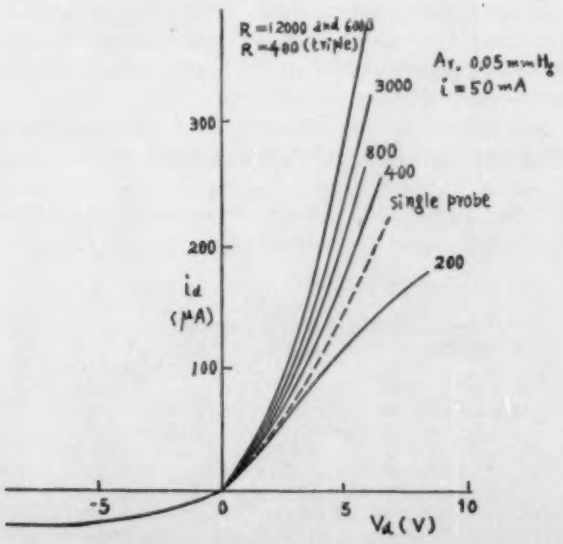

FIG. 6. Double probe characteristic with different values of R, comparing with single probe characteristic.

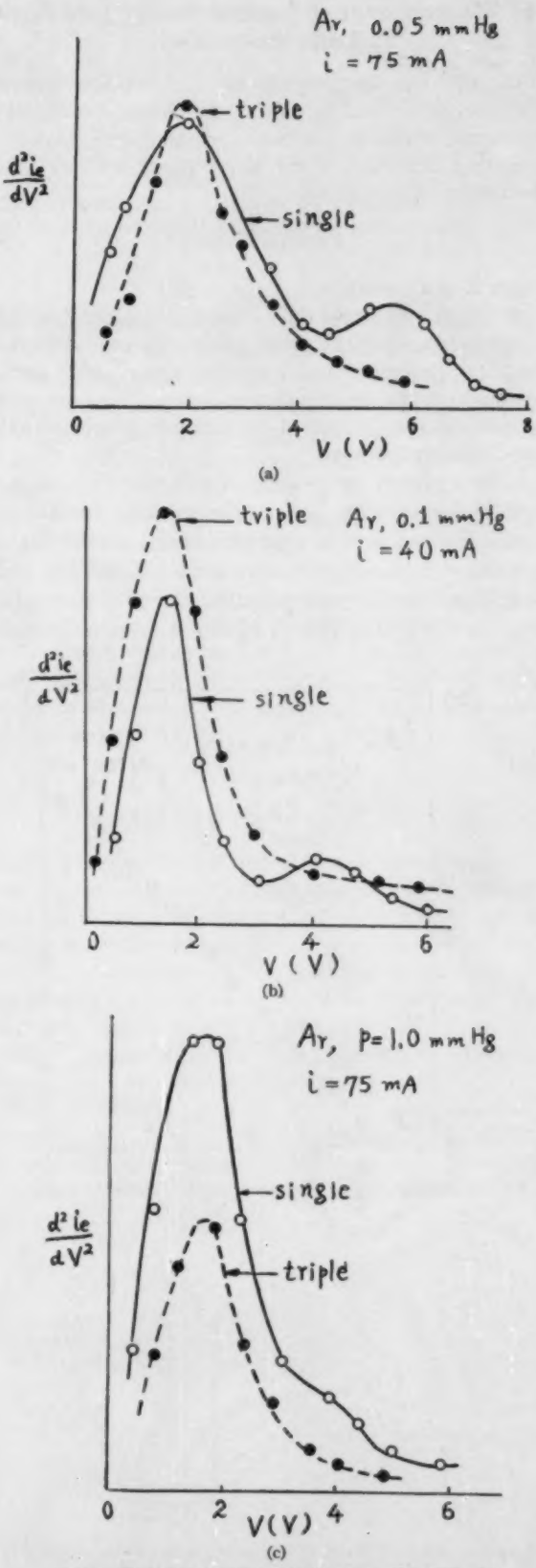

FIG. 7. Plot of the second derivatives $d^2 i_e/dV^2$ with retarding voltage.

(b) Measurement of Electron Energy Distribution by Triple Probe Method

Usually the electron energy distribution function $f(V)$ can be derived by taking the second derivative of the curve of electron current i_e plotted with respect to retarding potential in the single probe method, using the following expression:

$$f(V)=KV^{\frac{1}{2}}d^2i_e/dV^2, \tag{10}$$

where K is a constant.

As the double probe characteristic for large R is quite in agreement with the single probe characteristic when the triple probe method is applied, the electron energy distirbution can be found even when the single probe method can not be applied, for example, in an electrodeless discharge plasma.

Measurements of energy distribution by such a method are carried out under various conditions. Figure 7 shows typical examples of the second derivative d^2i_e/dV^2, showing features of the distribution function. These data are taken in the case when the surface area ratio R is 400. In this figure, the results obtained by the single probe method are also given as comparison. A distinct difference in the shape of the second derivative is observed between them. A small hump at high energy seen in the single probe measurement does not appear in that obtained by the new method.

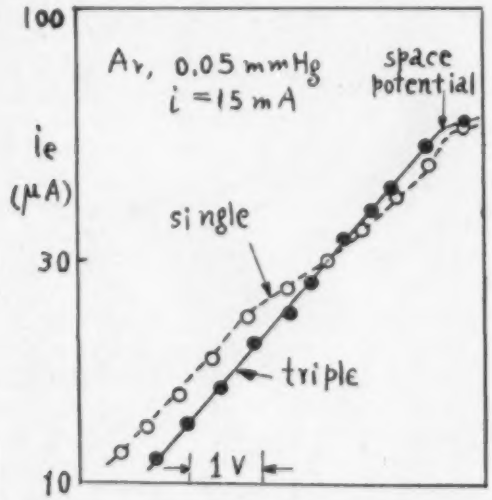

FIG. 8. Semilog plot of electron current *vs* probe potential.

In Fig. 8, the semilog plots of electron current *vs* probe potential are shown. The plot of the single probe method deviates from the straight line, while that of the triple probe method is on a straight line, showing the energy distribution to be Maxwellian. In our experimental condition, as the probes are located in a homogenous plasma at a distance of several cm from the cathode, the existence of high energy group of electron should not be expected. As the triple probe method is free from errors to a characteristic disturbance in the single probe method, we may conclude that the distribution curve obtained by the triple probe method is more justifiable than that by the single probe method.

Such disturbance results in a distortion of behavior of the neighboring space of the probe, when the electron current flowing into the probe is large. Consequently electron current flowing into the probe at small negative potential with respect to plasma or evaluated electron temperature is different from that when no distrubance exists.

V. CONCLUSION

The asymmetrical triple probe method is useful for measuring the electron energy distribution when there is no electrode as a reference of potential. The method is also helpful in making the measurement in dc plasma with the reference electrode more reliable. This method is free from a characteristic disturbance in the single probe method, which is a change of the plasma density and potential of neighboring space with increasing probe current. It follows that the discharge current flowing through the anode-probe space is different from that in the cathode-probe space.

From the measurement by using this method, it is seen that the existence of the high energy group of electrons often observed in the single probe method is sometime due to the disturbance.

The authors are indebted to Mr. T. Kojima for his assistance throughout the present work.

JOURNAL OF APPLIED PHYSICS VOLUME 31, NUMBER 1 JANUARY, 1960

Figure of Merit for Thermionic Energy Conversion*

N. S. Rasor
Atomics International, A Division of North American Aviation, Inc., Canoga Park, California
(Received August 3, 1959)

The optimum performance for emission-limited thermionic energy conversion is derived in convenient analytical form. The steps which are thereby indicated to reduce fundamental performance limitations are enumerated and briefly discussed. A figure of merit is defined with brief description of its usefulness and significance. A comparison of thermionic and thermoelectric conversion is thereby afforded by the analysis.

I. INTRODUCTION

SEVERAL analyses of the direct conversion of thermal energy to electrical energy by thermionic emission have been published.[1-4] However, these analyses do not yield a simple single parameter as a figure of merit for comparing prospective materials, such as that extensively used[5,6] in the development of thermoelectric conversion. In the following, a similarly useful figure of merit for the thermionic system is obtained by an analysis analogous to that used in the thermoelectric case. This parameter permits a quick estimate of the efficiency of a thermionic converter, quantitatively illustrates the relative importance of the various materials properties, and permits direct intuitive and quantitative comparison of thermoelectric and thermionic systems.

II. EFFICIENCY ANALYSIS

Figure 1 is a diagram of negative electric potential for a thermionic diode. V_c and V_a are the potential difference between the maximum negative potential of the system and the Fermi levels of the cathode (hot electrode) and anode, respectively; ϕ_c and ϕ_a are the respective work functions, T_c and T_a the respective temperatures, and J_c and J_a the saturation electron emission current densities of the respective electrodes, and V the potential drop across the external load. The potential curve between the two electrodes depends on the space charge formed there by the emitted electrons. The nature of the space charge and means for its suppression are important problems which have received detailed attention elsewhere,[7-10] and concerning which significant progress is presently being made. While such effects are important factors in the performance of existing devices, there already exist means by which they can, in principle, be made negligibly small. The primary purpose of the present analysis is to display the fundamental system requirements and limitations with the greatest simplicity consistent with generality. Therefore, the absence of space charge limitation will be assumed in the analysis, with subsequent consideration of such effects as perturbations. This is similar to the omission of contact resistance, nonuniformity, and other troublesome but nonessential effects from the classic thermoelectric analysis, which indeed have been largely overcome as that technology has matured.

The potential diagram for a thermonic diode delivering maximum power to its load, but without space charge limitation, is shown in Fig. 2. The Richardson-Dushman equation for the saturation emission currents will be assumed

$$J_c = AT_c^2 \exp(-e\phi_c/kT_c) \quad (1)$$

$$J_a = AT_a^2 \exp(-e\phi_a/kT_a), \quad (2)$$

where $A = 120$ amp/cm^2-°K^2 is the theoretical constant, e the electronic charge, and k the Boltzmann constant. This assumption neglects electrode patchiness, electron reflection, temperature dependence of the work function, and energy transfer between the electron gas and other gas present in the interelectrode space.[4] The influence of these effects on Eqs. (1) and (2) as used herein is either negligible or can be made arbitrarily small in most practical applications.

For simplicity it will be assumed that the anode temperature T_a is so low that J_a is negligibly small. The thermal efficiency of the emission-limited thermionic converter at its optimum output emf ($V_0 = \phi_c - \phi_a$) is

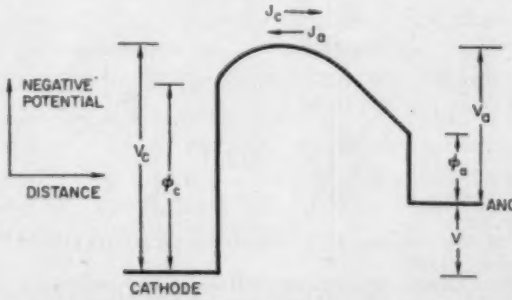

FIG. 1. Negative electric potential diagram for a space-charge-limited thermionic diode with arbitrary load.

* Supported in part by the U. S. Atomic Energy Commission under Contract No. AT(11-1)-GEN-8.

[1] W. Schlichter, dissertation, University of Gottingen (1915).
[2] M. J. O. Strutt, Proc. Inst. Radio Engrs. **40**, 601 (1952).
[3] H. Moss, Brit. J. Electronics **2**, 305 (1957).
[4] J. M. Houston, J. Appl. Phys. **30**, 481 (1959).
[5] A. F. Ioffe, *Semiconducting Thermoelements and Thermoelectric Cooling* (Infosearch, Ltd., London, 1956).
[6] C. Zener, Ind. Labs. **9**, 538 (1958).
[7] V. C. Wilson, J. Appl. Phys. **30**, 475 (1959).
[8] H. F. Webster, J. Appl. Phys. **30**, 488 (1959).
[9] Hernqvist, Kanefsky and Norman, RCA Rev. **19**, 244 (1958).
[10] G. N. Hatsopoulos and J. Kaye, J. Appl. Phys. **29**, 1124 (1958).

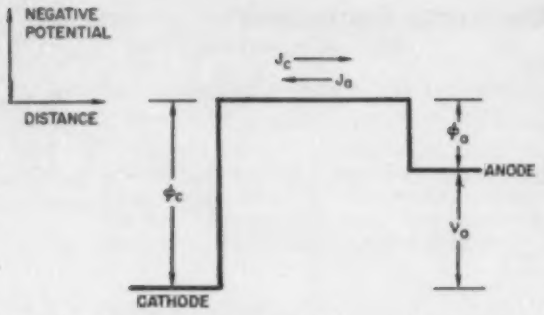

FIG. 2. Negative electric potential for an emission-limited thermionic diode with optimum load.

then given[4,11] by

$$\eta=\frac{J_c(\phi_c-\phi_a-V_w)}{J_c(\phi_c+2kT_c/e)+P_L}, \tag{3}$$

where V_w is the potential drop across the lead wires to the load. $P_L=P_r+P_m+(P_w-J_cV_w/2)$ is the net extraneous power loss per unit cathode emitting area due to radiation (P_r) heat conduction along the cathode lead wire (P_w), and other miscellaneous losses (P_m) such as gaseous heat conduction. By superposition, half of the Joule heat dissipated in this wire flows back to the cathode and thus subtracts from the conduction loss P_w. Thus the numerator of Eq. (3) is the electrical power per unit emitting area delivered to the load, while the denominator is the sum of the heat per unit emitting area required to emit the electrons from the cathode and supply its extraneous heat losses.

Since P_w and V_w are both functions of the lead wire size, Eq. (3) can be maximized with respect to this variable. The optimum lead configuration may be shown† to be given by

$$\frac{A_w}{X}=J_cA_e\left(\frac{\rho}{\eta K(T_c-T_a)}\right)^{\frac{1}{2}}\left(1-\frac{\eta}{2}\right)^{\frac{1}{2}}, \tag{4}$$

where A_w, X, ρ, and K are the area, length, average electrical resistivity, and thermal conductivity, respectively, of the cathode lead wire, and A_e is the effective electron emitting area of the cathode. As will be shown later, even under ideal conditions the efficiency η is usually less than 50%, allowing $\eta\ll 2$ to be used as a very good approximation in the remaining analysis. Using this optimum lead size, the optimized efficiency is found from Eq. (3) to be

$$\eta_0=\frac{F}{B^2}\left[\left(1+\frac{BC}{F}\right)^{\frac{1}{2}}-1\right]^2, \tag{5}$$

where $F=\rho K(T_c-T_a)/\phi_c^2$, $C=1-\phi_a/\phi_c$, and $B=1+2kT_c/e\phi_c+(P_r+P_m)/J_c\phi_c$.

As in the thermoelectric case, this fairly exact but formidable expression for the optimized efficiency may be greatly simplified by the use of a few generally valid but restrictive approximations, as follows. Up to this point it has been tacitly assumed that the anode is so cold that no electrons are emitted from it. However, for minimum P_L in a given system, the temperature of the anode should be as high as the absence of appreciable back-emission permits. It may be seen from Eqs. (1) and (2) that the ratio of anode to cathode emission currents is negligibly small if the anode temperature is slightly less than the optimum anode temperature T_{a0} defined by

$$\frac{T_{a0}}{\phi_a}\equiv\frac{T_c}{\phi_c}\equiv\alpha. \tag{6}$$

As will be shown below, values for J_c within an order of magnitude of 1 amp/cm² are required for efficient energy conversion. Therefore Eq. (1) gives to an adequate approximation

$$\alpha=e/k\ln(AT_c^2/J_c)\simeq 640°\text{K/v}\pm 6\% \tag{7}$$

for $1<J_c<10$ amp/cm² at 1500°K. Furthermore, it may be shown that $(BC/F)^{\frac{1}{2}}\gg 1$ if the cathode lead wire is made of a typical metal obeying the Lorentz (Wiedemann-Franz) relation $\rho K=L(T_c+T_a)/2$, where the constant $L=2.45\times 10^{-8}$ w-ohms/°K².

Assuming the anode to be operated at the optimum temperature given by Eq. (6), assuming for the moment

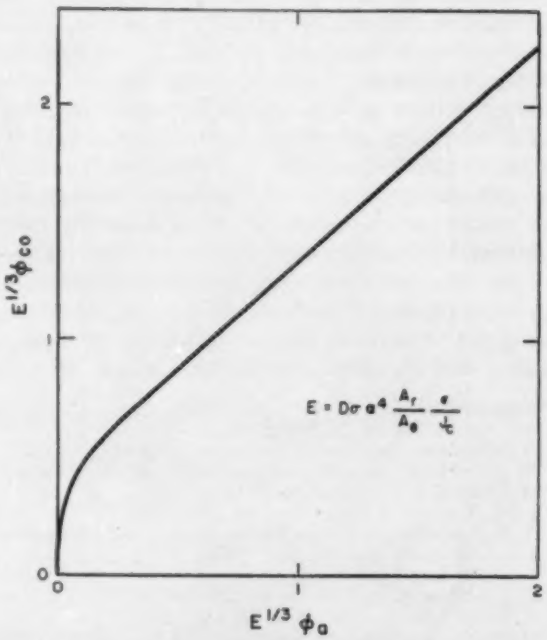

FIG. 3. Relation between anode work function ϕ_a and cathode work function ϕ_c for maximum conversion efficiency.

[11] G. N. Hatsopoulos, Ph.D. thesis, Massachusetts Institute of Technology (1956).

† The optimum values given by Houston (see reference 4) are not strictly correct. His otherwise logical description of the optimization may be corrected by replacing η in his Eqs. (12) through (15) by $\eta/(1-\eta)$

TABLE I. Performance summary for thermionic conversion.

	Performance for arbitrary anode and cathode	Performance for arbitrary anode, and optimum cathode	From Eq.
Given anode work function	ϕ_a	ϕ_a	
Cathode work function	ϕ_c (given)	For $\eta>1\%$ $\phi_{c0}=0.92\phi_a+0.41/E^{\frac{1}{3}}$	(13)
Optimum anode temperature	$T_{a0}=\alpha\phi_a$	$T_{a0}=\alpha\phi_a$	(6)
Required cathode temperature	$T_c=\alpha\phi_c$	$T_{c0}=\alpha\phi_{c0}$	(6)
Maximum efficiency	$\eta_0=\beta\dfrac{1-\phi_a/\phi_c}{1+E\phi_c^3[1-(\phi_a/\phi_c)^4]}$	$\eta_{\max}=\dfrac{\beta}{1+4E\phi_{c0}^3}$	(10) and (14)
where with $E\geqq 0.9(A_r\epsilon/A_eJ_e)(\text{ev})^{-3}$ for J_e in amp/cm²			(11)
	$\alpha\simeq 640°\text{K/v}$		(7)
	$\beta\simeq 0.8$		(8)

that miscellaneous heat losses (P_m) may be neglected, and using the approximations discussed in the preceding paragraph, Eq. (5) gives for the optimized efficiency

$$\eta_0=\eta_t\frac{\beta}{1+D(P_r/J_c\phi_c)}, \tag{8}$$

where $\eta_t=1-T_a/T_c=1-\phi_a/\phi_c=$maximum thermodynamic (Carnot) efficiency, $D=1/(1+2k\alpha/e)$, and $\beta/D=1-[2LD\alpha^2(1+T_a/T_c)/(1+DP_r/J_c\phi_c)]^{\frac{1}{2}}$. The parameters D and β/D are very insensitive to all variables (e.g., $0.82<\beta/D<1$), a value of ~ 0.9 being typical for both.

Finally, the radiative heat transfer term is given by

$$P_r=\frac{A_r}{A_e}\sigma\epsilon(T_c^4-T_a^4), \tag{9}$$

where A_r is the effective area for heat radiation from the cathode, ϵ is the effective emissivity of the cathode-anode system, and σ is the Stephen-Boltzmann radiation constant. Using Eqs. (6) and (9), Eq. (8) becomes

$$\eta_0=\beta\frac{1-\phi_a/\phi_c}{1+E\phi_c^3[1-(\phi_a/\phi_c)^4]}, \tag{10}$$

where

$$E=D\sigma\alpha^4\frac{A_r\epsilon}{A_eJ_c}. \tag{11}$$

Equations (10) and (11) yield the efficiency for arbitrary values of ϕ_c and ϕ_a. However, for a given value of ϕ_a, it may be seen from Eq. (10) that an optimum value of ϕ_c exists at which η_0 is a maximum. Physically, this maximum occurs when the gain in Carnot efficiency with increasing cathode temperature (increasing ϕ_c) is compensated by the rapid onset of radiation losses. Specifically, this maximum occurs when

$$3[\phi_{c0}/\phi_a-4/3]+(\phi_a/\phi_{c0})^3\equiv\frac{1}{E\phi_{c0}^3}, \tag{12}$$

where ϕ_{c0} is the optimum cathode work function defined by this equation. Equation (12) is plotted in Fig. 3, and can be represented to a good approximation by

$$\phi_{c0}=0.92\phi_a+0.41/E^{\frac{1}{3}} \tag{13}$$

for $0.1<E^{\frac{1}{3}}\phi_a<3$, which covers the entire region of present practical interest. The corresponding maximum value of η_0, which is thus the maximum attainable conversion efficiency, is found to be

$$\eta_{\max}=\frac{\beta}{1+4E\phi_{c0}^3}. \tag{14}$$

III. FUNDAMENTAL PERFORMANCE LIMITATIONS

The results of the foregoing analysis are summarized in Table I.

Thus the problem of developing a highly efficient thermionic converter reduces to: (1) obtaining a surface with the lowest usable work function for the anode; (2) obtaining a surface for the cathode with a work function near the optimum value [given by Eq. (13) or Fig. 2]; (3) constructing and operating these electrodes to give the smallest obtainable value of the parameter E defined in Eq. (11); (4) reducing extraneous heat losses, including use of the optimum lead size given by Eq. (4). The maximum efficiency of the resulting converter is then given by Eq. (14) if the optimum cathode work function is achieved, and by Eq. (10) if it is not.

Item (1) has a twofold critical importance. Firstly, for a low efficiency converter, the maximum obtainable efficiency is about inversely proportional to the cube of

the anode work function [Eqs. (13) and (14)]. Secondly, the temperature at which the cathode must operate for maximum efficiency is roughly proportional to the anode work function [Eqs. (6) and (13)]. The lowest usable work function is that which corresponds [through Eq. (6)] to the system heat sink temperature. Thus work functions as low as ½ ev, corresponding to room temperature as the optimum anode temperature, are of interest for thermionic conversion. Since the lowest work function presently known is greater than 1 ev, and there appears to be no fundamental reason why it cannot be lower, considerably increased efficiencies and substantially lower temperature requirements could result from development of surfaces with lower work functions. Such surfaces must be compatible with the methods of space charge neutralization, however.

Item (2) does not appear too formidable in itself since a variety of materials are available having work functions in the 1 to 5 ev region of interest for a converter cathode. Also, the efficiency maximum is relatively broad in ϕ_c. However, in a practical application, the highest temperature available from the heat source may limit the cathode temperature, and thus its work function, to values smaller than T_{c0} and ϕ_{c0}.

Item (3) permits further discrimination among those electrode materials most closely satisfying items (1) and (2). The material property affording the greatest latitude in the parameter E is the saturation current density J_e obtainable from the cathode surface. The relationship in Eq. (1) tends to obscure the important intuitive fact that this current density is an intrinsic property of a surface once a maximum permissible rate of its vaporization is imposed by a practical application. As is shown in the Appendix, the limitation on J_e is primarily determined for a surface by its ratio of cohesive energy to work function. Although existing data indicate that most known materials are incapable of emitting more than 10 amp/cm² without serious volatization, there is apparently no fundamental reason why surfaces capable of substantially higher emission cannot be developed. As stated previously, in some existing devices J_e is limited principally by interelectrode space charge. The present analysis may be applied, using observed values of J_e, when space charge limitation is small enough to be considered as a perturbation (i.e., when $V_c \cong \phi_c$ and $V_a \cong \phi_a$), and in any case gives the maximum performance obtainable.

Having obtained the largest possible emission current J_e, further reduction in the parameter E is possible by reducing the emissivity ϵ, and the heat-radiating to electron-emitting area ratio A_r/A_e. The latter ratio can in principle be made arbitrarily small in gas filled devices where the electron mean-free-path is sufficiently small to allow the electric field to penetrate small cavities. Using such an approach, "heat-shielded" cathodes have been developed[12] for high power rectifiers and thyratrons with an electron-emitting area more than 100 times the effective heat-radiating area. If this principle could be similarly applied to existing gas-filled converters,[7,9] quite high fractions of Carnot efficiency could be obtained using existing materials.

[12] E. F. Lowry, Electronics **6**, 280 (1933).

TABLE II. Fundamental correspondence of thermoelectric and thermionic converter performance.

	Thermoelectric	Thermionic
Fraction of Carnot efficiency	$0.5\dfrac{1}{1+K_L/K_e}$	$0.8\dfrac{1}{1+0.9(P_r/J_e\phi_c)}$
Usable energy transport	K_e	$J_e\phi_c$
Extraneous energy transport	K_L	P_r
Figure of merit	$\dfrac{TS^2}{\rho K}$	$\dfrac{A_e}{A_r}\dfrac{J_e}{\epsilon\phi_c^3}$

The only noteworthy extraneous heat loss relative to item (4) which has not been treated is that due to gaseous conduction. It is completely absent in the vacuum converter, and affects the efficiency to only a negligible extent in existing gas filled devices. For those cases where it might be important, an analysis similar to that subsequent to Eq. (8) may be carried out including P_m, yielding similar but somewhat more complex results.

Finally, for a thermionic converter operating in the range of practical power density and temperature implied by the typical value $\alpha = 640°\text{K/v}$, the ideal upper limit of efficiency may be seen from Eq. (14) to be $\sim 74\%$ (i.e., for $P_r = T_e = 0$). Of the $\sim 26\%$ intrinsic inefficiency, $\sim 16\%$ arises from cathode lead losses, and $\sim 10\%$ from the kinetic energy transported by the emitted electrons.

IV. INTUITIVE SIGNIFICANCE OF PARAMETERS

From Eqs. (10) and (14) it may be seen that the single dimensionless parameter

$$M = \frac{1}{E\phi_c^3} = \frac{1}{D\sigma\alpha^4}\frac{A_e J_e}{A_r \epsilon \phi_c^3} \tag{15}$$

is a convenient figure of merit for the thermionic converter. Converters having maximum conversion efficiencies greater than 16% are distinguished from those of lower efficiency by a value of M greater or less than unity, repspectively. Indeed for low efficiency converters (i.e., $M \ll 1$), the parameter M is approximately equal to the largest fraction of Carnot efficiency obtainable, and $M/4$ is approximately the maximum over-all efficiency obtainable by optimizing such a converter. Taking $A_e/A_r \simeq 1$ and substituting numerical values for the constants in Eq. (15) (using $\alpha = 640°\text{K/v}$), M is found to be essentially numerically equal to $J_e/\epsilon\phi_c^3$, for J_e in amp/cm² and ϕ_c in ev.

A direct comparison between thermionic and thermoelectric converters may readily be made using the results of the present analysis [Eqs. (8) and (15)] and the

analogous thermoelectric results obtained elsewhere.[5,6] The correspondence is displayed in Table II. K_L, K_e, and K, are the lattice, electronic, and total thermal conductivities, respectively, S the Seebeck coefficient and ρ the electrical resistivity of the thermoelectric material. T is the hot junction temperature.

It should be recognized that in both cases the figure of merit is essentially the electrical power delivered to the load divided by the heat lost from the heat source, for an inefficient converter with its heat sink at absolute zero temperature. Specifically

$$\frac{(TS)^2}{\rho} \Big/ KT \leftrightarrow A_e J_e \phi_e / A_r \sigma \epsilon T_e^4.$$

V. CONCLUSIONS

It has been found that the use of a few generally valid approximations permits the optimum efficiency of thermionic energy conversion to be expressed in simple analytical form. The resulting expressions are similar to those extensively used in thermoelectric conversion technology, and should be correspondingly useful in comparing prospective materials and configurations for thermionic converters. The optimum relationship between the work functions of the electrodes, their required or optimum operating temperatures, and a figure of merit for convenient quantitative comparison of thermionic conversion systems have been defined. Examination of steps toward improving thermionic converter performance reveals no fundamental limitation preventing achievement of conversion efficiencies as high as 74%.

APPENDIX: MAXIMUM ELECTRON EMISSION AS AN INTRINSIC SURFACE PROPERTY

The rate of vaporization of the emitting surface may be represented[13] by

$$q = Q \exp(-eE/kT_e), \tag{16}$$

where q is the flux density of evaporating atoms, E is the cohesive or adsorption energy, in electron potential units, of the emitting surface. Q is dependent on various factors such as temperature and the nature of the evaporating species. These factors do not in general cause Q to vary by more than an order of magnitude for present purposes, so that it may be considered constant compared with the extreme sensitivity of the exponential to its argument.

[13] E. H. Kennard, *Kinetic Theory of Gasses* (McGraw-Hill Book Company, Inc., New York, 1938), pp. 409 and 69.

TABLE III. Effect of E/ϕ_e on emitter vaporization rate.

E/ϕ_e	Evaporation rate (mm/yr)
1.8	1000
2.0	40
2.2	1
2.4	0.04
2.6	0.001

Combining Eqs. (1), (6), and (16) yields

$$J_e \simeq qP \exp\left[\frac{e}{k\alpha}\left(\frac{E}{\phi_e} - 1\right)\right], \tag{17}$$

where P likewise may be considered constant for purposes of the present illustration. Thus, since in any practical application q is limited to some maximum value, J_e is likewise limited to a value determined by q and the surface property E/ϕ_e. Indeed, since J_e is enormously more dependent on the property E/ϕ_e than on q, the suitability of a material as an emitter is primarily determined by this property. The importance of the property E/ϕ_e is illustrated in Table III for a typical value of J_e required for efficient conversion (10 amp/cm² at 1500°K). The value of P used was obtained from observed data for tungsten. It would thus appear that surfaces having $E/\phi_e < 2.0$ are totally unsuitable for use as a converter cathode, while those having $E/\phi_e > 2.4$ would be excellent. Using this criterion on the pure metals whose E/ϕ_e is known, tungsten and tantalum are marginal and the rest are distinctly unsuitable. Dispenser cathodes[14,15] and cathodes using an adsorbed film in equilibrium with its vapor[7] allow substitution of a high adsorption energy for a low cohesive energy, and permit substantially higher values of q. Examples have been found which are suitable for continuous emission of 10 amp/cm². Although little suitable data are available for evaluating the large number of refractory compounds which might be considered for use as a cathode, some of the data which do exist imply spectacular emission capabilities. For instance, the value of E/ϕ_e for zirconium carbide (ZrC), computed from the reported work function[16] (corrected for the temperature dependence of ϕ_e) and thermochemical data, is found to be in the vicinity of 5.

[14] A. W. Hull, Phys. Rev. **56**, 86 (1939).
[15] A. Venema *et al.*, Phillips Tech. Rev. **19**, 177 (1957).
[16] D. L. Goldwater and R. E. Haddad, J. Appl. Phys. **22**, 70 (1951).

JOURNAL OF APPLIED PHYSICS VOLUME 31, NUMBER 1 JANUARY, 1960

Specific Heat of High Purity Iron by a Pulse Heating Method*

D. C. Wallace, P. H. Sidles, and G. C. Danielson
Institute for Atomic Research and Department of Physics, Iowa State University of Science and Technology, Ames, Iowa
(Received June 25, 1959)

A dynamic pulse-heating method has been developed for measuring with an error of less than 2% the specific heats of metal wires from room temperature to 1000°C. The method consists essentially of recording the resistance of the sample wire while it is being heated by a pulse of large current and short time duration; then obtaining the temperature of the wire throughout the pulse with the aid of the measured resistance as a function of temperature; and finally computing the specific heat of the sample from the temperature as a function of time during the pulse, the measured power input to the wire, and the theoretically computed heat loss corrections. Results are given for high-purity iron over the temperature range 25° to 1050°C. Variations of the specific heat near the phase transitions are shown in detail.

I. INTRODUCTION

UNTIL quite recently most specific heat measurements were carried out by method-of-mixtures techniques. Under ideal conditions and when properly applied, these methods are capable of yielding very precise values of specific heat. However, in the case of samples which undergo a change in phase in the temperature range of interest, the complete liberation of the energy associated with the phase change is somewhat in doubt and the application of the method of mixtures in the temperature range above the phase change may be difficult. On the other hand, methods of thermal analysis are capable of yielding detailed information about the specific heat near a phase change and perform equally well above and below the phase change. The present investigation was undertaken to (1) extend the useful temperature range of the dynamic pulse-heating method of thermal analysis; (2) improve the accuracy of this method by refining techniques, instrumentation and heat loss corrections; and (3) evaluate the capability of the method near phase transformations. High purity iron was chosen as the sample material best suited for this evaluation.

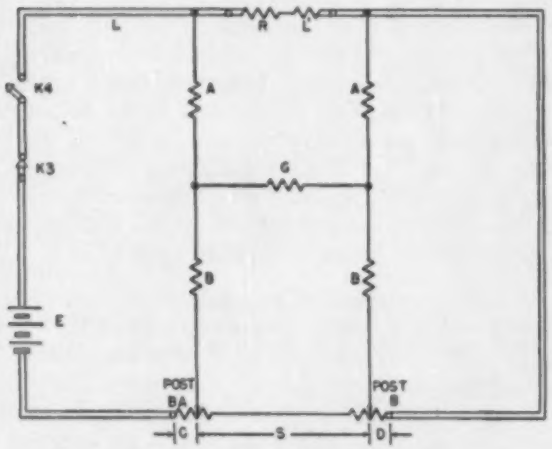

FIG. 1. Kelvin bridge and pulsing battery circuit.

In the dynamic pulse heating method of thermal analysis, continuous curves of such quantities as power input and sample temperature are obtained as a function of time throughout each pulse. The earliest attempt, known to us, to utilize this technique was described in 1939 by Avramescu[1] who measured the specific heat of copper and aluminum from room temperature to their melting points by means of a single pulse. While the data of Avramescu is not in good agreement with the best current values, his work demonstrated the potentiality of the dynamic pulse heating technique. Since 1939 several other investigators[2–6] have discussed dynamic pulse heating techniques for measuring specific heats.

For completeness, it should be pointed out that single point pulse heating methods of thermal analysis have also been investigated.[7–10] In the single point method, a measured quantity of heat ΔQ is delivered to the sample and the resulting temperature rise ΔT is determined. In principle these methods are quite similar to the dynamic pulse heating methods. However, they yield much less data per pulse and they are not suitable for making a detailed study of phase transitions.

This investigation was concerned only with the dynamic pulse heating technique. In contrast to previous investigations, a Kelvin bridge was used to measure the resistance of the sample throughout each pulse, instead

* Contribution No. 759. This work was performed in the Ames Laboratory of the U. S. Atomic Energy Commission. Based in part upon a thesis submitted by Duane C. Wallace to the Graduate School, Iowa State College, in partial fulfillment of the requirements for the degree of Master of Science, 1957.

[1] A. Avramescu, Z. tech. Physik **20**, 213 (1939).
[2] H. W. Baxter, Nature **153**, 316 (1944).
[3] V. I. Khotkovitch and N. K. Bagrov, Doklady Akad. Nauk. S.S.S.R. **81**, 1055 (1951). (English translation in U. S. Atomic Energy Commission Tr-1817, Technical Information Service, Oak Ridge, Tennessee).
[4] A. M. Nathan, J. Appl. Phys. **22**, 234 (1951).
[5] T. E. Pochapsky, Rev. Sci. Instr. **25**, 238 (1954).
[6] Strittmater, Pearson, and Danielson, Iowa Academy of Science **64**, 466–470 (1957). Also see R. C. Strittmater and G. C. Danielson, Iowa State College, Ames Laboratory of the U. S. Atomic Energy Commission Rept. ISC-666, 1955 (unpublished).
[7] E. Lecher, Verhandl. deut. physik. Ges. **9**, 647 (1907).
[8] E. Lapp, Ann. phys. **12**, 442 (1929).
[9] Kurrelmeyer, Mais, and Green, Phys. Rev. **59**, 921 (1941) (A); Rev. Sci. Instr. **14**, 349 (1943).
[10] L. Neel and B. Persoz, Compt. rend. **208**, 642 (1939).

of making separate measurements of current and voltage. Several shorter pulses, instead of one large pulse, were used to cover the temperature range of interest. Errors arising from heat losses by radiation and by conduction from the samples have been accurately taken into account.

II. APPARATUS

(A) Kelvin Bridge

The wire sample was connected into the "unknown" position of a Kelvin bridge and enclosed in a vacuum furnace. This bridge, which formed the heart of the measuring apparatus, was a specially calibrated Leeds and Northrup type 4306. A diagram of the bridge and pulsing battery circuit is given in Fig. 1, where the double lines represent heavy copper leads at places where small resistances were required.[11] The total series lead resistance in the bridge and battery circuit outside of the vacuum system is designated by L; that of the leads inside the vacuum system is designated by L'. A and B are the ratio arms of the bridge and S is the standard resistance. C is the unused portion of the plug box and D is the unused portion of the slide wire. Since the bridge would accommodate unknown resistances only as large as 1.0 ohm, the length and diameter of the sample were chosen such that its resistance would be slightly less than 1.0 ohm at 1000°C.

(B) Sample Holder

In this experiment, the samples were wires with diameters from 0.0254 to 0.0346 cm (10 to 14 mils) and lengths from 4 to 7 cm. The sample holder was designed with two requirements in mind: (1) to support the sample in the vacuum furnace and to allow it to be in thermal equilibrium with the furnace walls, and (2) to conduct the large pulsing current to the sample without appreciable heating of the sample holder leads. These requirements dictated opposite construction practices, as outlined below, and considerable time was spent in developing a sample holder which satisfied both. Essentially, then, the sample holder was a pair of current leads; the construction of one is shown in Fig. 2.

The solid copper rod at the lower end (hot zone) served as a heat sink whose temperature was the same as that of the furnace walls. The current lead was insulated from the nickel tubing at the upper end (room temperature) to prevent circulating electrical currents which would have arisen from thermal emfs. In consideration of the two requirements listed above, it was found that if the current lead wire were too large in cross-section, it would conduct heat away from the sample mounting electrode too fast and the temperature of the electrode would fall below the furnace wall temperature. On the other hand, if the current lead wire were too small, it could not carry the large pulsing current without heating. Brown and Sharpe gauge 10 copper wire was found to be a satisfactory compromise. The copper was protected with nickel tubing or with swaged-on nickel coating in order to prevent evaporation of the copper at the low pressures and high temperatures of the experiment.

Various techniques were used in order to mount the samples, including soldering, clamping, and spot welding. In the solder mounting, the end of the sample wire was placed into a snugly fitting hole drilled through the electrode, along with a small amount of copper-silver eutectic. The sample was then bonded to the electrode by heating in a vacuum furnace. This method was satisfactory for sample materials which did not interdiffuse with the solder at temperatures up to 1000°C. The clamp mounting was accomplished by placing the end of the sample wire into a slit which was cut through the electrode, and then closing this slit around the sample by tightening clamps on the electrode. The clamps were left on the electrodes during the experiment, in order to maintain the pressure contact at all temperatures. This method was satisfactory for sample materials which were harder than the copper electrode. The weld mounting was best accomplished by spot welding the end of the sample wire into a groove in the electrode, thus leading to only a very slight deformation of the wire at the point of its contact with the electrode. In the clamping and welding techniques, the sample wire was separated from the copper electrode with strips of another metal, for example platinum, when a diffusion barrier was needed.

To measure the temperature of the sample, a calibrated platinum to platinum—13% rhodium thermo-

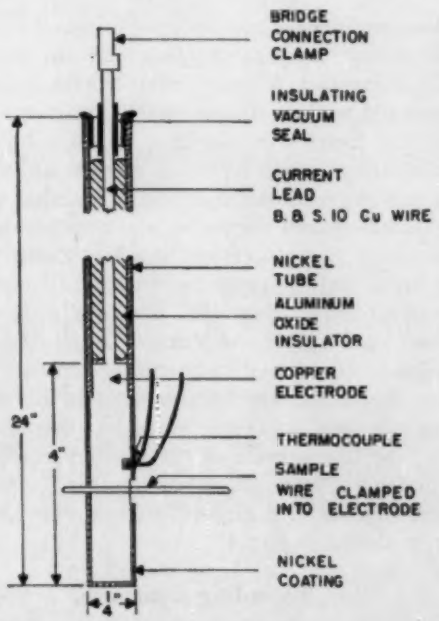

FIG. 2. Construction of a sample holder current lead. (Drawing is not to scale.)

[11] Leeds and Northrup Notebook E-53 (1), *Notes on the Kelvin Bridge* (Leeds and Northrup Company, Philadelphia, 1951).

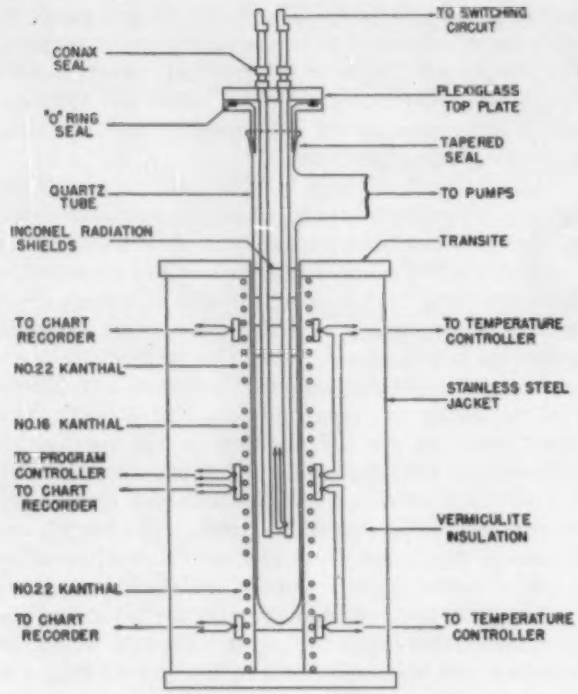

FIG. 3. Vacuum furnace with sample holder.

couple of B. & S. gauge 22 wires was used. The thermocouple bead was either crimped into a hole in the side of one of the electrodes or welded to the surface of the electrode. In the hot zone of the vacuum system, the thermocouple leads were protected with aluminum oxide insulators.

(C) Vacuum Furnace

The vacuum furnace was designed to provide a sample chamber whose temperature was uniform and automatically controlled. A quartz tube 48 mm in diameter was connected to the vacuum system and placed in the furnace. The furnace employed a center winding and two end windings which served as guards. Around each winding was placed an annular ring of stainless steel, to which chromel-alumel thermocouples were welded. The temperature of the center winding was controlled according to a preset program with a Minneapolis-Honeywell program controller. The top winding was maintained at the same temperature as the center with a Minneapolis-Honeywell temperature controller, activated by the differential output from a top winding thermocouple and a center winding thermocouple. Similarly, the temperature of the bottom winding was maintained at the same level with another temperature controller. The vacuum furnace, with sample holder in position, is shown in Fig. 3.

(D) Recording Apparatus

A block diagram of the recording apparatus is shown in Fig. 4. A switching circuit was constructed to route

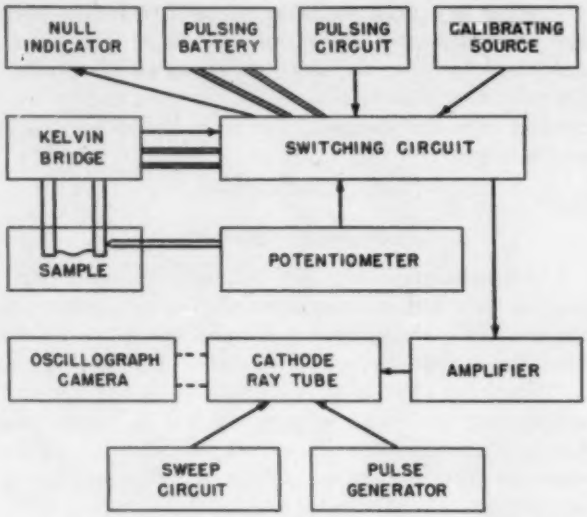

FIG. 4. Block diagram of specific heat apparatus.

signals properly for each of the four operations listed below:

(a) The emf of the sample thermocouple was measured with a Rubicon type B potentiometer with the aid of a Doelcam null indicator (model 2HG-1).

(b) The sample resistance was measured with the Kelvin bridge, the same null indicator, and a small amount of current from the pulsing battery.

(c) The sample was pulsed with a large current from the pulsing battery to obtain the specific heat measurement. During a pulse, all power to the furnace was turned off in order to eliminate ac pickup by the sample and the leads. The pulsing cycle consisted of operating the mercury relays K3 and K4 (Ebert HD1 and HD2, respectively) in such a way as to connect the pulsing battery to the bridge for about 40 milliseconds (see Fig. 1). The pulsing battery was made up of three 6-v lead storage cells in parallel. The galvanometer posts on the bridge were connected to the oscilloscope input, and the trace displayed the bridge unbalance voltage. During the sweep, time markers in the form of short negative pulses from an Electropulse generator (model 2120A) were applied to the cathode of the cathode-ray tube. The trace then appeared as a series of dots; the frequency of these dots was measured with a Beckman frequency meter (model 5571).

The oscilloscope itself was made up of the following components: a dc amplifier with a gain of 25 000 (Electronic Tube Corporation model EDA-M1), a specially constructed sweep circuit, and a cathode-ray indicator with 8 kv accelerating potential and very small spot size (slightly modified Dumont type 281-A).

(d) The oscilloscope was calibrated over the central 2.5 in. of the tube face with about 20 calibration lines. The necessary calibration voltages were obtained from a mercury battery and a Kelvin-Varley resistance net-

work. The oscilloscope traces were recorded with a Dumont oscilloscope camera (type 302) using type 44 Polaroid-Land film, with a speed rating of ASA 400.

III. THEORY

(A) Unbalanced Kelvin Bridge Calculation

The circuit of the Kelvin bridge and pulsing battery is shown in Fig. 1. From this diagram, four independent Kirchoff's Law equations can be written. In the present experiment, $(A+B)=1100$ ohms, $G=200\,000$ ohms, $(C+D+S)=0.1000$ ohm, and $(C+D+S+L)$ has a measured value of 0.1267 ohm. Therefore, S can be neglected compared to $(G+2B)$ and $(C+L)$ and D can each be neglected compared to $(A+B)$. With the aid of these approximations, the following two bridge equations are obtained:

$$R+L'=\frac{AESG+(C+D+S+L)[G(A+B)+2AB]E'}{BEG-[G(A+B)+2AB]E'}, \quad (1)$$

$$I=\frac{E}{(R+L')+(C+D+S+L)}, \quad (2)$$

where E=pulsing battery voltage, E'=voltage appearing across G, G=amplifier input resistance, R=sample resistance, S=standard resistance, L, L' are lead resistances, and I=current passing through the sample wire.

(B) Heat Loss Calculations

In the present experiment, the time rate of heat loss from the sample never totals more than 5% of the power input. Therefore, approximations are allowable in the calculation of these losses. The following three mechanisms are responsible for the heat losses.

(a) Heat is conducted through the ends of the wire into the electrodes. The heat flow equation for a wire heated by an electric current is[12]:

$$cda\frac{\partial\theta}{\partial t}=\frac{I^2R}{Jl}+Ka\frac{\partial^2\theta}{\partial x^2}-\sigma es(\theta^4-\theta_0^4), \quad (3)$$

where c=specific heat (cal/gm°C), d=density (gm/cm³), a=cross-sectional area of the wire (cm²), θ=temperature of the wire (°K), θ_0=temperature of the walls of the system (°K), t=time (sec), x=distance along the wire (cm) ($x=0$, l at the ends), I=current passing through the wire (amps), R=resistance of the wire (ohms), J=Joule's constant (taken to be 4.185 joules/cal), K=thermal conductivity (cal/sec cm°C), σ=Stefan-Boltzmann constant (taken to be 1.35×10^{-12} cal/cm² sec °K⁴), e=emissivity, and s=circumference of the wire. The boundary conditions are

$$\theta=\theta_0 \text{ at } x=0,l \text{ for all } t, \quad (4)$$

$$\theta=\theta_0 \text{ at } t=0 \text{ for all } x. \quad (5)$$

In this experiment, the following three approximations can be made:

(i) The power input I^2R is measured throughout each pulse, and is found to be nearly linear with time. Therefore, I^2R may be replaced by $u-wt$, where u and w are constants which are determined for each pulse.

(ii) $(\theta-\theta_0)$ is also found to be nearly linear with time and therefore may be replaced by ht where h is a constant which is determined for each pulse. [If one takes R to be linear with $(\theta-\theta_0)$, then (i) and (ii) are related through constants of the circuit.]

(iii) For $(\theta-\theta_0)$ small compared to θ_0, $(\theta^4-\theta_0^4)$ may be replaced by $4\theta_0^3(\theta-\theta_0)$.

With the aid of these three approximations and a change of variables,

$$T=(t/cd) \text{ and } y=(x/\sqrt{K}),$$

Eq. (3) becomes

$$\frac{\partial\theta}{\partial T}-\frac{\partial^2\theta}{\partial y^2}=M-NT, \quad (6)$$

where $M=u/Jal$ and

$$N=cd\left[\frac{w}{Jal}+\frac{4\sigma es\theta_0^3h}{a}\right].$$

The solution of Eq. (6) which satisfies the boundary conditions (4) and (5) is[13]

$$\theta=\Sigma_nC_n\sin\frac{n\pi y}{Y}, \; n=1, 2, 3, \cdots, \quad (7)$$

where $Y=y(l)$, and the Fourier coefficients are given by

$$C_n=\frac{4}{n\pi}\left(\frac{Y^2}{n^2\pi^2}\right)\left\{\left(1-\exp-\frac{n^2\pi^2T}{Y^2}\right)\left(M+\frac{NY^2}{n^2\pi^2}\right)-NT\right\}, \quad (8)$$

for odd n and $C_n=0$ for even n.

The rate at which heat is lost by conduction through both ends of the wire can be calculated at any time during a pulse by the following formula:

$$\frac{dQ}{dt}(\text{cond})=-2Ka\left(\frac{\partial\theta}{\partial x}\right)_{x=0} \text{ cal/sec}. \quad (9)$$

[12] See for example H. S. Carslaw and J. C. Jaeger, *Conduction of Heat in Solids* (Oxford University Press, London, England, 1947), Sec. 55.

[13] For more details on these calculations, see D. C. Wallace, M. S. thesis, Iowa State College, 1957 (unpublished).

By Eq. (7), we have

$$\left(\frac{\partial\theta}{\partial x}\right)_{x=0}=\frac{\pi}{l}\Sigma_n nC_n. \tag{10}$$

(b) Heat is lost from the sample by radiation from the surface of the wire. The rate at which heat is lost by this mechanism can be calculated at any temperature by the following formula:

$$\frac{dQ}{dt}(\text{rad})=-\sigma\epsilon sl(\theta^4-\theta_0^4)\ \text{cal/sec}. \tag{11}$$

(c) Heat may be lost from the wire by conduction through the surrounding gas. According to Dushman,[14] the energy transfer between a wire and the surrounding gas at low pressure is

$$\frac{dQ}{dt}(\text{gas})=\alpha\Delta_0 P\left(\frac{273.2}{\theta_0}\right)^{\frac{1}{2}}(\theta-\theta_0), \tag{12}$$

where α=an accommodation coefficient, Δ_0=the free molecular heat conductivity of the gas at 0°C (cal/sec cm² °K micron), P=pressure (microns), θ=temperature of the wire (°K), and θ_0=temperature of the walls of the system (°K).

Using the value of Δ_0 for nitrogen given by Dushman,[15] letting $\alpha=1$ and $P=0.01\ \mu$, and using temperatures which are representative of this experiment, we obtain from Eq. (12)

$$\frac{dQ}{dt}(\text{gas})<1\times10^{-5}\ \text{cal/sec cm}^2.$$

For sample wires used in this experiment, this loss term is less than $10^{-4}\%$ of the power input and so it is concluded that heat losses from this source are negligible.

(C) Specific Heat Calculation

For a thermodynamic system which is exchanging energy with its surroundings, the specific heat at constant pressure, denoted by C_p, may be written as

$$C_p=\frac{dQ}{d\theta}=\frac{(dQ/dt)(\text{in})-(dQ/dt)(\text{out})}{(d\theta/dt)}, \tag{13}$$

where dQ/dt (in) is the time rate at which energy is being supplied to the system, dQ/dt (out) is the time rate at which energy is lost from the system, and $d\theta/dt$ is the time rate of change of the temperature. For a wire of resistance R which is being heated by an electric current I, the rate at which energy is supplied is just the power I^2R. The rate at which energy is lost from the wire was calculated in the preceding section.

[14] S. Dushman, *Vacuum Technique* (John Wiley & Sons, Inc., New York, 1949), p. 52.
[15] See reference 14, p. 53.

Since the measurements in this experiment were made at constant pressure, the specific heat per gram of the material under investigation was obtained from the following formula:

$$C_p=\frac{1}{m(d\theta/dt)}\left[\frac{I^2R}{J}-\frac{dQ}{dt}(\text{cond})-\frac{dQ}{dt}(\text{rad})\right], \tag{14}$$

where m is the mass of the sample wire in grams, and where the heat loss from the sample by conduction into the surrounding gas has been neglected.

IV. PROCEDURE

(A) Data Collection

A length of wire sample was mounted in a sample holder and annealed at the highest temperature for which measurements were to be made (usually 1000°C) for 1 hr or more. Measurements were then made while the furnace was cooled to room temperature at a rate of about 40°C per hour. With many of the samples, measurements were also made while the furnace was reheated to 1000°C at the same rate of 40°C per hour; in such cases the data were accurately reproduced. The pressure did not rise above 1×10^{-5} mm of mercury throughout the experiment.

The resistance and temperature of the sample were determined at 3 to 5°C intervals, except near transition temperatures, where they were determined at 0.5°C intervals or less. The procedure for doing this was as follows. The emf of the sample thermocouple was first measured by balancing the potentiometer. The time when the potentiometer balance was reached, measured to the nearest second, was recorded along with the emf of the thermocouple. Next, the resistance of the sample plus sample holder leads, $R+L'$, was measured by balancing the Kelvin bridge. Also, the time when the bridge balance was reached, measured to the nearest second, was recorded. Finally, the temperature of the sample was again measured and recorded, along with the time when the potentiometer balance was reached. This set of measurements usually took about 30 sec; during this time the furnace temperature changed only about 0.3°C. A linear timewise interpolation then gave the temperature at the time when the Kelvin bridge was balanced.

At intervals of approximately 50°C, the sample was pulsed in order to collect specific heat data over a temperature range of about 100°C. Before each pulse, the emf of the pulsing battery and the emf of the calibration battery were measured with the potentiometer. The frequency of the time markers was also measured and recorded just before each pulse. The Kelvin bridge was then brought to balance, the camera shutter opened, and the pulsing cycle initiated. The oscillograph was then calibrated with about 20 lines of equally spaced voltage, covering the central 2.5 in. of the cathode-ray tube face. The camera was so constructed that the cathode-ray tube face could be viewed throughout the

exposure. The film was developed immediately after each exposure.

When the entire run was finished, the sample holder was removed from the vacuum system and the sample wire was observed under a microscope and cut off at each electrode. The sample was then weighed with a microbalance and the length of the wire was measured with a traveling microscope. The total resistance $(C+D+S+L)$, as shown in Fig. 1, was measured with a calibrated Leeds and Northrup precision Kelvin bridge. For each sample holder, the resistance L' was measured up to 1000°C furnace temperature with the sample holder in position and the sample electrodes shorted together.

Three auxiliary experiments were carried out to verify the accuracy of certain parts of the calculations.

(a) The internal resistance of the pulsing battery was about 0.001 ohm. Since, during a pulse, the current through this battery did not change by more than 10 amp, the voltage of the battery was assumed to be constant throughout each pulse. The validity of this assumption was verified by recording the voltage of the battery on the oscilloscope during many trial pulses.

(b) The resistance $R+L'$ was calculated at any time during a pulse by means of the unbalanced Kelvin bridge equation [Eq. (1)]. The specific heat recording apparatus was used to measure known resistances with the specific heat bridge purposely unbalanced. Some 15 resistances ranging from 0.001 to 1.00 ohms were measured this way, with three or four different "unbalances" for each one, and the accuracies were all well within 0.1%.

(c) It was assumed that, during a pulse, the sample holder current leads did not heat appreciably. The validity of this assumption was tested by pulsing the sample holder with the sample electrodes shorted together. Since no unbalance voltages were detected during such pulses, it was concluded that no heating took place.

(B) Data Analysis

At each measurement of temperature and resistance, the directly measured resistance was $(R+L')$. The sample resistance R was then determined at each temperature with the help of the measured L' *versus* temperature data. A graph of sample resistance as a function of temperature was prepared for use in the specific heat determination.

A reproduction of a typical film recording of pulse data is shown in Fig. 5. The positions of the lines and dots on each film were measured with a Gaertner traveling microscope, and a voltage E' was assigned to each dot by means of a linear interpolation between the calibration lines on either side of it. R was then calculated for each dot by means of Eq. (1) and the measured L'. A temperature θ was assigned to the sample at the time of each dot by reference to the R *versus* θ curve. The next step was to plot a curve of sample temperature

FIG. 5. Reproduction of an oscillograph film. The oscilloscope sweep is from right to left. The horizontal lines are voltage calibration lines, the bottom line corresponding to zero voltage. The series of dots is the trace made when the sample was pulsed. Each dot is a measure of the bridge unbalance voltage and of the time during the pulse. The temperature of the sample above the temperature of the furnace corresponds approximately to the voltage of each dot.

against dot number for each pulse. Since the time between dots was constant and known for each pulse, each curve was essentially a curve of temperature *versus* time. The slope of each curve was obtained at each point (dot), usually by means of a straight edge. The power delivered to the sample, I^2R, was also calculated at each point. The heat losses from the sample were calculated according to Eqs. (9) and (11). For iron samples, which are reported in this paper, values of the emissivity[16] and of thermal conductivity[17] were taken from tabulated results, and the diffusivity was obtained from the results of measurements currently being carried out at this laboratory.[18] It is shown in Sec. VI that considerable inaccuracies in the values of these quantities have a relatively small influence on the specific heat results.

The specific heat calculations outlined above were generally carried out with the aid of an IBM 650 computer and a program which was prepared in the Bell Laboratory interpretive system.[19] In this case, the slopes were obtained by a difference method. However, for many pulses, especially those which heated the sample through a phase transition, the data were graphically analyzed as outlined above.

The experimental values of the specific heat were finally plotted as a function of temperature and a smooth curve was graphically fitted to the experimental points.

V. RESULTS

Measurements have been made on platinum, nickel, iron, thorium, and uranium. In order to permit a critical evaluation of the experiment, data are presented here for high-purity iron. In the process of developing the experimental technique, six samples of iron were meas-

[16] C. J. Smithells, *Metals Reference Book* (Butterworth's Scientific Publications, Ltd., London, England, 1949), p. 470.
[17] R. W. Powell, Proc. Phys. Soc. (London) **51**, 407 (1939).
[18] P. H. Sidles, Iowa State College (private communcation). For the method of measurement of the thermal diffusivity, see P. H. Sidles and G. C. Danielson, J. Appl. Phys. **25**, 58 (1954).
[19] IBM Tech. Newsletter No. 11, International Business Machines Corporation, New York, New York (1956).

ured with the aid of four separate sample holders and calibrated thermocouples; the data below, however, are largely representative of two samples for which the best techniques had been obtained.

The iron wire was obtained from Johnson, Matthey and Company, Ltd. A report on the spectrographically standardized iron rods from which the wire was produced listed the following estimates of impurities:

(a) Principal impurities:

Carbon	0.03%
Oxygen	0.01%
Nitrogen	0.01%.

(b) Other foreign elements:

Copper	0.0001%
Nickel	<0.0005%
Sodium	<0.0001%
Silver	<0.0001%
Magnesium	<0.0001%
Silicon	<0.0001%.

Table I lists values of the apparent resistivity and specific heat of iron from room temperature to 1050°C. The apparent resistivity is the resistivity computed from the resistance at a given temperature and the room temperature dimensions. From the thermocouple calibrations[20] and from a consideration of the temperature uniformity of the sample wire, the limits of error on the sample temperatures of Table I are placed at ±1°C. The resistivity data of Table I are accurate to 0.5%. However, most of this error is attributed to the measurements of the cross-sectional areas of the wires. If the resistivity data are interpreted as resistance as a function of temperature, they are accurate to 0.1%.

TABLE I. Electrical resistivity and specific heat of high purity iron.

Temperature (°C)	Resistivity (μohm cm)	Specific heat (cal/g°C)	Temperature (°C)	Resistivity (μohm cm)	Specific heat (cal/g°C)
25	10.37	0.104_5	730	91.71	0.238
50	11.86	0.108	750	96.03	0.265
100	14.69	0.114_5	760	98.57	0.291
150	18.08	0.120	763	99.41[a]	...
200	21.89	0.125	765	...	0.321
250	26.20	0.130	769	...	0.385[b]
300	30.97	0.135	770	100.84	0.213
350	36.18	0.139_5	780	102.23	0.199
400	41.82	0.144_5	800	104.33	0.187
450	47.87	0.150_5	850	108.10	0.173
500	54.39	0.157	900	110.78	0.166
550	61.39	0.164_5	900	...	0.143_5
600	68.87	0.174_5	950	112.79	0.145_5
650	76.96	0.189	1000	114.49	0.147_5
700	85.85	0.213	1050	116.04[c]	0.150

[a] Point of inflection in resistance *versus* temperature curve.
[b] Peak in specific heat *versus* temperature curve (Curie temperature).
[c] Resistivity extrapolated from 1012°C.

[20] All thermocouples were calibrated by the National Bureau of Standards. The uncertainties in these calibrations were not more than 0.5° in the range 0° to 1100°C.

It has been previously observed[21] that the resistance of an iron wire increased when the wire was cooled through the $\alpha-\gamma$ phase transition, but that no change took place when it was heated through this transition. This effect was studied in the present investigation and was attributed to an irreversible change in the dimensions of the wire. From 21 cycles of heating and cooling through this transition for six iron samples and for various heating and cooling rates, it was found that on cooling the average change in resistance divided by the resistance, $\Delta R/R$, was 0.6%, with rms deviation 0.2%; and that on heating, $\Delta R/R$ was too small to measure (<0.02%). For slow cooling (0.5°C per minute), this resistance increase occurred over a 2°C temperature interval centered at 900°C; this was taken as the temperature of the phase transition upon cooling. This discontinuity is not included in the resistivity data of Table I.

For one sample, the area was measured before and after the wire had been cycled through the transition 10 times. The average change in area divided by the original area, $\Delta a/a$, was found to be $-0.34\pm0.08\%$ per cycle. In order to discuss this change from the point of view of a simple model, consider a wire of cross-sectional area a, length l, and resistance R at some temperature T below the $\alpha-\gamma$ transformation temperature. Assume that after heating to the γ phase and then returning to temperature T, the transformation back to the α-phase is complete and the resistivity, mass, and density of the sample are unchanged. Under these conditions, the expected relative change in area is given by[22] $\Delta a/a=-\frac{1}{2}\Delta R/R$, or about -0.3%. This is in agreement with the measured $\Delta a/a$.

Such a change in the dimensions of the iron wire may be due to preferred orientation of crystallites since the wire was prepared by drawing through dies. Similar dimensional changes in uranium have been attributed to preferred orientation.[23]

Various observations are not in agreement as to the resistance changes at the $\alpha-\gamma$ transition in iron. For example, Shimura, Eichen, and Spretnak[24] have reported that the resistance is unchanged on cooling but increases by about 1.3% on heating. These authors also give a brief summary of dilatometric and resistance measurements by various investigators at this transition.

The accuracy of the specific heat data of Table I is placed at 2%, except within about two degrees of the Curie temperature, where the accuracy is still believed to be within 4%. Heating rates for the sample were of the order of 10^3 to 10^4°C/sec for this experiment; variation of the heating rates by a factor of two or three at

[21] See reference 13, p. 40.
[22] Since the resistivity is given by $\rho=Ra/l$ and the volume by $V=al$, then $d\rho=dR(a/l)+R(da/l)-R(a/l^2)dl=0$, and $dV=adl+ldl=0$. These equations give at once the result $dl/l=-da/a=\frac{1}{2}(dR/R)$.
[23] H. H. Chiswik, Trans. Am. Soc. Metals 49, 822 (1957).
[24] Shimura, Eichen, and Spretnak, WADC Tech. Rept. 57-738 (1958) (unpublished).

any given temperature did not measurably affect the specific heat results. The position of the peak in the specific heat curve indicated a Curie temperature of 769°C, which is in good agreement with the results of other thermal analysis methods for high-purity iron.[25]

A temperature hysteresis effect was noted when the sample was pulse-heated through the $\alpha-\gamma$ phase transition. The heating rates just below the transition ranged from 2×10^3 to 3×10^3°C/sec and the temperature of the transition, taken as the temperature at which the specific heat became infinite, ranged from about 920 to 930°C (eight such pulses were taken). For this range of heating rates, the transition temperature was found to increase nearly linearly with heating rate. A somewhat smaller hysteresis effect (8–10°C) has been reported by

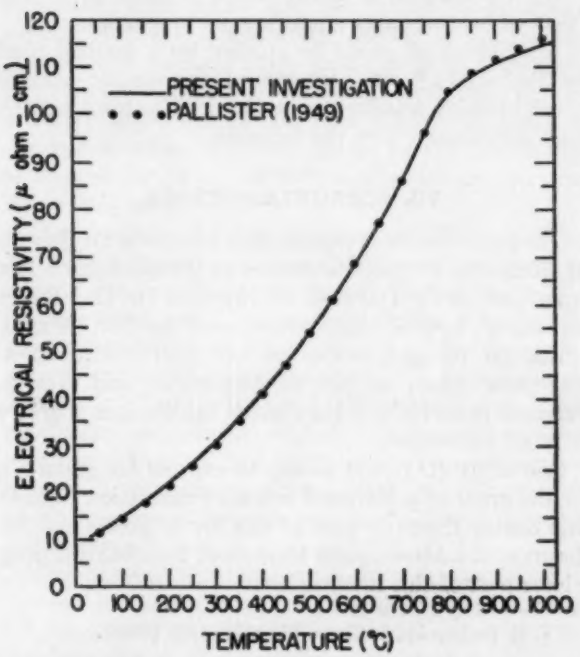

FIG. 6. Resistivity as a function of temperature for high-purity iron. The curve has an inflection point at 763°C. The dots show the values measured by Pallister.[28]

other investigators[26] who used much slower heating rates.

The latent heat of the $\alpha-\gamma$ transformation was calculated to be 3.9 ± 0.4 cal/g in the temperature range from 920 to 930°C. This result is in good agreement with tabulated values.[27]

Figure 6 shows a plot of the resistivity data given in

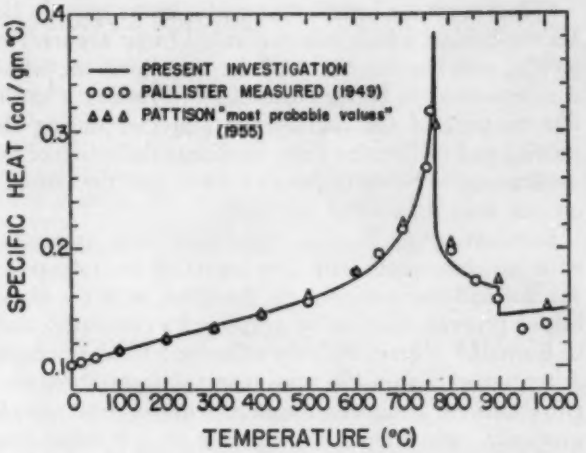

FIG. 7. Specific heat as a function of temperature for high-purity iron. The curve has a very high and narrow peak at 769°C (the Curie temperature), and is discontinuous at 900°C (the $\alpha-\gamma$ phase transition temperature). The circles show the values measured by Pallister[28] and the triangles show the values given as most probable by Pattison.[30]

Table I together with Pallister's[28] recent data on high purity iron. The reader is referred to Cleaves and Thompson[29] for a summary of earlier measurements of the resistivity of iron. Figure 7 shows a plot of the specific heat data given in Table I, together with the measured values reported by Pallister[28] and the "most probable" values reported by Pattison.[30]

VI. DISCUSSION

The major systematic errors in the experiment arose from the following sources.

(a) For the resistivity measurement, the major difficulty was the determination of the cross-sectional areas of the sample wires. These areas were therefore calculated from measured masses, lengths, and an assumed density of 7.867 g/cm³.[31] The diameters were measured with a micrometer, and the areas thus obtained generally agreed with the calculated areas within 0.5%.

(b) The possible error in cutting a sample wire from the electrode at each end was estimated to be not more than 0.005 cm, and the balance error in weighing the sample was not more than 0.002 mg. Hence, the mass of a sample was generally determined within 0.25%.

(c) The corrections for heat losses from the sample due to conduction through the wire ends were never greater than 4% of the power input, and the corrections for heat losses from the sample due to radiation were never greater than 0.5% of the power input. It was estimated that these correction terms were accurate to at least 10%; hence, the error introduced into the specific heat calculation was not more than 0.45%.

[25] H. E. Cleaves and J. C. Thompson, *The Metal Iron* (McGraw-Hill Book Company, Inc., New York, 1935), Chap. 5.
[26] B. A. Rogers and K. O. Stamm, Trans. Am. Inst. Mining and Met. Engr. **150**, 131 (1942). See also reference 25, p. 105.
[27] The value 3.93 cal/g has been reported by H. Esser and E. F. Baerlecken, Arch. Eisenhüttenw. **14**, 617 (1941). The value 3.9 cal/g has been reported by J. H. Awberry and E. Griffiths, Proc. Roy. Society (London) **A174**, 1 (1940). The results of earlier work are summarized in reference 25, p. 148.
[28] P. R. Pallister, J. Iron and Steel Inst. **161**, 87 (1949).
[29] See reference 25, p. 188.
[30] J. R. Pattison, J. Iron and Steel Inst. **180**, 359 (1955).
[31] See Reference 25, p. 274.

Other sources of small systematic errors were in the Kelvin bridge, which was calibrated to an accuracy of 0.01%, and the frequency of the time markers, which was measured to better than 0.01%. Systematic errors due to drift of the oscilloscope amplifier during the pulsing and calibrating time, nonlinear deflection of the oscilloscope between calibration lines, and the potentiometer were considered negligible.

Random errors in this experiment were associated with measurements with the traveling microscope of the dot and line positions on the films; with the slope-taking process, whether by graph or by computer; and, to a smaller degree, with the other graphical processes. A scatter of about 1% was expected from these contributions. A complete measurement for one sample generally gave 500 or more points on a specific heat *versus* temperature curve; the rms deviation of these points from the smooth curve drawn through them was generally 1% or less, as expected.

From Fig. 7 it can be seen that the specific heat at the Curie temperature was found to reach a very high and narrow peak. The accurate determination of the shape of this peak exemplifies an important advantage of the present method of measuring specific heats, namely, that the behavior of the sample, while it is being heated, is observed at intervals of time which may be made as small as desired. More exact information is obtained, therefore, regarding the variation of specific heat with temperature at a given temperature.

The measurements above the Curie temperature, and also those above 900°C, exemplify a second important characteristic of the present method, namely that, if the sample undergoes phase transitions at various temperatures, the sample can be studied at an equilibrium ambient temperature just above or just below any transition. To measure the specific heat just above a transition temperature, for example, it is not necessary to cool the sample through the transition. Such a cooling through the transition could produce strains in the lattice which would not anneal out at a lower temperature and would, therefore, affect the heat content.

Another advantage of the present method is that measurements can be carried out with only a very small amount of the test material.

The present experimental technique also offers the following interesting possibilities for further investigations.

(a) Since there appears to be very little loss of accuracy up to 1000°C, the temperature range of the experiment could probably be successfully extended to very high temperatures.

(b) Very accurate values for latent heats of transition should be obtainable by this method if slower heating rates are used.

(c) The method is ideally suited to the study of the effect of heating rates upon thermal properties.

(d) Nonmetals could be studied by a method used by Pochapsky,[32] who determined the specific heat of silver bromide relative to platinum by pulsing a platinum wire coated with the bromide.

VII. ACKNOWLEDGMENTS

The authors wish to express their thanks to Dr. Joseph M. Keller for helpful discussions on the conduction loss equations; to Dr. David G. Worden and Dr. Dan Redin for many helpful discussions; and to Mr. Wayne Rhinehart for suggestions on the electronic circuits. The perseverance of Mrs. D. Strandburg and Mrs. S. Peterson in carrying out the many calculations is gratefully acknowledged.

One of us (D.C.W.) wishes to express his gratitude for the grant of a National Science Foundation Fellowship during the early part of this investigation and for the grant of a Minneapolis-Honeywell Fellowship during a later part of this investigation.

[32] T. E. Pochapsky, J. Chem. Phys. 21, 1539 (1953).

Angular Distribution of Sputtered Material*

G. K. Wehner and D. Rosenberg
Mechanical Division of General Mills, Incorporated, Minneapolis, Minnesota
(Received July 20, 1959)

The angular distribution of material sputtered under normal Hg^+-ion incidence from flat, polycrystalline targets at 100 to 1000 ev was measured and plotted in polar diagrams. The distribution is "under cosine," approaching a cosine distribution, at higher ion energies. Mo and Fe show a more pronounced tendency to eject to the sides than Ni or Pt. Under oblique ion incidence atoms are sputtered preferentially in the forward direction.

INTRODUCTION

In 1935 Seeliger and Sommermeyer[1] found that sputtered atoms are ejected in accordance with Knudsen's cosine law, independently of the angle of ion incidence. This result was considered to be strong support for the evaporation theory of sputtering.[2] Seeliger and Sommermeyer made their measurements in the region of 10 kev ion energy and they pointed out that conditions may be quite different at lower ion energy. However, a determination of the distribution of ejected atoms at lower impinging ion energies has never been made.

In the region of lower ion energies (100 to 1000 ev) Wehner[3] obtained evidence that atoms sputtered at oblique ion incidence are ejected preferentially in a forward direction. Furthermore, it was found[4,5] that atoms sputtered from single crystals are ejected preferentially in the directions of their closest packing in the lattice, i.e., [110] in fcc and [111] in bcc metals. These results furnished strong evidence to support a momentum transfer or "billiard ball" model theory of sputtering and it seemed very likely that deviations from the cosine law should occur as well in the case of polycrystalline targets.

The angular distribution of material sputtered at various ion energies from flat polycrystalline metal targets should be of interest not only with respect to the formulation of a sputtering theory but also with respect to many other related problems in the field of sputtering. A knowledge of the angular distribution is necessary, for instance, in sputtering yield measurements whenever the amount of sputtered material is determined by means of a collector or a detector for sputtered atoms. It is also necessary in the study of the forces which arise at an electrode due to the ejection of sputtered atoms. In practical sputtering applications, knowledge of the angular distribution may help in designing the optimal electrode arrangement for controlled production of thin films such as in achieving deposits of high uniformity.

EXPERIMENTAL PROCEDURES AND RESULTS

All measurements reported here were made under normally incident Hg^+-ion bombardment in a demountable tube which has been described previously[6] in connection with our sputtering yield studies. A low pressure (~1 micron) mercury discharge (3 amp) between a pool-type cathode and an anode (voltage drop: ~30 volts) furnishes a dense low pressure plasma of essentially singly ionized Hg^+ ions. The target is immersed in this plasma and behaves like a large negative Langmuir probe. Probe measurements show that the plasma surrounding the target has a potential close to that of the anode, hence the negative voltage applied between target and anode determines the bombarding energy of the ions. With the Langmuir sheath thickness small (at ion current densities of the order of 5 ma/cm² and 500 ev ion energy it is of the order of 1 mm) the target is bombarded with ions under normal incidence. Target edges where ions strike obliquely are protected from sputtering by applying a 2 mm wide border of colloidal graphite which has a low sputtering rate. After a deposit of the desired density has been laid down, the ribbon is removed from the tube, and in a flat position the density distribution is determined photometrically.

The experiment of Seeliger and Sommermeyer was repeated at an ion energy of 200 ev with an arrangement such as shown in Fig. 1(a). A glass ring (4 cm diameter, 2 cm high) surrounds the plasma. A glass ribbon collector is laid flush against the inner wall of this cylinder over the whole circumference, receiving the sputtered

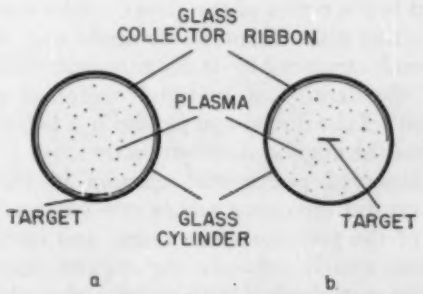

FIG. 1. Arrangements for the study of the angular distribution in sputtered deposits.

* This work was supported by the Office of Naval Research.
[1] R. Seeliger and K. Sommermeyer, Z. Physik **93**, 692 (1935).
[2] A. v. Hippel, Ann. Physik **81**, 1043 (1926); and E. Blechschmidt and A. v. Hippel, *ibid.* **86**, 1006 (1928).
[3] G. Wehner, J. Appl. Phys. **25**, 270 (1954).
[4] G. Wehner, J. Appl. Phys. **26**, 1056 (1955).
[5] G. Wehner, Phys. Rev. **102**, 690 (1956).
[6] G. Wehner, Phys. Rev. **108**, 35 (1957).

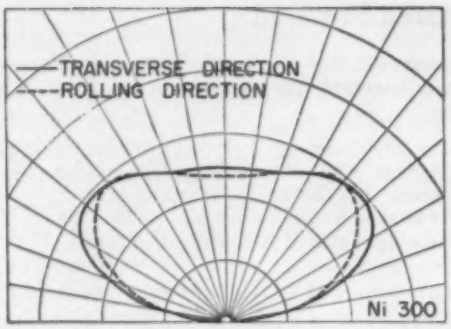

FIG. 2. Influence of preferred crystallite orientation caused by rolling on the angular distribution in Ni bombarded by 300 ev Hg^+ ions.

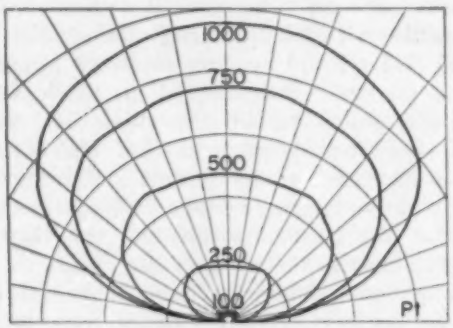

FIG. 3. Polar diagram of material sputtered from Pt by normally incident Hg^+ ions of 100 to 1000 ev energy.

material from the target. The target (0.5 cm wide strip) forms part of the inner cylinder wall. With the mean free path of the sputtered atoms large compared to the tube dimensions, a cosine distribution in this arrangement, where the target forms part of the cylinder wall, would cause the material to be deposited with equal density over the whole circumference. The experiment showed, however, that the angular distribution is definitely "under cosine," i.e., much more material is ejected to the sides than in the direction normal to the target surface. This being the case it turns out that measurements can be performed more simply and with greater accuracy with an arrangement such as shown in Fig. 1(b). Here the target strip is mounted in the center of the glass cylinder which holds the collecting glass ribbon on its inside wall. With the target small compared to its distance from the collector ribbon, the density of material sputtered over the entire 180° of the ribbon and plotted in a polar diagram then gives the angular distribution directly.

The observed preferential ejection in the closest packed crystal directions makes one suspect that the history of the polycrystalline target and its preferred orientation should influence the angular distribution. This point was checked with nickel strips which were cut either parallel with or normal to the rolling direction. Figure 2, obtained at 300 ev ion energy, shows that the difference is not very pronounced. In the following studies the samples were always cut in the rolling direction.

The change in angular distribution with the ion energy is shown in the polar diagrams of Figs. 3 to 7. The diagrams were drawn in such a way that the areas enclosed by the polar curves are proportional to the sputtering yields. A cosine distribution would appear in this representation as a circle touching the origin. Figures 3 and 4 show results for two face-centered cubic metals, Pt and Ni, in the energy range 100 to 1000 ev. Germanium representing a diamond lattice is shown in Fig. 5, and two body-cubic-centered metals (Mo and Fe) in Figs. 6 and 7. The angular distribution remains "under cosine" at energies below 1000 ev, with a tendency to approach a cosine distribution with increasing ion energy. It is interesting to compare these results with those of Rol, Fluit, and Kistemaker[7] who found an "over cosine" distribution at 20 kev, i.e., the target material tends to be sputtered more in the direction normal to the target surface. Seeliger and Sommermeyer collected their results at ion energies (10 kev) where the angular distribution probably just moves from "under cosine" to "over cosine." Another interesting result is the fact that Mo and Fe have a much greater tendency than Ni, Pt, or Ge to be sputtered to the sides, particularly at low ion energy.

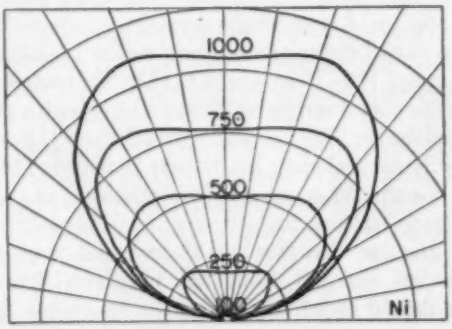

FIG. 4. Polar diagram of material sputtered from Ni by normally incident Hg^+ ions of 100 to 1000 ev energy.

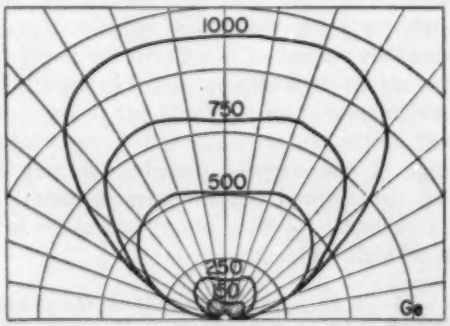

FIG. 5. Polar diagram of material sputtered from Ge by normally incident Hg^+ ions of 100 to 1000 ev energy.

[7] Lab. voor Masspectrografie, Amsterdam, Holland (personal communication).

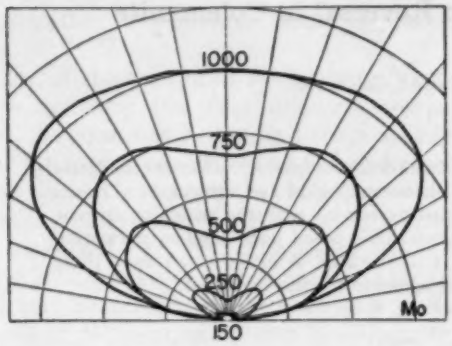

FIG. 6. Polar diagram of material sputtered from Mo by normally incident Hg^+ ions of 100 to 1000 ev energy.

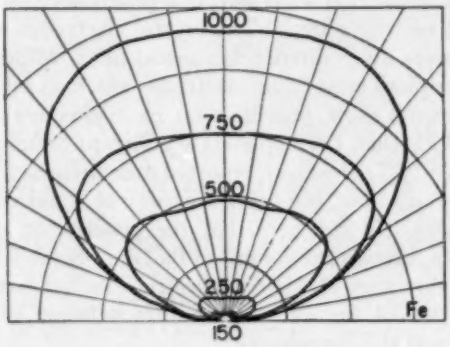

FIG. 7. Polar diagram of material sputtered from Fe by normally incident Hg^+ ions of 100 to 1000 ev energy.

In previous work we have shown,[5] qualitatively at least, that atoms are ejected preferentially in a forward direction when the target is bombarded under oblique incidence. It was desirable to substantiate this result by measuring and plotting the density of the deposit obtained by sputtering the target edge while at the same time preventing the center portion from being sputtered. For this purpose the target strip, arranged in the tube as shown in Fig. 1(b), was completely covered with a colloidal graphite layer with the exception of a 1 mm wide border along one target edge. The angular distribution for Ni obtained at 250 ev is shown in Fig. 8 and for Mo in Fig. 9. Again, Mo shows a greater tendency than Ni to eject material in the forward direction. It is of interest also to mention that Mo shows a much more pronounced increase in sputtering yield than Ni when the angle of incidence is changed from normal to more oblique incidence.[8]

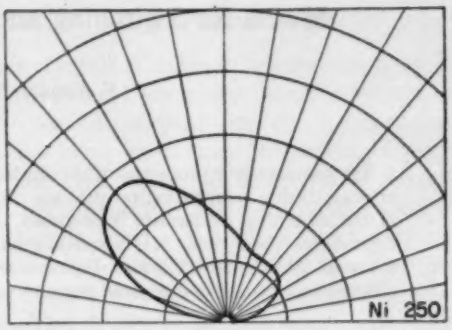

FIG. 8. Polar diagram of material sputtered from one edge of a Ni strip by obliquely incident Hg^+ ions of 250 ev.

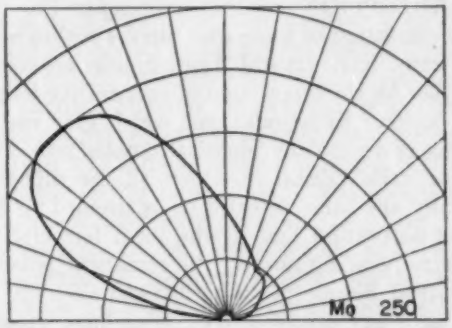

FIG. 9. Polar diagram of material sputtered from one edge of a Mo strip by obliquely incident Hg^+ ions of 250 ev.

ACKNOWLEDGMENTS

The authors wish to thank Emil Benz and Arthur Haut for the skillful glass work.

[8] G. Wehner, J. Appl. Phys., Oct. 1959.

JOURNAL OF APPLIED PHYSICS VOLUME 31, NUMBER 1 JANUARY, 1960

Model for Switching and Polarization Reversal in Colemanite

H. H. WIEDER
U. S. Naval Ordnance Laboratory, Corona, California
(Received July 6, 1959)

The characteristic properties of the displacement current transients obtained from ferroelectric colemanite crystals during polarization reversal are presented in detail. A phenomenological and semiempirical model of the switching mechanism is proposed. The model yields good agreement with the switching current dependence upon time, field amplitude and ambient temperature. It is based upon random nucleation followed by extensive sidewise displacement of the nucleated 180° domains. A model based upon three dimensional growth of nucleated domains is shown to be in poor agreement with experiment.

I. INTRODUCTION

POLARIZATION reversal represents the induced reorientation of molecular dipoles within a macroscopic ferroelectric crystal. These dipoles are coupled to each other by the interaction of cooperative long-range forces peculiar to ferroelectrics which give rise to the grouping of vectorially identical dipoles into domains. A ferroelectric crystal in which all the dipoles have essentially the same orientation is deemed to be in a state of saturation and in the ideal ferroelectric the saturation polarization and the remanent polarization are identical. Simultaneous optical and electrical experiments on a number of ferroelectrics have shown that the polarization reversal process may be described as the nucleation and subsequent growth of domains having an orientation of 180° with respect to the original polarization. Nucleation is considered to be the generation of needle-like spikes which may, or may not penetrate the entire crystal thickness in a direction normal to the crystal electrodes hence parallel to the ferroelectric axis and the applied electric field. The growth of these nuclei may take place either by a volume expansion in a direction normal to the ferroelectric axis, or by growth parallel to the ferroelectric axis or, conceivably by a combination of both. In either case, the growth process is expressed in terms of an average displacement velocity of the walls separating regions of oppositely directed polarization.

On the basis of such optical and electrical experiments carried out on $BaTiO_3$ single crystals, Merz[1] concluded that 180° nuclei grow in the direction of the ferroelectric axis with negligible lateral growth, due probably to the great forward and slight sidewise coupling of dipoles. On the other hand, Miller[2] showed that a considerable sidewise growth can take place in $BaTiO_3$. Indeed under special conditions, the polarization can be entirely reversed by the lateral expansion of a single nucleated domain.[3] Significant differences exist in the experimental methods employed by Merz and Miller. Merz had to apply a mechanical stress in a direction perpendicular to the ferroelectric axis in order to see under polarized light the difference between 180° domains, Miller, on the other hand, used etching techniques to delineate the motion of domain walls during a progressive but interrupted switching cycle. The crystal electrodes used by Merz were evaporated noble metal films, Miller, however, employs ionic liquid electrodes which, as subsidiary experiments show, provide a far more effective contact to $BaTiO_3$ than the imperfectly adherent metal films.

Recently Triebwasser[4] reported measurements similar to those of Miller, but using a variety of liquid and solid electrodes. He indicates that the penetration of 180° domains through the volume of $BaTiO_3$ c-domain crystal in the direction of the ferroelectric axis appears to be a function of the effective contact between the electrodes and the ferroelectric.

A rather similar situation is found in the case of Rochelle salt. The experiments of Mitsui and Furuichi[5] show extensive sidewise motion of domain walls yet the experiments of Marutake[6] show that a significant contribution to the polarization reversal process must be ascribed to domain wall motion in the direction of the ferroelectric axis. It is remarkable that in both Rocehlle salt and $BaTiO_3$, nucleation appears to follow very nearly the empirical law $dn/dt \propto \exp(-\alpha/E)$, dn/dt being the rate of nucleation, E the applied electric field and α an empirical factor defined as an activation field.

Electrical experiments which consist in the reversal of the remanent polarization by alternate, sequentially applied, voltage pulses and the observation of the resultant displacement currents yield remarkably similar results in the case of every ferroelectric which has been investigated to date. On the basis of these observations it seems reasonable to assume that the polarization reversal process in most ferroelectrics consists in the nucleation and subsequent growth of antiparallel domains. Although some doubts may exist as to the growth process, i.e., in some ferroelectrics or even in certain crystals of a particular ferroelectric, preferential growth may occur by the lateral displacement of domain walls, yet in others by forward displacement of domains and still others by a combinatorial effect; these modal differences are not too great and may be no obstacle in

[1] W. J. Merz, Phys. Rev. **95**, 690 (1954).
[2] R. C. Miller, Phys. Rev. **111**, 736 (1958).
[3] R. C. Miller and A. Savage, Phys. Rev. **112**, 755 (1958).
[4] S. Triebwasser, Bull. Am. Phys. Soc. Ser. II, **4**, 184 (1959).
[5] T. Mitsui and J. Furuichi, Phys. Rev. **90**, 193 (1953).
[6] M. Marutake, J. Phys. Soc. Japan **7**, 25 (1952).

the formulation of a general model for polarization reversal.

In spite of the superficial similarity between ferromagnetic switching and ploarization reversal in ferroelectrics, the equations governing domain wall displacement in the former cannot be applied to ferroelectrics since, as pointed out by Miller[3] and Chynoweth,[7] the displacement of domain walls in the latter is much more closely connected with the nucleation of 180° domains. Indeed it is likely that the entire process of polarization reversal may be formulated by a nucleation mechanism.

A study of polarization reversal in colemanite single crystals appeared tempting for a number of reasons. Although in most respects colemanite is a much more complex crystal than $BaTiO_3$, its ferroelectric properties adhere very closely to the simple phenomenological theory of polarization developed by Devonshire.[8] Colemanite, $CaB_3O_4(OH_3)\cdot H_2O$ is a natural crystalline compound having monoclinic symmetry both above and below the ferroelectric transition temperature of -7°C. Perfect cleavage may be obtained perpendicular to the monoclinic *b* axis which is also the polar and ferroelectric axis. The thermodynamic transition is of the λ-type. Ferroelectricity is assumed to be due to the ordering of certain hydrogen bonds within the unit cell. In many respects it is to be expected that colemanite should behave in the ferroelectric phase in an analog manner to other ferroelectrics in which hydrogen bonding plays a significant role. The thermodynamics of the ferroelectric transition and the dielectric properties of colemanite in the paraelectric and ferroelectric states have been published earlier.[9] Christ *et al.*[10] have described in detail its crystalline structure and morphology.

In contrast to $BaTiO_3$ colemanite is very weakly piezoelectric and does not exhibit any fatigue of polarization. Its surface properties are unaffected by water vapor at ordinary temperatures. It shows no secular changes in ferroelectric properties and is unaffected by repeated cycling across its transition temperature. These properties, in conjunction with the uncomplicated transition from the paraelectric to the ferroelectric state and the relatively small spontaneous polarization compared to that of $BaTiO_3$ make the polarization reversal process in colemanite of some interest for comparative purposes. Since optical techniques for the observation of domain dynamics are made difficult by the problem of temperature control below -7°C, the present study is restricted to an investigation of the electrical properties during switching and to the proposal of a phenomenological and semiempirical theory to account for the observed phenomena.

[7] A. G. Chynoweth, Phys. Rev. **110**, 1316 (1958).
[8] A. F. Devonshire, *Advances in Physics* (Taylor and Francis, Ltd., London, England, 1954), Vol. 3, p. 85.
[9] H. H. Wieder, J. Appl. Phys. **30**, 1010 (1959).
[10] Christ, Clark, and Evans, Acta Cryst. **11**, 761 (1958).

II. EXPERIMENTAL

Sample crystals of colemanite approximately 5 cm×2 cm² were obtained from mineral sample collections of the United States Geological Survey. Attempts at colemanite synthesis have thus far produced only small microscopic crystallites not suited for polarization reversal experiments. By carefully cleaving thin sections from a parent crystal a number of thin transparent plates were obtained free of occlusions or other faults. These sections were uniformly diced into squares 0.1 cm per side. The thickness of these specimens ranged between 0.01 cm and 0.02 cm. After cleaning and degreasing procedures, electrodes of silver were evaporated in vacuum upon the major crystal faces. The electroded crystals were placed in a coaxial silver plated brass sample holder. Light, spring loaded contacts provided electrical contact between the crystal electrodes and external circuits. Thermocouples placed in the immediate vicinity of the crystal served to monitor the ambient temperature. The sample holder was placed in turn in a thermostated Dewar flask where it was cooled by the convection flow of nitrogen gas evaporated from a liquid nitrogen bath by an immersion heater. The latter was in turn controlled by a thermistor sensing element placed within the Dewar enclosure and connected by a servo loop to the heater. Details of the construction of this cryostat are published elsewhere.[11] Specimen temperatures between $+25$°C and -100°C were obtainable and temperature control could be maintained at any fixed temperature to within ± 0.1°C. A total of 12 colemanite crystals were selected for further experiments because a preliminary check on their properties at -10°C indicated each of these to have an unbiased and undistorted hysteresis loop.

After reaching thermal equilibrium at some fixed temperature in the ferroelectric phase, each specimen was subjected to sequential, opposite polarity voltage pulses obtained from an electromechanical pulse generator of low impedance. The salient features of the latter have been described in detail elsewhere.[12]

An electric field applied to the crystal causes the flow of a displacement current into the crystal electrodes and reversal of the previous remanent polarization. The quantitative and qualitative properties of this displacement transient allowed an interpretation of polarization reversal in terms of the inherent properties of the ferroelectric crystal.

Figure 1 shows a reversal transient superposed on a normal or "unswitched" displacement current transient. In high quality crystals the unswitched transients represent simply the displacement current flowing into the linear capacitance as well as the stray capacitance of the circuit. It is reasonable to assume that a linear superposition of the polarization reversal transient and the

[11] Naval Ordnance Laboratory Tech. Memo 42-29 (unpublished).
[12] H. H. Wieder and D. A. Collins, Rev. Sci. Instr. **28**, 580 (1957).

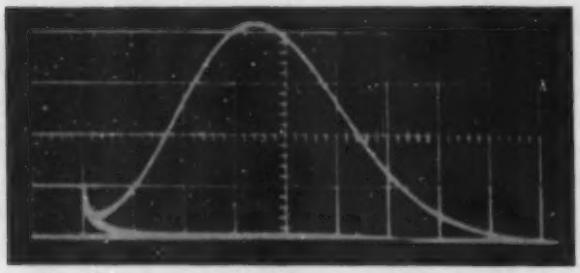

FIG. 1. Representative polarization reversal transient obtained when a positive pulsed electric field is applied to a colemanite crystal in the ferroelectric phase. It is superposed on a normal displacement current transient obtained when a subsequent positive pulse does not change the state of the remanent polarization.

capacitance charging transient produces the experimentally observed switching currents. The reversal transient would rise from 0 at $t=0$ to a peak current density J_m at $t=t_m$ and then decay in a near exponential function with time as can be surmised from Fig. 1. Figure 2 shows the integral of displacement current curves as obtained on a digital differential analyzer. The reversed polarization P, normalized with respect to $2P_s$ is plotted as a function of time t normalized with respect to t_m. Clearly, the polarization rises first exponentially, reaches an approximately linear slope and then approaches asymptotically with time the value $2P_s$.

The characteristic properties of the polarization reversal transients of colemanite crystals were found to be entirely analogous to other, previously reported ferroelectrics. These properties may be summarized as follows.

1. The integrated area under the switching transient is independent of the applied field E, and to a very close approximation is the same as $2P_s$ determined from hysteresis loop measurements. This is clearly illustrated in Fig. 3.

2. For low or moderately small applied fields the peak of the transient J_m, at a fixed ambient temperature, is proportional to $\exp(-\alpha/E)$. Figure 4 illustrates this relation as well as the linear dependence of J upon E at high fields. Although not shown here, the linear relation between J_m and $\exp(-\alpha/E)$ was verified to hold over more than three decades of J_m in the temperature region: minus 20°C to minus 100°C. The parameter α is an empirically defined activation field which is temperature dependent and in $BaTiO_3$ was shown to be related to both the nucleation process and the growth of 180° nuclei.

3. The time t_m in which the transient reaches its peak or the arbitrarily defined polarization reversal time $\tau_s(P \rightarrow 2P_s)$ are inversely proportional to the applied field at high E's. For low fields both t_m and τ_s are proportional to $\exp(\alpha/E)$. Both t_m and τ_s decrease as the temperature approaches the transition temperature.

4. The polarization P_m, reversed between $t=0$ and $t=t_m$ was found to be independent of both the ambient temperature and the applied field if normalized with respect to $2P_s$. Thus $(P_m/2P_s)=0.46$ as shown in Fig. 2. In essence the above outlined results constitutes the detailed behavior of the polarization current transient as a function of time, ambient temperature, and amplitude of applied field.

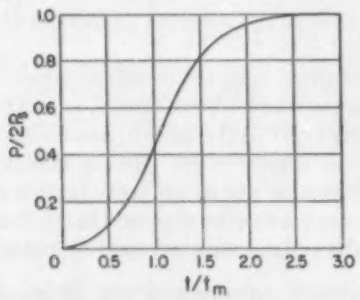

FIG. 2. A normalized plot of the change in polarization with time for the integrated experimental switching transient of Fig. 1.

The similarities in the behavior of colemanite to the earlier detailed studies upon $BaTiO_3$ are evident. It is reasonable therefore to attempt a description of a phenomenological and semiempirical model for polarization reversal in colemanite based upon earlier developed theoretical foundations for switching in barium titanate.

III. PHENOMENOLOGICAL MODEL THEORIES

Models of the polarization reversal mechanism have been proposed for $BaTiO_3$ by a number of authors and in a few cases have been tested against experimental data obtained at room temperature. The proposed models assume either a preliminary nucleation followed by growth of 180° domains, or a process in which nucleation and growth occur simultaneously. As stated earlier the growth process may be assumed either or both, parallel and normal to the ferroelectric axis. An effective model for polarization reversal should provide for the time dependence of the polarization current density $J(t)$, as well as the field and temperature dependence of this transient $J(E,T)$. An attempt to apply some of

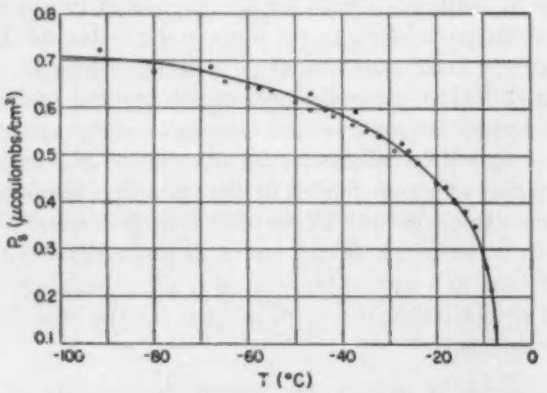

FIG. 3. Spontaneous polarization P_s as a function of temperature. Open circles represent measurements made from conventional hysteresis loops, filled dots were obtained from switching transients and plots such as shown in Fig. 2.

these theories to colemanite and to reconcile their predictions with the earlier described experimental results will now be attempted.

Merz[1] has proposed that at high electric fields, domain nucleation in $BaTiO_3$ takes place initially at a rapid rate and domain wall motion, in the direction of the ferroelectric axis is dominant for most of the polarization switching process. If nucleation is assumed to occur preferentially at one of the crystal electrodes, in the presence of an applied field E which is a step function with a very sharp rise time, then it is reasonable to assume the occurrence of polarization reversal in an essentially constant electric field.

Studies of switching transients obtained from $BaTiO_3$ as well as other ferroelectric crystals indicate that the amplitude of the polarization current density dP/dt, is proportional at any instant t, to the as yet unswitched polarization $(2P_s-P)$. The total change in polarization during switching is $2P_s$ and the amount of reversed polarization up to the time t is P. An empirical expression for the switching transient of $BaTiO_3$ in the tetragonal phase at $+25°C$ might be written as:

$$dP/dt=(2P_s-P)\beta t \qquad \begin{matrix} P=0 & t=0 \\ P\to 2P_s & t\to\infty \end{matrix} \qquad (1)$$

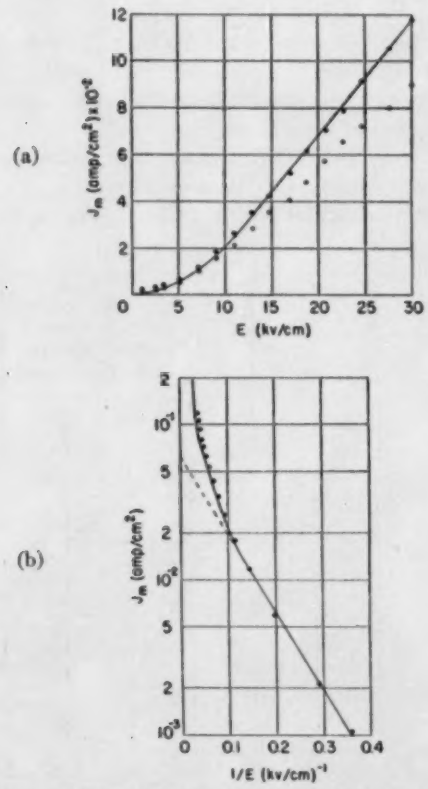

FIG. 4. (a) Filled dots show the experimental data obtained at $-37.5°C$ on sample k-3. The peak of the switching transient J_m, is shown to depend upon the magnitude of the applied field, E. Open circles represent the calculated values of J_m using Eq. (4). (b) At low fields J_m depends upon the applied field as $\exp(-\alpha/E)$ as shown for the nonlinear region of J_m *vs* E of Fig. 4(a).

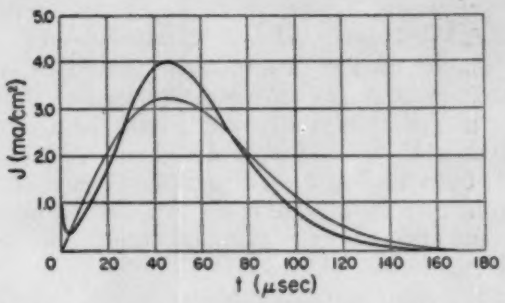

FIG. 5. An experimental switching transient, obtained at $-68°C$ for sample k-3 at a field of 15.9 kv/cm is compared to the calculated reversal transient using Eq. (3). The heavier drawn curve represents the experimental data.

where β is a field-dependent and temperature-dependent time constant of the switching process. Upon integrating (1) obtains:

$$P=2P_s[1-\exp(-\tfrac{1}{2}\beta t^2)] \qquad (2)$$

and the polarization current density $dP/dt=J$ may then be written as:

$$J=2P_s\beta t\exp(-\tfrac{1}{2}\beta t^2). \qquad (3)$$

It is readily seen that this leads to the same expresssion proposed by Pulvari and Kuebler[13] for $BaTiO_3$. The peak of the current transient J_m, is expressed as:

$$J_m=(2P_s/t_m)\exp(-\tfrac{1}{2}). \qquad (4)$$

This expression which appears valid in the case of $BaTiO_3$ is however not applicable to colemanite for the following reasons:

1. Equation (4) predicts that the product $J_m t_m=1.21\ P_s$. However it is found experimentally for colemanite that over a wide range of applied fields and ambient temperatures $J_m t_m=1.61\ P_s$ representing a discrepancy of the order of 33%.

2. If experimental values of t_m obtained as a function of the applied field at a fixed temperature are substituted in (4) the resultant calculated curve of J_m *vs* E does not agree with experiment as shown in Fig. 4(a).

3. Equation (3) as well as the relations proposed by Pulvari and Kuebler[13] do not yield the proper time dependence of the polarization current transient as can readily be seen from Fig. 5.

Another model for polarization reversal in $BaTiO_3$ was proposed recently by Burfoot.[14] His approach is based upon a qualitative interpretation of a nucleation rate which is random in time but dependent upon the empirical factor $\exp(-\alpha/E)$ and a domain growth largely dependent upon and controlled by the nucleation rate. His model assumes unrestricted nucleation without accounting either for coagulation of domains nor for possible overlap of nucleation sites by adjacent expanding nuclei. Nevertheless his model permits estimates of

[13] C. F. Pulvari and W. Kuebler, J. Appl. Phys. **29**, 1315 (1958).
[14] J. C. Burfoot, Proc. Phys. Soc. (London) **73**, 641 (1959).

order of magnitude. The prediction that the transient peak J_m should occur before $(t'/2)$ where t' is defined as the time required for J to decrease to 0.368 J_m is essentially confirmed by experimental transients obtained upon colemanite. For other parameters the agreement between predicted and experimental values is not very good. Calculated and experimental values of J_m for example even in the case of $BaTiO_3$ disagree by some 25% and further direct application to colemanite seems therefore of doubtful value.

In recent study on Barkhausen pulses in $BaTiO_3$, Chynoweth[7] proposed a relationship between the parameters of these pulses and the reversal of polarization in c-domain plates at room temperature. He proposed that if Barkhausen pulses are closely related to the nucleation probability of spike-shaped 180° domain nuclei, then their critical size is consistent with the empirically determined nucleation probability factor $\exp(-\alpha/E)$. Chynoweth considers two different growth conditions:

1. At low fields, random nucleation is followed by sideways expansion of nuclei normal to the ferroelectric axis. Due account is taken of the fact that nuclei expand to some average size before growth ceases. Comparison of parameters predicted from this model with a corresponding experimental transient led to moderate agreement.

2. At high fields nucleation is assumed to be still random in time and in the direction of the ferroelectric axis. Growth proceeds, however, by the rapid sidewise expansion of domains across some nucleation sites which are overrun. The effect of these ingested nucleation sites are calculated by a theoretical model such as developed by Avrami.[15]

Subsequently, Miller[2,3] has shown experimentally that extensive sidewise motion does occur in $BaTiO_3$ and that the second model of Chynoweth involving the ingestion of nucleation sites may apply to low fields as well. Although a mathematical error is to be found in both the calculations of Miller and Chynoweth, the arguments advanced in favor of this model are not invalidated and, as shall be shown presently, are directly applicable to colemanite.

IV. RANDOM NUCLEATION AND SIDEWISE WALL MOTION OF 180° DOMAINS

For random nucleation in the direction of the ferroelectric axis, the nucleation rate is given by:

$$(dN/dt)=kN_0e^{-kt}, \tag{5}$$

here the nucleation probability is k and the total number of available nucleation sites is N_0. The size of a nucleus at any time t, if nucleated at $t=y$, is given by:

$$g(t,y)=\sigma[r(t,y)]^\lambda, \tag{6}$$

where σ is a shape factor, $\lambda=1$, 2, or 3 and depends upon growth proceeding in one, two, or three dimensions; $r(t,y)$ is a growth parameter which depends on the time at which a nucleus was generated and the elapsed time since growth started. The total volume V, of all generated nuclei is at any time t:

$$V(t)=\int_0^t [g(t,y)(dN/dt)_{t-y}]dy. \tag{7}$$

Suppose that an applied field causes the nucleation of 180° domains in the form of thin spikes which thereafter grow in the forward direction at a faster rate than either the nucleation or the subsequent two dimensional sidewise growth velocity of the generated nuclei. The area s subtended by a two dimensionally growing nucleus at the major surface of the crystal S_0 is given by $s=\pi r^2$ if the area is circular, or $s=a^2$ if the area is rectangular and the sidewise growth velocity v is essentially constant, then $s(t)=[v(t-y)]^2$. The amount of the reversed polarization at any time t may then be represented by the total subtended area, $S(t)$ upon S_0 by all the expanding nuclei and therefore (7) and (5) may be used to write:

$$\frac{S(t)}{S_0}=\frac{v^2kN_0}{S_0}\int_0^t [(t-y)^2\exp(-kt)]dy. \tag{8}$$

The above equation represents the fraction of reversed polarization in time (t), provided that, nucleation is random in time and growth proceeds unhindered, but without overlap of nucleation sites.

Avrami[15] has shown that in the case of random nucleation if ingestion of nucleation sites does occur, Eq. (8) must be rewritten as follows: Letting γ_{ex} correspond to

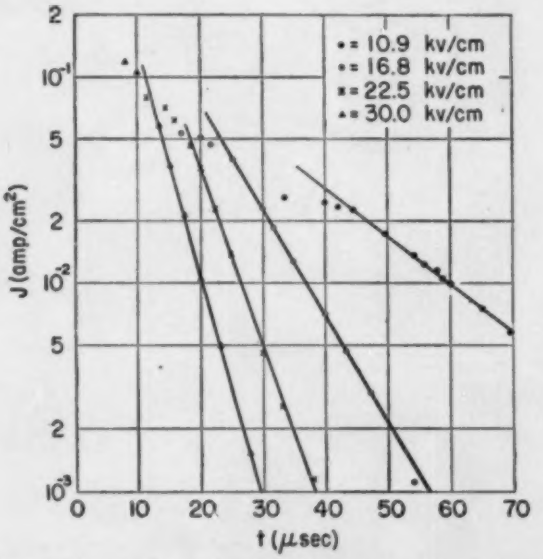

FIG. 6. A series of plots show the reverse slopes of experimental transients as a function of various applied fields at −37.5°C for sample k-3. The respective slopes are considered to be the nucleation probability, k.

[15] B. Avrami, J. Chem. Phys. 8, 212 (1940).

the fractional extended polarization with no ingestion, i.e., $S(t)/S_0=\gamma_{ex}$ and the fractional polarization reversed if ingestion is effective $\gamma=P/2P_s$, then $d\gamma_{ex}=d\gamma/(1-\gamma)$. Integration and subsequent substitution of (8) leads to:

$$-\log(1-\gamma)=\frac{2v^2N_0}{k^2S_0}\left[\frac{k^2t^2}{2}-kt+1-e^{-kt}\right]. \quad (9)$$

Letting $(2v^2N_0/S_0)=B$, Eq. (9) may be written as:

$$P=2P_s\left[1-\exp(-B/k^2)\left(\frac{k^2t^2}{2}-kt+1-e^{-kt}\right)\right]. \quad (10)$$

The instantaneous current density J expressed in terms of the polarization P reversed between $t=0$ and t is:

$$J=(B/k)(2P_s-P)(kt-1+e^{-kt}), \quad (11)$$

and the peak of the transient is then obtained by differentiating (11) with respect to t and maximizing the resultant expression. It follows that:

$$B=\frac{k^2[1-\exp(-kt_m)]}{[kt_m-1+\exp(-kt_m)]^2}. \quad (12)$$

To obtain verification of the calculated polarization current expressed in (11) with experimentally obtained switching transients the nucleation probability k must first be determined.

Chynoweth[7] has shown that for $BaTiO_3$ the reverse slopes of experimental transients obey quite well a logarithmic decay curve with time and this is found to be true of colemanite. Considering Eq. (11) it is to be noted that in the region where $kt\simeq 1$:

$$\log J \text{ is linear in } kt. \quad (13)$$

Therefore a semilog plot of J as a function of t for experimentally obtained switching transients should yield the nucleation probability k.

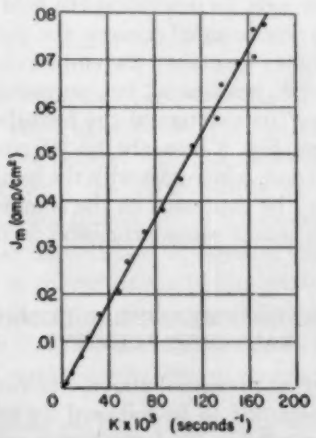

FIG. 7. J_m and k are directly proportional as shown for the experimental data obtained at −47°C for sample k-3. This is also in accord with Eq. (15).

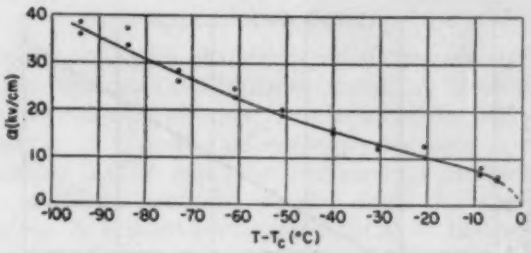

FIG. 8. The activation field α is shown to depend upon the temperature difference with respect to the transition temperature T_c. Open circles represent α calculated from plots such as shown in Fig. 4(b). Filled dots were calculated from similar plots at low values of E for $(\partial K/\partial E)$.

Figure 6 shows a series of such curves whose slopes represent the nucleation probability factor, k. Similar curves were also prepared in order to determine the dependence of k upon E for the range of field amplitudes between 1 kv/cm and 30 kv/cm and within the temperature range of −15°C and −100°C.

The values of k obtained in the manner, when plotted as a function of E, show a striking parallelism between the corresponding plots of $\log J_m$ *vs* E as shown in Fig.7. In addition the following results were noted.

1. For low E amplitudes, $(\partial k/\partial E)_T$ is proportional to $\exp(-\alpha/E)$ and α is, within the experimental error, the same activation field discussed earlier for J_m *vs* E. A comparison of the α values determined from the peak of the transient and from the k *vs* E curves is shown in Fig. 8.

2. The product kt_m is a constant which is independent of either field, temperature or spontaneous polarization. Its value is $kt_m\simeq 2.12$ within the temperature and field boundaries given earlier.

A search for agreement between the theoretical expression (11) and experimental transients led to very good results. Figure 9 shows the synthesis of such a theoretically derived transient and the corresponding experimental point by point plot. The value of B is calculated from (12) by introducing the experimental data of kt_m and values of $(2P_s-P)$ as a function of some arbitrary t are obtained from plots such as shown in

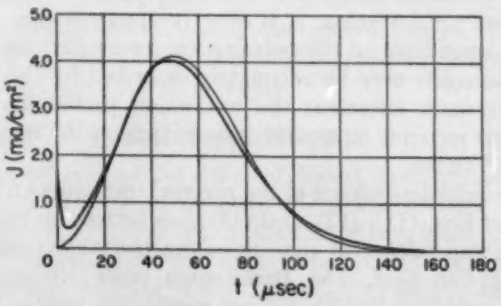

FIG. 9. The same experimental switching transient shown in Fig. 5 is compared to the theoretical curve calculated according to Eq. (11). The heavier drawn curve represents the experimental data.

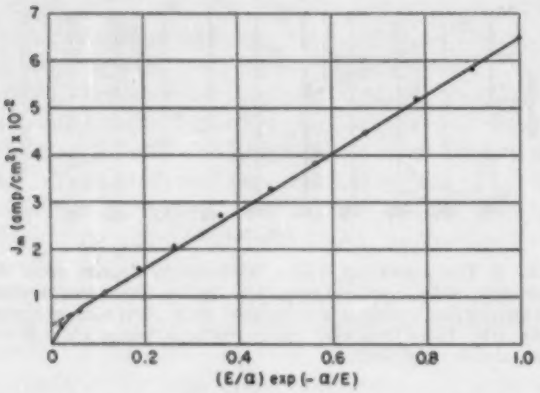

FIG. 10. The linearity expressed in Eq. (16) between J_m and $[E/\alpha \exp(-\alpha/E)]$ is shown for sample k-3 at -47°C. Similar results were also obtained at other temperatures.

Fig. 2. This agreement between the experimental and corresponding theoretical time dependence of J remained excellent irrespective of field amplitude or ambient temperature.

The values of J_m may be derived directly from Eqs. (11) and (12). Since $B=0.572\ k^2$ it follows that:

$$J_m=0.572\ k[kt_m-1+\exp(-kt_m)](2P_s-P_m). \quad (14)$$

The value of $(2P_s-P_m)$ may be calculated from (10) since both $B/k^2=0.572$ and $kt_m=2.12$ are known. It is thus found that $P_m/2P_s=0.44$, in very good agreement with the experimentally determined $P_m/2P_s=0.46$. Equation (14) may be expressed therefore as:

$$J_m=0.765\ kP_s. \quad (15)$$

Equation (15) thus states the proportionality between J_m and k, in agreement with the experimental data presented in Fig. 7. The ratio (J_m/kP_s) should remain constant and independent of the applied field or temperature. The average ratio for all field amplitudes at fixed, specific, temperatures has been calculated and is given in Table I. It is readily seen that the agreement between the temperature independent average value of (J_m/kP_s) and the constant predicted from (15) is quite good and well within the maximum error of measurement which is estimated to be of the order of 12%.

From the foregoing, it is directly apparent that the time dependence of the polarization reversal transients of colemanite may be adequately described by the use of one main criterion; the nucleation probability k, without recourse to specific information on the motion of 180° nuclei.

The field dependence of the reversal transients on the basis of Eqs. (11), (12), and (15) then follows by virtue of the dependence of the nucleation probability upon the applied field. The Barkhausen pulse studies of Chynoweth[7] on $BaTiO_3$ did not completely resolve the question whether the number of Barkhausen pulses are dependent upon E, evidence was presented however that the number of generated pulses may increase with field.

TABLE I.

Temperature	$(J_m/kP_s)_{Av}$	$(kt_m)_{Av}$
−10.0	0.770	2.122
−16.0	0.746	2.045
−27.5	0.743	2.193
−37.5	0.769	2.175
−47	0.744	2.146
−58.0	0.753	1.996
−68	0.731	2.128
−80	0.758	2.160
−91.5	0.754	2.198
−100	0.746	2.096

No Barkahusen studies have been made on colemanite as yet and it is still somewhat uncertain whether there is a direct causal relationship between nucleation and Barkhausen pulses since Miller[2] has shown that such pulses are also obtained when two latterally expanding domains join at a common interface.

For the exponential region of Fig. 4 where $J_m \propto \exp(\alpha/E)$ Eq. (15) and Fig. 8 give the field and temperature dependence of k. In the linear region where J_m, or respectively, $k \propto (E-\alpha)$, the temperature dependence of k may be expressed as $(\partial k/\partial T)_E \propto (1/\alpha)$. An empirical expression which provides the proper field and temperature dependence over both the linear and at least two decades of the exponential regions of J_m *vs* E is:

$$J_m \propto (E/\alpha) \exp(-\alpha/E). \quad (16)$$

A plot of this relation is illustrated in Fig. 10. The above equation is found to provide an excellent fit for all the experimental data obtained on colemanite over the entire range of 1 to 30 kv/cm and -15°C to -100°C. Equation (16) is similar to the empirical equation proposed by Pulvari and Kuebler[13] for the field dependence of J_m of $BaTiO_3$ at room temperature. Their expression as well as that of Merz[1] requires however an additional empirical parameter; the domain wall mobility μ, expressed in terms of the field dependence of the displacement velocity of a 180° wall in the direction of the ferroelectric axis. In describing the field dependence of the polarization reversal process, the parameter α is highly significant; however, its empirical role as an "activation field" remains as yet unresolved in terms of basic physical parameters of the ferroelectric lattice structure. From Fig. 8 it might be inferred that as a first approximation, α increases with the local crystalline field which may be expressed as the summation of the odd terms of a power series expansion in terms of the polarization.[15]

V. THREE-DIMENSIONAL DOMAIN WALL DISPLACEMENT

In the theory as presented above, nucleation of 180° domains was assumed to be followed by rapid growth in a direction parallel to the ferroelectric axis and to be followed subsequently by slower sidewise displacement of domain walls.

In the case of other ferroelectrics, specifically Rochelle salt and $KNbO_3$ there is some evidence that nuclei do not penetrate the crystal volume and the growth process, leading to saturation of the polarization, might be described by a domain wall expansion of three dimensions. It is of interest to consider for colemanite the extreme case in which the growth in three dimensions may be described by a single parameter such that the volume of a nucleus v, generated at $t=y$, may be described at any time t by:

$$v(t,y)=\sigma[g(t-y)]^3, \tag{17}$$

σ is a shape factor and g is the growth velocity which is considered to be uniform in any direction. The analysis, for the general case, assuming random nucleation, has been carried out by Jacobs and Tompkins[16] and proceeds in a manner parallel to that outlined above for the case of two-dimensional growth. It is shown that:

$$P=2\left\{P_s 1-\exp\frac{B'}{k^3}\left[-\frac{k^3t^3}{3!}+\frac{k^2t^2}{2!}-kt+1-\exp(-kt)\right]\right\}. \tag{18}$$

This leads to a polarization reversal transient defined by:

$$J=\frac{B'}{k^2}\left[\frac{k^2t^2}{2}-kt+1-\exp(-kt)\right][2P_s-P]. \tag{19}$$

Differentiating (19) with respect to t and maximizing, the value of B' is calculated to be:

$$B'=k^2\frac{kt_m-1-\exp(-kt_m)}{\{[(k^2t_m^2)/2]-[kt_m-1-\exp(-kt_m)]\}^2}. \tag{20}$$

Replacing the experimentally determined value of $kt_m=2.12$ in (20) yields $B'=1.222\ k^3$. Substitution of this value into (19) and solving for J_m:

$$J_m/(P_s k)=1.385. \tag{21}$$

In addition, from (18) it is found that $P_m/2P_s=0.51$ obviously in poor agreement with the experimental value of 0.46. The value of $J_m/(P_s k)$ from (21) is equally unreconcilable with the experimental data shown in Table I. Within the framework of the model of polarization reversal presented here it appears that growth in the direction of the ferroelectric axis, as in the case of $BaTiO_3$, is quite rapid and a model which considers growth in two dimensions would adequately explain the polarization reversal mechanism of colemanite.

[16] P. W. M. Jacobs and F. C. Tompkins, *Chemistry of the Solid State* edited by W. E. Garner (Academic Press, Inc., New York, 1955).

VI. SUMMARY AND CONCLUSION

Qualitatively the characteristics of the polarization reversal transients of colemanite crystals are found to be the same as that of other ferroelectrics. The field dependence of J_m and t_m are essentially the same as that found for $BaTiO_3$ and other ferroelectrics irrespective of crystalline structure. At low fields J_m rises as $\exp(-\alpha/E)$ without any apparent threshold field which might indicate a true coercivity such as found in magnetic materials. For high fields J_m rises nearly linearly with field. The nonlinear region between J_m and E or respectively t_m^{-1} and E such as found by Stadler[17] for $BaTiO_3$ is not reached in colemanite even at fields of 30 kv/cm.

The time dependence of the switching transient in colemanite is apparently quite different from that of $BaTiO_3$. If the comparison is made on the basis of a polarization reversal mechanism involving random nucleation of 180° domains and their subsequent lateral growth, then the product, kt_m, of the nucleation probability k and the time required for the transient to reach its peak t_m, is much larger in $BaTiO_3$ than in colemanite. This is to be inferred from the analysis presented by Chynoweth[7] and the experimental data of Pulvari and Kuebler[18] on $BaTiO_3$ and the information presented in this paper.

It is shown that a theoretical model for polarization reversal based upon random nucleation and a rate of growth independent of direction does not provide as satisfactory an agreement with experimental data on colemanite as a simpler model involving only lateral domain wall motion and two-dimensional growth. In the latter case a simple expression is obtained for the time dependence of the displacement current transient in which no explicit information is required on the velocity of domain wall displacement or the density of nucleation sites within the crystal but only on the nucleation probability k and the amount of the polarization which is not yet switched. The applicability of either the two-dimensional growth or the three-dimensional growth model to other ferroelectrics remains to be tested. In view of the great analogy between ferroelectrics, the polarization reversal process, as manifested by the displacement current transient parameters, might be described by a combination of some growth parallel to the ferroelectric axis and a considerable, radially symmetrical growth, normal to this axis.

ACKNOWLEDGMENTS

The support of the Office of Naval Research in the course of this work is gratefully acknowledged. The author is indebted to Mr. A. Levine for help in programming the theoretical and experimental data on a digital differential analyzer and to D. A. Collins for able assistance during the experimental phase of this study.

[17] H. L. Stadler, J. Appl. Phys. **29**, 1485 (1958).

JOURNAL OF APPLIED PHYSICS VOLUME 31, NUMBER 1 JANUARY, 1960

Variation in Ferroelectric Characteristics of Lead Zirconate Titanate Ceramics Due to Minor Chemical Modifications*

ROBERT GERSON
Electronic Research Division, Clevite Corporation, Cleveland 8, Ohio
(Received June 29, 1959)

Lead zirconate titanate ceramics with certain 3- or 5-valent additions (lanthanum, neodynium, tantalum, and niobium) are found to be characterized by low aging of electrical and mechanical properties, a well-defined hysteresis loop, and by high electrical and mechanical losses. Experimental investigations are reported on plain lead zirconate titanate and on a low-aging niobium modification.

The experiments included an electron microscope study of the ceramics and a number of electrical measurements. As a result of the study, the changed properties of the substituted material have been explained as being due to domain wall motion under low electric field. The results of electrical measurements supporting this conclusion, and a hypothesis accounting for the effects in terms of lattice vacancies, are presented.

The 3- or 5-valent additives described in the foregoing also cause greatly increased volume resistivity in the ceramic. This has not been satisfactorily explained.

INTRODUCTION

LEAD zirconate titanate ceramics are of interest because, while they are ferroelectric and possess the same structure as barium titanate, they have a higher Curie temperature and ferroelectric polarization. The present investigation concerns certain modifications in lead titanate zirconate ceramics which lead to considerable changes in their electrical and mechanical properties.[1–4] The modifications involve the addition of small quantities of the oxides of tri- or pentavalent elements (*viz.*, lanthanum, neodynium, tantalum, or niobium) which have the following effects:

(1) As in all ferroelectric ceramics, the modified ceramic exhibits some aging of its dielectric and mechanical properties after a drastic thermal or electrical excursion. The aging of the modified ceramic is, however, almost an order of magnitude smaller than that in the plain ceramic.

(2) The mechanical and electrical losses under low stress or field encountered in the modified material are considerably higher than in the unmodified ceramic.

(3) The dc resistivity of the modified ceramic is much higher than that of plain ceramic. At 200°C the two resistivities differ by three orders of magnitude.

(4) The dielectric constant of the modified material is higher, while its elastic stiffness modulus is somewhat lower than that of the unmodified material. In a sense, then, the addition results in a "softer" material, both electrically and mechanically.

(5) The modified material exhibits a relatively square hysteresis loop with a coercive voltage which is quite independent of applied field. Hysteresis loops of ferroelectric ceramics are usually not square, and usually the measured coercive field depends strongly on the peak driving field.

In general, the dielectric and mechanical properties of ferroelectric crystals below their Curie points are functions of the state of polarization and stress. A phenomenological theory due to Devonshire[5] has been quite successful in correlating many of the characteristics of the barium titanate single crystal, but the ceramic is more complicated. In a ceramic ferroelectric, each crystallite is twinned into many polarization domains. The contribution of domain-wall motion to the properties is superimposed on the single-crystal behavior, and in many of the ceramic modifications this domain contribution is of considerable importance. In particular, it is usually assumed that aging is due to a gradual change in the domain configuration.[6–8] Electrical hysteresis effects, whether in the single crystal or in the ceramic, are also a characteristic due to domain wall motion.

The lead titanate zirconate with the above additions differs markedly from the unmodified material in hysteresis and aging. This may indicate a change in the behavior of the domain walls. Furthermore, most of the other changed properties of the modified material can be regarded as influenced by domain-wall motion. The dielectric constant of ferroelectric ceramics, for example, has been considered to be partly due to a limited domain wall oscillation,[7,9,10] and the same oscillation in the case of 90° domain walls will result in increased compliance. Plessner[7] has pointed out that a wall trapped in an unsymmetrical potential well will contribute to the power factor as well as to the dielectric and elastic susceptibilities. Thus, many of the unusual properties of the modified ceramic can be ac-

* Supported by the Office of Naval Research.
[1] F. Kulcsar, J. Am. Ceram. Soc. (to be published).
[2] D. Berlincourt, Sandia Corporation Rept. SC-3859 (TR) (1956).
[3] D. Berlincourt, Sandia Corporation Rept. SC-4122 (TR) (1957).
[4] D. Berlincourt, Sandia Corporation Rept. SC-4203 (TR) (1958).
[5] A. F. Devonshire, Phil. Mag., Suppl. 3, 85-130 (1954).
[6] W. P. Mason, J. Acoust. Soc. Am. 27, 73 (1955).
[7] K. W. Plessner, Proc. Phys. Soc. (London) B69, 1261 (1956).
[8] M. C. McQuarrie and W. R. Buessem, Bull. Am. Ceram. Soc. 34, 402 (1955).
[9] C. Kittel, Phys. Rev. 83, 458 (1951).
[10] B. Lewis, Proc. Phys. Soc. (London) B73, 17 (1958).

counted for by the assumption that in this material the domain walls have freedom to oscillate under low alternating electrical or mechanical stress, but that the average position of the wall with no external stress applied is quite stable.

The experiments reported below were designed to test these ideas. The approach used has been to evaluate the ceramics microscopically (electron microscope studies were necessary to reveal domain structure in lead titanate zirconate, which is a relatively fine-grained material) and under electrical and mechanical excitation which would tend to reveal domain behavior.

The ceramic compositions used were as follows: Unmodified (plain) ceramic: $Pb_{0.95}Sr_{0.05}Zr_{0.53}Ti_{0.47}O_3$; Modified ceramic: $PbZr_{0.52}Ti_{0.48}O_3+1$ wt% Nb_2O_5.

Both of these materials are tetragonal but may contain rhombohedral phases in minor amounts. The c/a ratio in the tetragonal phase is about 1.020 for the plain ceramic and 1.024 for the modified material, the lower ratio in the plain ceramic being due to the presence of strontia.

FIG. 1. Electron micrograph of unpoled modified ceramic.

The average dielectric constant for unpoled ceramic at room temperature is 1100 for unmodified materials and 1250 for modified materials. The values were taken 24 hr after cooling from above the Curie point. For poled ceramic the free dielectric constants (1 kcps) are 1200 (parallel to poling) and 1350 (perpendicular to poling) for the unmodified material, while the corresponding values are 1500 and 1300 for the modified material. These values were taken 24 hr after poling.

MICROSCOPY

The logical first step in investigating domain processes was to reveal the domain structures. The small size of the domains required electron microscopy for their observation, and a surface polishing and etching treatment suitable for making replicas for the electron microscope had to be developed.

To prepare a replica a sample of ceramic about 6 mm sq and 1 mm thick was compression-molded into a cylinder of phenolformaldehyde type resin, with a flat surface of the ceramic lying in one of the end planes of the cylinder. The ceramic was polished with successively finer metallographic polishing papers, culminating with a 4/0 paper, and then polished at slow speed with Fisher Gamal (fine-grained alumina) in suspension on a felt cloth. Finally it was etched with a 10% aqueous solution of hydrofluosilicic acid at room temperature for a few seconds.

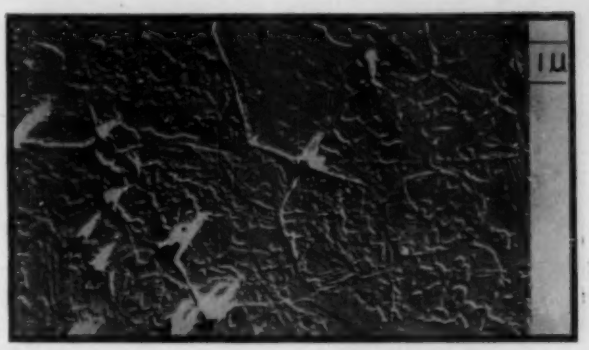

FIG. 2. Electron micrograph of unpoled plain ceramic.

A replica of Formvar (applied as a 1% solution in ethylene dichloride) with a collodion backing was made, the Formvar-collodion replica was lifted on a metal screen, the collodion was dissolved, and the Formvar replica was shadowed, first with palladium and then with carbon. After dissolving the Formvar in ethylene dichloride, an electron microscope was used for examination of the domain pattern.

Figures 1 and 2 show the electron micrograph of plain and modified ceramic. Both grain and domain boundaries are evident. A series of domain boundaries running parallel are walls between domains where the polarization vectors are at 90° to each other, while the irregular lines within a grain are usually 180° walls. While the plain ceramic pattern does not have the distinctiveness that is found in the modified ceramic, the two do not appear to differ greatly. Domain sizes, for example, are approximately the same in both materials.

One interesting result of this study was found in contrasting the micrograph of an unpoled ceramic with the same material after poling. (Figs. 3 and 4). In the polarized material practically all of the 180° twinning

FIG. 3. Electron micrograph of unpoled modified ceramic. This material was slightly over fired, and the grain boundaries are not easily seen.

FIG. 4. Electron micrograph of poled modified ceramic. The material is the same as in Fig. 3. Since there are many fewer domain boundaries after poling, the grain boundaries are visible in this photograph.

FIG. 5. Electron micrograph of unpoled modified ceramic, showing herringbone pattern of 90° twinning.

has disappeared, and the 90° twinning is very greatly reduced. The latter result differs from barium titanate, where the 90° twinning is little affected by poling. Berlincourt and Krueger[11] have arrived at this same result by study of the dimensional changes of the ceramics on poling.

In spite of the difference in domain sizes the twinning patterns observed are similar to those found in barium titanate.[12,13] For example, Fig. 5 shows a herringbone pattern of 90° twins, while Fig. 6 shows two 180° walls crossing a field of 90° twinning. Both of these are patterns previously observed in barium titanate.

EFFECT OF BIAS VOLTAGE

One of the fundamental manifestations of ferroelectricity is the nonlinearity of the polarization as electric field is applied. One aspect of this behavior is that the dielectric constant of a ferroelectric ceramic, measured with a low amplitude ac signal, varies when dc bias is applied. The amount of this variation depends on the particular type of ceramic, and the ceramics being studied are found to differ widely (Figs. 7 to 9). These measurements were made on a General Radio 716 C Bridge at 1 kcps. A large blocking capacitor between the sample and the bridge prevented the dc voltage from entering the bridge circuit. The bias in all cases was in the same direction as the original poling field.

The initial portion of the curve for the plain ceramic depends on the amount of aging it has undergone. The freshly poled unmodified ceramic shows a fairly linear variation in dielectric constant with dc bias, while the aged ceramic is not linear until it has been subjected to a substantial field. The relationship between dielectric constant and bias for the aged ceramic is thus altered irreversibly by the application of high dc bias, and when the bias is reduced the ceramic is again in a freshly poled condition. On the other hand, the low-aging ceramic shows a curve which is fairly linear and similar to those of the freshly poled plain material. In this sense, the low-aging ceramic is like a material which is permanently held in the excited condition, characteristic of plain ceramic immediately after poling.

It is quite probable that the decrease of dielectric constant with voltage is due to a higher degree of the alignment in the poled ceramic, bringing it closer to a *c* domain, or low dielectric constant, crystal in the direction of measurement. The implication of the data

FIG. 6. Electron micrograph of unpoled modified ceramic, showing 180° domain reversal in a field of 90° twinning.

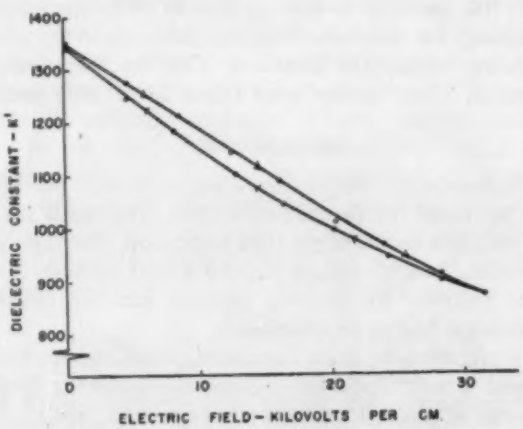

FIG. 7. Dielectric constant of plain ceramic as a function of bias field, ½ hr after poling.

[11] D. Berlincourt and H. H. A. Krueger, J. Appl. Phys. (to be published).
[12] V. J. Tennery and F. R. Anderson, J. Appl. Phys. **29**, 755 (1958).
[13] F. Kulcsar, J. Am. Ceram. Soc. **39**, 13 (1956).

is that this realignment occurs fairly readily in freshly poled (excited) plain material, or in materials containing niobium.

In aged plain ceramic, however, the process requires the application of a fairly high field.

EFFECT OF MEASURING FIELD ON DIELECTRIC CONSTANT

The dielectric constant of ferroelectric ceramics is usually found to be a function of the ac measuring field. At higher fields there are contributions to the polarization from domain switching which raise the dielectric constant and loss.[10] Some aspects of the effect have already been reported in poled lead zirconate titanate ceramics.[14] The present investigation is concerned with the behavior of unpoled ceramics and with the aging of the voltage-dependence effect.

Most of the measurements below were made at 100 cps (to avoid the heating caused by higher frequencies) on a General Radio 716-C capacitance bridge. Since the components in the bridge limit the voltage which may be applied, fairly thin samples (0.2 to 0.4 mm thick) were used. The electrodes were evaporated gold. In one experiment, involving fields above 5 kv per cm, a conventional Sawyer and Tower hysteresis circuit was used at 100 cps and photographs of the oscilloscope trace were measured.

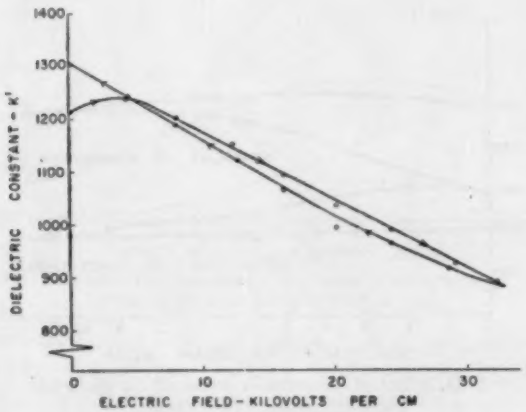

FIG. 8. Dielectric constant of plain ceramic as a function of bias field, four days after poling.

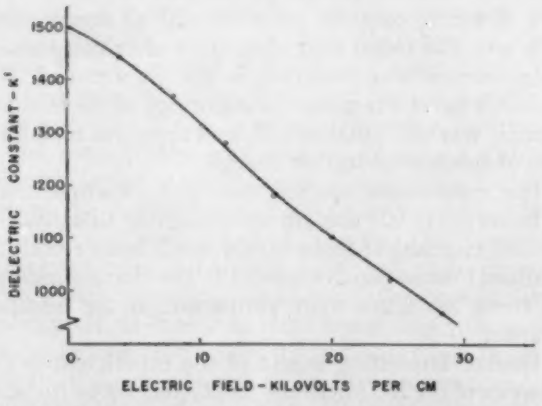

FIG. 9. Dielectric constant of modified ceramic as a function of bias field. Since this material ages very little, the curve does not depend appreciably on the time elapsed after poling.

[14] Berlincourt, B. Jaffe, H. Jaffe, and Krueger, U. S. Navy J. Underwater Acoust. 8, 479 (1958).

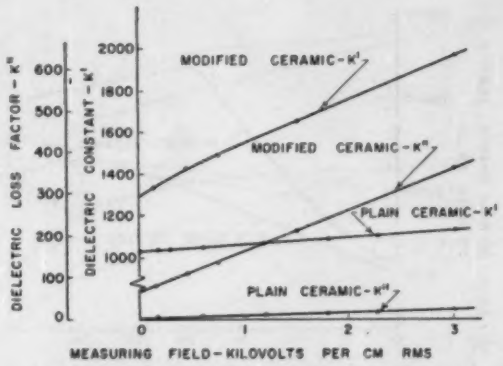
DIELECTRIC LOSS FACTOR - K''
DIELECTRIC CONSTANT - K'
MODIFIED CERAMIC - K'
MODIFIED CERAMIC - K''
PLAIN CERAMIC - K'
PLAIN CERAMIC - K''
MEASURING FIELD - KILOVOLTS PER CM RMS

FIG. 10. Effect of measuring field on the dielectric constant and dielectric loss factor of plain and modified ceramic. Both materials were aged, but the modified ceramic was de-aged by the measuring process.

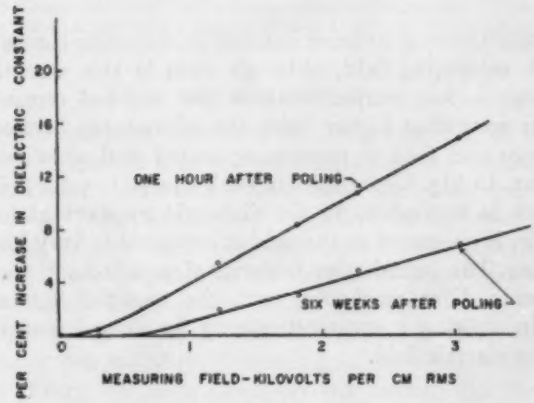
PER CENT INCREASE IN DIELECTRIC CONSTANT
ONE HOUR AFTER POLING
SIX WEEKS AFTER POLING
MEASURING FIELD - KILOVOLTS PER CM RMS

FIG. 11. Effect of measuring field on the dielectric constant of plain ceramic for aged and for freshly poled samples.

Curves of the dielectric characteristics of unpoled material as a function of the measuring field are presented in Fig. 10. At low fields all of the dielectric constants increase linearly as the field is raised. There is a very marked difference between modified and plain ceramic in the amount of loss and of increase in dielectric constant with field, but essentially no difference in the nature of the relationships. Both of these curves were taken by first measuring at the highest field and then going to lower fields. Under those conditions the modified material, but not the plain material, is in a de-aged condition.

In plain ceramic the behavior under ac measuring field is a function of the amount of aging it has undergone. Figure 11 represents the behavior of a sample which was measured after some months of aging, then repoled and measured 1 hr later. The freshly poled

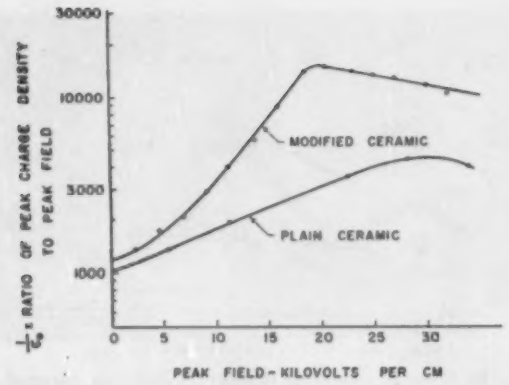

FIG. 12. Dielectric behavior of plain and modified ceramics under high ac field, calculated from oscillograph data. The quantity plotted as ordinate reduces to the dielectric constant at low fields.

sample shows a stronger increase in dielectric constant with measuring field, although even in this case the change is less marked than in the modified ceramic.

At somewhat higher fields the relationship between charge and field is more complicated and very nonlinear. In Fig. 12 the ratio of peak charge to peak field, which is equivalent to the dielectric constant at low fields, is presented as the field is increased to very high values. The quantitative behavior of modified and plain ceramic differ markedly, with the modified ceramic again showing a greater tendency for domain motion under electric field.

EFFECT OF COMPRESSION ON THE DIELECTRIC CONSTANT

Further evidence of the relative mobility of 90° domain walls in the modified ceramic is provided by experiments involving the mechanical deformation of the ceramic under compression. A convenient indicator of the amount of domain orientation which occurs during the process is the ratio between the dielectric constants in the directions parallel and perpendicular to compression. A compressive stress tends to orient a high proportion of the *c* axes of the crystallites perpendicular to the axis of compression, lowing the dielectric constant in these directions and raising it in the direction of compression (Figs. 13 and 14).

The experimental work was done on ceramic cubes of about one centimeter edge dimension, carefully lapped to make the sides parallel. The direction to be studied was painted with silver paste electrodes (these are satisfactory with thick samples). All samples were allowed to age for a minimum of four days before being tested. The capacity of the samples was measured before and during compression, and the aging of the capacity after compression was also determined. All measurements were made at 1 kcps on a General Radio 716-C capacity bridge. The compression was increased by uniform amounts to a maximum of about 10^8 newtons per square meter and then decreased to zero in the same manner. The total time under compression was about 25 min. It is seen that the maximum deviation in dielectric anisotropy from unity produced by the pressure is about 2.5 times as great in the modified ceramic as in the plain ceramic (Fig. 15). Here we define

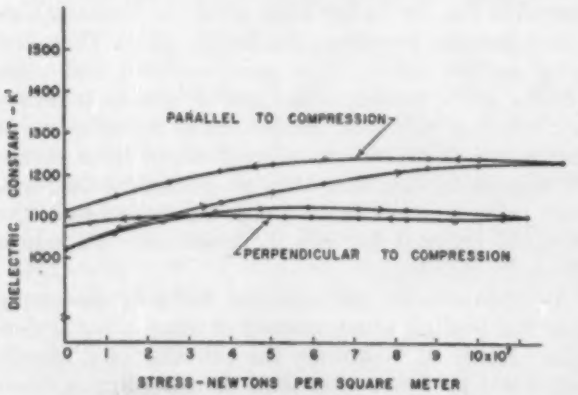

FIG. 13. Effect of compressive stress on the dielectric constant of plain ceramic.

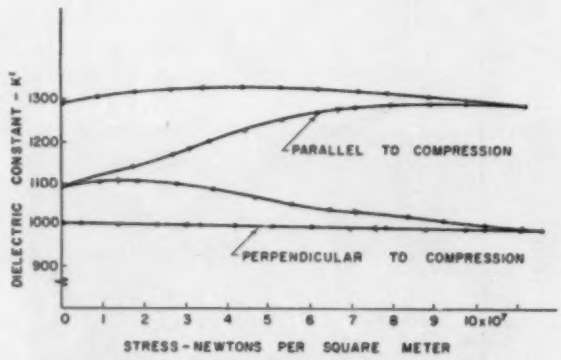

FIG. 14. Effect of compressive stress on the dielectric constant of modified ceramic.

the dielectric anisotropy as the ratio of the relative dielectric constant parallel to compression, to the relative dielectric constant perpendicular to compression.

It was also found that three days after compression no anisotropy was detectible in the plain ceramic. On the other hand, the dielectric anisotropy of the modified ceramic was still equal to 1.25, and there was no indication of substantial further change.

The conclusions reached from this experiment are as follows: (1) 90° domain switching due to externally applied mechanical stress occurs much more readily in modified than in plain ceramic. (2) The changes induced by stress are much more permanent in the modified ceramic.

Another interesting aspect of the experiment is the behavior of the K'' (dielectric loss factor) *versus* pressure curves (Fig. 16). For both plain and modified material the loss constants perpendicular to compression are considerably higher than those in the direction of compression. Possibly the reason for this is that an electric field in the direction of compression opposes stress-

induced domain growth, while perpendicular to the stress direction, the alternating field sometimes opposes and sometimes favors this motion. During the half-cycle in which field and stress are additive, considerable domain motion is to be expected. In both measurement directions K'' is higher for the modified than for the plain ceramic.

RESISTIVITY

The reason for the increased resistivity of lead zirconate titanate ceramics with off-valency additions has not been determined. Figure 17 is a comparison of the resistivity of plain and modified ceramic at temperatures up to 800°C. The measurements were not extended beyond this temperature because the possibility of lead oxide loss from the ceramic made the values uncertain. The results indicate that there is no change in conductivity mechanism over the temperature range studied. Possibly the oxygen vacancy concentration in the ceramic, which may be strongly influenced by impurity additions, determines its resistivity. It is known, for example, that the resistivity of titanium dioxide is a function of the oxygen pressure during measurement.[15] In addition, it is found with lead zirconate titanate, as with the alkaline earth titanates, that heating the material in the presence of a reducing agent causes it to become semiconducting. It has not been proved that the conductivity is due to oxygen vacancies, however, and the conductivity may well be associated with a completely different mechanism. The increased resistivity of the modified material may be caused by, for example, a compensation effect. The fact that bonding in these ceramics is partially ionic and partially covalent makes the determination of this mechanism quite difficult. It should be emphasized that variations do occur in measured resistivity from one batch of lead zirconate titanate material to another prepared under presumably identical conditions. These variations can amount to as much as one-half an order of magnitude, and they are probably due to minor changes in impurities and processing.

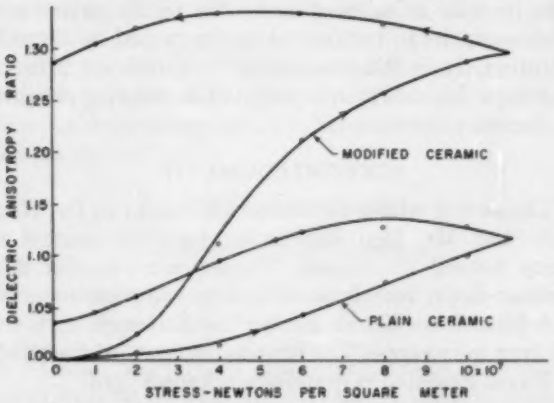

FIG. 15. Dielectric anisotropy produced by compressive stress in plain and in modified ceramic.

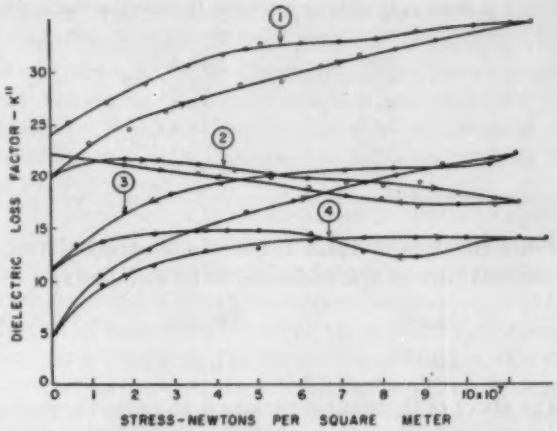

FIG. 16. Dielectric loss factor of plain and modified ceramic under compressive stress. Curve 1: Modified ceramic perpendicular to stress. Curve 2: Modified ceramic parallel to stress. Curve 3: Plain ceramic perpendicular to stress. Curve 4: Plain ceramic parallel to stress.

CONCLUSIONS

The hypothesis advanced for the occurrence of the changes found in lead zirconate titanate with niobium or lanthanum additions is that these effects are due to relatively high domain wall mobility in response to applied electric fields. In this respect these modified ceramics are assumed to be similar to plain ceramic immediately after an excitation process (voltage or temperature), which is also thought to possess high domain wall mobility, decreasing as the ceramic ages.

A theory has been developed to account for these effects. The common feature of the low-aging materials, both with 3- and 5-valent substituents, is the deliberate introduction into the lattice of materials which do not have the proper valence for the lattice positions which they probably assume. For example the ionic radii of the elements with which we are concerned are shown in Table I.

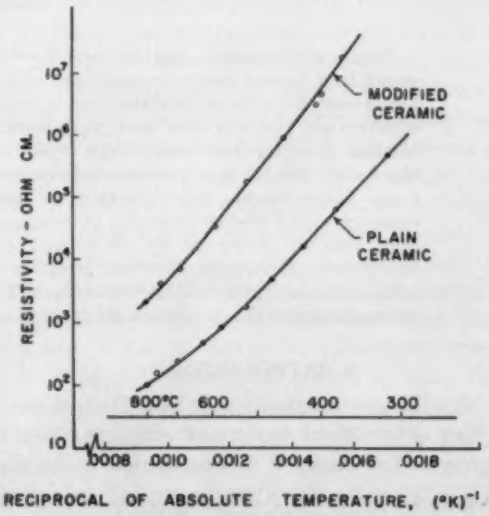

FIG. 17. Resistivity of plain and modified ceramic as a function of temperature.

[15] M. D. Earle, Phys. Rev. 61, 56 (1942).

TABLE I. Ionic radii of cations present in materials discussed.

Pb^{2+}	1.18 A
Ti^{4+}	0.64 A
Zr^{4+}	0.87 A
Sr^{2+}	1.18 A
La^{3+}	1.22 A
Nb^{5+}	0.70 A

From the data in Table I, one would expect the substitutional sites of the additions to be as follows:

La^{3+}	Pb site
Nb^{5+}	Ti, Zr site.

The effect of these substitutions is to cause vacancies, which maintain the valency balance, in the Pb position.[3] The vacancies, in a material whose ferroelectric properties are not destroyed by the disorder they introduce, may be expected to have a profound effect on domain wall motion under electrical and mechanical stress. This is because the elongation of the unit cell in the direction of the polarization results in very high local stresses on domains which have undergone 90° switching. These stresses may be relieved as switching continues by changes in the over-all dimensions of the ceramic. The presence of vacancies in the crystal minimizes the local stresses and makes some switching possible under low electrical or mechanical drive. The explanation of the reduced aging of the modified ceramics is that they are unable to store high stresses, since these are quickly relieved by domain motion.

While 180° domain switching causes no permanent deformation, there is probably a temporary deformation of the unit cell as it goes through the switching process, accounting for the energy requirement in this type of switching. Again the presence of vacancies in the lattice will facilitate the process.

Domain-wall motion is usually accompanied by hysteresis and is inherently a lossy process. Since one finds high mobility of domain walls in modified ceramic, it is not surprising that under low electrical and mechanical stress this material shows an increase in dielectric loss and a low mechanical Q.

Thus the marked changes in properties of lead zirconate titanate ceramics containing lanthanum or niobium substituents, such as the low aging and high electrical and mechanical losses, have been identified as related to a considerable increase in domain-wall mobility. The increase is believed to be due to the presence of lead vacancies in the crystal lattice caused by the substitution. It is felt that these data indicate a useful technique for the ceramic physicist in tailoring ceramics to desired properties.

ACKNOWLEDGMENTS

The author wishes to express his thanks to Dr. Hans Jaffe and Mr. Don Berlincourt for their counsel in many helpful discussions. Thanks are also due Mr. Delmar Kopp for his assistance in the measurements and Miss Rose Kozak for her careful work with the electron microscope. The financial support of the Office of Naval Research is gratefully acknowledged.

JOURNAL OF APPLIED PHYSICS VOLUME 31, NUMBER 1 JANUARY, 1960

Dislocation Structure and the Formation and Strength of Sodium Chloride Whiskers

W. W. WEBB
Union Carbide Metals Company, Division of Union Carbide Corporation, Niagara Falls, New York
(Received July 22, 1959)

Details of dislocation structure have been determined for a variety of NaCl whiskers and microcrystals grown from porous substrates moistened with supersaturated aqueous solution. Some of the smaller needle-like crystals have the single dislocation with an axial screw component usually assumed for whiskers. Larger whiskers and platelets often have much more complicated dislocation structures and may have higher dislocation densities than normal bulk crystals. Strengths were compared with dislocation structures and it was found that the nearly theoretical strengths observed in some of these whiskers are not due to merely a size effect but are directly related to the dislocation structure. Even crystals with high dislocation densities exhibited high strength in bending provided that all of the dislocations were so arrayed that they were not influenced by the applied stress. Regular dislocation arrays often occur naturally with this growth mechanism. However, irregular dislocation structures often associated with growth irregularities invariably resulted in low strength. Techniques for application of x-ray diffraction microscopy to determination of the dislocation structure of microcrystals are described.

I. INTRODUCTION

MORE is now known about NaCl whiskers than any other of the variety of whiskers which have been grown. Amelinckx[1–3] has succeeded in decorating individual dislocations in NaCl whiskers using the method of Barber, Harvey, and Mitchell,[4] and in developing etch pits at the intersection of dislocations with surfaces, and Webb[5] has reported preliminary corrobo-

[1] S. Amelinckx, *Growth and Perfection of Crystals* (John Wiley & Sons, Inc., New York, 1958), p. 139.
[2] S. Amelinckx, Phil. Mag. 44, 337 (1953).
[3] S. Amelinckx, J. Appl. Phys. 29, 1610 (1958).
[4] Barber, Harvey, and Mitchell, Phil. Mag. 2, 704 (1957).
[5] W. W. Webb, *Growth and Perfection of Crystals* (John Wiley & Sons, Inc., New York, 1958), p. 230.

rative observations of dislocations in NaCl whiskers using x-ray diffraction methods. Observations of mechanical properties of sodium chloride whiskers have been reported by Gluyai[6] and Gordon,[7] and Amelinckx[1] has observed the process of plastic deformation by means of etch pit techniques. Detailed mechanisms for two methods of growth have been worked out by Amelinckx.[1,2] No direct observations of the relation between detailed dislocation structure and strength of whiskers or microcrystals of any material have been reported in spite of the unique mechanical properties reported for many whiskers.

It is the object of this paper to report some features of the dislocation structure of NaCl whiskers determined using x-ray diffraction and etch pit techniques, and some related observations of deformation, strength, and morphology, and to utilize this work and published information to deduce a relatively complete description of the dislocation structure of NaCl whiskers, its origin and relation to mechanical properties. Some previously unavailable experimental details of the application of diffraction microscopy to detection of dislocations in whiskers are also given.

II. EXPERIMENTAL

(A) Preparation of Crystals

Whiskers of sodium chloride (and other alkali halide crystals) can be prepared readily in two distinct ways:

1. Crystallization in air from aqueous films on porous substrates such as unglazed ceramic or organic membranes as practiced by Kober,[8] Tauber and Kleiner,[9] Gluyai,[10] Amelinckx,[11] and Charsley and Rush.[12]

2. Crystallization in aqueous solutions containing "poisons" consisting of large, adsorbable organic molecules such as polyvinyl alcohol, as practiced by Evans,[13] Amelinckx,[1] and Gordon.[7]

Other techniques have also been reported, but most of the research to date has utilized crystals grown by one of the above methods.

Two variations of the first method with substrates of porous ceramic following Gluyai[10] and of cellophane following Amelinckx[11] were used in the present work. The well formed crystals obtained grew at rates between 10 and 1000 μ/hr by addition of material primarily at the base. Needles between 5 and 50 μ in thickness were obtained on both substrates and platelets in the same thickness range and up to 2 mm in width were obtained on the cellophane substrate. Lengths up to 15 mm were common. Some crystals were hollow or contained intermittent pores. All of the observed growth characteristics were consistent with the mechanisms proposed by Amelinckx[2,11] which involve addition of material at helical growth steps immersed in the aqueous film on the base of the whisker.

For comparison with observations on whiskers grown in "poisoned" aqueous solutions, the differences between that method of growth and growth from a porous substrate are noted. Growth in poisoned solutions occurs by addition of material at the free tip of the whisker, and branches at 90 degrees to the principal whisker axis are common.[1] In contrast, on whiskers grown from a porous substrate where material is added to the whiskers primarily at the base, branches are not formed. A small amount of "poison" is inevitably included in whiskers grown in solution, while those grown from a porous substrate can be of high purity.

Periodic microscopic observations and measurements of the positions of accidental defects or deliberately induced artifacts and the crystal ends indicated where material was added to the crystals during growth.

(B) Detection of Dislocations

1. Diffraction Methods

X-ray diffraction methods reveal individual dislocations in whiskers through two distinct manifestations: (a) gross lattice orientation changes due to the elastic strains associated with individual screw dislocations or dislocation arrays and (b) local perturbations of diffracted intensity at dislocation sites.

(a) *Lattice orientation.*—Eshelby[14] has shown that a screw dislocation component parallel with the major axis of a thin elongated crystal should produce an elastic twisting of the crystal lattice around the major axis. The magnitude of the twist is proportional to the net Burgers vector component parallel to the major axis and to the reciprocal of the cross section area of the crystal. Hence, by measurement of the elastic twist of the lattice around whisker axes, the net components of the Burgers vectors of screw dislocations parallel with the axes are determined. Eshelby[14,15] has derived appropriate solutions for the elasticity problem, and Dragsdorf and Webb[16] have described in detail experimental techniques for the measurements. In contrast with other methods for detection of dislocations, the sensitivity of this relatively specialized measurement increases as the size of the crystal decreases down to the minimum size ($\sim$1 μ) at which the diffracted intensity can be detected in a reasonable period of time. Only screw components parallel to the major crystal axis are detected and, indeed, even screw dislocations parallel

[6] F. Gluyai, Z. Physik **138**, 317 (1954).
[7] J. E. Gordon, *Growth and Perfection of Crystals* (John Wiley & Sons, Inc., New York, 1958), p. 219; See also, C. C. Evans and D. M. Marsh, Rept. No. 55, Tube Investments Research Laboratories, Cambridge, England.
[8] P. A. Kober, J. Am. Chem. Soc. **39**, 944 (1917).
[9] H. Tauber and I. S. Kleiner, J. Am Chem. Soc. **54**, 2392 (1932).
[10] Z. Gluyai, Z. Physik **125**, 1 (1948).
[11] S. Amelinckx, Physica **24**, 390 (1958).
[12] P. Charsley and P. E. Rush, Phil. Mag. **3**, 508 (1958).
[13] C. C. Evans, quoted by Amelinckx in reference 1 (1957).
[14] J. D. Eshelby, J. Appl. Phys. **24**, 176 (1953).
[15] J. D. Eshelby, Phil. Mag. **3**, 440 (1958).
[16] R. D. Dragsdorf and W. W. Webb, J. Appl. Phys. **29**, 817 (1958).

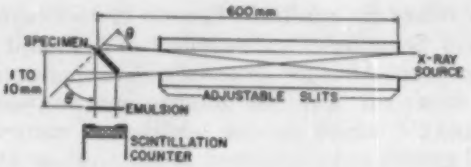

FIG. 1. Schematic drawing of apparatus geometry for diffraction microscopy. The emulsion is placed in the diffracted beam after the crystal has been aligned for Bragg reflection of characteristic radiation with the help of the scintillation counter.

with the crystal axis may give no manifestation of their presence through an "Eshelby twist" if there happens to be a pair having opposite signs of the Burgers vector screw components that are so arrayed that their lattice twists effectively cancel.

The above technique relies on measurements of high resolution Laue spots under near focusing conditions, so additional information on crystalline perfection similar to that obtained by the Guinier-Tennevin technique[17] is obtained by inspection of Laue spots. The resolution is such that lattice misorientations as small as 0.05 deg can be routinely detected and smaller misorientations may be observed if specifically sought.

(b) *Diffraction microscopy.*—Local perturbations of diffracting power in the vicinity of dislocations afford a means of detecting and mapping dislocations using a refinement of the well known Berg-Barrett technique[18,19] of x-ray diffraction microscopy. Lang,[20] Newkirk,[21] and Borrmann *et al.*[22] have refined these techniques sufficiently to make possible detection and mapping of individual dislocations in bulk crystals having relatively small dislocation densities, $<10^6$ cm^{-2}. The exact correspondence between the diffraction maps and the locations of dislocations determined by decoration and by etch pit techniques has been amply demonstrated by Lang and by Newkirk in silicon and in LiF.

The theory of the diffraction contrast observed in dislocations has not been worked out in exact detail, but a theory based on local lattice constant change and orientation changes has recently been proposed by Bonse[23a] and recently a further analysis of this problem by Newkirk[23b] has appeared. One criterion for contrast is that there must be a component of the dislocation Burgers vector along the diffraction vector (that is, perpendicular to the diffracting lattice planes).

Lang[24] has given an analysis of the pertinent diffraction geometry, and Webb[5] has reported preliminary results of the application of diffraction microscopy to whiskers, but the experimental details unique to the study of whiskers have previously been reported only orally,[25] so are described here.

Figure 1 shows the diffraction geometry schematically. The x-ray source placed 600 mm from the specimen is a standard diffraction tube arranged so the projected area of the anode spot is about 1 mm square. Adjustable slits at the specimen limit the size of the beam, although the entire specimen is usually illuminated and a set of adjustable slits in front of the anode can be used to reduce the effective source size, whenever necessary. The crystal is mounted on a eucentric goniometer head in an Eulerian cradle[26] on a diffractometer equipped with a scintillation counter with a large window to facilitate orientation for diffraction from various sets of diffracting planes. Photographic plates are held close to the specimen with a rigid micromanipulator to record the diffraction micrographs.

Eastman NTB nuclear plates and Eastman High Resolution plates are used. With hard radiations, MoKα and AgKα, NTB plates, 25 to 50 μ thick, permit exposure times on the order of a few minutes with a useful photographic resolution of 5 to 10 μ. Thinner NTB plates are satisfactory with softer radiations. For special situations where ultimate resolution is required, "high resolution" plates are exposed for periods up to 48 hr to obtain a useful photographic resolution of better than 5 μ.

The geometry of the system is so chosen that the beam divergence, the wave length range between $K\alpha_1$ and $K\alpha_2$, and the natural diffraction width of a perfect crystal all yield roughly the same resolution limit. Under normal conditions, the critical geometric factor is the specimen-to-emulsion distance which has been maintained between 2 and 10 mm to yield resolutions consistent with the photographic resolution available from short exposures. By limiting the x-ray beam width to <0.1 mm to eliminate diffraction of $K\alpha_2$ radiation, placing the emulsion 1 mm from the specimen, and using long photographic exposures on high resolution plates, substantially better resolution is available for special purposes.

Crystals that are much larger than 1 mm (the maximum effective x-ray source size) in a direction perpendicular to the diffracting planes or that are deformed yield diffraction micrographs from only a part of their volume for any particular orientation. Lang[20] has examined bulk crystals by translating the crystal and film together through a narrow ribbon beam. For relatively small crystals, such as most whiskers, it suffices to rotate the crystal through a small angle, say 1 deg, around an

[17] A. Guinier and J. Tennevin, Acta Cryst. **2**, 133 (1949).
[18] W. Berg, Krist **89**, 286 (1934); Naturwissenschaften **19**, 391 (1931).
[19] C. S. Barrett, Trans. Am. Inst. Mining Met. Engrs. **161**, 15 (1945); see also C. S. Barrett *Structure of Metals* (McGraw-Hill Book Company, Inc., New York, 1952), pp. 95–99.
[20] A. R. Lang, J. Appl. Phys. **29**, 597 (1958).
[21] J. B. Newkirk, J. Appl. Phys. **29**, 995 (1958); Phys. Rev. **110**, 1465 (1958).
[22] Borrmann, Hartwig, and Irmler, Z. Naturforsch. **13a**, 423 (1958).
[23] (a) W. Bonse, Z. Physik **153**, 278 (1958); (b) see also M. J. Whalen and P. B. Hirsch, Berlin Conference on Electron Microscopy (1958).
[24] A. R. Lang, Acta Met. **5**, 358 (1957).
[25] W. W. Webb, oral presentation at Pittsburgh Diffraction Conference (1958).
[26] T. C. Furnas, Jr., and David Harker, Rev. Sci. Instr. **26**, 449 (1955); see also T. C. Furnas, "Single crystal orienter," General Electric Company (1957).

axis perpendicular to the plane defined by the incident and diffracted beams or to use a larger effective x-ray source size. There is, then, a small loss in resolution which depends on specimen-emulsion spacing, but the technique is useful in many cases.

In order to determine Burgers vector directions, to locate precisely dislocation sites within the crystals, and to distinguish between diffraction contrast due to dislocations and that due to surface features, it is necessary to record diffraction micrographs using several orientations of the crystal with respect to the x-ray beam. To describe the orientations used, the angle ψ between the growth direction $\bar{A}$ and the diffraction vector $(\bar{S}-\bar{S}_0)$ and the angle ϕ between $(\bar{S}-\bar{S}_0)$ and the normal $\bar{N}$ to one of the largest faces of the crystal are defined. The vector $\bar{S}_0$ describes the direction of the incident beam and $\bar{S}$ is the diffracted beam. In all of the experiments discussed, the plane including $\bar{A}$ and $(\bar{S}-\bar{S}_0)$ and the plane including $\bar{S}$ and $\bar{S}_0$ are orthogonal. Figure 2 shows these angles identified for a platelet at $\psi=90°$, $\phi=90°$, a useful arrangement.

The emulsion (not shown in Fig. 2) is placed perpendicular to $\bar{S}$, the diffracted beam, and measurements of the positions of features in two (or more) diffraction micrographs suffice to locate them by appropriate geometric projections.

2. *Etch Pit Techniques*

A variety of etching techniques have been used to detect dislocations in NaCl by the development of etch pits. In the present work, an etch developed by Moran[27] consisting of a 1% solution of mercuric chloride in anhydrous ethanol followed by a carbon tetrachloride rinse was found most useful. Pyramidal and occasionally flat-bottomed pits were obtained on whiskers. The flat-bottomed pits produced by this etch were not reproducible and are apparently not associated with dislocations, so in the etch pit patterns presented here they should probably be disregarded.

III. GENERAL OBSERVATIONS

(A) Growth Forms

Well formed, fully transparent filamentary crystals in the form of needles of square cross section from 2 to about 200 μ thick and platelets from 2 to 20 μ by 20 to 2000 μ in cross section were produced in lengths up to 1 cm. Platelets formed on cellophane membrane substrates, but not on porous ceramic substrates. Needle-like whiskers growing on the cellophane membrane were only tenuously attached, and a touch with a needle sufficed to upset them so that a lateral surface lay on the moist cellophane. Subsequently, the upset whiskers usually resumed growth as platelets, as Amelinckx[11] predicted.

Growth steps occur on the lateral surfaces of many whiskers, but they remain at a fixed distance from the outer end during growth. They are due to a change in the thickness of the whisker initially formed by addition of material at the base from solution rather than due to thickening by migration of a film of solution up the sides of the whisker and deposition of additional material on the lateral faces subsequent to initial growth.

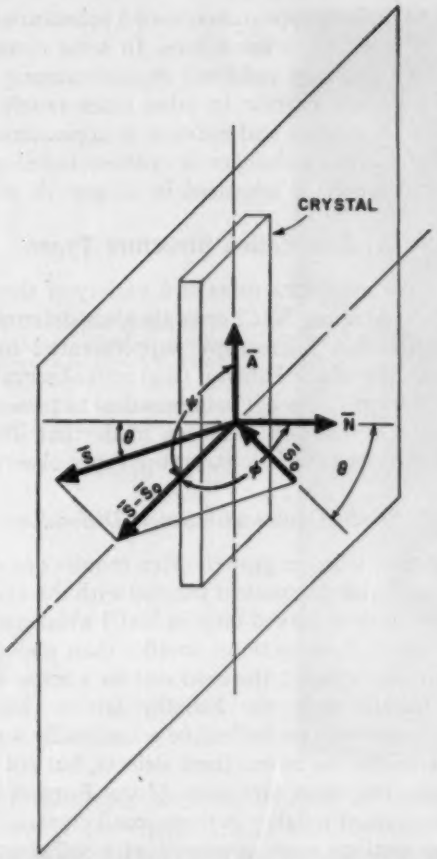

FIG. 2. Definitions of crystal orientation with respect to diffraction vectors. The incident beam is $\bar{S}_0$, $\bar{S}$ is the diffracted beam, $\bar{A}$ the major axis (growth direction) of the crystal, and $\bar{N}$ is a normal to the largest lateral crystal faces. The angle between $\bar{A}$ and $\bar{S}-\bar{S}_0$ is ψ and that between $\bar{N}$ and $\bar{S}-\bar{S}_0$ is ϕ.

With only one exception, the growth occurred in a [100] direction and the lateral surfaces were found to be (100) planes. The exception, a platelet with a [110] growth direction, appears to have formed by tipping of a whisker to about a 45° angle with the substrate so that growth occurred on part of one lateral surface to yield a platelet with a [110] growth direction with (100) planes parallel to the wide lateral surfaces, and (110) planes parallel to the narrow lateral surfaces.

In addition to the well formed, fully transparent filamentary crystals of needle- or plate-like form, many irregular crystals of variable form were found. Some of these have abrupt changes in cross-sectional area. Some platelets which vary in thickness or width divided into a cluster of parallel needles on variation of growth conditions. The fraction of crystals formed which are regu-

[27] P. R. Moran, J. Appl. Phys. **29**, 1768 (1958).

lar and smooth in appearance varied substantially with details of the growth conditions. In some cases it was difficult to find any euhedral crystals among the ill-formed crystals, whereas in other cases nearly all the crystals were smooth and uniform in appearance. Some examples of sudden changes in cross-sectional area and cross-sectional shape appeared in all growth attempts.

(B) Dislocation Structure Types

The dislocation structures of a variety of shapes and sizes of filamentary NaCl crystals were determined by x-ray diffraction microscopy supplemented by x-ray measurements of the Eshelby twist and observations of etch pit patterns. Since it is impractical to present all of the results, a selection has been made that illustrates most of the characteristic structure types observed.

1. Small Needles with Single Dislocation

Theories of whisker growth often require one dislocation with a screw component parallel with the axis. Such structures were observed only in NaCl whiskers having nearly square cross sections, smaller than about 20 by 20 μ. In these crystals, the evidence for a screw dislocation is usually only the Eshelby lattice twist. The diffraction microscopy technique occasionally was sufficiently sensitive to reveal these defects, but not clearly enough for the exact directions of the Burgers vectors to be ascertained reliably in these small crystals. Where the cross sections were measured with sufficient precision to yield good values of the net Burgers vector component parallel to the whisker axis, the values obtained fell between 2 and 4 A. This is consistent with a prime Burgers vector $b=a/2[110]=3.97$ A with an axial component 2.81 A as expected from the work of Amelinckx[1] but is not uniquely demonstrated by these experiments. However, that this is the most probable configuration will be demonstrated from results on more complex structures to be discussed. One example yielded an axial component of 5.6 A consistent with $b=a[100]$ or $a[110]$. To indicate the distinctness of the manifestation of lattice twist due to these small Burgers vectors, Fig. 3 shows a pair of high resolution Laue spots, one from a small NaCl whisker with a net Burgers vector around 2 A and the other from a metal whisker that shows no evidence for dislocations.

A few tubular NaCl needles about 20 to 80 μ thick

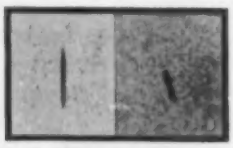

FIG. 3. Equatorial high resolution Laue spots from (left) a metal whisker about 5 μ thick with no Eshelby twist and (right) a NaCl whisker about 12 μ thick with an Eshelby twist due to an axial screw dislocation Burgers vector component of about 6 A. Difference in length of spots is due to different lengths of whiskers in beam. Magnification 7×.

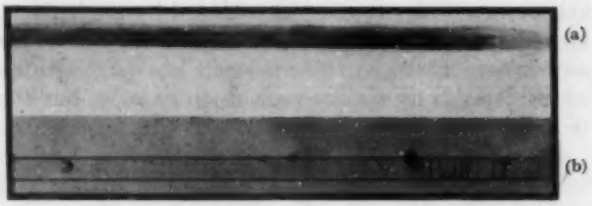

FIG. 4. (a) Part of diffraction micrograph of whisker containing 2 dislocations. Diffracting planes (200) perpendicular to growth direction ($\psi=90°$, $\phi=90°$). High resolution plate ~66×. (b) Photomicrograph of part of whisker yielding pattern shown in Fig. 4(a). Transmitted light. Note thin, dark line parallel to growth direction due to internal pore along dislocation core in part of crystal. Transverse lines are edges of growth steps on the surface. Transmitted light ~66×. Different portions of the crystal represented in the two illustrations.

with about 5-μ wall thickness were found growing on porous ceramic substrates. Several were observed to have a pronounced Eshelby twist. Diffraction micrographs of these crystals showed no evidence for lattice defects other than the Eshelby torsional strain and the hole along the whisker axis.[5] The axial twists correspond to Burgers vectors ~100 A (following Eshelby,[15] a small correction for the pore is included in the Burgers vector calculation). The fact that the axial pore corresponds to the dislocation core was demonstrated by cracking one of the crystals parallel with its axis, thus relaxing the elastic strain after which the Eshelby twist was found to have disappeared as expected. Hollow dislocation cores have also been observed in α-Al_2O_3 whiskers by Webb and Forgeng,[28] but in this case, the holes are only ~1 μ thick.

A number of relatively large crystals up to 1 mm diam, formed by growth on a cellophane membrane, were observed to contain many nearly parallel holes about 1 to 5 μ in diam. The arrangement of the holes was similar to complex dislocation structures observed in platelets to be discussed below, and it was inferred from this that these holes also form at dislocation cores and are an extreme case of the "hopper crystal" growth described by Amelinckx.[2,11]

2. Paired Dislocations in Nearly Perfect Whiskers

Many strong NaCl needles and narrow platelets up to about 25 by 50 μ were found to be entirely free of Eshelby twist. Prior to study of these crystals by diffraction microscopy, there were two alternative explanations for this observation: either these whiskers are free of screw dislocations parallel with the growth axis, or they contain a symmetrically spaced pair having opposite Burgers vectors. Diffraction microscopy results have confirmed the second alternative in all cases studied. Figure 4(a) is an enlargement of a diffraction micrograph showing two parallel dislocations in part of a crystal that had no Eshelby twist. A photomicrograph, Fig. 4, of part of the crystal producing this pattern

[28] W. W. Webb and W. D. Forgeng, J. Appl. Phys. **28**, 1449 (1957).

reveals that one of the dislocations has a hollow core over part of its length. The hollow portion of the dislocation does not show diffraction contrast in any orientation. Growth steps on the surface, such as those shown in Fig. 4(b), do not yield a strong contrast effect in diffraction micrography.

The greatest perfection (on a dislocation density basis) found in any of the NaCl whiskers studied was found in platelets on the order of $10\,\mu \times 250\,\mu$ in cross section and about 10 mm long. Only two dislocations at most were present in these crystals. Figure 5 shows an attempt to reproduce two diffraction micrographs of part of one of these crystals. There are two dislocations present parallel to the axis, one near each edge. The diffraction contrast is barely visible in these photographs since they were recorded on high resolution (low contrast) plates to reveal the smallest defects. No other defects were detected. Several micrographs recorded by diffraction from planes perpendicular to the whisker axis were so arranged that the possibility of confusion of enhanced diffraction from the edges of the crystal with manifestations of dislocations was eliminated. The Burgers vectors of these dislocations are both oriented in or near [110] type directions in the plane of the platelet such that the screw components are opposite. Figure 6 is a photomicrograph of this platelet which formed by unidirectional growth of part of one side of a thin whisker (visible at top of the platelet) which had fallen onto the cellophane substrate. The tip is highly imperfect, but most of the imperfections did not propagate into the main body of this platelet during growth.

FIG. 6. Photomicrograph in reflected light of platelet yielding diffraction pattern shown in Fig. 5; whisker, part of which developed into platelet, is visible at top. Transverse lines are growth steps. ~100×.

3. Imperfect Needles and Platelets

A small fraction of the needle-shaped crystals, less than $50\,\mu$ thick, exhibit large Eshelby twists corresponding to Burgers vectors on the order of 20 to 400 A but show none of the characteristic manifestations of dislocations in diffraction micrographs nor, in some cases, could any unusual defects be seen in microscopic examination. It is most likely that these crystals actually contain a high density of arrayed dislocations too closely spaced to permit resolution of individual defects by diffraction microscopy. Several of these needles were shown by high resolution Laue techniques to contain several parallel elongated crystallites misoriented by rotations up to 1 deg around the [100] longitudinal axis of the crystal.

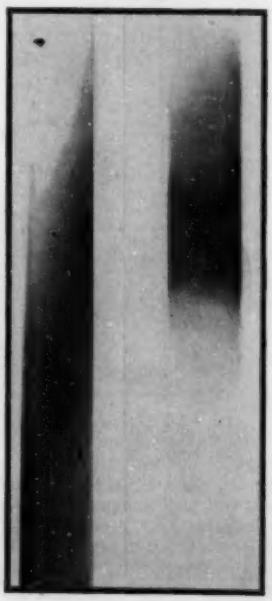

FIG. 5. Diffraction micrographs of a small part of nearly perfect NaCl platelet. Lines of faint contrast due to two dislocations are barely visible near edges of the patterns. The diffraction contrast is most visible near the left-hand edge of the left-hand pattern. Black specks and slight mottling are irreproducible artifacts. Diffracting planes (200) $\phi=90°$, $\psi=90°$ left, $\psi=0°$ right. High resolution plate ~100×.

The majority of the larger platelets contain spectacular arrays of dislocations parallel to the growth direction. Figure 7 shows a set of diffraction micrographs of a platelet $22\,\mu$ by $760\,\mu$ in cross section by 5 mm long. Microscopic examination showed no visible internal structure except at the tip; some surface growth steps were visible on the surface, as shown in the photomicrograph taken with reflected light in Fig. 8. There may be correspondence between some of the visible structures at the tip and several of the defects shown in that part of the diffraction micrographs. The fact that nearly all of the dislocation lines can be identified in diffraction micrographs taken both from diffracting planes perpendicular to the plane of the platelet and parallel to the growth direction but perpendicular to the plane of the platelet suggests that with a few possible exceptions, all of the Burgers vectors lie near [110] directions at 45 deg to the growth axis. Two slightly crooked dislocations *may* be pure screw dislocation with [001] Burgers vec-

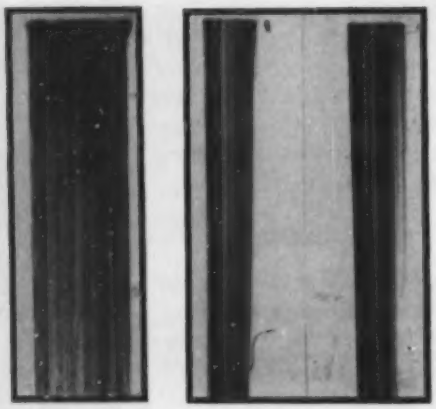

(a) (b)

FIG. 7. (a) Diffraction micrograph of large platelet (shown in Fig. 8) containing many nearly parallel dislocations with screw components parallel to the growth direction. Note several irregular dislocations near center of platelet Diffraction from (200) type planes at $\psi=0°$, $\phi=90°$ with crystal rocked through the diffraction angle. NTB 17×. (b) Diffraction micrographs of platelet shown in Fig. 8 Diffracting planes (200) at $\psi=90°$, $\phi=90°$, and perpendicular to platelet faces. Platelet rotated 180 degrees around growth direction between exposures to $\phi=270$ deg and one plate printed in reverse for comparison. Not all individual dislocations are resolved in these prints. NTB 17×.

tors in the growth directions since they do not appear on diffraction at $\psi=90$ deg, although they may be hidden by other nearby dislocation lines. Most dislocations run the entire length of the crystals, but a few terminate at lateral surfaces, as can be seen in Fig. 7(a).

Irregular dislocation networks with triple points, curved dislocation lines, and straggling dislocations that terminate at lateral surfaces are observed in some crystals. The networks are similar to those Amelinckx[1] observed by decoration of dislocations in sodium chloride whiskers grown in poisoned solutions.

Some examples of some irregularities observed in one platelet 5 to 10 μ thick are shown in Figs. 9 and 10.

The small-scale diffraction micrographs presented in Figs. 9(a) and (b) show evidence between A and A' for combination of a pair of adjacent dislocations parallel to the growth direction with mutually perpendicular (110) type Burgers vectors to form a (100) edge dislocation with Burgers vector perpendicular to the growth direction for part of the length. Where this occurs there is no contrast in Fig. 9(b) because the Burgers vector and diffraction vector are there mutually perpendicular. Figure 10 is a larger-scale print of part of Fig. 9(a) showing that the closely spaced dislocations are irregular and crooked with occasional triple points with branches intersecting the surface. Along one edge of the platelet at B some heavy local plastic deformation has formed clusters of unresolved dislocations that appear as dark blurs. Several closely spaced dislocations near this same edge are perturbed at C where a change in the growth thickness of the platelet occurs. It is not clear whether several dislocations combine and possibly annihilate here or whether they meet the lateral surface at the growth steps due to the thickness change. The straight diagonal lines near D are slip bands induced by careless handling. They are discussed further below.

FIG. 8. Photomicrograph in reflected light of platelet yielding diffraction micrographs shown in Figs. 7(a) and (b). All visible detail is on surface, except at tip. No internal defects could be detected optically, even with transmitted light. ~17×.

4. *Plastic Deformation*

Light plastic deformation in bending of relatively imperfect whiskers usually resulted in slip on several sets of (110) slip planes. The Burgers vector directions, [110] type, in each slip band can be deduced from the relative intensities diffracted from the slip bands with various sets of diffracting planes. Diffraction microscopy results on a lightly deformed, relatively imperfect platelet about 200 μ wide are presented in Figs. 11 and 12. The micrographs were briefly exposed to avoid overdarkening of the slip bands, so the grown-in dislocations

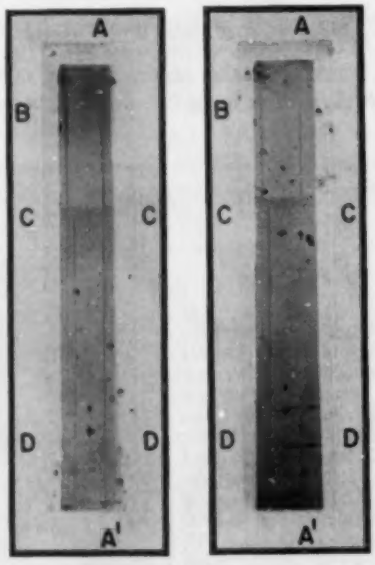

(a) (b)

FIG. 9. Diffraction micrographs of a platelet containing several irregular dislocations—a combining dislocation pair between A and A', edge damage at B, a change in thickness at C, and some light slip bands near D. Note that the combined pair, A-A', shows no contrast in (b) in the combined section since the Burgers vector is there perpendicular to the diffraction vector. See enlargement of top portion of (a) shown in Fig. 10. (a) $\psi=90°$, $\phi=90°$; (b) $\psi=0$, $\phi=90°$. NTB 15×.

are underexposed and are barely visible. The three diffraction micrographs in Fig. 11 may be compared with the etch pit pattern in Fig. 12, and a one-to-one correspondence between slip bands will be found. These slip bands contain many closely spaced dislocations that are only partially resolved in the etch pit patterns and are not at all resolved in the diffraction micrographs. Very small amounts of slip do, however, sometimes yield resolvable dislocation structures in the slip bands in these crystals. Only those dislocations having a component of their Burgers vector perpendicular to the diffracting planes (parallel to the diffraction vector) show in a diffraction micrograph. Figure 13 shows the contrast expected from various [110] Burgers vectors for the three diffraction micrographs shown in Fig. 11. Comparison demonstrates that only [110] type Burgers vectors are represented.

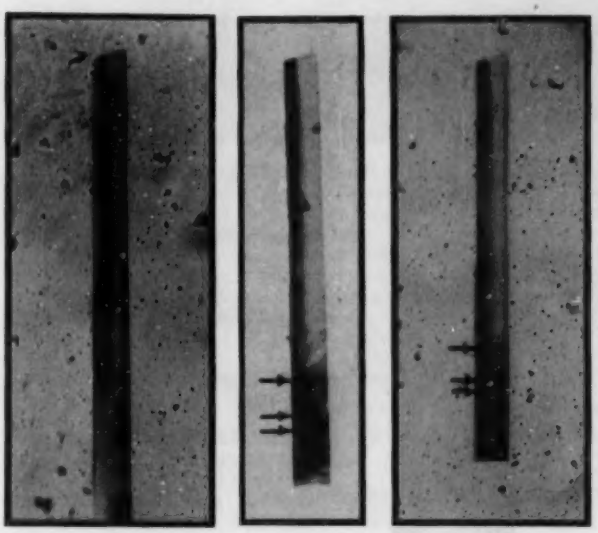

FIG. 11. Diffraction micrographs of a platelet plastically deformed in bending showing axial dislocations and slip bands. (a) (200) planes $\psi=90°$, $\phi=90°$; (b) (200) planes $\psi=0°$, $\phi=90°$; (c) (220) planes $\psi=45°$, $\phi=90°$. Note that differences in relative intensities of various sets of slip bands with change in orientation of diffracting planes agree with those predicted in Fig. 13 for [110] Burgers vectors in 110 slip planes. NTB 17×.

IV. MECHANICAL PROPERTIES AND DISLOCATION STRUCTURE

The unique property from which the current interest in whiskers and microcrystals of nominally plastic materials originated is the exceptional mechanical strength of these crystals. This exceptional strength, which often approaches the theoretical strength of perfect crystals, is attributed in many cases to the absence or paucity of dislocations. It is a well known feature of the mechanical properties of whiskers that there is startling variability from specimen to specimen. Crystals of identical appearance may display nearly theoretical strength or may be weak. In spite of concern about this variability, no direct experimental comparison of mechanical strength with dislocation structure in whiskers has previously been accomplished due to the lack of a reliable method for direct determination of the dislocation structure of individual specimens.

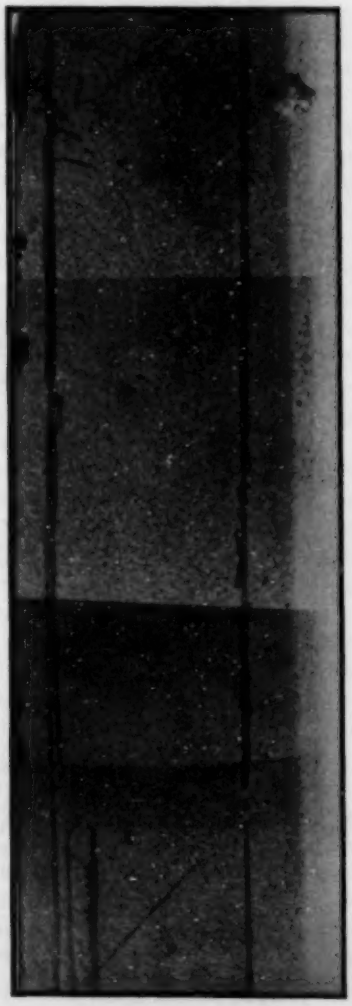

FIG. 10. Enlargement of part of the diffraction micrograph shown in Fig. 9(a) showing irregular dislocation structure in detail.

With the object of determining the relationship between dislocation structure and strength in whiskers of sodium chloride, bend tests were carried out on typical samples of the various types described in the preceding section of this paper, and some bend tests have been carried out on specimens for which the dislocation structure has been determined in great detail by diffraction microscopy.

(A) Average Mechanical Properties

Free bend tests of a large sample (about 20) of sodium chloride crystals were carried out by progressively bending and relaxing firmly mounted crystals with a precision micromanipulator and measuring the strains attained without permanent damage. Details of technique were described by Webb and Forgeng.[29] The experi-

[29] W. W. Webb and W. D. Forgeng, Acta Met. 6, 462 (1958).

FIG. 12. Etch pit pattern of platelet yielding diffraction micrographs in Fig. 11. Note correspondence of slip bands. Prominent reference marks for comparison marked with arrows. 29×.

ments indicate that nearly all whiskers with less than 100 μ^2 cross-sectional area could be expected to show high elastic limits at >1% elastic strain. The mode of failure was usually by brittle fracture. The behavior of nearly all relatively large crystals with cross-sectional areas >1000 μ^2 was also consistent; the elastic limits were always low, and failure occurred by plastic deformation. In the intermediate size range, behavior was less consistent, and no a priori prediction of strength or mode of failure was possible. For example, stressing of different parts of the same crystal occasionally produced brittle fracture on the first test at high stress and plastic yielding at about the same stress on the second. Detailed observations of the elastic limit and mode of failure of crystals of known dislocation structure in this intermediate size range are described later.

Whiskers which failed by plastic deformation after sustaining substantial elastic strains exhibited a sharp yield point and could subsequently be further plastically deformed at stresses <0.1 initial yield stress. This result was not investigated quantitatively because the bend test method was not regarded as sufficiently precise, but the qualitative result was fully reproducible. This pronounced yield point is in contrast with the results on the bulk crystals and on whiskers grown in poisoned aqueous solutions which apparently do not show sharp yield points.[30,31] Brenner has attributed the lack of a sharp yield point in many whiskers grown in poisoned solutions to a solution hardening effect due to inclusion of molecules of the poisoning agent during growth.[32]

On deforming some weak whiskers in tension, slip was often confined to a single set of slip planes in relatively large regions of the crystal with the result that very large plastic strains (on the order of 50%) were obtained without fracture. Figure 14 shows one of these crystals. The very broad slip bands formed in this way indicate that slip is initiated at only a few sites and then propagates by broadening of the slip band at stresses sufficiently low that initiation of slip in unperturbed portions of the crystal is avoided. Evans has observed similar slip bands in alkali halide whiskers grown from poisoned solutions.[7]

(B) Aging Effects

In contrast with the behavior of ordinary large NaCl crystals[30,31,33] prolonged exposure to the atmosphere had no apparent effect on the ability of the microcrystals to plastically deform. Even after storage in air for a year, most filamentary crystals that did not have nearly theoretical strength could be plastically deformed readily.

An experiment was carried out to determine whether the difference between microcrystals and bulk crystals might be due to a paucity of diffusion paths for impurities along dislocations in the whiskers. Dislocations were introduced into a set of similar platelets each about 100 μ wide and 10 μ thick by dropping 150-μ aluminum oxide abrasive grains on them from a height of about 20 cm. That many clusters of dislocation loops are introduced by this treatment was shown by diffraction

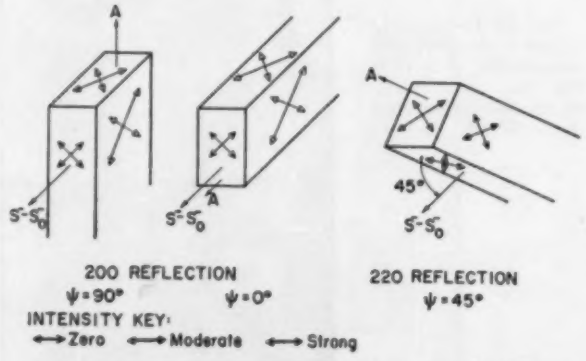

FIG. 13. Diffraction contrast intensity for various [110] Burgers vectors in the diffraction geometry used in Fig. 11. The most obvious feature confirming this scheme is the lack of contrast from slip bands running from upper right to lower left in Fig. 11(c).

[30] W. Dekeyser, Acta Met. 4, 557 (1956).
[31] Gorum, Parker, and Pask, J. Am. Ceram. Soc. 41, 161 (1958).
[32] S. S. Brenner, *Growth and Perfection of Crystals* (John Wiley & Sons, Inc., New York, 1958), p. 157.
[33] Joffe, Kirpitschewa, and Lewitsky, Z. Physik 22, 286 (1924).

microscopy, results of which are presented in Figs. 15–17. Half of the crystals were immediately plastically deformed by free bending about 30 deg; none fractured. All were then stored for 90 days in air and were again plastically deformed in bending. All could still be further deformed without fracture. Apparently the difference between aging effects in these filamentary crystals and bulk NaCl crystals is not due to differences in dislocation structure since introduction of neither small dislocation loops nor slip bands leads to deleterious aging characteristics under conditions that result in brittleness in bulk sodium chloride crystals.

(C) Direct Association of Strength and Deformation Mechanisms with Grown-In Dislocation Structure

With the object of determining the relationships between dislocation structure and strength in whiskers, tests of yield strength in bending were carried out on six relatively perfect platelets and whiskers, several crystals that had been deliberately damaged, and numerous relatively imperfect crystals after the dislocation structure of all of these crystals had been determined in some detail by diffraction microscopy. In a few cases, the dislocation structures generated by the bend test were also studied.

It was determined that with only one exception those relatively perfect crystals that contained only one or two dislocations running the full length of the crystal parallel with the growth direction, such as those illustrated in Figs. 5 and 6 would withstand elastic strains between 0.2 and 1% before precipitous failure, either by plastic deformation or brittle fracture. One crystal failed by plastic bending near one end and after remounting failed at roughly the same strain, 0.23%, by brittle fracture near the other end. Both acicular crystals and platelets were included in this group. Pains were taken to avoid surface damage before testing.

Within the limits of observation in the diffraction micrographs (about 10 μ), all the dislocations in the strong crystals were straight. The Burgers vectors were in every case at an angle of $\sim$45 deg with the growth direction (and, thus, the dislocation line direction), so the dislocations were of mixed edge and screw character. In the cases where a careful determination of Burgers vector direction was made by diffracting from several different sets of planes, the Burgers vectors appeared to be in or near [110] type directions at 45 deg to the [100] growth direction. All of the less detailed determinations are also consistent with this type of dislocation. Therefore, glide of the grown-in dislocations in the strong crystals might be expected only on (100) glide planes . Although all of the dislocations in strong crystals appeared straight, the possibility of dislocation segments lying in (100) planes perpendicular to the growth direction and, thus, glissile on (110) planes is not excluded by the diffraction microscopy results since the

FIG. 14. Photomicrograph of plastically deformed whisker showing heavy slip in very wide slip bands. Original width of the crystal is that of widest parts shown where slip has occurred on (110) planes at a 45-deg angle to plane of photomicrograph reducing thickness by about $\frac{1}{2}$. Surface steps due to slip bands are visible. Narrow sections are reduced in width by about $\frac{1}{2}$ by slip on (110) planes perpendicular to the plane of the photomicrograph. Transmitted light, magnification 74×.

critical glissile segment length long enough to glide at ordinary stresses is $\sim$0.1 μ, which could not be resolved by the diffraction techniques. Although the stress for glide of existing dislocations on (100) planes in NaCl type structures should be substantially higher than on (110) planes, the difference is too small to account for the near-theoretical strength.

However, in the platelets the grown-in Burgers vector directions were all in the plane of the platelet so that a careful bend test around a bend axis in the plane of the platelet exerts no force on them. Furthermore, all of the dislocations observed in strong crystals were on or near the neutral axis during bending, so were not stressed to the maximum fiber stress. Therefore, the observation that the presence of certain grown-in dislocations is not necessarily detrimental to whisker strength is not so surprising. In fact, the one dislocation configuration that was observed to yield nearly theoretical strength in bending is an array of one or more straight or nearly straight edge dislocations of mixed character parallel to the growth direction and near the neutral axis in bending. The well known observation that the strengths of whiskers measured in bend tests are consistently higher than those found in tension tests is accounted for by this sort of dislocation structure.

Platelets containing many dislocations, like those shown in Figs. 7 to 10, invariably failed at immeasurably low strain ($<$0.01%) by plastic deformation and could be plastically deformed heavily before cracking, as shown in Fig. 14. This was also true of the other relatively large crystals up to about 0.5 mm thick, although some of them occasionally failed by brittle fracture.

The strengths of several nearly perfect platelets containing a few dislocations that were either not straight or that displayed local branching or other irregularities of the type illustrated in Figs. 9 and 10 were determined. None of them displayed near-theoretical strength, and plastic deformation was initiated at some of these irregularities. Details of the initiation of slip in some of these crystals will be published later.

(D) Extraneous Damage and Whisker Strength

In order to investigate the possibility that a substantial portion of the known variability of strength of whiskers in any given size range is due to surface damage

and to estimate the ease with which damage is incurred, the effect on strength and perfection of deliberate attempts to introduce damage was studied.

In order to estimate the sensitivity of NaCl whiskers to accidental deformation and, at the same time, to determine the sensitivity of the diffraction microscopy technique for detection of isolated dislocations, nearly perfect platelets of high strength (see Figs. 15, 5, and 6, for example) were subjected to various attempts at deformation. Lightly rubbing the surface with a needle or with another whisker produced no defect visible in diffraction micrographs and no measurable loss of elastic strength. However, holding a whisker lightly with a pair of watchmaker's forceps invariably produced gross damage even when the nominal jaw pressure was low, probably because stress concentrations occurred at rugosities on the jaws of the forceps. Handling a mass of detached whiskers usually resulted in damaged edges with accompanying catastrophic loss of strength. The diffraction micrographs in Figs. 9 and 10 show the sort of highly localized damage that results. Often, slip bands extending well across the crystal also appear having evidently nucleated at the sites of local edge damage. Isolated slip bands are usually extremely difficult to detect in the optical microscope but, as is evident from Figs. 9 to 13, are obvious in diffraction micrographs.

Another estimate of the susceptibility of whiskers to surface damage was obtained by dropping aluminum oxide abrasive grains on the surface from various heights following the technique of Gilman.[34] Sprinkling the surface with 150-μ corundum grit produced prominent blotches in the diffraction microscopy patterns, Fig. 16, which were found to match perfectly with the pattern of rosettes found in a subsequent etch pit pattern, Fig. 17. The rosettes formed by dropping corundum grit on NaCl are nearly identical with those formed on larger LiF crystals by Gilman, and can be identified as clusters of small dislocation loops. On diffracting at $\psi=90$ deg from (002) planes perpendicular to the growth direction, the blotches at regions of deformation were at the same positions but were not the same shape as expected. Too many dislocation loops of very small size were formed to permit resolution of individual loops in diffraction micrographs.

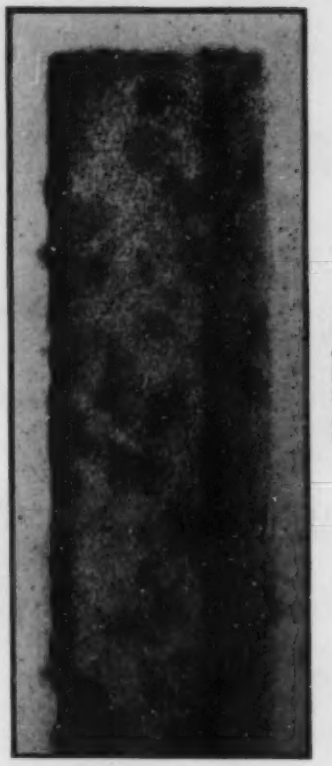

FIG. 16. Diffraction micrograph of platelet shown in Fig. 15 after impact by free-falling, 150-μ alundum grains, same diffraction conditions as above. 180×.

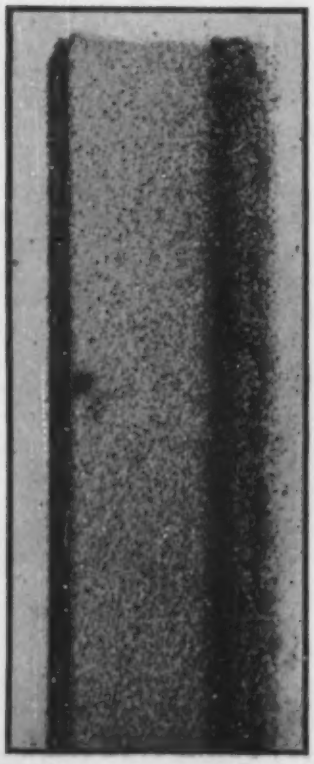

FIG. 15. Diffraction micrograph of nearly perfect platelet before deformation. (Diffuse spot near center of left edge is an artifact introduced during enlargement.) Diffraction from (200) planes. $\psi=90°$, $\phi=90°$. NTB plate. 180×.

From observations of grain size and height of free fall required to initiate plastic deformation (taking into account the asphericity of particles), it was estimated that the stress required to initiate local plastic deformation is greater than 10^8 dyne cm^{-2} which is about the same as the yield strengths of nearly perfect NaCl whiskers measured by bend tests.

V. DISCUSSION AND SUMMARY

(A) Diffraction Methods for Whisker Structures

The x-ray techniques of diffraction microscopy utilizing variations of diffracted intensity from the neighbor-

[34] J. J. Gilman, *Dislocations and Mechanical Properties of Crystals* (John Wiley & Sons, Inc., New York, 1957), p. 117.

hood of dislocations and measurements of lattice twists appear capable of yielding rather detailed results on many of the features of dislocation structure of NaCl whiskers, just as is possible for larger crystals. There is no fundamental difference between the principles involved in applying this method to large crystals and to whiskers, although details of technique differ. In either case, the fact that individual dislocations are not resolved at spacings much less than 10 μ leads to an uncertainty about whether all dislocations are detected.

A complete theory of the contrast effect should lead to improved techniques. Nevertheless, as it stands, x-ray diffraction microscopy and x-ray measurements of lattice twists together may be considered a reliable *nondestructive* method for characterizing most of the details of the dislocation structure of small crystals.

(B) Dislocation Structure of NaCl Whiskers

If one considers the dislocation structures of the NaCl microcrystals examined in the present study and those examined by Amelinckx[1] in terms of dislocation density, one sees nothing particularly startling, since the observed dislocation densities are about 10^4 to 10^7 cm^{-2} which is higher than is found in bulk crystals of the same materials. However, the fact that a dislocation density of 10^6 cm^{-2} corresponds to only one 1-cm-long dislocation in a whisker of 10 μ square in cross section is somewhat more intriguing.

The most common products of the efforts to grow NaCl whiskers on a porous substrate are the small (less than 100-μ^2 cross section), strong whiskers that have been little discussed here because little needed to be said. These crystals often contain 1, 2, or 3 dislocations parallel with the growth direction, probably with $a/2[110]$ Burgers vectors and no other dislocations. (Thus, these are mixed dislocations with the screw component parallel to the growth direction along the whisker axis.) Measurements of the Eshelby twist established the approximate magnitudes of the axial component of the Burgers vectors. Some relatively small whiskers, $\sim$100 μ^2 in cross section, have very large Eshelby lattice twists corresponding to net screw dislocation Burgers vector components $\sim$100 A. In a few cases, these contained single dislocations with a hollow core; in others, there was no diffraction microscopy evidence for a single dislocation and no axial hole for a hollow core, so it can only be inferred that a large number of dislocations are presently spaced too closely to be resolved by diffraction microscopy.

In the larger whiskers, particularly the platelets, variety in dislocation structure is apparent. Some of them contain many straight, nearly parallel dislocations, while others have only one or two. Although whiskers of nearly square cross section containing two dislocations are common, thin platelets with one dislocation near each edge were also common. Crystals containing irregular networks were also found. Fairly large pores, some of them containing water, were often found in some of the more imperfect larger crystals. Thin holes along some dislocation cores were also occasionally observed.

Comparison of the structures found in the present study with those observed using decoration and etching techniques by Amelinckx[1] for whiskers grown in poisoned solutions suggests that (1) the heat-treatment required for decoration sometimes does not change the dislocation structure drastically, and (2) the differences in dislocation structures between NaCl whiskers grown in poisoned solutions and some of the less perfect of those grown in air on porous substrates are slight.

(C) Growth

There is now little doubt that the screw dislocation mechanism suggested by Amelinckx[10] for basal growth of alkali halide whiskers on a wet, porous membrane applies to the whiskers studied in this report. It is evident that many of the relatively large needles and platelets grow through the cooperative action of a substantial group of dislocations. Very few pure screw dislocations were discovered and only then in a crystal with [110] growth direction. However, the mixed [110] type Burgers vectors are active in the growth processes.

The usual dislocation densities are in the range 10^4 to 10^5 cm^{-2}. It is not obvious why this particular density occurs. However, the size and dislocation density of the whiskers are probably determined by the crystal originally nucleated on the moist substrate. The evident reluctance of the whisker cross sections to change

FIG. 17. Etch pit pattern of platelet yielding diffraction micrograph shown in Fig. 16. Reflected light. $\sim$180$\times$.

drastically during growth except with gross perturbation of the growth process supports this conjecture.

It is likely that the changes in the dislocation structure noted at pronounced cross section changes are an effect of a growth perturbation rather than a cause of the cross section change. Although many crystals have some irregular grown-in dislocations that have screw components meeting lateral surfaces, there is no branching at these sites probably only because no growth can occur on the lateral whisker surfaces where there is no supply of supersaturated solution.

The dislocations observed in platelets are either propagated from the whisker which had been upset onto the the moist substrate to initiate platelet growth or are nucleated at inclusions or surface damage. The occurrence in the most nearly perfect platelets of dislocations near one or both edges may be due to the propagation of the axial dislocation from the ends of the whisker from which the platelet started.

The irregular branched dislocations that are detrimental to strength appear particularly where several mixed dislocations are propagated close together. There is no difference in Burgers vector between the straight and irregular dislocations, except where irregular dislocations combine or branch.

The crystals studied in detail were preselected for reasonably regular appearance, and it is probable that still more complicated dislocation structures exist among the very irregular crystals that were rejected. Every crystal containing visible growth irregularities that was examined by diffraction microscopy was found to have corresponding irregularities of the dislocation structure; for example, see Fig. 11.

(D) Strength, Deformation, and Dislocation Structure

The dependence of the strength in bending on the dislocation structure of NaCl whiskers is indicated by the present study. In essence, it has been found that whiskers (both needles and platelets) are "strong"; that is, they support elastic strains in excess of 0.25% in bending *if* they contain only one or two straight dislocations that run parallel to the growth axis of the whisker for its full length. This is to be expected since this configuration provides no dislocation generators for gross plastic deformation at low stresses.

It is not quite so obvious why whiskers that contain one or two $a/2[110]$ mixed dislocations with the screw component parallel to the growth direction (such as those in Figs. 5 or 6) should be stronger than whiskers with 20 dislocations of approximately the same sort (such as those in Figs. 7 and 8). In some cases, the difference is that some of the multitude of dislocations are not so neatly arrayed so that there are changes in direction, branches, or nodes, etc. that can provide effective dislocation generators of various types that are active under small bending stresses.

The fact that whiskers selected for mechanical testing are invariably preselected for regular, uniform cross sections and smooth surfaces free of gross morphological irregularities influences the average results. Whiskers containing many dislocations may have some stragglers that decrease their strength, *without* suffering pronounced aberrations in growth form that would lead to rejection for testing. On the other hand, in a nearly perfect whisker, exit of one or two dislocations through a lateral surface or gain of another at the base during growth should lead to a pronounced change in growth form that would exclude that crystal from selection for strength testing. Therefore, it appears likely that preselection of whiskers for good growth form leads to selection of crystals with either (a) only one or two necessarily straight dislocations or (b) many dislocations, some of which provide effective dislocation sources. As limiting cases of this idea, all whiskers of irregular growth form (and hence irregular dislocation structures) are found to be weak and nearly all very thin whiskers of uniform cross section (and hence simple regular dislocation structures) are strong. It is quite likely that the various conflicting observations on the strengths of alkali halide whiskers are due to differences between the whiskers studied. Various bases for selecting crystals for test may lead to concomitant selection of different types of dislocation structures, and various techniques for growth may lead to differing proportions of the various sorts of dislocation structures.

ACKNOWLEDGMENT

It is a pleasure to acknowledge the inspired cooperation and assistance of N. P. Bertolone on all of the x-ray experiments and on many other aspects of this research, the assistance of A. F. Silvaggi on the growth and handling of whiskers, and valuable discussions with Dr. W. F. Sheely.

JOURNAL OF APPLIED PHYSICS VOLUME 31, NUMBER 1 JANUARY, 1960

Novel Mechanism for Mass Transport during Whisker Growth—Cesium Chloride from Aqueous Films

W. W. Webb and N. P. Bertolone
Union Carbide Metals Company, Division of Union Carbide Corporation, Niagara Falls, New York
(Received August 3, 1959)

Capillary rise of a saturated solution within a hollow whisker has been found to provide a mechanism yielding growth at the tips of cesium chloride whiskers on a moist substrate in air at room temperature. The driving force for crystal growth is local supersaturation due to evaporation of water from solution at the tip of the capillary pore in each whisker. Screw dislocations provide the lattice steps on the whisker tips.

I. INTRODUCTION

AMONG the variety of whisker growth mechanisms described by Nabarro and Jackson in their recent review[1] are many variations involving growth at the surface lattice steps that are inexhaustibly provided by the intersection of screw dislocations with the growing surface. Growth involving dislocation mechanisms can occur either at the free tip or the attached base of a whisker. For example, sodium chloride whiskers grow at room temperature within aqueous supersaturated solutions containing a small amount of vinyl alcohol by deposition of salt from the solution on the growing tip at steps provided by the intersection of dislocations with the surface.[2] Sodium chloride whiskers also form in air on a moistened porous substrate such as cellophane membrane or porous ceramic by growth at lattice steps on the bases of the whiskers which are in contact with the supersaturated aqueous film on the porous substrate.[3] Tip growth of polycrystalline $NaClO_3$ in air from a moist substrate has been reported by Kato[4] and explained by Sears[5] by migration of a surface film of liquid up the lateral surfaces of the crystal to the tip.

The purpose of this paper is to describe another (previously unreported) mechanism for mass transport during whisker growth on a moist substrate that leads to addition of material at the free tip of the whisker.

II. EXPERIMENTAL OBSERVATIONS

Clean glass microscope slides were immersed in a hot (60 to 70°C), nearly saturated solution of cesium chloride containing 1860 g/l CsCl, then rapidly withdrawn and placed under a microscope. The thin film of the liquid (~0.1 mm) that remained on the slide cooled to nearly room temperature in a few seconds, since the slide was not heated appreciably during the quick dip in the hot solution. During cooling, flat dendritic fern-like crystals spread rapidly through the aqueous film, forming a layer that covered the surface of the film. The interstices in the network then filled in by thickening of the dentrites until only a few pores remained in the crystalline layer. Figure 1 shows this layer after completion of crystallization with the dendritic crystals still clearly discernible. At this stage, nearly all of the remaining moisture was contained in solution trapped below the crystalline layer. At some of the pores, mounds a few microns high then formed and whiskers began to grow from them. Whisker growth progressed at about 5μ/sec for 2 to 4 min, followed by much slower growth for an additional 2 to 10 min. Figure 2 shows a profile view of a slide after completion of whisker growth. That there is a simple crystallographic relationship between the whisker axes and the substrate was indicated by the fact that all of the whiskers formed on each dendritic crystal were oriented in one of three preferred directions. The whisker axes were found by x-ray diffraction methods to be in [111] directions. Measurement of the angles between the three observed whisker growth directions on a substrate crystal yielded values in agreement with the characteristic 70.53° angles between [111] (tetrahedral) directions. Therefore, whiskers are probably part of the crystal forming their substrate.

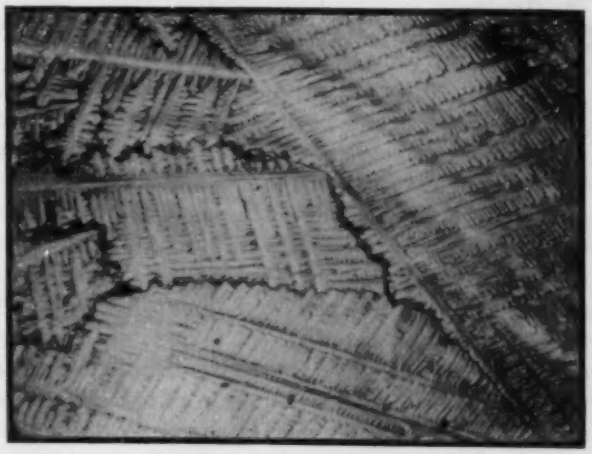

FIG. 1. Photomicrograph of dendritic crystal layer taken after growth is completed. Dendritic film on the surface of the slide has extended across the entire surface. Whiskers are not visible in this photograph. There are six dendritic crystals in view; each group of parallel dendrites comprises a single crystal. Transmitted light.

[1] R. N. Nabarro and P. J. Jackson, in *Growth and Perfection of Crystals* (John Wiley & Sons, Inc., New York, 1958), p. 13.
[2] S. Amelinckx, Physica **24**, 390 (1958).
[3] Z. Gluyai, Z. Physik **138**, 317 (1954).
[4] N. Kato, J. Phys. Soc. Japan **10**, 1024 (1955).
[5] G. W. Sears, J. Chem. Phys. **26**, 1549 (1957).

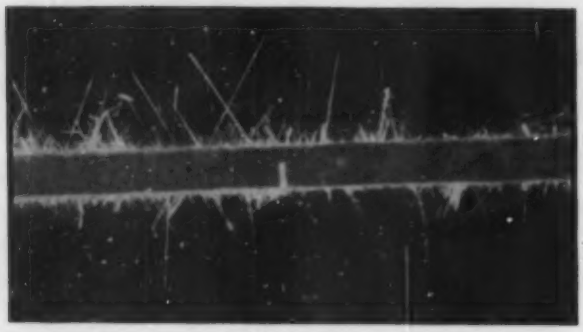

FIG. 2. Photomicrograph showing profile view of slide with whiskers in place on the substrate. Diagonal lighting.

Whiskers grew to lengths between 1 and 10 mm, usually with diameters of about 10 μ. A few reached diameters of approximately 100 μ. Microscopic inspection showed each whisker to be a hollow cylinder. Typical whiskers are shown in Figs. 3 and 4 after removal from the substrate and immersion in nitrobenzene (index of refraction $n=1.53$ compared with $n=1.64$ for CsCl). Air trapped in the axial pore prevented complete penetration of the nitrobenzene. The pores shown are about 5 μ in diameter in approximately 10 μ-diameter whiskers.

Viewing this whisker growth with a microscope, it could be clearly seen that solution rose inside the hollow whiskers during their period of rapid growth. After the liquid column broke, because of depletion of the solution under the substrate, the whisker growth rate decreased drastically. Lengthening of the whiskers occurred by addition of cesium chloride at the tips and not by addition at the ends attached to the substrate. This was deduced from the observation that visible natural defects and deliberate artifacts on the lateral surfaces of the whiskers remained at constant distances from the substrate, while the distances from them to the tips increased as the whisker grew.

An x-ray diffraction method[6,7] was applied to two whiskers to investigate the presence of screw dislocations parallel to the axis of the whiskers. The high-resolution Laue technique reveals the presence of screw displacements in whiskers by identification of a gross elastic torsional strain associated with them. Large screw dislocation displacements were, indeed, found. The computed Burgers vectors were approximately 250 A and 770 A in these two whiskers, taking into account a correction for the pore given by Eshelby.[8] Visible twisting of longitudinal striations in all of the whiskers observed microscopically suggests that screw dislocation displacements occur in all of these whiskers.

[6] Webb, Dragsdorf, and Foregeng, Phys. Rev. **108**, 498 (1957).
[7] R. D. Dragsdorf and W. W. Webb, J. Appl. Phys. **29**, 817 (1958).
[8] J. Eshelby, Phil. Mag. **3**, 440 (1958).

III. DISCUSSION

The experimental observations suggest a simple growth mechanism. Following formation of a nearly complete crystalline layer on the surface of the supersaturated solution during initial cooling on the slide, there are only a few holes through which evaporation of water from the solution can take place. As evaporation proceeds, crystal growth occurs around each pore, producing a hollow hillock or fumarole where the solution reaches maximum supersaturation by local loss of water to the atmosphere. As this process continues, the solution rises in the pore by capillary action and crystal growth occurs at the rim of the pore so that a hollow needle is formed. In order for this process to continue without eventually blocking the capillary hole by internal crystal growth, the supersaturation of the solution must be low compared to that at the whisker tip. Probably growth at the tip occurs by deposition at spiral lattice steps generated by the screw dislocations parallel to the whisker axis. After the solution is depleted so that insufficient liquid remains to fill the capillaries, further slow growth that is observed probably occurs by transport in a thin, adsorbed liquid film within the axial capillary pores.

It remains to estimate whether the magnitudes of the effects associated with the proposed mechanisms are consistent with the observations. Capillary rise is entirely adequate to pull fluid into the capillary pores in the whiskers. The maximum possible capillary rise expected is given by

$$h=(2\gamma/r\rho g) \qquad (1)$$

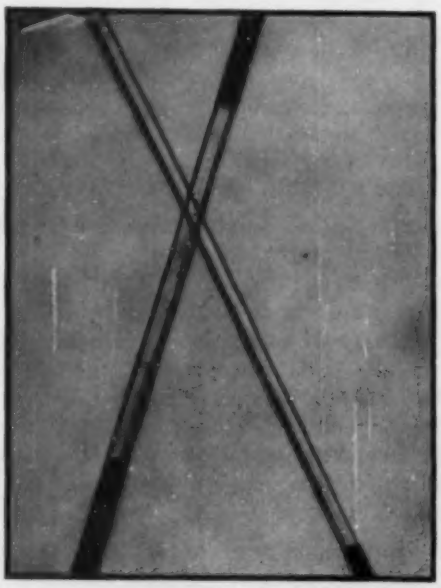

FIG. 3. Photomicrographs of cesium chloride whiskers immersed in nitrobenzene. Dark sections are air bubbles that have prevented penetration of the nitrobenzene into the pores. Transmitted light.

where γ is the interfacial energy, r capillary radius, ρ the solution density, and g the acceleration of gravity. Using $\gamma=80$ erg cm^{-2}, $r=10\mu$, $\rho\cong 2$ g cm^{-3}, $g=980$ cm sec^{-2} yields ~ 80 cm which is on the order of 100 times the length of the longest whisker found. The interfacial energy γ is taken to be 80 erg cm^{-2} which is estimated from measurements on potassium chloride in contact with saturated solution,[9] and from theoretical calculations.[10] The approximate rate of evaporation from the solution surface at the tip of the capillary was calculated from the vapor pressure of the solution, cross-sectional area of the capillary pore, and relative humidity using an estimated diffusion boundary layer thickness equal to the whisker thickness. The estimated evaporation rate corresponds to a growth rate $\sim 5\mu$ sec^{-1} which is just equal to the average observed growth rate. This exact agreement is fortuitous in view of the numerous approximations involved in computing the evaporation rate. In order to determine directly whether the growth rate is sensitive to evaporation, as would be expected from this model, a stream of warm, dry air was blown across a group of growing whiskers. The growth rate immediately increased substantially. Conversely, on passing air saturated with water over the crystals, growth stopped.

The interior surfaces of the whisker pore are concave and the bottom surfaces of the dendritic layer are not smooth and are probably not composed of close-packed planes free of surface steps, so that growth of the solid phase would be expected to occur at very low supersaturations, as this sort of surface can grow with a very small activation energy. Since plugging of the capillary pores by internal crystal growth does not occur, the solution within the pores must be virtually at equilibrium with the solid phase.

At the tips of the whiskers, growth at lattice steps in the surface should begin at a supersaturation given by[11]

$$\alpha=\exp\frac{\gamma\Omega}{\rho_c kT}-1 \qquad (2)$$

where γ is the interfacial energy (erg cm^{-2}) between solid CsCl and the solution, Ω is the molecular volume (cm^3), ρ_c is a critical radius of curvature (cm) of the steps, k is the Boltzmann constant (erg deg^{-1}), and T is the absolute temperature (deg). Since the dislocation

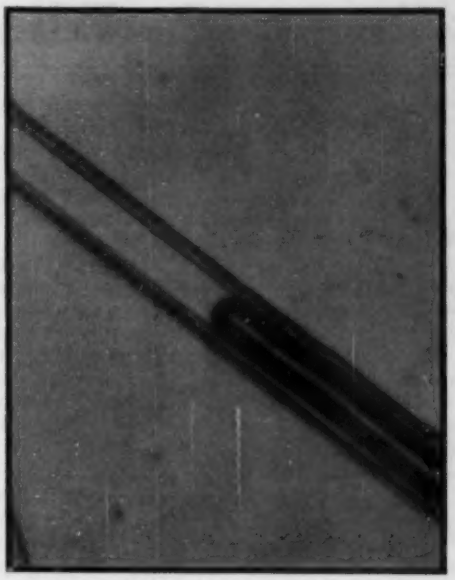

FIG. 4. High magnification photomicrograph of cesium chloride whisker showing small wall irregularities and meniscus at nitrobenzene-air interface inside capillary. Transmitted light.

core is hollow, the critical radius ρ_c is taken as the pore radius of 2.5 microns. With these numbers, Eq. (2) yields a minimum supersaturation ratio $\alpha\cong 3\times 10^{-4}$ at which growth should begin to occur at lattice steps on the whisker tip. For comparison, two dimensional homogeneous nucleation would not yield an appreciable growth rate for supersaturation ratios below $\alpha\cong 3\times 10^{-3}$. The principal source of uncertainty in these calculations is the estimate of the interfacial energy which may be incorrect by as much as $\pm 50\%$.

Probably lattice steps on the whisker tip are essential to provide active growth sites for continuation of whisker growth, so whiskers form only at those pores in the dendritic substrate that happen to fulfill the requirement of a net screw dislocation slip vector perpendicular to the pore axis. Others probably plug by isotropic crystallization as the solution evaporates. The very large Burgers vectors are understandable since the capillary pores eliminate most of dislocation core energy. Although the diameter of the axial capillary is probably governed by rate processes rather than equilibrium energetics, it is interesting to note that the observed pore size is about the size computed from the theory of Frank[12] for hollow dislocations with large Burgers vectors.

[9] G. W. Sears, J. Chem. Phys. **29**, 979 (1958).
[10] R. Shuttleworth, Proc. Phys. Soc. (London) **A62**, 167 (1949).
[11] N. Cabrera and M. M. Levine, Phil. Mag. **1**, 450 (1956).
[12] F. C. Frank, Acta Cryst. **4**, 497 (1951).

Letters to the Editor

Hall Mobility of Holes in AgBr*

ROLAND C. HANSON† AND FREDERICK C. BROWN
University of Illinois, Urbana, Illinois
(Received August 5, 1959)

THE literature contains conflicting evidence for the mobility of holes in polar crystals such as the silver halides.[1-3] Experiments on the drift of carriers at 80°K and below fail to show hole currents in AgCl[4,5] but indicate that holes make a small but definite contribution to photocurrents in high-purity AgBr.[6] The early results of Lehfeldt[4] on the overwhelming importance of electrons served as a basis for the Gurney-Mott theory of the photographic process. More recent theories of latent image formation regard the hole as mobile and as playing an important role in the photographic process.[7]

There is no serious doubt that holes possess some freedom of motion in the silver halides at room temperature, as shown by the experiments of Wagner[8] and Luckey and West.[9] The latter studied the increase in dark conductivity of AgBr as a function of bromine pressure and found the excess conductivity proportional to the square root of the bromine pressure. Similar experiments have been carried out over a wide range of pressures by a group of Russian workers.[10] An explanation for the increase in conductivity was first given by Wagner who proposed that the crystal absorbs an excess of bromine, the excess appearing in the form of silver ion vacancies and holes. For small bromine pressures the concentration of vacancies will remain virtually unchanged because of the large Frenkel disorder normally present. The increase in conductivity was thought to be due almost entirely to the presence of holes. Observations, given below, of the Hall effect for the added carriers show that this is a reasonable mechanism and that the mobility of holes is much greater than the mobility of ionic defects but substantially less than the mobility of electrons in the range of temperature from 25°C to 150°C.

The Hall effect for holes was observed using sensitive high-impedance ac techniques similar to those of Macdonald and Robinson.[11,12] Crystals of high-purity silver bromide were mounted between colloidal graphite current electrodes (area 1.0×0.2 cm, separation 1.0 cm). The current electrodes were carefully balanced to ground in a bridge circuit where a small third electrode served as the Hall probe. The sample and electrodes were mounted in a glass tube so that bromine or chlorine gas could be introduced from a connecting manifold. Pressure of the halogen gas was controlled by the temperature of a side tube on the manifold and the temperature of the sample was controlled by a small oven. A transverse magnetic field up to 10^4 oersteds could be applied. Voltages from 0.1 to 50 volts at frequencies from 50 to 2000 cycles per second were applied to the current electrodes. Signals as small as 1.0 μv could be observed above noise at the Hall electrode by means of a high-impedance preamplifier, narrow-band amplifier, and a phase sensitive detector. A strip chart recorder was used to display the signal in the presence of drift.

The conductivity, σ, of a crystal at a given temperature was found to increase by an amount, $\Delta\sigma$, upon admitting bromine or chlorine gas as described by Luckey and West.[9] Tests made on on samples of different thickness and purity indicate that the phenomena is a volume effect and that the excess conductivity readily disappears when the halogen is pumped off. A Hall effect of positive sign was observed in the presence of halogen. At 30°C a typical change in potential of the Hall probe upon reversal of the magnetic field (10^4 oersted) was of the order of 100 μv with one volt across the current electrodes. The Hall voltage was found to be linearly dependent upon magnetic field and applied electric field and independent of frequency in the range of frequencies where the impedance of the preamplifier was much larger than the crystal impedance.

TABLE I. Typical data showing conductivities and Hall angles.

T(°C)	H (kilo-oersted)	Bromine pressure (mm Hg)	σ (ohm^{-1} cm^{-1} ×10^7)	$\Delta\sigma$ (ohm^{-1} cm^{-1} ×10^7)	$1+\frac{\sigma}{\Delta\sigma}$	observed θ_0 (radians ×10^5)	corrected θ_p (radians ×10^5)
27	8.42	230	0.255	4.85	1.05	11.0	11.5
57	9.80	270	3.38	34.2	1.10	9.7	10.6
57	9.80	66	3.38	17.1	1.20	8.6	10.3
111	8.42	234	119	424	1.28	3.6	4.6
111	8.42	66	119	261	1.45	3.2	4.6
111	8.42	24	119	152	1.78	2.7	4.7

In order to compute the Hall mobility, it is necessary to consider the effect of the ionic component of the current upon the Hall field. The situation is similar to the case of a semiconductor with two types of carriers except that in our case one type of carrier is ionic (silver interstitials and vacancies) and has a mobility much less than that of the holes. It can be shown that the Hall angle for the holes, θ_p, is related to the observed electric field angle by the relation[13]

$$\theta_p=\mu_p H/c=[1+(\sigma/\Delta\sigma)]\theta_0$$

where θ_0 is the ratio of transverse component to longitudinal component of electric field. Table I shows that consistent values of θ_p can be obtained in this way for different halogen pressures at a given temperature. The correction of Eisenberg, Russell, and Greene,[14] due to the shorting of the Hall field by the current electrodes, was used in reducing the final data. At a temperature of 27°C the best value of Hall mobility obtained from several runs on different crystals was $\mu_p=1.7\pm0.5$ cm²/volt sec. The corresponding carrier density is approximately 10^{12} cm^{-3} for a bromine pressure in the vicinity of 200 mm of Hg. Because of small differences between runs, the relative mobility at various temperatures can be found a little more accurately than the absolute values and is shown for one crystal in Fig. 1.

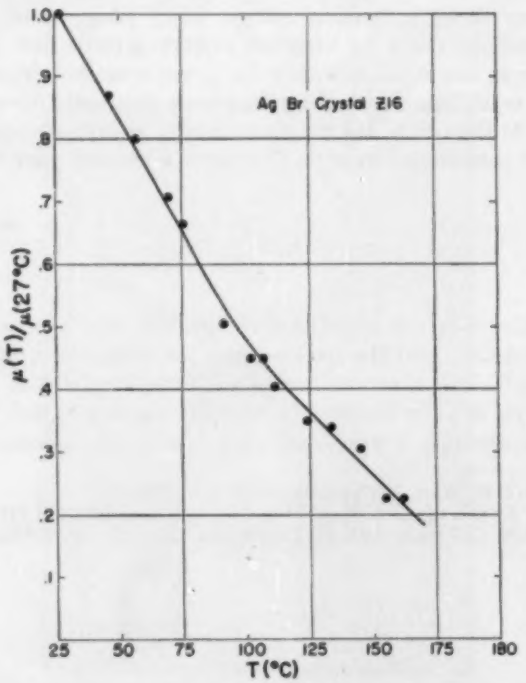

FIG. 1. Temperature dependence of the Hall mobility of holes in a high-purity zone-refined[6] AgBr crystal. The mobility is plotted relative to the value at room temperature, $\mu(27°C)=1.7\pm0.5$ cm²/volt sec. Similar results were obtained for other less pure samples.

In discussing the results it should be remarked that electrons have a mobility about 40 times larger than the mobility of holes at the temperatures of these measurements.[15] A high effective mass and a polaron effect for holes could contribute to this result, but if the hole is a relatively localized imperfection, the band approximation may break down. The low value of mobility helps explain the previous experimental difficulty of separating hole from electron currents in the silver halides.[3,5] Figure 1 shows that the Hall mobility of holes decreases somewhat more steeply with increasing temperature than the mobility of electrons. The latter are probably scattered mainly by optical mode lattice vibrations at these temperatures.[6] An attempt is being made to extend the temperature range of the hole measurements.

[1] F. Seitz, Revs. Modern Phys. 23, 328 (1951).
[2] L. P. Smith in *Semiconducting Materials*, edited by H. K. Henisch, (Butterworths Scientific Publications, Ltd., London, 1951).
[3] F. C. Brown, J. Phys. Chem. Solids 4, 206 (1958).
[4] W. Lehfeldt, Nachr. Ges. Wiss. Jahresber. Geschäftsjahr Math.-physik. Kl. Fachgruppen Göttingen, II 1, 171 (1935).
[5] R. S. Van Heyningen and F. C. Brown, Phys. Rev. 111, 462 (1958).
[6] Burnham, Brown, and Knox (to be published).
[7] J. W. Mitchell, Repts. Progr. in Phys. 20, 433 (1957).
[8] C. Wagner, Z. physik. Chem. (Leipzig) B32, 447 (1936).
[9] G. W. Luckey and W. West, J. Chem. Phys. 24, 879 (1956).
[10] Shamovskii, Dunina, and Gosteva, Soviet Phys. "Doklady" 1, 124 (1956).
[11] J. R. Macdonald and J. Robinson, Phys. Rev. 95, 44 (1954).
[12] J. R. Macdonald, Rev. Sci. Instr. 25, 144 (1954).
[13] Arrived at by an analysis similar to that given in W. Shockley, *Electrons and Holes in Semiconductors* (D. Van Nostrand Company, Inc., Princeton, New Jersey, 1950), p. 217.
[14] Eisenberg, Russell, and Greene, Rev. Sci. Instr. 19, 685 (1948).
[15] Yamanaka, Itoh, and Suita, in *Photographic Sensitivity*, edited by S. Fujisawa (Maruzen Company, Ltd., Tokyo, 1958), Vol. 2, p. 175.
* Supported in part by the U. S. Air Force Office of Scientific Research.
† Corning Glass Works Foundation Predoctoral Fellow for 1958–1959.

Thermal Expansion of Silicon

LEON MAISSEL
Philco Corporation, Philadelphia 44, Pennsylvania
(Received July 10, 1959)

THERE are a number of areas in the semiconductor industry where a knowledge of the coefficient of thermal expansion of silicon is necessary. Among these are the design of transistor base tabs and the selection of glasses for the sealing of infrared windows.

A literature search, however, revealed that data on this coefficient are both scarce and conflicting. Besides the original measurement by Fizeau,[1] only three determinations have been published in recent years. These are by Erfling,[2] by Straumanis and Aka,[3] and by Gibbons.[4] For the room temperature range, the values they obtained were, respectively, 2.42, 4.15, and 2.33×10^{-6}. None of these workers made determinations above 100° C—the range of temperatures at which the value of the expansion coefficient becomes important in most of the applications referred to in the foregoing.

The measurements reported in the following were obtained by a straightforward optical method. Specimens were laid in a groove in a flat plate, one end in contact with a fixed peg and the other pushing against a mirror which was free to pivot about an axis perpendicular to and above the specimen. Deflections of the mirror with increasing specimen length were measured by the deflection of a light beam. The apparatus was made entirely of quartz (the reflecting surface of the mirror was sputtered nichrome) and was placed in a region of uniform temperature in an atmosphere of argon. Specimens were approximately 2 in. long and $\frac{1}{4}$ in. square in cross section. The values quoted have been corrected for the thermal expansion of the quartz and are all $\times10^{-6}$ per°C.

Several specimens of both (111) and (110) crystal orientations were measured. While they did not differ significantly within the estimated experimental error ($\pm0.3\times10^{-6}$ per°C), the (110) values were consistently lower. They have therefore been tabulated separately (see Table I).

As can be seen, good agreement with the room temperature values of Erfling and Gibbons has been obtained.

TABLE I.

Temperature range (°C)	111 orientation	110 orientation
50–100	2.5	2.7
100–200	3.1	3.0
200–300	3.5	3.4
300–400	3.9	3.8
400–500	4.3	4.1
500–600	4.7	4.4
600–700	5.0	4.5
700–800	4.9	4.5
800–850	4.6	4.3

[1] H. Fizeau, Compt. rend. 68, 1125 (1869).
[2] H. D. Erfling, Ann. Physik 41, 471 (1942).
[3] H. D. Straumanis and E. Z. Aka, J. Appl. Phys. 23, 330 (1952).
[4] D. F. Gibbons, Phys. Rev. 112, 136 (1958).

Influence of X-Rays on the Electrification of NaCl Crystals

ANNA SZAYNOK
Department of Physics, Institute of Technology, Warsaw, Poland
(Received March 9, 1959)

WHEN crystals of NaCl are irradiated with x-rays and subsequently pulverized, measurements show that the electrical charges produced as a result of such pulverization are predominantly positive in nature.[1] Measurements were carried out by means of apparatus described by Kunkel and Hansen.[2] In this method, the pulverized salt is introduced from the top into a thermally isolated column. The salt particles are made to fall through an electric field set up between a pair of vertical, plane parallel plates of a condenser. A rotating disk provides periodic illumination, making it possible to photograph the tracks of the falling particles, which appear as bright spots against the dark background. The sodium chloride crystals used in this work were grown from aqueous solution.

Figure 1, curve A, shows the result of the measurements using NaCl crystals which were not irradiated with x-rays. Evidently, a symmetrical charge distribution results. There is a distinct maxi-

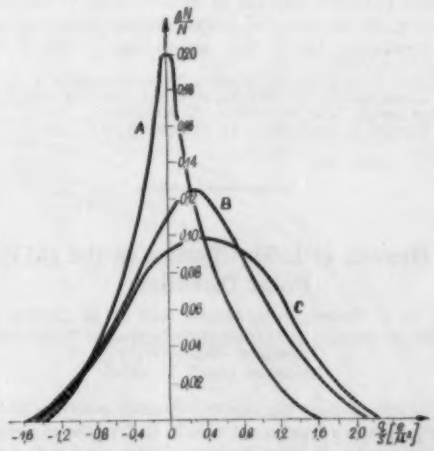

FIG. 1. The charge distribution in dust cloud produced from NaCl crystals. q/s, the ratio of dust particle charge q to its area s in units of electrons/sqμ; N/N, the ratio of the number of particles N with value q/s between q/s and $q/s+(q/s)$, to the total number of particles N. A: Curve for NaCl Crystals not irradiated with x-rays. B: Curve for NaCl crystals irradiated with x-rays (initial parts of tracks). C: Curve for NaCl crystals irradiated with x-rays (end parts of tracks).

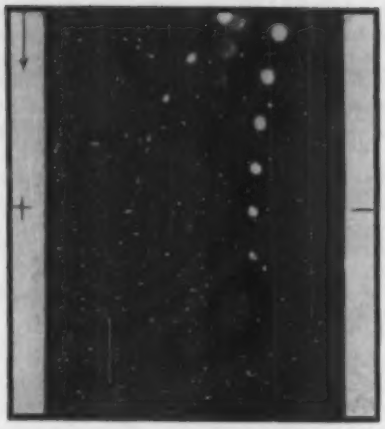

FIG. 2. Deviation of the particle tracks, giving evidence for the presence of photoelectric effect. The arrow indicates the direction of movement of the particles, and the plus and minus signs denote the direction of the field.

mum for those particles which are either uncharged or have a very small charge. The mean charge per unit surface is 0.441 electron/sqμ.

Next, NaCl crystals irradiated with x-rays were employed for the measurements. The *F*-center concentration amounted to about 10^{16} cm^{-3}. Considerable photoelectric effect was noted as a result of the illumination of falling dust particles during measurement (about 37%). The falling particles showed track discontinuities due to loss of electrons (Fig. 2). The maximum deviation of tracks appears in the area where there is the strongest intensity of light. This phenomenon of photoemission from crystals containing *F* centers is well known.[3] The charge distribution in the dust cloud shows a preponderance of positive charge (Fig. 1, curves *B* and *C*). In plotting curve *B*, only the initial parts of the tracks of the particles have been taken into consideration, i.e., before the particles began to lose electrons, as a result of the photoelectric effect. The mean charges amounted to 0.584 electron/sqμ. In plotting curve *C*, only the final parts of the tracks of the particles in the same dust cloud, i.e., after the loss of electrons due to the photoelectric effect, have been taken into consideration. Here, the mean charge amounted to 0.668 electron/sqμ. The shift of curve *B* towards the positive might have been caused by the presence of small quantities of light scattered into the upper part of the measuring chamber, or tribo electrification taking place during crushing. The shift of the curve *C* towards the positive is caused by the photoelectric effect taking place during the measurement. It is suggested that the increase of mean charge in the dust cloud is caused by the increase of lattice defects in the crystals as a result of irradiation with x-rays, as proposed by W. B. Kunkel.[4]

[1] A. Szaynok, Zeszyty Nauk. Politech. Wroclaw. Chem. **5**, 21 (1958).
[2] W. B. Kunkel and J. W. Hansen, Rev. Sci. Instr. **21**, 308 (1950).
[3] L. Apker and E. Taft, Phys. Rev. **79**, 964 (1950).
[4] W. B. Kunkel, J. Appl. Phys. **21**, 820 (1950).

Growth of InSb Crystals in the ⟨111⟩ Polar Direction*

H. C. GATOS, P. L. MOODY, AND M. C. LAVINE
Lincoln Laboratory, Massachusetts Institute of Technology, Lexington, Massachusetts
(Received August 28, 1959)

IT was observed that the crystallographic polarity of the ⟨111⟩ direction plays a significant role in the degree of perfection of InSb crystals grown in that direction. When the end of the ⟨111⟩ seed crystal terminating in Sb atoms (B {111} surface) was employed, single crystals of InSb were invariably obtained by the Czochralski method. However, by employing the other end of the same seed, terminating with In atoms[1-4,†] (A surface), twinning or large grain formation frequently occurred early in crystal

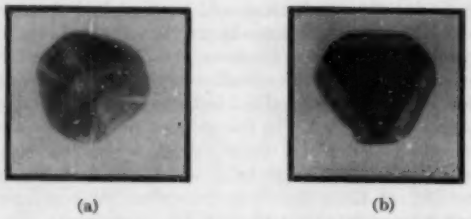

FIG. 1. InSb crystal (about 0.75 in. in diam) grown in the A ⟨111⟩ direction. Some of the grains are evident. (a) As viewed from the seed end. (b) Cross section perpendicular to the growth direction about 0.5 in. from initiation of growth.

growth. Growth conditions were identical in both cases; i.e., the seed was rotated at 10 rpm and pulled at 0.75 in./hr. A crystal of InSb grown from the A end of an ⟨111⟩ seed is shown in Fig. 1.

In addition, differences in dislocation densities were observed between the single crystals grown in the B ⟨111⟩ direction and the single-crystal portions grown in the A ⟨111⟩ direction. No effort was made to determine the absolute values of the dislocation densities involved. Our present observations on InSb are probably characteristic of the III-V compounds in general and they perhaps answer the question[4] as to whether the perfection of a GaAs crystal grown in the ⟨111⟩ direction depends on the polarity of the seed crystal.

Gatos and Lavine[5] have proposed an atomic model which explains the differences observed between the behavior of the A and B {111} surfaces of the III-V compounds; i.e., the higher reactivity of the B surfaces, as determined by dissolution rates, and the more noble electrode potential of the A surfaces. The model accounts for the differences in etching behavior and for the appearance of dislocation etch pits on the A and not on the B surfaces of six III-V compounds studied (InSb, GaSb, AlSb, InAs, GaAs, and InP). According to the proposed model, tetrahedrally bonded atoms of the B surfaces have an unshared pair of electrons [Fig. 2-I(b)], which is responsible for the high reactivity of the B surfaces with electron-seeking agents. The atoms of the A surfaces have their fourth tetrahedral orbital unfilled [Fig. 3-I(a)]. In addition to explaining differences in chemical reactivity, this model points to pronounced differences in electronic properties between the A and B surfaces.

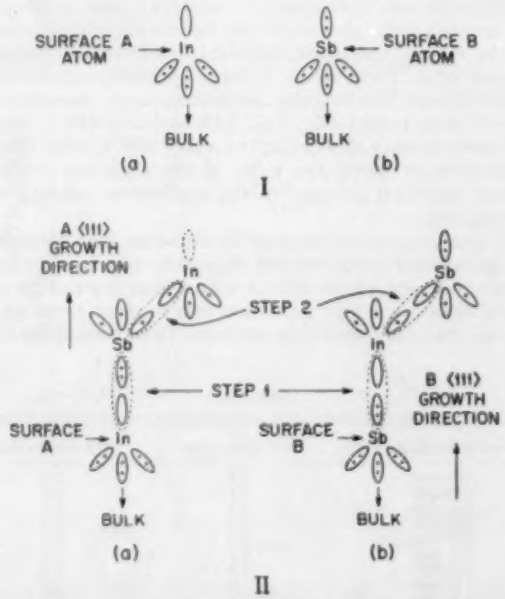

FIG. 2. Atomic model of A and B surfaces of InSb (I) and the addition of atoms in the A and B ⟨111⟩ directions (II).

The observed differences in crystal perfection are undoubtedly related to the above behavior of A and B surfaces and can be viewed in terms of the same atomic model. Let us consider the addition of atoms onto the A surface in the A ⟨111⟩ direction [Fig. 2-II(a)]. With only three of the s-p orbitals occupied, it is likely that the electronic configuration of the A surface atoms is distorted from the tetrahedral symmetry. In the course of adding a B atom onto an A surface atom (step 1), it is necessary that the A atom acquire the sp^3 tetrahedral configuration. Once B atoms are added, then A atoms follow, each A atom sharing its three electrons with three B atoms (step 2). Since group III atoms are not tetrahedrally bonded in their normal trivalent state, step 2 will result in a strained configuration. It is not pertinent to the present argument whether the addition of B atoms or the addition of A atoms is the growth determining step and this point will not be elaborated here. However, the bond readjustment associated with the addition of atoms in the A ⟨111⟩ direction is believed responsible for the tendency of the crystal to grow in some other orientation. The present argument is not altered if there is ordering in the melt or even if the melt contains distinct molecules of the III-V compound. In this case the addition of atoms might proceed by B-A layers rather than by steps 1 and 2.

With regard to growth in the B ⟨111⟩ direction, it can be seen in [Fig. 2-II(b)] that an A atom is added by sharing the filled orbital of a B surface atom which has retained its tetrahedral configuration (step 1). As a result, by sharing its three electrons with three new B atoms, the A atom acquires a tetrahedral electron configuration without undergoing bond distortion (step 2).

The present model does not deal with the physical mechanism of crystal growth. Furthermore, it does not take into consideration possible surface states or quantum mechanical aspects. It does, however, explain qualitatively, the effect of the A and B surfaces on the perfection of crystals grown in the A and B ⟨111⟩ directions. The relationship of this model to the mechanisms of crystal growth is being developed.

* The work reported in this paper was performed by Lincoln Laboratory, a center for research operated by Massachusetts Institute of Technology with the joint support of the U. S. Army, Navy, and Air Force.

[1] E. P. Warekois and P. H. Metzber, Pittsburgh Diffraction Conference Abstracts (November, 1958) p. 48; J. Appl. Phys. **30**, 960 (1959).

[2] J. G. White and W. C. Roth, J. Appl. Phys. **30**, 946 (1959).

[3] E. P. Warekois, unpublished results.

[4] S. G. Ellis, J. Appl. Phys. **30**, 947 (1959).

† An absolute identification of the {111} A and B surfaces of InAs,[1] GaSb,[1] GaAs,[2] InSb[3], and other III-V intermetallic compounds[3] has been obtained recently by x-ray diffraction techniques. As a consequence of this work, one can now conveniently identify the A surfaces of the III-V compounds by the presence of dislocation etch pits which develop in a number of etching media.[4] Ordinarily, the B {111} surfaces do not develop dislocation etch pits.

[5] H. C. Gatos and M. C. Lavine (submitted to J. Electrochem. Soc.).

Spontaneous Magnetizations of Some Gadolinium Alloys

SIGURDS ARAJS AND D. S. MILLER
Edgar C. Bain Laboratory for Fundamental Research, United States Steel Corporation Research Center, Monroeville, Pennsylvania

(Received July 8, 1959)

THE spontaneous magnetization of a ferromagnetic substance is a quantity of fundamental significance. No thorough and adequate investigations of the spontaneous magnetization of ferromagnetic rare earth metals and alloys from absolute zero to their respective Curie points have been made so far. The only known attempt is due to Behrendt[1] who determined the temperature dependence of the spontaneous magnetization of a single crystal Dy in the ⟨11$\bar{2}$0⟩ direction using the usual extrapolation of the magnetic isotherms.

This letter is the product of an attempt to obtain the spontaneous magnetizations of ferromagnetic rare earth metals and their alloys from absolute zero to the corresponding ferromagnetic Curie temperature using the available magnetic data. It has been found that only the information on Gd-Y and Gd-La systems[2] is such that fairly reliable values of spontaneous magnetizations as a function of temperature can be found. For Gd,[2-5] Er,[3] and Ho[6,7] more accurate high magnetic field data as a function of temperature are needed. For Dy,[1,8] Tb[9] and similar systems, where the ferromagnetism is followed by an antiferromagnetic (or metamagnetic) ordering which can be destroyed by higher magnetic fields, the determination of the spontaneous magnetization is difficult because low magnetic field extrapolation must be used. For Eu, which appears to be ferromagnetic below 90°K[10], no magnetic isotherms have been published up to the present. The ferromagnetism in Tm is still an open question. According to Rhodes *et al*[6] Tm is not ferromagnetic. Leipfinger,[7] however, from his measurements (which are not accurate enoughfo r reliable determination of the spontaneous magnetizations) concludes that Tm is ferromagnetic.

TABLE I. Smoothed values of spontaneous magnetization of Gd-Y and Gd-La alloys expressed in σ_{OT} (cm³ sec^{-2} oe^{-1}) and μ_{eff} (Bohr magnetons per Gd atom).

T (°K)	10.0 at.% Y σ_{OT}	μ_{eff}	16.7 at.% Y σ_{OT}	μ_{eff}	25.0 at.% Y σ_{OT}	μ_{eff}	33.3 at.% Y σ_{OT}	μ_{eff}	10.0 at.% La σ_{OT}	μ_{eff}
0	250.0	7.48	240.0	7.52	228.0	7.63	209.4	7.56	234.0	7.23
10	249.3	7.46	239.4	7.50	227.2	7.60	208.6	7.53	233.0	7.20
20	248.0	7.42	238.2	7.47	225.8	7.55	207.5	7.49	231.2	7.15
30	246.5	7.37	236.5	7.41	224.0	7.49	206.0	7.43	228.8	7.07
40	244.9	7.33	234.5	7.35	222.0	7.43	204.0	7.36	226.3	7.00
50	242.5	7.26	232.3	7.28	220.0	7.36	201.5	7.27	223.5	6.91
60	240.0	7.18	229.5	7.19	217.2	7.27	199.0	7.18	220.3	6.81
70	237.0	7.09	226.5	7.10	214.5	7.18	196.0	7.07	216.8	6.70
80	233.7	6.99	223.5	7.00	211.0	7.06	192.4	6.94	213.2	6.59
90	230.2	6.89	219.8	6.89	207.5	6.94	188.5	6.80	209.2	6.47
100	227.0	6.79	215.7	6.76	203.8	6.82	184.4	6.66	205.2	6.34
110	223.0	6.67	211.7	6.63	199.0	6.66	180.0	6.50	201.0	6.21
120	218.8	6.55	207.5	6.50	194.5	6.51	174.0	6.28	196.3	6.07
130	214.2	6.41	202.6	6.35	189.3	6.33	168.0	6.06	191.5	5.92
140	209.0	6.25	198.0	6.21	183.8	6.15	161.5	5.83	186.6	5.77
150	203.4	6.09	193.0	6.05	177.5	5.94	154.5	5.58	181.4	5.61
160	198.0	5.92	187.0	5.86	171.5	5.74	146.5	5.29	175.5	5.42
170	192.6	5.76	181.0	5.67	164.0	5.49	138.0	4.98	170.0	5.25
180	187.0	5.59	174.3	5.46	155.5	5.20	126.5	4.57	163.0	5.04
190	181.0	5.42	167.0	5.23	146.0	4.88	111.0	4.01	155.5	4.81
200	174.5	5.22	158.5	4.97	135.5	4.53	91.0	3.28	147.0	4.54
210	167.0	5.00	150.0	4.70	124.0	4.15	67.8	2.45	134.5	4.16
220	159.4	4.77	141.0	4.42	109.5	3.66			120.0	3.71
230	150.0	4.49	128.0	4.01	85.0	2.84			80.9	2.50
240	138.0	4.13	109.5	3.43	4.1	0.14			40.0	1.24
250	122.5	3.67	85.0	2.66						
260	103.0	3.08	34.5	1.08						
270	74.1	2.22								

The deduced spontaneous magnetizations per gram, σ_{OT}, and μ_{eff} in Bohr magnetons per Gd atom, of Gd-Y and Gd-La alloys

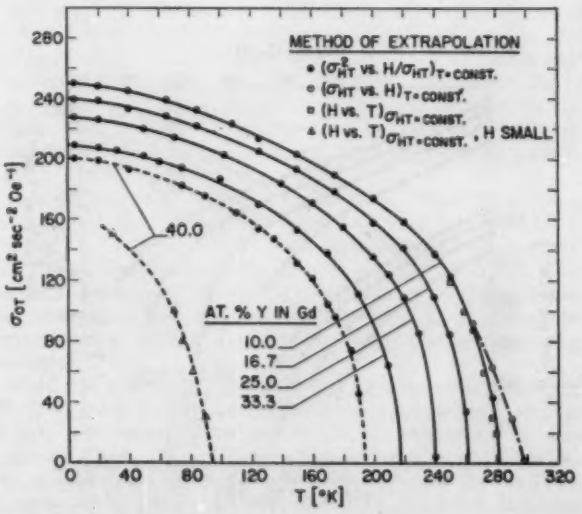

FIG. 1. Spontaneous magnetization of some Gd-Y alloys as a function of temperature.

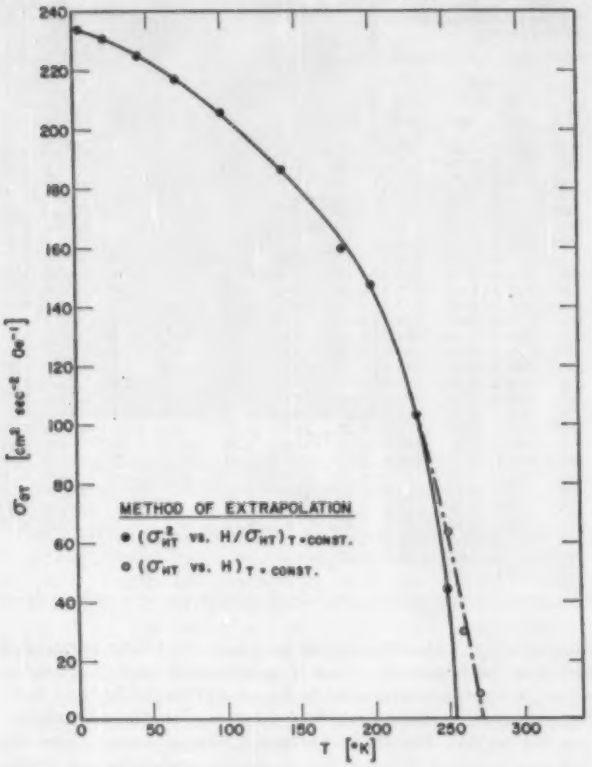

FIG. 2. Spontaneous magnetization of 10.0 at.% La in Gd alloy as a function of temperature.

from original magnetic measurements of Thoburn, Legvold, and Spedding[3] are given in Table I. Figures 1 and 2 show σ_{0T} of these alloys as a function of absolute temperature. The methods for obtaining the spontaneous magnetization from the magnetic moment per gram, σ_{HT}, at the magnetic field H and the absolute temperature T, are indicated in these figures. These techniques give the same results except in the region near the Curie temperature where the $(\sigma_{HT}$ *vs* $H)_{T=\text{const}}$ extrapolation yields too high values of the spontaneous magnetization. The method due to Belov and Coriaga,[11] Arrott[12] and Kouvel,[13] utilizing the $(\sigma_{HT}^2$ *vs* $H/\sigma_{HT})_{T=\text{const}}$ plots, is especially useful because it provides the values of the spontaneous magnetization in the temperature region near the ferromagnetic Curie point. It also is simpler than others because it directly utilizes measured quantities. For all the Gd-Y and Gd-La alloys, except 40.0 atom percent Y in Gd alloy, the high magnetic field extrapolations were used. This could not be done for the 40.0 atom percent Y in Gd alloy because of the existence of a field dependent antiferromagnetism (or metamagnetism). In this case the spontaneous magnetization near the Curie temperature was determined from $(H$ *vs* $T)\sigma_{HT=\text{const}}$ plots using low magnetic field extrapolations.

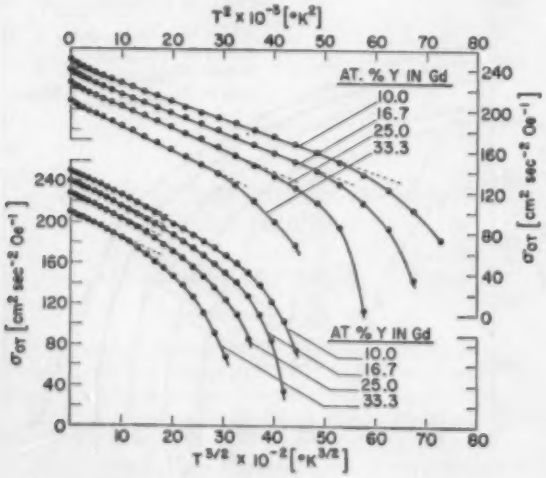

FIG. 3. Spontaneous magnetization of some Gd-Y alloys compared with $T^{3/2}$ and T^2 laws.

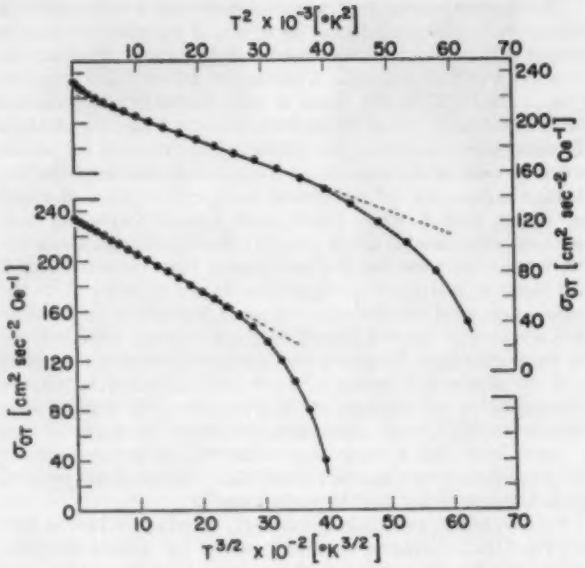

FIG. 4. Spontaneous magnetization of 10.0 at.% La in Gd alloy compared with $T^{3/2}$ and T^2 laws.

Figures 3 and 4 show that the decrease in spontaneous magnetization with increasing temperatures from the absolute zero of these Gd-Y and Gd-La alloys is representable within the experimental error by $T^{\frac{3}{2}}$ law in accordance with the predictions of various spin-wave theories[14] and the theory of Kondorskii.[15] Deviations from the $T^{\frac{3}{2}}$ law start to occur at about 90, 80, 70, and 60°K for the 10.0, 16.7, 25.0, and 33.3 atom percent Y in Gd alloys, respectively. For the 10.0 atom percent La in Gd alloy the departure from the $T^{\frac{3}{2}}$ law occurs at about 120°K. The T^2 relationship is satisfied over a limited range of temperatures beginning somewhat above the absolute zero. Although the T^2 law has been predicted by Stoner[16] using a highly idealized collective electron model, we hardly can expect it to be applicable in rare earth metals and their alloys because their magnetic behavior is primarily determined by the highly localized f electrons. Thus the observed T^2 dependence may have only an empirical meaning. In the region near the Curie temperature the square of the spontaneous magnetization is linear in $1/T$. The ferromagnetic Curie temperatures determined from the σ_{0T}^2 *versus* $1/T$ plots are shown in Table II in comparison with Thoburn's values.

TABLE II. Curie temperatures of Gd-Y and Gd-La alloys.

Alloy composition	θ_f Calculation (from σ_{0T}^2 *vs* $1/T$ plots)	θ_f (Thoburn)
10.0 at.% Y	282±1°K	281±1°K
16.7	262±1	262±1
25.0	241±1	241±1
33.3	222±1	211±1
10.0 at.% La	253±1	258±1

The authors are indebted to A. D. Damick of this laboratory for his assistance in performing a large part of the numerical calculations. Also the discussions with A. Arrott of the Scientific Laboratory of the Ford Motor Company are greatly appreciated.

[1] D. R. Behrendt, "Magnetic properties of neodymium and dysprosium single crystals," Ph.D. thesis, Iowa State College (1956); Behrendt, Legvold, and Spedding, Phys. Rev. **109**, 1544 (1958).
[2] W. C. Thoburn, "Magnetic properties of Gd-La and Gd-Y alloys," Ph.D. thesis, Iowa State College (1956); Thoburn, Legvold and Spedding, Phys. Rev. **94**, 1143 (1958).
[3] J. F. Elliott, "The ferromagnetic properties of the rare earth metals," Ph.D. thesis, Iowa State College (1953).
[4] J. F. Elliott, Phys. Rev. **91**, 28 (1953).
[5] Legvold, Spedding, Barson, and Elliott, Revs. Modern Phys. **25**, 129 (1953).
[6] Rhodes, Legvold, and Spedding, "Magnetic properties of holmium and thulium," U. S. Atomic Energy Commission Report ISC-701 (December, 1955); Rhodes, Legvold, and Spedding, Phys. Rev. **109**, 1547 (1958).
[7] H. Leipfinger, Z. Physik **150**, 415 (1958).
[8] Elliott, Legvold, and Spedding, Phys. Rev. **94**, 1143 (1954).
[9] Thoburn, Legvold, and Spedding, Phys. Rev. **112**, 56 (1958).
[10] C. H. La Blanchetais and M. F. Trombe, Compt. rend. **243**, 707 (1956).
[11] K. D. Belov and A. N. Goriaga, Fiz. Metal. i Metalloved. Akad. Nauk S.S.S.R. **2**, 3 (1956) (in Russian).
[12] A. Arrott, Bull. Am. Phys. Soc., Ser. 2, **2**, 8 (1957); Phys. Rev. **108**, 1394 (1957).
[13] J. S. Kouvel, "Methods for determining the Curie temperature of a ferromagnet," General Electric Research Laboratory Report No. 57-RL-1799 (September, 1957).
[14] S. Van Kranendonk and J. H. Van Vleck, Revs. Modern Phys. **30**, 1 (1958).
[15] E. S. Kondorskii and A. S. Pakhomov, Soviet Phys. JETP **5**, 269 (1957).
[16] E. C. Stoner, Proc. Roy. Soc. (London) **A165**, 372 (1938).

Alternative Forms of Some Exponential and Power Functions for Graphical Representation

C. C. HARRIS
University of Leeds, Leeds, England
(Received July 6, 1959)

A CONVENIENT plot for exponential functions with, unknown asymptotes was given by Mengelsdorf.[1] Thus using here different symbols and the suffix notation of difference equations, the equation

$$Y=Ae^{-bX}+k \tag{1}$$

may be represented by the pair of equations

$$X_r=X_{r-1}+\Delta \tag{2}$$

and

$$Y_r=Y_{r-1}e^{-b\Delta}+k(1-e^{-b\Delta}), \tag{3}$$

r is an integer and $\Delta>1$ and is constant. Consequently, Eq. (2) defines an arithmetical progression. Equation (3) is obtained by eliminating X_{r-1} and X_r between Eqs. (1) and (2).

As $r\to\infty$, $Y_{r-1}=Y_r=k$ and by plotting Y_r against Y_{r-1} both b and k are readily obtained. It will be noted that A is absent from Eq. (3).

By a similar procedure, simple alternative methods for representing graphically two size distribution equations may be derived from which a generalized equation follows .These methods may have wider application and their essential details are presented briefly in the following.

The Rosin-Rammler and Gaudin size-distribution equations are, respectively,

$$Y=\exp(-bX^n) \tag{4}$$

and

$$Y=1-BX^N, \tag{5}$$

in which Y is the fraction by weight or volume of material greater than the screen aperture size X. The remaining symbols represent parameters.

The equation

$$X_{r-1}=qX_r \quad (q \text{ constant}) \tag{6}$$

defines a geometrical progression and this has experimental significance because the most important sieve series form a geometrical scale with $q=2^{\frac{1}{2}}$. It is convenient in the present application for r to increase as X decreases [compare Eq. (2)]. Thus, by eliminating X_{r-1} and X_r between Eqs. (4), (5), and (6), Eqs. (4) and (5) become, respectively,

$$Y_{r-1}=Y_r{}^Q \tag{7}$$

$$Y_{r-1}=(1+q^N)+q^NY_r. \tag{8}$$

These are the required alternative equations and their graphical representation is clear; however, the absence of both b and B should be noted.

As $r\to\infty$, $X\to 0$ and $Y_{r-1}=Y_r=1$. This boundary condition can be used to assess loss of extremely fine materials, essentially a problem involving an unknown asymptote.

The alternative equations may be generalized into

$$Y_{r-1}=(1+q^N)+q^NY_r{}^Q, \tag{9}$$

which reduces to Eq. (7) when $N=0$ and to Eq. (8) when $n=0$. This and other generalized equations can describe distributions not satisfied by the original Eqs. (4) and (5). More detailed information has been given elsewhere.[2]

These and similar procedures for transforming explicit relationships into a pair of recurrence relations or difference equations can be of value in the analysis of data; they deserve to be better known. The writer is happy to join Professor Mangelsdorf in bringing this method to general attention.

[1] P. C. Mengelsdorf, J. Appl. Phys. **30**, 442 (1959).
[2] C. C. Harris, Second Symposium on Coal Preparation (Leeds University, 1957), Paper 8.

Dislocation Arrays in Depth and Recrystallization Produced by Surface Deformation of Single Crystals of Copper at High Temperature

JOHN M. BAILEY AND ALLAN T. GWATHMEY
Departments of Physics and Chemistry, University of Virginia, Charlottesville, Virginia
(Received August 5, 1959)

CAREFULLY prepared faces on crystals of 99.999% pure copper have been deformed by sliding sapphire styli of various radii on the surface in known directions. The arrangement of dislocations created on {111} faces was studied by means of an etchant which formed pits at clean dislocations intersecting the surface. A method was developed for investigating the change in dislocation distributions with depth below the surface by electrolytic sectioning.

The speed of sliding was 0.001 cm/sec. Experiments were conducted in hydrogen at temperatures up to 800°C, and in air. The etchant was a modification of that developed by Lovell and Wernick[1] and consisted of 4 g $FeCl_3\cdot 6H_2O$, 20 g conc. HCl, 1 g CH_3COOH, 8 drops bromine, and 150 cc distilled water. The specimen was etched by immersing for 5–10 sec. The most distinct pits were obtained when the orientation of the surface was within 1.5° of (111).

Figure 1(a) shows the end of a wear track formed by a 794 μ stylus sliding on a (111) face in a direction lying 20° from $[\bar{1}\bar{1}2]$. The load on the stylus was 25 g, and the deformation temperature was 200°C. Results were the same at room temperature. The positions of etch pits beyond the end of the wear track, where the deformation had still not become complex, indicated the arrangement of dislocations along {111} slip planes intersecting the surface.

When the deformation was performed at temperatures between 250°C and 550°C, the deformed region recrystallized spontaneously. At temperatures above 500°C, polygonization also became evident, and accompanied or replaced recrystallization. Figure 1(b) shows the end of a wear track formed by the 794 μ stylus at 800°C. The lines of etch pits outside the groove indicated that considerable polygonization of the deformed region had occurred.

(a)

(b)

FIG. 1. Wear tracks formed by sapphire stylus sliding on (111) face of 99.999% pure single crystal of copper; hydrogen atmosphere. (a) Deformed at 200°C. (b) Deformed at 800°C. ×325.

A similar series of experiments was conducted, using a 63 μ radius stylus. The more concentrated stress produced recrystallization at temperatures from 250°C to 800°C. Above 600°, both spontaneous recrystallization and polygonization were observed.

Very little polygonization was obtained by annealing for 5 hr at 800°C specimens which had been deformed at low temperatures. This agrees with the results of others[2] who studied deformation of 99.999% pure copper. The wide dislocations in copper climb with great difficulty. However, the results of our experiments indicate that polygonization is easily obtained when thermal activation and mechanical stress are applied simultaneously, as has been found in creep studies on other metals.[3]

The techniques described above may be combined with electropolishing to give a general method of studying the change in dislocation distributions with depth below the surface. Thin layers of metal of known thickness were successively removed by electrolytic polishing, and each new subsurface was etched to show the positions of dislocations. By superposition of micrographs of successive etched subsurfaces, a three-dimensional picture of the dislocation lines in the deformed surface region was obtained. Figures 2(a)–(c) indicate the decrease in dislocation density with depth below a scratch formed in hydrogen at 500°C. The original surface and subsurfaces at 200 μ and 50 μ depth are shown. A

(a)

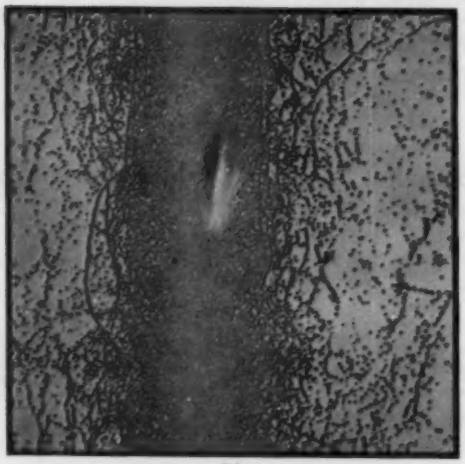

(b)

(c)

FIG. 2. Depth display of dislocations below wear track formed on (111) face by 794-μ sapphire stylus sliding in a direction near [$\bar{1}$12]; 25-g load. (a) Original surface. (b) 20 μ removed. (c) 50 μ removed. ×325.

subgrain boundary which predated the deformation can be used as a reference mark in matching the micrographs. Both recrystallization and a suggestion of polygonization were observed in the original surface.

Spontaneous recrystallization was found to penetrate 25–50 μ under various conditions, but evidence of plastic deformation was detectable as far as 150 μ below the original surface. This is an order of magnitude greater than the penetration of lattice damage due to abrasion of metal single crystals as revealed by electron diffraction.[4]

The authors gratefully acknowledge the support provided by the Office of Naval Research and the General Motors Corporation in this work. Mr. Bailey was holder of the General Motors Fellowship in Physical Chemistry for the sessions 1957–1958 and 1958–1959.

[1] L. C. Lovell and J. H. Wernick, J. Appl. Phys. 30, 590 (1959).
[2] F. W. Young, Jr., J. Appl. Phys. 29, 760 (1958); Wei, Parthasarathi, and Beck, *ibid.* 28, 874 (1957).
[3] A. Hultgren and B. Herrlander, Trans. Am. Inst. Mining, Met. Petrol. Engrs. 172, 493 (1947); R. W. Guard, *Creep and Recovery* (American Society for Metals, Cleveland, Ohio, 1957), p. 251.
[4] W. Kranert and H. Raether, Ann. Physik 43, 520 (1943); Nogata, Tomada, and Ide, Tech. Repts. Osaka Univ. 4, 7 (1954).

Behavior of InSb Surfaces during Heat Treatment*

D. Haneman
Barus Research Laboratory of Physics, Brown University, Providence, Rhode Island
(Received June 8, 1959)

IT has been observed that when InSb crystals are heated above a certain temperature below the bulk mp (523°C), small flat-topped hillocks form at various places on the surfaces. These hillocks then migrate over the surface.

An InSb filament was mounted so that a polished and etched (11$\bar{1}$) surface could be continuously viewed under a microscope while the filament was heated by passing current through it in vacuum. [The (11$\bar{1}$) surface develops chemical etch pits while the opposite (111) surface does not.] A thermocouple was constructed of 0.005-in. diam Chromel and Alumel wires, fused to make a junction region of dimensions not exceeding 0.005 in. This junction was pressed under the tension of the wires into a small cavity on the (11$\bar{1}$) face, and the specimen was so prepared that maximum heat developed in the region surrounding the thermocouple, which region was kept under continuous observation.

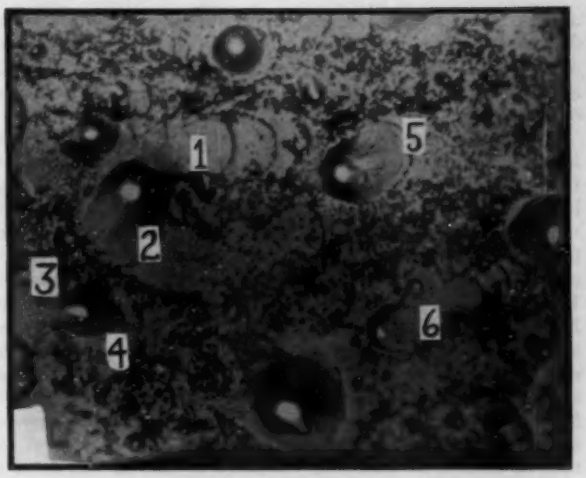

FIG. 2. Same surface as shown in Fig. 1 after heated above 420°C in vacuum. ×288.

When the specimen was slowly heated, no changes were observed under a magnification of 200 until a temperature was attained at which the thermocouple registered 400°C. Small hillocks then formed. These proceeded to travel over the surface, with velocities of up to 20 μ/sec when the surface passed through the critical temperature at a rate of the order of a few degrees C per min. The hillocks were observed to form on all surfaces.

The detailed manner in which the motion proceeds can be seen from Figs. 1 and 2, which refer to a (11$\bar{1}$) surface of another specimen at different stages of heat treatment. The surface of this specimen, oriented to within $\frac{1}{4}$ degree by x-ray measurements, was initially prepared by grinding and polishing, and etching in a mixture of 2 parts of HNO_3 (70%), 1 part of HF (50%), and 1 part of CH_3COOH (98%), which caused etch pits to develop. A (11$\bar{1}$) preferential etch consisting of a mixture of equal quantities of HF (50%) and H_2O_2 (30%) was then given, followed by rinsing in distilled water. The surface was heated by electron bombardment in high vacuum to the point where the hillocks formed, as shown in Fig. 1, and was also argon ion bombarded.

For subsequent heat treatment the 8-mm diam cylindrical crystal was supported by three Mo screws inside a mild steel tube heated by rf induction, in a vacuum of about 10^{-7} mm (ample for preventing observable oxidation). No changes in the

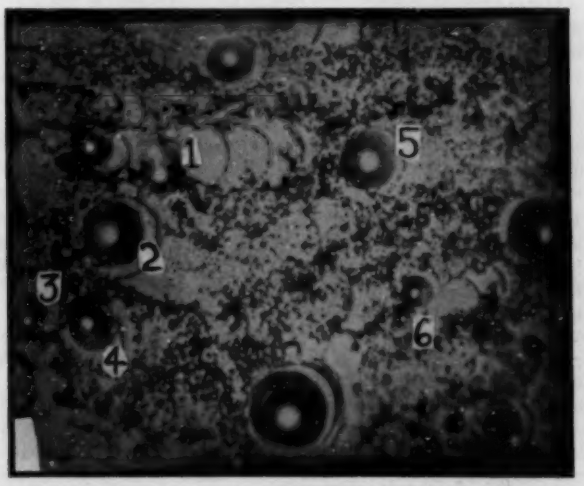

FIG. 1. (11$\bar{1}$) surface of InSb etched in argon ion bombarded. ×288.

FIG. 3. Region around coalesced hillocks one and two shown in Fig. 2 focused on melted region. ×576.

appearance of the surface were noted under a magnification of 288, as shown in Fig. 1, after heating to temperatures of about 420°C. When the crystal was heated to a higher temperature, but still below the melting point, the changes shown in Fig. 2 were obtained.

Referring to the numbered hillocks in Fig. 1, it is seen that hillocks 1 and 2 have moved towards each other and joined, forming a single hillock. The same process at a less advanced stage is evident for hillocks 3 and 4, and hillocks 5 and 6 have clearly moved, leaving a melted "wake." More such phenomena can be found by close inspection of the photographs. A focused photomicrograph of the melted region around hillock 2 is shown in Fig. 3. Note the streaky appearance. The detailed origin of the hillocks is not as yet understood. There is evidence (unpublished electron diffraction studies of evaporated films) that antimony evaporates preferentially from a heated InSb surface. It is possible that excess indium in the surface collects around favored sites to form the observed hillocks which, being indium rich (mp of indium is 155°C), are probably molten at about 400°C and can thus be mobile. No particular formation of hillocks was noted in the vicinity of chemical etch pits, which mark the emergence point of dislocations before the specimen was heated.

The surface temperature at which the hillocks form is of interest. The reading of 400°C given by the fine-wire thermocouple pressed into the surface may be somewhat low if there is an appreciable temperature drop between the part of the junction in actual contact with the surface and the remainder of the junction. Indications are that this may be the case.

* This work was supported by a contract with the U. S. Air Force, Air Force Cambridge Research Center, Air Research and Development Command.

Minority Carrier Current in a Linearly Graded Drift Field

D'AVID P. KENNEDY
Product Development Laboratory, International Business Machines Corporation, Poughkeepsie, New York
(Received June 29, 1959)

INVESTIGATIONS have been made into the influence of a linearly graded drift field upon the magnitude of hole current in an n-type semiconductor. It is assumed this field is characterized in magnitude and direction by the expression

$$\epsilon = \epsilon_0[1-(x/w)]. \tag{1}$$

The hole current is established for a field directed to aid or oppose the current resulting from diffusion alone. Further, this current is shown for each direction of field when the source of minority carriers is located at the point of maximum drift field ($x=0$) or minimum drift field ($x=W$).

Diffusion and drift represent the principal mechanisms of hole current; therefore

$$J_p = -qD_p(d\psi_p/dx)+q\mu_p\psi_p\epsilon_0[1-(x/w)]. \tag{2}$$

In this study an infinite minority carrier lifetime is assumed; thus Eq. (2) is divergence free and must satisfy the relation

$$0=(dJ_p/dx)=(d^2\psi_p/dz^2)+bz(d\psi_p/dz)+b\psi_p$$
$$b=q\epsilon/kTW, \quad z=(W-x). \tag{3}$$

A solution of Eq. (3) can be obtained by assuming the minority carrier concentration potential, $\psi_p(z)$, is given by

$$\psi_p(z)=\sum_{m=0}^{\infty} A_m z^m. \tag{4}$$

Substituting Eq. (4) into (3) yields the recurrence formula

$$A_m=(m+2)A_{m+2}; \tag{5}$$

thus Eq. (4) has the form

$$\psi_p(z)=A_0k_0(b;z)+A_0k_1(b;z). \tag{6}$$

The terms $k_0(b;z)$ and $k_1(b;z)$ are given by

$$\text{(a)}\ k_0(b;z)=1-\frac{bz^2}{2}+\frac{b^2z^4}{2\cdot4}-\frac{b^3z^6}{2\cdot4\cdot6}+\frac{b^4z^8}{2\cdot4\cdot6\cdot8}-\cdots,$$
$$\text{(b)}\ k_1(b;z)=z-\frac{bz^3}{3}+\frac{b^2z^5}{3\cdot5}-\frac{b^3z^7}{3\cdot5\cdot7}+\frac{b^4z^9}{3\cdot5\cdot7\cdot9}-\cdots, \tag{7}$$

where

$$\text{(a)}\ \partial/\partial z\{k_0(b;z)\}=-bzk_0(b,z),$$
$$\text{(b)}\ \partial/\partial z\{k_1(b;z)\}=1-bzk_1(b;z). \tag{8}$$

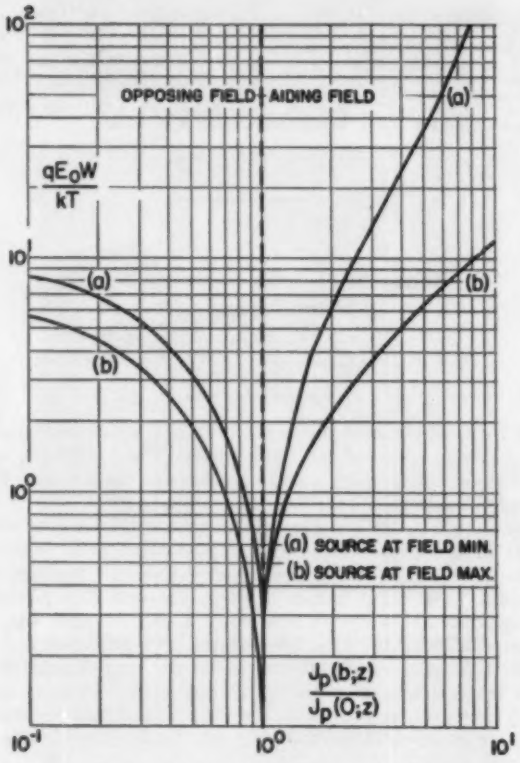

FIG. 1. Influence of graded drift field on the current ratio of Eq. (13).

Two sets of boundary conditions are imposed upon Eq. (6),

$$\text{(a)}\ \psi_p(z)=\begin{cases}\psi_{p0} & z=0\\ 0 & z=W\end{cases},$$
$$\text{(b)}\ \psi_p(z)=\begin{cases}\psi_{p0} & z=W\\ 0 & z=0\end{cases}. \tag{9}$$

Each situation requires a constant potential minority carrier source, ψ_{p0}, at one end of the semiconductor material with an ideal sink at the other end. Equation (9a) and Eq. (9b) establish the source of carriers at a location of minimum drift field ($z=W$) and maximum drift field ($z=0$), respectively.

Solutions of Eq. (3), subject to the boundary conditions imposed by Eq. (9), are given by

$$\text{(a)}\ \psi_p(z)=\psi_{p0}\frac{k_0(b;z)k_1(b;W)-k_1(b;z)k_0(b;W)}{k_1(b;W)}$$
$$\text{(b)}\ \psi_p(z)=\psi_{p0}\frac{k_1(b;z)}{k_1(b;W)} \tag{10}$$

From Eq. (2) and Eqs. (10), the minority carrier currents are given by

$$\text{(a)}\quad J_p = qD_p\psi_{p0}\frac{k_0(b;W)}{k_1(b;W)}$$
$$\text{(b)}\quad J_p = -\frac{qD_p\psi_{p0}}{k_1(b;W)}. \tag{11}$$

Equation (11a) establishes the magnitude of hole current resulting from a minority carrier source located at the minimum of an opposing drift field. Similarly, Eq. (11b) establishes this hole current when the source is located at the maximum of an aiding drift field.

Equations (11) can be normalized by using the magnitude of hole current resulting from diffusion alone ($b=0$),

$$J_p(0;z) = \frac{qD_p\psi_{p0}}{W}; \tag{12}$$

therefore

$$\text{(a)}\quad \frac{J_p(b;z)}{J_p(0;z)} = W\frac{k_0(b;W)}{k_1(b;W)}$$
$$\text{(b)}\quad \frac{J_p(b;z)}{J_p(0;z)} = \frac{W}{k_1(b;W)}. \tag{13}$$

Figure 1 is a graphical representation of the expressions appearing within Eqs. (13). In an aiding field the magnitude of hole current is shown to differ significantly for the two sets of boundary conditions assumed in this analysis. A larger magnitude of current exists within this semiconductor material when a minority carrier source is located at the point of maximum drift field.

The assumed boundary conditions of Eqs. (9) introduce a small difference in total hole current in the presence of an opposing drift field. Locating the source of minority carriers at a point of minimum or maximum field yields an approximately equal magnitude of minority carrier current.

I would like to express my appreciation to Mr. F. J. Goth and Mr. J. H. Beaudette, who were responsible for the computations of Eqs. (13). Through their efforts, IBM 704 computer programs were developed to permit a graphical representation of the solutions for this problem.

Low Melting Sulfide-Halogen Inorganic Glasses

S. S. Flaschen, A. David Pearson, and William R. Northover
Bell Telephone Laboratories, Inc., Murray Hill, New Jersey
(Received July 20, 1959)

THIS letter is a preliminary report of the discovery of a new family of glasses in ternary reactions of arsenic with sulfur and the halogen iodone. The glasses exhibit unique low melting properties; transitional in character between the common inorganic glasses and the organic polymers.

Synthesis of glasses in the ternary system arsenic-sulfur-iodine can be accomplished by direct reaction of the elements. High purity (99.99+%) end members were preweighed into clean fused silica test tubes and flame heated to reaction (500–600°C) under a nonoxidizing atmosphere. The reaction tubes were lightly covered with aluminum foil to minimize corrections for volitalization loss at high iodine concentrations. Because of the high fluidities of the system, a short (*ca* 5 min) agitation is sufficient to produce a uniform product. Sample size studied ranged from 20 to 250 g.

To aid in the determination of crystallization tendencies and liquid immiscibility phenomena, the reacted melts were allowed to air cool slowly to room temperature. Standard physical, optical, and x-ray techniques of analysis were employed in evaluation of samples and determination of phase boundaries (Fig. 1). The ternary system shows an extensive area of glass formation,

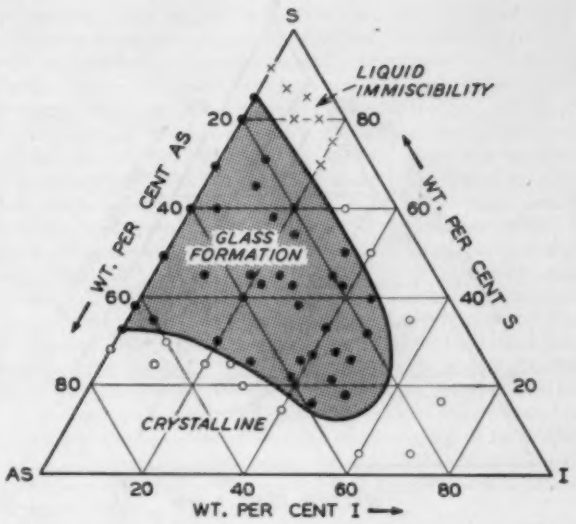

FIG. 1. The phase diagram of glass formation in the system As-S-I.

limited at high sulfur concentrations by liquid immiscibility with sulfur compounds and at low sulfur concentrations by crystalline phase formation.

The glasses are similar in major properties to those of the previously reported As-Tl-S-Se systems.[1] Generally, they exhibit good chemical durability. They are insoluble in water, acids including HF, and weak bases. They are decomposed by strong alkali and strong oxidizing agents. Glasses of high sulfur content show surface hydrolysis in boiling water. Unlike the previously reported sufide-selenide systems the higher iodine glasses are nonflammable and appear resistant to air oxidation to above 300°C. The glasses are insulators. Resistivities at 25°C are in excess of 10^{12} ohm-cm. Compare the work of Goriunova and Kolomiets[2] on the electrical conductivities of other low melting glass systems. Thin continuous transparent glassy films have been obtained in this system by vacuum evaporation.

The ternary iodine glasses possess remarkably low melting points. They appear as the first examples of ionorganic glasses having high fluidities ranging down continuously to below 100°C. An analysis of the 30 poises viscosity temperatures is shown in Fig. 2. The softening points of the glasses are illustrated in Fig. 3.

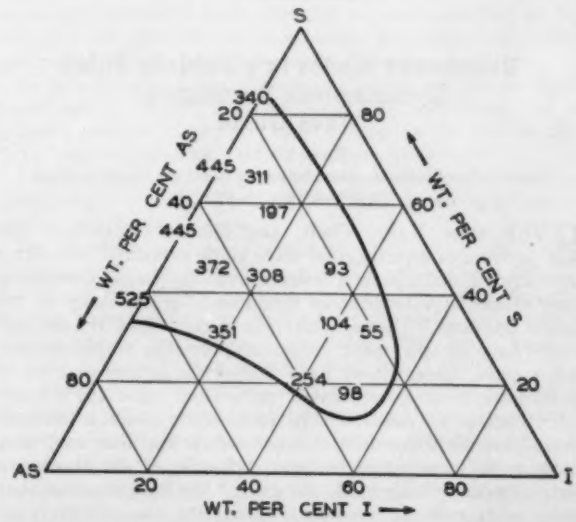

FIG. 2. Glass melt, 30 poises viscosity temperatures in the system As-S-I.

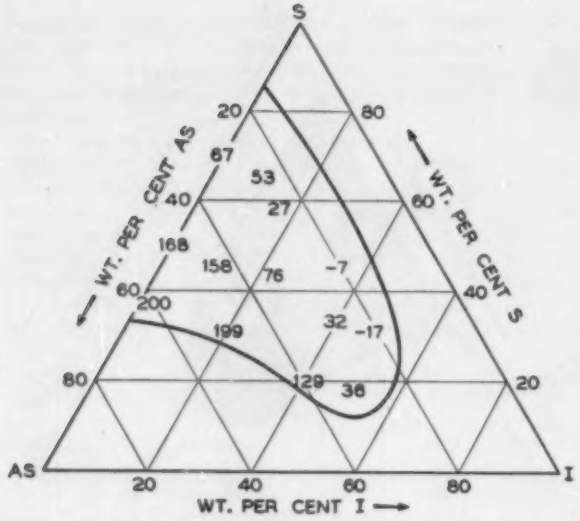

FIG. 3. Softening points of glasses in the system As-S-I.

These temperatures represent the initiation of measurable yield to short term applied stresses. The temperature coefficients of viscosity are found to be 5 to 6 times higher than those of the silicate and related oxy-glass systems. We believe the structures of these glasses to be based upon extended chains involving polymeric $(-S-S-)_n$ bonding, the role of the 7 electron iodine species being one of a chain terminator. In studies in progress, the halogen bromine is also found to have a similar effect in increasing the binary arsenic-sulfur melt fluidities. Considerable variation in properties also appears possible by means of a number of post transition element additives. As an example of possible chain cross-linking phenomena the addition of trace amounts (0.5–1.0 wt%) of Pb^{II} causes a pronounced increase in the viscosities of the ternary compositions.

We anticipate that work in progress will lead to further characterization of the properties and structures of this new family of glasses.

[1] Flaschen, Pearson, and Northover, J. Am. Ceram. Soc. **42**, 450 (1959).
[2] N. A. Goriunova and B. T. Kolomiets, Bull. Acad. Sci. U.S.S.R., Phys. Ser. (Columbia Technical Translations) **20**, 1372 (1956).

Evanescent Modes in a Partially Filled Gyromagnetic Rectangular Wave Guide

CHEN TO TAI
Instituto Tecnológico de Aeronáutica, São José dos Campos, Brasil
(Received July 29, 1959)

EVER since Kales, Chait, and Sakiotis[1] formulated the problem of a rectangular wave guide partially filled with a gyromagnetic material as a nonreciprocal microwave component many others have contributed significantly in the study of this class of problems.[2–7] In particular, the works of Lax, Button, and Roth[2,3] have revealed many interesting properties of the modes in such a guide. Recently, we have studied the general problem of an inhomogeneous gyromagnetic rectangular wave guide based upon a scalar formulation. The formulation yields a modified Sturm-Liouville differential equation which has been used as a guidance to investigate the basic behavior of the transverse electric modes existing inside the guide.* We have observed that modes with complex propagation constant, henceforth being designated as evanescent modes, are also members of an orthogonal

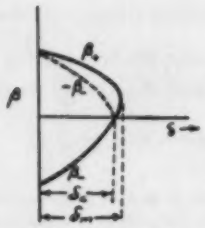

FIG. 1. The propagation constant of the fundamental mode as a function of δ.

set of modes although they are not carriers of power flowing in the guide. While many investigators seem to be aware of the existence of these modes,[8] none has given an explicit demonstration to that effect.

The purpose of this correspondence is to present such a demonstration based upon the asymptotic form of the characteristic equation. The behavior of the so-called "fundamental wave-guide mode" near and beyond cutoff is also briefly discussed.

The characteristic equation which governs the propagation constant of a partially filled guide has been derived by Lax and Button.[3] It can be written in the form

$$p k_a \cot k_a(L-\delta)+q\beta+k_m \cot k_m\delta=0, \tag{1}$$

where β = propagation constant of the guided wave, L = width of the guide, δ = thickness of the gyromagnetic material being placed at the one side of the guide, $k_a=(\omega^2\epsilon_0/\nu_0-\beta^2)^{\frac{1}{2}}$, $k_m=(\omega^2\epsilon_1/\nu_1-\beta^2)^{\frac{1}{2}}$, $p=\nu_0/\nu_1$, $q=\nu_2/\nu_1$, ϵ_1 = dielectric constant of the gyromagnetic material, $\nu_0=1/\mu_0$. ν_1 and ν_2 are the parameters of the magnetic reluctivity tensor of the gyromagnetic material being defined as follows:

$$[\nu]=[\mu]^{-1}=\begin{bmatrix}\nu_1 & 0 & i\nu_2\\ 0 & \nu_0 & 0\\ -i\nu_2 & 0 & \nu_1\end{bmatrix}.$$

It is assumed that the time factor is $e^{-i\omega t}$, and $[\nu]$ is Hermitian. By using a typical sample of magnetic material Lax and Button have solved Eq. (1) for all the real values of β in terms of δ. Two modes were identified. They have been designated as the fundamental wave-guide mode and the ferrite dielectric mode.

It is quite obvious from Eq. (1) that purely imaginary values of β are not permissible solutions for that equation except for the degenerate case corresponding to $q=0$. Thus, if evanescent modes exist at all they must have complex propagation constants. Let us denote

$$\beta=\beta'+i\beta''.$$

Now consider the case that

$$|\beta| \gg |\omega(\epsilon_0/\nu_0)^{\frac{1}{2}}| \quad \text{and} \quad |\omega(\epsilon_1/\nu_1)^{\frac{1}{2}}|, \tag{2}$$

then the following approximations are valid:

$$k_a \simeq i\beta, \quad \text{and} \quad k_m \simeq i\beta. \tag{3}$$

Under these conditions Eq. (1) reduces to

$$p \cot i\beta(L-\delta)-iq+\cot i\beta\delta=0. \tag{4}$$

By separating the real and the imaginary parts of Eq. (4), and assuming further that

$$|\beta'\delta| \gg 1, \tag{5}$$

we obtain the following asymptotic solutions to Eq. (4):

$$2\beta''(L-\delta)=n\pi, \quad n=\pm1, \pm2, \cdots, \tag{6}$$

$$\tanh\beta'(L-\delta)=-(q\pm1)/p, \quad n=\text{odd}, \tag{7a}$$

or

$$\coth\beta'(L-\delta)=-(q\pm1)/p, \quad n=\text{even}. \tag{7b}$$

We have excluded the case for $n=0$ in Eq. (6) which corresponds to the asymptotic solution for those modes with real β. The plus and the minus signs in Eqs. (7a), (7b) must be chosen such that the sign of β' will be consistent with the solutions of these two equations. The asymptotic solutions as given by Eqs. (6) and (7) are valid only when the solutions thus obtained satisfy

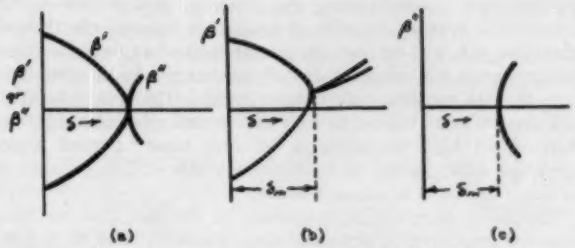

FIG. 2. The propagation constant in the neighborhood of the cutoff for a guide partially filled with (a) dielectric material; (b) and (c) gyromagnetic material.

the conditions stated by Eqs. (2) and (5). This normally occurs at the values of δ very near to that of L. When these conditions are not satisfied we must use Eq. (1) directly in solving for β' and β'' that corresponds to resolve two simultaneous equations involving β', β'', and δ. Without good computing facilities it is not easy to pursue these solutions. However, it may be of some interest to discuss briefly the nature of the fundamental waveguide mode near and beyond the cutoff.

For a typical sample, Lax and Button have computed the real propagation constant as a function of δ for the fundamental mode. Their figure is reproduced in Fig. 1 where the dotted curve, labeled $-\beta_-$, is the mirror image of the curve labeled β_-. The curves β_+ and $-\beta_-$ are the ones originally plotted by Lax and Button. For clarity we have slightly exaggerated the convex part of curve β_+. For analytical reasons it is better to treat β_+ and β_- as two branches of a continuous curve. The distance δ_c was interpreted by Lax and Button as the cutoff thickness of that mode. Actually it can be verified that at δ_c where $\beta=0$, the derivative of β with respect to δ is positive. The curve becomes single valued at $\delta=\delta_m$ which should be interpreted as the cutoff thickness. For $\delta_m>\delta>\delta_c$, the fundamental mode consists of two forward waves. In that sense it also shares the unidirectional property of the ferrite dielectric mode. What happens to the curve for $\delta>\delta_m$ is similar to the cutoff phenomena for a guide partially filled with a dielectric material. The main difference is that β starts to go to the complex domain for the gyromagnetic case. The splitting of β into β' and β'' is sketched in Fig. 2. The two branches of β' for $\delta>\delta_m$ may swing either both upward or both downward or in the opposite sense depending upon the values of the constants of the material. The two branches of β'', however, always go to the opposite directions. It is clear from our sketch that the undirectional property also applies to the evanescent modes when the two branches of β' both swing to the same direction.

[1] Kales, Chait, and Sakiotis, J. Appl. Phys. **24**, 816 (1953).
[2] Lax, Button, and Roth, J. Appl. Phys. **25**, 1413–1421 (1954).
[3] B. Lax and K. J. Button, J. Appl. Phys. **26**, 1184–1187 (1955).
[4] S. Weibaum and H. Boyet, J. Appl. Phys. **27**, 519–524 (1956).
[5] H. Seidel, J. Appl. Phys. **28**, 218–226 (1957); Bell System Tech. J. **36**, 409–426 (1957).
[6] T. M. Straus, I.R.E. Wescon Record, Pt. I, 135–146 (1958).
[7] R. F. Soohoo, Proc. Inst. Radio Engrs. **46**, 788–789 (1958).
[8] Details of this study will be published soon.
[9] Symposium on Electromagnetic Theory, I.R.E. Trans. Antennas and Propagation, AP-4, No. 3 (July, 1956).

Reviving the Classical Theory of Friction by a Modern Dislocation Theory of Deformation Revision*

JOHN H. DISMANT†
University of North Dakota, Grand Forks, North Dakota
(Received August 17, 1959)

THIS deformation and dislocation theory approach appears to consolidate, revise, and simplify all of the older theories of friction and allied phenomena.

Based on I-Ming Feng's plastic and elastic deformation theory of wear, this new approach adds the dislocation concept of deformation. Now all facets of this vast field of friction can apparently be accounted for by a modern modification of the older and hitherto rejected classical (Ammonton's)[1] theory of friction, which incidently stood as the only acceptable theory of friction for over 200 years. The classical theory considered the asperites or irregularities of a surface as sliding over one another, similar to the sliding of one inclined plane over another. It is necessary to point out that for this sliding action to function these small asperites or irregularities must act as rigid bodies. In view of modern developments on crystalline materials, it appears impossible for areas as small as these irregularities must be (possibly 10^{-2} to 10^{-4} sq cm in section) to support each other as rigid bodies for sliding to occur. Modern developments indicate the asperites would flow through each other by some type of deformation, the kind and quantity depending on the dislocations developed and moving. This then becomes a new revised classical theory of friction with low coefficients of friction related to elastic deformations and high coefficients of friction related to the irreversible plastic deformations, and modifications of the elastic and plastic effects are provided by the motion and generations of dislocations which allow this approach to apparently account for all major frictional phenomena.

At this point, it is well to recall that the classical (Ammonton's) theory of friction was rejected only when it was demonstrated that the frictional force was much greater than the slider mass multiplied by the distance it was raised. A number of years were required to replace this classical theory of friction and as late as 1953 the *Encyclopedia Britannica* still used it to describe friction.

The field of lubrication is generally separated into hydrodynamic (or bulk) and boundary (or thin film) phenomena. This new approach in no way affects the present hydrodynamic theory of lubrication. However, fine points of the revised classical theory, as reviewed previously, leads to predictions of an entirely new hypothesis of the mechanism of boundary lubrication and thin film bearings. This new hypothesis is that boundary lubricants cause the surface crystals to become elastically harder by restrictions on the motion and generation of dislocations, as described by Cottrell[2] for oxide films and demonstrated by Barrett.[3] In other words, the actual yield point strength will be increased on the asperites by the action of the coherent film of a boundary lubricant, and similarily for thin metallic films on bearings.

Experimental evidence by the author appears to bear out this hypothesis for one such compound on very fine copper wire springs where 0.4-mil copper wire springs dipped in a 5% oleic acid solution shows an average yield point loading of 145% compared to 100% for undipped springs, that is an average increased yield point strength of 45%. This yield point strengthening apparently diminishes as the wire size increases since 0.6-mil wire indicated only 33% increase and 0.10-mil wire shows none, which also provides a potential explanation of the wear-in period.

In this revised theory sliding and rolling friction are again considered as derived from the same basic mechanism but by different manifestations. The basic mechanism for both is effectively that described by Tabor[4] for rolling friction only.

Further, the observed high and low speed and loading variation effects observed in friction are both plausibly accounted for by this revised classical theory.

For the critical subject of the stick-slip (chattering) phenomenon there appear to be at least six plausible explanations provided by the new revised theory as compared to only one for the existing welding theory of friction. Perhaps all six explanations may be individually or concurrently applicable. The most intriguing however is based on geometric reasoning from Cottrell's[5] "turbuent plastic flow" in crystals, with work hardening shifting the dislocation force to various equivalent crystallographic planes to provide a multitude of directional force components in any given polycrystalline material; the instantaneous summation of all these component forces with their directional properties yields the momentary direction and magnitude of the bulk stick-slip (chattering) force. This summation is however anticipated to be

very sensitive in both the direction and magnitude of the individual components and their interrelations so that the next instant the summation of the component forces may yield an entirely different bulk direction and magnitude. Further, this explanation operates in three dimensions which is in agreement with at least some published work on frictional sliding tracks.

Welding properties of friction are considered a major phenomenon only at the time of seizure and even then fifty percent of the friction energy must be used by the deformation to keep from violating the second law of thermodynamics, since it will take at least as much energy to make a weld as to break it.

* John H. Dismant, Ph.D. thesis, University of Utah (1955).
† Summer Professor Consultant, Oklahoma City Air Material Command, Tinker Air Force Base, Oklahoma.
[1] G. Ammonton's, Mem. acad. roy. Soc. Paris 206 (1699).
[2] A. H. Cottrell, *Dislocations and Plastic Flow in Crystals* (Oxford University Press, New York, 1953), pp. 55–56.
[3] C. S. Barrett, Acta Met. 1, 2 (1953).
[4] D. Tabor, Phil. Mag. 43, 1055 (1952).
[5] Reference 3, p. 157.

Maser Behavior: Temperature and Concentration Effects*

T. H. Maiman
Hughes Aircraft Company, Research Laboratories, Culver City, California
(Received July 20, 1959)

IT has been conventional practice to operate solid-state masers at temperatures in the liquid-helium range. Operation at much higher temperatures is certainly possible in principle, but two effects make this difficult. The magnetic susceptibility of a paramagnetic material is an inverse function of absolute temperature, and in addition thermal relaxation times rapidly decrease with an increase in temperature. Neither of these restrictions however is severe enough to prevent maser action in ruby at temperatures well above the helium region. Our laboratory reported successful performance of an x-band ruby maser at 50°K with solid nitrogen used as a coolant[1]; at the same time Ditchfield and Forrester reported similar results.[2]

Recently, efforts have been made in this laboratory to increase the maser operating temperature further, and maser action has been successfully attained up to 195°K with dry ice used as the coolant.

Preliminary measurements have been made on a maser operating at 77.4°K. With a 0.20% ruby crystal,[3] a gain band-width product of about 14 Mc was obtained, and an effective noise temperature of approximately 100°K (excluding input losses) was observed. This temperature is in satisfactory agreement with a value of 95°K which was calculated by taking into account cavity losses and the spin temperature of the ruby. Efforts to reduce the noise temperature by optimizing crystal and cavity parameters as well as experiments to study in more detail the contributions to the noise temperature are in progress.

Preliminary studies to determine the effect of paramagnetic-ion density on maser performance were also made. It was found that ruby crystals having a chromium concentration larger than approximately 0.1% exhibited poorer performance (gain-band-width product) at 4.2°K than that of more dilute crystals at the same temperature. Sufficient data are not available at this time to allow definite conclusions to be drawn; however, an explanation based on cross-relaxation effects follows.[4,5] In sufficiently dilute paramagnetic crystals the cross-relaxation times are long compared with the thermal relaxation times, even at very low temperatures, and therefore they do not essentially interfere with normal maser operation. However, as the spin density is increased, the cross-relaxation rate is also increased and can become competitive with the thermal processes. In the limit, an equilibrium emissive condition is prevented. In a 0.7% crystal for example, we found that by saturating the pumping transition, we could reduce the absorption of the maser transition, but we were unable to obtain negative spin temperatures. One expects that if the lattice temperature is raised an order of magnitude or more, the thermal relaxation rate will increase by a large factor but that the cross-relaxation rate will remain essentially unchanged. In this situation, even in a reasonably concentrated crystal, the cross-relaxation rate may be small compared with the thermal relaxation rate, and therefore at high temperatures we may expect normal maser operation with crystal concentrations which exhibit reduced or no maser action at low temperatures.

The above argument is supported by the fact that we have observed amplification and oscillation in a 0.7% ruby at 77.4°K, but, as noted above, we were not even able to produce negative temperatures in the same crystal at 4.2°K.

In all of these experiments, the ruby was operated in the "push-pull" pumping mode[6] with the signal frequency at 9.14 kMc and the pump frequency at 23.1 kMc.

The maser design used is a standard configuration in our laboratory and was developed in connection with a Signal Corps contract.[1,7] The cavity was constructed from a solid block of ruby cut to the correct dimensions and coated with silver; holes in the coating served as coupling irises. The cavity was resonant in the TE_{011} mode at x-band and used the TE_{103} mode for the K-band pumping transitions. Since the dielectric constant of ruby is large ($\epsilon \sim 10$), the cavity dimensions for the dominant mode are quite small (approximately 0.28 by 0.28 by 0.14 in.). Coupling to the cavity was achieved by constructing a wave-guide transition having dimensions that gradually tapered from those of standard x-band wave guide to the dimensions of the cavity. The transition contained a piece of clear sapphire to keep the wave guide above cutoff. The K-band pumping power was similarly coupled through a taper transition to a perpendicular face of the cavity. A drawing of the transition section and cavity is shown in Fig. 1.

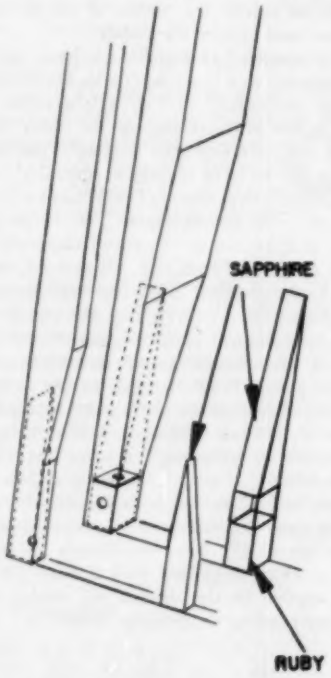

FIG. 1.

The taper transitions, which were designed to take advantage of the small cavity dimensions, permitted the placement of a small permanent magnet (weighing 12 ounces) inside of the working Dewar to furnish the required magnetic field of 4000 gauss.

The over-all weight of the liquid-nitrogen maser, including the Dewar, magnet, and microwave plumbing, was 3½ lb.

The author gratefully acknowledges the technical assistance of I. J. D'Haenens in constructing the apparatus and in making the measurements; he also appreciates helpful discussions with Dr. G. Birnbaum.

* This work was supported in part by the U. S. Army Signal Corps.

[1] T. H. Maiman, NSIA-ARDC Conference on Molecular Electronics (Washington, D. C., November 13–14, 1958), pp. 71–74.
[2] C. R. Ditchfield and P. A. Forrester, Phys. Rev. 1, 448–449 (1958).
[3] Crystal concentrations quoted here are given as weight percent of Cr_2O_3 to Al_2O_3 as determined by chemical analysis.
[4] Bloembergen, Shapiro, Pershan, and Artman, Phys. Rev. 114, 445 (1959).
[5] S. Shapiro and N. Bloembergen, Technical Report No. 306, Croft Laboratory, Harvard University (June 18, 1959).
[6] Makhov, Kikuchi, Lambe, and Terhune, Phys. Rev. 109, 1399 (1958).
[7] T. H. Maiman, Signal Corps Contract No. DA 36-039 SC-74951 Second Quarterly Progress Report (March 1, 1958 through May 30, 1958) et seq.

Books Reviewed

Prompt, noncritical reviews appear in this column. Critical reviews of many of the books described here will appear in Physics Today, The Review of Scientific Instruments, *or* American Journal of Physics.

Principles of Quantum Electrodynamics. (Volume 3 of Pure and Applied Physics). Pp. 234. Academic Press, Inc., New York, 1959. Price $8.00.

This translation of Thirring's well-known treatise is a welcome addition to the English literature on field theory. Though applications are restricted to electrodynamics the author has formulated the subject so that the reader may generalize the formulation to other fields as well. Special features, not to be readily found elsewhere in the literature, comprise a discussion of fluctuation phenomena, measurability, and a careful discussion of the restrictions imposed on matrix elements by the requirement of Lorentz invariance. The book is not elementary and does not serve as an introduction to the novice. However, to the initiate the beauty of both mathematical development and physical interpretation is wondrous to behold.

Methods of Experimental Physics. Volume 6, Solid State Physics. Part A: Preparation, Structure, Mechanical and Thermal Properties. Pp. 466. Academic Press, Inc., New York, 1959. Price $11.80.

This book is the first of two books to be devoted to solid state physics in a series concerned with methods of experimental physics. The book consists of a coordinated collection of articles each of which is written by authors experienced in the field. The subjects covered are: preparation and purification of materials, crystal structure determination, mechanical properties, thermal properties, and studies of solids subject to high pressures. The book is a reference book of broad utility and is designed to be useful to graduate students, research workers, and teachers.

Great Experiments in Physics. Edited by Morris H. Shanos. Pp. 370. Henry Holt and Company, Inc., New York, 1959. Price $4.40.

This book describes approximately twenty classic achievements in physics. Extracts from the original publications are reproduced and the editor has added biographical, historical, and scientific commentaries. Four typical subjects are "Accelerated motion" by Gallileo, "Light diffraction" by Fresnel "X-rays" by Roentgen, "The neutron" by Chadwick. Any person interested in the history of science should have no difficulty understanding these commentaries.

Progress in Cryogenics. Volume 1. Edited by K. Mendelssohn. Pp. 259. Academic Press, Inc., New York, 1959. Price $11.00.

This book is a collection of articles on a wide variety of low-temperature problems having current scientific or technical interest. The subjects covered are: superconducting circuits, thermoelectric cooling, evacuated powder insulation, distillation, mechanical properties of metals, frozen free radicals, specific heat measurements, and ultrasonic attenuation in metals.

Introduction to the Theory of Quantized Fields. N. N. Bogoliubov and D. V. Shirkov. Pp. 647+lxxiii. Interscience Publishers, Inc., New York, 1959. Price $17.00.

This book is a solid introduction to the theory of fields bringing the reader up to date on the situation as it stood at the end of 1956. In addition to a discussion of renormalization techniques and Green's function methods, the book is distinguished by a lengthy account of dispersion relations with application to meson-nucleon interactions. It is regrettable that in view of this elaborate treatment the Chew-Low theory together with the nature of the 33 resonance is not expounded by the authors. General absence of discussion of contact between experiment and theory is weak.

Space Technology. Edited By Howard Seifert. John Wiley & Sons, Inc., New York, 1959.

A collection of talks given by many experts in a UCLA graduate level extension course covering practically all aspects relating to space exploration. The series was filmed and has been widely distributed. To those not involved in the space program, the book is still of interest but for the most part, not one that can be skimmed lightly. The table of contents includes: "The unknown cosmos," "Interplanetary operations," "Time dilation effects in space travel," and "Crew performance in a space vehicle," to mention a few of the 33 chapters included. The work is divided into five main divisions following an introduction: "Flight dynamics"; "Propulsion and structures"; "Communications"; Guidance and control"; "Man in space"; and the "Present and future applications of space technology." Not much is said concerning ion propulsion and nothing about photon propulsion. Nor is anything included on space law. An Appendix is included listing about 100 multiple-choice questions given as an examination on the Space Technology course based on these lectures. Answers are also given.

Semiconductors and Transistors. Douglas M. Warschauer. Pp. 250+xvii. McGraw-Hill Book Company, Inc., New York, 1959. Price $6.50.

This intermediate-level text describes the physical principles underlying the behavior of semiconductors, transistors, and other solid-state devices, as well as their application to various useful circuits. It covers the physics pertinent to semiconductors, discusses their characteristics, and the way in which diodes and transistors operate by giving a description of the working of the basic *p-n* junction. Calculus is not used in presenting the concepts involved; physical concepts are discussed and clarified in elementary terms.

Books Received

Notes on the Quantum Theory of Angular Momentum. Eugene Ganberg and George Edward Pake. Pp. 56. Stanford University Press, Stanford California, 1959. Price $1.25.

Geist und Materie. Erwin Schrodinger. Pp. 77. Vieweg and Sohn, Braunschweig, 1959.

Tabellen von Exponentialfunktionen und-integralen Zur anwendung auf Gebieten der Thermodynamik Hableiter-theorie und Gaskinetik. SIEGFRIED OBERLANDER. Pp. 151. Akademie-Verlag, Berlin, 1959.

Hochfrequenz-Messtichnik. O. ZINKE AND H. BRUNSWIG. Pp. 234. S. Hirzel Verlag, Stuttgart, 1959.

Techniques Modernes et Applications de la Cryometrie. Y. DOUCET. Pp. 215+x. Dunod, Paris, 1959. Price 450 fr.

Analytical Elements of Mechanics. Vol. I. THOMAS R. KANE. Pp. 192+lviii. Academic Press, Inc., New York, 1959.

Scientific Russian without Tears. J. W. PERRY. Pp. 26. Reprinted from *The Chemical Bulletin*. Chicago Section ACS, Inc., Chicago 6, Illinois, 1959. Price $1.00.

Atlas of γ-Ray Spectra from Radiative Capture of Thermal Neutrons. L. V. GROSHEV, V. N. LUTSENKO, A. M. DEMIDOV, AND V. I. PELEKHOV. Pp. 198. Pergamon Press, New York, 1958. Price $20.00.

Gas Chromatography. Second Edition. A. I. M. KEULEMANS AND C. G. VERVER, EDITORS. Pp. 217+xvii. Reinhold Publishing Corporation, New York, 1959. Price $7.50.

Announcements

The *Journal of Mathematical Physics*, a new AIP bimonthly, makes its appearance in February. Edited by Elliott Montroll, the journal offers new mathematical methods for the solution of physical problems as well as original research in physics furthered by such methods. Review papers on mathematical topics for physicists also will appear occasionally.

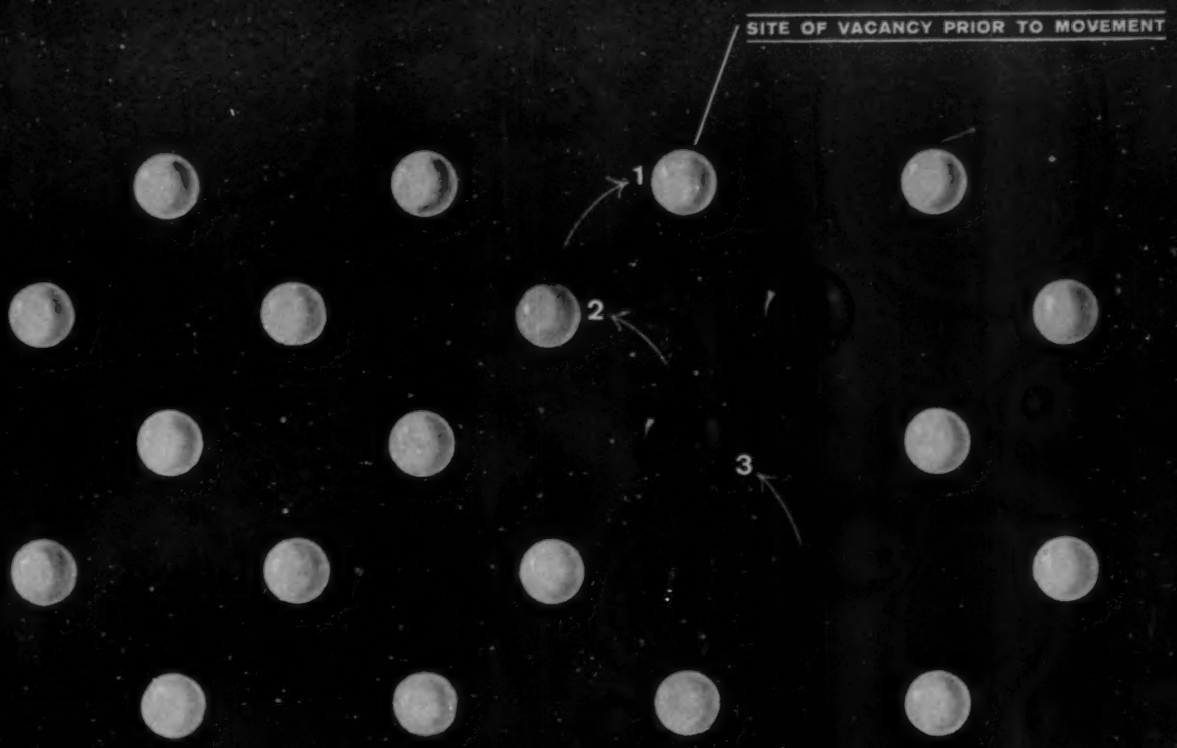

Report from IBM ▲ *Yorktown Research Center, New York*

HOW ATOMS JUMP IN SOLID SOLUTIONS

It is known that in many solid solutions, such as alpha brass, atomic rearrangement can be induced by an applied stress. Experiments of this nature have confirmed that the atomic mobility required for this rearrangement derives chiefly from the presence of lattice vacancies. A simple example is seen in the reorientation of a pair of solute atoms.

The time required for these atom jumps is under investigation by metallurgists at IBM Research.

By observing this rearrangement—a relaxation effect seen as a peak in a curve of internal friction vs. temperature—it is possible to measure atom mobility at temperatures far below those at which ordinary diffusion experiments can be carried out. It is also possible to freeze an excess of defects into the lattice of an alloy by quenching rapidly from high temperatures to produce an abnormally short relaxation time.

Through these experiments IBM scientists are determining how the equilibrium concentration and mobility of vacancies change with temperature. They seek to learn the manner in which the excess of vacancies retained after quenching disappears within the alloy.

IBM.RESEARCH

Investigate the many career opportunities available in exciting new fields at IBM.
International Business Machines Corporation, Dept. 579M, 590 Madison Avenue, New York 22, New York.

LOW VOLTAGE DC POWER SUPPLIES

6, 12, and 28 volt

	Voltage	Current	Price
Model 125B	6.3	1.5a	$47.00
Model 119	12.6	0.9a	$43.50
Model 227	28.0	1.2a	$59.00

These small "Uniplugs" operate on 115 volts AC to furnish a DC output with low ripple voltage. Useful at many jobs in the lab. The octal plugin feature makes them very economical as they can be removed from equipment which is no longer in use,

C. J. APPLEGATE & CO.

1840 24th Street *Phone Hillcrest 2-8750* Boulder, Colorado

ENGINEERS

WHO WANT TO DO

ORIGINAL THINKING

Men who seek the challenge of the new will find just such opportunity for original thought at Project Matterhorn an AEC thermonuclear research program at Princeton University's Forrestal Research Center. Your association with some of the leading scientists of our time will enhance your professional standing and enable you to use your talents to their fullest.

Salaries are comparable to industry. Unusual benefits include 1 month's vacation, retirement plan, life insurance, major medical insurance, etc.

ELECTRONICS ENGINEERS OR PHYSICISTS

DEVELOPMENT WORK: To develop scientific apparatus used with thermonuclear devices. Covers broad field of electronics, optics, nuclear instrumentation, pulse circuits, etc.

ELECTRONICS ENGINEERS, JR. & SR.

TRANSMITTER & POWER-TYPE RF EQUIPMENT: For super power tube equipment being developed to heat plasma with the goal of reaching thermonuclear temperatures. Experience with amplifiers, oscillators, transmitters or pulse circuitry desirable.

Please send resume to R. B. Starbuck

P.O. BOX 451, PRINCETON, NEW JERSEY

Scylla

Tobe... first with condensers for thermonucleonics

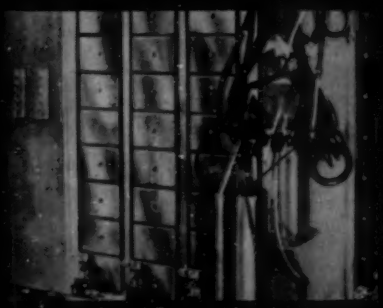

Naval Research Lab's Condenser Battery

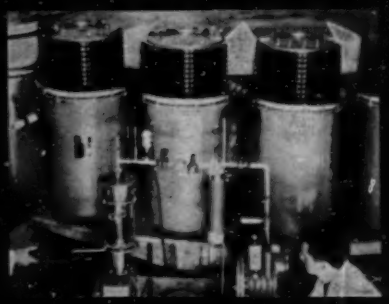

Columbus II

Of particular interest to the thousands of international visitors to the historic Geneva Atoms-For-Peace Conference, was the display of thermonuclear fusion research equipment which the U.S. Government set up. Significantly, several of these devices use Tobe low-inductance condensers. Three of the machines are shown here.

Even now — long after the conference — inquiries and orders are being received from every corner of the globe. The postmarks read like a roll call at the United Nations: Great Britain, Japan, Italy, U.S.S.R., France, Brazil, The Netherlands, Sweden and many others.

Scientists and engineers of these countries are in perfect accord in their recognition of Tobe thermonuclear condensers.

We invite inquiries for a single energy storage capacitor or a complete energy storage system including capacitors, racks, interconnecting lines, protective devices and charging power supply. For further technical information or engineering aid, write to Cornell-Dubilier Electric Corp., Marketing Office, Norwood, Massachusetts.

CDE **CORNELL-DUBILIER ELECTRIC CORPORATION**
Affiliated with **Federal Pacific Electric Company**

Industrial Research PHYSICISTS and Electronic Engineers

Electronics . Optics
Sonics . Instrumentation
Automation . Measurements

—If you are a physicist or electronic engineer and have broad technical interest in any of the above fields, then the Physics Department of Continental Can Company offers you a unique opportunity for interesting non-defense work and professional growth.

THE POSITIONS

We have openings for both recent graduates and more experienced individuals and one, with the title of General Physics Laboratory Director, for an outstanding man who has demonstrated considerable creative ability.

THE WORK

We are pioneering long-range and radically new processes and products arising out of the company's major position in high-speed fabrication of metal, glass, paper, fiber, cork and plastic containers, and other products. In addition, we render consulting services to other divisions.

THE BENEFITS

Salary structure is excellent, and there are numerous benefits including company-paid hospitalization and life insurance, relocation assistance. Staff members are *encouraged* to keep ahead in their profession.

THE LOCATION

The division's new laboratories are located within easy reach of the University of Chicago, The John Crerar Library, Argonne National Laboratory and of the finest southern and western residential suburbs.

You are invited to investigate these opportunities at Continental Can Company, in complete confidence. A few minutes now can mean a jump of years in your professional progress.

Please write or call collect to Dr. Harold K. Hughes, Director of Physics Research

CONTINENTAL CAN COMPANY, INC.

Central Research & Engineering Division
7622 S. Racine Avenue
Chicago 20, Illinois
VIcennes 6-3800, Ext. 305

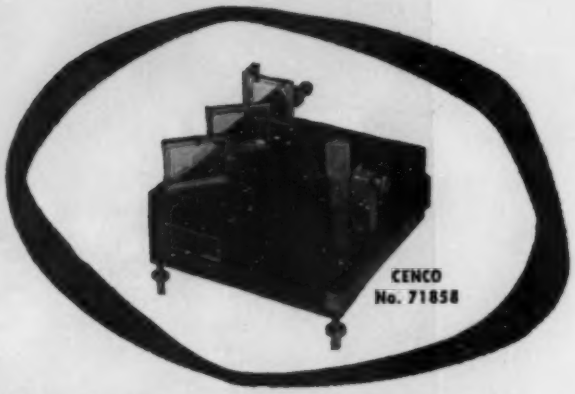

NOW! *a low cost Michelson*
INTERFEROMETER

This precision instrument is ingeniously designed to provide .2% accuracy at minimum cost. Directly calibrated in inches. Clear, well defined fringes are observable and measurable. Refractive properties of transparent materials can be easily studied. Sturdily constructed for classroom or laboratory research.

Complete with monochromatic mercury light and illustrated experiment manual . . . only $209.95

cenco

CENTRAL SCIENTIFIC CO.
A Subsidiary of Cenco Instruments Corporation
1718-A Irving Park Road • Chicago 13, Illinois
Branches and Warehouses—Mountainside, N. J. Boston • Birmingham • Santa Clara • Los Angeles • Tulsa Houston • Toronto • Montreal • Vancouver • Ottawa

MS-9 SERIES PACKAGED Helium Mass Spectrometer LEAK DETECTORS

Finds leaks in hermetically sealed components

WITH/WITHOUT AUTOMATIC ROUGHING STATION, BACKFILL CONSOLE

This is the most accurate, trouble-free
LEAK DETECTOR
you can buy

fast...simple...safe

• Quick and Easy to Operate
Flip a switch and the built-in automatic station does the work for you, electrically (no air supply required) ...lets you make up to 120 tests per hour...safety interlocks eliminate operator error, permits use of non-technical personnel.

• Guaranteed Accurate and Safe
Constant 10^{-10} cc/sec accuracy guaranteed by the patented VEECO VEETUBE®...it cleans itself...uses safe, inert helium as tracer gas.

• Thoroughly Tested
Each MS-9 undergoes a full week (168 hrs) of test run and inspection before shipment.

FREE MS-9 BROCHURE contains full details on performance, specifications, operation and advantages. There is an MS-9 series Leak Detector to fill your exact need. Write Department A-1435.

Veeco
VEECO VACUUM CORP.
86 J Denton Avenue, New Hyde Park
Long Island, New York
HIGH VACUUM & LEAK DETECTION EQUIPMENT

CAREER PROGRESS AT

Your opportunity for personal progress at Allied Research is as unlimited as the broad spectrum of basic and advanced engineering activities currently underway at this compact, research-oriented organization.

Purposefully probing the frontiers of theoretical and applied knowledge, Allied Research continually pioneers fresh areas for your growth and advancement.

This fast-paced rate of purposeful development within the Allied Research organization since its formal establishment in 1951 continues to present new opportunities at all levels.

Openings for senior and staff levels. PhD, MS or BS for:

Meteorologists

• Physical meteorology • physics of the upper atmosphere • satellite meteorology.

Physicists—Astrophysicists

• Nuclear weapons effects at extreme altitudes • plasma physics, electromagnetic theory • radiation theory, nuclear physics or operations research, electromagnetic propagation, atmospheric physics • fundamental electromagnetic communications problems.

Systems Engineers

• Systems and development background • experience in feed back controls; exposure to analog computers.

Electrical Engineers

• Systems planning of ionospheric research equipment • R. F. Transmission.

Mark this day for your first step in finding a fulfilling career at Allied Research.

Salaries are substantial, incentives worthwhile, and tuition assistance for postgraduate studies can help you achieve maximum accomplishment. Harvard and M.I.T. are conveniently located for engineers interested in pursuing such courses. Mr. Norman Metzger will accord your resume prompt attention in absolute confidence.

ALLIED RESEARCH ASSOCIATES, INC.

43 Leon Street, Boston, Massachusetts
GArrison 7-2434

RESEARCH • ENGINEERING • DEVELOPMENT

unequalled for **VERSATILITY**

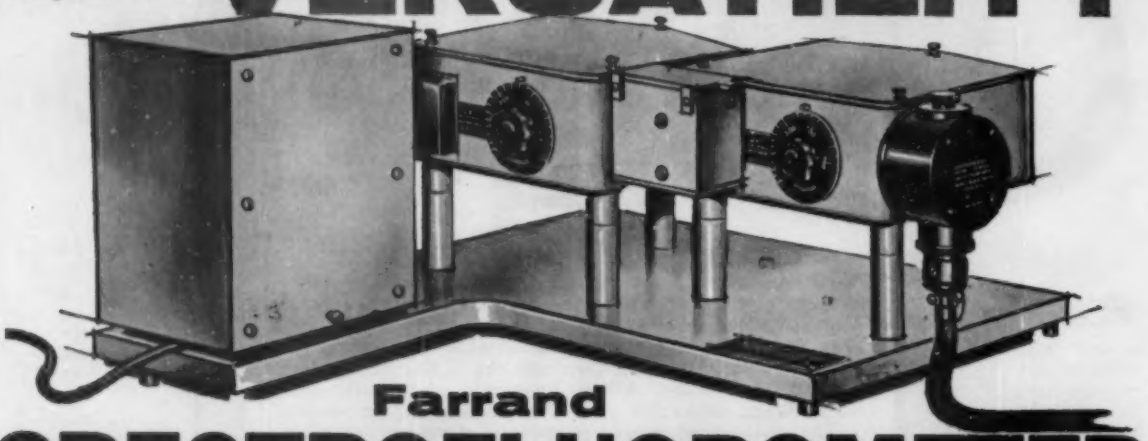

Farrand

SPECTROFLUOROMETER

Versatile instrument for photo-fluorometric assay, identification and analysis of chemical constituents in the Ultraviolet, Visible and Infrared. Measurements are much more discriminating than obtained through colorimetric or spectrophotometric methods. Can be used for micro or macro volumes. Models for manual, oscilloscope or chart recording available.

Technical data available on request
Specify Bulletin No. 820AP

FARRAND OPTICAL CO., INC.
BRONX BLVD. AND EAST 238th STREET • NEW YORK 70, N. Y.
Engineering Research Development Design and Manufacture of Precision Optics Electronics and Scientific Instruments

CHEMISTS
PHYSICISTS

Rapid and steady growth has created new openings in Melpar's Physical Sciences Laboratory for several experienced solid state chemists or physicists. Must be skilled in both theoretical and applied techniques, involving the selection, synthesis, application and testing of a wide variety of materials. Broad areas of interest include infrared, electroluminescence, semiconductors, nonlinear amplifiers, thermoelectricity, electro-chemistry, and fabrication of microcircuits.

Send complete resume to: **Professional Employment Supervisor**

MELPAR, INC.

A Subsidiary of Westinghouse Air Brake Co.

3317 Arlington Boulevard, Falls Church, Va.
In Historic Fairfax County. *(10 MILES FROM WASHINGTON, D. C.)*

PHYSICISTS

Opportunities in advanced reactor development at The Knolls Atomic Power Laboratory. The new groups being formed around key members of KAPL's professional staff afford physicists who join us now, unusual opportunities to work in close liaison with acknowledged leaders in reactor technology. Experimental facilities for nuclear investigations at KAPL rank with the finest in the nation and include seven reactor critical assemblies, one of which permits study of core configurations at power reactor temperatures and pressures. You are invited to inquire about the following openings: **Experimental Physicists** to plan, conduct and interpret results of reactor physics experiments. Develop new critical experiments, techniques and analytical methods of solving experimental reactor physics problems. Assist in the formulation and direction of critical experimentation. Should have MS or PhD in Physics. **Analytical Physicists** to interpret physics data and its application to design. Develop theory, analyze phenomena and predict nuclear performance and characteristics of reactors. Should have MS or PhD in Nuclear Engineering or Physics. **Nuclear Analysts** to evaluate reactor nuclear designs, using analytical and machine computational techniques. Predict nuclear performance of reactors. Develop and improve analytical techniques for the solution of nuclear design problems. Qualifications should include MS in Engineering or Physics with experience in nuclear analysis of reactors. **Also Openings in these areas:** Advanced Mathematics / Computer Programming / Controls Development / Coolant Chemistry & Engineering / Electrical Design / Facilities & Construction / Shielding Design / Heat Transfer, Fluid Flow / Instrumentation Development / Mass Spectrometry / Materials Application / Mechanical Design / Physical Metallurgy / Powerplant Equipment / Pressure vessel Design / Radiochemistry / Radiological Engineering / Reactor Plant Operation / Solid State Physics / Stress Analysis / Systems Analysis / Welding & Fabrication / X-Ray Diffraction.

U.S. Citizenship Required / Please write in confidence, including salary requirements to Mr. A. J. Scipione, Dept. 37-MA.

Knolls Atomic Power Laboratory

OPERATED FOR A. E. C. BY

GENERAL ELECTRIC

SCHENECTADY, N. Y.

. . . to broaden man's knowledge of the Universe that surrounds him . . . enabling him to reach out and grasp radical, new theories that make for a better and safer world.

At High Voltage Engineering Corporation basic developments important to medicine, science, and industry are now being conducted through the use of high energy particles. With the use of Van De Graaff and Linear Electron Accelerators, High Voltage is making startling discoveries from the Earth's crust to the wear of a sprocket gear.

If this type of research interests you, if you would like to team up with recognized experts in their fields, and if you are a Physicist with experience in

- **ION PHYSICS**
- **ION OPTICS**
- **HIGH VACUUM TECHNOLOGY**
- **ELECTROSTATICS**

Then you are cordially invited to submit your resume to Mr. Gordon R. Hamilton, Jr., Personnel Manager, or visit our representatives at the meeting of the American Physical Society at the Hotel New Yorker, New York City, New York, January 27 through January 30, 1960.

HIGH VOLTAGE ENGINEERING CORP.

BURLINGTON, MASSACHUSETTS

THERMIONIC GENERATORS

Senior Physicist—Engineer wanted for large project developing Portable Thermionic Generators.

Advanced degree preferred. Experience in Thermionic Emission, High Vacuum Techniques and Heat Transfer desirable.

Small to medium sized rapidly growing organization located 70 miles from New York City in Southern Connecticut.

Excellent opportunity for right man.

Please send replies to Journal of Applied Physics, Box 160A, 335 East 45th Street, New York 17, N.Y.

Physics Research

General Dynamics Corporation
Stromberg-Carlson Division

Positions are available for doctorate physicists in the Research Division of Stromberg-Carlson, Rochester, New York. A few years of creative work beyond the Ph.D. is needed in some cases—not in all.

One category of research involves initiation of new programs in the field of "molecular electronics" with special emphasis on magnetic thin films and on semiconductor high-frequency devices.

A second category has to do with basic research in solid state physics with considerable opportunity for self-direction. Microwave resonance effects and the properties of semiconducting and insulating thin films are representative of studies currently in progress.

All of these positions offer the greatest opportunity for original scientific achievement.

A letter stating your interests and background would be appreciated. Please write:

Robert L. Ford
Manager of Technical Personnel

STROMBERG-CARLSON
A DIVISION OF **GENERAL DYNAMICS**

1421 North Goodman Street
Rochester 3, New York

A new volume in the HARVARD MONOGRAPHS IN APPLIED SCIENCE

The Scattering and Diffraction of Waves

By RONOLD W. P. KING and TAI TSUN WU. A comprehensive summary and critique of important recent research and theory concerning those aspects of diffraction and scattering that properly fall under the broad heading of reflections from surfaces of complex shapes. Attention is directed primarily toward the electromagnetic phases of these phenomena and wherever appropriate, reference is made to parallel problems in acoustics. $6.00

IMPORTANT NOTE: Harvard University Press is now handling distribution and sales for all volumes in the HARVARD MONOGRAPHS IN APPLIED SCIENCE. A complete descriptive circular is available on request.

Proceedings of an International Symposium on the Theory of Switching

Annals of the Computation Laboratory of Harvard University. Vols. 29, 30. Reports by foremost world authorities in 39 papers at a symposium devoted to an evaluation of the state of the art of switching. Subjects covered include: abstract models, contact networks, magnetic and transistor logic, switching systems, new switches. 2 vols.: 742 pages, 435 illustrations. $15.00

Order through your bookseller

HARVARD UNIVERSITY PRESS
Cambridge 38, Massachusetts

NEW OPPORTUNITIES AT ZENITH®

Chicago, Ill., and Redwood City, Calif. The continuing expansion program at Zenith has created new opportunities for engineers with experience in the fields of:

MICROWAVE CIRCUITS ELECTRON-BEAM DYNAMICS LOW-NOISE AMPLIFIERS
SEMICONDUCTOR DEVICES TV AND RADIO RECEIVER DESIGN ENGINEERS

B.S. through Ph.D levels in E.E. or Physics.

The fast-wave **electron-beam parametric amplifier,** conceived at Zenith, has opened up challenging new fields for research and development activity from UHF to SHF bands. Broad company interests in the microwave-tube area provide fertile atmosphere for original ideas and individual initiative.

An expanding research program in new fields centered around **compound semiconductors** provides opportunities for individuals with backgrounds in the solid-state art. Development of special devices for highly specific purposes, in collaboration with applications engineers, represents another area of active interest in the semiconductor field.

Positions are now available in the Research Department at Chicago; some openings are available in the San Francisco Bay Area. Congenial small-group atmosphere prevails, with all the advantages of a large, progressive company.

Interested applicants please contact: **DR. ALEXANDER ELLETT, Zenith Radio Corporation**
6001 Dickens Avenue, Chicago 39, Illinois
BErkshire 7-7500

Free to WRITERS
seeking a book publisher

Two fact-filled, illustrated brochures explain subsidy publishing, and tell how to publish your book, get 40% royalties, national publicity, sales promotion and advertising.

We publish every type of book, from the little volume of verse and the first novel, to the scholarly study and the critical essay.

It is acknowledged that publication is one of the foundation stones of a scientist's and scholar's career. To gain recognition, prestige and advancement, the scholar must seek publication. Exposition Press under our special academic imprint, Exposition–University Books, offers you a complete publishing service.

Your inquiries and manuscripts are invited. An editorial report will be returned promptly without any obligation to you.

Write to Alonzo Paxson, Editorial Dept.

Exposition Press, 386 Park Ave. So., N.Y. 16

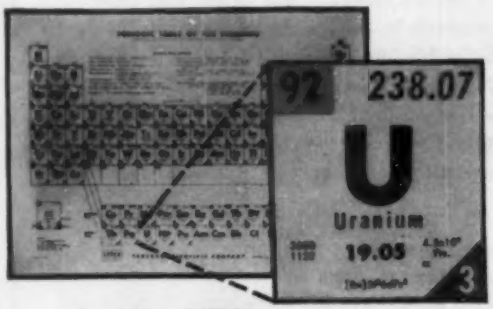

←This unit is ⅛ actual size

Another NEW
LECTURE ROOM
PERIODIC TABLE
LARGER • EASY TO READ • COLORFUL
INCLUDES ATOMIC DATA

Includes all elements and number of naturally occurring radioactive and stable isotopes. Shows atomic number in large type, also weight, density, boiling and melting points, electronic configuration, half-life, and important atomic constants for physics and chemistry. New lecture room size, 62" x 52", in 4-colors on heavy plastic coated stock.

No. 12056 with wood strips and eyelets, each, $7.50

cenco®
CENTRAL SCIENTIFIC CO.
A Subsidiary of Cenco Instruments Corporation
1718-A Irving Park Road • Chicago 13, Illinois
Branches and Warehouses—Mountainside, N. J.
Boston • Birmingham • Santa Clara • Los Angeles • Tulsa
Houston • Toronto • Montreal • Vancouver • Ottawa

A Superior Detector for Infra-Red Spectroscopy

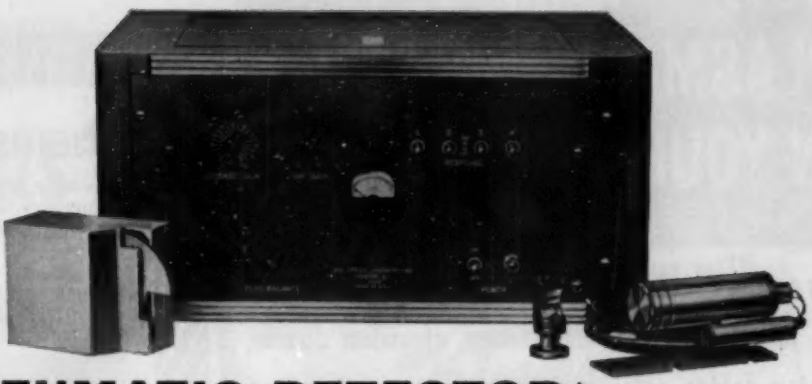

GOLAY PNEUMATIC DETECTOR*

Among the characteristics that render the Golay Detector superior to other types of detectors for use in infra-red spectroscopy are:

1. **An effective sensitive area 1/32" in diameter.**
2. **Sensitivity of 6×10^{-11} watts RMS-ENI when used with "chopped beam" method and with recording time constant of 1.6 second.**
3. **Uniform sensitivity from the ultra-violet through the visible and the entire infra-red, and up to the micro-wave region.**
4. **Improved, drift-free, A. C. operated amplifier with step gain controls and four response periods.**

Write for EPLAB Bulletin No. 10

*Fundamental and experimental aspects of this detector are discussed in the following publications: Rev. Sci. Inst. *18*, 347 and 357 ('47); ibid. *20*, 816 ('49); Proc. IRE *40*, 1161 ('52).

278-8

THE EPPLEY LABORATORY, INC.
SCIENTIFIC INSTRUMENTS
6 Sheffield Ave. • Newport • Rhode Island • U.S.A.

application unlimited!
CENCO Lerner Lab-Jack®

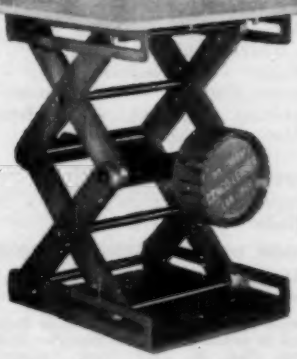

Model 19088
each $37.50

An all-purpose utility lab support. Smoothly lifts up to 100 lbs. with precision control of vertical adjustments thru elevation of 3" to 10". Saves time, prevents breakage. 8" x 8" top auxiliary plate increases work area.

cenco®
CENTRAL SCIENTIFIC CO.
A Subsidiary of Cenco Instruments Corporation
1718-A Irving Park Road • Chicago 13, Illinois
Branches and Warehouses—Mountainside, N. J. Boston • Birmingham • Santa Clara • Los Angeles • Tulsa Houston • Toronto • Montreal • Vancouver • Ottawa

SCIENTISTS ENGINEERS
CALIFORNIA
offers you and your family

- A world center of the electronics-missile-space industries for CAREER ADVANCEMENT
- The High Sierra and the Pacific Ocean for RECREATION
- And for your children some of the nation's FINEST PUBLIC SCHOOLS
- World Famous Universities for ADVANCED STUDY
- MAJOR CULTURAL CENTERS

while living in such places as
Exciting San Francisco
Fabulous Southern California
Cultural Palo Alto

Companies pay interview, relocation and agency expenses

Submit resume in confidence to:
PROFESSIONAL and TECHNICAL RECRUITING ASSOCIATES
(a Division of the Permanent Employment Agency)
Suite A
825 San Antonio Road
Palo Alto, Calif.

NOW— 15,000°F. PLASMA FLAME SPRAY IN YOUR OWN PLANT

Apply coatings of high melting point materials such as tungsten, tungsten carbide, molybdenum, chromium carbide, titanium oxides, calcium zirconate, rare earth oxides. Operates at 10,000°-15,000°F.

Plasma flame spraying hi-temperature crucible

Now any material that can be melted without decomposing can be sprayed. Despite high melting temperature, object sprayed stays cool.

High fluidity of particles and high velocity of impingement bond the particles together to produce high density coatings semi-fused to work. Absence of air eliminates oxidation.

The METCO Plasma Flame Spray Gun is a valuable new tool for the metalworking research department or production line. Operates on inexpensive inert gases with high electrical power conversion efficiency, long component life. Continuous gas streams, as high as 30,000°F., with accurate control of temperature, generated at costs of ⅓ to ½ those of oxygen-fuel gas equipment for equivalent heat output. No combustion—uses inert gases. No flashback or explosion hazards—push-button operation.

Write today for free bulletin describing the METCO Plasma Flame Gun.

METCO

Metallizing Engineering Co., Inc.

Flame Spray Equipment and Supplies

1143 Prospect Avenue, Westbury, Long Island, N. Y.

In Great Britain METALLIZING EQUIPMENT CO., Ltd. Chobham-near-Woking, England

Please send me free bulletin on the Metco Plasma Flame Spray Gun.

Name _____ Title _____

Company _____

Address _____

City _____ Zone _____ State _____

SCIENTISTS and ENGINEERS

Dynamic new division of **Ford Motor Company** is now in initial stages of expanding military and commercial programs.

Positions are at Aeronutronic's new $22 million Research Center at Newport Beach in Southern California. Work in an intellectual environment as stimulating as the location is ideal—close to most of Southern California's cultural, educational, and recreational centers.

Outstanding growth opportunities for qualified engineers and scientists are open in the following fields:

OFFICE OF ADVANCED RESEARCH

THEORETICAL RESEARCH—Hydrodynamic and radiation processes in tenuous gases at very high temperatures, ionization produced by soft X-radiation, hydrodynamics of solids at high pressures including studies of equations of state, infrared properties of the atmosphere and of hot gases, conversion of chemical energy into sound and the condensation rate of supersaturated vapors. Theoretical physicists are needed to work in these fields. Specific experience is not necessary. However, a general background in theoretical and mathematical physics is required.

You are invited to address inquiries to M. H. Johnson, Advanced Research Staff, at our Newport Beach address.

Other unusual opportunities are open for qualified engineers and scientists in the following areas:

SPACE TECHNOLOGY OPERATIONS

Astrodynamics • Space Environment • Theoretical Physics • Electronics • Radar • Information Links • Automatic Controls • Mathematics • Propulsion Research • Combustion • Materials • Aeromechanics

COMPUTER OPERATIONS

Input-Output Equipment • Storage Units • Display Devices

TACTICAL WEAPON SYSTEMS OPERATIONS

Aero-Thermodynamics • Aero-Chemistry and Propulsion • Astronautics

Qualified applicants for the above three divisions are invited to send resumes and inquiries to Mr. Jim Harris, Bldg. 15, Ford Road, Newport Beach, California. Telephone ORiole 3-2520.

AERONUTRONIC

a Division of FORD MOTOR COMPANY

NEWPORT BEACH,

SANTA ANA—MAYWOOD, CALIFORNIA

need high vacuum components?

The Stokes McLeod type High Vacuum Gage is the only McLeod type gage that combines absolute standards of accuracy and precision with convenience and rugged construction for practical laboratory or industrial service. Four models are available with ranges of .01-5000; .1-500; 1-5000 microns and .01-50 millimeters Hg.

STOKES makes a complete line of vacuum components . . . advance-designed and engineered to help make your vacuum systems more productive. Each unit reflects Stokes' unparalleled experience, pioneering leadership and wealth of basic vacuum technology.

The product list includes: Diffusion Pumps, Vapor Booster Pumps, Mechanical Pumps, Mechanical Booster Pumps, Vacuum Gages, and Valves.

Send for technical data on any or all . . . without obligation.

High Vacuum Division
F. J. STOKES CORP.
5562 Tabor Road, Phila. 20, Pa.

STOKES

FIND THE ANSWER TO YOUR ELECTRONIC, OPTICAL AND INFRA-RED PROBLEMS WITH

Kinney®

PRECISION EVAPORATED FILMS

Have you explored the possibilities of controlling REFLECTION, TRANSMISSION, ABSORPTION and EMISSIVITY with KINNEY Precision Evaporated Films? Here are advanced techniques, backed by years of research and successful production of optical and electrical films applied to a broad range of surfaces and substances. These development and production facilities are available to you: Front and Back Surface Mirrors—any metals... Low Reflection Films—any wave length... Semi-Transparent Films . . . Dichroics . . . Beam Splitters . . . R.F. Shielding . . . Anti-Electrostatic Films.

KINNEY offers Infra-Red Reflecting Films, designed to your specifications . . . can be deposited upon Glass, Plastic or Metal and many other materials.

KINNEY Infra-Red Low Reflection Films provide peak transmission of desired wave length on Glass, Quartz, Germanium, Silicon, Arsenic Trisulphide and many other materials.

KINNEY provides precise deposition of films for Dark Mirrors and Beam Splitters as well as Absorbing Films.

KINNEY also provides these important Electrical Aids: Anti-Electrostatic Films... Transparent Conducting Films . . . Solderable Films on Glass, Phenolics, etc.

Write for information regarding your specific problems . . . no obligation.

MAIL THIS COUPON FOR YOUR COPY OF BULLETIN NO. 4900.1

VACUUM EQUIPMENT DIVISION
THE NEW YORK AIR BRAKE COMPANY
1321A ADMIRAL WILSON BLVD. · CAMDEN · N. J.

Please send copy of Bulletin No. 4900.1 describing KINNEY Precision Evaporated Films.

Name_____

Company_____

Address_____

City_____ Zone____ State_____

INDEX TO ADVERTISERS

Name	*Page*
AERONUTRONIC, DIV. OF FORD MOTOR CO.	xxx
ALLIED RESEARCH ASSOCIATES	xxiii
APPLEGATE & CO., C. J.	xx
ARNOLD ENGINEERING CO.	iii
AVCO EVERETT RESEARCH LAB.	Insert at p. ix
BELL TELEPHONE LABS.	v
CENTRAL RESEARCH LABS., INC.	vi
CENTRAL SCIENTIFIC CO.	vii, xxii, xxviii, xxix
COLLINS RADIO CO.	xvi
CONTINENTAL CAN CO.	xxii
CORNELL-DUBILIER ELECTRIC CORP.	xxi
EASTMAN-KODAK CO.	xiii
EPPLEY LAB., INC.	xxix
EXPOSITION PRESS	xxviii
FARRAND OPTICAL CO.	xxiv
FORRESTAL RESEARCH CENTER	xx
GENERAL ELECTRIC, KAPL	xxv
GENERAL RADIO CO.	Cover 4
HARSHAW CHEMICAL CO.	xv
HARVARD UNIVERSITY PRESS	xxvii
HIGH VOLTAGE ENGINEERING CORP.	xxvi
I.B.M. CORP.	xix
KEITHLEY INSTRUMENTS, INC.	xi
KINNEY MFG. CO., N. Y. AIR BRAKE CO	xxxi
LOS ALAMOS SCIENTIFIC LAB.	viii
McGRAW-HILL BOOK COMPANY, INC.	x
MELPAR, INC.	xxiv
METALLIZING ENGINEERING CO.	xxx
MITRE CORP.	xiv
PERMANENT EMPLOYMENT AGENCY	xxix
PHILIPS ELECTRONICS, INC.	Cover 2
RADIO CORP. OF AMERICA	xvii
SPACE TECHNOLOGY LABS.	Cover 3
STOKES CORP., F. J.	xxxi
STROMBERG-CARLSON	xxvii
UNITED AIRCRAFT CORP.	xii
VEECO VACUUM CORP.	xxii
WELCH SCIENTIFIC CO., W. M.	xviii
WESTINGHOUSE BETTIS ATOMIC POWER LAB.	iv
ZENITH RADIO CORP.	xxviii

POSITIONS AVAILABLE

NUCLEAR INSTRUMENTATION

Permanent positions are available in our expanding Nuclear Physics Section for personnel with at least 2 years of nuclear instrumentation experience and a B.S. degree in Physics or Electrical Engineering.

If you desire interesting and challenging research work, write to:

A. J. Paneral
ARMOUR RESEARCH FOUNDATION
of Illinois Institute of Technology
10 West 35th Street Chicago 16, Ill.

RESEARCH
CHEMISTS—PHYSICISTS
B.S.—M.S.

Research in analysis of solid state materials using spark source mass spectrometer. Experience in mass spectrometric techniques, instrumentation, electronic circuitry desirable but not essential. Send resume to:

M. F. McConkey
Industrial Relations, Dept. H-89
WESTINGHOUSE
RESEARCH LABORATORIES
Beulah Road, Churchill Borough
Pittsburgh 35, Pennsylvania

Staff in electrical engineering. Attractive positions combining teaching (graduate and undergraduate) and research are available. Appointment at any level from assistant professor up, depending on qualifications. A person with interests in electrical energy conversion and modern electrical machines is especially sought but openings in other fields are available. Applicants must have Ph.D. or equivalent evidence of research potential. Write Chairman, Division of Engineering, Brown University, Providence 12, R. I.

SCIENTISTS, ENGINEERS—Detection, Communications, Weapon Systems R&D, Digital, Analogue Computer, Transistor, Maser, Microwave, Infrared Circuits. Minimum: Ph.D. $20K, M.S. $17K, B.S. $16K for work in nationwide operations. Resume.

BASIC & EXPERIMENTAL PHYSICS
Box 689, Falmouth, Mass.

* Διαφέρομεν δὲ καὶ ταῖς τῶν πολεμικῶν μελέταις τῶν ἐναντίων τοῖσδε. Τήν τε γὰρ πόλιν κοινὴν παρέχομεν καὶ οὐκ ἔστιν ὅτε ξενηλασίαις ἀπείργομέν τινα ἢ μαθήματος ἢ θεάματος, ὃ μὴ κρυφθὲν ἄν τις τῶν πολεμίων ἰδὼν ὠφεληθείη, πιστεύοντες οὐ ταῖς παρασκευαῖς τὸ πλέον καὶ ἀπάταις ἢ τῷ ἀφ' ἡμῶν αὐτῶν ἐς τὰ ἔργα εὐψύχῳ.

THUCYDIDES

*

"We feel superior to our enemies in the art of war for these reasons: We throw open our city to all, and we never drive any stranger away to prevent him from learning or seeing anything; we conceal nothing, even though the knowledge of it may aid our foes; for we do not trust to preparations and crafty devices so much as to our natural courage in the hours of danger."

Present conditions no longer permit a situation quite so ideal as Thucydides' "open city" as a realistic basis for national security. Work in basic research, however, is relatively free from the restrictions that are necessary for security in other areas. Basic research at the Physical Research Laboratory of Space Technology Laboratories, Inc., is conducted in an academic atmosphere which takes full account of the fact that free communication is essential to the development of science.

STL's Physical Research Laboratory is engaged in frontier research in the physical sciences, as applicable to ballistic missile and space vehicle systems, and to space technology generally. Analytical and experimental investigations of particular interest are fundamental studies in the fields of magnetohydrodynamics, plasma physics and low temperature solid state physics.

Members of STL's Senior Staff will be attending the annual meeting of the American Physical Society, New Yorker Hotel, New York City, January 27-30, 1960. They will be available for local interviews for those who are interested in openings now available at STL.

For an appointment please call Mr. T. W. Griesinger at the STL suite, Hotel New Yorker, LOngacre 3-6839 or send resumes and inquiries to:

SPACE TECHNOLOGY LABORATORIES, INC.

P.O. BOX 95002, LOS ANGELES 45, CALIFORNIA

For Those Working With Pulses . . .

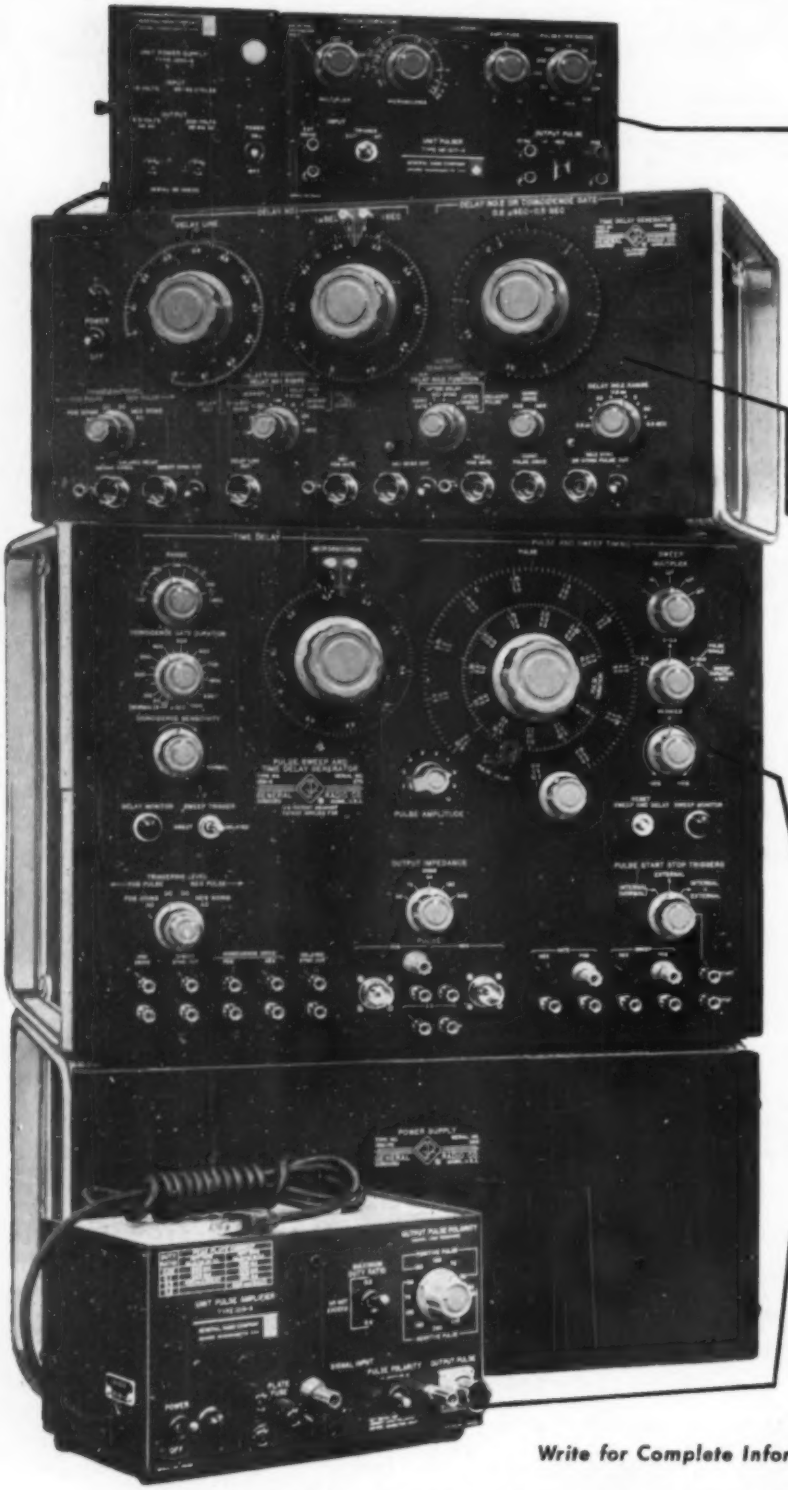

Type 1217-A UNIT PULSER . . . $235
(with power supply $275)

A compact, versatile, and inexpensive source of pulse waveforms. Several Pulsers can be easily combined to form a generator of composite signals.

Repetition Rate: 30c, 60c; 100c to 100 kc in 1-2-5 sequence. 15c to 100 kc continuous with external drive.
Pulse Duration: 0.2 to 60,000 μsec, continuously adjustable.
Rise Time: 0.05 μsec **Decay Time:** 0.15 μsec

Type 1392-A TIME-DELAY GENERATOR . . . $985

The most precise and flexible delay generator available. Two independent delay circuits (0 to 1.1 sec and 0.5 μsec to 0.5 sec) can be "series connected" for 0 to 1.6 sec range in delay. Coincidence circuitry makes possible exact delays and pulse bursts. Input circuits accept almost any waveform from dc to over 300 kc to initiate action. Built-in provision for time modulation.

Type 1391-B PULSE, SWEEP, AND TIME-DELAY GENERATOR . . . $1975

Complete, accurate, wide-range time measurements and pulse-waveform synthesis with one instrument. Fast rise and decay times — better than 0.015 μsec. No duty ratio restrictions.

Pulse Duration: 25 mμsec to 1.1 sec
Pulse Repetition Rate: 0 to 250 kc
Sweep Duration: 3 to 120,000 μsec
Time Delay: 1 μsec to 1.1 sec
Delay Repetition Rate: 0 to 400 kc

Type 1219-A UNIT PULSE AMPLIFIER . . . $200

Provides 55-watts peak power over a wide range of output impedances. Provides current pulses up to 600 ma; voltage pulses in excess of 250v at durations as small as 0.1 μsec. Drive requirements, 20v negative or 2.5v positive pulse.

Write for Complete Information

GENERAL RADIO COMPANY

Since 1915 — Manufacturers of Electronic Apparatus for Science and Industry

WEST CONCORD, MASSACHUSETTS

NEW YORK AREA: Tel. N. Y. WOrth 4-2722, N. J. WHitney 3-3140 **CHICAGO:** Tel. VIllage 8-9400
PHILADELPHIA: Tel. HAncock 4-7419 **WASHINGTON, D. C.:** Tel. JUniper 5-1088
SAN FRANCISCO: Tel. WHitecliff 8-8233 **LOS ANGELES 38:** Tel. HOllywood 9-6201
In CANADA, TORONTO: Tel. CHerry 6-2171

With the cooperation of Dr. G. W. Pierce of Harvard and Dr. W. G. Cady of Wesleyan, we designed our first quartz-crystal frequency standard in 1926. Even earlier, in 1922, our first broadcast station crystal oscillator unit was delivered to the Bell System for use in the pioneer New York radio station, WEAF. Today, almost every U. S. broadcasting station has a General Radio frequency monitor.